

THE ST. ANTHONY COMPLEX,
NORTHWESTERN NEWFOUNDLAND.
A PETROLOGICAL STUDY OF THE RELATIONSHIP
BETWEEN A PERIDOTITE SHEET AND ITS
DYNAMOTHERMAL AUREOLE

CENTRE FOR PART 1 AND STUDIES

**TOTAL OF 10 PAGES ONLY
MAY BE XEROXED**

(Without Author's Permission)

REBECCA ANNE JAMIESON

THE ST. ANTHONY COMPLEX, NORTHWESTERN NEWFOUNDLAND:
A PETROLOGICAL STUDY OF THE RELATIONSHIP BETWEEN
A PERIDOTITE SHEET AND ITS DYNAMOTHERMAL AUREOLE

by

Rebecca Anne Jamieson, B.Sc.



A Thesis submitted in partial fulfillment
of the requirements for the degree of

Doctor of Philosophy

Department of Geology
Memorial University of Newfoundland
St. John's, Newfoundland

January, 1979

ABSTRACT

The St. Anthony Complex consists of a suite of alkaline basaltic rocks (the Ireland Point Volcanics), greenschist and epidote amphibolite facies metasedimentary and metabasic rocks (the Goose Cove Schist), amphibolite to transitional granulite facies metabasites (the Green Ridge Amphibolite), an assemblage of dunite, troctolite, gabbro, and anorthosite (the Long Ridge Metagabbro), and a lherzolite-harzburgite massif (the White Hills Peridotite). These rocks are interpreted as a partial ophiolite and an underlying dynamothermal aureole formed during its tectonic emplacement.

The overall metamorphic grade increases from the base of the St. Anthony Complex to the peridotite contact. Lithological and structural discontinuities occur within the aureole, with the epidote amphibolite to amphibolite facies transition marked by a metasomatic mylonite zone. Temperatures of 850°C to 950°C have been calculated for the amphibolites and peridotites in the contact zone, while the transition from greenschists to undeformed volcanics corresponds to temperatures of 300°C to 350°C. This indicates an overall thermal gradient of 750° to 800°C/km. Pressure estimates range from 7 to 10 kb near the peridotite contact to 2 kb or less at the greenschist-volcanic transition.

The lithological evidence and the pressure and temperature estimates suggest that the aureole is composite, formed by the juxtaposition of progressively shallower units during the dynamothermal metamorphism which accompanied the tectonic emplacement of the peridotite.

Thermal models indicate that heating by conduction and friction contributed to the high contact temperatures. The evidence is consistent with a model involving westward transportation of oceanic lithosphere over tholeiitic gabbros, alkaline basalts, and turbidites to form the St. Anthony Complex, before final emplacement along late thrust faults as part of the Hare Bay Allochthon.

Comparison of the St. Anthony Complex with other peridotite-aureole complexes shows general similarities in geological setting, lithology, and metamorphic grade. It is concluded that the formation of dynamothermal aureoles beneath transported peridotite is a normal process accompanying the early stages of tectonic peridotite emplacement.

TABLE OF CONTENTS

VOLUME 1

Abstract	i
List of Figures	v
List of Tables	ix
CHAPTER 1. INTRODUCTION	1
1.1. The Ophiolite Aureole Problem	1
1.2. Regional Setting	4
1.2.1. The Newfoundland Appalachians	4
1.2.2. The Humber Zone	4
1.2.3. The Hare Bay Allochthon	7
1.3. Previous Work	9
1.4. Purpose and Scope of Study	12
1.5. Acknowledgements	13
CHAPTER 2. THE GEOLOGY OF THE ST. ANTHONY COMPLEX	15
2.1. The Ireland Point Volcanics and Related Rocks	15
2.1.1. Gabbro	15
2.1.2. Variolitic Pillow Lava	17
2.1.3. Pillow Breccia	19
2.1.4. Vesicular Pillow Lava	19
2.1.5. Porphyritic Pillow Lava	20
2.2. The Goose Cove Schist	21
2.2.1. Metasediments	22
2.2.2. Banded Metavolcanics	23
2.2.3. Spotted Metavolcanics	24
2.2.4. Epidote Amphibolite	25
2.3. The Green Ridge Amphibolite	25
2.3.1. Biotite Amphibolite	26
2.3.2. Quartz Amphibolite	27
2.3.3. Plagioclase Amphibolite	29
2.4. The Long Ridge Metagabbro	30
2.5. The White Hills Peridotite	31
2.5.1. Jacupirangite and Syenite	31
2.5.2. Peridotite	32
2.6. Post-tectonic Dykes	34
2.7. Structure	34
2.8. Discussion	38
CHAPTER 3. PETROLOGY AND GEOCHEMISTRY	41
3.1. The Ireland Point Volcanics and Related Rocks	41
3.1.1. Petrography	41
3.1.2. Geochemistry	43
3.1.3. Mineral Chemistry	47
3.1.4. Petrogenesis	49
3.2. The Goose Cove Schist	57
3.2.1. Petrography	57
3.2.2. Geochemistry	60
3.2.3. Mineral Chemistry	62
3.2.4. Petrogenesis	67

3.3. The Green Ridge Amphibolite	74
3.3.1. Petrography	74
3.3.2. Geochemistry	79
3.3.3. Mineral Chemistry	82
3.3.4. Petrogenesis	86
3.4. The Long Ridge Metagabbro	93
3.4.1. Petrography	93
3.4.2. Geochemistry	95
3.4.3. Mineral Chemistry	95
3.4.4. Petrogenesis	97
3.5. The Jacupirangite - Syenite Association	99
3.6. The White Hills Peridotite	101
3.6.1. Petrography	101
3.6.2. Geochemistry	103
3.6.3. Mineral Chemistry	105
3.6.4. Petrogenesis	110
3.7. Discussion	113
 CHAPTER 4. THE THERMAL STRUCTURE OF THE ST. ANTHONY COMPLEX	 115
4.1. Geothermometry and Geobarometry	115
4.1.1. The Ireland Point Volcanics	116
4.1.2. The Goose Cove Schist	117
4.1.3. The Green Ridge Amphibolite	119
4.1.4. The Long Ridge Metagabbro	123
4.1.5. The White Hills Peridotite	124
4.2. Metamorphic Profiles	125
4.3. Thermal Models	130
4.3.1. Introduction	130
4.3.2. The Conduction Model	132
4.3.3. The Friction Model	136
4.3.4. Combined Conduction and Friction Models	141
4.3.5. The Effects of Reactions on Heat Production	143
4.3.6. Limitations and Implications of the Thermal Models	144
 CHAPTER 5. THE GEOLOGICAL HISTORY OF THE ST. ANTHONY COMPLEX	 149
5.1. Pre-tectonic History	149
5.2. Syntectonic History	153
5.3. Post-tectonic History	158
5.4. Regional Implications	158
5.4.1. The Hare Bay Allochthon	158
5.4.2. Other Areas in Western Newfoundland	159
 CHAPTER 6. THE OPHIOLITE AUREOLE PROBLEM	 162
6.1. Geological Setting	162
6.2. Relationships of Peridotites to their Aureoles	163
6.3. Metamorphism	164
6.4. Discussion	168
6.5. Summary and Conclusions	172
 REFERENCES	 174

APPENDIX I. ROCK ANALYSES	196
i. Sample Preparation	196
ii. Major Element Analyses	196
iii. Trace Element Analyses	198
APPENDIX II. MINERAL ANALYSES	200
i. Analytical Method	200
ii. Amphibole	201
iii. Pyroxene	206
iv. Feldspar	207
v. Olivine	207
vi. Epidote	207
vii. Chlorite	207
viii. Mica	207
ix. Oxides	208
APPENDIX III. THERMAL MODELS	209
APPENDIX IV. PUBLICATIONS AND MANUSCRIPTS RELATING TO STUDY	215

LIST OF FIGURES

VOLUME 1

FIGURE II.i. Nomenclature of calcic and sub-calcic amphiboles	202
II.ii. Amphibole substitutions	205

VOLUME 2

FIGURE 1.1. Alpine peridotite emplacement and associated metamorphism	1
1.2. Model for the development of Humber Zone geology	2
1.3. Geology of the Humber Arm and Hare Bay Allochthons	3
FIGURE 2.1. Rhythmic layering in gabbro, Partridge Point	5
2.2. Variolitic pillow lava, Ireland Point	5
2.3. Map of Quirpon Harbour area	6
2.4. Variolitic pillow lava overlying black shale, east of Ireland Point	7
2.5. Pillow breccia, Ireland Point	7
2.6. Vesicular pillow lava, Ireland Bight	8
2.7. Porphyritic pillow lava, Stark's Bight	8
2.8 (a-d). Transition from the Ireland Point Volcanics to the Goose Cove Schist	9
2.9. Deformed pillow breccia, Stark's Bight	11
2.10. Folded marble and chert, Fischot Island	11
2.11. Semi-pelitic schist with quartz aggregates, Three Mountain Harbour	12
2.12. Psammite, Lobster Point	12
2.13. Pelite, Goose Cove West	13
2.14. Finely laminated cherty horizon, east of Goose Cove	13

FIGURE 2.15.	Massive, coarse-grained greenschist, Duck Point	14
2.16.	Banded greenschist, Goose Cove	14
2.17 (a, b).	Variable deformation in banded greenschist	15
2.18 (a, b).	Variable deformation in spotted greenschist	16
2.19.	Deformed pillows in spotted greenschist, Cremaillere Harbour	17
2.20.	Banding in spotted greenschists, Savage Point	17
2.21.	Epidote amphibolite	18
2.22.	Map of the Howe Harbour area	19
2.23.	Biotite amphibolite with epidote amphibolite inclusion	20
2.24.	Biotite amphibolite with melted quartz amphibolite inclusion, Northeast Island	20
2.25.	Relict igneous layering in metagabbro, Wild Cove	21
2.26.	Folded marble band, Northeast Island	21
2.27.	Partially melted quartz amphibolite, Northeast Island	22
2.28.	Compositional layering in quartz amphibolite, Three Mountain Summit	22
2.29.	Quartz amphibolite with band of very coarse-grained quartz and feldspar	23
2.30.	Inhomogeneously deformed metagabbro, Long Ridge	23
2.31.	Interlayered dunite, troctolite, and gabbro, Long Ridge	24
2.32.	Interlayered syenite, alkaline pyroxenite, and hornblende gneiss	24
2.33.	Lens of alkaline pyroxenite surrounded by interlayered syenite and hornblendite, Northern Long Pond	25
2.34.	Rectangular jointing in harzburgite, White Hills	25
2.35.	Fold in peridotite contact zone, Western Long Pond	26
2.36.	Ultramafic mylonite, Milan Arm Melange	26
2.37.	Post-tectonic diabase dyke, Lobster Point	27
2.38.	Brecciated metasedimentary schist, Goose Cove West	27
2.39.	Folded calc-silicate layer in amphibolite, Northeast Island	28
2.40.	F ₃ fold in epidote amphibolite, Three Mountain Summit	28
2.41.	Hare Bay thrust fault, Ireland Point	29
FIGURE 3.1 (a, b).	Variolitic pillow lava	32
3.2.	Kaersutite microlites, massive flow	33
3.3.	Plagioclase microlites, vesicular pillow lava	33
3.4.	Vesicular glass shard, pillow breccia	34
3.5 (a, b).	Porphyritic pillow lava	35
3.6.	Gabbro	36
3.7.	Diorite	36
3.8.	Effects of alteration on the geochemistry of the Ireland Point Volcanics	37
3.9.	Immobile element geochemistry of the Ireland Point Volcanics	38
3.10.	Immobile element geochemistry of the Ireland Point Volcanics	39
3.11.	Immobile element geochemistry of the Cape Onion and Maiden Point volcanics	40
3.12.	Immobile element geochemistry of the Cape Onion and Maiden Point volcanics	41
3.13.	Geochemistry of volcanic rocks in relation to tectonic setting	42
3.14.	Pyroxene quadrilateral, volcanic rocks	43
3.15.	Pyroxene variation diagrams, volcanic rocks	44
3.16.	Amphibole compositions, Ireland Point Volcanics	45

FIGURE 3.17. Compositions of the Ireland Point Volcanics in the basalt tetrahedron	46
3.18. Experimental phase relations, hydrous basaltic systems	48
3.19. Phase relations in the system $\text{CaO} - \text{MgO} - \text{Al}_2\text{O}_3 - \text{SiO}_2 - \text{Na}_2\text{O} - \text{H}_2\text{O}$, 5 kb	49
3.20. Variolitic pillow lava with olivine growth across boundary	50
3.21. Quartz aggregate in psammite	50
3.22. Semi-pelitic schist with folded muscovite	52
3.23. Rotated garnets in ferruginous metachert	52
3.24. Massive greenschist with relict diabasic texture	54
3.25. Spotted greenschist with deformed aggregates after plagioclase porphyroclasts	54
3.26. Banded greenschist showing S_1 and F_2	55
3.27. Epidote amphibolite with amphibole intergrowth	55
3.28. Geochemistry of the Goose Cove Schist	56
3.29. Geochemical comparison of the Goose Cove Schist and the Ireland Point Volcanics	57
3.30. Co-existing chlorite and amphibole compositions	58
3.31. Feldspar compositions, Goose Cove Schist and Green Ridge Amphibolite	59
3.32. Amphibole compositions, Goose Cove Schist	60
3.33. Metamorphic mineral assemblages, Goose Cove Schist and Green Ridge Amphibolite	61
3.34. ACF diagram, Goose Cove Schist	62
3.35. Experimental phase relations, greenschist facies	63
3.36 (a, b). Biotite amphibolite	65
3.37. Quartz amphibolite	66
3.38. Two-pyroxene amphibolite	66
3.39. Plagioclase amphibolite	67
3.40. Geochemistry of quartz and plagioclase amphibolites	68
3.41. Composition - volume diagram, biotite amphibolite	71
3.42. Geochemistry of biotite amphibolite	72
3.43. Immobile element geochemistry, Green Ridge Amphibolite, and comparison with greenschists and volcanics	73
3.44. Amphibole compositions, Green Ridge Amphibolite	74
3.45. Pyroxene quadrilateral, Green Ridge Amphibolite and Long Ridge Metagabbro	75
3.46. ACF diagram, Green Ridge Amphibolite	76
3.47. Melt compositions, Green Ridge Amphibolite	77
3.48. Experimental amphibolite - garnulite phase relations	78
3.49. Deformed dunite, Long Ridge	80
3.50 (a, b). Coronitic metagabbro	80
3.51. Relict igneous clinopyroxene in metagabbro	81
3.52. Geochemistry of the Long Ridge Metagabbro	82
3.53. Amphibole compositions, Long Ridge Metagabbro	83
3.54 (a-c). Jacupirangite - syenite assemblage	85
3.55. Geochemistry of the jacupirangite - syenite assemblage	87
3.56. AFM diagram, jacupirangite - syenite assemblage	88
3.57 (a, b). Basal mylonite, White Hills Peridotite	90
3.58. Plagioclase exsolution from orthopyroxene	91
3.59. Amphibole lherzolite, base of White Hills Peridotite	91
3.60. Geochemistry of the White Hills Peridotite	92

FIGURE 3.61.	Peridotite compositions in the system $\text{CaO} - \text{MgO} - \text{Al}_2\text{O}_3 - \text{SiO}_2$	93
3.62.	Orthopyroxene compositions, White Hills and other peridotites	94
3.63.	Pyroxene quadrilateral, White Hills and other peridotites	95
3.64.	Spinel prism, White Hills Peridotite	96
3.65.	Amphibole compositions, White Hills Peridotite	97
3.66.	Plagioclase to spinel lherzolite transition	98
FIGURE 4.1.	Phase relations relating to sub-greenschist facies conditions	99
4.2.	Garnet - biotite geothermometry, biotite amphibolites	100
4.3.	Compositions of the Long Ridge Metagabbro in the system $\text{CaO} - \text{MgO} - \text{Al}_2\text{O}_3 - \text{SiO}_2 - \text{H}_2\text{O}$	104
4.4.	Olivine - spinel compositions, White Hills Peridotite	105
4.5.	Metamorphic section, Fischot Islands	106
4.6.	Metamorphic section, Three Mountain Summit	107
4.7.	Metamorphic section, Brimstone Pond	108
4.8.	Composite thermal gradient through the St. Anthony Complex	109
4.9.	Temperature distribution as a function of time, T_p , and T_R for the conduction model	111
4.10.	Maximum temperatures reached through aureole, regardless of time, by conduction	112
4.11.	Contact temperatures for different thermal properties	114
4.12.	Contact temperatures as a function of time for the case where $T_p = 950^\circ\text{C}$, $T_R = 300^\circ\text{C}$, for the conduction model	115
4.13.	Relationship between heat production, shear strength, and rate of motion for frictional heating model	117
4.14.	Relationship between temperature increase at contact, time, and heat production for the frictional heating model	118
4.15.	Decrease in heat production with a linear decrease in shear strength	119
4.16.	Contact temperature as a function of time for $T_R = 300^\circ\text{C}$, frictional heating model	120
4.17.	Contact temperature as a function of time, frictional heating model with decreasing shear strength	121
4.18.	Thermal gradient as a function of heat produced at the contact, frictional heating model	122
4.19.	Combined friction and conduction models for $T_p = 950^\circ\text{C}$, $T_R = 300^\circ\text{C}$, and decreasing shear strength	123
4.20.	Alternative model for the formation of narrow, inverted metamorphic sequences	125
FIGURE 5.1.	Pre-emplacement development of the St. Anthony Complex	127
5.2.	Syn-emplacement development of the St. Anthony Complex	127
5.3.	Late syn-emplacement development of the St. Anthony Complex	127
FIGURE 6.1.	Pyroxene compositions, various peridotite - aureole complexes	131
6.2.	Garnet compositions, various peridotite - aureole complexes	133
6.3 (a, b).	Amphibole compositions, various peridotite - aureole complexes	134

PLATE 1.	Position of the St. Anthony Complex in the Appalachian Orogen	back pocket
2.	Geological map of the northern part of the Hare Bay Allochthon	"
3.	Lithological map of the southeastern part of the St. Anthony Complex	"
4.	Structural map of the southeastern part of the St. Anthony Complex	"

LIST OF TABLES

VOLUME 1

TABLE I.i.	Precision and accuracy of major element analyses	197
I.ii.	Precision and accuracy of trace element analyses	199
TABLE II.i (a).	Sample calculation of ferric iron content of amphibole	203
TABLE III.i.	Conduction model, similar thermal properties	210
III.ii.	Maximum temperatures attained in country rocks by conduction for similar thermal properties	212
III.iii.	Maximum contact temperatures for conduction model with dissimilar thermal properties	213
III.iv.	Contact temperatures, frictional heating model	214

VOLUME 2

TABLE 1.1.	Correlation between the Hare Bay and Humber Arm Allochthons	4
TABLE 3.1.	Abbreviations of mineral names	30
3.2.	Petrography of the Ireland Point Volcanics	31
3.3.	Crystallization sequence of the Ireland Point Volcanics	47
3.4.	Petrography of the Goose Cove Schist metasediments	51
3.5.	Petrography of the Goose Cove Schist metabasites	53
3.6.	Petrography of the Green Ridge Amphibolite	64
3.7.	Average compositions of epidote, biotite, and quartz amphibolites	69
3.8.	Calculated chemical changes for metasomatic transformation of epidote and quartz amphibolite into biotite amphibolite	70
3.9.	Petrography of the Long Ridge Metagabbro	79
3.10.	Petrography of the jacupirangite - syenite assemblage	84
3.11.	Petrography of the White Hills Peridotite	89
TABLE 4.1.	Garnet - biotite geothermometry, biotite amphibolite	101
4.2.	Calcite - dolomite geothermometry, marble	102
4.3.	Orthopyroxene - clinopyroxene geothermometry, amphibolite and peridotite	103
4.4.	Parameters and data sources for thermal models	110
4.5.	Effect of variable thermal properties on contact temperatures produced by conduction	113
4.6.	Initial country rock temperatures required to produce observed contact temperatures by conduction	116
4.7.	Heat produced by dehydration reactions	124

TABLE 5.1.	Lower and Middle Ordovician tectonic and depositional events in western Newfoundland	126
TABLE 6.1.	Geological settings of various peridotite - aureole complexes	128
6.2.	Peridotite - aureole geology, various ophiolite - aureole complexes	129
6.3.	Mineral assemblages, various ophiolite - aureole complexes	130
6.4.	Two-pyroxene temperature estimates for the Lizard compared to those from the St. Anthony Complex	132
6.5.	Garnet - clinopyroxene temperature estimates for various ophiolite - aureole complexes	132
TABLE I.iii.	Rock analyses, Ireland Point Volcanics	136
I.iv.	Rock analyses, Goose Cove Schist	137
I.v.	Rock analyses, Green Ridge Amphibolite	138
I.vi.	Rock analyses, Long Ridge Metagabbro	139
I.vii.	Rock analyses, White Hills Peridotite	140
I.viii.	Rock analyses, other rocks	141
TABLE II.i(b).	Amphibole analyses	142
II.ii.	Pyroxene analyses	143
II.iii.	Feldspar analyses	144
II.iv.	Olivine analyses	145
II.v.	Epidote analyses	146
II.vi.	Chlorite analyses	147
II.vii.	Mica analyses	148
II.viii.	Oxide analyses	149
II.ix.	Garnet analyses	150

CHAPTER 1. INTRODUCTION

1.1. The Ophiolite Aureole Problem

The origin of the narrow zones of high grade metamorphic rocks which commonly occur beneath ophiolite suites remains unresolved by current models of ophiolite genesis and emplacement (e.g. Coleman, 1977). Commonly referred to as dynamothermal aureoles, these strongly deformed rocks are inversely zoned over a structural thickness of several hundred metres from upper amphibolite facies rocks in tectonic contact with peridotite, down into epidote amphibolite and greenschist facies rocks, which grade into underlying undeformed volcanic or sedimentary rocks (Williams and Smyth, 1973; Woodcock and Robertson, 1977). The fault-bounded slivers of high grade metamorphic rocks commonly found beneath ophiolites and alpine peridotites (e.g. Woodcock and Robertson, 1977), and the amphibolite blocks commonly incorporated in ophiolitic melanges (Gansser, 1974) are probably the disrupted equivalents of these aureoles. Since models for the emplacement of the associated peridotites commonly depend on the interpretation of the metamorphism, the aureoles have assumed a great deal of importance in spite of their small volume.

Traditionally, these rocks were interpreted as contact aureoles formed around high temperature, diapiric, peridotite intrusions (e.g. Smith, 1958; MacKenzie, 1960; Green, 1964a, b, c; MacGregor, 1964). Despite the use of the term "intrusion", it was generally accepted that the peridotites were emplaced as solids (MacGregor, 1964; Ragan, 1967; Green, 1967); emplacement as a "crystal mush" (mainly olivine crystals with a small amount of interstitial liquid) was considered a possible

alternative. "Forcible intrusion" of hot mantle diapirs, resulting in intense internal deformation and dynamothermal metamorphism, was the preferred emplacement mechanism (Green, 1967). Diapiric emplacement implies the transfer of peridotite upwards through its surroundings. Although even "hot" peridotite is denser than most crustal rocks, the "increased rheidity" of the peridotites, owing to their high temperature, was supposed to account for their mobility, and the existence of ultramafic bodies with contact aureoles was cited as proof that crystalline peridotite was capable of moving in the crust through pressure differentials of several kilobars (Green, 1967). Despite statements to the contrary (Green, 1967), this has yet to be proven by geophysical analysis. To emplace dense rocks upwards through less dense material requires the buoyant force provided by a column of peridotite less dense than the surrounding mantle (e.g. Loomis, 1972b), an upward path provided by extension in the overlying crust, or a tectonic "push" from the sides or below.

Ophiolites and alpine peridotites are now generally interpreted as tectonically emplaced fragments of oceanic lithosphere or sub-continental mantle (e.g. Dietz, 1963; Gass, 1968; Moores, 1970; Dewey and Bird, 1971; Coleman, 1971; Nicolas and Jackson, 1972). This implies transport of the peridotites with, or over, their surroundings, generally by thrusting. Plate interactions are one means of tectonically emplacing mantle peridotite into high levels of the crust. However, this interpretation fails to reconcile the tectonic emplacement of ophiolite suites with the development of high temperature metamorphic aureoles beneath them. As a result, the cause of the dynamothermal metamorphism has been

the subject of much speculation. Malpas et al. (1973) suggested that high temperature aureoles are normally associated with ophiolite nappes emplaced by overthrusting, in contrast to the high pressure metamorphism associated with ophiolites emplaced along Benioff zones in accretionary melanges (Fig. 1.1). Explanations which have been proposed include the following:

(1) the generation of frictional heat during overthrusting (Church and Stevens, 1971; Church, 1972; Malpas et al., 1973; Williams and Smyth, 1973; Malpas, 1976; Woodcock and Robertson, 1977; Malpas, in press).

(2) inherent heat associated with young oceanic lithosphere emplaced shortly after its formation (Church and Stevens, 1971; Church, 1972; Malpas et al., 1973; Williams and Smyth, 1973; Malpas, 1976; Woodcock and Robertson, 1977; Malpas, in press).

(3) the juxtaposition of a rising ultramafic body with progressively shallower, lower-grade metamorphic rocks to form a composite aureole (Karamata, 1974);

(4) the imbrication of ophiolite slices with previously amphibolitised ocean floor rocks during emplacement (Thayer, 1969; Coleman et al., 1976);

(5) a complex sequence of diapiric intrusion and metamorphism in subduction zones (Pamic, 1977);

(6) the generation of heat from exothermic metamorphic reactions such as serpentinisation (Dewey and Bird, 1971).

This work attempts to clarify the ophiolite aureole problem through a detailed study of the St. Anthony Complex of northwestern Newfoundland, where a transported peridotite is underlain by a well

preserved, well exposed, and relatively accessible dynamothermal aureole.

1.2. Regional Setting

1.2.1. The Newfoundland Appalachians

The St. Anthony Complex, which occupies most of the area between Hare Bay and Pistolet Bay at the northeastern tip of the Great Northern Peninsula of Newfoundland, is located at the northern limit of exposure of the Appalachian orogen (Plate 1). The geology of the Appalachians can be interpreted in terms of the evolution of the Iapetus ocean from its formation in the Late Precambrian to its destruction in the Ordovician (Wilson, 1966; Dewey and Bird, 1971; Williams and Stevens, 1974; Williams, 1976). Williams (1976) has divided the orogen into four tectonic and lithostratigraphic zones which are, from west to east, the Humber, Dunnage, Gander, and Avalon zones. In terms of the current tectonic model for the Appalachians, the Humber Zone, which includes the St. Anthony Complex, represents the ancient eastern continental margin of North America, the Dunnage Zone represents the remnants of the Iapetus ocean basin and an associated volcanic arc, and the Gander Zone represents the western margin of the continental platform represented by the Avalon Zone.

1.2.2. The Humber Zone

Within the Humber Zone in western Newfoundland, the following elements of an ancient Atlantic-type continental margin have been recognized (Williams and Stevens, 1974) (Plate 1, Fig. 1.2):

(1) Precambrian basement (Long Range Mountains) of Grenville age (1130 to 840 Ma; Pringle et al., 1971);

(2) late Precambrian plateau basalts (Lighthouse Cove Formation) and coarse clastic rocks (Bradore Formation and succeeding units) formed during rifting of the craton (Williams and Stevens, 1969; Strong and Williams, 1972; Strong, 1974);

(3) a Lower Cambrian to Middle Ordovician continental shelf sequence consisting of shallow water marine sediments, mainly carbonates, which formed a broad carbonate bank (St. George Group) which reached its maximum development in the Lower Ordovician (e.g. Rodgers, 1968);

(4) a thick prism of late Precambrian to Cambrian deep water clastic rocks (Humber Arm Supergroup, Maiden Point Formation, Fleur de Lys Supergroup) derived from the craton to the west, and deposited on the continental slope and rise (e.g. Church, 1969; Stevens, 1970; Smyth, 1973);

(5) igneous and metamorphic rocks of the adjacent ocean basin (Bay of Islands Complex, St. Anthony Complex) (e.g. Stevens, 1970; Church and Stevens, 1971; Malpas, 1976).

Destruction of this continental margin began with the early Ordovician Taconic orogeny which marked the earliest phase in the closing of the Iapetus ocean. This proceeded diachronously from east to west, so that deposition continued undisturbed on the continental shelf while deformation was occurring in the ocean basin (Stevens, 1970; Williams and Stevens, 1974).

The earliest phase of the deformation involved the displacement of oceanic lithosphere over supracrustal rocks, probably in response to the initiation of an east-dipping subduction zone (e.g. Strong et al., 1974). The dynamothermal metamorphism which accompanied this stage of emplacement took place between 480 and 460 Ma, proceeding diachronously

from north to south (Dallmeyer and Williams, 1975; Dallmeyer, 1977).

The sedimentary rocks of the continental slope and rise were then caught up in the thrusting, so that the outer part of the continental margin collapsed into a series of westerly-directed thrust sheets. Two large transported sequences, the Humber Arm and Hare Bay allochthons, formed as a result, each consisting of a series of thrust slices separated by melange zones (e.g. Williams, 1975).

The assembly of the allochthons on the outer edge of the continental margin caused rapid subsidence of the adjacent continental shelf in middle Arenig times (Williams and Stevens, 1974). Deposition of carbonates and black shales (Table Head Formation) in the lower Llanvirn was followed by westward transgression of easterly-derived, chromite-bearing flysch (Goose Tickle Formation) formed by erosion of the advancing thrust sheets (Stevens, 1970).

The allochthons ultimately overrode the autochthonous rocks of the continental shelf. Their emplacement was complete by the late Middle Ordovician, when neoautochthonous rocks of the Long Point Group were deposited above the southwestern extremity of the Humber Arm Allochthon (Rodgers, 1965; Stevens, 1970).

The eastern part of the Humber Zone contains a smaller Taconic allochthon (Coney Head Complex) (Williams, 1977b) and a series of continental margin deposits (Fleur de Lys Supergroup), ophiolitic melange (Birchy Schist) and ophiolite complexes (Advocate and Point Rousse Complexes) (Church, 1969; Williams et al., 1977). The extremely complex metamorphic and structural relationships of these rocks (e.g. Williams et al., 1972, 1974; Kennedy, 1975) probably result from protracted Ordovician deformation

as the region was deeply buried beneath successive westerly-directed thrust sheets (DeWit and Strong, 1975; Bursnall and DeWit, 1975; Williams et al., 1977), with subsequent Acadian modification of the terrain. Still further to the east, in the Dunnage Zone, a Lower to Middle Ordovician volcanic arc formed above the east-dipping subduction zone (Kean and Strong, 1975; Dean, 1978).

1.2.3. The Hare Bay Allochthon

The geology of the St. Anthony Complex cannot be isolated from its context as the highest structural slice of the Hare Bay Allochthon (Fig. 1.3). The Hare Bay Allochthon, like the broadly similar Humber Arm Allochthon, comprises a lower group of thrust slices consisting mainly of sedimentary rocks, and an upper group of thrust slices consisting mainly of igneous and metamorphic rocks (Table 1.1).

The lowest slice in the Hare Bay Allochthon is the Northwest Arm Formation of Tremadocian age (Tuke, 1968). It consists of black shale, argillite, limestone, and chert and is commonly chaotically deformed; it is equivalent in age to the Middle Arm Point Formation of the Humber Arm Supergroup.

The Maiden Point Formation spans the entire length of the Hare Bay Allochthon (Cooper, 1937; Tuke, 1968; Smyth, 1973). It consists mainly of quartzo-feldspathic flysch containing blue quartz, plutonic fragments, and minor quartz pebble conglomerate; it is lithologically correlative with the late Precambrian to Cambrian Irishtown and Summerside Formations of the Humber Arm Supergroup. However, it contains mafic igneous rocks, unknown in the comparable units of the Humber Arm Supergroup,

which are important for correlations within the Hare Bay Allochthon. South of Hare Bay, tholeiitic basalts at the structural base of the Maiden Point Formation near Croque and Grandois have been correlated with the rift-related plateau lavas of the autochthonous late Precambrian Lighthouse Cove Formation (Smyth, 1973). North of Hare Bay, variolitic pillow lavas at the structural top of the Maiden Point Formation at Quirpon Harbour, and gabbros that intrude the sediments at St. Anthony, are petrologically similar to rocks in the structurally overlying Cape Onion and St. Anthony slices (Jamieson, 1977a).

The Grandois Group structurally overlies the Maiden Point Formation near St. Julien Island, but its relationship to the higher thrust slices in the Hare Bay Allochthon is not known (Smyth, 1973). The sandy limestone of the Irish Formation and the polymictic conglomerate of the St. Julien Island Formation are unknown elsewhere in western Newfoundland; the provenance of the acid volcanic clasts in the St. Julien Island Formation is one of the major unsolved problems in interpreting the history of the Hare Bay Allochthon. The Grandois Group is assigned a Middle to Upper Cambrian age because it contains some Maiden Point-like greywackes, and has a rough lithological similarity to the Cook's Brook Formation of the Humber Arm Supergroup (Smyth, 1973; Williams and Smyth, in press).

The Milan Arm Melange consists of a variety of igneous, metamorphic, and sedimentary blocks in a chaotically deformed black shale matrix. It differs from the melange zones separating the various thrust slices in scale and in the variety of lithologies it contains, and is the best example of ophiolitic melange in western Newfoundland (Williams, 1975).

The Cape Onion Formation, which has been interpreted as a thrust slice overlying the Milan Arm Melange (Williams et al., 1973), may actually be a very large block within it (DeLong, 1976; Williams and Smyth, in press). It consists of variolitic pillow lavas with minor sills and dykes, which overlie black shales containing Tremadocian graptolites (Williams, 1971). It is lithologically correlative with the Ireland Point Volcanics of the St. Anthony Complex (Jamieson, 1977a), and similar to the Skinner Cove Formation of the Humber Arm Allochthon in lithology (alkali basalt) and structural setting.

The St. Anthony Complex, the highest structural slice of the Hare Bay Allochthon, consists of a peridotite sheet, interpreted as the basal part of an ophiolite suite by analogy with the Bay of Islands Complex, and its underlying dynamothermal aureole (Williams et al., 1973; Williams and Smyth, 1973). It includes the Ireland Point Volcanics, the Goose Cove Schist, the Green Ridge Amphibolite, the Long Ridge Metagabbro, and the White Hills Peridotite (Williams, 1975; Williams and Smyth, in press; Plate 3, 4).

1.3. Previous Work

The St. Anthony area was the first part of North America to be exploited by Europeans for its mineral resources -- Norsemen smelted bog iron ore at L'Anse aux Meadows in about 1000 A.D. (Ingstad, 1969).

Alexander Murray conducted the first geological expedition to the area in 1864 (Murray, 1866). He examined the sedimentary sequence to the south and west of Hare Bay, and the diorites, serpentinites, and slates to the north, which he correlated with the Lower Silurian (now

Ordovician) Quebec Group. He observed pillow lava ("green slate" with a "nodular structure") at Ireland Point, amphibolite ("black hornblende slate") at Three Mountain Summit, and greenschist ("chloritic slates") at Cremaillere (Crevailliere) Harbour, and also recorded copper mineralization at Goose Cove.

The next geological study was done inadvertently when R. A. Daly's ship became icebound at Quirpon en route to Labrador in June, 1901. Daly described a sequence of variolitic pillow lavas interbedded with sediments extending from Quirpon Harbour south for several miles (Daly, 1903). No attempt was made to follow up this work, but his conclusion that the volcanics were deposited in "sea-water of some depth" was published as a contribution to the debate on the origin of pillow lavas.

A small copper mine was opened at Goose Cove in 1908, working a small massive sulphide deposit which occurs within the greenschists. About 1800 tons of ore was mined between 1908 and 1912 (Stephenson, 1937), but never shipped; it is still piled around the open mine shafts. One of the shafts penetrated to the thrust fault at the base of the Goose Cove Schist (H. R. Peters, pers. comm., 1975), a depth of about 30 metres in this area.

The first report dealing specifically with the geology of the Hare Bay region was published by Cooper in 1937. He noted the similarity of the White Hills Peridotite to the Bay of Islands Complex and interpreted the surrounding greenschists and amphibolites as a contact aureole caused by the intrusion of a peridotite sheet. He made the first stratigraphic interpretation of the area, and considered the pillow lavas at Ireland Point to be a volcanic member of the Maiden Point sandstone which he

recognized to the south of Hare Bay and northeast of the schists. Cooper realized the importance of thrust faulting in the area, observing that the peridotite and its aureole had been thrust over the underlying rocks after the metamorphism had occurred. A supplementary report on the Goose Cove copper deposit was written by his assistant (Stephenson, 1937).

Mapping of the area was begun in some detail in 1963 in order to test the hypothesis proposed by Rodgers and Neale (1963) that the rocks of the Hare Bay region were allochthonous. The studies confirmed that the clastic sequence and overlying igneous and metamorphic rocks were transported over Lower Middle Ordovician carbonate and flysch (Gillis, 1966; Tuke, 1968). Tuke (1968) recognized three separate tectonic slices which were comprised of the Lower Ordovician Northwest Arm Formation, the Maiden Point Formation of possible Cambrian age, and the White Hills Peridotite and its surrounding metamorphic rocks of unknown age.

The next breakthrough came with the recognition that the mafic and ultramafic rocks of western Newfoundland are ophiolite complexes that can be interpreted as oceanic lithosphere thrust over the continental margin during the closing of the proto-Atlantic Ocean (Stevens, 1970; Church and Stevens, 1971; Dewey and Bird, 1971). Church and Stevens (1971) described the White Hills Peridotite as a partial ophiolite, transported with its underlying dynamothermal aureole as a part of the Hare Bay Allochthon.

The southern half of the Hare Bay Allochthon was mapped by Smyth (1971, 1973) and further work on the northern half was done by Williams et al. (1973). Williams and Smyth (1973) discussed the geology of the White Hills Peridotite and its surrounding metamorphic rocks, describing

the aureole as a continuous sequence of amphibolites and greenschist formed from the undeformed Ireland Point Volcanics during peridotite emplacement. This work established the current model for the formation of the St. Anthony Complex, but no detailed petrological study of the aureole rocks was carried out.

Williams (1975) and Williams and Smyth (in press) formalized the stratigraphic nomenclature of the Hare Bay Allochthon. The St. Anthony Complex was defined as including the White Hills Peridotite, the Green Ridge Amphibolite, the Goose Cove Schist, and the Ireland Point Volcanics; it consists of a large thrust sheet between Hare Bay and Pistolet Bay as well as outliers three kilometres east of Raleigh, one kilometre southwest of Cape Onion, and at the Fischot Islands, Quirpon Island, and Croque Head (Plate 2, Bostock et al., 1976).

1.4. Purpose and Scope of Study

The study of the St. Anthony Complex was undertaken with the following objectives:

(1) to test the validity of the starting hypotheses, i.e., that the White Hills Peridotite is in tectonic, not intrusive, contact with its aureole, that the metamorphic sequence from polydeformed amphibolites to undeformed volcanics is continuous, and that the formation of the aureole was related to the emplacement of the peridotite and not to some other event;

(2) to determine what the protoliths of the metamorphic rocks were and their pre-tectonic relationships to the peridotite;

(3) to describe the metamorphic petrogenesis of the aureole rocks;

(4) to establish the shape of the pressure-temperature gradient through the aureole, and to speculate on the geological conditions relating to peridotite emplacement which produced this gradient;

(5) to generalize about the origin of dynamothermal aureoles with ophiolites and other alpine peridotites by a comparison of the St. Anthony Complex with other occurrences.

These problems required a detailed petrological and geochemical study based on mapping of representative sections of the St. Anthony Complex.

1.5. Acknowledgements

The study of the St. Anthony Complex was suggested by Dave Strong, who provided supervision, suggestions, constructive criticism, encouragement, and financial support through the four years at Memorial University. The work has benefited greatly through discussions with supervisory committee members Bob Stevens, Tom Calon, Hank Williams, and Ken Collerson, and with M.U.N. colleagues Ray Talkington, Don Baker, Alan Thompson, George Einarson, John Malpas, Campbell DeLong, Svend Stouge, and Chris Lynas. At various times Grant Cawthorn (University of the Witwatersrand), Philip England (Cambridge University), Gary Kirby (University of Southampton), Barry Doolan (University of Vermont) and Ron Smyth (Newfoundland Department of Mines and Energy) were of enormous help.

Joan Burry and Carol Ann Gallagher provided capable field assistance. Maurice Simmonds of Goose Cove, our boatman for two years, and the Aylward family of Harbour de Veau were very helpful. The study

would not have been possible without the technical assistance of Dave Press, Alan Thompson, Gert Andrews, Jaan Vahtra, Wilf Marsh, Foster Thornhill and Lloyd Warford. The final draughts of the maps were done by Gill Campbell, and the typing was done by Glenys Woodland.

Financial support was provided by the National Research Council of Canada, through a 1967 Science Scholarship held by the author from 1974 to 1978, and operating grant A-7975 and microprobe grant E-2723 held by D. F. Strong.

Last, but not least, the assistance of the CFA String Band (past and present) and fellow members of the Waterford Association for Studying Trivial Exercises Diligently, who kept the entire study in its correct perspective, is gratefully acknowledged.

CHAPTER 2. THE GEOLOGY OF THE ST. ANTHONY COMPLEX

The St. Anthony Complex was divided into the Ireland Point Volcanics, the Goose Cove Schist, the Green Ridge Amphibolite, and the White Hills Peridotite by Williams (1975) and Williams and Smyth (in press). A fifth unit, the Long Ridge Metagabbro, has been identified on the basis of this work. Included in this discussion of the St. Anthony Complex are volcanic and gabbroic rocks which occur in the structurally underlying Cape Onion and Maiden Point slices but are closely related to the Ireland Point Volcanics. A geological map of the northern half of the Hare Bay Allochthon (Plate 2), and lithological (Plate 3) and structural (Plate 4) maps of the St. Anthony Complex are located in the back pocket.

2.1. The Ireland Point Volcanics and Related Rocks

The Ireland Point Volcanics form a belt lying directly above the Hare Bay thrust fault for several kilometres along the north shore of Hare Bay (Plate 2, 3). Similar volcanic rocks make up most of the Cape Onion Formation at Quirpon Harbour; gabbros which intrude the Maiden Point Formation just below the Hare Bay thrust from Howe Harbour to St. Anthony are petrologically similar to these volcanics (Jamieson, 1977a). This group of igneous rocks can be subdivided into five units -- gabbro, variolitic pillow lava, pillow breccia, vesicular pillow lava, and porphyritic pillow lava.

2.1.1. Gabbro

A series of small sill-like intrusions occurs near the top of

the Maiden Point Slice along the north shore of Hare Bay and at St. Anthony with minor outcrops near Cape Onion and on Quirpon Island (Plate 2, Plate 3). Blocks of gabbro occur within the melange zone separating the Maiden Point and St. Anthony slices along the north shore of Hare Bay, and within the Milan Arm Melange.

The gabbros are mainly homogeneous, medium- to coarse-grained rocks, although rhythmic layering is well-developed at Partridge Point (Fig. 2.1), and irregular plagioclase-rich pockets containing acicular amphibole occur on the southern side of St. Anthony Bight. The rusty-weathering gabbro typically consists of large, tabular, black clinopyroxene crystals with interstitial white plagioclase. Epidote commonly replaces the feldspar, giving it a pale green tinge, and rare veins of prehnite are present. Chilled margins are poorly developed, and contact metamorphism of the surrounding sediments is evident only in the shales at St. Anthony.

The gabbro is undeformed except locally in faults and small shear zones; many of the contacts are modified by small-scale thrusts probably related to the emplacement of the overlying St. Anthony Slice. The sediments which it intrudes are deformed adjacent to the Hare Bay thrust. Cleavage in the country rocks generally passes into the gabbro where it intrudes coarse-grained sandstones. However, at Partridge Point, fine-grained gabbro cuts schistose shales. The discrepancy may be due to the difference in competency between the shales and the sandstones. Alternatively, it might mean that deformation of the Maiden Point Formation had already begun when the gabbro was intruded, a relationship first suggested by Cooper (1937). The absence of gabbro

cutting the St. Anthony Complex, and the presence of gabbroic blocks in the melange separating the thrust sheets indicate a pre-thrusting age of intrusion.

2.1.2. Variolitic Pillow Lava

Distinctive variolitic pillow lava occurs stratigraphically above Maiden Point sediments at Quirpon Harbour (Daly, 1903), makes up most of the Cape Onion Formation (DeLong, 1976), and forms the lowest structural unit of the Ireland Point Volcanics (Jamieson, 1977a). The closely-packed pillows range from 1 to 3 metres in long dimension. They are zoned from a dark aphanitic margin 2 to 5 centimetres in width, through a transitional zone up to 10 centimetres wide containing numerous, sharply defined, pale green to brown, spherical varioles 2 to 15 millimetres in diameter in a dark, aphanitic matrix, to a core composed entirely of light grey-green to grey-brown variole material (Fig. 2.2). The pillow rims contain very small spherical vesicles which are commonly filled with calcite.

At Quirpon Harbour, overturned variolitic pillow lava stratigraphically overlies fine grained black sandstones of the Maiden Point Formation along the east side of Jacques Cartier Island (Fig. 2.3). The volcanics and sandstone form the overturned limb of a west-facing anticline, whose upper limb is probably represented by upright variolitic pillow lavas on Quirpon Island. On the west side of Jacques Cartier Island the lavas are faulted against black shales containing green tuffaceous layers, which may originally have been in stratigraphic contact with the volcanics.

Variolitic pillow lava is the dominant rock type of the Cape Onion Formation (Williams, 1975; DeLong, 1976) which also includes dykes, pillow breccia, pyritic black shale, chert, and tuff, and totals about 1000 metres in thickness. Near Ship Cove, the pillow lava stratigraphically overlies black shale containing Tremadocian graptolites (Williams, 1971); this is the only fossil locality associated with the volcanic rocks.

A variolitic pillow lava unit 75 to 80 metres thick occurs above the Hare Bay thrust at Ireland Point, Ireland Bight, Hodidou Point, and between Ireland Point and Stark's Bight. The pillow lavas are upright, and undeformed except immediately adjacent to the basal thrust. Some massive flows, one with a pillowed top, are interbedded with the variolitic pillow lavas, but dykes and sills are absent. One-half kilometre east of Ireland Point, variolitic pillow lava stratigraphically overlies limy black shale (Fig. 2.4). The shales, which are depressed by the weight of the overlying lavas, pass downward into sandstones resembling parts of the Maiden Point Formation, but shearing due to the proximity of the Hare Bay thrust makes the stratigraphic or tectonic nature of the shale-sandstones contact uncertain.

The occurrence of distinctive variolitic pillow lavas associated with shales and fine-grained sandstones at three localities north of Hare Bay can hardly be a coincidence. It is therefore concluded that they were originally part of a single unit of Tremadocian volcanic rocks which was disrupted by thrust faulting during the emplacement of the Hare Bay Allochthon.

2.1.3. Pillow Breccia

A horizon of pillow breccia 20 to 25 metres thick occurs above the variolitic pillow lava between Ireland Bight and Ireland Point. It contains isolated fragments of purple vesicular pillow lava, 5 to 30 centimetres across, in a grey, pumiceous, calcite-rich matrix which forms 50 to 60 percent of the rock (Fig. 2.5). A few broad, hydrothermally altered zones resembling dykes occur within the breccia. Where undeformed, the breccia dips moderately to the northeast, but it commonly has a strong schistosity parallel to the Hare Bay thrust.

2.1.4. Vesicular Pillow Lava

Highly vesicular pillow lava forms the main part of the Ireland Point Volcanics. It is continuous from Ireland Bight to Stark's Bight, with minor outcrops east of Hodidou Point and at Lock's Cove, and its estimated maximum thickness is 900 metres at Ireland Point. It overlies the pillow breccia at Ireland Point and grades upwards into the Goose Cove Schist along the east coast of Stark's Bight. The pillows, which rarely exceed 1 metre in their long dimension, are full of irregular vesicles and calcite amygdales 1 millimetre to 2 centimetres across (Fig. 2.6). The pillow lavas, everywhere highly altered, are generally purple but commonly contain green epidote-rich veins and alteration patches. The interpillow material is calcite, which locally contains purple manganiferous bands. Minor tuff, agglomerate, and deformed pillow breccia occur within the pillow lavas at Stark's Bight. The pillow fragments in the breccia are identical to the vesicular pillow lavas. Massive green flows occur near the base of the unit between Ireland Bight

and Ireland Point; one of these flows near Ireland Point contains pyrite and chalcopyrite mineralization along a fault.

2.1.5. Porphyritic Pillow Lava

Porphyritic pillow lava is restricted to a small area at the head of Stark's Bight. The base of the unit is faulted against vesicular pillow lava, but near the top, porphyritic flows surround vesicular pillows (and vice versa), indicating that the two lithologies are interbedded there. The porphyritic pillows are virtually undeformed, in contrast to the flattened vesicular pillow lavas at the same locality, presumably reflecting a difference in competency. The pillows, 1 to 2 metres across, are light green and have a spotted appearance resulting from the high concentration of plagioclase phenocrysts (Fig. 2.7). The latter may be over 2 centimetres long and comprise over 50 percent of many pillow cores. The pillow rims are commonly aphyric but contain abundant small, spherical vesicles. Blue-green chlorite and epidote occur in the vesicles and small fractures, and replace some of the phenocrysts.

In summary, the Ireland Point Volcanics and the similar basalts and gabbros at Quirpon Harbour, Cape Onion, and St. Anthony are interpreted as part of an originally continuous igneous suite. The variolitic pillow lavas at Cape Onion, which are intruded by sills and dykes which decrease in number upwards (DeLong, 1976), probably formed the lower part of the sequence, while the lack of intrusions in the Ireland Point Volcanics suggests that they formed a higher part of the sequence. The sudden appearance of pillow breccia and highly vesicular pillow lava

above variolitic pillow lava at Ireland Point suggests that the volcanics were part of a pile which built upward to a water depth where explosive activity was possible. The combined estimates for the Cape Onion and Ireland Point volcanics indicate a thickness of at least 2 km.

2.2. The Goose Cove Schist

Reconnaissance mapping by Cooper (1937), Williams et al. (1973), and Williams and Smyth (1973; in press) has shown that the Goose Cove Schist forms the lower part of the dynamothermal aureole beneath the White Hills Peridotite (Plate 2). It also underlies the western two-thirds of the Fischot Islands, 11 km south of Goose Cove, and forms parts of St. Anthony Complex outliers which occur east of Raleigh, southwest of Cape Onion, and on Quirpon Island.

In most localities, the Goose Cove Schist is truncated by the Hare Bay thrust and sits directly on thrust zone melange. Where its basal contact is preserved, it grades downwards into the Ireland Point Volcanics. Vesicular pillow lava becomes strongly deformed along the eastern shore of Stark's Bight (Fig. 2.8). Fractures in the pillow interiors develop obliquely to the foliation, while the pillow margins become interleaved with interstitial carbonate and transformed into purple and green schist. The proportion of schistose matrix to relict pillow cores increases until the pillow lavas are entirely transformed into a flaky, pale green and purple, calcite-rich schist which resembles tuff. The boundary between the Ireland Point Volcanics and the Goose Cove Schist is arbitrarily drawn at the place where primary volcanic structures are obliterated; this is approximately where a strongly

deformed pillow breccia outcrops at water level (Fig. 2.9). At this locality, deformed epidote veins and altered volcanic fragments in the breccia show that the alteration of the vesicular pillow lava preceded its deformation. A few metres above this level, the predominance of grey-green schists over purple-grey schists coincides approximately with the actinolite-in isograd.

The Goose Cove Schist is here divided into three greenschist facies lithological units -- metasediments, banded metavolcanics, and spotted metavolcanics -- and a unit of epidote amphibolite facies metabasic rocks (Plate 3). All are characterized by a single penetrative schistosity, S_1 , which is complexly folded by at least two fold generations, F_2 and F_3 , although these folds are not developed to the same extent throughout the Goose Cove Schist (Plate 4). Its total structural thickness is variable but averages about 450 metres.

2.2.1. Metasediments

Metasedimentary rocks form most of the Goose Cove Schist on the Fischot Islands, and occur near water level from Duck Point to Goose Cove, in the eastern part of the Goose Cape Peninsula and on Notre Dame Island, at Cremaillere Harbour, and near Three Mountain Summit (Plate 3). Pelites and psammites dominate, with minor chert, tuff, and marble.

A green psammite directly overlies melange along the west coast of Fischot Island. Except for its pale green colour and incipient schistosity it is very similar to Maiden Point sandstones within and below the melange. It is succeeded by a dark grey semi-pelite containing wispy, deformed quartz aggregates, and grey and green, laminated, pelitic schists. A few dull green, friable zones within the pelites probably

represent tuffaceous horizons. Buff weathering carbonate and rare black chert bands a few centimetres thick, containing thin, tightly folded garnetiferous layers are also present (Fig. 2.10). A pale grey-green metabasite containing coarse-grained green amphibole is interpreted as a pre-tectonic dyke or sill within the metasediments (Fig. 2.15).

Except for carbonate, the metasedimentary lithologies present on the Fischot Islands are also represented around Goose Cove. The dark grey, quartz-rich semi-pelite occurs on the south side of Three Mountain Harbour and south of Duck Point (Fig. 2.11) and pre-tectonic metabasic sills are present at Duck Point and Lobster Point. Psammitic rocks predominate east of Goose Cove (Fig. 2.12) while pelitic rocks predominate at Duck Point (Fig. 2.13). Metatuffs occur at water level between Goose Cove and Greenwood Cove. A pale grey, laminated, siliceous horizon some 10 metres thick occurs within the banded greenschists surrounding Three Mountain Summit, not far below the transition to epidote amphibolites (Fig. 2.14). It probably represents a chert or siliceous siltstone, and within it a band containing black wisps flattened parallel to the compositional layering resembles tuff.

2.2.2. Banded Metavolcanics

Banded greenschist is typical of the Goose Cove Schist north of Hare Bay, although it is relatively rare on the Fischot Islands. It is structurally above the metasediments, although the two are commonly infolded. It consists of dark green, fine-grained metabasic rocks with compositional banding defined by varying proportions of epidote and amphibole (Fig. 2.16). There is a range from striped rocks with finely

spaced, laterally continuous lamellae (Fig. 2.17), to mainly massive rocks with irregularly distributed streaks of epidote or calcite (Fig. 2.17). Although many of these schists resemble tuffs, most are presumed to be the higher grade (decarbonatized) equivalents of the flaky, calcite-rich, pale grey-green schists at the transition from the Ireland Point Volcanics, and are thus referred to as metavolcanics. A small massive sulphide deposit just east of Goose Cove, deformed with the banded greenschists, was mined between 1908 and 1912.

2.2.3. Spotted Metavolcanics

A distinctive metavolcanic unit forms many of the east-west trending ridges between St. Anthony and Goose Cove and is the most common basic greenschist unit on the Fischot Islands. It contains abundant white spots, interpreted as the sites of plagioclase phenocrysts, which have been deformed and replaced by fine-grained epidote, calcite, and albite, in a dark green matrix (Fig. 2.18). In zones of low strain, deformed pillows are clearly recognizable (Fig. 2.19), so that the rocks closely resemble their presumed protoliths, the porphyritic pillow lavas at Stark's Bight (cf. Fig. 2.7). The spotted metavolcanics differ in having deformed "plagioclase" in a dark green, amphibole-rich matrix, contrasting with the undeformed, although altered, plagioclase in a pale green, epidote-rich matrix which forms the pillow lavas at Stark's Bight. In zones of high strain, the pillows become stretched out and ultimately unrecognizable, while the aggregates replacing the former "plagioclase phenocrysts" become elongated by factors of 10 or 20 to 1, forming a strong lineation. At Savage Point, a friable, laminated

schist containing feldspar porphyroblasts which probably represents a crystal tuff, may be the protolith for some of the more intensely deformed spotted greenschists (Fig. 2.20). The less deformed spotted metavolcanics form topographic highs over large areas (Plate 3), but near Three Mountain Summit, where they are strongly deformed and interleaved with the banded greenschists, they are a volumetrically minor part of the Goose Cove Schist.

2.2.4. Epidote Amphibolite

In the vicinity of Three Mountain Summit, the Goose Cove Schist becomes progressively darker and coarser-grained, until a fine- to medium-grained, dark grey epidote amphibolite predominates. The same progressive change is noted on the Fischot Islands, where faulting repeats the epidote amphibolites three times along the south coast (Plate 3). Epidote is abundant, concentrated in thin bands which are commonly tightly folded (Fig. 2.21). Upward through the unit the epidote occurs mainly in coarse-grained knots and stringers which may in part be hinges of small isoclinal folds with strongly thinned limbs. Black, medium-grained hornblende becomes the main matrix mineral, until at the top of the unit the rock consists of a true amphibolite containing sparse, coarse-grained bands of epidote.

2.3. The Green Ridge Amphibolite

The Green Ridge Amphibolite forms the upper part of the metamorphic aureole of the White Hills Peridotite. It is well-exposed on Three Mountain Summit, on the east coast of the Fischot Islands, on

Long Ridge east of the White Hills, in the Deer Park (an upfaulted inlier of amphibolite in the eastern White Hills) and south of Brimstone Pond at the western extremity of the White Hills (Plate 2) (Fig. 2.22).

The transition from epidote amphibolite to amphibolite facies rocks is marked by the disappearance of epidote, the development of coarse-grained black hornblende, and a change from structures dominated by tight folds to structures dominated by a flat-lying schistosity. The boundary of the Green Ridge Amphibolite is here defined as the base of the mylonitic biotite amphibolite zone which is exposed at the level of the epidote-out isograd on Three Mountain Summit and the Fischot Islands. At its top the Green Ridge Amphibolite is in tectonic contact with the White Hills Peridotite, except east of the White Hills where it is apparently gradational upward into the Long Ridge Metagabbro.

The Green Ridge Amphibolite is divided into three lithological units -- biotite amphibolite, quartz amphibolite, and plagioclase amphibolite, with a total structural thickness of about 250 m.

2.3.1. Biotite Amphibolite

A red-brown weathering, mylonitic, biotite-rich amphibolite occurs above the epidote amphibolite unit of the Goose Cove Schist on the Fischot Islands and Three Mountain Summit, and is assumed to continue beneath the White Hills although it is not exposed there (Plate 3). It ranges from a strongly foliated rock containing alternating brown, biotite-rich and black, hornblende-rich layers, to a massive, conchoidally-fracturing rock containing porphyroclasts of garnet, hornblende, and plagioclase in a fine-grained matrix. The biotite amphibolite is finer

grained and more intensely deformed than the surrounding rocks, and contains inclusions of the adjacent amphibolites which have been deformed with the mylonite. On Three Mountain Summit the inclusions are mainly of epidote amphibolite (Fig. 2.23), while on Northeast Island inclusions of partially melted quartz amphibolite are present (Fig. 2.24). The formation of the mylonite thus postdates the amphibolite facies metamorphism, but since it is structurally conformable with the foliation in the overlying quartz amphibolites and is affected by F_3 folding, it predates the late phases of deformation of the St. Anthony Complex. The biotite amphibolite is interpreted as a late syn-metamorphic mylonite zone. Locally, owing to its compositional layering and mineralogy, it resembles metasediments, particularly on the south coast of Fischot Island where it is poorly defined; in that locality biotite amphibolite may be partly pelitic in origin.

2.3.2. Quartz Amphibolite

Medium- to coarse-grained black, quartz-rich amphibolite showing coarse compositional layering parallel to a strong foliation is typical of the Green Ridge Amphibolite. The greatest lithological variety within the amphibolite is on the Fischot Islands.

On the west side of Fischot Island, where the amphibolites are truncated by a fault which repeats the metamorphic sequence, most of the Green Ridge Amphibolite consists of metagabbro. It consists of roughly equal proportions of interlayered black, hornblende-rich, and pale grey, plagioclase-rich amphibolite and preserves transposed igneous layering (Fig. 2.25). The hornblende-rich layers are indistinguishable

from typical quartz amphibolites, while the plagioclase-rich layers closely resemble the plagioclase amphibolite described in the following section. The rocks are informally referred to in later discussions as the Wild Cove metagabbro.

Within the amphibolites on the east coast of the islands, a marble and calc-silicate horizon occurs about 25 metres above the biotite amphibolite zone. It contains pink and green, zoned calc-silicate nodules, and a prominent marble band on Northeast Island. Refolded isoclinal folds in these rocks reveal a structural complexity not evident in the lithologically homogeneous parts of the quartz amphibolites (Fig. 2.26), showing the main foliation to be a second generation, S_2 , feature (cf. Smyth, 1973).

The upper part of the quartz amphibolite unit on the east coast of the Fischot Islands is laced with thin, diffuse, leucocratic veins (Fig. 2.27). These veins locally coalesce into small pockets containing coarse-grained quartz, feldspar, and biotite, and are interpreted to have formed by incipient partial melting of the amphibolites. On the northern part of Northeast Island, the diffuse veining becomes coarser in scale and the rocks locally resemble migmatites.

North of Hare Bay, the exposed quartz amphibolite consists entirely of medium- to coarse-grained metabasites. Coarse compositional banding resulting from variations in the proportions of hornblende and plagioclase is common (Fig. 2.28), but no partially melted rocks are seen. Rare, coarse-grained, quartz-feldspathic bands a few millimetres to a few centimetres thick are present. The most prominent is a single layer at the top of Three Mountain Summit, consisting of very large,

white, tabular plagioclase crystals, some oblique to the foliation and some with long dimensions parallel to it, in a matrix of translucent grey quartz (Fig. 2.29). Both the coarse compositional banding and the thin quartzo-feldspathic veins are parallel to the main foliation in the amphibolites, which in the White Hills is parallel to the base of the peridotite. At Brimstone Pond, within 50 metres of the contact, the compositional banding becomes coarser in scale and the proportion of hornblende decreases as grey clinopyroxene becomes common.

2.3.3. Plagioclase Amphibolite

At Brimstone Pond, the Deer Park, and between Eastern and Western Long Ponds, a grey, diffusely banded, inhomogeneously deformed amphibolite occurs adjacent to the peridotite. It contains a much higher proportion of plagioclase than the quartz amphibolites, and the amphibole is green rather than black. The rocks have undergone extensive retrograde metamorphism and some are thoroughly veined by prehnite. The plagioclase amphibolite grades downward into the quartz amphibolite, and has a tectonic upper contact against peridotite, except on Long Ridge where it apparently grades into the Long Ridge Metagabbro. At its western end it is less than 5 metres thick, but on Long Ridge it is probably 30 to 50 metres thick.

2.4. The Long Ridge Metagabbro

At the southern end of Long Ridge, 2 kilometres west of St. Anthony, ultramafic and gabbroic rocks occur which have been described as an outlier of the White Hills Peridotite (Williams et al., 1973; Williams and Smyth, in press). This study has shown them to be unlike

either the White Hills Peridotite or the Green Ridge Amphibolite, and they are described separately here as the Long Ridge Metagabbro (Plate 3).

The Long Ridge Metagabbro consists of dunite, troctolite, gabbro, and anorthosite which have undergone inhomogeneous deformation and metamorphism. Most of the gabbroic rocks are amphibolitized, but lack the penetrative foliation and coarse-grained black hornblende which are characteristic of most of the Green Ridge Amphibolite. Narrow zones of fine-grained, grey amphibolite with a strong foliation surround lenses of medium- to coarse-grained, virtually undeformed metagabbro (Fig. 2.30). At the western edge of the complex, well-foliated metagabbro closely resembles plagioclase amphibolite. It is therefore probable that the Long Ridge Metagabbro grades downward into the Green Ridge Amphibolite with increasing deformation, although the two are not seen in direct contact.

Ultramafic rocks occur in the southwestern part of the assemblage. They are almost completely serpentized, but smooth, brown-weathering dunite containing sparsely distributed black chromite is preserved as islands in a matrix of blue serpentine at the western edge of the area. In one outcrop, undeformed dark green troctolite and grey gabbro are interlayered with the dunite (Fig. 2.31). This is interpreted as original igneous layering; other evidence concerning the original relationships among the rocks in the complex has been destroyed by faulting and deformation.

Light grey-green metagabbro, consisting of roughly equal proportions of amphibolitized clinopyroxene and saussuritized plagioclase, forms most of the Long Ridge Metagabbro. Some small, bright green,

spherical coronas around olivine are preserved in the least deformed gabbros. A few white plagioclase-rich bands, restricted to the northeastern part of the assemblage, were probably anorthosite layers, although no igneous structures are preserved in this locality.

2.5. The White Hills Peridotite

The White Hills Peridotite makes up the two flat-topped massifs which are topographically and structurally the highest level of the St. Anthony Complex. Outliers occur on the western side of Howe Harbour and peridotite blocks are found within the Milan Arm Melange (Plate 2). This study focusses on the eastern margin of the peridotite, where the basal contact zone is exposed in stream sections and cliff faces.

2.5.1. Jacupirangite and Syenite

Along the northeastern margin of the White Hills is an assemblage of alkalic rocks, including jacupirangite, pyroxenite, hornblendite, and syenite (Plate 3), which is unknown elsewhere in the St. Anthony Complex. Although lithologically the rocks bear no resemblance to the White Hills Peridotite, they apparently form part of the same structural unit. The assemblage ranges from undeformed, homogeneous, alkaline ultramafic rocks in tectonic contact with peridotite through increasingly deformed and amphibolitized banded gneisses, to leucocratic mylonites at the base. Although the basal contact is not exposed, the mylonites are probably structurally concordant with the Green Ridge Amphibolite since both are foliated parallel to the base of the White Hills Peridotite.

Within this assemblage, three main lithologies can be recognized. Medium- to coarse-grained, purple-black jacupirangite (or alkaline pyroxenite, depending on the proportion of clinopyroxene to ilmenite and apatite) directly underlies the peridotite. Below this, the degree of deformation increases, amphibole replaces clinopyroxene, and white feldspar-rich bands appear, forming a black and white hornblende gneiss foliated parallel to the base of the peridotite (Fig. 2.32). In the northernmost stream locality (Plate 3), a striped rock occurs which consists of thin bands of pure white syenite alternating with thin bands of pure black hornblendite (Fig. 2.33). This zone is at least 4 metres thick, and contains a lens of undeformed pyroxenite and a few very coarse-grained pockets of hornblende. The base of the assemblage is marked by a syenitic mylonite which contains streaks of amphibole and pyroxene defining a strong L-S fabric in a matrix of fine-grained feldspar. The distribution of these lithologies is not uniform, since the hornblende gneiss unit is the only one which crops out at all four localities, but their relative order of appearance does not change from place to place.

2.5.2. Peridotite

No attempt was made to subdivide the White Hills Peridotite into lithological units, nor was any pattern established in the small area that was mapped. It consists mainly of harzburgite, with minor dunite, lherzolite, pyroxenite, and gabbro, with a mylonitic fabric in the basal zone.

The harzburgite is red-brown, with a hackly surface of resistant orthopyroxene crystals standing out against a smooth-weathering olivine matrix. Compositional layering in the harzburgite is defined by variations in the amount of orthopyroxene, and is parallel to a strong foliation. Elongated orthopyroxene crystals define a mineral lineation in the plane of the foliation (Fig. 2.34), and are attenuated by extension along crescent-shaped fractures perpendicular to the direction of the lineation. Some olive-green weathering peridotite could be identified as lherzolite by the presence of clinopyroxene, but in general it is not macroscopically distinguishable from harzburgite. Smooth, red-brown dunite containing small black chromite crystals is irregularly distributed as sharply bounded layers or oblique bands, or diffusely bounded, irregular pods. Pyroxenite bands, generally less than 20 centimetres thick, cut all other lithologies including each other.

Within 50 metres of its base, the peridotite develops a mylonitic foliation associated with isoclinal folds a few centimetres to 2 metres across (Fig. 2.35). Both the foliation and the axial planes of the folds are nearly flat-lying, parallel to the basal contact. Sheet-like layers of brown amphibole occur in the plane of this foliation, particularly along the southern margin of the peridotite. Where these rocks are strongly serpentized, the amphibole layers remain essentially unaltered, while the fine-grained, olivine-rich layers are completely replaced by pale grey serpentine. This results in the formation of the distinctive, brown and grey, banded ultramafic mylonites found in the Milan Arm Melange and at Howe Harbour (cf. Williams and Smyth, 1973) (Fig. 2.36).

The White Hills Peridotite is variably serpentized. Intense serpentization is generally confined to fault zones and to the basal contact zone. In the interior of the peridotite, bright blue-green veins of hard serpentine 1 to 5 centimetres wide, containing some fibrous chrysotile, form angular networks which cut all the tectonic fabrics.

2.6. Post-tectonic Dykes

The St. Anthony Complex is cut by a number of northeast-trending mafic dykes, undeformed except for minor joints and faults, which cut all the other rock types. A long lamprophyre dyke, or a set of smaller ones, runs from Goose Cove West to Cremaillere Harbour. Diabase dykes a metre thick occur on the Fischot Islands and the Goose Cape Peninsula (Fig. 2.37) . These dykes were not studied in detail, but representative samples were analysed (Appendix I).

2.7. Structure

Each of the major units of the St. Anthony Complex is characterized by a different structural style. The deformation is inhomogeneous, particularly in the Goose Cove Schist; zones of very high and very low strain can be identified within the metamorphic rocks. Pre-emplacement structures are prominent only in the peridotite, syn-emplacement structures affect all the units, and post-emplacement structures occur in the easternmost part of the area (Plate 4).

The Ireland Point Volcanics, which dip moderately to the northeast, are undeformed except adjacent to the Hare Bay Thrust, and near the transition to the Goose Cove Schist, where vesicular pillow lavas

and pillow breccias become intensely deformed until primary volcanic structures are obliterated, as described in Section 2.2. Small faults are common in the volcanic rocks.

A penetrative schistosity, S_1 , is the foliation associated with the greenschist facies metamorphism throughout the Goose Cove Schist. It is defined by the preferred orientation of amphibole, chlorite and mica. It is parallel to the banding in the metavolcanic rocks, and also approximately parallel to primary compositional layering in the psammites. F_1 folds are rarely seen except in the laminated metasediments, where isoclinal, intrafolial folds occur locally (Fig. 2.14).

S_1 is weakly developed in the spotted metavolcanics which form the east-west ridges north of Three Mountain Summit. However, a strong lineation in the plane of S_1 is formed by the greatly elongated "plagioclase" crystals. The relatively mild deformation in these rocks is partly attributable to a competency difference between the protoliths of the greenschists. This is well illustrated at Stark's Bight, where undeformed porphyritic pillow lava occurs with sheared vesicular pillow lava, and in many parts of the Goose Cove Schist, where slightly deformed pockets or recognizable pillows of spotted greenschist commonly occur within tightly folded banded greenschists. Epidote-rich, finely-laminated banded greenschists (Fig. 2.17) may be the highly strained equivalents of the porphyroclastic rocks.

Locally (for example, at Goose Cove West and Wild Cove), zones of breccia up to 50 centimetres wide contain fragments of schist in a weakly foliated matrix with the same mineralogy as the schist. These zones are parallel to the surrounding foliation (Fig. 2.38).

S_1 is folded by at least two generations of folds, F_2 and F_3 , which are not always developed everywhere in the Goose Cove Schist. F_2 consists of strongly asymmetric, parallel to similar folds, ranging from a few centimetres to a few metres across (Fig. 2.13, 2.17). The fold limbs are widely variable in attitude, and are presumably controlled by later structures, but F_2 fold hinges commonly trend east-west (Plate 4). Lineations parallel to these fold axes suggest that the direction of motion within the Goose Cove Schist was also east-west (cf. Bell, 1978; Williams, 1978). In the greenschists, these folds are not associated with an axial planar foliation, although rarely in the banded meta-volcanics some translation of S_1 to form a weak S_2 foliation is visible. Commonly, brecciation occurs in F_2 hinge zones, and fold limbs are truncated by other F_2 folds. In the epidote amphibolite zone of the Goose Cove Schist, coarse-grained epidote concentrates in F_2 hinges; where the fold limbs are thinned, the epidote-rich hinges define a new lineation.

The Green Ridge Amphibolite is characterized by a flat-lying penetrative foliation defined by the preferred orientation of black hornblende (Fig. 2.29). On Three Mountain Summit and Long Ridge the hornblende also defines a north-south trending lineation. Unlike the S_1 foliation of the Goose Cove Schist, this foliation is not tightly folded. Where marbles and amphibolites are interbanded on the east side of Fischot Island, the foliation is axial planar to F_2 folds (Fig. 2.39), and is therefore S_2 (Smyth, 1973). The same terminology is extended to the amphibolites north of Hare Bay, although folds related to S_2 have not been recognized there.

East of Goose Cove, a series of asymmetric folds several tens of metres across affects the Goose Cove Schist and the amphibolites on Three Mountain Summit. These folds, here termed F_3 , have flat-lying lower limbs and steeply-dipping upper limbs which form the prominent ridges north of Three Mountain Summit (Fig. 2.40, Plate 4). They are mainly northwest-southeast trending, but swing around to east-west in the vicinity of Goose Cove. The interference of F_2 and F_3 produces extremely complex structural geometry in the area around Three Mountain Summit, which has not been studied in detail.

The White Hills Peridotite is characterized by tectonic layering and a strong foliation which predate its displacement. This fabric is complex and polyphase in detail but is simply referred to as S_{p1} here. It is cut by S_{p2} , a mylonitic foliation developed in the lowest 50 metres of the peridotite which increases in intensity toward the basal contact. The foliation is associated with a decrease in the grain size of the peridotite and with isoclinal folds in the contact zone (Fig. 2.35). It is parallel to the basal peridotite contact, to the foliation in the syenitic mylonite, and to the foliation in the surrounding Green Ridge Amphibolite, and is undoubtedly related to the tectonic emplacement of the White Hills Peridotite.

The latest syn-emplacement structure is the Hare Bay thrust (Fig. 2.41) which cuts through the St. Anthony Complex from the black shales underlying the pillow lavas at Ireland Point to the peridotite at Howe Harbour. It therefore post-dates the internal deformation and metamorphism of the St. Anthony Complex but served as the means of

emplacing an already assembled metamorphic complex over underlying rocks and ultimately onto the continental margin.

Post-emplacement, upright folding affects the Fischot Islands, where the St. Anthony Complex now dips moderately to the east, and the Goose Cove area, where the Goose Cape Peninsula forms an antiform (Plate 4). It dies out rapidly west of Goose Cove and does not appear to affect the White Hills. The folds trend north-northeast to south-southwest and are probably Acadian in age (Smyth, 1973).

North-south and east-west trending vertical faults of unknown age affect the eastern part of the St. Anthony Complex (Plate 4). On the Goose Cape Peninsula they do not cause much displacement, but around Cremaillere Harbour the metamorphic sequence is locally disrupted.

2.8. Discussion

While the field evidence supports the conclusions of Williams and Smyth (1973) that the dynamothermal metamorphism within the St. Anthony Complex was related to the emplacement of the White Hills Peridotite from east to west, in detail the lithological, metamorphic, and structural relationships are much more complex than previously described.

The Ireland Point Volcanics can be linked to the continental margin sediments of the Maiden Point Formation through their similarity to the variolitic pillow lavas at Quirpon Harbour and Cape Onion and the gabbros intruding the Maiden Point Formation at St. Anthony. The gradational relationships between vesicular pillow lava and greenschist along the east side of Stark's Bight, the similarity between the porphyritic pillow lavas and the spotted greenschists, and the occurrence of

Maiden Point-like psammities in the Goose Cove Schist link the lower part of the aureole to the same continental margin setting. Field identification of the protoliths of the Green Ridge Amphibolite is more difficult. The large volume of homogeneous amphibolite, locally associated with marble, suggests a mainly volcanic origin, while at Wild Cove and adjacent to the White Hills Peridotite, the protoliths were probably gabbros.

This study has identified two units, occurring structurally beneath the White Hills Peridotite and above the Green Ridge Amphibolite, which appear anomalous in their geological setting. The Long Ridge Metagabbro consists of dunite, troctolite, gabbro, and anorthosite similar to the "Critical Zone" assemblages of many ophiolite complexes which mark the transition from cumulate dunites to gabbroic rocks (e.g. Malpas, 1976). In this context, its structural setting beneath the peridotite, and its apparent gradation from undeformed metagabbro into plagioclase amphibolite appear out of place. The origin of the jacupirangite-syenite assemblage is even more enigmatic. It is difficult to reconcile the presence of undersaturated alkaline rocks with their structural setting beneath the White Hills Peridotite, since similar lithologies are unknown in ophiolite complexes at any level. The lack of intrusive contacts, and the gradation from undeformed jacupirangite adjacent to deformed peridotite to syenitic mylonite structurally concordant with the base of the peridotite, indicate tectonic juxtaposition of the alkaline rocks with the White Hills Peridotite during the emplacement of the St. Anthony Complex.

While there is an overall increase in metamorphic grade from the Ireland Point Volcanics to the top of the Green Ridge Amphibolite,

the metamorphic sequence is not continuous, since it is disrupted by a major mylonite zone at the epidote amphibolite to amphibolite facies transition. This overall increase in metamorphic grade does not coincide with an increase in the intensity of deformation; the entire metamorphic sequence is structurally complex. Throughout the aureole, zones of low strain, such as the weakly deformed metagabbros on Long Ridge and spotted metavolcanics at Cremaillere Harbour, contrast with zones of high strain, such as the syenitic mylonite and the biotite amphibolite units. These may reflect changes in the locus of motion within the thrust sheet during emplacement (cf. Elliott, 1976; Malpas, 1976, in press). The lithological and structural variations raise the possibility that the aureole is composite in origin.

CHAPTER 3: PETROLOGY AND GEOCHEMISTRY

Before a discussion of the formation of the St. Anthony Complex is possible, the pre-tectonic identity and subsequent metamorphic history of the aureole rocks must be established. Geochemistry is one of the few remaining clues to the origin of the strongly deformed greenschists and amphibolites which make up most of the aureole, and can also be used to compare units for fundamental similarities and differences. The petrology of the aureole rocks is critical for determining the physical conditions under which the St. Anthony Complex formed. The combined geochemical and petrological data should indicate whether or not the St. Anthony Complex formed as a continuous metamorphic and lithological sequence, a question fundamental to determining its origin.

3.1. The Ireland Point Volcanics and Related Rocks

The igneous rocks of the St. Anthony Complex comprise the variolitic, vesicular, and porphyritic basalts of the Ireland Point Volcanics. In this section, the petrology of these volcanic rocks and the related gabbros and variolitic basalts north of Hare Bay is considered in detail, and comparisons are made with other volcanic rocks in the Hare Bay Allochthon. This amplifies a preliminary discussion (Jamieson, 1977a) but the conclusions are not significantly different.

3.1.1. Petrography

Four petrographic groups can be defined, corresponding to field-based subdivisions of the volcanic and gabbroic rocks (Table 3.2).

The first group includes the variolitic pillow lavas at Ireland Point and Quirpon Harbour and massive flows associated with them at Ireland Point. The pillow lavas contain varioles, olivine phenocrysts, and titanaugite microlites with hornblende rims in a devitrified matrix (Fig. 3.1). The massive flows lack varioles and olivine, and contain interlocking laths of plagioclase, titanaugite, and hornblende (Fig. 3.2).

The second group includes the vesicular pillow lavas and two lithologies derived from them. The pillow lavas from Ireland Bight to Stark's Bight contain plagioclase microlites in a mafic, highly vesicular, devitrified matrix (Fig. 3.3). The pillow breccias at Ireland Point contain fragments of vesicular pillow lava in a calcite-rich, pumiceous matrix (Fig. 3.4). The deformed pillow lavas on the east side of Stark's Bight contain bands with a relict trachytic texture interleaved with a schistose calcite- and chlorite-rich matrix.

The third group includes porphyritic pillow lavas at Stark's Bight which contain a high proportion of plagioclase phenocrysts with minor olivine and clinopyroxene in a fine-grained matrix of plagioclase and clinopyroxene (Fig. 3.5).

The fourth group includes the gabbros of the Maiden Point Formation at Howe Harbour, Ireland Bight, and St. Anthony. Most consist of medium- to coarse-grained titanaugite, plagioclase and hornblende and vary mainly in the proportion of plagioclase (Fig. 3.6) with minor amounts of leucocratic, plagioclase- and hornblende-bearing diorite on the southwest side of St. Anthony Bight (Fig. 3.7).

The variolitic pillow lavas and gabbros can be classified as alkali basalts by the presence of plagioclase, titanaugite, and hornblende,

with olivine in the pillow lavas (e.g. Wilkinson, 1974). The vesicular and porphyritic lavas are basaltic, but the degree of alteration precludes a more precise petrographic classification. On the basis of their present mineralogy, the volcanic and gabbroic rocks can all be termed spilites (e.g. Cann, 1969; Vallance, 1974).

3.1.2. Geochemistry

Major and trace element analyses and CIPW norms for 38 samples from the Ireland Point Volcanics, 23 from the gabbros, and 15 from other volcanic rocks are listed in Appendix I, along with descriptions of the analytical techniques and estimates of the precision and accuracy of the analyses. The locations of the analysed samples are shown in Plate 3, Fig. 2.5, and Fig. 2.21.

The effects of the pervasive alteration of the Ireland Point Volcanics must be evaluated before conclusions about their geochemistry can be drawn. SiO_2 and Al_2O_3 are affected by the replacement of glass by chlorite and calcite, MgO is affected by the replacement of olivine by carbonate and glass by chlorite and albite, CaO is affected by the chloritization of clinopyroxene, the albitization of plagioclase, and the addition of calcite, and Na_2O is affected by albitization. The ratio $\text{Fe}_2\text{O}_3/\text{FeO}$ has increased in the hematized vesicular basalts. The abundance of fine-grained sphene in the basalts suggests that TiO_2 has not been mobile on a large scale.

The predicted alkali element mobility is borne out by the alkali variation diagram of Hughes (1973), which shows the relative Na_2O enrichment of the Ireland Point Volcanics and the gabbros (Fig. 3.8b).

Figure 3.8a shows the scatter in CaO and MgO + FeO with respect to average alkali basalt compositions (Manson, 1968). Total FeO, Al_2O_3 , MnO, TiO_2 and P_2O_5 are relatively unaffected. The trace elements Zr, Y, Nb, Ni, Cr, and V are relatively stable, but Ba, Rb, Sr, Cu, and Zn are scattered. The direction of the change depends on the nature of the alteration, in particular on the amount of secondary calcite in the samples, which causes loss of SiO_2 , MgO, and Na_2O and gain of CaO and K_2O .

Since there is abundant evidence of major element mobility, even in the least altered samples, the geochemical description of these basalts must rely on the immobile element behaviour. A number of recent papers have attempted to use Ti, Zr, P, Y, and Nb to classify altered basic rocks (Pearce and Cann, 1973; Floyd and Winchester, 1975; Winchester and Floyd, 1976; Ridley et al., 1974; Pearce et al., 1975, 1977; Smith and Smith, 1976). While the value of using minor and trace elements to determine the original tectonic setting of basalts is debatable, these components successfully distinguish alkali and tholeiitic basalts and can be used to discriminate between generally similar groups of rocks. Plots involving TiO_2 , Zr, Y, Nb, P, V, Cr, and Ni were used to compare the various types of basaltic rocks north of Hare Bay with each other and with volcanic rocks from elsewhere in the Appalachians.

The variation diagrams of Fig. 3.9 show considerable overlap among the variolitic and vesicular pillow lavas and the gabbros, although the vesicular pillow lavas have consistently higher concentrations of Zr and Y, which may reflect slightly different source areas or melting

histories for the magmas. On all the plots the basalts fall close to the alkali-tholeiitic boundary, and are therefore classified as "transitional". The compositions of the porphyritic pillow lavas reflect dilution by plagioclase, which is poor in the elements considered in the diagrams, supporting the earlier conclusion that these rocks are cumulates (Jamieson, 1977a). Fig. 3.10 shows plots involving Ni and Cr, which separate the variolitic pillow lavas from the vesicular pillow lavas and the gabbros. The variolitic pillow lavas are enriched in Cr and Ni, as would be predicted by the presence of olivine and abundant clinopyroxene in these rocks, while the plagioclase-rich vesicular pillow lavas and gabbros are poor in Cr and Ni. The porphyritic pillow lavas, with their rare olivine and clinopyroxene phenocrysts, plot between the two extremes.

The results of Fig. 3.9 are reproduced in Fig. 3.11, with the fields for the variolitic and vesicular basalts shown with the data for the Cape Onion and Maiden Point volcanics. The Cape Onion variolitic pillow lavas overlap completely with the Ireland Point Volcanics, but the Maiden Point basalts show higher Zr and Y and lower Nb and P_2O_5 , and fall within the field of tholeiitic rocks. In Fig. 3.12, the Cape Onion and Ireland Point Volcanics are shown to overlap with respect to Cr and Ni, while the Maiden Point Volcanics have relatively low Cr, Ni, and Ti and high V.

On the basis of these diagrams it is concluded that the Cape Onion Volcanics are geochemically as well as petrographically similar to the Ireland Point Volcanics (cf. Jamieson, 1977a) and the variolitic basalts of Quirpon Harbour, and that they can be considered part of the same suite of rocks. The volcanic rocks from St. Lunaire and Croque

Harbour, however, show minor but consistent differences from the Ireland Point Volcanics and cannot be said to be part of the same suite of rocks.

Finally, the data were compared to other volcanic rocks from western Newfoundland and the Appalachians and modern oceanic rocks. Data from the Bay of Islands Complex (Malpas, 1976), the Betts Cove Ophiolite (Upadhyay, 1973), the Maiden Point Formation (Smyth, 1973), the Snooks Arm Group (Jenner, 1977), and plateau lavas of western Newfoundland (Strong, 1974; Williams and Strong, 1972), the Catoctin volcanics (Reed and Morgan, 1971), and ocean ridge basalts (Aumento and Loncarevic, 1969; Kay et al., 1970; Gunn and Roobol, 1977; Flower et al., 1977). Since trace element data for these rocks are commonly not complete, the comparison relies on major elements, and Zr and Y where available. The data are divided into five groups -- ocean floor basalts (Newfoundland ophiolites and modern oceanic rocks), rift-related volcanics (western Newfoundland and Catoctin), possible oceanic island volcanics (Snook's Arm), the Ireland Point Volcanics, and the St. Lunaire and Croque Harbour Volcanics.

In general, diagrams involving only two co-ordinates give poor separation for these groups, since alkaline and tholeiitic rocks from all the environments are shown as gradational trends, with the transitional Ireland Point Volcanics in the middle. Fig. 3.13 shows triangular plots which give somewhat better resolution. The Ti-Zr-Y diagram (Fig. 3.13a) shows the separation of the Ireland Point Volcanics from both the ocean floor and the rifting basalts. The Maiden Point Volcanics analysed in this study (trace element data are not given in Smyth, 1973) range from the field of the Ireland Point Volcanics into the field of the ocean

floor basalts, while the Snook's Arm volcanics overlap with all the other groups. In terms of the fields defined by Pearce and Cann (1973), the Ireland Point Volcanics are "within plate" basalts. The data were also plotted in the $\text{FeO-MgO-Al}_2\text{O}_3$ diagram of Pearce et al. (1977) which separates oceanic and continental "within plate" basalts (Fig. 3.13b). In spite of the possible effects of alteration, this diagram correctly classifies the oceanic and rifting basalts, while showing the variolitic Ireland Point Volcanics as "oceanic island" basalts and the Maiden Point volcanics as "continental", overlapping completely with the rift-related volcanics from the Appalachians. The Ireland Point Volcanics are once again shown ranging from tholeiitic to alkalic compositions.

On the basis of these diagrams, it is concluded that the Ireland Point Volcanics are neither ocean floor nor continental rifting basalts, but may have formed part of an oceanic island. They are not related to the Maiden Point Formation volcanics, which closely resemble rift-related tholeiitic basalts from elsewhere in the Appalachians.

3.1.3. Mineral Chemistry

Microprobe analyses of clinopyroxene, amphibole, and feldspar from the least altered pillow lavas and gabbros are listed in Appendix II.

Clinopyroxene

The clinopyroxenes of the variolitic basalts and the gabbros are rich in Ti and Al and trend from Ca-rich diopside to salite within the pyroxene quadrilateral (Fig. 3.14). In contrast, clinopyroxene from the Croque Harbour Volcanics is relatively poor in Ca, Al, and Ti.

Clinopyroxene compositions can be used to classify the host basalts (e.g. Le Bas, 1962), and have been used to determine the tectonic setting of altered volcanic rocks (Nisbet and Pearce, 1977). By these methods, the Croque Harbour basalts can be classified as subalkaline, ocean floor basalts, while the Ireland Point - Cape Onion volcanics can be classified as alkaline to peralkaline "within plate" basalts (Fig. 3.15). These results are compatible with the conclusions drawn on the basis of the immobile element geochemistry.

Amphibole

Owing to the scarcity of coarse-grained amphibole in the volcanic rocks, only gabbroic amphibole was analysed, but the similar optical properties and parageneses of the amphiboles from the intrusive and extrusive rocks suggests that they have similar compositions. In both cases, brown hornblende commonly occurs after titanaugite, less commonly occurs as phenocrysts, and generally contains patches of blue-green hornblende.

The brown amphibole ranges from Ti-rich pargasite to kaersutite (Appendix II), but since the compositions are gradational, they are loosely referred to here as "kaersutite". (Na + K) is close to the ideal pargasite value of 1.0 and Al^{IV} is close to the ideal pargasite value of 2.0 (Fig. 3.16). Al^{VI} is low by comparison, the Y-site being rich in Ti^{4+} and Fe^{3+} instead. Amphibole phenocrysts from the leucocratic diorites have particularly high concentrations of Ti and Al^{IV} . The high (Na + K), Ti, and Al^{IV} are typical of amphiboles from basic alkalic rocks (Wilkinson, 1961; Aoki, 1963; Mason, 1968).

Blue-green amphibole which sporadically replaces the kaersutite is an Fe-rich, Ti-poor hastingsite. The high (Na + K) and Al^{IV} characterize it as an igneous rather than a metamorphic amphibole, which may have formed in response to late magmatic deuteric activity.

Feldspar

All the feldspars analysed were albite, $\text{An}_{0.3}$ to $\text{An}_{6.6}$ (including gabbroic plagioclase which appeared to be calcic on the basis of its twinning). The albite is presumed to be secondary after a more calcic composition. The anorthite content was the lowest in the vesicular pillow lava, and highest in the gabbro.

3.1.4. Petrogenesis

This discussion focusses on two problems -- the crystallization history of the basalts, and the origin of the variolitic structures. The crystallization history is considered first in order to provide a framework for the discussion of the varioles.

Crystallization History

The mineralogy and immobile element geochemistry of the Ireland Point Volcanics indicate an alkaline affinity which is supported by the normative compositions (calculated with Fe_2O_3 reduced to 1.5%). The basalts range from slightly nepheline-normative to slightly hypersthene-normative, and all contain normative olivine (Fig. 3.17). In conventional terminology, they range from alkali basalts to olivine tholeiites, or in a general sense are "transitional". The tendency is for the gabbros to become more ne-normative with differentiation, and for the basalts

to become more hy-normative higher in the sequence. However, the pervasive geochemical alteration of the rocks makes their normative compositions unreliable petrogenetic indicators.

The primary mineralogy of the basalts, summarized in Table 3.3, is a better guide to their petrogenesis. In the variolitic pillow lavas, olivine was the first phase to crystallize, followed by titanaugite. The absence of olivine from amphibolite-rich samples and the presence of amphibole rims on titanaugite indicates that olivine and pyroxene reacted with the liquid to produce kaersutite (cf. Donaldson, 1977). Plagioclase was the last phase to crystallize. In the gabbros, olivine is absent, iron-titanium oxide (ilmenite?) is an important early phase, and titanaugite and kaersutite are abundant, with kaersutite eventually replacing titanaugite as the primary mafic phase in the diorites. The low concentrations of Cr and Ni and the absence of olivine in the gabbros suggest that they are the intrusive equivalents of the massive flows within the Ireland Point Volcanics. The intrusive event appears to have been short-lived, since the gabbros are a widespread but homogeneous and volumetrically minor group.

The change from variolitic to vesicular basalts coincides with a change in mineralogy to a plagioclase-mafic glass assemblage. This probably resulted from a combination of two factors -- a change in the liquid composition towards trachybasalt through the crystallisation of olivine and clinopyroxene, and a relatively lower pressure of crystallization, suggested by the high vesicularity, which would expand the primary phase field of plagioclase. Some liquids which accumulated large amounts of plagioclase and some olivine and clinopyroxene were later erupted as porphyritic basalts.

Fig. 3.18 shows the experimental results of Yoder and Tilley (1962) and Holloway and Burnham (1972) on the basalt-H₂O system. For clarity, similar data from other studies on natural and synthetic systems are not plotted in this diagram (Nesbitt and Hamilton, 1970; Helz, 1973, 1976; Cawthorn and O'Hara, 1976). Variations in P_{H_2O} , f_{O_2} , and bulk composition affect the temperatures at which phases appear, but they do not alter their order of appearance. At $P > 2$ kb, this order is olivine (and/or magnetite), followed by clinopyroxene, followed by amphibole as the result of reaction between olivine, clinopyroxene, and liquid, finally followed by plagioclase. At $P \leq 2$ kb, plagioclase precedes amphibole in the crystallisation sequence. These relationships are essentially identical to those observed in the variolitic basalts, and fix a minimum pressure of 2 kb. Since this is excessive for volcanic rocks, even in deep water, eruption probably took place rapidly from a depth of a few kilometres.

Projections from olivine and clinopyroxene in the system CaO-MgO-Al₂O₃-SiO₂-Na₂O-H₂O (Fig. 3.19) using the method of Cawthorn and O'Hara (1976) support the model of a continuous trend of liquid compositions, with the porphyritic basalt compositions modified by plagioclase accumulation. Deviations from the 5 kb phase relations determined by Cawthorn and O'Hara (1976) are accounted for by a lower pressure of crystallization, increasing the stability of plagioclase at the expense of amphibole (Fig. 3.18), and particularly in Fig. 3.19b, by the effects of chemical alteration. Low pressure (less than 5 kb) control on the crystallization of the Ireland Point Volcanics is indicated by the phase relations.

Origin of the Varioles

Recent discussions of variolitic structures have proposed three kinds of origin:

(1) varioles form by liquid immiscibility (e.g. Carstens, 1963; Gelinas et al., 1976)

(2) varioles form by alteration processes (e.g. Philpotts, 1977)

(3) varioles are a cooling phenomenon (e.g. Mével, 1975, 1976).

The choice among these alternatives rests heavily on the interpretation of textural relationships, which can be controversial even in unaltered, well-described examples (Gelinas et al., 1976; Hughes, 1977; Philpotts, 1977; Gelinas et al., 1977). The problem is complicated by the use of the term "variole" to describe a variety of spherical structures in basic igneous rocks (cf. Lofgren, 1971). To avoid confusion about the kind of structure referred to in the following discussion, the main features of the varioles in the Ireland Point, Cape Onion, and Quirpon Harbour volcanic rocks are described below.

The varioles are entirely restricted to the pillow lavas; they do not occur in massive flows, dykes, or gabbros of similar bulk composition. They are leucocratic, spherical masses, averaging 4 mm in diameter, which appear a few cm from the pillow rim as isolated bodies within a melanocratic matrix of selvage material. Over the next 5 to 15 cm, they coalesce to form pillow cores of continuous variole material which make up about 50% of the pillows by volume (Fig. 2.2). The varioles lack any kind of radiating or concentric internal structure, and contain the same primary phases as their matrix. Although the

interface between the leucocratic varioles and their melanocratic matrix is sharp, olivine phenocrysts and titanite microlites commonly grow across the boundary without visibly affecting it (Fig. 3.20). In general, chlorite pervasively replaces the glass, clinopyroxene, and olivine of the matrix, while within the varioles pyroxene is fresh, altered olivine crystals and veinlets contain more calcite than chlorite, and the glass is replaced by albite and calcite.

The liquid immiscibility hypothesis requires that a magma separate into acidic and basic fractions in response to the free-energy requirements of the system (Roedder, 1978). Droplets of one liquid (in basalts, generally the acidic one) form in the other and coalesce to minimize the free surface energy of the system, forming larger spheres in a matrix of contrasting composition. At the time of formation, the two liquids must be in equilibrium with each other and with the crystalline phases in the magma (Bowen, 1928), although this does not require the simultaneous precipitation of identical phases from both liquids (Philpotts, 1977). High interfacial tension will exist at the boundary between the liquid droplet and its host (Philpotts, 1977) but may be modified by turbulence in the lava (Gelinas et al., 1978). Within the variole, crystal growth proceeds from the rim to the core, and crystal settling may occur (Philpotts, 1972).

The alteration hypothesis requires the redistribution of elements in a basalt to produce approximately spherical aggregates of altered glass (generally felsic) in a matrix of contrasting composition. In spilitic pillow lavas, alteration can enrich pillow cores in albite and pillow rims in chlorite (Vallance, 1969), producing compositional

zoning. If the alteration process involves devitrification, spherulitic structures may be produced.

The cooling hypothesis is based on experimental work showing that crystal forms in quenched basalts depend on the degree of supercooling (ΔT) (Lofgren, 1974). At high ΔT , spherulitic growth occurs proceeding from core to rim, while at low ΔT , tabular crystal forms are produced. Varioles may thus represent spherulitic crystal aggregates formed inside a quenched, glassy margin by growth from a highly supercooled liquid (e.g. Mével, 1976). Alteration might subsequently obliterate the radial structure within the spherulites.

In the case of the Ireland Point Volcanics, textural evidence can be found for and against all three hypotheses. Each is considered separately in terms of its ability to explain the distribution, size, shape, mineralogy, and alteration of the varioles.

The restriction of the varioles to pillow lavas, and their concentric distribution with respect to the pillow margins suggests a genetic relationship between rapid cooling and variole formation. This argues against stable liquid immiscibility but does not preclude metastable immiscibility. However, if immiscible liquid droplets did separate upon rapid cooling, they must have grown very quickly to reach diameters of several millimetres. The varioles are at least two orders of magnitude larger than immiscible droplets formed in modern submarine tholeiitic pillow lavas (A. R. Philpotts, written communication, 1978). The size of the varioles relative to the olivine and pyroxene crystals would require more efficient diffusion of felsic than mafic components through the melt, whereas the reverse is more likely. The occurrence of skeletal

titanaugite and olivine phenocrysts across variole boundaries requires either simultaneous growth of crystallographically continuous phases from two liquids, or the penetration of a liquid-liquid interface by delicate crystals without breaking or forming a meniscus. As pointed out by Philpotts (1977), a phase in equilibrium with both liquids in an immiscible system is likely to crystallize only from the one which is closer to it in composition. Even if both liquids contain identical phases at the time they separate, their reaction relationships with these phases will differ. Therefore, the formation of hornblende from reaction between olivine, clinopyroxene, and melt is unlikely to have occurred in both the varioles and the matrix. While these observations weaken the argument for liquid immiscibility, the regular spherical shape of the varioles supports the hypothesis.

The alteration hypothesis is even less satisfactory. The distribution and regular shapes of the varioles suggest a remarkably uniform secondary process, which has affected the variolitic pillow lavas but not the vesicular ones. This process must also have involved very efficient diffusion, since the mafic components which would have migrated out of the variole sites must have been homogeneously absorbed by the matrix. Most importantly, the alteration pattern now preserved suggests that the variole boundaries were present at the time the alteration occurred. However, since the variole formation would postdate the crystallization, this hypothesis does explain the crystal growth across the interfaces.

If the varioles did not form as drops of immiscible liquid, and if they formed prior to spilitization, the time of formation is

probably the cooling interval. As a result of quenching before plagioclase nucleation, the pillow rims would be supersaturated with respect to feldspar. In the warm pillow core, nucleation of minute plagioclase crystals might occur, but the degree of supercooling would inhibit the growth of large crystals (cf. Lofgren, 1971, 1974). Heat transfer from core to rim, accompanied by volatile diffusion, could induce the coalescence of these nuclei into spherical aggregates (cf. Grovesnor, 1962, p. 321) whose internal structure would depend on the kinetics of crystal growth in the glass. This hypothesis differs from the other two in being dependent on the cooling process itself, which is consistent with the distribution of the varioles. It also explains why the varioles do not occur in the plagioclase-rich vesicular basalts, why they have sharp boundaries and a uniform size, and why the distribution of the mafic phases is independent of the variole boundaries. This cooling stage must be encountered frequently in submarine basalts, where varioles, generally consisting of radiating plagioclase crystals, are common (e.g. Furnes, 1973; Lofgren, 1974). However, the Ireland Point Volcanics lack the radiating spherulitic structures that are generally observed.

In summary, the Ireland Point Volcanics and the related rocks form a suite of alkaline to transitional basalts. The crystallization of the lower members of the suite involved olivine, titanite, and kaersutite, but plagioclase dominates in the upper units. Variolitic structures in pillow lavas at the base of the Ireland Point Volcanics are probably a cooling phenomenon.

3.2. The Goose Cove Schist

The Goose Cove Schist, the lower part of the dynamothermal aureole of the White Hills Peridotite, grades downward into the Ireland Point Volcanics and upward into the Green Ridge Amphibolite. It includes greenschist and epidote amphibolite facies metasedimentary and metabasic rocks. The metasedimentary rocks consist mainly of psammite and pelite, with minor marble and chert, while the metabasic rocks consist of banded and spotted greenschists, which are the metamorphic equivalents of the Ireland Point Volcanics, and minor pre-tectonic basic sills or dykes within the metasediments.

3.2.1. Petrography

Metasediments

The assemblage quartz-plagioclase-muscovite-chlorite forms over 90% of the clastic metasediments, which range from psammite to pelite depending on the relative proportions of quartz and feldspar to mica and chlorite (Table 3.4). At lower grades, sericite and albite replace detrital alkali feldspar and plagioclase, while muscovite and chlorite replace detrital mica. At higher grades, garnet and biotite form at the expense of chlorite. The schistosity (S_1) develops by the preferred orientation of mica and chlorite, and by the recrystallization of quartz from detrital grains into lensoid aggregates of interlocking crystals and ultimately into bands of polygonal crystals (Fig. 3.21). Compositional layering, defined by alternating quartz-rich and mica-rich bands, is parallel to the schistosity. In pelitic rocks, crenulation of S_1 occurs by bending of the sheet silicates, but is not associated with penetrative

recrystallization (Fig. 3.22). Tiny, euhedral garnets first appear along S_1 foliation planes, but as their size increases the foliation tends to be deflected around them.

Rare marbles and some calcite-rich tuffaceous horizons occur within the pelites. These consist mainly of calcite and epidote with variable proportions of actinolite and chlorite, depending on the bulk composition of the layers (Table 3.4). Except where epidote is concentrated in bands parallel to S_1 , the foliation is poorly developed.

Fine-grained, laminated, metacherts occurring on the Fischot Islands are rich in magnetite, hematite, and spessartine. S_1 is defined by muscovite and chlorite and is parallel to the compositional layering defined by the varying proportions of quartz and iron oxides. Quartz generally has irregular, interlocking grain boundaries, while the larger garnets contain sigmoidal and spiral inclusion trails (Fig. 3.23).

Metabasites

Four petrographic types of metabasic rocks can be defined within the Goose Cove Schist (Table 3.5). These include massive, spotted, and banded greenschists, as well as epidote amphibolites.

The massive greenschists (mapped with the banded greenschists) include coarse-grained, weakly foliated pre-tectonic dykes and sills within the Goose Cove Schist. They are distinguished by a relict diabasic texture, in which large, ragged, pale green hornblende (after clinopyroxene?), intergrown with tabular to lathlike albite (after calcic plagioclase), is set in matrix of finer-grained, granular albite, epidote and chlorite (Fig. 3.24). Deformation is reflected in weak alignment of hornblende and chlorite, and recrystallization of albite.

The spotted greenschists are characterized by large white aggregates of epidote, calcite, albite, and muscovite occupying the sites of plagioclase "porphyroclasts" which are presumed to be the deformed equivalents of the large phenocrysts in the porphyritic pillow lava unit at Stark's Bight (Fig. 3.25). These occur in a fine-grained matrix rich in amphibole and chlorite. With increasing grade, blue-green hornblende replaces actinolite and chlorite becomes less common. The amphibole and chlorite define the S_1 foliation, which is generally, although not always, strongly developed. The aggregates formed from the porphyroclasts are lensoid, with aspect ratios of up to 20:1 in the plane of this foliation, and define a prominent lineation. In the most intensely deformed rocks, the aggregates merge into discontinuous bands of epidote, calcite, and albite; these rocks are similar in appearance to the banded greenschists described below.

The typical banded greenschists are distinguished by thin, pale green bands of epidote, sodic plagioclase, and calcite in a fine-grained, dark-green matrix of amphibole, chlorite, and epidote (Table 3.5). Pale green actinolite occurs at low grades, but blue-green hornblende is more common in the upper part of the sequence. Chlorite is common but never abundant, and disappears at higher grades. The penetrative S_1 foliation, defined by the alignment of amphibole and chlorite, is parallel to the compositional layering. It is folded by tight, asymmetric F_2 folds (Fig. 3.26), which involve crenulation of S_1 in fold hinges, but are not associated with a penetrative S_2 foliation.

At Three Mountain Summit, with the gradual increase in grain size, loss of chlorite, and decrease in the proportion of epidote-rich

bands to matrix, the banded greenschists grade into epidote amphibolite facies rocks. These are characterized by epidote, blue-green hornblende containing abundant ovoid inclusions of quartz and sphene, and granular matrix quartz and zoned oligoclase. Epidote is not nearly as common a matrix phase as in the greenschist facies rocks, being concentrated in coarse-grained bands and lenses instead. These epidote-rich aggregates form separate metadomains in which the assemblage epidote-actinolite-albite-calcite persists after these minerals have disappeared from the matrix. At the highest grades, therefore, the epidote amphibolites consist of calc-silicate-rich layers in a matrix which is essentially identical to the quartz amphibolites described in Section 3.3. Near the top of the epidote amphibolite sequence, intergrowths of actinolite, epidote, and plagioclase surrounded by rims of blue-green hornblende occur on the margins of these bands (Fig. 3.27). Like the banded greenschists, the epidote amphibolites are characterized by an S_1 foliation, defined by the alignment of hornblende crystals, which is parallel to the compositional layering and which is folded by asymmetrical tight to isoclinal F_2 folds.

3.2.2. Geochemistry

Metasediments

Seven representative metasedimentary rocks were analysed for major and trace elements (Appendix I). Their geochemistry is dominated by SiO_2 , which ranges from 75% in some psammites to 50% in the garnetiferous metacherts. The high concentrations of FeO, Fe_2O_3 , and MnO, and relatively low concentration of SiO_2 in the "cherts" suggest that "iron formation" would be a more appropriate term.

In the clastic rocks, the bulk chemistry reflects the abundance of mica and chlorite, with pelites having higher concentrations of Al_2O_3 and K_2O than psammities. Trace element concentrations are highly variable, particularly for Zr and Sr which reflect the distribution of zircon and calcite in the samples. By comparison with the metabasites, the metasediments have high Rb, Ba, Nb, and Pb, and low Cr and Ni (Fig. 3.28).

Metabasites

Forty-two metabasic rocks from the Goose Cove Schist were analysed for major and trace elements, including 9 massive greenschists, 10 spotted greenschists, 14 banded greenschists, and 9 epidote amphibolites. The three greenschist facies groups have similar basaltic compositions (Fig. 3.28), with variable Al_2O_3 , CaO, FeO_T , and $\text{Fe}_2\text{O}_3/(\text{Fe}_2\text{O}_3 + \text{FeO})$ reflecting the varying proportions of porphyroclasts and epidote. A few samples of massive greenschists are distinguished by high TiO_2 , MgO, P_2O_5 , Zr, Nb, Y, Cr, and Ba.

The epidote amphibolite facies rocks, while petrographically gradational with the banded greenschists, have consistently different chemical compositions, with high SiO_2 , TiO_2 , FeO_T , $\text{FeO}_T/(\text{FeO}_T + \text{MgO})$, K_2O , Zr, Rb, Y, V, and Ga, and low Al_2O_3 , MgO, Cr, and Ni. The distinction is probably not attributable to the loss or gain of mobile components with metamorphic grade, since the "immobile" elements Ti, Al, Zr, and Y are involved (e.g. Smith and Smith, 1976), and K and Rb, which tend to be depleted with progressive metamorphism (e.g. Field and Elliott, 1974), are actually higher in the epidote amphibolites than

in the greenschists. The geochemical data suggest that the Goose Cove Schist is composed of two different types of basaltic rocks. As will be shown in Section 3.3, the epidote amphibolites are essentially the same as the quartz amphibolites of the overlying Green Ridge Amphibolite.

The field evidence suggests that much of the Goose Cove Schist is composed of the greenschist facies equivalents of the vesicular and porphyritic pillow lavas of the Ireland Point Volcanics, which have been interleaved with carbonate during deformation. The compositions of the Goose Cove Schist and the volcanic rocks were plotted as ratios of the components to TiO_2 , to offset the effect of the likely addition of CaO to the greenschists. The examples given in Fig. 3.29 show that the greenschists fall along a trend between the vesicular and porphyritic pillow lavas, confirming their derivation from similar rocks and also suggesting that the amount of plagioclase in the protoliths is the main cause of chemical variation in the greenschists.

3.2.3. Mineral Chemistry

Microprobe analyses of chlorite, epidote, plagioclase, and amphibole were obtained from samples of each petrographic type except the metasediments. Owing to the fine grain size of the greenschists, it was not possible to analyse the complete mineral assemblage in some samples. The results are given in Appendix II.

Chlorite

Chlorite from five greenschists was analysed. In each case, it is ripidolite (as defined by Deer et al., 1970, p. 233) with a composition close to $\text{Fe}_x \text{Mg}_{9.5-x} \text{Al}_{2.5} (\text{Si}_{5.5} \text{Al}_{2.5}) \text{O}_{20} (\text{OH})_{16}$. The

Fe/Mg ratio depends on the host rock composition, but is always less than 1.0. On an ideal stoichiometric basis of 20 cations to 28 oxygens (equivalent to $O_{20} (OH)_{16}$), the chlorites are essentially unoxidized, with a maximum calculated Fe_2O_3 of 0.34.

The chlorite compositions are plotted in Fig. 3.30 using the epidote projection of Harte and Graham (1975). This plot shows a tendency for the ratio Mg/Fe to decrease with increasing grade in rocks with comparable bulk compositions.

Epidote

Epidote from all the samples is close to the composition $Ca_{2.0} Fe^{3+}_{0.8} Al_{2.2} Si_{3.0} O_{12} (OH)$, which corresponds to Ps_{27} . Total iron, calculated as Fe^{3+} , ranges from 0.58 to 0.86. The most variable compositions are from the greenschist facies samples, where epidote from porphyroclasts or calc-silicate bands may differ from the matrix epidote in composition. These differences, which are not consistent in terms of the ratio Fe^{3+}/Al , may reflect a lack of equilibration. The high Fe^{3+}/Al ratios suggest a high oxygen fugacity in the environment of crystallisation (e.g. Holdaway, 1972; Liou, 1973), which is supported by the common occurrence of hematite in the Goose Cove Schist. No systematic change in epidote composition with metamorphic grade was detected.

Plagioclase

Figure 3.31 shows the frequency of plagioclase compositions from rocks with different mineral assemblages corresponding to different grades. With the exception of two analyses from one sample, there is a compositional gap between An_7 and An_{18} , with both greenschists and

epidote amphibolites having compositions which fall on either side. This coincides with the "peristerite gap" (Brown, 1962), a lack of feldspar compositions in the range An_5 to An_{20} which characterises the transition from the greenschist to the amphibolite facies. The two intermediate analyses (An_{11}) may be feldspars that have unmixed on a submicroscopic scale, since the same sample also contains albite.

Within this overall trend, some unusual patterns occur. Most greenschist facies samples contain either albite (An_{0-5}) or oligoclase (An_{18-22}) but not both. The more calcic compositions are from very fine-grained samples, and may reflect a bias in the analyses towards coarser-grained plagioclase. The most calcic albite analysed (An_7) is from an epidote amphibolite sample containing complex intergrowths of hornblende, actinolite, epidote, and plagioclase; in this case, calcic albite may be a metastable product of the reaction among these phases. Otherwise, the most calcic albite analysed is An_5 . A second gap occurs in epidote amphibolite samples between An_{26} and An_{31} . All the epidote amphibolite samples contain two plagioclase compositions -- either albite and oligoclase, or albite and andesine, or oligoclase and andesine -- but none has been found which contains all three compositions. This probably reflects incomplete reactions producing andesine from albite/oligoclase and epidote or, possibly, retrograde reactions.

Amphibole

Amphibole analyses were obtained from the entire range of greenschist and epidote amphibolite facies rocks. The results were recalculated in terms of minimum, intermediate, and maximum ferric iron

using a program developed by B. Doolan (unpublished) based on the stoichiometric recalculation schemes of Stout (1972) and Papike et al. (1974). All the data are plotted and discussed in terms of the intermediate Fe^{3+} values. The details of the method are described in Appendix II.

Figure 3.32 shows the data for the greenschist and epidote amphibolite facies rocks plotted in terms of $(\text{Na} + \text{K})$ and Al^{IV} . This plot separates several possible types of substitutions (towards edenite, glaucophane, pargasite, and tschermakite), while it depends very little on the Fe^{3+} , since the parameters plotted have opposite effects on its calculated value and tend to cancel out (Appendix II). This plot is used throughout this work for showing amphibole compositions.

The amphibole compositions range from actinolite to hastingsite. All plot close to the tie line between tremolite ($\text{Ca}_2 \text{Mg}_5 \text{Si}_8 \text{O}_{22} (\text{OH})_2$) and Al-pargasite ($\text{NaCa}_2 \text{Mg}_3 \text{Al}_2 \text{Si}_5 \text{Al}_3 \text{O}_{22} (\text{OH})_2$), reaching a maximum Al^{IV} content of about 1.7. The trend is continuous, with greenschist facies amphiboles having $\text{Al}^{\text{IV}} < 1.3$ and epidote amphibolite facies amphiboles having $\text{Al}^{\text{IV}} > 1.3$.

The amphiboles which coexist with chlorite are aluminous actinolites, with $0.2 < \text{Al} \leq 1.3$. The only exception is a hornblende which replaces chlorite in a massive greenschist from Lobster Point. Within the greenschist, amphibole becomes more aluminous with increasing grade. The epidote amphibolites contain hornblende with $1.3 \leq \text{Al} \leq 1.7$ with the following exceptions. Two samples, one from just above the chlorite-out isograd, and one from close to the top of the epidote amphibolite unit on Three Mountain Summit contain actinolite in calc-silicate layers and hornblende in the matrix. This is the result

of the difference in bulk composition between the epidote-rich bands and the epidote-poor matrix. The sample from the base of the epidote amphibolites shows no sign of reaction involving actinolite, and contains no amphibole compositions between actinolite and aluminous hornblende. The sample from the top of the epidote amphibolites contains complex intergrowths of actinolite, hornblende, epidote, and albite, and amphiboles which span the range from actinolite to aluminous hornblende along the same trend as that defined by the combined greenschist and epidote amphibolite facies data.

There is no evidence of a miscibility gap between hornblende and actinolite (cf. Cooper and Lovering, 1970). The paucity of data between $Al^{IV} > 1.0$ and $Al^{IV} < 1.3$ is interpreted as resulting from a rapid transition from less aluminous to more aluminous compositions corresponding to the loss of chlorite from the metamorphic assemblage. This agrees with the experimental observations of Liou et al. (1974) and the conclusions of Graham (1974) on compositional changes in amphibole at the chlorite-out isograd. In support of this conclusion is the absence of exsolution lamellae in amphibole of any composition. The data of Cooper and Lovering (1970) are based primarily on actinolite rimming hornblende, suggesting that a retrograde reaction was involved. Reaction kinetics, and the P-T path of metamorphism may determine the presence or absence of a miscibility gap in the calcic amphiboles from any given area.

Using $(Al^{IV} + Na + K)$ as an index, it can be seen that there is an increase in the trivalent octahedral cations $(Al^{VI} + Fe^{3+})$ with increasing grade, but that Ti^{4+} changes very little. Fe/Mg is much

more dependent on host rock composition than grade (Fig. 3.32), although there is a tendency for Mg/Fe to decrease with increasing grade in rocks of similar composition (Fig. 3.30).

The relationship of a set of amphibole compositions to the tremolite -- Al-pargasite join can be used as a guide to the P/T gradient of metamorphism (B. Doolan, pers. comm., 1978; Steffe, 1978). Fig. II.ii (Appendix II) shows the compositional trends of amphiboles from high pressure metamorphic terrains, and from high temperature metamorphic terrains. The Goose Cove Schist amphibole trend is much closer to the high temperature path.

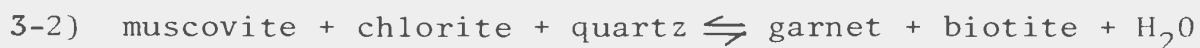
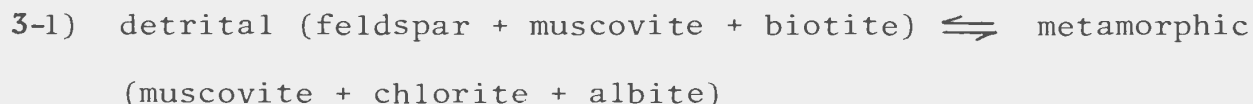
3.2.4. Petrogenesis

Metasediments

Only psammites and pelites are widespread enough for any generalizations about their metamorphic petrogenesis to be made, and even here, the scarcity of metasediments in the upper part of the Goose Cove Schist means that only greenschist facies assemblages are present.

Figure 3.33 summarizes the mineral assemblages present in the clastic metasediments. Muscovite and chlorite are abundant at low grades. Garnet appears somewhat before biotite, and where biotite is abundant muscovite and chlorite decrease sharply in abundance, chlorite disappearing first. The disappearance of calcite coincides approximately with the appearance of epidote and sphene. Once formed, epidote persists even in quartz-rich samples, although it is most common in chlorite-rich layers. Garnet is not present in the semi-pelitic rocks near the base of Three Mountain Summit.

The prograde reactions probably take the following form, as in many metamorphic terrains (Miyashiro, 1973, and references therein):



The appearance of garnet before biotite differs from the order of their appearance in the Dalradian sequence (e.g. Atherton, 1977) which has come to be regarded as the typical regional metamorphic sequence. However, the absence of garnet from the semi-pelitic horizon near the top of the greenschists close to Three Mountain Summit suggests that the early garnet is spessartine, stabilized by MnO at relatively high temperatures and low pressures (e.g. Hsu, 1968; Okrush, 1971; Vernon, 1976, p. 106). This relationship is clearly illustrated by the abundance of spessartine in the manganese-rich "cherts" on the Fischot Islands.

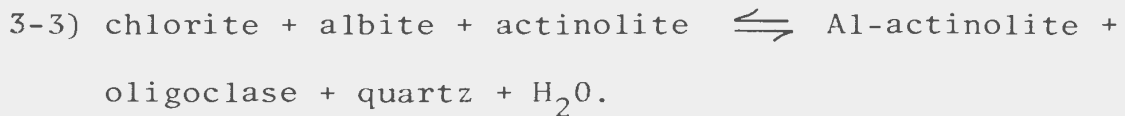
Metabasites

The transition from the greenschist facies to the amphibolite facies in metabasic rocks is of considerable petrological interest, since it occurs in many metamorphic terrains under a wide range of P/T conditions. It has been the subject of many field studies (e.g. Wiseman, 1934; Miyashiro, 1958; Cooper, 1972; Graham, 1974), but few experimental studies have been done (e.g. Liou et al., 1974) because of the difficulty of equilibrating the relevant assemblages in the laboratory. The transition commonly includes a zone of epidote amphibolite facies rocks, depending on the pressure of metamorphism, oxygen fugacity, and possibly bulk rock composition. All stages of this complex transition occur within the Goose Cove Schist.

Observations relevant to the petrogenesis of the Goose Cove Schist include the following. The essential greenschist facies assemblage is plagioclase + epidote + chlorite + amphibole. The plagioclase includes both albite and oligoclase, and the amphibole ranges from actinolite to hornblende with increasing Al^{IV} . The essential epidote amphibolite facies assemblage is plagioclase + epidote + amphibole + quartz. The plagioclase is generally oligoclase, but albite and andesine also occur, while the amphibole is blue-green hornblende. The mineral assemblages are summarized in the ACF diagram of Fig. 3.34; the bulk compositions of the rocks plot very close to the epidote-actinolite join, explaining why chlorite is never an abundant phase. The transition from the greenschist to the epidote amphibolite facies is thus marked by the disappearance of chlorite, the appearance of quartz, and by changes in the compositions of plagioclase and amphibole. The two metamorphic assemblages approximately coincide with two different bulk compositions, both basaltic, which differ mainly in minor and trace element constituents. The compositional difference is thus unlikely to influence the distribution of the major phases, but may affect the occurrence of accessory minerals like sphene and iron oxides.

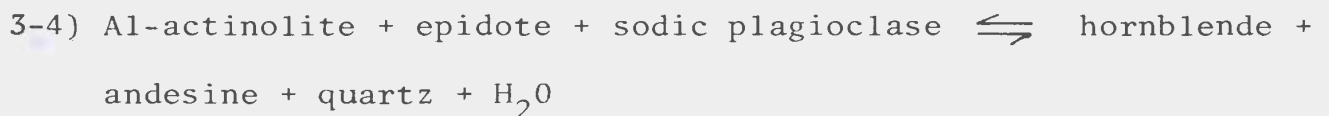
The disappearance of chlorite defines an isograd separating greenschist facies assemblages from epidote amphibolite facies assemblages. The gradual change in feldspar and amphibole compositions suggests that there is a broad zone through which chlorite reacts with actinolite to produce aluminous actinolite, and that the "chlorite-out" isograd merely defines the upper limit of the reaction zone. Epidote breakdown may also be involved, but its continued abundance above the isograd, its

constant composition, and the occurrence of both albite and oligoclase above and below the isograd suggest that this is not a fundamental part of the transition. The reaction can be written as:



It is a divariant reaction, taking place over a range of temperatures and pressures as the minerals involved gradually change in composition until one of the reactants (in this case, chlorite) is used up.

The disappearance of chlorite marks the first stage in the conversion of a greenschist to an epidote amphibolite, and ultimately to an amphibolite. Feldspar and amphibole compositions continue to change with increasing grade, reflecting the breakdown of epidote to produce the assemblage andesine + hornblende + quartz which defines the amphibolite facies. This assemblage occurs at the top of the Goose Cove Schist in the matrix between coarse-grained epidote-rich aggregates. The reaction is epitomized by the complex intergrowths seen at the margins of the calc-silicate bands near the top of the epidote amphibolite zone (Fig. 3.27), where hornblende surrounds epidote, pale green amphibole, and plagioclase. The ideal reaction can be written as:



As for the chlorite-consuming reaction, this proceeds over a range of pressures and temperatures as the compositions of plagioclase and amphibole change, until epidote is used up. The reaction marks the upper limit of albite occurrence in the Goose Cove Schist.

Metastable assemblages persist to the top of the epidote amphibolite zone. In the epidote-rich bands, the assemblage epidote +

albite + actinolite persists as a separate metadomain because of its different bulk composition, while the matrix of these rocks contains the amphibolite facies assemblage hornblende + andesine + quartz. When the epidote in these bands finally begins to break down at the top of the epidote amphibolite unit on Three Mountain Summit, a wide range in plagioclase and amphibole compositions can occur in a single sample.

Figure 3.35 reproduces the summary diagram of Liou et al. (1974) showing the experimentally determined relationships between the greenschist, the epidote amphibolite, and the amphibolite facies. It is evident that there is a zone between curves (1) and (2) which represents the breakdown of chlorite to form aluminous amphibole. The relative slopes of the "chlorite-decreasing" and "chlorite-out" curves suggest that this transition zone may disappear at high pressure. The relationship between the high pressure epidote amphibolite facies (strictly, epidote + albite + hornblende; Miyashiro, 1973) and the low pressure assemblage actinolite + calcic plagioclase (Miyashiro, 1973), is shown by the relative positions of curves (2) and (3). At low pressures, epidote breaks down before chlorite, and calcic plagioclase is produced before aluminous amphibole, while at high pressures the relationship is reversed. Most significant is the dependence of epidote stability on oxygen fugacity, increased f_{O_2} increasing the thermal stability of epidote. Since increased f_{O_2} may decrease the thermal stability of Fe-chlorite (Liou et al., 1974), the two effects combine to expand the stability field of epidote amphibolite assemblages to lower pressures and higher temperatures.

The Goose Cove Schist commonly contains small amounts of hematite, and epidote with a composition of about Ps_{27} . These observations

suggest that f_{O_2} during the metamorphism was higher than that of the QFM buffer, but not as high as that of the HM buffer, which would produce epidote with a maximum Fe^{3+} content, corresponding to Ps_{33} (Fig. 3.35). Therefore, the results of Liou et al. (1974), based on the QFM buffer, can only be used as a qualitative guide to the metamorphic conditions.

Besides the problem of oxygen fugacity, there is a problem in determining the probable partial pressure of H_2O . Although the Goose Cove Schist was almost certainly a fluid-saturated system, a significant amount of calcite is present in its lower levels. If sufficient CO_2 was present in the environment to lower P_{H_2O} with respect to P_{TOT} , this would lower the temperatures at which the dehydration reactions occur. The reaction most strongly affected would be the breakdown of chlorite. Although carbonate tends to be restricted to the epidote-rich bands and the porphyroclast sites, and may thus have affected only small metadomains within the rock, its presence must be taken into account. However, calcite disappears from the assemblage below the "chlorite-out" isograd (Fig. 3.33). Therefore, P_{CO_2} may not have affected the maximum thermal stability of chlorite, although it could have had a considerable effect on the position of the "chlorite-decreasing" curve, allowing maximum pressures of greater than 4.5 kb for the intersection of curves (1) and (2) (Fig. 3.35).

If the NNO buffer can be taken as an approximation to the oxygen fugacity conditions within the Goose Cove Schist, and if this does not affect chlorite stability, and if $P_{H_2O} = P_{TOT}$, the shaded areas in Fig. 3.35b represent the stability fields of the observed greenschist

and epidote amphibolite facies assemblages. The stability of epidote requires conditions on or above curve (3a), and a broad zone in which chlorite decreases in abundance. Both aluminous actinolite and hornblende occur, and epidote amphibolite is a stable assemblage. Extrapolating curve (1) to its intersection with curve (2), the stability field of the Goose Cove Schist can be roughly defined as lying between 1.75 kb and 4.5 kb, and between 450°C and 650°C. High P_{CO_2} could increase the maximum pressure, while high f_{O_2} could decrease the lower temperature, so that this P-T range can only be considered an approximation to the actual conditions.

In summary, the Goose Cove Schist contains two "isograds" which represent the limits of divariant mineral assemblages. The "chlorite-out" isograd defines the maximum stability of the assemblage actinolite-epidote-chlorite, while the "epidote-out" isograd defines the maximum stability of the assemblage epidote-albite-hornblende. The Goose Cove Schist thus contains three stable metamorphic mineral assemblages, characteristic of the greenschist, epidote amphibolite, and amphibolite facies (although the amphibolite facies is restricted to the matrix of samples which still contain epidote aggregates). These assemblages and the reactions relating them can be compared to the experimental work of Liou et al. (1974), with the qualifications described above. In the absence of any mineral geobarometers or geothermometers, a P-T range of 1.75 to 4.5 kb and 450° to 650°C is consistent with the petrology of the Goose Cove Schist.

3.3. The Green Ridge Amphibolite

The Green Ridge Amphibolite comprises the upper half of the dynamothermal aureole beneath the White Hills Peridotite. It is composed entirely of amphibolite facies rocks, with the exception of a narrow zone close to the peridotite contact at Brimstone Pond (Fig. 2.21) which contains both augite and hypersthene and is therefore transitional into granulite facies rocks. A horizon of calcareous rocks occurs within the amphibolites on the Fischot Islands.

3.3.1. Petrography

The fundamental petrographic distinction between the amphibolite facies rocks of the Green Ridge Amphibolite and the epidote amphibolite and greenschist facies rocks of the Goose Cove Schist is the absence of prograde epidote in the former. The Green Ridge Amphibolite can be subdivided into "biotite", "quartz", and "plagioclase" amphibolites on the basis of petrographic characteristics (Table 3.6).

Biotite Amphibolite

The biotite amphibolite unit which separates the epidote amphibolites and quartz amphibolites on Three Mountain Summit and the Fischot Islands has been interpreted as a late-tectonic mylonite zone formed from the surrounding rocks by metasomatism (Chapter 2; Jamieson and Strong, 1978). The term "amphibolite" is a misnomer for many of these rocks, where biotite may be more abundant than hornblende, but is retained here in a loose sense to emphasize their metamorphic grade and gradational relationship with true amphibolites.

The biotite amphibolites are characterized by hornblende, biotite, garnet, plagioclase and quartz, the proportion of biotite and quartz increasing relative to hornblende with increasing intensity of deformation in the rocks. Compositional layering is defined by alternating bands of equigranular hornblende and biotite containing small euhedral garnets with circular inclusion patterns. This layering is disrupted by isoclinal folding, boudinage, and small shear zones, as biotite replaces hornblende along grain boundaries and cleavages. The typical biotite amphibolite contains vestiges of hornblende-rich layers and porphyroclasts of hornblende, garnet, and plagioclase in a fine-grained, biotite- and quartz-rich matrix (Fig. 3.36a). Ultimately, a massive rock containing scattered, rounded porphyroclasts of plagioclase, garnet, and rare hornblende, in a matrix of fine-grained biotite, quartz, and plagioclase is produced; this can be described as mylonite according to the definition of Bell and Etheridge (1973). The porphyroclastic garnet commonly contains circular or planar inclusion trails of magnetite and quartz which are not continuous with the foliation in the matrix (Fig. 3.36b). This foliation is best defined in layered rocks, where it is parallel to the compositional banding, and least well defined in the porphyroclastic rocks, where the preferred orientation of fine-grained biotite is inhomogeneously developed.

Quartz Amphibolite

Quartz amphibolite is the typical lithology of the Green Ridge Amphibolite. On the east coast of the Fischot Islands it is partially melted, and close to the peridotite contact in the western White Hills it contains assemblages transitional into hornblende granulite (Table 3.5).

The quartz amphibolites typically consist of medium- to coarse-grained green hornblende containing inclusions of quartz, sphene, ilmenite, and plagioclase, with interstitial plagioclase and quartz (Fig. 3.37). Plagioclase occurs both as anhedral, saussuritised crystals of similar size to the hornblende, and as smaller, clear, twinned matrix grains. Quartz is the most abundant matrix mineral, occurring as small grains with interlocking boundaries, or large crystals which show extensive sub-grain development. Small grains of sphene with rounded rhombic outlines are common in the lower part of the quartz amphibolites, but are replaced by ilmenite at higher grades.

On the east coast of the Fischot Islands, quartz-rich wisps and coarse-grained quartz- and feldspar-rich segregation veins occur in the amphibolites (Fig. 2.24). In the matrix to these veins, quartz blebs are very common at hornblende-plagioclase grain boundaries, commonly forming embayments into the amphibole. Within the larger segregations, zones rich in quartz and potassium feldspar with myrmekitic intergrowths surround patches rich in biotite, andesine and dark green hornblende. The veins are interpreted as partial melts of the surrounding amphibolites, while coarse-grained, quartz- and feldspar-poor amphibolites occurring on Northeast Island may represent the residual material.

Pyroxene- and brown hornblende-bearing amphibolites occurring within 75 metres of the peridotite contact at Brimstone Pond have a similar bulk composition to the quartz amphibolites, and are presumed to be their high grade equivalents. Bands of hornblende alternate with bands of granoblastic pale green clinopyroxene, defining a compositional

banding. Brown hornblende replaces pyroxene along grain boundaries and cleavages. Although a small amount of red, pleochroic hypersthene is present (Fig. 3.38), it is generally replaced by serpentine. A single sample from Lock's Cove contains garnet rather than pyroxene. The pyroxene-bearing amphibolites are transitional into granulite facies assemblages.

The main fabric of the quartz amphibolites is a foliation defined by aligned hornblende crystals, termed S_2 because it is axial planar to F_2 folds on the Fischot Islands. Elongated hornblendes, with (010) in the plane of S_2 , commonly define a lineation. Hornblende commonly assumes a subidiomorphic shape, while interstitial quartz and feldspar are anhedral and have sutured grain boundaries. The larger quartz crystals, including those in the partial melt segregations and in the coarse-grained quartz-feldspar bands north of Hare Bay (e.g. Fig. 2.25), show extensive sub-grain development.

Plagioclase Amphibolite

The third type of basic amphibolite occurs adjacent to the peridotite in the White Hills, and in the metagabbro at Wild Cove on the Fischot Islands. It is distinguished by the pale green colour of the hornblende, by the abundance of coarse-grained plagioclase (invariably saussuritized), and by the scarcity of quartz, sphene, and opaque oxides, which are generally secondary where present. Clinopyroxene, generally partially replaced by pale green hornblende, is common in the plagioclase amphibolites from the White Hills (Fig. 3.39). Locally, hornblende is zoned or mottled with a darker green to pale brown amphibole resembling the hornblende in the quartz amphibolites.

Amphibolite occurring adjacent to the peridotite at Howe Harbour has been grouped with the plagioclase amphibolites on the basis of its geochemistry and the appearance of the amphibole, although it contains no plagioclase. It consists mainly of coarse-grained, weakly foliated, pale brown hornblende, with serpentine aggregates after pyroxene. An amphibolite block from the Milan Arm Melange is also classed with the plagioclase amphibolites on the basis of its geochemistry and the abundance of plagioclase and pale brown hornblende.

A foliation, defined by the alignment of hornblende and elongated aggregates of coarse-grained plagioclase, is inhomogeneously developed in the plagioclase amphibolites (Fig. 3.39). It is weakest in rocks close to the peridotite contact, where extensive retrograde alteration, which can amount to incipient rodingitization, locally obliterates the prograde mineralogy and fabric.

Calcareous Rocks

A folded marble band about 20 cm thick occurs on the eastern side of the Fischot Islands about 25 metres above the base of the quartz amphibolite sequence. It consists of coarse-grained, granoblastic calcite and dolomite with scattered flakes of phlogopite and tremolite. It is bordered by zones of calc-silicate assemblages which grade outward into the surrounding amphibolites, and zoned calc-silicate nodules occur along strike. These contain zones in which one mineral or mineral pair predominates, the assemblage depending on the distance from the marble band or core of the nodule, and the relative amounts of calcite and quartz present.

3.3.2. Geochemistry

Ten samples of biotite amphibolite, 23 samples of quartz amphibolite, and 12 samples of plagioclase amphibolite were analysed for major and trace elements (Appendix I). These groups can be clearly distinguished on the basis of their bulk chemistry.

The differences between the quartz and plagioclase amphibolites are illustrated in Fig. 3.40. The quartz amphibolites have higher TiO_2 , FeO_T , $\text{FeO}_T/(\text{FeO}_T + \text{MgO})$, P_2O_5 , Zr, Zn, Y, and V, and lower CaO, Al_2O_3 , Cr, and Ni than the plagioclase amphibolites. The diagrams also show that although the plagioclase amphibolites share some chemical characteristics which distinguish them from the quartz amphibolites, they are not a homogeneous group. This indicates that there was more than one protolith for these rocks.

Plagioclase amphibolite from the Wild Cove metagabbro on the Fischot Islands is probably related to the mafic layers, which chemically resemble quartz amphibolite, by means of plagioclase accumulation, a relationship suggested by the high normative plagioclase of these samples. In contrast, the CaO-rich plagioclase amphibolites from the White Hills and Quirpon Island have high normative diopside, but their normative plagioclase is no higher than that of the quartz amphibolites. This suggests that the low TiO_2 , Zr, P_2O_5 , Y, Nb, and $\text{FeO}_T/(\text{FeO}_T + \text{MgO})$ reflect derivation from a different type of basaltic protolith rather than from a plagioclase-enriched equivalent of the quartz amphibolites. Amphibolite from the Milan Arm Melange is similar to the latter group except for high Ba and Rb, and alkalis, which may be the result of metasomatism from the shale matrix. The amphibolite from Howe Harbour, which does not contain plagioclase but has similar low concentrations of TiO_2 , MnO,

$\text{FeO}_T/(\text{FeO}_T + \text{MgO})$, Zr, and Y, and high MgO and Al_2O_3 , may have been derived from yet another basic protolith, or may have acquired some chemical characteristics through metasomatic reaction with the nearby peridotite.

Comparison with the data from the Goose Cove Schist shows that the quartz amphibolites are very similar to the epidote amphibolites except for the higher CaO and lower MgO of the epidote amphibolites, presumably a reflection of their mineralogy, and the lower iron oxidation ratio and alkalies of the quartz amphibolites, which probably reflect their higher metamorphic grade. The similarity suggests derivation from similar, if not identical, basaltic protoliths. The similarity is also reflected in gradational petrographic characteristics, and indicates that their separation in the field, based on differences in structural style and the presence of an intervening mylonite zone, probably does not reflect a fundamental difference in the origin of the two units.

The field relationships and mineralogy of the biotite amphibolites indicate that they are part of a syntectonic shear zone derived from the surrounding amphibolites by metasomatism. If the volume change of the rocks, or the magnitude of transfer of one of the chemical components is known, the net chemical change involved in the metasomatic reaction can be calculated, using the following equation (Gresens, 1967):

$$x_n = a \left(f_v \cdot \frac{\rho_B}{\rho_A} \right) - x_A$$

where

x_n = the change in component n

f_v = the ratio of the volume of the parent rock A to the product rock B

a = number of grams of parent rock A

ρ_A, ρ_B = density of rock A, B

X_A, X_B = concentration of component n in A, B.

Using the average compositions of the epidote, biotite, and quartz amphibolites (Table 3.7), and assuming first an isovolumetric reaction and then an isochemical reaction (Table 3.8), the composition-volume diagram of Fig. 3.41 was derived. The clustering of points on the $\Delta X_n = 0$ axis close to $f_v = 1.0$ suggests that the metasomatism was close to isovolumetric (cf. Gresens, 1967), and that SiO_2 , Al_2O_3 , TiO_2 , and MnO were essentially immobile. The calculated results for the major and trace elements using the constant volume equation are listed in Table 3.8. CaO , MgO , FeO , Na_2O , Y, and V have been lost from the amphibolites while K_2O , P_2O_5 , Ba, Rb, Zr, Nb, Cu have been added. The results for the quartz and epidote amphibolites are very similar except for the magnitude of transfer for CaO and MgO , so that the mylonite zone can be considered as having developed in rocks that were nearly chemically homogeneous.

In order to check that the calculated chemical changes are not artifacts of averaging the compositions of the parent and product rocks, all the data were plotted on variation diagrams as ratios of the elements to Al. If Al is immobile, as indicated by the above calculations, the direction of transfer of each element is indicated by the slope of the curve. In general, the graphical results derived from these diagrams are similar to the calculated results, with the exception of two samples of biotite amphibolite which appear to have undergone net addition of SiO_2 (Fig. 3.42). It is therefore concluded that the metasomatic transformation of quartz and epidote amphibolite into biotite amphibolite was isovolumetric and involved addition of K_2O , P_2O_5 , Ba, Rb, Zr, Nb,

Cu, loss of CaO, MgO, FeO, Na₂O, Y, and V, and little or no change in SiO₂, Al₂O₃, TiO₂, MnO, Sr, Cr, Zn, and Ni in most cases.

Since the protoliths of the amphibolites generally cannot be determined by direct observation, their immobile element compositions were plotted with those of the Ireland Point Volcanics, the Goose Cove Schist, and the statistically determined fields for various types of basalt (Fig. 3.43). The diagrams show some overlap between the Ireland Point Volcanics and the Green Ridge Amphibolite, but demonstrate the more "tholeiitic" character of the latter. They also emphasize the compositional gap between the plagioclase and quartz amphibolites, and the compositional differences between the Goose Cove Schist and the Green Ridge Amphibolite.

3.3.3. Mineral Chemistry

Plagioclase, hornblende, pyroxene, biotite, garnet, and oxides from the quartz, plagioclase, and biotite amphibolites were analysed. The results are listed in Appendix II.

Plagioclase

Feldspar from all three groups was analysed, but only one usable analysis was obtained from the highly altered plagioclase in the plagioclase amphibolites. The data cluster in the andesine field (Fig. 3.31), between An₃₁ and An₄₁, with a tendency towards more calcic compositions at higher grades. A compositional gap between An₂₅ and An₃₁ corresponds to the transition from epidote amphibolite to quartz amphibolite and suggests the presence of a solvus in this range analogous to the "peristerite" solvus at lower grades. There was no difference between

porphyroclastic and matrix plagioclase in the biotite amphibolites, or between plagioclase in the biotite and quartz amphibolites, indicating that metamorphic grade rather than bulk composition controls the plagioclase composition.

Amphibole

Amphiboles from the Green Ridge Amphibolite are hornblendes with $1.0 < Al^{IV} \leq 1.7$, and most cluster at the Al^{IV} -rich end of the trend that characterises the Goose Cove Schist amphiboles (Fig. 3.44). Hornblende from the quartz amphibolites is essentially identical to the epidote amphibolite hornblendes with respect to (Na +K) and Al^{IV} . Amphiboles from the plagioclase amphibolites have lower Al^{IV} , but are gradational into the quartz and epidote amphibolite hornblende compositions. The only amphiboles that diverge significantly from the tremolite- Al-pargasite join are the brown, Ti-rich hornblendes from the two-pyroxene amphibolites from Brimstone Pond. These are enriched in alkalis with respect to Al^{IV} , a trend noted in granulite facies amphiboles from the Adirondacks (Engel and Engel, 1962) and in high temperature melting experiments (Spear, 1976), suggesting a fundamental relationship between the change from amphibolite to granulite facies assemblages and the alkali content of the amphibole.

Zoned hornblendes from the biotite amphibolites show a tendency to have core compositions on the main trend and rim compositions which are enriched in Al^{IV} and $(Al^{VI} + Fe^{3+})$. This may reflect the relative enrichment in trivalent cations as Ca, Mg, Fe, and Na are lost from the rocks during metasomatism.

Figure 3.44 illustrates the increase in Ti^{4+} content of the hornblendes from the epidote amphibolites to the two-pyroxene amphibolites, coinciding with a change in colour from blue-green or green to brown. This trend is characteristic of many amphibolite facies terrains where hornblende coexists with a Ti-rich phase (e.g. Binns, 1965; Leake, 1965; Raase, 1974).

Pyroxene

Clinopyroxene occurs in both quartz and plagioclase amphibolites near the contact with the White Hills Peridotite. Hypersthene does not occur in the plagioclase amphibolites but coexists with clinopyroxene in quartz amphibolites within 30 metres of the peridotite contact at Brimstone Pond. The clinopyroxene from the quartz and plagioclase amphibolites form distinct groups in the pyroxene quadrilateral (Fig. 3.45), reflecting the different bulk compositions of the host rocks. The CaO-rich plagioclase amphibolites contain salite, $\text{Wo}_{48} \text{En}_{38} \text{Fs}_{14}$, while the quartz amphibolites contain augite, $\text{Wo}_{43} \text{En}_{38} \text{Fs}_{18}$, which coexists in one sample with hypersthene, $\text{Wo}_3 \text{En}_{57} \text{Fs}_{40}$. Relict igneous clinopyroxene, distinguished petrographically in one sample, contains less Ca than metamorphic salite in the same sample, and has a higher Mg/Fe ratio than the augite in the quartz amphibolites.

Biotite

Biotite is restricted to the mylonite at the base of the Green Ridge Amphibolite, where it occurs as a replacement product of hornblende, as inclusions in garnet, and as a matrix mineral. In general, Fe/Mg ranges from 0.9 to 2.0 and reflects the bulk rock composition,

and there are no major differences among grains in a single sample.

Garnet

Almandine, with varying proportions of spessartine and grossular, is common in the biotite amphibolites. The proportion of Mn in the garnets decreases from core to rim, a common phenomenon in metamorphic rocks, generally attributed to the strong partitioning of Mn into garnet at the early stages of growth which depletes the environment in Mn during the later stages of growth (e.g. Hollister, 1966; Tracy et al., 1976). The variability of garnet compositions in a sample of banded biotite amphibolite probably reflects compositional heterogeneity of the rock, since the garnets are all small, euhedral, and unzoned. Almandine coexists with brown hornblende in one quartz amphibolite sample from Lock's Cove.

Oxides

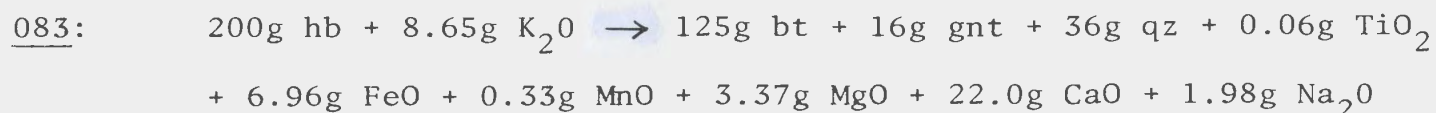
Opaque oxides are common accessories in the quartz and biotite amphibolites. The most abundant oxide is ilmenite, generally close to its ideal composition. In the amphibolites from the east coast of the Fischot Islands, the ilmenite is partially replaced by very fine-grained sphene. In the pyroxene-bearing amphibolites from Brimstone Pond, ilmenite-hematite and magnetite-ulvospinel solid solutions coexist, with magnetite greatly subordinate to ilmenite. In these rocks, there is a range of compositions from $\text{Ilm}_{87} \text{Hm}_{13}$ and $\text{Mt}_{91} \text{Uv}_9$ to nearly pure ilmenite and magnetite, suggesting that retrograde re-equilibration has occurred. The maximum temperature and oxygen fugacity estimates,

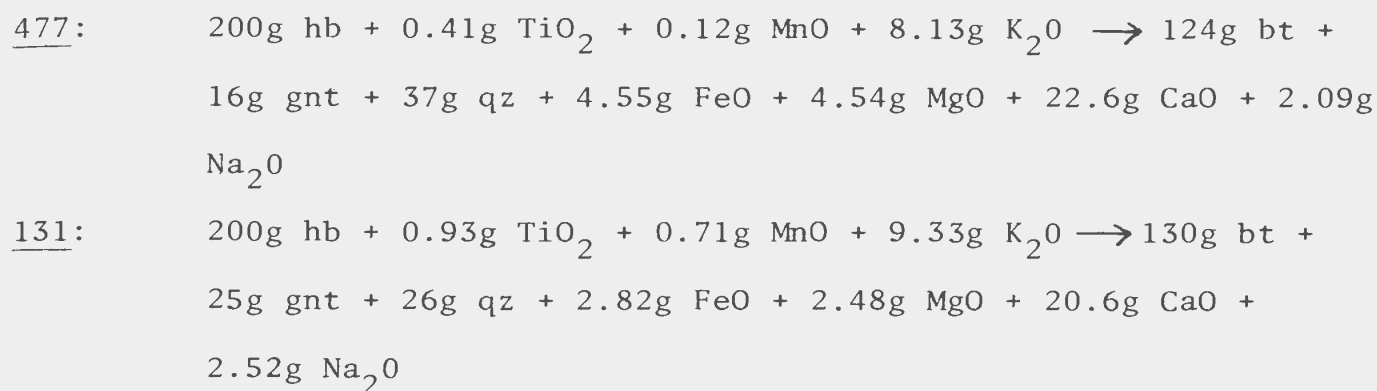
based on the calibration of Buddington and Lindsley (1964) are 600°C and $f_{O_2} = 10^{-18}$.

3.3.4. Petrogenesis

The relationships between the mineral compositions and whole rock compositions for the Green Ridge Amphibolite are illustrated in the ACF diagram of Fig. 3.46. The quartz amphibolites, which have a simple mineralogy dominated by hornblende, andesine, and quartz, plot close to the hornblende-plagioclase tie-line. The more calcic plagioclase amphibolites, which commonly contain clinopyroxene but never orthopyroxene, plot in the hornblende-plagioclase-clinopyroxene field. The biotite amphibolites, in which biotite and garnet replace hornblende as the main mafic minerals, trend towards the AF side of the diagram as a result of CaO loss during metasomatism. Relationships involving biotite in these samples are not adequately represented in this diagram, since K_2O is not considered, but in general, the mineralogy of the amphibolites reflects their bulk compositions.

In the biotite amphibolites, metasomatism has resulted in the formation of garnet and the replacement of hornblende by biotite. The mineral reactions can be treated in the same way as the bulk rock reactions using the equations given by Gresens (1967). Assuming no change in volume or in the amounts of Al_2O_3 and SiO_2 , and using representative mineral analyses from each of the three samples analysed with the electron microprobe, the following reactions can be written:

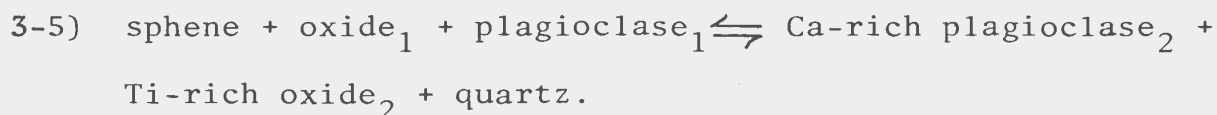




These reactions satisfactorily account for the mineralogy of the rocks, and indicate the same kinds of chemical changes as calculated from the whole rock geochemistry. The loss of CaO and addition of K₂O are particularly noteworthy.

It is difficult to identify isograds within the Green Ridge Amphibolite, because the assemblage hornblende-plagioclase is stable in basic rocks over a broad range of temperatures and pressures. The "epidote-out" isograd which marks the transition from epidote amphibolite to amphibolite facies rocks has been described in Section 3.2.4.

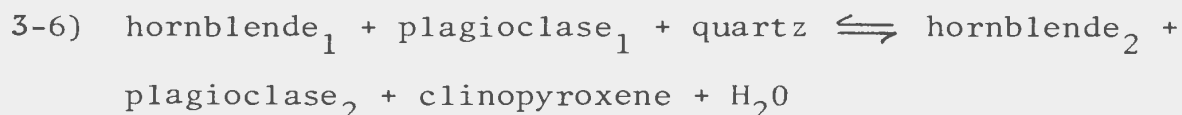
The first change in mineralogy within the amphibolites is the appearance of ilmenite at the expense of sphene, although sphene does persist at higher grades as rims and intergrowths with ilmenite. The breakdown of sphene is not associated with a change in the composition of hornblende, but may involve the formation of a more calcic plagioclase through a reaction of the type



The disappearance of sphene from high grade metabasalts has been described (e.g. Liou et al., 1974; Hunt and Kerrick, 1977) but the

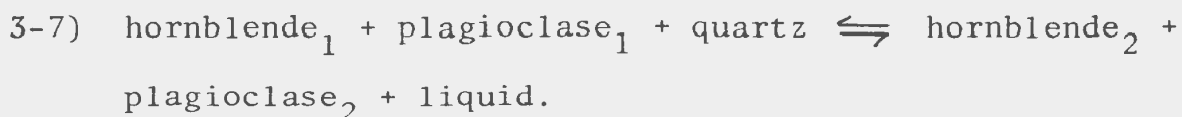
reactions involved have not been studied in detail, so that it is not possible to estimate the conditions at which the reaction occurred.

Above the "sphene-out" isograd no further change in the mineral assemblage occurs until clinopyroxene appears in the amphibolite by the reaction



The position of this isograd was not defined in the quartz amphibolites because a continuous section including both clinopyroxene-bearing and clinopyroxene-free assemblages was not studied. In the White Hills the plagioclase amphibolites generally contain clinopyroxene, so that the relative importance of metamorphic grade or bulk composition in controlling its distribution is unclear. In both quartz and plagioclase amphibolites, the clinopyroxene is replaced by hornblende, indicating a reversal of the prograde reaction.

Within the quartz amphibolites, the maximum metamorphic grade is defined by two different types of assemblage which occur in different parts of the St. Anthony Complex. On the east coast of the Fischot Islands, partial melting of amphibolite has produced leucocratic pockets rich in quartz, potassium feldspar, and plagioclase. The melting relationship can be roughly expressed by the reaction



Relevant experimental work includes studies of the melting of amphibolites (Binns, 1968, 1969; Spear, 1976) and the crystallization and melting of hydrous basaltic systems (Helz, 1973, 1976; Holloway and Burnham, 1972).

Helz (1976) gives detailed compositional and mineralogical data for equilibrium partial melting of basalt at $P_{H_2O} = P_T = 5$ kb. The melts have the following characteristics:

1) The compositions change continuously with increasing temperature: SiO_2 decreases and CaO increases in a linear fashion, FeO and MgO increase exponentially at high T and K_2O decreases exponentially at low T .

2) The melt compositions of tholeiitic basalts do not vary greatly with the starting bulk composition, except for Na/Ca which depends directly on the Na/Ca of the starting material.

3) Melts of both ne-normative and hy-normative basalts are quartz-normative and most are also corundum-normative.

4) As long as hornblende is a residual phase, f_{O_2} has little effect on the melt composition. As long as P_{H_2O} is high enough to stabilize hornblende, its value has little effect on the melt composition. However, for a given T , the amount of water available affects the degree of partial melting and thus the melt composition.

5) The melts are broadly trondhjemitic in composition.

The temperature of the beginning of melting in the Fischot Islands amphibolites is constrained by the absence of pyroxene in the residuum. This requires a maximum temperature of $785^{\circ}C$ at 2.65 kb, and a melting range of $690^{\circ}C$ to $800^{\circ}C$ at 5 kb (Binns, 1968). Helz (1976) does not report pyroxene in the residuum below $875^{\circ}C$ at 5 kb. This discrepancy would undoubtedly affect the melt compositions in the temperature range 800° - $875^{\circ}C$. The difference may be partly attributable to the starting materials -- quartz-normative metamorphic amphibolite

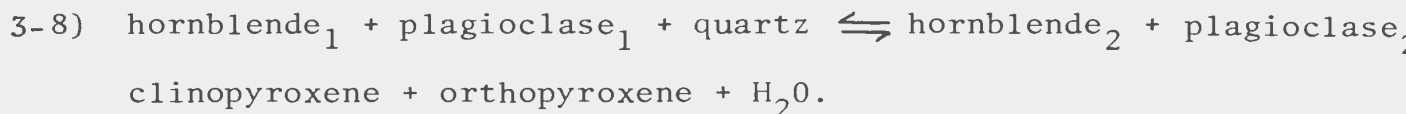
in the case of Binns (1968, 1969), and olivine- and hypersthene-normative fresh basalts with water in the case of Helz (1973, 1976). In this respect, the work of Binns (1968, 1969) is more comparable to the Fischot Islands amphibolites.

Five leucocratic bands from the Green Ridge Amphibolite were analysed. Of these, two probably represent metamorphic concentrations of quartz and feldspar since partial melting textures are absent, the feldspar compositions are similar to those in the surrounding amphibolites, and the bulk compositions are poor in incompatible elements for their high SiO_2 content. Of the two samples from the Fischot Islands, one is a relatively pure quartz-feldspar band which probably represents a segregation vein of melt from the amphibolites; the other is very rich in potassium feldspar, hornblende, and biotite, and probably represents the mixing of a small amount of melt with the surrounding amphibolite. The fifth sample was from an amphibolite block in the Milan Arm Melange, and proved to be extensively altered. Only one sample, from the segregation vein on the Fischot Islands, is discussed here.

The composition of this sample is shown in the Qz-Ab-An-Or system (Fig. 3.47), with the melt paths determined by Helz (1976). The tendency for Na/Ca to depend on bulk composition is illustrated by the Qz-Ab-An diagram. Sample 275 falls in the middle temperature range, 800-850°C, by comparison with the Picture Gorge experimental data. By comparison with the oxide data of Helz (1976), the melt composition corresponds to temperatures of 800°-825°C in terms of CaO, SiO_2 , FeO, and alkalies, and is rather higher for MgO and lower

for Al_2O_3 . These estimates correspond approximately to the maximum melt temperature of 800°C at 5 kb reported by Binns (1968) for a hornblende-bearing residuum. The sample does not contain normative corundum, but is slightly diopside-normative. Allowing for the experimental errors, the uncertainty in pressure, and the possible effects of alteration on the alkali content of the sample, temperatures of 700° to 800°C are favoured for the melting of the Fischot Islands amphibolites.

Near Brimstone Pond at the western end of the White Hills, the assemblage hornblende-clinopyroxene-orthopyroxene-plagioclase, transitional into the granulite facies, occurs. There is no evidence of partial melting in these rocks. The relationship can be expressed by the reaction



Clinopyroxene appears before orthopyroxene, but does not appear to be involved in the hypersthene-forming reaction since its composition does not change, while the hornblende composition changes markedly (Fig. 3.44). These amphibolites are olivine and hypersthene normative, although there is a range of compositions between them and the quartz-normative amphibolites of the Fischot Islands.

Experimentally determined reactions for the breakdown of amphibolite facies assemblages in basic rocks are shown in Fig. 3.48 (Binns, 1968, 1969; Spear, 1976). Also shown are the melting curves for basalt under different $P_{\text{H}_2\text{O}}$ conditions (Holloway and Burnham, 1972). The lack of partial melting textures and the presence of clinopyroxene and orthopyroxene in the Brimstone Pond amphibolites can be explained

by having P_{H_2O} less than P_T , high f_{O_2} , or by the olivine-normative character of the rocks. The first explanation seems to be the most likely, since high f_{O_2} apparently suppresses the occurrence of orthopyroxene in the rocks (Spear, 1976) and since the water-saturated melting curve for olivine tholeiite (Holloway and Burnham, 1972) is close to the curve for quartz-normative compositions (Binns, 1968). From Fig. 3.48 it is apparent that different mineral assemblages could occur at the same temperature and pressure in rocks of the same composition if P_{H_2O} is variable. Since $P_{H_2O} < P_T$ has the effect of driving the melting curve of basalt towards higher temperatures for a given pressure, and of driving the stability of the amphibolite assemblage to lower temperatures at the same pressure, $P_{H_2O} < P_T$ for the Brimstone Pond amphibolites, and $P_{H_2O} = P_T$ in the Fischot Islands amphibolites would explain the differences between them. This explanation has been advanced for the formation of granulite facies assemblages in general (e.g. Althaus, 1968).

In summary, the plagioclase and quartz amphibolites were derived from basic igneous rocks, as their widespread uniformity and compositional similarity to modern igneous rocks suggests. Some plagioclase and quartz amphibolites originated as part of a layered gabbro, but in general they appear to have been derived from different types of basic rocks. The biotite amphibolites were formed by metasomatism in a syn-tectonic mylonite zone, resulting in the formation of garnet and biotite at the expense of hornblende. Within the amphibolites, little change in mineralogy occurred until very high temperatures were achieved adjacent to the peridotite. Partial melting occurred under water-

saturated conditions on the Fischot Islands, while orthopyroxene-bearing assemblages formed under water-undersaturated conditions at Brimstone Pond.

3.4. The Long Ridge Metagabbro

The Long Ridge Metagabbro comprises the inhomogeneously deformed association of dunite, troctolite, gabbro, and anorthosite occurring just to the east of Western Long Pond. It was originally mapped as an outlier of the White Hills Peridotite (Williams et al., 1973) but is distinguished from it and the surrounding Green Ridge Amphibolite by lithology, structure, and composition.

3.4.1. Petrography

The dunite, now nearly entirely serpentized, originally consisted of olivine and chromite (Table 3.9). Olivine crystals 1 to 3 mm across, showing undulose extinction and the development of kink bands, are transected by bands of recrystallized, polygonal, nearly strain-free olivine crystals which define a foliation (Fig. 3.49). The chromite occurs as small, subhedral, opaque to slightly translucent, red-brown crystals. The large olivine crystals and the arrangement of chromite grains in bands at a high angle to the foliation suggest that the dunites are deformed cumulates.

The troctolites contain olivine, plagioclase, and minor chromite, with coronas invariably developed between the olivine and the plagioclase. The chromite occurs as small, euhedral, translucent red-brown grains. In the least altered troctolites, the coronas consist of olivine rimmed by clinopyroxene, adjacent to fibrous

amphibole rims (after orthopyroxene?) on plagioclase. In the most altered troctolites, the coronas consist of vermicular spinel intergrown with tremolitic amphibole (Fig. 3.50).

The gabbros of the Long Ridge Metagabbro range from slightly amphibolitized, undeformed rocks to strongly deformed metagabbro resembling the plagioclase amphibolites of the Green Ridge Amphibolite. The relict clinopyroxene occurs as tabular, twinned crystals incipiently altered along cleavages to fibrous amphibole, while the rims are replaced by mosaics of acicular to equidimensional tremolitic amphibole (Fig. 3.51). Rarely in olivine-bearing gabbro, clinopyroxene is rimmed by spinel-amphibole symplectite. With increasing alteration, the clinopyroxene is completely replaced by mats of randomly-oriented, subhedral, tremolitic amphibole, while in the deformed metagabbros, this amphibole forms elongated lens-shaped clusters which tend to merge into bands. The amphibole-rich bands alternate with elongated aggregates of saussuritized plagioclase to form well-foliated amphibolite. The transition from partially amphibolitized gabbro to deformed amphibolite can occur over a few centimetres. Rare granular, colourless, metamorphic, clinopyroxene occurs in the amphibolites. One amphibolitized metagabbro contains small amounts of tourmaline and corundum.

The anorthosite bands originally consisted of calcic plagioclase, but have been altered to intermediate plagioclase and clinozoisite. The plagioclase is coarse-grained andesine with deformation twins and extensive subgrain development, while the interstitial clinozoisite is generally strongly zoned.

3.4.2. Geochemistry

Nine samples from the Long Ridge Metagabbro were analysed for major and trace elements (Appendix I). The different lithologies are clearly separated on SiO_2 variation diagrams (Fig. 3.52). The dunites have very high MgO , and low Al_2O_3 , CaO , iron-magnesium ratios and alkalies, while the anorthosites have low MgO , and high Al_2O_3 , CaO , iron-magnesium ratios and alkalies. The troctolites and gabbros span the range between the two extremes. Trace element concentrations show parallel trends, with high Cr and Ni in the dunites and high Sr, Zr, and Ba in the anorthosites. The gabbros fall between the extremes with the exception of enrichment in TiO_2 , V, Cu, and Y.

Data from the White Hills Peridotite and the plagioclase amphibolite unit of the Green Ridge Amphibolite are also plotted in Fig. 3.52. The dunites from the Long Ridge Metagabbro are very similar to, although somewhat richer in FeO than, the ultrabasic rocks of the White Hills Peridotite, which is to be expected from their mineralogy. More remarkable is the similarity of the plagioclase amphibolite compositions to those of the Long Ridge Metagabbro. This supports the suggestion made on the basis of the field evidence that the metagabbros grade into the plagioclase amphibolites with increasing deformation.

3.4.3. Mineral Chemistry

Olivine, clinopyroxene, amphibole, and spinel from the Long Ridge Metagabbro dunites, troctolites, and gabbros have been analysed (Appendix II); the saussuritized plagioclase was unsuitable for analysis.

Olivine

Fresh olivine occurs in the dunite and the troctolite. The olivine in the dunite is Fo₈₉, which is less magnesian than olivine from harzburgites in the White Hills (see Section 3.5.4), but similar to olivine from the cumulate dunites of the Bay of Islands Complex (Malpas, 1976). The olivine in the troctolite is less magnesian, about Fo₈₇, which is consistent with its occurrence in a rock with a higher iron-magnesium ratio.

Clinopyroxene

The compositions of the relict igneous clinopyroxene and granular metamorphic clinopyroxene from the Long Ridge Metagabbro are shown in Fig. 3.45 with data from the plagioclase amphibolites of the Green Ridge Amphibolite and the gabbros from the Bay of Islands Complex for comparison. The igneous clinopyroxenes, including all the data from the Bay of Islands Complex, the relict pyroxenes from the Long Ridge Metagabbro, and one relict pyroxene from a plagioclase amphibolite, are characterized by decreasing Ca with increasing Fe/Mg, a pattern similar to the tholeiitic trend for clinopyroxenes. The metamorphic clinopyroxenes, including the granular pyroxene from the strongly deformed metagabbros and the pyroxenes from the plagioclase amphibolites, are characterized by high Ca which does not change greatly with increasing Fe/Mg. Clinopyroxene from the olivine-plagioclase coronas in the troctolites could belong to either group on the basis of its Ca-Fe-Mg content, but is distinguished from both by its high Al₂O₃ content (3 wt%).

Amphibole

The Long Ridge Metagabbro amphiboles are either intergrown with clinopyroxene, or occur in aggregates which can be assumed to have completely replaced clinopyroxene. On a plot of $(Na + K)$ versus Al^{IV} (Fig. 3.53), they plot parallel to but slightly below the tremolite - Al-pargasite join. The compositions range from actinolitic hornblende to common hornblende (Appendix II), and overlap with the hornblendes from the plagioclase amphibolites. They have high Mg/Fe, and low Ti, reflecting the bulk compositions of their host rocks. Hornblendes which are intergrown with clinopyroxene range from $Al^{IV} > 0.6$ to $Al^{IV} \leq 1.5$ in composition, probably reflecting disequilibrium, while hornblendes from completely amphibolitized rocks are more homogeneous, with $Al^{IV} \simeq 1.2$.

Spinel

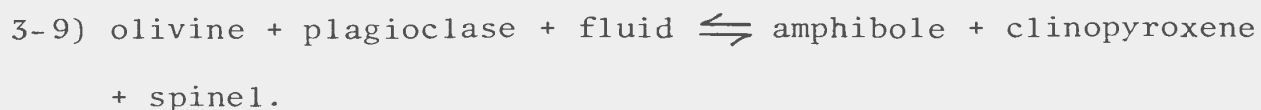
Two kinds of spinel occur in the Long Ridge Metagabbro. Chromite occurs in the dunite (Uv_1 Chr_{57} Sp_{38} Mf_4) and in the troctolite (Uv_1 Chr_{54} Sp_{44} Mf_1). The differences in composition reflect the enrichment in Fe and Al with respect to Mg and Cr in the plagioclase-bearing troctolites. Vermicular spinel intergrown with hornblende in the coronas was too fine-grained for a quantitative analysis but its composition is approximately Sp_{71} Hc_{29} (Fig. 3.68).

3.4.4. Petrogenesis

The geochemical data shown in Fig. 3.52 suggest that the Long Ridge Metagabbro is a differentiated igneous suite dominated by olivine-plagioclase-clinopyroxene equilibria. The crystallization sequence deduced from the petrographic relationships is olivine + chromite \rightarrow

olivine + chromite + plagioclase \rightarrow olivine + plagioclase + clinopyroxene \rightarrow plagioclase + clinopyroxene, with local plagioclase accumulation forming the anorthosites. This sequence is the same as that described by Malpas (1976) and is typical of the "Critical Zone" of many ophiolite complexes. This zone, termed by Malpas (1973) the "seismic Moho", is characterised by troctolites, gabbros, and anorthosites overlying a thick cumulate dunite sequence which marks the transition from the upper mantle to the lower oceanic crust. While it is present in the ophiolites of the Bay of Islands Complex, it has not been identified in the White Hills Peridotite. Since the Long Ridge Metagabbro is structurally beneath the White Hills Peridotite, it is clearly in the wrong position to represent in situ Critical Zone rocks. However, it may have originated at the oceanic crust-mantle transition, and have been caught up beneath the peridotite during its tectonic displacement from the upper mantle.

The corona structures between olivine and plagioclase indicate subsolidus re-equilibration occurred in these rocks (cf. Griffin and Heier, 1973; Gardner and Robins, 1974; Talkington and Gaudette, in prep.). Two types of coronas were produced -- one consisting of homogeneous aluminous clinopyroxene rimming olivine and fibrous amphibole rimming plagioclase, the other consisting of fibrous amphibole adjacent to both olivine and plagioclase, with interstitial amphibole-spinel symplectite. The reaction involved is of the form



In general, studies of coronitic textures developed between olivine and plagioclase in gabbroic rocks suggest that either an increase in pressure with stable or fluctuating temperature, or nearly isobaric cooling at high pressure (i.e. a very shallow slope, dP/dT) is required (Green and Ringwood, 1967; Ito and Kennedy, 1971; Griffin and Heier, 1973). Pressures of 7 to 10 kb are necessary to stabilize spinel (e.g. Kushiro and Yoder, 1966; Herzberg, 1976b). If the Long Ridge Metagabbro originally formed part of a magma chamber near the base of the oceanic crust (a depth of 5 km), as suggested by its geological setting, it must have undergone a pressure increase during cooling in order to form spinel-bearing coronites. Possibly the early displacement of the White Hills Peridotite resulted in deep burial of the Long Ridge Metagabbro, producing high pressures during cooling.

3.5. The Jacupirangite - Syenite Association

Immediately below the White Hills Peridotite on its northeastern margin occurs a suite of alkalic undersaturated rocks. The lithologies include undeformed jacupirangite and alkaline pyroxenite (titanaugite-ilmenite-apatite-kaersutite) in contact with the White Hills Peridotite, hornblende gneiss (kaersutite-albite), and syenitic mylonite (albite-clinopyroxene-olivine-amphibole) at the base of the sequence (Table 3.10), (Fig. 3.54).

The mafic rocks are characterized by very high concentrations of TiO_2 , P_2O_5 , FeO , and CaO , while the felsic rocks have high concentrations of Na_2O , Al_2O_3 , and SiO_2 (Fig. 3.55; Appendix I). The ratio $FeO_T/(FeO_T + MgO)$ remains constant throughout the sequence. High

concentrations of Zr, Ba, Rb, Nb, Sr, and Y in the mafic rocks and the occurrence of small amounts of primary carbonate suggest affinities with carbonatites. These elements are relatively depleted in the felsic rocks.

The mafic silicates are typical of those found in alkalic undersaturated rocks. The clinopyroxene and hornblende are rich in Ti, Al, and Na (Fig. 3.15 & 3.65) and the biotite is very rich in Ti (Appendix II). Feldspar is invariably close to albite in composition.

The distribution of minor and trace elements is not like the pattern expected for a strongly differentiated igneous sequence. The data do follow the pattern expected for a pair of immiscible liquids in which TiO_2 , P_2O_5 , Ba, Rb, Zr, and other trace elements are strongly partitioned into the mafic liquid (in this case, jacupirangite) while Na_2O , SiO_2 , and Al_2O_3 are strongly partitioned into the felsic liquid (in this case, syenite) (Watson, 1976). The AFM plot of Fig. 3.56 supports this hypothesis -- the mafic and felsic rocks plot on opposite sides of the natural liquid immiscibility field delineated by Philpotts (1976) and along trends similar to those found in lunar basalts which show immiscible behaviour at late stages in their differentiation histories (Rutherford et al., 1974). It is concluded that the jacupirangite-syenite suite originated as part of an alkalic igneous complex, which may originally have included carbonatite, and which underwent fractionation by liquid immiscibility. Its petrological history appears to have had nothing to do with the White Hills Peridotite with which it is now structurally associated. For a more detailed discussion, see Appendix IV (Jamieson and Talkington, in prep.).

3.6. The White Hills Peridotite

The White Hills Peridotite consists of harzburgite, dunite, lherzolite, and rare gabbro, with a complex igneous, metamorphic, and structural history pre-dating the transport of the peridotite and its emplacement with the St. Anthony Complex. By analogy with the Bay of Islands ophiolite complex, it is assumed here that the ultramafic rocks represent a slice of upper oceanic mantle. The following discussion focusses on the basal contact zone of the White Hills Peridotite, where the development of isoclinal folding, a mylonitic fabric, and distinctive mineral assemblages suggests that the emplacement of the peridotite was accompanied by extensive recrystallization in the contact zone.

3.6.1. Petrography

The typical lithology of the White Hills Peridotite is porphyroclastic harzburgite (Table 3.11). Enstatite, elongated along (100) slip planes, occurs in a matrix of medium-grained olivine crystals which are elongated parallel to the foliation (S_{P1}) and have well-developed kink bands and ragged grain boundaries. The enstatites contain diopside exsolution lamellae parallel to (100), and are commonly surrounded by a fine-grained aggregate of enstatite and diopside. Locally, lherzolite containing medium-grained diopside occurs, but clinopyroxene is generally present only in trace amounts associated with orthopyroxene. Interstitial brown spinel, with the characteristic "holly leaf" texture described by Mercier and Nicolas (1975), is common.

Within 30 metres of the basal contact, a mylonitic texture is developed in the peridotite. The grain size of the matrix olivine

decreases until only a few large, deformed olivine crystals remain in a matrix of minute, irregular, elongated grains. Enstatite, surrounded by fine-grained aggregates of ortho- and clinopyroxene, is greatly elongated parallel to (100) (Fig. 3.57). The mylonitization results in a bimodal grain size distribution, with porphyroclasts, generally enstatite (5 to 20 mm), in a very fine-grained matrix ($50 - 100\mu$). The enstatite porphyroclasts contain diopside exsolution lamellae, as well as elongated olivine inclusions and embayments of olivine from the matrix. Clinopyroxene, optically indistinguishable from olivine in the fine-grained matrix, was detected by XRD (J. Vahtra, pers. comm., 1978).

Plagioclase and pargasite occur locally in the basal peridotites. In one sample, plagioclase exsolution lamellae occur with diopside along (100) in enstatite, and anhedral plagioclase in the matrix is associated with aggregates of enstatite crystals (Fig. 3.58). Pargasite, concentrated in thin, monomineralic, coarse-grained sheets parallel to the S_{p2} foliation, is common within 10 metres of the basal contact (Fig. 3.59). These amphibole bands commonly have developed a "pinch and swell" structure with clusters of large (2-5 mm) crystals connected by stringers of smaller ones, so that the formation of the amphibole pre-dates the S_{p2} deformation. The pargasite generally occurs in lherzolite, where it is associated with olive-green spinel, diopside, and small flakes of phlogopite, but it is locally present in brown spinel-bearing harzburgites. Where the pargasite-bearing peridotites are serpentinized, brown bands of unaltered phlogopite and amphibole alternate with grey bands of serpentine, forming the

banded ultramafic mylonites described by Williams and Smyth (1973).

Locally, deformed gabbroic rocks characterized by plagioclase, clinopyroxene, and green spinel occur in the contact zone. Near the southern end of Western Long Pond, an isoclinally folded, fine-grained band occurring about 20 m above the contact contains abundant orthopyroxene, and pale green spinel that is concentrated in bands parallel to the folded S_{p1} foliation. Equidimensional clinopyroxene and orthopyroxene which contains fine diopside lamellae occur in a matrix of granular pyroxene and saussuritized plagioclase. Near the northern end of Eastern Long Pond, a mylonitic gabbroic band occurring adjacent to the basal contact contains rare orthopyroxene, abundant brown pargasite, and porphyroclasts of bottle-green spinel containing inclusions of magnetite and exsolution lamellae of hematite. The pargasite occurs both as irregular crystals replacing clinopyroxene, and in discrete bands associated with magnetite.

Post-kinematic low-grade metamorphism has affected the peridotite in the contact zone. Fine-grained talc, locally overgrown by acicular tremolite, may totally replace enstatite and also occurs as veins. Brown spinel is replaced along cracks by opaque oxides and surrounded by zones of fine-grained magnetite and colourless chlorite. Most of the contact zone peridotite has been pervasively serpentized, with pargasite the only ferromagnesian mineral unaffected by the alteration. These secondary minerals are undeformed, overgrowing the mylonitic fabric.

3.6.2. Geochemistry

Twelve peridotites, including three from the contact zone,

one pyroxenite, and one gabbroic mylonite were analysed (Appendix I). Variation diagrams against MgO show that the basal zone peridotites are lherzolitic in composition, with slightly higher Al_2O_3 and CaO, and lower MgO and Ni than the typical White Hills harzburgite (Fig. 3.60). Pargasite-rich peridotite from the contact has anomalously high alkalis, but for all other components plots between lherzolite and pyroxenite. A projection from Mg_2SiO_4 onto the plane CaSiO_3 - MgSiO_3 - Al_2O_3 in the system $\text{CaO-MgO-Al}_2\text{O}_3\text{-SiO}_2$ (O'Hara, 1968) (Fig. 3.61) shows a trend from dunite to pyroxenite and from enstatite-rich compositions toward diopside, with a slight enrichment in the A component of the serpentinized (magnetite-rich) dunites. The contact zone rocks plot with lherzolite at the CaSiO_3 -rich end of the trend, with the pargasite-rich lherzolite falling directly on the line joining the harzburgites and the pyroxenite.

The geochemical data suggest that the ultramafic mylonites of the contact zone were originally lherzolites, or that the pyroxenite bands which are common in the interior of the peridotite massif have become tectonically mixed with harzburgite in the basal zone. Williams and Smyth (in press) describe the basal mylonites as consisting of interleaved amphibolite and peridotite. However, in Fig 3.61, which shows the field of Green Ridge Amphibolite compositions plotted with the peridotite data, the compositions of the contact zone rocks clearly trend toward pyroxenite rather than amphibolite. It is considered more likely that the amphibole in the basal mylonites originated in situ, and that its resistance to alteration, in contrast to its olivine-rich matrix, explains the appearance of the black and white banded

mylonites which occur locally in the eastern White Hills, on the shores of Howe Harbour, and in the Milan Arm Melange. The alkali enrichment in the pargasite-bearing mylonites may be the result of metasomatism from the amphibolites of the aureole, but probably was introduced with the fluid at the time the amphibole was formed.

3.4.3. Mineral Chemistry

Olivine, orthopyroxene, clinopyroxene, spinel, plagioclase, amphibole, phlogopite, and chlorite from 5 basal zone samples were analysed and compared with data from the interior of the White Hills Peridotite and from other Alpine peridotites.

Olivine

All the White Hills Peridotite samples analysed contain magnesian olivine, Fo_{88} to Fo_{89} . This is similar to, although somewhat less forsteritic than, olivine from most Alpine peridotites (e.g. Thayer, 1967), but resembles olivine from the Bay of Islands lherzolites (Malpas, 1976) and reflects the bulk compositions of the rocks.

Orthopyroxene

The orthopyroxene is magnesian bronzite, ranging from $\text{Wo}_1 \text{En}_{89} \text{Fs}_{10}$ to $\text{Wo}_1 \text{En}_{86} \text{Fs}_{13}$. A few more calcic compositions are attributable to the inclusion of very small diopside exsolution lamellae in some analyses. It is more similar to orthopyroxene from lherzolites than the enstatite from most Alpine peridotites (harzburgites) (Malpas, 1976; Dick, 1977).

The White Hills orthopyroxene compositions are plotted with some analyses from the Lizard (Green, 1964c), the Bay of Islands (Malpas,

1976) and the Ronda (Dickey, 1970) peridotites in Fig. 3.62 and 3.63. The White Hills orthopyroxenes are similar to lherzolitic orthopyroxenes from the other peridotites, with the exception of the Ca-rich compositions from the Lizard (attributable to the inclusion of diopside lamellae in the mineral separates used for the analyses). There is a slight tendency for Ca to increase with increasing Fe/Mg, a trend also observed by Dick (1977). Since high Fe/Mg ought to correspond to a lower temperature pyroxene, while the pyroxene solvus shows that enstatite is slightly enriched in Ca at high temperature (e.g. Davis and Boyd, 1966; Dixon and Presnall, 1977), this contradicts the expected equilibrium behaviour. The trend has been interpreted as the result of partial melting, which would deplete the orthopyroxene in Fe, Ca, and Al (Dick, 1977).

Figure 3.62 shows a plot of Al_2O_3 versus $\text{Mg}/(\text{Mg} + \text{Fe}_T)$ in the orthopyroxene compared with data presented by Dick (1977), Malpas (1976), Green (1964c), and Dickey (1970). The White Hills enstatites are rich in Al_2O_3 , and fall into two groups. One group, with higher $\text{Mg}/(\text{Mg} + \text{Fe}_T)$ plots close to the Bay of Islands, Lizard, and Ronda data, and at the high temperature end of the trend shown by Dick (1977) except for somewhat lower $\text{Mg}/(\text{Mg} + \text{Fe}_T)$. The second group includes only orthopyroxene from the pargasite-rich peridotite and the folded gabbroic band, and has low $\text{Mg}/(\text{Mg} + \text{Fe}_T)$ for its Al_2O_3 content, suggesting a control of the orthopyroxene composition by the coexisting mineral assemblage, and by bulk composition.

Figures 3.62 and 3.63 also illustrate the enrichment of the orthopyroxene cores in Al_2O_3 with respect to the rim and matrix

compositions, while there is no difference in Fe, Mg and only slight enrichment in Ca. However, greater Ca enrichment in the cores would be observed if the exsolved diopside lamellae were recalculated with the enstatite to give a homogeneous pyroxene. The pyroxene which is exsolving plagioclase has the same composition as plagioclase-free pyroxene.

Clinopyroxene

Clinopyroxene compositions are more variable (Fig. 3.63). Diopside in exsolution lamellae and from the interior of the peridotite is enriched in Ca and Al relative to diopside from the recrystallized matrix of the contact zone peridotites. Diopside from the folded, orthopyroxene-bearing gabbroic band is similar to the recrystallized clinopyroxene while the clinopyroxene from the amphibole-rich gabbroic band is rich in Fe and Al, reflecting the bulk composition of the rock.

There are regular changes in $Mg/(Mg + Fe_T)$ in coexisting ortho- and clino-pyroxenes which correspond broadly to the changes in bulk composition from harzburgite to gabbro (Fig. 3.63). There is a pattern of Ca-poor clinopyroxene coexisting with Ca-rich orthopyroxene for core, rim, and matrix compositions. This reflects the shape of the pyroxene solvus in the $CaO-MgO-Al_2O_3-SiO_2$ system (e.g. Dixon and Presnall, 1977).

Spinel

Aluminous, magnesium-rich spinels occur in the basal zone of the White Hills Peridotite (Fig. 3.64). $Mg/(Mg + Fe_T)$ averages about

0.7, and $\text{Cr}/(\text{Cr} + \text{Al})$ averages about 0.13. Exceptions are the slightly Fe-enriched brown spinels from the harzburgite adjacent to the folded gabbroic band. The compositions of the green spinels in the gabbroic bands reflect the bulk compositions of the rocks, with low $\text{Cr}/(\text{Cr} + \text{Al})$ (0 - .02) and variable, low $\text{Mg}/(\text{Mg} + \text{Fe}_T)$, and are similar to the vermicular green spinel of the Long Ridge Metagabbro.

The spinel compositions contrast sharply with the Cr-rich spinels from harzburgites in the White Hills Peridotite (R. Talkington, pers. comm., 1978) and other Alpine peridotites, and with chromite from the Long Ridge Metagabbro. The compositions are more similar to lherzolitic spinels, but the low $\text{Cr}/(\text{Cr} + \text{Al})$ resembles the composition of spinel in the granulite facies, amphibole-bearing, metaperidotites of the Finero Complex (Medaris, 1975).

In one sample, brown spinel is replaced by magnetite and chlorite. The relict spinel cores are essentially identical to the unaltered spinels from other basal zone peridotites. Semi-quantitative analyses of the opaque veins within the altered spinel give a magnesioferrite-rich composition ($\text{Chr}_{24}\text{Sp}_{20}\text{Mf}_{49}\text{Mt}_6$) while the opaque rims bordering the spinel are closer to magnetite ($\text{Chr}_{12}\text{Sp}_5\text{Hc}_2\text{Mt}_{80}$).

Amphibole

The orange-brown amphiboles from the basal zone of the White Hills Peridotite are Ti-rich pargasites with compositions close to $\text{K}_{0.2}\text{Na}_{0.7}(\text{Na}_{0.1}\text{Ca}_{1.9})\text{Fe}_{0.5}\text{Mg}_{3.5}\text{Ti}_{0.3}\text{Al}_{0.6}(\text{Si}_6\text{Al}_2)\text{O}_{22}(\text{OH})_2$. High Ti and low Mg/Fe in hornblende from a gabbroic band reflect the bulk composition of the rock. They have higher Mg/Fe and (Na + K) than

the brown hornblende from the Green Ridge Amphibolite. The compositions plot close to pargasite in terms of (Na + K) and Al^{IV} (Fig. 3.65), and are well removed from the amphibolite facies hornblendes although they might be considered the end of the trend towards pargasite displayed by the pyroxene-bearing rocks in the contact zone of the Green Ridge Amphibolite. The differences support the suggestion, based on the geochemistry of the rocks, that the amphibole bands are part of the peridotite assemblage and do not result from interleaving of peridotite and amphibolite in the contact zone.

One sample contains tremolite ($Na_{0.1} Ca_{1.9} Mg_{4.8} Fe_{0.2} Si_8 O_{22} (OH)_2$) overgrowing talc, clearly the result of post-tectonic metamorphism.

The composition of the pargasite is more similar to primary amphibole from lherzolite xenoliths and St. Paul's Rocks (e.g. Melson et al., 1972; Francis, 1976) than to amphibole from metaperidotite (Trommsdorf and Evans, 1972; Springer, 1974; Rice et al., 1974). It has higher (Na + K) and Ti than the pargasite in the recrystallized marginal zones of the Lizard peridotite. This compositional difference, and the petrographic observation that the amphibole bands are deformed, suggest that the pargasite is a primary phase.

Phlogopite

Amphibole-rich bands in the peridotites adjacent to the contact contain flakes of Ti-rich phlogopite with the structural formula $K_{1.5} (Na_{0.2} Fe_{0.6} Mg_{4.4}) (Ti_{0.5} Cr_{0.1} Al_{0.2}) (Al_{2.7} Si_{5.3}) O_{20} (OH)_4$.

Feldspar

Plagioclase occurs as exsolution lamellae in enstatite in one contact zone peridotite, and is a common matrix phase in the gabbroic bands. In the peridotite, the plagioclase is fresh, unzoned andesine, with a composition close to An_{45} in both the exsolution lamellae and the matrix. Plagioclase exsolved from pyroxene is commonly of sodic or intermediate composition (Dickey, 1970; Morse, 1975; Emslie, 1975) due to the instability of Na in the pyroxene structure at $P < 18$ kb (e.g. Kushiro, 1969). Plagioclase in the amphibole-rich gabbroic band is sodic labradorite, An_{53} .

Chlorite

Chlorite and magnetite commonly replace spinel in the contact zone. The chlorite is nearly homogeneous penninite (using the classification of Deer et al., 1970, p. 233) with the formula $Mg_{9.4} Fe_{0.6} Al_{1.8} Si_{6.4} O_{20} (OH)_6$ and trace amounts of Cr, Ni, and alkalis.

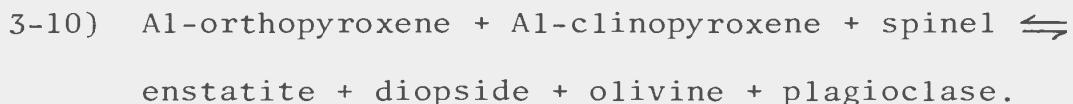
3.4.4. Petrogenesis

In general, the mineralogy of the mylonitic basal peridotites appears to be inherited from an original high temperature-high pressure lherzolite (cf. Malpas, 1976; Dick, 1977; Melson et al., 1972). However, the restriction of pargasite and plagioclase to the basal mylonites, and the formation of post-tectonic talc, tremolite, chlorite, and serpentine require further explanation.

The deformation of the pargasite bands in the ultramafic mylonites indicates a pre- or syn-emplacement (S_{p2}) origin for the amphibole. Melson et al. (1972) concluded that similar pargasite bands

in peridotite mylonites from St. Paul's Rocks formed from normal lherzolites in the presence of limited amounts of water. Since pargasite locally is observed to replace clinopyroxene, and the bulk composition of the amphibole lherzolites is not greatly different from amphibole-free lherzolites, this explanation is considered likely for the White Hills Peridotite as well. Its restriction to the contact zone probably indicates a syn-tectonic origin by replacement of clinopyroxene during the early stages of peridotite displacement. $^{40}\text{Ar}/^{39}\text{Ar}$ dating of similar amphiboles from the ultramafic mylonites at the base of the Bay of Islands Complex gave an age of 477 ± 10 Ma, compared to amphiboles from basic amphibolites which gave ages of 458 ± 10 Ma and 468 ± 10 Ma (Dallmeyer and Williams, 1975). The results are consistent with a syntectonic origin for the pargasite.

The exsolution of plagioclase from enstatite in the basal zone of the White Hills Peridotite indicates that the following reaction is occurring:



Experimental studies in the system $\text{CaO-MgO-Al}_2\text{O}_3\text{-SiO}_2$ show that the reaction is nearly isobaric at 8.5 kb (Herzberg, 1976b, 1978) but that in Na_2O -bearing systems it is displaced to higher pressures (Green and Hibberson, 1970; Emslie, 1970). Above 10.5 kb, sodic plagioclase may coexist with spinel (Herzberg, 1976a). The experimental results plotted in Fig. 3.66 suggest that the plagioclase exsolved from orthopyroxene in the pressure range 8 to 11 kb as the result of upward displacement of the peridotite. The restriction of exsolved plagioclase to the

basal mylonites may reflect reaction kinetics. Wilshire and Jackson (1975) showed that redistribution of Al_2O_3 in pyroxene could occur in response to strain. In the case of the White Hills Peridotite, the deformation of the rocks in the contact zone may have promoted Al_2O_3 mobility and resulted in local exsolution of plagioclase, while plagioclase was not formed in less deformed rocks of similar bulk composition and under similar ambient pressure and temperature conditions.

Gabbro bands in the eastern part of the White Hills Peridotite contain green spinel forming at the expense of plagioclase and clinopyroxene (R. W. Talkington, pers. comm., 1978). The same reaction is probably responsible for the presence of green spinel in the gabbroic bands at the base of the White Hills Peridotite, where deformation has destroyed the original textural relationships among the minerals. In one sample, amphibole commonly replaces clinopyroxene. The mineral assemblages are similar to those in the coronitic metagabbros of the Long Ridge Complex, suggesting recrystallization under granulite facies conditions.

The compositions of olivine, enstatite, and amphibole in unserpentinized basal peridotites are richer in iron than those of phases formed by deserpentinization (cf. Trommsdorf and Evans, 1972; Frost, 1975; Vance and Dungan, 1977) and it is therefore concluded that the rocks were not serpentinized prior to their emplacement.

Within 5 metres of the basal contact, post-tectonic talc and tremolite replace orthopyroxene, and chlorite and magnetite replace spinel. With $P_{\text{H}_2\text{O}} = P_{\text{TOT}}$, the assemblage talc-chlorite-magnetite would be stable in the temperature range 550° to 700°C (Springer, 1974). Below 550°C , serpentinization would take place. This suggests that

the cooling of the contact zone peridotites to temperatures below 700°C began only after the deformation had ceased, and that cooling proceeded slowly enough to permit talc-bearing retrograde assemblages to form before pervasive serpentinization occurred.

3.7. Discussion

Although there is a continuous range in metamorphic grade within the St. Anthony Complex from low greenschist to low granulite facies, pre-metamorphic lithological discontinuities have been recognized on the basis of geochemistry, and a major post-metamorphic structural discontinuity has been identified. The transition from the Ireland Point Volcanics to the Goose Cove Schist is apparently gradational in terms of metamorphism (the actinolite-in isograd) and lithology, although in the lower part of the Goose Cove Schist there is a lateral change from metabasites to metasediments. However, the transition from the greenschist to the epidote amphibolite facies (the chlorite-out isograd) approximately coincides with a change in the bulk composition of the metabasites, indicating a cryptic lithological discontinuity at this level. The Goose Cove Schist is separated from the Green Ridge Amphibolite by a mylonite zone which is localized at the level of the epidote-out isograd. Although the mylonite is a prominent structural discontinuity, the surrounding rocks originally represented a continuous lithological, and gradational metamorphic, sequence. Another lithological discontinuity occurs near the top of the Green Ridge Amphibolite, where quartz amphibolite gives way to plagioclase amphibolite adjacent to the contact with the White Hills Peridotite.

Therefore, the dynamothermal aureole beneath the White Hills Peridotite was not superimposed upon an originally continuous sequence of rocks, but must have been assembled in the course of metamorphism.

The following chapter attempts to determine a pressure and temperature gradient through the St. Anthony Complex, and to combine this with the lithological and petrological evidence to reconstruct its syn-tectonic history.

CHAPTER 4. THE THERMAL STRUCTURE OF THE ST. ANTHONY COMPLEX

The field and petrological data described in the preceding chapters can be synthesized to produce cross-sections of the aureole in which the positions of isograds, and metamorphic pressures and temperatures, where known, can be shown. These cross-sections summarize the data and give a detailed picture of the apparent thermal gradient preserved in the metamorphic rocks of the St. Anthony Complex. Theoretical models of temperature distribution in the aureole can then be compared with the observed gradient.

4.1. Geothermometry and Geobarometry

The compositions of key minerals or mineral assemblages can be used to define pressures, temperatures, or P-T paths in metamorphic rocks, subject to the following assumptions and limitations:

(1) The mineral assemblages considered were in equilibrium at the time of their formation, and the measured compositions have not been affected by later events. This can be tested to some degree by petrographic observations and by examining the mineral assemblages for compositional homogeneity. If equilibrium has been achieved on only a local scale (e.g. in compositional metadomains) this must be considered before the results are extrapolated to an entire sequence of rocks.

(2) The constraints of the experimental calibrations to which the data are compared must be met by the natural example as closely as possible. The simpler the system, the more useful the data are likely to be.

(3) If complex mineral assemblages giving P-T paths are used, more than one set is required to fix the metamorphic conditions.

4.1.1. The Ireland Point Volcanics

In order to model the thermal gradient through the aureole, it is necessary to estimate the pre-tectonic temperature of the rocks over which the peridotite was emplaced. An approximation to this can be reached by examination of the secondary mineral assemblages in the Ireland Point Volcanics. A pre-emplacement age for the low-grade metamorphism of these rocks is indicated by the occurrence of altered fragments of vesicular basalt in deformed pillow breccias and the deformation of epidote veins in altered volcanic rocks along the east side of Stark's Bight. However, since the Ireland Point Volcanics have not been established as the protoliths for the Green Ridge Amphibolite, the temperature estimates based on their metamorphic assemblages are valid only for the pre-emplacement conditions in the Goose Cove Schist.

The Cape Onion Volcanics, which are well-removed from the effects of the dynamothermal metamorphism, contain secondary calcite and chlorite with minor prehnite (DeLong, 1976). Epidote is rare, and actinolite is absent. These observations suggest temperatures of about 300°C and pressures of less than 2 kb (Fig. 4.1) (Nitsch, 1971; Schermerhorn, 1975). The Ireland Point Volcanics below the transition to the Goose Cove Schist contain calcite, chlorite, and epidote, with prehnite and pumpellyite absent. Actinolite does not occur in the undeformed volcanics, and its appearance approximately coincides with the obliteration of the volcanic structures which has been used to define the transition from

the Ireland Point Volcanics to the Goose Cove Schist. This fixes the maximum pre-tectonic temperature at about 360°C and the pressure at less than 2 kb (Nitsch, 1971). However, the presence of abundant calcite in veins, vesicles, and the groundmass of the volcanic rocks suggests a high partial pressure of CO₂. This would suppress the appearance of prehnite and pumpellyite (Glassley, 1974), but apparently does not greatly affect the stability of actinolite. Thus the minimum pre-tectonic temperature may have been considerably less than the 300°C suggested by the rarity of prehnite and pumpellyite in the Cape Onion Volcanics, but the maximum pre-tectonic temperature probably did not exceed 360°C, as suggested by the absence of actinolite in the Ireland Point Volcanics.

On the basis of these observations, a temperature of 360°C for the base of the Goose Cove Schist is shown in the thermal profiles (Fig. 4.5-4.8) and temperatures of 250°C, 300°C, and 350°C are used in the theoretical models to span the range of likely pre-tectonic conditions.

4.1.2. The Goose Cove Schist

The Goose Cove Schist consists of greenschist and epidote amphibolite facies rocks containing epidote, actinolite or hornblende, chlorite, albite or oligoclase, and commonly calcite or quartz in basic rocks. Its lower limit is defined by the penetrative deformation and the appearance of actinolite, the chlorite-out isograd occurs within the sequence, and the epidote-out isograd approximately coincides with the top of the sequence. In metasedimentary rocks, biotite replaces chlorite and muscovite in the upper greenschist facies. Mineral assemblages

within the Goose Cove Schist are not good indicators of metamorphic conditions, since the isograds are actually zones in which the compositions of the complex mineral solid solutions change over intervals which depend on P, T, bulk composition, f_{O_2} , and P_{H_2O} . In the absence of an independent geothermometer or geobarometer, P-T ranges must be used.

The thermal gradient suggested below for the Goose Cove Schist is based entirely on assemblages in metabasic rocks, which occur throughout the metamorphic sequence north of Hare Bay. In the metasedimentary rocks, even where they are most common on the Fischot Islands, mineral assemblages diagnostic of particular pressures and temperatures do not occur.

The appearance of actinolite at the base of the Goose Cove Schist indicates a temperature of about 360°C (Nitsch, 1971). The chlorite-out isograd ranges from 450°C to 550°C in the pressure range 1.5 to 4.5 kb, but is nearly isothermal at 550°C above 2.5 kb (Liou et al., 1974; Fig. 3.35). The epidote-out isograd (NNO buffer) varies from 550°C to 650°C for the same pressure interval. In the absence of an independent pressure estimate, a value of 550°C for the disappearance of chlorite, and an intermediate value of 600°C for the disappearance of epidote are assumed.

The chlorite-biotite reaction in metasedimentary rocks is dependent on many factors such as the composition of the coexisting muscovite and chlorite, and the values of P_{H_2O} and P_{CO_2} (e.g. Mather, 1970). In the Goose Cove Schist it falls between the actinolite-in and the chlorite-out isograds of the metabasic rocks, that is, in the range

350° to 550°C. Naggar and Atherton (1970) estimated a temperature of about 500°C for the disappearance of chlorite in pelitic rocks which also contained cordierite and staurolite. However, these minerals are absent from the psammites and semi-pelites of the Goose Cove Schist, suggesting lower temperatures and a reaction of the form muscovite + chlorite \rightleftharpoons biotite. Small garnets in the lower part of the meta-sedimentary sequence are probably spessartine produced at about 400°C, while the absence of garnet in metasediments close to the chlorite-out isograd near Three Mountain Summit suggests temperatures of less than 525°C (cf. Naggar and Atherton, 1970). These temperatures are consistent with the positions of the rocks relative to the metabasites.

4.1.3. The Green Ridge Amphibolite

Within the Green Ridge Amphibolite, the most useful minerals and mineral assemblages for geothermometry and geobarometry are the biotite-garnet pairs of the biotite amphibolite, the calcite-dolomite pairs in the marble band on the Fischot Islands, the two-pyroxene assemblages from the Brimstone Pond area, and the partial melts on the eastern side of the Fischot Islands.

The biotite amphibolites contain biotite and garnet which have formed together at the expense of hornblende. Geothermometers based on K_D (Fe, Mg) for garnet-biotite pairs have been calibrated by Perchuk (1970), Thompson (1976), and Ferry and Spear (1978). The data from the St. Anthony Complex are plotted in the diagrams given by these authors (Fig. 4.2) and the resulting temperature estimates are given in Table 4.1. The estimates are generally comparable within the error of

the method, although the experimental results of Ferry and Spear (1978) give lower temperatures at high K_D and higher temperatures at low K_D . Average temperatures are used except for Mn-rich garnet cores which are compensated for only by the calibration of Perchuk (1970).

Sample 131, a typical biotite amphibolite from near the top of Three Mountain Summit, contains garnet, plagioclase, and hornblende porphyroclasts in a fine-grained, biotite-rich matrix. The cores of garnets containing biotite inclusions give temperatures of 610°C and matrix garnet-biotite pairs give estimates of 625°C ; the rims of the garnet porphyroclasts give estimates of 571°C . Sample 477 is a layered biotite amphibolite from near the base of the mylonite zone on Whale Grotto Mountain. Small euhedral garnets in biotite-rich bands give temperatures ranging from 482° to 381°C . Sample 083 is a hornblende-rich biotite amphibolite from the lower margin of the mylonite zone on Three Mountain Summit, and gives a temperature estimate of 449°C . The range of temperature estimates is consistent with the model that the biotite amphibolites formed a mylonite zone which was initiated during the metamorphism of the St. Anthony Complex and continued to act as a zone of high strain and metasomatism after the peak of metamorphism had passed.

The marble and calc-silicate horizon which occurs about 25 metres above the base of the quartz amphibolite unit on the Fischot Islands provides reliable temperature data for the lower part of the Green Ridge Amphibolite. The marble contains equidimensional Mg-calcite and dolomite with polygonal grain boundaries, suggesting that equilibrium was reached. Temperatures were estimated using the equation given by

Rice (1977), based on the combined data of Graf and Goldsmith (1965) and Goldsmith and Newton (1969) for the calcite-dolomite solvus. The results are shown in Table 4.2. A range of MgCO_3 solution in calcite was observed within individual grains, probably reflecting later re-equilibration, and yielding calculated temperatures of 486° to 842°C . However, there is a definite cluster of compositions, including grain averages, at $x_{\text{MgCO}_3}^{\text{cal}} \simeq 0.1$, with an overall average of $x_{\text{MgCO}_3}^{\text{cal}} = 0.106$. The average gives a temperature estimate of 682°C , which is probably accurate within 50°C .

The assemblages in the zoned calc-silicate bands adjacent to the marble can be used to estimate pressure in a qualitative way. Since they are zoned they do not represent equilibrium assemblages, but stages of a metasomatic reaction between the marble and the surrounding amphibolite. Since the relevant reactions shift to higher temperature with increasing pressure, and the temperature is known to be about 680°C , pressure can be estimated from experimental work on mixed-volatile "impure marble" systems. The highest grade assemblages in these rocks contain diopside but no forsterite. This indicates temperatures of 500°C at 0.5 kb and 650°C at 5 kb (Hunt and Kerrick, 1977). On this basis, a pressure of close to 5 kb is favoured, and pressures of less than 3 kb are unlikely.

The occurrence of partially melted amphibolite along the east coast of the Fischot Islands can be used to estimate temperatures. Comparison with the experimental work of Helz (1976), Binns (1968, 1969), and Holloway and Burnham (1972), discussed in Chapter 3, indicates that the melting occurred in the range 700° to 800°C at pressures of

4 to 5 kb. The lower temperature, representing the beginning of melting, is in good agreement with the temperature of 680°C for the marble band which occurs close to partially melted amphibolites.

The temperature within 25 metres of the contact between the Green Ridge Amphibolite and the White Hills Peridotite was estimated using the compositions of coexisting hypersthene and augite in the transitional hornblende granulites near Brimstone Pond at the western end of the White Hills. Experimental and theoretical work on the pyroxene solvus (e.g. Davis and Boyd, 1966; Wood and Banno, 1973; Wells, 1977; Mori, 1977; Powell, 1978; Herzberg, 1978) indicates that although there are limitations, pyroxene geothermometry gives geologically reasonable results. The calibration of Wells (1977), using a combination of recent experimental work and data from natural samples where independent temperature estimates were available, seems to be one of the most consistent. The results using this calibration are listed in Table 4.3. Temperatures of 849° to 869°C were calculated for the hypersthene-augite pair of sample 552. The average temperature of 859°C is as good as it is possible to get for the temperature of the amphibolites close to the peridotite contact, since amphibolites within 20 metres of the peridotite have undergone retrograde metamorphism which has obliterated the orthopyroxene. In the thermal models for the Green Ridge Amphibolite, a minimum temperature of 850°C is used, although at the contact it may have been as high as 900°C .

A two-pyroxene temperature of 860°C in rocks which have not undergone partial melting indicates either maximum pressures of 3.5 kb for the formation of the hornblende granulites, since for $P_{\text{H}_2\text{O}} = 0.6 P_{\text{TOT}}$

melting begins at 850° to 870°C in the range 3 to 4 kb (Fig. 3.48), or a partial pressure of H_2O less than $0.5 P_{\text{TOT}}$.

4.1.4. The Long Ridge Metagabbro

In the Long Ridge Metagabbro, the assemblage plagioclase + amphibole + diopside + spinel formed from plagioclase and olivine in the presence of a fluid. A study by Ford (1972) on the system $\text{CaO-MgO-Al}_2\text{O}_3\text{-SiO}_2\text{-H}_2\text{O}$ showed that the assemblage anorthite + clinoamphibole + diopside + spinel + vapour exists over the range 7 to 10 kb and 825° to 910°C (Fig. 4.3a); the isothermal 850°C , 10 kb section contains the compositions of all the coronitic metagabbros in the anorthite + clinoamphibole + diopside + spinel stability field (Fig. 4.3b). The absence of enstatite fixes the upper temperature at 910°C . Given the geological setting of the Long Ridge Metagabbro, a lower pressure estimate is considered more reasonable, but even for 7 kb, burial to depths of more than 20 km is required. This is highly unlikely for a gabbro even at the base of the oceanic crust (~ 5 km) and suggests that the coronites formed in response to a tectonic pressure increase imposed during their cooling interval.

The relationship between the formation of the corona structures in these metagabbros and the dynamothermal metamorphism of the St. Anthony Complex cannot be firmly established. However, if the pressure increase was related to the beginning of overthrusting of the White Hills Peridotite, the coronite assemblages can be used as a guide to the maximum conditions close to the peridotite contact. The intermediate temperature estimate of 850°C is remarkably

close to the estimates for the upper part of the Green Ridge Amphibolite.

4.1.5. The White Hills Peridotite

Determination of the temperature of the White Hills Peridotite at the time of its emplacement is fundamental to thermal models of the St. Anthony Complex. The basal peridotites differ from the typical harzburgites of the interior of the peridotite by having a mylonitic fabric overprinting the S_{p1} fabric, by the occurrence of pargasite in sheets parallel to this foliation, by the presence of orthopyroxene exsolving plagioclase, by the presence of spinel somewhat enriched in Fe associated with the amphibole lherzolites, and by the presence of post-kinematic talc and tremolite after enstatite and chlorite-magnetite coronas after spinel. These features enable limits to be placed on the temperature of the peridotite in the contact zone at the time of emplacement.

The presence of pargasitic amphibole in the basal lherzolites fixes the maximum temperature of the rocks at about 1050°C (Milhollen et al., 1974, and references therein). Two-pyroxene geothermometry on these samples yields temperatures of 911° to 958°C for the porphyroclast rims and the recrystallized matrix pyroxenes (Wells, 1977) (Table 4.3). The exsolution of plagioclase from orthopyroxene suggests pressures of 8.5 to 10 kb over a wide temperature range (Herzberg, 1976, a,b; Emslie, 1970; Green and Hibberson, 1970) (Fig. 3.66), although a refined P-T grid for spinel lherzolites involving a correction for Al_2O_3 in clinopyroxene (Herzberg, 1978) indicates temperatures of 925° to 1000°C and pressures of 7 to 8 kb for this reaction. On the qualitative metamorphic olivine-spinel plot of Evans and Frost (1975) the spinel-olivine

pair from the pargasite-bearing peridotite plots between 700° and 1200°C at significantly lower temperatures than olivine-spinel pairs from elsewhere in the White Hills (Fig. 4.4). The gabbroic mylonite sample, G12, contains the assemblage spinel + diopside + amphibole + plagioclase, with a trace of orthopyroxene detected by XRD (J. Vahtra, pers. comm. 1978). This is similar to the mineralogy of the coronites of the Long Ridge Metagabbro, although it is in a rock with a different bulk composition, and suggests temperatures of close to 900°C .

The study of the exsolved plagioclase raised questions about the behaviour of Al_2O_3 in pyroxenes under condition of intense strain (cf. Wilshire and Jackson, 1975) which may have implications for the validity of the two-pyroxene geothermometry. The possibility of post-kinematic pyroxene re-equilibration should also be considered, although the basal zone mylonites have apparently undergone little textural recovery (T. J. Calon, pers. comm., 1978). The only absolute controls on the emplacement temperature of the peridotite are the stability of amphibole (1050°C) and the lack of pre-emplacement serpentization (550°C). With these reservations in mind, temperatures of 1050°C , 950°C , and 850°C are used for the White Hills Peridotite in the thermal models. For the estimated pressure of 8 kb, corresponding to a depth of 25 km, these temperatures yield geothermal gradients of 30° to $50^{\circ}\text{C}/\text{km}$, not unreasonable for oceanic regimes.

4.2. Metamorphic Profiles

In order to summarize the structural, metamorphic, and geothermal data for the St. Anthony Complex, three cross-sections, restored to the horizontal, have been constructed. Since no continuous

section from undeformed volcanics to the peridotite was investigated, the three sections are used to derive a composite metamorphic and thermal profile through the aureole. The sequences described are from the Fischot Islands, Three Mountain Summit, and Brimstone Pond, covering the St. Anthony Complex from east to west.

The Fischot Islands consist of a sequence of lowest greenschist to upper amphibolite facies rocks, but the continuity is interrupted by faulting. The section is thus drawn in two parts (Fig. 4.5). The eastern side of the islands comprises a thick sequence of amphibolite and upper greenschist facies metabasites, which are continuously exposed from a basal fault to their disappearance at the coast. The thicknesses shown are based on the maximum exposures of each unit, for example, as shown in section B-B' in Plate 4, without compensation for the syn-emplacement folding (F_2 and F_3). The western section, based on A-A', consists of a thick sequence of greenschist facies metasediments and a very thin sequence of epidote amphibolite to amphibolite facies metabasites. Exposure is continuous from the basal thrust and melange in the west to the fault which truncates the amphibolites in the east. The two sections differ not only in their relative levels in the St. Anthony Complex -- mainly the Goose Cove Schist in the west and mainly the Green Ridge Amphibolite in the east -- but in their vastly different thicknesses of the epidote amphibolite and biotite amphibolite units.

The Three Mountain Summit profile (Fig. 4.6) is based on cross-sections of the St. Anthony Complex north of Hare Bay. The structural thickness used is measured perpendicular to S_1 in the greenschists, but no attempt has been made to compensate for the complex

folding in the Goose Cove Schist. The quartz amphibolite thickness shown is that estimated for the eastern White Hills, although only a small part is exposed at the top of Three Mountain Summit. The position of the Long Ridge Metagabbro is also shown, although its relationship to the aureole rocks is unclear. While the quartz amphibolite and greenschist unit thicknesses are directly comparable to the Fischot Islands profiles, the thicknesses of the transitional epidote and biotite amphibolite units are intermediate to the eastern and western Fischot Islands profiles.

The Brimstone Pond profile (Fig. 4.7) includes only the amphibolites close to the peridotite contact, since the lower parts of the section are not exposed. Estimates of the overall thicknesses of the Green Ridge Amphibolite and the Goose Cove Schist based on the map of Williams and Smyth (in press) (Plate 2), suggest they are comparable to the Three Mountain Summit and Fischot Islands estimates.

Each section provides some critical evidence concerning the thermal gradient through the aureole, but unfortunately none is complete. In the composite thermal profile shown in Fig. 4.8, the Brimstone Pond section provides the upper amphibolite facies temperatures, the Fischot Islands covers the lower part of the amphibolites, and the Three Mountain Summit profile covers the Goose Cove Schist. The shape of the derived thermal gradient depends critically on the thicknesses of the epidote and biotite amphibolites which mark the transition from the Goose Cove Schist to the Green Ridge Amphibolite. The two units range in thickness from 100 to 150 metres each on the eastern Fischot Islands, to 40 to 50 metres each on Three Mountain Summit, to only a few

metres each on the western Fischot Islands. The epidote amphibolite unit is too thin for its temperature range, resulting in a break in the geothermal gradient at the greenschist to amphibolite facies transition (Fig. 4.8). Since this coincides with the occurrence of the biotite-rich mylonite zone, the most reasonable explanation is that the mylonite has cut out part of the epidote amphibolite unit. This has resulted in an overall thinning of the St. Anthony Complex and a disruption of the metamorphic sequence.

The accuracy of the thermal profiles shown in Fig. 4.8 depends on the accuracy of the field data and the accuracy of the methods used to estimate the pressures and temperatures. The probable errors in both are shown by error boxes. For example, the main uncertainty in field data comes where a thick unit is characterized by a divariant reaction, so that the position of the probable temperature is placed at the centre of the zone, with error bars indicating the thickness of the zone.

The thermal gradients shown are based on the present overall structural thicknesses of the St. Anthony Complex. However, post-metamorphic folding in the Goose Cove Schist, involving at least two phases of tight folds, has occurred. The folding has undoubtedly affected the thickness of the Goose Cove Schist, although without a detailed structural analysis it is impossible to say exactly how. Although the foliation accompanying the amphibolite facies metamorphism is axial planar to second phase folds and concordant with the peridotite contact, there is a possibility of post-metamorphic thinning, for example at the biotite amphibolite mylonite zone. Therefore, the apparent thermal gradient preserved in the St. Anthony Complex is not that which

was present at the time of metamorphism, making it unrealistic to model the thermal structure of the entire aureole.

A systematic change from higher to lower pressure through the aureole is apparent from the profile shown in Fig. 4.8. Pressures of 7 to 10 kb are estimated for the metamorphism of the White Hills Peridotite and the Long Ridge Metagabbro. These may not reflect the conditions of dynamothermal metamorphism, but indicate a deep-seated origin for the rocks at the top of the St. Anthony Complex. The Fischot Islands melts and calc-silicate assemblages suggest pressures of close to 5 kb, while the two-pyroxene amphibolites from Brimstone Pond probably formed at pressures of about 4 kb. The presence of epidote amphibolite and a zone where chlorite decreases in the Goose Cove Schist suggests pressures of 2 to 4.5 kb. In the Ireland Point Volcanics, the absence of pumpellyite and actinolite indicates pressures of less than 2 kb. The pressure gradient, and the systematic changes in lithology through the aureole, indicate that the metamorphic history of the St. Anthony Complex is more complicated than previously envisaged (cf. Williams and Smyth, 1973). Instead of a single metavolcanic pile, the metamorphic profiles point to both a lateral and vertical stacking of units during the transportation of the peridotite. The St. Anthony Complex thus represents a composite sequence made up of metamorphic and lithological units translated along cryptic dislocations which may have been nearly parallel to metamorphic isograds. For this reason, the thermal models discussed in the following section concentrate on accounting for the temperature at the peridotite-amphibolite contact, with the implications for the external part of the aureole considered separately.

4.3. Thermal Models

4.3.1. Introduction

The fundamental problem concerning the origin of dynamothermal aureoles associated with transported peridotites is the source of heat. Was the metamorphism caused by the conduction of heat from a high temperature peridotite into the surrounding rocks (i.e. conventional contact metamorphism) or was it caused by frictional heating as the peridotite was thrust over the surrounding rocks? Before the recognition of many peridotite massifs as transported bodies, their aureoles were assumed to be the result of heating by conduction from hot, intrusive peridotites (e.g. MacKenzie, 1960; MacGregor, 1964; Green, 1964b). Ophiolites are thought to have originated as relatively cool oceanic crust and upper mantle, thus lacking the heat content necessary to produce contact metamorphism, yet they are commonly associated with dynamothermal aureoles (Williams and Smyth, 1973; Woodcock and Robertson, 1977). This has led many workers to suggest that ophiolites and their aureoles are contemporaneous, originating as hot, oceanic crust-mantle sequences, which have formed in marginal basins or similar environments close to their sites of emplacement (e.g. Church and Stevens, 1971; Malpas, 1976; Coleman, 1977). The St. Anthony Complex provides an excellent opportunity to study a tectonically emplaced peridotite with a well-developed metamorphic aureole, where the thermal conditions are sufficiently well-defined to permit theoretical models to be developed.

The question is basically this: was conduction or friction responsible for the high temperatures and steep thermal gradients in

the Green Ridge Amphibolite? In the following discussions, the conduction and friction models are discussed separately to clarify their main characteristics. Conduction of heat from the peridotite to its surroundings must have occurred unless they were initially at the same temperature. The widespread compositional homogeneity of the quartz amphibolites indicates that they were originally basalts, with minor associated marbles and gabbro, while the plagioclase amphibolites may have been derived from either basalts or gabbros. In modern oceanic regimes, basalts are commonly altered to lower greenschist facies assemblages even in near surface environments (Cann, 1969; Miyashiro et al., 1971). In the case of the St. Anthony Complex, the pre-tectonic temperature of the Ireland Point Volcanics can be used as a guide to the pre-tectonic temperature of the basaltic protoliths of the Green Ridge Amphibolite, although structural and lithological discontinuities within the St. Anthony Complex make it unlikely that they were originally part of the same rock unit. It is therefore likely that conduction of heat from the White Hills Peridotite (950°C) to the protoliths of the Green Ridge Amphibolite (300°C) occurred. It is also evident from the structure of the rocks that the emplacement of the White Hills Peridotite involved lateral motion between the peridotite and the underlying rocks, suggesting that some frictional heat could have been generated. The central part of the discussion considers how the two models might be combined, and the way in which each might have contributed to the metamorphism of the St. Anthony Complex. Then the effects of endothermic and exothermic reactions on the heat production in the aureole are considered. Finally, the limitations of the theoretical

models are discussed and their probable relationships to the actual observations are evaluated.

A fundamental assumption throughout is that the dynamic metamorphism of the St. Anthony Complex is entirely related to the tectonic emplacement of the White Hills Peridotite, that is, that a narrow, high-temperature aureole was not superimposed upon a pre-existing sequence of metamorphic rocks (cf. Church, 1972), and that the aureole does not result from tectonic inversion and thinning of a normal metamorphic sequence. Since it is not possible to rule out the latter model on the basis of the results of this study, it is considered at the end of the chapter. In all cases, a thermal model must result in a temperature of 850° to 950°C at the contact to be considered successful, with a steep thermal gradient (about $800^{\circ}\text{C}/\text{km}$) in the upper 250 metres of the aureole. The physical parameters used in the models, and the sources of the data, are given in Table 4.4. Most of the results are presented in graphical form; the tables on which the graphs are based are given in Appendix III.

4.3.2. The Conduction Model

The rate at which heat is conducted from a hot body of rock to an adjacent cooler one depends on the following factors (Lovering, 1936):

- 1) the initial temperature distribution
- 2) the time elapsed after the rocks are juxtaposed
- 3) the thermal properties of the rocks
- 4) endothermic and exothermic reactions in the rocks
- 5) loss of heat by other means (e.g. convection of water)
- 6) the shapes of the bodies.

This discussion assumes that a planar contact separates a thick peridotite sheet from the country rocks, that there is no relative motion between the peridotite and its surroundings, and that heat is lost by conduction only. The other variables are treated as follows:

(1) The temperature distribution is varied within the likely extremes, based on the thermal data of the previous sections. The initial temperature of the peridotite is assumed to be 1050° , 950° , and 850°C in turn, for initial country rock temperatures of 350° , 300° , and 250°C .

(2) The time at which the maximum contact temperature is achieved is always immediately after emplacement. Maximum temperatures away from the contact are reached later. The exact times depend on the thickness of the heat source, which is here taken as 1000 metres. Changing this value does not affect the shapes of the curves, but only the numerical values of the times involved (less time for a thinner sheet). The temperature distributions in the country rock at a given time after emplacement are shown in Fig. 4.9 (a-i). The maximum temperatures achieved in the country rocks at different times are shown in Fig. 4.10 (a-c). The thermal gradients for various points at various times are listed in Appendix III.

It must be emphasized that for all the models, the times calculated are those necessary for the given ambient temperature to be reached, not the time necessary for the mineral assemblages to equilibrate to that temperature. Geologically reasonable times for the metamorphic assemblages to form are likely to be much higher, but numerical estimates are not possible without data (generally unavailable) on rates of reaction.

(3) The thermal properties of the peridotite and the amphibolite have been estimated from many sources (see Table 4.4). For simplicity, in most models it is assumed that the peridotite and the country rock are homogeneous materials with identical thermal properties. Fig. 4.11 and Table 4.5 show the effects of different thermal properties on the maximum contact temperature reached, based on likely extreme values for the conductivity and diffusivity, and the curves given by Lovering (1936).

(4) The effects of endothermic and exothermic reactions are ignored at this stage, but are discussed in section 4.3.5.

The complete results are given in Appendix III. Here only the intermediate case, where $T_P = 950^{\circ}\text{C}$ and $T_R = 300^{\circ}\text{C}$, is discussed in detail. The other cases are identical in form and implications; the results for all the contact temperature calculations are given in Table 4.6 for easy comparison.

For this case, the maximum contact temperature is 625°C , reached immediately after emplacement and maintained for 10^3 years. Initially, the thermal gradients in the upper 200 m of the aureole are very steep, on the order of $2000^{\circ} - 1000^{\circ}\text{C/km}$. Within 10^3y they have levelled out to about 250°C/km throughout the aureole, and ultimately fall off to 15°C/km as the entire system reaches temperatures of 400°C .

If the maximum temperature reached by each point in the country rock is preserved (e.g. locked into the mineral assemblages by the slow rates of retrograde reactions), thermal gradients of 600°C/km in the upper 100 m, and 450°C/km in the upper 250 m of the aureole result. The maximum temperatures in the outer parts of the aureole

are reached within $10^4 - 10^5$ y of the time of emplacement (see Appendix III for details).

These models assume that the thermal properties of the peridotite and the country rock are the same. Lovering (1936) has discussed the effects of differing thermal properties on the contact temperatures. The maximum temperature reached depends on the ratio

$$4.1) \quad \left(\frac{K}{\sqrt{\kappa}} \right)_P \bigg/ \left(\frac{K}{\sqrt{\kappa}} \right)_R = \mathcal{K}$$

where K = conductivity and κ = diffusivity. Table 4.5 shows the effect of varying \mathcal{K} for the 950°C , 300°C model. The thermal constants given in most reference works (e.g. Lovering, 1936; Birch et al., 1942; Clark, 1966; Nafe and Drake, 1968) suggest that K and κ for peridotite are higher than K and κ for basalt, which means that \mathcal{K} will be greater than 1.0. For the maximum likely difference, $\mathcal{K} = 2.0$, the maximum contact temperature is 736°C (compared to 625°C for $\mathcal{K} = 1.0$). Based on more probable literature values ($K_P = 7.0 \times 10^{-3}$, $K_R = 5 \times 10^{-3}$, $\kappa_P = 10^{-2}$, $\kappa_R = 0.8 \times 10^{-2}$), $\mathcal{K} = 1.25$, leading to a maximum contact temperature of 661°C . The thermal gradients through the aureole in this case follow the same pattern as for $\mathcal{K} = 1.0$, but higher temperatures are achieved at different times.

Fig. 4.12 shows the contact temperature as a function of time for the case where $T_P = 950^\circ\text{C}$, $T_R = 300^\circ\text{C}$, the thermal properties are identical, and the peridotite is 1000 m thick.

From these conduction models, the following conclusions can be drawn:

(1) The contact temperature achieved by simple conduction does not reach the observed value of 850°C for any likely values of T_p , T_R , or thermal properties. Temperatures over 800°C are reached only by considering the case for $T_p = 1050^{\circ}\text{C}$, $T_R = 300^{\circ}\text{C}$ - 350°C , and $\mathcal{K} = 1.8$ - 2.0 , conditions which are considered extreme.

(2) High thermal gradients are achieved close to the contact soon after the peridotite is emplaced. If the maximum temperatures reached in the aureole are preserved, the resulting thermal gradients of $600^{\circ} - 450^{\circ}\text{C/km}$ are at the lower limit of those observed in the St. Anthony Complex.

(3) The maximum temperatures and thermal gradients close to the contact are achieved at the time of emplacement; both T_c and dT/dx decrease rapidly for $t > 10^3$ years.

(4) Working backwards, for temperatures of 850°C to be reached at the contact by conduction alone, the initial temperature of the country rock must have been 750°C for $T_p = 950^{\circ}\text{C}$, $T_R = 300^{\circ}\text{C}$, and $\mathcal{K} = 1.0$, or 725°C for $\mathcal{K} = 1.25$. This means that conduction would only produce the observed temperatures if the country rocks were already at high temperatures (Table 4.6).

4.3.3. The Friction Model

The amount of heat (q) generated by friction along a plane surface in an infinite, homogeneous medium depends on the following factors (Carslaw and Jaeger, 1959; Reitan, 1968; Graham and England, 1976):

- 1) the rate of motion
- 2) the time after the beginning of motion

- 3) the shear strengths of the rocks
- 4) endothermic and exothermic reactions in the rocks
- 5) the thermal properties of the rocks
- 6) loss of heat by other means.

This discussion assumes that the rocks have similar thermal properties and that heat is not removed by convection or some other means. The other variables are treated in the following manner:

(1) The rate of motion, u , is varied from 1 to 20 cm/y. The higher rates are not commonly observed in modern plate motions, but might be achieved in the early stages of thrusting, or as the result of plate convergence at oblique angles, or where two plates approach each other at relatively high velocities (Fig. 4.13).

(2) The time after the beginning of motion is plotted as $\log t$ (y) (Fig. 4.14) and is varied from 10 to 10^7 years.

(3) The shear strength, \mathcal{T} , is varied from 1 to 3 kb, probable ranges based on the data of Griggs et al. (1960) and Clark (1966) for rocks at high temperatures and confining pressures, with stress applied at low angles to the plane of the maximum stress difference. Two situations are considered. \mathcal{T} is initially considered to be independent of temperature, and the resulting values of q for different \mathcal{T} and u are plotted in Fig. 4.13. It is most probable, however, that \mathcal{T} decreases at high temperatures, particularly as water is released by dehydration reactions and as partial melting begins. Following the method described by Graham and England (1976), \mathcal{T} is considered independent of T up to a critical temperature C (T_C of Graham and England, 1976), after which it decreases in a linear fashion over a temperature interval B . The

effects of decreasing \mathcal{T} on q for various values of C and B are shown in Fig. 4.15.

The assumption that \mathcal{T} is constant, or decreases in a linear fashion with temperature, is known to be incorrect; \mathcal{T} is a complex function of T , P , strain rate, time, grain size, fluid availability, etc (Weertman and Weertman, 1965a, b; Jaeger and Cook, 1969; Jonas et al, 1969; Kirby and Raleigh, 1975; White and Knipe, 1978). Therefore, \mathcal{T} will vary even at constant T and P as metamorphism proceeds, owing to the interplay of mechanical effects such as work hardening, reaction-enhanced ductility, and creep. An analysis of these factors is beyond the scope of this thesis, largely because the microstructural analysis necessary to determine deformation mechanisms has not been attempted. Before the friction model can be rigorously tested, these factors should be evaluated; the model discussed below is therefore a very simplified, limiting case.

(4) As for conduction, discussion of the effects of exothermic and endothermic reactions is postponed to section 4.3.5.

The equations used are those given in Graham and England (1976), simplified after Carslaw and Jaeger (1959).

(1) The amount of heat generated at the contact by friction is given by

$$4-2) \quad q = u\mathcal{T}$$

(2) The temperature increase at the contact generated by this amount of heat is given by

$$4-3) \quad \Delta T_{(x=0)} = \frac{q}{\rho C_p} \cdot \left(\frac{t}{\pi \kappa} \right)^{1/2}$$

(3) The thermal gradient at the contact generated by the heat produced is given by

$$4-4) \quad \frac{dT}{dx} (x=0) = \frac{q}{\rho C_p K} = q/K$$

These equations show that the temperature increase at the contact is independent of the initial temperature of the rocks (as long as \mathcal{T} is independent of T). If friction alone is considered, there is an implicit assumption that $T_P = T_R$. The important variable is q , not T_P or T_R . However, the ultimate temperature reached depends on the initial temperature at the contact.

Fig. 4.13 shows the quantity of heat generated at the contact (q) for various shear strengths (\mathcal{T}) and rates of motion (u). The relationships are linear (see equation 4-2); e.g. for $\mathcal{T} = 3$ kb and $u = 20$ cm/y, $q = 48$ hfu. Fig. 4.14 shows the temperature increase at the contact (ΔT) for various q , plotted against the time since the beginning of thrusting. Temperatures increase exponentially with time for constant q (see equation 4-3). Fig. 4.15 shows the change in q as \mathcal{T} falls off above a temperature C . Since \mathcal{T} is assumed to change in a linear fashion, the change in q is also linear:

$$4-5) \quad q = q_0 \cdot \left(1 - \frac{(T-C)}{B} \right) \quad (\text{after Graham and England, 1976})$$

The value of the contact temperature produced by frictional heating is thus a complex function. Fig. 4.16 shows T_c as a function of the time since the beginning of thrusting, assuming an initial contact temperature of 300°C , for $q = 32, 16$, and 8 hfu, assuming that \mathcal{T} does not change with T . The curves show that T_c reaches 850°C within $10^4 - 10^5$ years, and continues to increase exponentially thereafter. On the basis of the temperatures calculated for the St. Anthony Complex, motion must have stopped after 850°C was reached, or \mathcal{T} must have

fallen off with T so that T_c levelled off at about 850°C .

If \mathcal{T} is a function of T , the contact temperature is obviously very dependent on the values chosen for C , B , and q . The maximum contact temperature approaches the limiting value $C + B$ after increasing exponentially with time up to C . The example plotted in Fig. 4.17 illustrates the principles. T_c is shown as a function of time, assuming \mathcal{T} is constant to 700°C and falls in a linear fashion over the next 200°C , for $q = 16$ hfu (corresponding to $\mathcal{T} = 2$ kb, $u = 10$ cm/y). The plot is identical to Fig. 4.16 up to 700°C , but T does not continue to increase exponentially. Its rate of increase falls off, so that T approaches the limiting value of 900°C at $t > 10^6$ years.

From the frictional heating models, the following conclusions can be drawn (subject to the limitations discussed previously):

(1) For reasonable rates of motion and shear strengths, contact temperatures of 850°C can easily be achieved within 10^6 years of the beginning of motion.

(2) As long as thrusting continues, the maximum contact temperature depends on the way in which \mathcal{T} varies, approaching asymptotically the T at which $\mathcal{T} \rightarrow 0$. In general, \mathcal{T} will decrease with T , but numerical values for its behaviour at high temperature are poorly known and other factors such as strain rate and reaction effects have been ignored. The values for \mathcal{T} , C , and B shown in Fig. 4.17, which have been chosen to approximate the conditions in the St. Anthony Complex, may not be realistic.

(3) The thermal gradients at the contact depend on the amount of heat generated and the conductivity of the rocks. To achieve a

gradient of 800°C/km requires heat production of 48 hfu (Fig. 4.18). This is much higher than the 16 hfu estimated using $\mathcal{T} = 2\text{ kb}$ and $u = 10\text{ cm/y}$, requiring conditions like $\mathcal{T} = 3\text{ kb}$ and $u = 20\text{ cm/y}$. While not impossible, these values are probably upper limits. The estimated value of 16 hfu produces a thermal gradient of only 270°C/km at the contact. This is a major deficiency of the frictional heating model and is considered again in a later section.

(4) As long as motion continues, temperatures increase with time, and the thermal gradient is constant as long as q is constant.

4.3.4. Combined conduction and friction models.

Heat transfer by conduction must have occurred as long as there was a temperature difference between the peridotite and the underlying rocks. Since the peridotite was emplaced by overthrusting, some heat was probably generated by friction. It seems inevitable that both effects contributed to raising the temperature of the country rocks. The previous sections have shown that the temperature increase by conduction is a maximum at the time of emplacement, and decreases with time, while the temperature increase by friction increases exponentially with time until the heat production stops because of decreasing shear strength or the cessation of motion.

To estimate the ways in which the effects might combine, a model was calculated using the following assumptions: $T_p = 950^{\circ}\text{C}$, $T_R = 300^{\circ}\text{C}$, $u = 10\text{ cm/y}$, $\mathcal{T} = 2\text{ kb}$ ($\therefore q = 16\text{ hfu}$), $C = 700^{\circ}\text{C}$, $B = 200^{\circ}\text{C}$. The results are shown in Fig. 4.19, where T_c is plotted against time, which should be compared with the conduction-only model of Fig. 4.12

and the friction-only models of Fig. 4.16 and 4.17. The model shows that for t_1 (0-10 years), the contact temperature is 625°C resulting from conduction of heat from the peridotite into the underlying rocks. For t_2 ($10 - 10^4$ years), the contact temperature increases by frictional heating to 700°C , the temperature at which the shear strength begins to decrease. For t_3 ($10^4 - 10^6$ years) the contact temperature continues to increase, but the rate of increase falls with increasing T until the limiting value of 900°C is approached. If motion stops after 10^6 years (at 10 cm/y this means the thrust sheet has moved 100 km) a maximum contact temperature of 880°C is reached. The section of the graph labelled t_4 shows how the temperature falls if, after a maximum of 880°C is reached, the heat is dissipated by conduction through a zone 1000 metres either side of the contact. In this situation, the contact temperature falls to 150°C in 300,000 years after motion has ceased (i.e., very rapidly on the exponential t scale shown for the total elapsed time since the beginning of thrusting). Also, in Fig. 4.19, the model is repeated for the case where $C = 700^{\circ}\text{C}$ and $B = 50^{\circ}\text{C}$, to approximate the conditions where partial melting occurs in the range $700 - 750^{\circ}\text{C}$. In this case, the limiting temperature of 750°C is approached after 10^5 years of motion.

The results show that it is possible to model the contact temperature in the aureole of a transported peridotite without resorting to unusually high initial temperatures for the country rocks or the peridotite, unusually high shear strengths, or unusually high rates of thrusting. It is concluded that a thermal model involving heating by both conduction and friction fits the observations within the many limitations imposed by the model and by the data to which the model

is compared. The effects of some of these limitations are discussed in Section 4.3.6.

4.3.5. The Effects of Reactions on Heat Production

Endothermic and exothermic reactions at the contact affect the amount of heat available, the first by using up the heat produced by conduction and friction, the second by adding to it. Close to the contact with the White Hills Peridotite, partial melting (observed on the Fischot Islands) is the main heat-consuming reaction, while the dehydration of amphibole to produce pyroxene (observed at Brimstone Pond) is the main heat-producing reaction.

Yoder (1976, p. 93) estimates the enthalpy of melting (ΔH_m) of basalt at 73.5 cal/g. For amphibolite it is probably lower, and a value of 50 cal/g, combined with a density of 3.0 g/cm³, gives $\Delta H_m = 150 \text{ cal/cm}^3$. The heat flux necessary to melt a 1 cm thick layer of amphibolite is thus 150 cal/cm². If the amount of heat produced at the contact is 16 hfu ($16 \times 10^{-6} \text{ cal cm}^{-2} \text{ s}^{-1}$), it would take 10^7 seconds (about 1 year) to melt the rock at the contact entirely. Although information on rates of reaction is not available, these figures suggest that partial melting of amphibolite could consume most of the heat produced at the contact. Combined with the decrease in T once partial melting has begun, it is likely that the maximum temperature reached by the partially melted rocks would not greatly exceed the melting temperature.

For the dehydration of amphibole, estimation of ΔH_r is difficult owing to scarce and contradictory data for ΔH_f . Table 4.7

shows the results obtained using the data of Robie and Waldbaum (1968) for the reaction: pargasite + 4 quartz \rightleftharpoons diopside + 3 enstatite + albite + anorthite + H₂O. At T = 1100° to 1200°C, and assuming amphibole to form 50% of the rock, a value for ΔH_r of about 18 cal/cm³ is obtained. This may be wildly inaccurate, but comparison with the estimate for the melting reaction suggests that it is probably reasonable within an order of magnitude. In a layer of rock 1 cm thick, a heat flux of 18 cal/cm² would be produced, of which half would be dissipated upwards and half downwards. This would correspond to 1.8 hfu if the reaction took one year to complete. The heat would be transferred from the reaction zone through the rock at a rate given by $f = \frac{kt}{a^2}$, which is approximately equal to 1.0 for basalts (P. E. England, pers. comm., 1977). Considering the uncertainty associated with these estimates, it is probably realistic to conclude that the heat released by dehydration reactions could contribute locally to high temperatures and thermal gradients but would not greatly affect the thermal structure of the aureole as a whole.

4.3.6. Limitations and Implications of the Thermal Models

As well as those discussed previously, the limitations of the models discussed in this section include the following:

(1) The theoretical models involve many simplifying assumptions which could affect the solutions considerably. For example, in rocks undergoing both deformation and dehydration, heat would be carried out of the system by the circulation of water. The temperatures calculated here are considered a maximum for the times involved.

(2) Even in the simplified cases, the numerical values of

the parameters used in the equations are poorly known. For example, if the heat production at the contact is reduced by a factor of 10, through different estimates for shear strengths or velocities of motion, then it would take 5 m.y. to raise the temperature at the contact by 200°C and severe constraints would be placed on the frictional heating model. If heat production were raised by a factor of 10 by heats of reaction or different estimates for τ and u , the rocks at the contact would melt almost as soon as motion began, again limiting the models (see Fig. 4.14).

(3) Neither the friction nor the conduction model produces a thermal gradient as steep as that observed in the St. Anthony Complex. However, that gradient is based on the present structural thickness of the aureole which is not likely to be that pertaining at the time of metamorphism. If strains of 100% occurred during the dynamothermal metamorphism, which is possible given the structural style of the rocks (T. J. Calon, pers. comm. 1978), then the original thickness of the aureole would be doubled and the thermal gradient halved. This would result in a gradient of 300° to 400°C/km, which is compatible with the calculated models (Fig. 4.18).

(4) The observed pressure gradient and lithological change through the aureole show that it is a composite sequence, implying lateral and vertical transposition of units. Within this sequence, every foliation plane could have acted as a thrust surface, along which translation occurred simultaneously with the metamorphism, until an apparently continuous aureole showing a gradational metamorphic sequence was produced. Modelling of the entire thermal structure of the aureole

requires the assumption of a steady state system in the rocks being heated, which is obviously not the case. For this reason, the thermal models discussed here have dealt only with the temperature and thermal gradient produced at the thrust contact.

(5) The effect of thermal re-equilibration of the disturbed geothermal gradient resulting from overthrusting has not been considered. The results of Oxburgh and Turcotte (1974) and Graham and England (1976) suggest that the effects of heating by friction and conduction in the narrow zone adjacent to the contact considered here will be much more important than thermal relaxation in the early history of thrusting. Equilibration of the geothermal gradient does not have a major effect on the temperature at the thrust plane until times on the order of several millions of years have passed, depending on the thickness of the overriding sheet and the original geothermal gradients involved.

An important implication of the models discussed here is that there is no need for the peridotite to have been hot at the time of its emplacement in order for a high temperature aureole to have been produced. This discussion has assumed a peridotite temperature of about 950°C because the particular conditions of the White Hills Peridotite suggest it. However, for q in the range of 10 to 20 hfu, frictional heat raises the temperature at the contact to the limiting value imposed by the shear strength within 10^4 to 10^5 years (Fig. 4.16; Appendix III). This is almost independent of the initial temperature because of the exponential increase of T with time. Since the peridotite will also undergo high temperature metamorphism in the contact zone as a result of frictional heating, high-temperature assemblages there may

be a consequence of emplacement rather than reflecting the conditions in the rocks prior to emplacement. Loss of heat by conduction will first cool down the peridotite near the contact, and friction will subsequently heat it up, resulting in convergent metamorphism in the peridotite and the country rocks in the contact zone.

These models have assumed that the high temperature metamorphism and inverted thermal gradient are the result of the peridotite emplacement. However, an alternative model for the origin of the St. Anthony Complex is conceivable. Zwart (1974), on the basis of studies in the Scandinavian Caledonides, has suggested that metamorphic nappes with inverted geothermal gradients can form as very large shear zones in a normal metamorphic sequence (Fig. 4.20). High strain within these zones would result in thinning of the metamorphic sequence and a distribution of isograds at low angles to the upper shear surface. Subsequent transport along a later, high level thrust fault, followed by erosion, could leave a thin inverted sequence of metamorphic rocks beneath a peridotite sheet.

This model could account for the east to west changes in lithology and base to top pressure gradient of the St. Anthony Complex, and the presence of smaller scale mylonites such as the biotite amphibolite unit. It also explains how high temperatures could be achieved in rocks where heat loss through fluid transport almost certainly occurred and why there is complex post-metamorphic (post-S₁) deformation. However, it requires that a metamorphic sequence some 15 km thick (based on probable pressures of metamorphism for the Green Ridge Amphibolite)

including transitional granulite facies rocks, partially melted amphibolites, and strongly deformed volcanics, be formed and then reduced to less than 1 km in thickness. These lithologies do not occur in modern ocean basins and ophiolite complexes (e.g. Malpas, 1976; Coleman, 1977; Gass and Smewing, 1973; DeWit and Stern, 1976; Miyashiro et al., 1971).

It is possible to combine the two extremes by proposing that high grade metamorphism was imposed on a normal oceanic sequence through a temperature increase by frictional heating along the upper shear surface shown in Fig. 4.20 and a pressure increase by the crustal thickening resulting from the overthrusting. The detailed structural analysis which could test the models by determining the nature of the early, syn-metamorphic structures in the St. Anthony Complex has not been attempted here.

In conclusion, it should be emphasized that the thermal models presented here represent extreme cases. A dynamic conduction model, in which a high temperature peridotite moved across and progressively heated the underlying rocks, could remove some of the difficulties in producing the observed high temperatures. However, given the geological evidence that the St. Anthony Complex represents the leading edge of the peridotite-aureole sheet as it was emplaced onto the continental margin, it is difficult to escape the conclusion that frictional heating contributed to the high temperature metamorphism. As previously noted, uncertainties in the estimation of shear strengths at high pressures and temperatures make the numerical results of the frictional heating model highly speculative; more refined calculations must await more detailed information on the physical parameters used and on more structural data, particularly the determination of deformation mechanisms within the St. Anthony Complex.

CHAPTER 5. THE GEOLOGICAL HISTORY OF THE ST. ANTHONY COMPLEX

The geological, petrological, geochemical, and geophysical data of the preceding chapters can be synthesized to portray the evolution of the St. Anthony Complex, answering the following questions. What were the original relationships of the rocks before they were juxtaposed during deformation and metamorphism? What can the present disposition of the rocks reveal about the tectonic events which formed the St. Anthony Complex? Can this study clarify any regional relationships in western Newfoundland? What are the implications for the origin of dynamothermal aureoles associated with ophiolites around the world? The final question will be discussed at length in the concluding chapter.

5.1. Pre-tectonic History

The pre-tectonic history of the St. Anthony Complex must be compatible with the regional history of western Newfoundland, which has been summarized in Chapter 2. The work of Stevens (1970), Smyth (1973), Williams and Stevens (1974), Williams (1975), Malpas (1976), Williams and Smyth (in press) and many others has shown that western Newfoundland formed an Atlantic-type continental margin on the western side of the Iapetus ocean. Elements of this continental margin which have been preserved include the late Precambrian rift facies volcanic and clastic rocks, the Cambro-Ordovician carbonate bank built up at the shelf edge, the westerly-derived flysch prism deposited on the continental slope and rise, and the igneous and metamorphic rocks of the oceanic crust and the distal marine sediments overlying them (Fig. 1.2a).

The St. Anthony Complex includes undeformed basalts, poly-deformed metabasites and metasediments, and a peridotite tectonite. The basalts are part of a suite of Tremadocian, mildly alkaline rocks which is widespread north of Hare Bay and includes gabbros which intrude the Maiden Point Formation. The upper part of the Ireland Point Volcanics includes protoliths of the Goose Cove Schist, and grades into the green-schists with increasing metamorphic grade and degree of deformation. The Goose Cove Schist also includes psammites like those of the Maiden Point Formation. The Green Ridge Amphibolite, mainly metabasic rocks with minor marble and pelite, cannot be directly correlated with any undeformed rocks in the area. Its immobile element geochemistry suggests derivation from a tholeiitic to "transitional" basaltic parent which may have had affinities to the more alkalic Ireland Point Volcanics. The metagabbro, anorthosite, and dunite of the Long Ridge Metagabbro are unlike most other rocks in the Hare Bay Allochthon, but resemble Critical Zone sequences of the Bay of Islands Complex and other ophiolites. The metagabbros are chemically similar to the plagioclase amphibolites at the top of the Green Ridge Amphibolite and probably grade into them with increasing deformation. At the base of the White Hills Peridotite, a thin, deformed, jacupirangite-syenite unit occurs which is unlike any other Cambro-Ordovician rocks in western Newfoundland; the closest comparable rocks are the Cambrian alkalic intrusions of the St. Lawrence rift system (e.g. Doig, 1970; Philpotts, 1978). The White Hills Peridotite is strikingly similar to the basal ultramafics of the Bay of Islands Complex and presumably formed in the sub-oceanic upper mantle; differences in detail are attributable to slightly different petrological histories.

These relationships suggest that the upper part of the St. Anthony Complex was derived mainly from an ocean basin, but that the lower part was derived from a Tremadocian igneous and sedimentary sequence which formed close to a continental slope or rise. The scarcity of volcanic detritus in the Maiden Point Formation (Smyth, 1973), suggests that these rocks were not closely associated with a large arc system; any island arc in existence at this time must have been well to the east. The alkalic volcanic pile was probably constructed on oceanic basement, in part represented by the White Hills Peridotite, the Long Ridge Metagabbro, and possibly the Green Ridge Amphibolite. The sense of emplacement of the St. Anthony Complex suggests that the units should be unstacked with the presently lowest in the west, and the presently highest in the east (e.g. Williams et al., 1973) and the pressure gradient through the aureole suggests that the higher units were derived from greater depth. This interpretation leads to the reconstruction shown in Fig. 5.1.

The Ireland Point Volcanics and their equivalents were erupted over and intruded into distal continental margin sediments, forming a volcanic pile at least 1 to 2 km thick. The basalts, with their definite alkaline affinities, are not typical oceanic tholeiites but resemble more closely the rocks formed on ridge flanks or within oceanic plates away from a spreading centre. For these reasons they have been shown as a seamount adjacent to a continental rise -- possible modern analogues include the seamounts of the Newfoundland Basin (Sullivan and Keen, 1977) or the Canary Islands (Dillon and Sougy, 1974). The term "seamount" here is used loosely -- whether the volcanic pile formed on a ridge

flank or as an isolated mass away from a major spreading centre depends on the proximity of the ridge to the continental margin at the time. However, the intrusion of the gabbro into coarse-grained sandstones, and the lack of mid-ocean ridge tholeiite compositions in the St. Anthony Complex suggests isolation from a spreading centre. East of the seamount (or group of seamounts) oceanic crust underlain by mantle tectonite extended to a spreading centre. Fragments of this oceanic crust and upper mantle subsequently became thrust back towards the continental margin as the Green Ridge Amphibolite, the Long Ridge Metagabbro, and the White Hills Peridotite.

The outstanding anomaly in this reconstruction is the presence of highly undersaturated alkaline rocks now adjacent to the peridotite. Rocks like jacupirangite, carbonatite, and syenite are rare in ocean basins, although their scarcity may be partly a function of poor preservation and exposure, since they are generally small, deep-seated intrusive bodies (e.g. Gittins, 1966). In modern oceanic basins, alkaline ultrabasic rocks occur in association with continental margins (e.g. the Canary and Cape Verde Islands, Dillon and Sougy, 1974) or where fracture zones or hinge faults intersect subduction zones associated with island arcs (DeLong et al., 1975). An intriguing speculation is that these rocks were related to the Cambro-Ordovician alkalic activity which occurred in the St. Lawrence graben and throughout the North Atlantic region (Doig, 1970; Philpotts, 1978). Carbonatite and syenite were emplaced at Mutton Bay on the Strait of Belle Isle at 586 Ma (Doig and Barton, 1968) and although this may have been 200 km or more from the site where the jacupirangite now associated with the

White Hills Peridotite was emplaced (at an unknown time), the distance is not great in terms of a rift system several thousand kilometres long with several major branches (Doig, 1970). In modern times, continuity of zones of structural weakness between continental margins and the adjacent ocean basins is not unusual (e.g. Burke and Dewey, 1973; Keen, 1974; Simpson and Bothner, 1978). A fracture zone originating in the on-shore rift valley and extending into the ocean basin might have served as the site of alkaline magmatism related to the jacupirangite and the alkali basalts. Whatever its origin, the presence of the jacupirangite-syenite suite in the St. Anthony Complex strengthens the links between the continental and oceanic regimes already noted above.

5.2. Syntectonic History

Table 5.1 summarizes the depositional and tectonic events of the Lower and Middle Ordovician of western Newfoundland, based on stratigraphic ages and a few radiometric dates (Stevens, 1970; Williams and Stevens, 1974; Tuke, 1968; Williams, 1975; Dallmeyer, 1977; Williams, 1971). Since flysch eroded from the ultramafic thrust sheets was being deposited in the narrowing ocean basin at the same time that carbonate deposition was continuing on the shelf, it is apparent that the destruction of the ocean basin and adjacent continental margin proceeded diachronously from east to west. That it also proceeded diachronously from north to south has been shown by the radiometric dates of the ophiolite aureoles (Dallmeyer, 1977) and the pattern of closure-related deposition in western Newfoundland (Williams and Stevens, 1974). Therefore, events recorded in the better-known and more complete record of the Humber Arm

Allochthon probably occurred somewhat later than in the Hare Bay Allochthon.

The emplacement of the St. Anthony Complex occurred in two stages -- the first involved ductile deformation and was accompanied by dynamothermal metamorphism, the second involved brittle thrusting.

In the Lower Ordovician, possibly early Arenig time, displacement of oceanic crust and upper mantle peridotite began, probably in response to the east-dipping subduction which built up the Ordovician island arc sequence of Notre Dame Bay (Strong, 1973; Strong et al., 1974; Williams and Stevens, 1974; Dean, 1978). This event may have post-dated the eruption of the Tremadocian Cape Onion - Ireland Point volcanics by only a few million years. This raises the possibility that there was a disturbed geothermal gradient in the area where the thrust sheets originated, supporting the suggestion of Armstrong and Dick (1974) that dislocation of thin overthrust sheets may be associated with high geothermal gradients and thermal weakening of the crust and mantle. The vertical and lateral displacement of the White Hills Peridotite produced dynamothermal metamorphism of the underlying rocks, mainly by frictional heating. High pressures generated early in this process, owing to subduction, burial by thick thrust sheets, or tectonic overpressure, resulted in the formation of coronites in gabbros near the base of the oceanic crust. An $^{40}\text{Ar}/^{39}\text{Ar}$ cooling age of 480 ± 5 Ma was obtained for the Green Ridge Amphibolite (Dallmeyer, 1977), and since rapid thrusting was probably accompanied by rapid uplift, the cooling age may not differ very much from the actual age of the recrystallization. In the Humber Arm Allochthon, the same stage was only reached 20 Ma

later, probably in the latest Arenig (Dallmeyer and Williams, 1975). Lateral and vertical telescoping of units within the St. Anthony Complex is indicated by the pressure change through the aureole, and by regular west to east lithological variations. These include the thickening of the plagioclase amphibolite unit from 1 metre in the west to 20-30 metres in the east where it grades upwards into the Long Ridge Metagabbro, the restriction of jacupirangite to the northeastern part of the White Hills, the change from "drier" hornblende granulites in the west to "wetter" partially melted amphibolites in the southeast, the change in the Goose Cove Schist from mainly metabasites in the west to mainly metasediments in the east, and the restriction of garnet amphibolite to the west. These variations suggest that metamorphism within the St. Anthony Complex was diachronous, as the peridotite and its aureole overrode progressively higher and more westerly rocks during its emplacement (Fig. 5.2). The aureole rocks consequently suffered a long period of deformation, possibly including changes in the orientation of the stress field (e.g. as the thrust sheet flattened out at higher levels), resulting in complex structures throughout the St. Anthony Complex.

A major mylonite zone was initiated at this stage at the level of the epidote amphibolite to amphibolite facies transition, which acted as a channel for fluids causing metasomatism during deformation in the waning stages of the metamorphism of the St. Anthony Complex. The mylonite zone was probably active for a long time, and transposed the upper part of the aureole over the lower part, cutting out parts of the epidote amphibolite zone of the Goose Cove Schist in the process.

Dynamothermal metamorphism in the St. Anthony Complex eventually ended, possibly because the rates of motion necessary to generate frictional heat were not maintained, or because the rocks at shallow crustal levels had low shear strengths and did not respond in a ductile manner to stress, or because heat dissipation from the St. Anthony Complex was too rapid as it reached the surface. It is also possible that the White Hills Peridotite and its aureole ran into a physical barrier of some kind, possibly related to the end of easterly-directed subduction.

Mass wasting of the thrust sheets may have occurred continuously, or may have begun only after the first dynamothermal stage of emplacement. Detritus shed from the thrust slices was accumulating as the Goose Tickle flysch by the upper Llanvirn when it was deposited on the carbonates and shales of the Table Head Formation. By analogy with the Humber Arm Allochthon, easterly-derived sediments may have accumulated from the Arenig on. Between the Arenig, when the dynamothermal metamorphism occurred, and the lower Middle Ordovician, when the Goose Tickle Formation was deposited over the sunken shelf deposits, the Hare Bay Allochthon was being assembled as a series of thrust slices piling up from east to west. The Milan Arm Melange was probably deposited at this time (late Arenig to Llanvirn) as an olistostrome in front of the upper thrust slices, collecting debris shed into it (including the Cape Onion Volcanics as a huge block) and then overridden and deformed by these thrust sheets.

This stage of the emplacement of the St. Anthony Complex involved brittle dislocation along what is now the Hare Bay thrust,

which broke up the alkali basalt suite and brought the St. Anthony Complex against the Maiden Point Formation. The thrust fault truncates all the units of the St. Anthony Complex, thus post-dating the metamorphism. The final episode of emplacement may have involved the type of motion described by Elliott (1976) where thrusting proceeds in the direction of the downslope on the surface of the thrust sheet, even if the lower surface dips in the opposite direction. This process can ultimately result in the "piggy-backing" of thrust sheets that is observed in the Hare Bay and Humber Arm Allochthons, and may have produced the thrust-related splay faults and ductile deformation zones described by Atkinson (1976).

Motion along high-level, brittle thrust faults, facilitated by high fluid pressure in the shaley melange zones between the thrust sheets (e.g. Hubbert and Rubey, 1959; Stevens, 1970) brought the assembled Hare Bay Allochthon over the now-submerged continental shelf. In southwestern Newfoundland, this was accomplished by the early Middle Ordovician, as dated by the neoautochthonous Long Point Formation, and in the Hare Bay area cannot have pre-dated the deposition of the Llanvirn Goose Tickle Flysch. Since the earliest motion of the thrust sheets in the Hare Bay area, as dated by the Green Ridge Amphibolite, occurred at 480 Ma, compared to 460 Ma for the Bay of Islands Complex, but the final emplacement in both cases was Llanvirn or slightly later, a greater transport distance or a slower assembly process for the Hare Bay Allochthon is implied.

5.3. Post-tectonic History

After the emplacement of the thrust sheets in the early Middle Ordovician, the only major structural event to affect the St. Anthony Complex was an episode of upright folding, probably of Acadian age (Smyth, 1973). This affected the eastern part of the St. Anthony Complex, particularly the Fischot Islands and the Goose Cape Peninsula, but had virtually no effect in the west. A series of post-tectonic, northeast trending diabase and lamprophyre dykes cut the St. Anthony Complex. A lamprophyre dyke near Goose Cove has been dated at 408 ± 17 Ma (K-Ar; Wanless et al., 1968). Uplift and erosion, probably in several stages and most recently in the Pleistocene, have produced the present topography.

5.4. Regional Implications

5.4.1. The Hare Bay Allochthon

On the basis of the evidence presented here it seems likely that two different volcanic sequences are associated with the Maiden Point Formation. An early one, related to late Precambrian rifting and correlative with the Lighthouse Cove Formation, was subsequently buried beneath the sediments of the continental slope and rise and underwent high pressure metamorphism under conditions transitional between greenschist and blueschist facies, with the development of sodic amphibole-bearing assemblages (Jamieson, 1977b, and unpublished data). The later (Ordovician) sequence included the Ireland Point, Cape Onion, and Quirpon Harbour volcanics and was related to within-plate volcanic activity. These rocks underwent only very low-grade alteration and little

deformation except where directly involved in the dynamothermal metamorphism associated with the formation of the St. Anthony Complex. In the vicinity of St. Lunaire and Quirpon, however, the two types of basalts are spatially associated, suggesting that the Hare Bay Allochthon is greatly thinned in the northeast.

Unfortunately the work presented here does nothing to clarify the origin of the St. Julien Island polymictic conglomerate. The source of the rhyolite and microgranite clasts remains obscure. The only new possibility raised by this study is that the seamounts which included the Ireland Point and Cape Onion volcanics might also have included more differentiated, acidic rocks not preserved in the allochthon.

5.4.2. Other Areas in Western Newfoundland

The obvious implications of this study for the history of the Bay of Islands Complex will be discussed in the concluding chapter. Elsewhere in the Humber Arm Allochthon, the origin of the Ireland Point and Cape Onion volcanics may be related to that of the much more alkaline Skinner Cove Formation, which also has petrological and geochemical affinities to within-plate alkaline sequences (Strong, 1974; Baker, in prep.) but is not associated with continentally-derived sediments. Although there is now some doubt that their ages are similar (D. Baker, pers. comm., 1977) the broad lithological similarity and identical structural setting suggest that they may have formed by similar processes. In this sense, there is more geological control on the origin of the Ireland Point Volcanics, and if the Skinner Cove Formation had a similar origin certain hypotheses (such as a fore-arc basin setting) could be

eliminated. Since there is no direct relationship between the rocks, further speculation is not very useful.

It has recently been suggested that the Little Port Complex and possible correlatives in the Lewis Hills (referred to as the "Coastal Complex" by Karson and Dewey, 1978) originated in a transform fault zone which ran perpendicular to the spreading centre at which the Bay of Islands ophiolites were formed, and obliquely to the adjacent continental margin. According to this hypothesis, the impingement of the transform zone onto the margin led to the diachronous emplacement of the ophiolites. At Hare Bay, there is no evidence that a transform fault had anything to do with the origin or emplacement of the St. Anthony Complex. However, since the upper levels of the ophiolite are not preserved there, this does not negate the hypothesis. If the suggestion is correct, it is possible that the St. Anthony Complex, some 350 km north of the Lewis Hills, originated beyond the transform zone. If the suggestion is not correct, the origin of the "Coastal Complex" remains enigmatic. Some of the rocks associated with it, particularly the Old Man Cove Slice, are very similar to the Goose Cove Schist, and may have originated in a dynamothermal aureole. However, the extremely inhomogeneous deformation, variety of rock types, and evidence for contemporaneous magmatism and deformation are unlike the geological relationships seen in the St. Anthony Complex.

The history of the St. Anthony Complex also has implications for the much more complex geology of the Baie Verte area (e.g. Williams et al., 1977). At Hare Bay it has been shown that units of different origin can be structurally juxtaposed with no apparent break, that

units of metamorphic origin can resemble stratigraphic units, etc. In short, a complex sequence of deformed metamorphic rocks should be treated as a stratigraphic sequence with great caution and then only when less deformed equivalents can be traced into the rocks. The history of geological interpretations of the Baie Verte area illustrates this (e.g. Williams, 1977a). Specific features of the St. Anthony Complex which have a bearing on the geology of the Baie Verte area include support for the suggestion that the root zone for the ophiolites was 100 km or more from their present location (e.g. Williams, 1977a), that subduction was east-dipping (Strong et al., 1974; Williams and Stevens, 1974), and that garnet amphibolites associated with the Baie Verte ultramafics are parts of dynamothermal aureoles (L. Riccio, pers. comm. to D. F. Strong, 1974). The St. Anthony Complex also shows that the western margin of Iapetus had a more complex volcanic history than previously thought, so that the volcanic sequences of the Baie Verte area (e.g. Snook's Arm) need not fit snugly into a "ridge" or "arc" model (cf. Jenner, 1977).

Polydeformed greenschists resembling the Goose Cove Schist which are thought to have formed in structural aureoles associated with the transport of ophiolites and other plutonic rocks occur along the western side of White Bay, from the Fischot Islands through Croque Head to Coney Arm (Smyth, 1973; Williams, 1977b). This implies that dynamothermal metamorphism, far from being a localized feature in western Newfoundland, was a necessary consequence of tectonic transport in the area.

CHAPTER 6. THE OPHIOLITE AUREOLE PROBLEM

The association of ophiolites with dynamothermal aureoles is an apparent contradiction which has led to controversy concerning the origin and emplacement of ultramafic rocks in orogenic belts (e.g. Green, 1967; Thayer, 1967; Maxwell, 1969). Within the St. Anthony Complex, the sequence of high grade amphibolites to undeformed volcanics preserves a record of the emplacement of the White Hills Peridotite from the mantle to the crust. If other dynamothermal aureoles are similar, comparison with the St. Anthony Complex could lead to some generalizations regarding peridotite emplacement processes. In Tables 6.1 to 6.3 information from the Bay of Islands, Mount Albert, Lizard, Tinaquillo, Red Hills, Brezovica, Krivaja, and Ronda peridotites is summarized and compared to data from the St. Anthony Complex. Several of these are still widely interpreted as mantle diapirs, and at least one, the Ronda peridotite, probably underwent both a diapiric and a tectonic emplacement phase. Some examples of ophiolites associated with high grade metamorphic rocks have not been included because of structural discontinuities between the peridotite and the aureole, or because of scanty published descriptions.

6.1. Geological Setting

All the peridotite-dynamothermal aureole complexes considered here except the Ronda originated in an oceanic setting, as indicated by the abundance of spilitic pillow lavas and marine sediments associated with them, although they are not generally parts of complete ophiolite suites. Some are associated with ophiolitic melange. The peridotites

are all broadly alpine in character, but differ in the proportions of harzburgite, lherzolite, and basic layers, and in the amount of ophiolite superstructure preserved. In all cases, the peridotite and its aureole have been preserved as complete structural units because of emplacement as parts of large thrust sheets (Table 6.1).

6.2. Relationships of the Peridotites to their Aureoles

In all cases, the peridotite can be interpreted as a sheet overlying its aureole, although metamorphic rocks probably dating from an early diapiric event overlie the Ronda peridotite (Loomis, 1972; Lundeen, 1978), and the Tinaquillo peridotite is also reported to have aureole rocks overlying it (MacKenzie, 1960). The peridotite at the contact is generally mylonitic, with a strong foliation parallel to the contact. The contact, where visible, is planar and tectonic, and interbanding of peridotite and aureole rocks parallel to the contact over several metres can occur. The aureole rocks at the contact are generally reported to be relatively coarse-grained, and homogeneous, compared to the underlying amphibolites which are strongly foliated and compositionally layered parallel to the contact. The aureoles grade into the surrounding rocks with decreasing intensity of deformation and metamorphic grade, and some are interpreted as being superimposed on regionally metamorphosed rocks. The aureoles are commonly reported to be 500 to 1000 metres thick. For all the sub-oceanic peridotites, metabasites occur in the inner part of the aureole, while metasediments, if present, occur farther away from the peridotite contact. At the Ronda, the only sub-continental peridotite considered here, the aureole rocks are metasedimentary gneisses (Table 6.2).

6.3. Metamorphism

Recrystallized assemblages in the peridotite contact zones are commonly obliterated by serpentization. Pre- or syn-tectonic amphibole, generally green or brown pargasite, is commonly present in the contact zone, although in the case of the Tinaquillo peridotite the distribution of amphibole does not appear to be related to the contact. Plagioclase occurs in the contact zones of the Lizard and White Hills peridotites, while metamorphic garnet is present in the Bay of Islands basal zone. Late- or post-tectonic talc and tremolite occur locally.

In the aureole, the contact zone rocks may be pyroxene- or garnet-bearing amphibolites, granulites, garnet granulites, or eclogites, with equivalent grades in metasediments. Garnet is common in the contact zone except in the St. Anthony Complex, the Red Hills, and the Lizard. The amphibolites are commonly enriched in CaO and MgO/FeO close to the contact; this is generally attributed to metasomatism but is interpreted as a primary compositional feature in the St. Anthony Complex.

Estimated emplacement temperatures for the peridotites range from 900° to 1200°C, with corresponding contact temperatures in the aureole of 700° to 900°C at variable pressures (Table 6.3).

Pyroxene, garnet, and amphibole compositions are compared to data from the St. Anthony Complex in Figs. 6.1 to 6.3. Some of the variability is probably attributable to analytical technique -- microprobe for the St. Anthony Complex and Bay of Islands Complex, conventional wet analysis of mineral separates for the others.

Fig. 6.1b shows the compositions of aureole pyroxenes from the various localities. Tie lines join coexisting ortho- and clinopyroxenes from the Lizard aureole; two-pyroxene data from the same samples are not given elsewhere. The arrow shows the trend of clinopyroxene compositions toward diopside with decreasing distance from the peridotite contact, and therefore increasing temperature. The Yugoslavian clinopyroxenes are jadeitic (2% Na_2O and 6% Al_2O_3), reflecting their occurrence in eclogites.

Fig. 6.1a shows the compositions of pyroxenes from the basal zones of the peridotites. In all cases the data are from amphibole-bearing lherzolites, which is reflected in their relatively Fe-rich compositions.

Two-pyroxene temperatures were calculated for the Lizard peridotite and aureole, and are compared to the St. Anthony Complex estimates in Table 6.4. While the peridotite temperatures of 872° and 883°C agree with the White Hills estimates within the 70°C error of the method, the granulite temperatures, 976° and 946°C , are 100°C higher than the estimates for the Brimstone Pond amphibolites. If the temperature estimates are correct, the granulites must have recrystallized under extremely low water pressures, and at higher temperatures than the adjacent peridotite. Since this seems unlikely, the pyroxene compositions may be suspect, but without more detailed information on the Lizard mineral parageneses no further conclusions can be drawn.

Figure 6.2 shows the compositions of garnets from garnetiferous amphibolites or granulites in the aureoles. The arrows show the

compositional trends toward the peridotite reported from the Bay of Islands aureole (Malpas, 1976) and inferred from the Mount Albert aureole (MacGregor, 1964). The experimental results of Råheim and Green (1974) show that at constant pressure, garnet in equilibrium with clinopyroxene becomes enriched in Ca and Fe with increasing temperature, and at constant temperature garnet becomes enriched in Mg with increasing pressure. These results suggest that the Bay of Islands compositional trend reflects a pressure increase towards the peridotite contact, while the Mount Albert trend is primarily controlled by temperature. Pyrope-rich garnets from the Dinarides eclogites reflect a high pressure origin, while garnet from the St. Anthony Complex (from a single sample an unknown distance from the peridotite contact) plot at the low temperature end of the Mount Albert trend.

The garnet and clinopyroxene compositions have been used with the calibration of Råheim and Green (1974) to estimate the equilibration temperatures, assuming pressures of 5 kb for the Mount Albert aureole, 10 kb for the Bay of Islands, and 15 kb for the Central Dinarides. The results are given as ranges in Table 6.5. Mount Albert garnet amphibolites give the lowest temperatures (725° - 925° C), the Bay of Islands the highest (750° - 950° C), and the Dinarides intermediate estimates (730° - 875° C). Although there is considerable uncertainty in the pressure and in the location of the samples with respect to the peridotite contacts, the results are compatible with the metamorphic parageneses and suggest that temperatures of $800^{\circ} \pm 100^{\circ}$ C were achieved.

The compositions of amphiboles from the aureole amphibolites are plotted in Fig. 6.3a. The plot shows considerable scatter, largely

owing to lack of information about the amphibole parageneses, but the compositions generally overlap with the St. Anthony Complex data, trending towards pargasite with higher grade. The Dinarides compositions are somewhat enriched in (Na + K) with respect to Al^{IV} , which is consistent with a high pressure origin (Steffe, 1978).

Peridotite amphibole compositions are plotted in Fig. 6.3b. The pargasites from the base of the Bay of Islands Complex are very similar to the White Hills Peridotite amphiboles, but those from the Lizard and Tinaquillo peridotites are relatively poor in alkalies. All fall within the range of primary amphibole compositions from St. Paul's Rocks, and constrain the maximum emplacement temperatures of the host peridotites to $1050^{\circ}C$.

The metamorphic phase assemblages and mineral compositions for the other peridotite-aureole complexes suggest that temperatures of $800^{\circ}C$ were commonly achieved in the contact zones of the aureoles, under variable pressure conditions, but insufficient data are available from the other areas to determine P-T gradients. The Ronda mineralogical data have not been considered here because of the different lithologies involved. Temperature estimates of $725^{\circ}C$ given by Loomis (1972b), Westerhof (1977), and Lundeen (1978) are lower than those for metabasic rocks in contact with sub-oceanic peridotite, and both high pressure (9 kb) and low pressure (3.5 kb) assemblages are preserved. The thermal gradient calculated by Loomis (1972b) for the Casares unit overlying the peridotite has a much shallower T/x slope than the one estimated for the St. Anthony Complex.

6.4. Discussion

Given the many points of similarity among peridotite-aureole associations around the world, the results of this study of the St. Anthony Complex may be applicable in a broader sense. In particular, the concepts of frictional heating, and of the vertical and lateral translation of units to form a composite aureole can explain some features common to most peridotite aureoles and clarify the general problem of solid state peridotite emplacement.

If the St. Anthony Complex is typical, dynamothermal aureoles associated with alpine-type peridotites and ophiolites are formed by metamorphism at progressively shallower depths as the peridotite is displaced over tholeiitic gabbros, then volcanics, and finally sediments. This would explain the lithological zonation commonly reported within the aureoles, where CaO-MgO rich, coarse-grained amphibolites, probably derived from gabbros, occur close to the peridotite and metasediments occur in the lower parts of the aureoles.

The tendency for similar contact temperatures to be reached in many peridotite aureoles can be interpreted as the result of frictional heating, which would raise the temperature of the rocks to a limiting value determined mainly by the shear strengths of the rocks. In rocks with similar physical properties, similar temperatures would be reached regardless of the ambient geothermal conditions. In rocks with different properties, different temperatures would be reached, which may explain why the Ronda aureole, composed of metasedimentary rocks rather than metabasic ones, apparently recrystallized at somewhat

lower temperatures. On the other hand, if the high temperatures were produced solely by conduction from hot peridotites, the peridotite and its surroundings must always have been at the right relative temperatures to produce contact temperatures of about 800°C. Alternatively, if the temperature of the contact zone rocks has been inherited from deep-seated rocks transported with the peridotite from depth, a similar coincidence of circumstances is required in order to juxtapose rocks at temperatures close to 800°C with peridotite under a variety of pressure conditions.

Most discussions of the formation of dynamothermal aureoles with either diapirically or tectonically emplaced peridotite have concluded that anomalously hot mantle material was involved (e.g. Green, 1964; Loomis, 1972; Malpas, 1976). Most estimates of the emplacement temperatures of the peridotites are based either on the presence of a high temperature contact aureole, or on the presence of high temperature mineral assemblages within the peridotites (e.g. Green, 1963, 1967). However, the presence of a dynamothermal aureole does not provide adequate information on the emplacement temperature of the associated peridotite, since the high temperatures could be produced by frictional heating, while the high temperature mineral assemblages in the peridotites described generally formed prior to emplacement into the crust. The peridotite emplacement temperature must be estimated from assemblages which formed during the emplacement event, which in most cases means the mineral assemblages in the marginal mylonites of the peridotites.

In the St. Anthony Complex, the Bay of Islands Complex, the Lizard peridotite, and the Tinaquillo peridotite, the presence of pre- or syn-tectonic amphibole limits the emplacement temperature to 1050°C

or less. The available two-pyroxene temperatures from the marginal zones of the St. Anthony Complex, the Lizard, and Mount Albert (MacGregor and Basu, 1976) indicate recrystallization at temperatures of 950°C or less. The Ronda peridotite, which originally equilibrated in the mantle at temperatures of $1100\text{-}1200^{\circ}\text{C}$ and pressures of 20-35 kb, re-equilibrated during its ascent at temperatures of $800\text{-}1000^{\circ}\text{C}$ and pressures of 5-13 kb (Obata, 1977). These data indicate that temperatures of 1000°C are probably close to a maximum for peridotite emplacement, rather than the minimum suggested by Green (1967).

Temperatures of $800\text{-}1000^{\circ}\text{C}$ are high compared to the temperatures estimated for many alpine-type peridotites and the basal parts of ophiolites. For a peridotite at the depth of 8 to 10 km implied by the stratigraphy of the Bay of Islands Complex, these temperatures require geothermal gradients of close to $100^{\circ}/\text{km}$. However, the presence of metamorphic garnet in the ultramafic mylonites and garnetiferous amphibolites implies pressures greater than the 3 kb suggested by the present stratigraphy. The mineral assemblages at the base of the White Hills Peridotite indicate recrystallization at pressures of 7 to 10 kb, that is, at depths much greater than a reconstructed ophiolite stratigraphy would suggest. If there has been considerable vertical translation of peridotite in zones of high strain in the basal zone, as suggested by Mercier (1976), the hotter parts of the ophiolites could have been derived from much greater depths than their present thickness indicates. Temperatures of $800\text{-}1000^{\circ}\text{C}$ might then be produced under normal geothermal conditions, and the hotter material transported from depth during the early displacement of the peridotite from the upper mantle.

The concept of the initiation of peridotite emplacement at depth within the mantle is based on the evidence from western Newfoundland, but if friction is the main source of heat, there is no theoretical necessity for deep-seated, hot peridotite to have been involved in the formation of the dynamothermal aureoles. However, since the heat produced by friction depends on the shear strengths of the rocks, serpentinitized peridotites probably do not produce dynamothermal aureoles. The presence of garnet amphibolites and granulites in many aureoles indicates that metamorphism begins deep within the crust, so that disruption of the ophiolite-aureole complex during transport to the surface is likely.

It is concluded that alpine-type peridotites with dynamothermal aureoles are likely to have been tectonically rather than diapirically emplaced into the crust, although a diapiric history within the mantle is likely. Although the processes leading to the formation of the dynamothermal aureoles must be extremely complex, the following pattern is suggested. Peridotite is displaced through the upper mantle, either diapirically or along incipient thrusts, and eventually displaced from the mantle along thrust faults. As the peridotite overrides crustal rocks, a composite aureole is formed by the upward translation and juxtaposition of rocks from different levels which are strongly deformed and undergo high temperature metamorphism as the result of frictional heating. The whole complex is eventually emplaced in an orogenic belt along high level, brittle thrust faults. Thus, dynamothermal metamorphism is probably the rule, rather than the exception,

during the early stages of ophiolite emplacement, but the results are not likely to be preserved.

6.5. Summary and Conclusions

(1) The St. Anthony Complex comprises a suite of alkaline basaltic pillow lavas and pyroclastics (the Ireland Point Volcanics), greenschist and epidote amphibolite facies metabasic and metasedimentary rocks (the Goose Cove Schist), amphibolite to transitional granulite facies metabasites and rare marbles (the Green Ridge Amphibolite), a complex association of dunite, troctolite, gabbro, and anorthosite (the Long Ridge Metagabbro), and a harzburgite-lherzolite massif (the White Hills Peridotite). These rocks are interpreted as a partial ophiolite and a dynamothermal aureole formed during its tectonic emplacement.

(2) The metamorphic grade increases nearly continuously from the base of the St. Anthony Complex to the amphibolite-peridotite contact, while the degree of recrystallization in the peridotite decreases upwards from the contact. However, cryptic lithological and structural discontinuities occur within the aureole, and a major late-tectonic mylonite zone occurs at the epidote amphibolite to amphibolite facies transition.

(3) Estimates of metamorphic temperatures indicate that the basal mylonites of the White Hills Peridotite recrystallized at 900-950°C, and the adjacent two-pyroxene amphibolites and metagabbros at 850-900°C. The transition from undeformed volcanics to greenschists occurs at about 350°C. This corresponds to an overall thermal gradient

of 750-800°C/km, and an estimated pressure change from 7-10 kb at the peridotite contact to about 2 kb at the greenschist-volcanic transition. A break in the thermal gradient occurs at the level of the biotite amphibolite mylonite zone, indicating that post-metamorphic thinning of the sequence occurred at the epidote amphibolite-amphibolite facies transition.

(4) The P-T estimates and lithological data suggest that the dynamothermal aureole is composite, formed by the juxtaposition of progressively shallower units during the metamorphism which accompanied peridotite emplacement.

(5) Thermal models suggest that both frictional heat and conduction of heat from the peridotite contributed to the high temperatures in the contact zone. They do not account for the steep thermal gradient through the aureole, further supporting the model of a composite metamorphic sequence.

(6) The evidence is consistent with a model of westward transportation of the White Hills Peridotite, to override oceanic gabbros and basalts, an alkali basalt suite that may have been part of a seamount, and turbidites of the continental slope and rise, before final emplacement along high level thrust faults as part of the Hare Bay Allochthon.

(7) Comparison with other occurrences of dynamothermal aureoles beneath transported peridotites shows general similarities in geological setting, lithology, and metamorphic grade. It is concluded that the formation of dynamothermal aureoles does not require anomalously hot peridotite, but that it is a normal process accompanying the early stages of tectonic peridotite emplacement.

REFERENCES

- ABBEY, S., 1975. Studies in "Standard Samples". Geol. Surv. Can. Pap. 74-41.
- ALTHAUS, E., 1968. Der Einfluß des Wassers auf metamorphe Mineralreaktionen. Neues Jahrb. Mineral. Monat. 9, pp. 289-306.
- AOKI, K., 1963. The kaersutites and oxykaersutites from alkaline rocks of Japan and surrounding areas. Jour. Petrol., 4, pp. 198-210.
- ARMSTRONG, R. L. and DICK, H. J. B., 1974. A model for the development of thin overthrust sheets of crystalline rock. Geology, 2, pp. 35-40.
- ATHERTON, M. J., 1977. Metamorphism of the Dalradian rocks of Scotland. Scot. Jour. Geol., 13, pp. 331-370.
- ATKINSON, S. J., 1976. Ophiolite emplacement onto continental margins. Nature, 264, pp. 164-165.
- AUMENTO, F. and LONCAREVIC, B. D., 1969. The Mid-Atlantic Ridge near 45°N. III. Bald Mountain. Can. Jour. Earth Sci., 6, pp. 11-23.
- BADHAM, J. P. N. and KIRBY, G. A., 1976. Ophiolites and the generation of ocean crust: data from the Lizard Complex, Cornwall. Bull. Geol. Soc. France, 18, pp. 885-888.
- BAKER, D., 1978. Petrology and geochemistry of the Skinner Cove Volcanics. M.Sc. Thesis, Memorial University of Newfoundland, in preparation.
- BECK, H., 1978. The St. Anthony Complex. W.A.S.T.E.D. Memoir 1 (abst.), p. 21.
- BELL, T. H., 1978. Progressive deformation and reorientation of fold axes in a ductile mylonite zone: the Woodroffe thrust. Tectonophysics, 44, pp. 285-320.
- BELL, T. H. and ETHERIDGE, M. A., 1973. Microstructure of mylonites and their descriptive terminology. Lithos, 6, pp. 337-348.
- BENCE, T. and ALBEE, A., 1968. Empirical correction factors for the electron microanalysis of silicates and oxides. Jour. Geol., 76, pp. 382-401.
- BINNS, R. A., 1965. The mineralogy of metamorphosed basic rocks from the Willyama complex, Broken Hill district, New South Wales. Part I: Hornblendes. Mineral. Mag., 35, pp. 306-326.
- BINNS, R. A., 1968. Experimental studies of metamorphism at Broken Hill, in "Broken Hill Mines - 1968". Aust. Inst. Min. Metall., Melbourne, pp. 199-204.

- BINNS, R. A., 1969. Hydrothermal investigations of the amphibolite-granulite facies boundary. Spec. Publ. Geol. Soc. Aust., 2, pp. 341-344.
- BIRCH, F., SCHAIRER, J. F. and SPICER, H. C. (Ed.), 1942. Handbook of physical constants. Geol. Soc. Am. Spec. Pap., 36, 325p.
- BOETTCHER, A. L., MYSEN, B. O., and MODRESKI, P. J., 1975. Melting in the mantle: Phase relationships in natural and synthetic peridotite-H₂O and peridotite-H₂O-CO₂ systems at high pressures. Phys. Chem. Earth, 9, pp. 855-867.
- BOSTOCK, H. H., CUMMINGS, L. M., WILLIAMS, H., and SMYTH, W. R., 1976. Geological map of the Strait of Belle Isle region. Geol. Surv. Can. Open File 347.
- BOWEN, N. L., 1928. The Evolution of the Igneous Rocks. Princeton University Press, Princeton, N.J., 1928.
- BROWN, W. L., 1962. Peristerite unmixing in the plagioclases and metamorphic facies series. Norsk. Geol. Tidss. 42, pp. 354-382.
- BUDDINGTON, A. F. and LINDSLEY, D. H., 1964. Iron-titanium oxide minerals and synthetic equivalents. Jour. Petrol., 5, pp. 310-357.
- BURKE, K. and DEWEY, J. F., 1973. Plume-generated triple junctions -- key indicators in applying plate tectonics to old rocks. Jour. Geol., 81, pp. 406-433.
- BURSNALL, J. T. and de WIT, M. J., 1975. Timing and development of the orthotectonic zone in the Appalachian Orogen of northwest Newfoundland. Can. Jour. Earth Sci., 12, pp. 1712-1722.
- CANN, J. R., 1969. Spilites from the Carlsberg Ridge, Indian Ocean. Jour. Petrol., 10, pp. 1-19.
- CARSLAW, H. S. and JAEGER, J. C., 1959. Conduction of Heat in Solids. 2nd ed. Oxford University Press, New York, 510p.
- CARSTENS, H., 1963. On the variolitic structure. Nor. Geol. Unders. Arb., 223, pp. 26-42.
- CAWTHORN, R. G. and O'HARA, M. J., 1976. Experimental evidence for amphibole fractionation in calc-alkaline magma genesis. Amer. Jour. Sci., 276, pp. 309-329.
- CHALLIS, G. A., 1965. High-temperature contact metamorphism of the Red Hills ultramafic intrusion - Wairau Valley, New Zealand. Jour. Petrol., 6, pp. 395-419.
- CHALLIS, G. A., 1965. The origin of New Zealand ultramafic intrusions. Jour. Petrol., 6, pp. 322-364.
- CHURCH, W. R., 1969. Metamorphic rocks of the Burlington Peninsula and adjoining areas of Newfoundland, and their bearing on continental drift in the North Atlantic, in "North Atlantic - Geology and Continental Drift", M. Kay (ed.). Am. Assoc. Petrol. Geol. Mem. 12, pp. 212-233.

- CHURCH, W. R., 1972. Ophiolite: its definition, origin as oceanic crust, and mode of emplacement in orogenic belts, with special reference to the Appalachians. In: "The Ancient Oceanic Lithosphere", E. Irving (ed.), Publ. of the Earth Physics Branch, Dept. of Energy, Mines and Resources, Ottawa, 42, pp. 71-85.
- CHURCH, W. R., and STEVENS, R. K., 1971. Early Paleozoic ophiolite complexes of the Newfoundland Appalachians as mantle-oceanic crust sequences. Jour. Geophys. Res., 76, (4), pp. 1460-1466.
- CLARK, S. P. (Ed.), 1966. Handbook of Physical Constants (revised edition). Geol. Soc. Am. Mem., 97, pp. 459-482.
- COLEMAN, R. G., 1971. Plate tectonic emplacement of upper mantle peridotites along continental edges. Jour. Geophys. Res., 76, pp. 1212-1222.
- COLEMAN, R. G., 1977. Ophiolites: Ancient Oceanic Lithosphere? 229p. Springer-Verlag, Berlin, Heidelberg, New York.
- COLEMAN, R. G., GARCIA, M., and ANGLIN, C., 1976. The amphibolite of Briggs Creek: a tectonic slice of metamorphosed oceanic crust in south-western Oregon? Geol. Soc. Am. Abst., 8, p. 363.
- COOMBS, D. S., LANDIS, C. A., NORRIS, R. J., SINTON, J. M., BORNS, D. J., and CRAW, D., 1976. The Dun Mountain ophiolite belt, New Zealand, its tectonic setting, constitution, and origin, with special reference to the southern portion. Amer. Jour. Sci., 276, pp. 561-603.
- COOPER, A. F., 1972. Progressive metamorphism of metabasic rocks from the Haast schist group of southern New Zealand. Jour. Petrol., 13, pp. 457-492.
- COOPER, A. F. and LOVERING, J. F., 1970. Greenschist amphiboles from Haast River, New Zealand. Contrib. Mineral. Petrol., 27, pp. 11-24.
- COOPER, J. R., 1937. Geology and mineral deposits of the Hare Bay area. Nfld. Dept. Nat. Res., Geol. Sec. Bull., 9, 36p.
- DALLMEYER, R. D., 1977. Diachronous ophiolite obduction in western Newfoundland: evidence from $^{40}\text{Ar}/^{39}\text{Ar}$ ages of the Hare Bay metamorphic aureole. Amer. Jour. Sci., 277, pp. 61-72.
- DALLMEYER, R. D. and WILLIAMS, H., 1975. $^{40}\text{Ar}/^{39}\text{Ar}$ ages from the Bay of Islands metamorphic aureole: their bearing on the timing of Ordovician ophiolite obduction. Can. Jour. Earth Sci., 12, pp. 1685-1690.

- DALY, R. A., 1903. Variolitic pillow-lava from Newfoundland. Amer. Geol., 32, pp. 65-78.
- DAVIS, B. T. C. and BOYD, F. R., 1966. The join $\text{Mg}_2\text{Si}_2\text{O}_6$ - $\text{Ca Mg Si}_2\text{O}_6$ at 30 kb pressure and its application to pyroxenes from kimberlites. Jour. Geophys. Res., 71, pp. 3567-3576.
- DEAN, P. L., 1978. The volcanic stratigraphy and metallogeny of Notre Dame Bay, Newfoundland. M.Sc. Thesis, Memorial University of Newfoundland, 204p.
- DEER, W. A., HOWIE, R. A. and ZUSSMAN, J., 1970. An Introduction to the Rock-Forming Minerals. Longman, London, 528p.
- DE JONGH, W. K., 1973. X-Ray fluorescence analysis applying theoretical matrix corrections. Stainless steel. X-Ray Spectrom., 2, no. 4.
- DE LONG, R. C., 1976. Geology, petrography, and possible petrogenesis of the Cape Onion Formation, Newfoundland. Unpubl. B.Sc. Honours Thesis, Memorial University of Newfoundland., 72p.
- DE LONG, S. E., HODGES, F. N. and ARCULUS, R. J., 1975. Ultramafic and mafic inclusions, Kanaga Island, Alaska, and the occurrence of alkaline rocks in island arcs. Jour. Geol., 83, pp. 721-736.
- DEWEY, J. F. and BIRD, J. M., 1971. Origin and emplacement of the ophiolite suite: Appalchian ophiolites in Newfoundland. Jour. Geophys. Res., 76, pp. 3179-3206.
- DEWIT, M. J. and STERN, C. R., 1976. A model for ocean-floor metamorphism, seismic layering, and magnetism. Nature, 264, pp. 615-619.
- DEWIT, M. J. and STRONG, D. F., 1975. Eclogite-bearing amphibolites from the Appalachian mobile belt, N.W. Newfoundland: dry versus wet metamorphism. Jour. Geol., 83, pp. 609-627.
- DICK, H. J. B., 1977. Partial melting in the Josephine Peridotite I: The effect on mineral composition and its consequence for geobarometry and geothermometry. Amer. Jour. Sci., 277, pp. 801-832.
- DICKEY, J. S., 1970. Partial fusion products in alpine-type peridotites: Serrania de la Ronda and other examples. Mineral. Soc. Am. Spec. Pap. 3, pp. 33-49.
- DIETZ, R. S., 1963. Alpine serpentinites as oceanic rind fragments. Geol. Soc. Am. Bull., 74, pp. 947-952.
- DILLON, W. P. and SOUGY, J. M. A., 1974. Geology of West Africa and Canary and Cape Verde Islands. In "The Ocean Basins and Margins", A.E.M. Nairn and F. G. Stehli (eds), Plenum, New York, pp. 315-390.

- DIXON, J. R. and PRESNALL, D. C., 1977. Geothermometry and geobarometry of synthetic spinel lherzolite in the system $\text{CaO-MgO-Al}_2\text{O}_3\text{-SiO}_2$. Extended Abst., 2nd Int. Kimberlite Conference.
- DOIG, R., 1970. An alkaline rock province linking Europe and North America. *Can. Jour. Earth Sci.*, 7, pp. 22-28.
- DOIG, R. and BARTON, J. M., 1968. Ages of carbonatites and other alkaline rocks in Quebec. *Can. Jour. Earth Sci.*, 5, pp. 1401-1407.
- DONALDSON, C. H., 1977. Kaersutite overgrowths on highly aluminous titanaugite in the Quarsut sill. *Mineral. Mag.* 41, pp. 297-300.
- ELLIOTT, D., 1976. The motion of thrust sheets. *Jour. Geophys. Res.*, 81, pp. 949-963.
- EMSLIE, R. F., 1970. Liquidus relations and subsolidus reactions in some plagioclase-bearing systems. *Carn. Inst. Wash. Yb.*, 69, pp. 148-155.
- EMSLIE, R. F., 1975. Pyroxene megacrysts from anorthositic rocks: new clues to the sources and evolution of the parent magmas. *Can. Mineral.*, 13, pp. 138-145.
- ENGEL, A. E. J. and ENGEL, C. G., 1962. Hornblendes formed during progressive metamorphism of amphibolites, northwest Adirondack Mountains, New York. *Geol. Soc. Am. Bull.*, 73, pp. 1499-1514.
- ERNST, W. G., 1970. Tectonic contact between the Franciscan melange and the Great Valley sequence - crustal expression of a late Mesozoic Benioff zone. *Jour. Geophys. Res.*, 75, pp. 886-901.
- EVANS, B. W. and FROST, B. R., 1975. Chrome spinel in progressive metamorphism -- a preliminary analysis. *Geochim. Cosmochim. Acta*, 39, pp. 959-972.
- FERRY, J. M. and SPEAR, F. S., 1978. Experimental calibration of the partitioning of Fe and Mg between biotite and garnet. *Contrib. Mineral. Petrol.*, 66, pp. 113-117.
- FIELD, D. and ELLIOTT, R. B., 1974. The chemistry of gabbro/amphibolite transitions in south Norway. II. Trace elements. *Contrib. Mineral. Petrol.*, 47, pp. 63-76.
- FLETT, J. S., 1946. Geology of the Lizard and Meneage: Great Britain *Geol. Surv. Mem.*, 208p.
- FLOWER, M. F. J., ROBINSON, P. T., SCHMINCKE, H.-U., and OHNMACHT, W., 1977. Petrology and geochemistry of igneous rocks, DSDP Leg 37. In: Aumento, F., Melson, W. G. et al. "Initial Reports of the Deep Sea Drilling Project", 37, Washington, U. S. Gov't Printing Office), pp. 658-680.

- FLOYD, P. A. and WINCHESTER, J. A., 1975. Magma type and tectonic setting discrimination using immobile elements. *Earth Planet. Sci. Lett.*, 27, pp. 211-218.
- FORD, C. E., 1972. Phase relations in the system $\text{CaO-MgO-Al}_2\text{O}_3\text{-SiO}_2\text{-H}_2\text{O}$. NERC Prog. in Exp. Pet., 2, pp. 266-272.
- FRANCIS, D. M., 1976. The origin of amphibole in lherzolite xenoliths from Nunivak Island, Alaska. *Jour. Petrol.*, 17, pp. 357-378.
- FROST, B. R., 1975. Contact metamorphism of serpentinite, chloritic blackwall, and rodingite at Paddy-Go-Easy Pass, Central Cascades, Washington. *Jour. Petrol.*, 16, pp. 272-313.
- FURNES, H., 1973. Variolitic structure in Ordovician pillow lava and its possible significance as an environmental indicator. *Geology*, 1, pp. 27-30.
- GANSSEER, A., 1974. The ophiolitic melange, a world-wide problem on Tethyan examples. *Eclogae. Geol. Helv.*, 67, pp. 479-507.
- GARDNER, P. M. and ROBINS, B., 1974. The olivine-plagioclase reaction: geological evidence from the Seiland petrographic province, Northern Norway. *Contrib. Mineral. Petrol.*, 44, pp. 149-156.
- GASS, I. G., 1968. Is the Troodos Massif of Cyprus a fragment of Mesozoic ocean floor? *Nature*, 220, pp. 39-42.
- GASS, I. G. and SMEWING, J. D., 1973. Intrusion, extrusion, and metamorphism at constructive margins: evidence from the Troodos Massif, Cyprus. *Nature*, 242, pp. 26-29.
- GELINAS, L., BROOKS, C., and TRZCIENSKI, W. E., 1976. Archean variolites - quenched immiscible liquids. *Can. Jour. Earth Sci.*, 13, pp. 210-230.
- GELINAS, L., TRZCIENSKI, W. E. and BROOKS, C., 1977. Archean variolites and the hypothesis of quench immiscible liquids re-examined: a reply to criticisms. *Can. Jour. Earth Sci.*, 14, pp. 2945-2958.
- GILLIS, J. W., 1966. Great Northern Peninsula. In: *Geol. Soc. Can. Pap. 66-1* (S. E. Jenness, ed.), pp. 178-181.
- GITTINS, J., 1966. Summaries and bibliographies of carbonatite complexes. In: "Carbonatites", ed. O. J. Tuttle, J. Gittins, Interscience Publ., pp. 417-541.
- GLASSLEY, W. E., 1974. Geochemistry and tectonics of the Crescent volcanic rocks, Olympic Peninsula, Washington. *Geol. Soc. Am. Bull.*, 85, pp. 785-794.

- GOLDSMITH, J. R. and NEWTON, R. C., 1969. P-T-X relations in the system CaCO_3 - MgCO_3 at high temperatures and pressures. *Amer. Jour. Sci.*, 267A, pp. 160-190.
- GRAF, D. L. and GOLDSMITH, J. R., 1965. Dolomite-magnesian calcite relations at elevated temperatures and CO_2 pressures. *Geochim. Cosmochim. Acta*, 7, pp. 109-128.
- GRAHAM, C. M., 1974. Metabasite amphiboles of the Scottish Dalradian. *Contrib. Mineral. Petrol.*, 47, pp. 165-185.
- GRAHAM, C. M. and ENGLAND, P. C., 1976. Thermal regimes and regional metamorphism in the vicinity of overthrust faults: an example of shear heating and inverted metamorphic zonation from southern California. *Earth Planet. Sci. Lett.*, 31, pp. 141-152.
- GREEN, D. H., 1963. Alumina content of enstatite in a Venezuelan high temperature peridotite. *Geol. Soc. Am. Bull.*, 74, pp. 1397-1402.
- GREEN, D. H., 1964a. A re-study and re-interpretation of the geology of the Lizard Peninsula, Cornwall. In: "Present Views of Some Aspects of the Geology of Cornwall and Devon", K.F.G. Hosking and G. J. Shrimpton (eds.). *Roy. Geol. Soc. Cornwall*, pp. 87-115.
- GREEN, D. H., 1964b. The metamorphic aureole of the peridotite at the Lizard, Cornwall. *Jour. Geol.*, 72, pp. 543-563.
- GREEN, D. H., 1964c. The petrogenesis of the high-temperature peridotite intrusion in the Lizard area, Cornwall. *Jour. Petrol.*, 5, pp. 134-188.
- GREEN, D. H., 1967. High temperature peridotite intrusions. In: "Ultramafic and Related Rocks", P. J. Wyllie (ed.), John Wiley, New York, pp. 212-222.
- GREEN, D. H. and HIBBERSON, W., 1970. The instability of plagioclase in peridotite at high pressure. *Lithos*, 3, pp. 209-221.
- GREEN, D. H. and RINGWOOD, A. E., 1967. An experimental investigation of the gabbro to eclogite transformation and its petrological applications. *Geochim. Cosmochim. Acta*, 31, pp. 767-833.
- GRESENS, R. L., 1967. Composition-volume relations of metasomatism. *Chem. Geol.*, 2, pp. 47-65.
- GRIFFIN, W. L. and HEIER, K. S., 1973. Petrological implications of some corona structures. *Lithos*, 6, pp. 315-335.

- GRIGGS, D. T., TURNER, F. J. and HEARD, H. C., 1960. Deformation of rocks at 500 to 800°C. In: "Rock Deformation", D. Griggs and J. Handin (eds.). Geol. Soc. Am. Mem., 79, pp. 39-104.
- GROSVENOR, A. W., 1962. Basic Metallurgy. Volume 1 - Principles. American Society for Metals, Metals Park, Ohio, 697p.
- GUNN, B. and ROOBOL, M. J., 1977. Geochemistry of the igneous rocks. In: "Initial Reports of the Deep Sea Drilling Project," 37, (Washington, U. S. Gov't Printing Office), F. Aumento, W. G. Melson et al. (eds.), pp. 735-756.
- HARTE, B. and GRAHAM, C. M., 1975. The graphical analysis of greenschist to amphibolite facies mineral assemblages in metabasites. Jour. Petrol., 16, pp. 347-370.
- HAWORTH, R. T., POOLE, W. H., GRANT, A. C., SANFORD, B. V., 1976. Marine geoscience survey northeast of Newfoundland. Geol. Surv. Can. Pap. 76-1A, pp. 7-15.
- HELZ, R. T., 1973. Phase relations of basalts in their melting range at $P_{H_2O} = 5$ kb as a function of oxygen fugacity, Part I. Mafic phases. Jour. Petrol., 14, pp. 249-302.
- HELZ, R. T., 1976. Phase relations of basalts in their melting ranges at $P_{H_2O} = 5$ kb. Part II. Melt compositions. Jour. Petrol. 17, pp. 139-193.
- HERZBERG, C. T., 1976a. Influence of normative albite to anorthite ratio on mineral parageneses in peridotites. NERC Prog. in Exp. Pet., 3, pp. 249-251.
- HERZBERG, C. T., 1976b. The plagioclase-lherzolite to spinel-lherzolite facies boundary, its bearing on corona structure formation and tectonic history in the Norwegian Caledonides. NERC Prog. in Exp. Pet. 3, pp. 233-235.
- HERZBERG, C. T., 1978. Pyroxene geothermometry and geobarometry: experimental and thermodynamic evaluation of some subsolidus phase relations involving pyroxenes in the system CaO-MgO-Al₂O₃-SiO₂. Geochim. Cosmochim. Acta, 42, pp. 945-957.
- HOLDAWAY, M. J., 1972. Thermal stability of Al-Fe epidote as a function of f_{O_2} and Fe content. Contrib. Mineral. Petrol., 37, pp. 307-340.
- HOLLISTER, L. S., 1966. Garnet zoning: an interpretation based on the Rayleigh fractionation model. Science, 154, pp. 1647-1651.
- HOLLOWAY, J. R. and BURNHAM, C. W., 1972. Melting relations of basalt with equilibrium water pressure less than total pressure. Jour. Petrol., 13, pp. 1-29.

- HSU, L. C., 1968. Selected phase relationships in the system Al-Mn-Fe-Si-O-H : a model for garnet equilibria. *Jour. Petrol.* 9, pp. 40-83.
- HUBBERT, M. K. and RUBEY, W. W., 1959. Role of fluid pressure in mechanics of overthrust faulting I. Mechanics of fluid-filled porous solids and its application to overthrust faulting. *Geol. Soc. Am. Bull.*, 70, pp. 115-166.
- HUGHES, C. J., 1973. Spilites, keratophyres, and the igneous spectrum. *Geol. Mag.*, 109, pp. 513-527.
- HUGHES, C. J., 1977. Archean variolites -- quenched immiscible liquids: Discussion. *Can. Jour. Earth Sci.*, 14, pp. 137-139.
- HUNT, J. A. and KERRICK, D. M., 1977. The stability of sphene; experimental redetermination and geologic implications. *Geochim. Cosmochim. Acta*, 41, pp. 279-288.
- INGSTAD, H., 1969. Westward to Vinland: The Discovery of Pre-Columbian Norse House-sites in North America. St. Martin's Press, New York, 250p.
- IRVINE, T. N., 1965. Chromian spinel as a petrogenetic indicator, Part I. Theory. *Can. Jour. Earth Sci.*, 2, pp. 648-672.
- ITO, K. and KENNEDY, G. C., 1971. An experimental study of the basalt-garnet granulite-eclogite transition. In: "The structure and physical properties of the earth's crust", J. G. Heacock (ed.), *Amer. Geophys. Un. Geophys. Mon.*, 14, pp. 303-314.
- JAEGER, J. C., 1968. Cooling and solidification of igneous rocks. In: "Basalts: The Poldervaart Treatise on Rocks of Basaltic Composition", Vol. 2, Interscience Pub., New York, pp. 503-536.
- JAEGER, J. C. and COOK, N. G. W., 1969. Fundamentals of rock mechanics. Chapman and Hall, London, 513p.
- JAMIESON, R. A., 1977a. A suite of alkali basalts and gabbros associated with the Hare Bay Allochthon of western Newfoundland. *Can. Jour. Earth Sci.*, 14, pp. 346-356.
- JAMIESON, R. A., 1977b. The first metamorphic sodic amphibole identified from the Newfoundland Appalachians -- its occurrence, composition, and possible tectonic implications. *Nature*, 265, pp. 428-430.
- JAMIESON, R. A. and STRONG, D. F., 1978. Dynamic and chemical implications of a late syntectonic shear zone within the ophiolite aureole, St. Anthony Complex, northwestern Newfoundland. *GAC/MAC G.S.A. Abst. w. Prog.* 3, 1978 Ann. Mtg., Toronto, pp. 428-429.

- JAMIESON, R. A., and TALKINGTON, R. W. (in prep.). A jacupirangite-syenite association beneath the White Hills Peridotite, northwestern Newfoundland. (ms under review).
- JENNER, G. A., 1977. Geochemistry of the upper Snooks Arm Group, Newfoundland. M.Sc. thesis, Univ. Western Ontario, 123p.
- JONAS, J. J., SELLARS, C. M. and TEGART, W. J. McG., 1969. Strength and structure under hot-working conditions. Metall. Rev., 130, pp. 1-24.
- KARAMATA, S., 1968. Zonality in contact metamorphic rocks around the ultramafic mass of Brezovica (Serbia, Yugoslavia). 23rd. Int. Geol. Congr., Prague, Vol. 1., pp. 197-207.
- KARAMATA, S., 1974. Dynamo-thermal metamorphism related to emplacement of ultramafics on examples from the Dinarides. Ann. Soc. Geol. Belgique, 97, pp. 541-545.
- KARSON, J. and DEWEY, J. F., 1978. Coastal Complex, western Newfoundland: an Early Ordovician oceanic fracture zone. Geol. Soc. Am. Bull., 89, pp. 1037-1049.
- KAY, R., HUBBARD, N. J. and GAST, P. W., 1970. Chemical characteristics and origin of oceanic ridge volcanic rocks. Jour. Geophys. Res., 75, pp. 1585-1613.
- KEAN, B. F. and STRONG, D. F., 1975. Geochemical evolution of an Ordovician island arc of the central Newfoundland Appalachians. Amer. Jour. Sci., 275, pp. 97-118.
- KEEN, M. J., 1974. The continental margin of eastern North America, Florida to Newfoundland. In: "The Ocean Basins and Margins", A. E. M. Nairn and F. G. Stehli (eds.), Plenum, New York, pp. 41-78.
- KENNEDY, M. J., 1975. The Fleur de Lys Supergroup: stratigraphic comparison of Moine and Dalradian equivalents in Newfoundland with the British Caledonides. Jour. Geol. Soc. Lond., 131, pp. 305-310.
- KIRBY, S. H. and RALEIGH, C. B., 1975. Mechanisms of high-temperature, solid-state flow in minerals and ceramics and their bearing on the creep behaviour of the mantle. In: "Mechanisms of Plate Tectonics", E. Irving (ed.), Tectonophysics, 19, pp. 165-194.
- KUSHIRO, I., 1969. Clinopyroxene solid solutions formed by reactions between diopside and plagioclase at high pressures. Min. Soc. Amer. Spec. Pap. 2, pp. 179-191.

- KUSHIRO, I. and YODER, H. S., 1966. Anorthite-forsterite and anorthite-enstatite reactions and their bearing on the basalt-eclogite transformation. *Jour. Petrol.*, 7, pp. 337-362.
- LANPHERE, M. A., COLEMAN, R. G., KARAMATA, S. and PAMIĆ, J., 1975. Age of amphibolites associated with alpine peridotites in the Dinaride ophiolite zone, Yugoslavia. *Earth Planet. Sci. Lett.*, 26, pp. 271-276.
- LEAKE, B. E., 1965. The relationship between composition of calciferous amphibole and grade of metamorphism. In: "Controls of Metamorphism", W. S. Pitcher and G. W. Flinn (eds.), *Geol. Jour. Spec. Iss. #1*, Oliver and Boyd, Edinburgh and London, pp. 299-318.
- LEAKE, B. E., 1968. A catalog of analysed calciferous and subcalciferous amphiboles together with their nomenclature and associated minerals. *Geol. Soc. Am. Spec. Pap.* 98, 210p.
- LEAKE, B. E. et al, 1969. The chemical analysis of rock powders by automatic X-Ray fluorescence. *Chem. Geol.*, 5, pp. 7-86.
- LE BAS, M. J., 1962. The role of aluminum in igneous clinopyroxenes with relation to their parentage. *Amer. Jour. Sci.*, 260, pp. 267-288.
- LIOU, J. G., 1973. Synthesis and stability relations of epidote, $\text{Ca}_2\text{Al}_2\text{FeSi}_3\text{O}_{12}(\text{OH})$. *Jour. Petrol.*, 14, pp. 381-413.
- LIOU, J. G., KUNIYOSHI, S. and ITO, K., 1974. Experimental studies of the phase relations between greenschist and amphibolite in a basaltic system. *Amer. Jour. Sci.*, 274, pp. 613-632.
- LOFGREN, G., 1971. Spherulitic textures in glassy and crystalline rocks. *Jour. Geophys. Res.*, 76, pp. 5635-5648.
- LOFGREN, G., 1974. An experimental study of plagioclase crystal morphology: isothermal crystallization. *Amer. Jour. Sci.* 274, pp. 243-273.
- LOOMIS, T. P., 1972a. Contact metamorphism of pelitic rock by the Ronda ultramafic intrusion, southern Spain. *Geol. Soc. Am. Bull.*, 83, pp. 2449-2474.
- LOOMIS, T. P., 1972b. Diapiric emplacement of the Ronda high-temperature ultramafic intrusion, southern Spain. *Geol. Soc. Am. Bull.*, 83, pp. 2475-2496.
- LOVERING, T. S., 1935. Theory of heat conduction applied to geologic problems. *Geol. Soc. Am. Bull.*, 46, pp. 69-94.
- LOVERING, T. S., 1936. Heat conduction in dissimilar rocks and the use of thermal models. *Geol. Soc. Am. Bull.*, 47, pp. 87-100.

- LUNDEEN, M. T., 1978. Emplacement of the Ronda peridotite, Sierra Bermeja, Spain. *Geol. Soc. Am. Bull.*, 89, pp. 172-180.
- MACGREGOR, I. D., 1964. A study of the contact metamorphic aureole surrounding the Mount Albert ultramafic intrusion. Unpub. Ph.D. Thesis, Princeton Univ., 195p.
- MACGREGOR, I. D. and BASU, A. R., 1976. Geological problems in estimating mantle geothermal gradients. *Amer. Mineral.*, 61, pp. 715-724.
- MACKENZIE, D.B., 1960. High-temperature alpine-type peridotite from Venezuela. *Geol. Soc. Am. Bull.*, 71, pp. 303-318.
- MACKENZIE, D.B., 1961. Is the Tinaquillo, Venezuela, "pseudogabbro" metamorphic or igneous? - A Reply. *Geol. Soc. Am. Bull.*, 72, pp. 1571-1574.
- MALPAS, J., 1973. A restored section of oceanic crust and mantle in western Newfoundland (abst.). *Geol. Soc. Am. Abst. w. Prog.*, 5, p. 192.
- MALPAS, J. G., 1976. The petrology and petrogenesis of the Bay of Islands ophiolite suite, western Newfoundland. Unpub. Ph.D. Thesis, M.U.N., 431p.
- MALPAS, J. G. (in preparation). The dynamothermal aureole of the Bay of Islands ophiolite suite. (manuscript under review).
- MALPAS, J., STEVENS, R. K. and STRONG, D. F., 1973. Amphibolite associated with Newfoundland ophiolite: its classification and tectonic significance. *Geology*, 1, pp. 45-47.
- MALPAS, J. and STRONG, D. F., 1975. A comparison of chrome spinels in ophiolites and mantle diapirs of Newfoundland. *Geochim. Cosmochim. Acta*, 39, pp. 1045-1060.
- MANSON, V., 1968. Geochemistry of basaltic rocks: Major elements. In: "Basalts: The Poldervaart Treatise on Rocks of Basaltic Composition", Vol. 1, Interscience Pub., New York, pp. 215-269.
- MASON, B., 1968. Kaersutite from San Carlos, Arizona, with comments on the paragenesis of this mineral. *Mineral Mag.*, 36, pp. 997-1002.
- MATHER, J. D., 1970. The biotite isograd and the lower greenschist facies in the Dalradian rocks of Scotland. *Jour. Petrol.*, 11, pp. 253-275.
- MAXWELL, J. A., 1968. Rock and Mineral Analysis. Interscience Pub., 584p.
- MAXWELL, J. C., 1969. "Alpine" mafic and ultramafic rocks -- the ophiolite suite: a contribution to the discussion of the paper "The origin of ultramafic and ultrabasic rocks" by P. J. Wyllie. *Tectonophysics*, 7, pp. 489-494.
- MEDARIS, L. G., 1972. High-pressure peridotites in southwestern Oregon. *Geol. Soc. Am. Bull.*, 83, pp. 41-58.

- MEDARIS, L. G., 1975. Coexisting spinel and silicates in alpine peridotites of the granulite facies. *Geochim. Cosmochim. Acta*, 39, pp. 947-958.
- MELSON, W. G., HART, S. R. and THOMPSON, G., 1972. St. Paul's Rocks, equatorial Atlantic: petrogenesis, radiometric ages, and implications on sea-floor spreading. *Geol. Soc. Am. Mem.*, 132, pp. 241-272.
- MERCIER, J.-C. C., 1976. Single-pyroxene geothermometry and geobarometry. *Amer. Mineral.*, 61, pp. 603-615.
- MERCIER, J.-C. C., NICOLAS, A., 1975. Textures and fabrics of upper-mantle peridotites as illustrated by xenoliths from basalts. *Jour. Petrol.*, 16, pp. 454-487.
- MÉVEL, C., 1975. Les zonations chimiques dans les pillow-lavas spililitiques du Chenaillet et des Gets. *Pétrologie*, 1, pp. 319-333.
- MÉVEL, C., 1976. Les zonations chimiques dans les pillow-lavas métamorphisés du vallon de Péas (Hautes Alpes). *Bull. Soc. Géol. France*, 18, pp. 985-990.
- MILLHOLLEN, G. L., IRVING, A. J. and WYLLIE, P. J., 1974. Melting interval of peridotite with 5.7 per cent water to 30 kilobars. *Jour. Geol.*, 82, pp. 575-587.
- MIYASHIRO, A., 1958. Regional metamorphism of the Gosaisyo-Takanuki district in the central Abukuma Plateau. *Jour. Tok. Univ. Fac. Sci., Sec. 2*, 11, pp. 219-272.
- MIYASHIRO, A., 1973. Metamorphism and metamorphic belts. George Allen and Unwin Ltd., London, 492p.
- MIYASHIRO, A., SHIDO, F. and EWING, M., 1971. Metamorphism in the Mid-Atlantic Ridge near 24° and 30°N. *Phil. Trans. R. Soc. Lond. A*, 268, pp. 589-603.
- MOORES, E. M., 1970. Ultramafics and orogeny, with models of the U.S. Cordillera and Tethys. *Nature*, 228, pp. 837-842.
- MORI, T., 1977. Geothermometry of spinel lherzolites. *Contrib. Mineral. Petrol.*, 59, pp. 261-279.
- MORI, T., 1978. Experimental study of pyroxene equilibria in the system of CaO-MgO-FeO-SiO₂. *Jour. Petrol.*, 19, pp. 45-65.
- MORSE, S. A., 1975. Plagioclase lamellae in hypersthene, Tikkoatokhakh Bay, Labrador. *Earth Planet. Sci. Lett.*, 26, pp. 331-336.

- MURRAY, A., 1866. Report of the Geological Survey of Newfoundland for the years 1864-1865, 43p.
- NAFE, J. E. and DRAKE, C. L., 1968. Physical properties of rocks of basaltic composition. In: "Basalts": The Poldervaart Treatise on Rocks of Basaltic Composition, H. H. Hess and A. Poldervaart (eds.), Interscience Pub., New York, Vol. 2, pp. 483-502.
- NAGGAR, M. H. and ATHERTON, M. J., 1970. The composition and metamorphic history of some aluminum silicate-bearing rocks from the aureoles of the Donegal granites. Jour. Petrol., 11, pp. 549-589.
- NESBITT, R. W. and HAMILTON, D. L., 1970. Crystallization of an alkali olivine basalt under controlled P_{O_2} , H_{H_2O} conditions. Phys. Earth Planet. Inter., 3, pp. 309-315.
- NICOLAS, A. and JACKSON, E. D., 1972. Repartition en deux provinces des péridotites des chaînes alpines longeant la Méditerranée: implications géotectoniques. Schweiz. Mineral. Petrog. Mitt., 52, pp. 479-495.
- NISBET, E. G. and PEARCE, J. A., 1977. Clinopyroxene composition in mafic lavas from different tectonic settings. Contrib. Mineral. Petrol., 63, pp. 149-160.
- NITSCH, K. H., 1971. Stabilitätsbeziehungen von Prehnit und Pumpellyit-haltigen Paragenesen. Contrib. Mineral. Petrol., 30, pp. 240-260.
- OBATA, M., 1976. The solubility of Al_2O_3 in orthopyroxenes in spinel and plagioclase peridotites and spinel pyroxenite. Amer. Mineral., 61, pp. 804-816.
- OBATA, M., 1977. Petrology and petrogenesis of the Ronda high-temperature peridotite intrusion, southern Spain. Unpub. Ph.D. thesis, Mass. Inst. Tech., 220p.
- OBATA, M. and DICKEY, J. S., 1976. Phase relations of mafic layers in the Ronda peridotite. Carn. Inst. Wash. Yb., 75.
- O'HARA, M. J., 1968. The bearing of phase equilibria studies in synthetic and natural systems on the origin and evolution of basic and ultrabasic rocks. Earth Sci. Rev., 4, pp. 69-133.
- OKRUSCH, M., 1971. Garnet-cordierite-biotite equilibria in the Steinach Aureole, Bavaria. Contrib. Mineral. Petrol., 32, pp. 1-23.
- OXBURGH, E. R. and TURCOTTE, D. L., 1974. Thermal gradient and regional metamorphism in overthrust terrains with special reference to the Eastern Alps. Schweiz. Mineral. Petrog. Mitt., 54, pp. 641-662.

- PAMIĆ, J., 1971. Amphibolites associated with the large Krijava-Konjuh ultramafic massif (Yugoslavia). Bull. Sci. A, 16, pp. 3-4.
- PAMIĆ, J. J., 1977. Variation in geothermometry and geobarometry of peridotite intrusions in the Dinaride central ophiolite zone, Yugoslavia. Amer. Mineral. 62, pp. 874-886.
- PAMIĆ, J. and MAJER, V., 1977. Ultramafic rocks of the Dinaride central ophiolite zone in Yugoslavia. Jour. Geol., 85, pp. 553-569.
- PAMIĆ, J., ŠČAVNIČAR, S. and MEDJIMOREC, S., 1973. Mineral assemblages of amphibolites associated with Alpine-type ultramafics in the Dinaride ophiolite zone (Yugoslavia). Jour. Petrol., 14, pp. 133-157.
- PAPIKE, J. J., CAMERON, K. L., and BALDWIN, K., 1974. Amphiboles and pyroxenes: characterization of other than quadrilateral components and estimates of ferric iron from microprobe data. Geol. Soc. Am. Ann. Mtg., Miami, Abs. w. Prog., pp. 1053-1054.
- PEARCE, J. A. and CANN, J. R., 1973. Tectonic setting of basic volcanic rocks determined using trace element analyses. Earth Planet. Sci. Lett., 19, pp. 290-300.
- PEARCE, T. H., GORMAN, B. E. and BIRKETT, T. C., 1975. The TiO_2 - K_2O - P_2O_5 diagram: a method of discriminating between oceanic and non-oceanic basalts. Earth Planet. Sci. Lett., 24, pp. 419-426.
- PEARCE, T. H., GORMAN, B. E. and BIRKETT, T. C., 1977. The relationship between major element chemistry and tectonic environment of basic and intermediate volcanic rocks. Earth Planet. Sci. Lett., 36, pp. 121-132.
- PERCHUK, L. L., 1970. Equilibrium of biotite with garnet in metamorphic rocks. Geochem. Int., 7, pp. 157-179.
- PHILPOTTS, A. R., 1972. Density, surface tension, and viscosity of the immiscible phase in a basic, alkaline magma. Lithos, 5, pp. 1-18.
- PHILPOTTS, A. R., 1976. Silicate liquid immiscibility: its probable extent and petrogenetic significance. Amer. Jour. Sci., 276, pp. 1147-1177.
- PHILPOTTS, A. R., 1977. Archean variolites -- quenched immiscible liquids: Discussion. Can. Jour. Earth Sci., 14, pp. 139-144.
- PHILPOTTS, A. R., 1978. Rift-associated igneous activity in eastern North America. In: "Petrology and Geochemistry of Continental Rifts", E. R. Neumann and I. B. Ramberg (eds.), D. Reidel Publ. Co., Dordrecht, Holland, pp. 133-154.

- POWELL, R., 1978. The thermodynamics of pyroxene geotherms. Phil. Trans. R. Soc. Lond. A., 288, pp. 457-469.
- PRINGLE, I. R., MILLER, J. A., and WARRELL, D. M., 1971. Radiometric age determinations from the Long Range Mountains, Newfoundland. Can. Jour. Earth Sci., 8, pp. 1325-1330.
- RAASE, P., 1974. Al and Ti contents of hornblende, indicators of pressure and temperature of regional metamorphism. Contrib. Mineral. Petrol., 45, pp. 231-236.
- RAGAN, D. M., 1967. The Twin Sisters dunite, Washington. In: "Ultramafic and Related Rocks", P. J. Wyllie (ed.), John Wiley and Sons, New York, pp. 160-167.
- RAHEIM, A. and GREEN, D. H., 1974. Experimental determination of the temperature and pressure dependence of the Fe-Mg partition coefficient for coexisting garnet and clinopyroxene. Contrib. Mineral. Petrol., 48, pp. 179-204.
- REED, J. C. and MORGAN, B., 1971. Chemical alteration and spilitization of the Catoctin greenstones, Shenandoah National Park, Virginia. Jour. Geol., 79, pp. 526-548.
- REITAN, P. H., 1968. Frictional heat during metamorphism: Quantitative evaluation of concentration of heat generation in time. Lithos, 1, pp. 151-163.
- REITAN, P. H., 1968. Frictional heat during metamorphism: 2. Quantitative evaluation of concentration of heat generation in space. Lithos, 1, pp. 268-274.
- RICE, J. M., 1977. Contact metamorphism of impure dolomitic limestone in the Boulder aureole, Montana. Contrib. Mineral. Petrol., 59, pp. 237-259.
- RICE, J. M., EVANS, B. W. and TROMSDORFF, V., 1974. Widespread occurrence of magnesiocummingtonite in ultramafic schists, Cima di Gagnone, Ticino, Switzerland. Contrib. Mineral. Petrol., 43, pp. 245-251.
- RIDLEY, W. I., RHODES, J. M., REID, A. M., JAKES, P., SHIH, C., and BASS, M. N., 1974. Basalts from Leg 6 of the Deep Sea Drilling Project. Jour. Petrol., 15, pp. 140-159.
- ROBIE, R. A. and WALDBAUM, D. R., 1968. Thermodynamic properties of minerals and related substances at 298.15°K (25.0°C) and one atmosphere (1.013 bars) and at higher temperature. U. S. G. S. Bull. No. 1259.
- RODGERS, J., 1965. Long Point and Clam Bank Formations, western Newfoundland. Proc. Geol. Assoc. Can. 16, pp. 83-94.

- RODGERS, J., 1968. The eastern edge of the North American continent during the Cambrian and early Ordovician. In: "Studies of Appalachian Geology: Northern and Maritime", E-an Zen, W. S. White, J. B. Hadley, J. B. Thompson, Jr. (eds.), Interscience Pub., New York, pp. 141-149.
- RODGERS, J. and NEALE, E. R. W., 1963. Possible Taconic klippen in western Newfoundland. Amer. Jour. Sci., 261, pp. 713-730.
- ROEDDER, E., 1978. Silicate liquid immiscibility in magmas and in the system $K_2O-FeO-Al_2O_3-SiO_2$: an example of serendipity. Geochim. Cosmochim. Acta, 42, pp. 1597-1617.
- RUTHERFORD, M. J., HESS, P. C. and DANIEL, G. H., 1974. Experimental liquid line of descent and liquid immiscibility for basalt 70017. Proc. 5th Lunar Sci. Conf., 1, pp. 569-583.
- SANDERS, L. D., 1955. Structural observations on the southeast Lizard. Geol. Mag., 92, pp. 231-240.
- SCHERMERHORN, L. J. G., 1975. Pumpellyite-facies metamorphism in the Spanish pyrite belt. Petrologie, 1, pp. 71-86.
- SIMPSON, R. W. and BOTHNER, W. A., 1978. Possible extension of the South Atlas Fault of North Africa into the Gulf of Maine. Geol. Soc. Am. Abst. w. Prog., Annual Meeting, Toronto, p. 493.
- SMITH, C. H., 1958. Bay of Islands igneous complex, western Newfoundland. Geol. Surv. Can. Mem., 290, 132p.
- SMITH, R. E. and SMITH, S. E., 1976. Comments on the use of Ti, Zr, Y, Sr, K, P, and Nb in classification of basaltic magmas. Earth Planet. Sci. Lett., 32, pp. 114-120.
- SMYTH, W. R., 1971. Stratigraphy and structure of part of the Hare Bay Allochthon, Newfoundland. Proc. Geol. Assoc. Can., 24, pp. 47-57.
- SMYTH, W. R., 1973. The stratigraphy and structure of the southern part of the Hare Bay Allochthon, NW Newfoundland. Unpub. Ph.D. Thesis, Memorial University of Newfoundland, 172p.
- SPEAR, F. S., 1976. Ca-amphibole composition as a function of temperature, fluid pressure, and oxygen fugacity in a basaltic system. Carn. Inst. Wash. Yb., 75, pp. 775-779.
- SPRINGER, R. K., 1974. Contact metamorphosed ultramafic rocks in the western Sierra Nevada foothills, California. Jour. Petrol., 15, pp. 160-195.

- STEFFE, D., 1978. A study of compositional relationships among the calcic and sub-calcic amphiboles. Unpub. M.Sc. Thesis, University of Vermont.
- STEPHENSON, K., 1937. Geology and mineralogy of the Goose Cove copper deposits of northern Newfoundland. Unpub. manuscript.
- STEVENS, R. K., 1970. Cambro-Ordovician flysch sedimentation and tectonics in West Newfoundland and their possible bearing on a Proto-Atlantic Ocean. Geol. Assoc. Can. Spec. Pap., 7, pp. 165-177.
- ST. JULIEN, P. and HUBERT, C., 1975. Evolution of the Taconian orogen in the Quebec Appalachians. Amer. Jour. Sci., 275A, pp. 337-362.
- STOUT, J. H., 1972. Phase petrology and mineral chemistry of coexisting amphiboles from Telemark, Norway. Jour. Petrol., 13, pp. 99-145.
- STRONG, D. F., 1973. Lush's Bight and Robert's Arm groups of central Newfoundland: possible juxtaposed oceanic and island-arc volcanic suites. Geol. Soc. Am. Bull., 84, pp. 3917-3928.
- STRONG, D. F., 1974. An "off-axis" alkali volcanic suite associated with the Bay of Islands ophiolite, Newfoundland. Earth Planet. Sci. Lett., 21, pp. 301-309.
- STRONG, D. F., 1974. Plateau lavas and diabase dykes of northwestern Newfoundland. Geol. Mag., 111, pp. 501-514.
- STRONG, D. F., DICKSON, W. F., O'DRISCOLL, C. F., KEAN, B. F., STEVENS, R.K., 1974. Geochemical evidence for an east-dipping Appalachian subduction zone in Newfoundland. Nature, 248, pp. 37-39.
- STRONG, D. F., STEVENS, R. K., MALPAS, J. and BADHAM, J. P. N., 1974. A new tale for the Lizard. Proc. Ussher Soc. (Abst.), 3, p. 242.
- STRONG, D. F., and WILLIAMS, H., 1972. Early Paleozoic flood basalts of northwestern Newfoundland: their petrology and tectonic significance. Proc. Geol. Assoc. Can., 24, pp. 43-54.
- SULLIVAN, K. D. and KEEN, C. E., 1977. Newfoundland seamounts: petrology and geochemistry. In: "Volcanic Regimes in Canada", W. R. A. Baragar, R. G. Coleman, and J. M. Hall (eds.), Geol. Assoc. Can. Spec. Pap., 16, pp. 461-476.
- TALKINGTON, R. W. and GAUDETTE, H. E. Microprobe analysis and origin of corona structures in lherzolite, Knox County, Maine, U.S.A. Ms. in prep.
- THAYER, T. P., 1967. Chemical and structural relations of ultramafic and feldspathic rocks in Alpine intrusive complexes. In: "Ultramafic and related rocks", Wyllie, P. J. (ed.), Wiley, New York, pp. 222-239.

- THAYER, T. P., 1969. Peridotite-gabbro complexes as keys to the petrology of mid-ocean ridges. *Geol. Soc. Am. Bull.*, 80, pp. 1515-1522.
- THAYER, T. P. and BROWN, C. E., 1961. Is the Tinaquillo, Venezuela, "pseudogabbro" metamorphic or igneous? *Geol. Soc. Am. Bull.*, 72, pp. 1565-1570.
- THOMPSON, A. B., 1976. Mineral reactions in pelitic rocks: II. Calculation of some P-T-X (Fe-Mg) phase relations. *Amer. Jour. Sci.*, 276, pp. 425-454.
- TRACY, R. J., ROBINSON, P. and THOMPSON, A. B., 1976. Garnet composition and zoning in the determination of temperature and pressure of metamorphism, central Massachusetts. *Amer. Mineral.*, 61, pp. 762-775.
- TROMMSDORFF, V. and EVANS, B. W., 1972. Progressive metamorphism of antigorite schist in the Bergell tonalite aureole (Italy). *Amer. Jour. Sci.*, 272, pp. 423-437.
- TUKE, M. J., 1968. Autochthonous and allochthonous rocks in the Pistolet Bay area in northernmost Newfoundland. *Can. Jour. Earth Sci.*, 5, pp. 501-513.
- UPADHYAY, H., 1973. The Betts Cove ophiolite and related rocks of the Snook's Arm Group, Newfoundland. Unpub. Ph.D. Thesis, Memorial University of Newfoundland, 224p.
- VALLANCE, T. G., 1969. Spilites again: some consequences of the degradation of basalts. *Proc. Linnean Soc. N.S.W.*, 94, pp. 8-51.
- VALLANCE, T. G., 1974. Spilitic degradation of a tholeiitic basalt. *Jour. Petrol.*, 15, pp. 79-96.
- VANCE, J. A. and DUNGAN, M. A., 1977. Formation of peridotites by deserpentinization in the Darrington and Sultan areas, Cascade Mountains, Washington. *Geol. Soc. Am. Bull.*, 88, pp. 1497-1508.
- VERNON, R. H., 1976. *Metamorphic Processes: Reactions and Micro-structure Development*. George Allen and Unwin Ltd., London, 247p.
- WANLESS, R. K., STEVENS, R. D., LACHANCE, G. R., and EDMONDS, C. M., 1968. Age determinations and geological studies. *Geol. Surv. Can. Pap.* 67-2, Part A, 141p.

- WATSON, B. E., 1976. Two liquid partition coefficients: experimental data and geochemical implications. *Contrib. Mineral. Petrol.*, 56, pp. 119-134.
- WEERTMAN, J. and WEERTMAN, J. R., 1965a. Mechanical properties, mildly temperature-dependent. In: "Physical Metallurgy", R. W. Cahn (ed.), John Wiley and Sons, New York, pp. 735-792.
- WEERTMAN, J. and WEERTMAN, J. R., 1965b. Mechanical properties, strongly temperature-dependent. In: "Physical Metallurgy", R. W. Cahn (ed.), John Wiley and Sons, New York, pp. 793-820.
- WELLS, P. R. A., 1977. Pyroxene thermometry in simple and complex systems. *Contrib. Mineral. Petrol.*, 62, pp. 129-139.
- WESTERHOF, A. B., 1977. On the contact relations of high-temperature peridotites in the Serrania de Ronda, southern Spain. *Tectonophysics*, 39, pp. 579-591.
- WHITE, S. H., and KNIPE, R. J., 1978. Transformation- and reaction-enhanced ductility in rocks. *Jour. Geol. Soc. Lond.*, 135, pp. 513-516.
- WILKINSON, J. F. G., 1961. Some aspects of the calciferous amphiboles oxyhornblende, kaersutite, and barkevikite. *Amer. Mineral.*, 46, pp. 340-354.
- WILKINSON, J. F. G., 1974. The mineralogy and petrography of alkali basaltic rocks. In: "The Alkaline Rocks", H. Sørensen (ed.), John Wiley and Sons, pp. 67-95.
- WILLIAMS, G. D., 1978. Rotation of contemporary folds into the X direction during overthrust processes in Lakesfjord, Finnmark. *Tectonophysics*, 48, pp. 29-40.
- WILLIAMS, H., 1971. Mafic-ultramafic complexes in western Newfoundland Appalachians and the evidence for their transportation: a review and interim report. *Proc. Geol. Assoc. Can.*, 24, pp. 9-25.
- WILLIAMS, H., 1975. Structural succession, nomenclature, and interpretation of transported rocks in western Newfoundland. *Can. Jour. Earth Sci.*, 12, pp. 1874-1894.
- WILLIAMS, H., 1976. Tectonic-stratigraphic subdivisions of the Appalachian orogen. *Geol. Soc. Am. Abst. w. Prog.*, 8, p. 300.
- WILLIAMS, H., 1977a. Ophiolitic melange and its significance in the Fleur de Lys Supergroup, northern Appalachians. *Can. Jour. Earth Sci.*, 14, pp. 987-1003.

- WILLIAMS, H., 1977b. The Coney Head Complex: another Taconic allochthon in west Newfoundland. *Amer. Jour. Sci.*, 277, pp. 1279-1295.
- WILLIAMS, H., HIBBARD, J. P. and BURNSNALL, J. T., 1977. Geological setting of asbestos-bearing ultramafic rocks along the Baie Verte Lineament, Newfoundland. *Geol. Surv. Can. Pap.* 77-1A, pp. 351-360.
- WILLIAMS, H., KENNEDY, M. J. and NEALE, E. R. W., 1972. The Appalachian structural province. In: "Variations in Tectonic Styles in Canada", Price, R. A. and Douglas, R. J. W. (eds.), *Geol. Assoc. Can. Spec. Pap.*, 11, pp. 182-261.
- WILLIAMS, H., KENNEDY, M. J., and NEALE, E. R. W., 1974. The northeastward termination of the Appalachian orogen. In: "The Ocean Basins and Margins", Vol. 2, Nairn, A. E. M. and Stehli, F. G. (eds.), pp. 79-123.
- WILLIAMS, H. and SMYTH, W. R., 1973. Metamorphic aureoles beneath ophiolite suites and Alpine peridotites: tectonic implications with west Newfoundland examples. *Amer. Jour. Sci.*, 273, pp. 594-621.
- WILLIAMS, H. and SMYTH, W. R., in press. The Hare Bay Allochthon, northwestern Newfoundland. *Geol. Surv. Can. Bull.* (to accompany regional map).
- WILLIAMS, H., SMYTH, W. R., and STEVENS, R. K., 1973. Hare Bay Allochthon, northern Newfoundland. *Geol. Surv. Can. Pap.* 73-1, Part A, pp. 8-14.
- WILLIAMS, H. and STEVENS, R. K., 1969. Geology of Belle Isle: Northern extremity of the deformed Appalachian miogeosynclinal belt. *Can. Jour. Earth Sci.*, 6, pp. 1145-1157.
- WILLIAMS, H. and STEVENS, R. K., 1974. The ancient continental margin of North America. In: "The Geology of Continental Margins", C. A. Burk, and C. L. Drake (eds.), pp. 781-796.
- WILLIAMS, H. and TALKINGTON, R. W., 1977. Distribution and tectonic setting of ophiolites and ophiolitic melanges in the Appalachian orogen. In: "North American Ophiolites", R. G. Coleman and W. P. Irwin (eds.), *State of Oregon Dept. of Geology and Mineral Resources Bulletin*, 95, pp. 1-11.
- WILSHIRE, H. G. and JACKSON, E. D., 1975. Problems in determining mantle geotherms from pyroxene compositions of ultramafic rocks. *Jour. Geol.*, 83, pp. 313-329.
- WILSON, A. D., 1955. A new method for the determination of ferrous iron in rocks and minerals. *Bull. Geol. Surv. Gt. Brit.*, 9, pp. 56-58.

- WILSON, J. T., 1966. Did the Atlantic close and then re-open? *Nature*, 211, pp. 676-681.
- WINCHESTER, J. A. and FLOYD, P. A., 1976. Geochemical magma type discrimination: application to altered and metamorphosed basic igneous rocks. *Earth Planet. Sci. Lett.*, 28, pp. 459-469.
- WISEMAN, J. D. H., 1934. The central and south-west highland epidiorites -- a study in progressive metamorphism. *Quart. Jour. Geol. Soc. Lond.*, 90, pp. 354-417.
- WOOD, B. J. and BANNO, S., 1973. Garnet-orthopyroxene and orthopyroxene-clinopyroxene relationships in simple and complex systems. *Contrib. Mineral. Petrol.*, 42, pp. 109-124.
- WOODCOCK, N. H. and ROBERTSON, A. H. F., 1977. Origins of some ophiolite-related metamorphic rocks of the "Tethyan" belt. *Geology*, 5, pp. 373-376.
- YODER, H. S., 1976. Generation of basaltic magma. *National Academy of Sciences, Washington, D. C.*, 265p.
- YODER, H. S. and TILLEY, C. E., 1962. Origin of basalt magmas: an experimental study of natural and synthetic rock systems. *Jour. Petrol.*, 3, pp. 342-352.
- ZWART, H. J., 1974. Structure and metamorphism in the Seve-Köli nappe complex (Scandinavian Caledonides) and its implications concerning the formation of metamorphic nappes. *Cent. Soc. Geol. Belgique. Geologie des Domaines Cristallins, Liege*, pp. 129-144.

APPENDIX I. ROCK ANALYSES

(i) Sample Preparation

Samples selected for analysis were trimmed to remove weathered surfaces and broken into chips less than 1 cm in diameter. Chips containing weathered surfaces or veinlets of secondary minerals were discarded, and the remainder washed. A representative sample of these chips was crushed in a Siebtechnik tungsten-carbide swing mill for 1 to 3 minutes, depending on the sample composition, to less than 200 mesh.

(ii) Major Element Analyses

Fused pellets were prepared by mixing 0.500 g of sample with 4.500 g of lithium tetraborate fluxing agent, fusing for 15 minutes in a Claisse fluxer, and casting in platinum molds.

The analyses were performed on a fully automated Philips 1450 X-Ray fluorescence spectrometer, using a silver anode tube, at 50 kV and 40 mA. Corrections were performed using a standard Philips alpha-correction program (de Jongh, 1973). Precision and accuracy data are given in Table I.i.

Ferrous iron was determined by the visual titration method of Wilson (1955) as described in Maxwell (1968, p. 419-421).

Loss of volatiles on ignition was determined by weighing 0.5 g of sample into a porcelain crucible and heating at 1050°C for two hours, followed by cooling in a dessicator and subsequent reweighing to determine the loss of volatiles in weight per cent.

Table I.i. Precision and accuracy of major element analyses, XRF on fused pellets.

I.i. (a) PRECISION OF METHOD (6 different pellets, sample RJ76-542):

Element	Mean	Standard Deviation	Standard Error of Mean	Range	
				Low	High
SiO ₂	46.02	0.48	0.11	45.26	46.81
TiO ₂	2.30	0.02	0.004	2.27	2.34
Al ₂ O ₃	12.62	0.23	0.05	11.97	13.00
Fe ₂ O _{3T}	12.40	0.12	0.03	12.17	12.58
MnO	0.15	0.004	0.001	0.14	0.16
MgO	9.29	0.10	0.02	9.11	9.47
CaO	6.72	0.04	0.01	6.64	6.79
Na ₂ O	3.66	0.06	0.01	3.56	3.84
K ₂ O	0.12	0.003	0.001	0.11	0.13
P ₂ O ₅	0.25	0.02	0.003	0.21	0.28

(b) PRECISION AND ACCURACY OF REPLICATE DETERMINATIONS (21 determinations, single pellet, BCR-1)

Element	Accepted* Value	Mean	Standard Deviation	Standard Error of Mean	Range		Differen
					Low	High	
SiO ₂	54.85	54.18	0.151	0.033	53.91	54.42	-1.2%
TiO ₂	2.22	2.14	0.007	0.001	2.13	2.15	-3.6
Al ₂ O ₃	13.68	13.36	0.176	0.038	13.04	13.68	-2.3
Fe ₂ O _{3T}	13.52	13.44	0.058	0.013	13.35	13.56	-0.6
MnO	0.19	0.17	0.004	0.001	0.16	0.18	-10.5
MgO	3.49	3.51	0.043	0.009	3.44	3.60	+0.6
CaO	6.98	7.00	0.020	0.004	6.94	7.03	+0.3
Na ₂ O	3.29	3.27	0.065	0.014	3.15	3.37	-0.6
K ₂ O	1.68	1.66	0.012	0.003	1.64	1.68	-1.2
P ₂ O ₅	0.33	0.34	0.014	0.003	0.32	0.36	+3.0

*Abbey, 1975.

(iii) Trace Element Analyses

Ten g of rock powder were mixed with 1.3 g of phenolformaldehyde binding agent, shaken for 10 minutes, pressed into a 40 mm disc at 25 tons, and baked at 200°C for 10 minutes (technique modified after Leake et al., 1969).

The analyses were done by X-Ray fluorescence, using the silver anode tube. Corrections were based on calibration curves with matrix corrections done using the Compton peak of Ag. Precision and accuracy data are given in Table I.ii.

Table I.ii. Precision and accuracy of trace element analyses
(13 determinations, single pellet, W-1).
XRF on pressed pellets.

<u>Element</u>	<u>Accepted*</u> <u>Value</u>	<u>Mean</u>	<u>Standard</u> <u>Deviation</u>	<u>Difference</u>
Zr	105	98	2	-6.7%
Sr	190	189	6	-0.5
Rb	21	22	2	+4.8
Zn	86	85	2	-1.2
Cu	110	117	4	+6.4
Ba	160	171	12	+6.9
Nb	9.5	8	1	-15.8
Y	25	24	2	-4.0
Pb	8	7	3	-12.5
Ni	78	70	3	-10.3
Cr	120	92	6	-23.3
V	240	240	5	--
Ga	16	20	2	+25.0

*Abbey (1975).

APPENDIX II. MINERAL ANALYSES

(i) Analytical Method

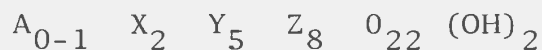
Mineral compositions were measured using a three-spectrometer JEOL JXA-50A automated electron microprobe with Krisel programming. Normal operating conditions were 15 kV accelerating voltage, 0.02 microamps sample current, and a beam diameter of 2 microns, except for feldspar which was measured with a beam defocussed to about 5 microns. The data were corrected on line by the Bence-Albee method (1968). Mineral standards similar in composition and structural type to the minerals being analysed were used for calibration; the standard compositions were checked periodically and recalibrated as necessary to ensure consistent results. For a good calibration, the precision of replicate analyses is estimated to be within 5 percent, with accuracy on the basis of standard compositions estimated to be within 10 percent. Some minerals, particularly garnet and spinel, proved difficult to calibrate, partly owing to a lack of suitable standards for the compositions involved; the precision and accuracy associated with these analyses is lower.

Analyses were done on polished thin sections. Several areas in each section were selected, and the phases of interest in each analysed. The analyses quoted in Tables II.i to II.viii are averages of several spots in each grain, or part of a grain as indicated. Most analyses are identified by sample number, spot number, mineral name, and a sequential number, with "C" indicating core and "R" indicating rim (e.g. 504-1 HB-2 indicates sample 504, spot 1, hornblende 2 out of the total number of hornblendes in the sample analysed). Analyses of

individual points were accepted on the basis of good totals (98-102 for anhydrous minerals) and good stoichiometry.

(ii) Amphibole

Amphibole analyses were recalculated on the basis of 23 0, according to the ideal structural formula



where Z (tetrahedral) : $Si + Al^{IV} = 8.000$

Y (octahedral M1 to M3) : $Al^{VI} + Ti + Fe^{3+} + Fe^{2+} + Mn + Mg + Ca = 5.000$

X (octahedral M4) : $Ca + Na + Fe^{2+} + Mn = 2.000$

A : $Na + K + Ca = 0 - 1.000$

Ferric iron was calculated using a program written by B. Doolan of the University of Vermont based on the methods of Stout (1972) and Papike et al. (1974). The minimum and maximum amounts of ferric iron are determined using the charge balance equation

$$Na (M4) + Al^{IV} = A\text{-site} + Al^{VI} + 2Ti + Fe^{3+}$$

and the following criteria:

1) Minimum Fe:

(a) Na (M4) = 0.000. In this case, some Fe^{3+} is calculated, depending on the charge balance equation.

(b) Na (M4) > 0.000 but a minimum determined by the charge balance equation. In this case, $Fe^{3+} = 0.000$ and total Fe is calculated as Fe^{2+} .

FIGURE 11.1: Nomenclature of calcic and sub-calcic amphiboles (after Leake, 1968; Steffe, 1978)

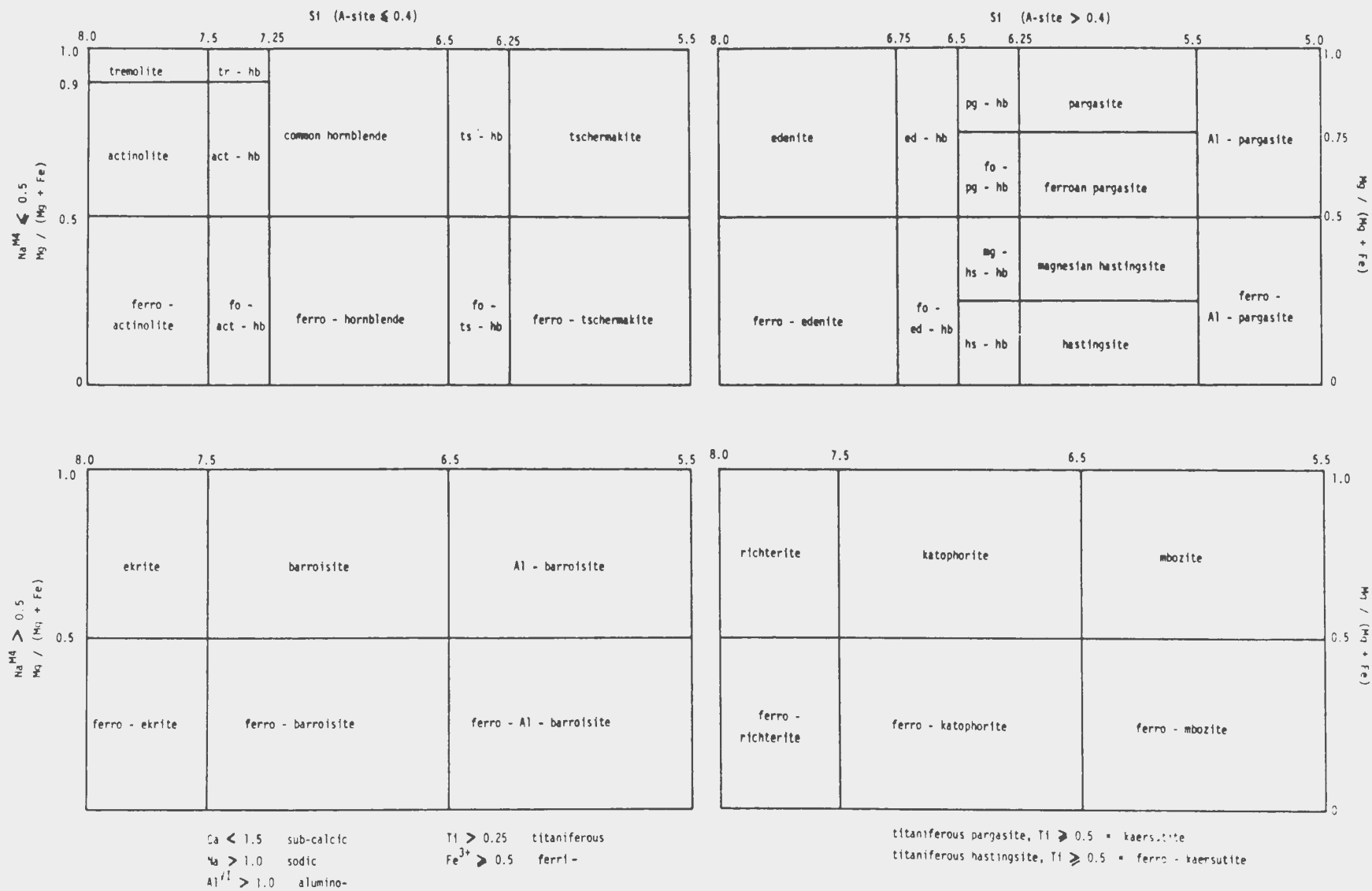


Table II.i.(a) Example of complete ferric iron calculation, using a program written by B. Doolan (University of Vermont)

		130-1	HB-2	
		<u>MINIMUM</u>	<u>INTERMEDIATE</u>	<u>MAXIMUM</u>
SiO ₂		43.62	43.62	43.62
TiO ₂		1.18	1.18	1.18
Al ₂ O ₃		12.02	12.02	12.02
Fe ₂ O ₃		2.30	5.60	8.90
FeO		13.72	10.75	7.78
MnO		0.26	0.26	0.26
MgO		11.61	11.61	11.61
CaO		11.31	11.31	11.31
Na ₂ O		1.70	1.70	1.70
K ₂ O		0.10	0.10	0.10
TOT		97.82	98.15	98.48
Z	Si	6.444	6.393	6.342
	Al ^{IV}	1.556	1.607	1.658
Y	Al ^{VI}	0.537	0.469	0.402
	Fe ³⁺	0.256	0.618	0.975
	Ti	0.131	0.130	0.129
	Fe ²⁺	1.520	1.247	0.946
	Mn			0.032
	Mg	2.556	2.536	2.516
X	Mg			
	Fe ²⁺	0.175	0.071	
	Mn	0.033	0.032	0.001
	Ca	1.790	1.776	1.762
	Na	0.002	0.121	0.238
A	Ca			
	Na	0.485	0.362	0.242
	K	0.019	0.019	0.019

2) Maximum Fe:

- (a) Na (M4) = maximum, calculated by eliminating Mn and Fe^{2+} from M4. This reduces the amount of Na in the A-site, reducing the total number of cations in the structural formula and requiring a minimum Fe^{2+} for charge balance.
- (b) $\text{Al} + 2\text{Ti} + \text{Fe}^{3+} \leq 2.000$.
- (c) No Fe^{3+} or Ti^{3+} in the Z-site.

Examples of the complete calculations are given in Table II.i.(a). All the St. Anthony Complex amphibole analyses are listed in Table II.i.(b), but only the structural formulae for the intermediate Fe^{3+} are given, along with the minimum and maximum calculated Fe_2O_3 .

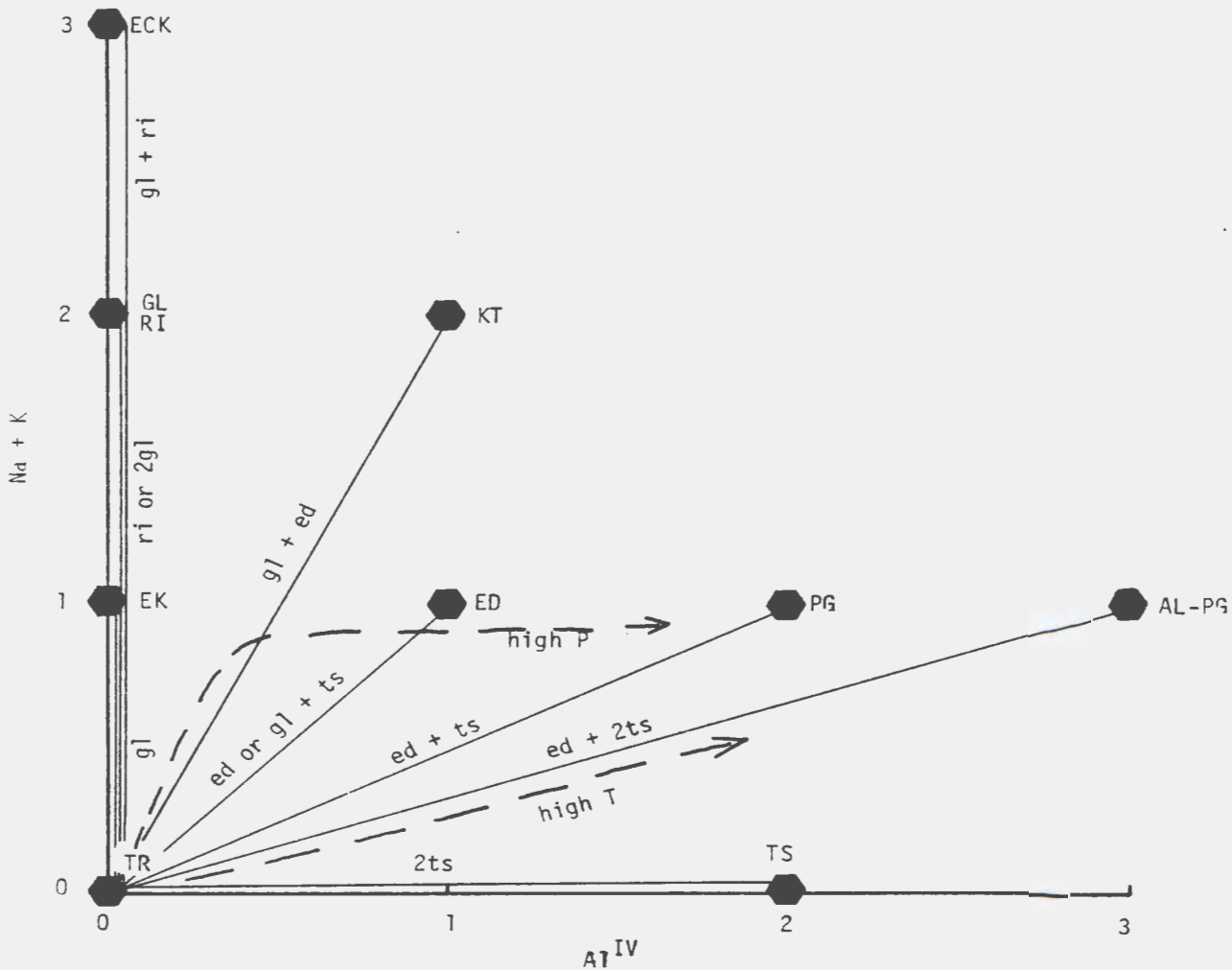
Amphibole chemistry can be considered in terms of four types of substitutions, beginning with tremolite ($\text{Ca}_2 \text{Mg}_5 \text{Si}_8 \text{O}_{22} (\text{OH})_2$):

- 1) $\text{Na (A)} + \text{Al}^{\text{IV}} \rightleftharpoons \text{Si (edenite - Na Ca}_2 \text{Mg}_5 \text{Si}_7 \text{Al O}_{22} (\text{OH})_2)$,
- 2) $\text{Na (M4)} + \text{Al}^{\text{VI}} \rightleftharpoons \text{Mg} + \text{Ca (glaucophane - Na}_2 \text{Mg}_3 \text{Al}_2 \text{Si}_8 \text{O}_{22} (\text{OH})_2)$,
- 3) $\text{Al}^{\text{IV}} + \text{Al}^{\text{VI}} \rightleftharpoons \text{Si} + \text{Mg (tschermakite - Ca}_2 \text{Mg}_3 \text{Al}_2 \text{Si}_6 \text{Al}_2 \text{O}_{22} (\text{OH})_2)$,
- 4) $\text{Na (A)} + \text{Na (M4)} \rightleftharpoons \text{Ca (richterite - Na}_2 \text{Ca Mg}_5 \text{Si}_8 \text{O}_{22} (\text{OH})_2)$.

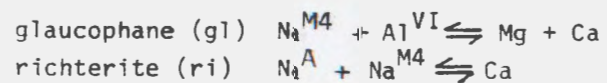
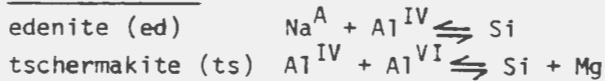
The substitutions $\text{Fe}^{2+} \rightleftharpoons \text{Mg}$ and $\text{Al} \rightleftharpoons \text{Fe}^{3+}$ are superimposed on these, leading to the wide, and sometimes confusing, variety in amphibole compositions and nomenclature. Abbreviated forms of the formal names for the St. Anthony Complex amphiboles, according to Fig. II.i., are listed in Table II.i.(b).

Diagrams involving Na and Al are the most useful for showing compositional relationships among amphiboles. Since reducing the number of cations tends to increase the value of Al^{IV} and decrease the value of

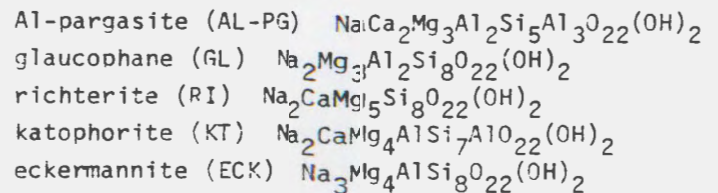
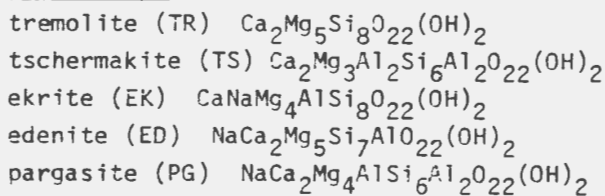
FIGURE II.ii: Amphibole substitutions involving Na and Al for Mg end members plotted in terms of Na+K and Al^{IV}. High pressure and high temperature trends from Steffe (1978).



Substitutions:



End Members:



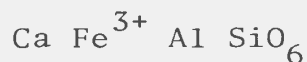
(Na + K), plots involving these parameters tend to cancel out the effect of variations in Fe^{3+} . A plot of (Na + K) against $\text{Al}^{\text{IV}} - \text{A}/2$ is virtually independent of Fe^{3+} (Steffe, 1978), but for the sake of simplicity, this additional correction has been ignored here. Sample plots using (Na + K) and Al^{IV} calculated for different values of Fe^{3+} showed no difference in the overall trend of amphibole compositions. Fig. II.ii. shows the positions of the ideal amphibole and members in terms of (Na + K) and Al^{IV} . The use of $(\text{Na} + \text{K})_{\text{TOT}}$ is preferred for the calcic amphiboles, since it separates the edenite and tschermakite substitutions, which plots involving Na (M4) do not, and since the value of Na (A) is generally dependent on Fe^{3+} and therefore poorly known. For relationships among sodic amphiboles, however, diagrams using Na (M4) are generally more useful.

(iii) Pyroxene

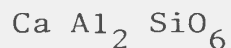
Pyroxene compositions were recalculated on the basis of 6 oxygens, with ferric iron estimated assuming an ideal number of 4.000 cations. The following end members were calculated using the method of Cawthorn and Collerson (1974) as modified by Doolan, Collerson, and Knapp (in preparation):

Wollastonite	$\text{Ca}_2 \text{ Si}_2 \text{ O}_6$
Enstatite	$\text{Mg}_2 \text{ Si}_2 \text{ O}_6$
Ferrosilite	$\text{Fe}_2 \text{ Si}_2 \text{ O}_6$
Jadeite	$\text{Na Al Si}_2 \text{ O}_6$
Acmite	$\text{Na Fe}^{3+} \text{ Si}_2 \text{ O}_6$
Ti-Tschermak	$\text{Ca Fe}^{2+} \text{ Ti SiO}_6$

Fe-Al Tschermak



Ca-Tschermak



(iv) Feldspar

Feldspar structural formulae were calculated on the basis of 32 oxygens. All the iron was calculated as ferric iron, and albite ($\text{NaAl Si}_3\text{O}_8$), anorthite ($\text{Ca Al}_2 \text{Si}_2\text{O}_8$) and orthoclase ($\text{KAl Si}_3\text{O}_8$) end members were calculated.

(v) Olivine

Olivine structural formulae were calculated on the basis of 4 oxygens. Ferric iron was not estimated, and only forsterite ($\text{Mg}_2 \text{SiO}_4$) and fayalite ($\text{Fe}_2 \text{SiO}_4$) end members were calculated.

(vi) Epidote

Epidote structural formulae were calculated on the basis of 12.5 oxygens, corresponding to the ideal formula $\text{Ca}_2 (\text{Al}, \text{Fe}^{3+})_3 \text{Si}_3 \text{O}_{12} (\text{OH})$, with ferric iron calculated on the basis of 8 cations to 12.5 oxygens.

(vii) Chlorite

Chlorite analyses were recalculated on the basis of 28 oxygens, corresponding to the ideal formula $(\text{Mg}, \text{Al})_{12} (\text{Si}, \text{Al})_8 \text{O}_{20} (\text{OH})_{16}$, with ferric iron estimated on the basis of 20 cations to 28 oxygens.

(viii) Mica

Biotite and phlogopite analyses were calculated on the basis of 22 oxygens, corresponding to the ideal formula $\text{K}_2 (\text{Mg}, \text{Al})_6 (\text{Si}, \text{Al})_8$

$O_{20} (OH)_4$. Ferric iron was not estimated.

(ix) Oxides

Spinel, including magnetite, were recalculated on the basis of 32 oxygens, with ferric iron calculated assuming 24.000 cations. The following end members were calculated:

Ulvospinel	$Fe^{2+}TiO_4$
Chromite	$Fe^{2+}_2 Cr_2O_4$
Magnesiochromite	$Mg Cr_2 O_4$
Spinel	$Mg Al_2O_4$
Hercynite	$Fe_2 Al_2O_4$
Magnesioferrite	$Mg Fe^{3+}O_4$
Magnetite	$Fe^{2+} Fe^{3+}_2 O_4$

Ilmenite analyses were recalculated, in terms of hematite (Fe_2O_3) and ilmenite ($FeTiO_3$) end members, on the basis of 6 oxygens and 4 cations.

APPENDIX III. THERMAL MODELS

This section lists the tables upon which the graphs and data discussed in Chapter 4 are based. A complete list of parameters and data sources is given in Table 4.4.

Table III.i. Conduction Model (Similar Thermal Properties).

Temperature reached at distance x from contact in time t (see Fig. 4.9).

$$f = \kappa t/a^2$$

κ = diffusivity = 10^{-2} cm²/s

a = half thickness of peridotite sheet
= 500 m

f = dimensionless time factor (from Jaeger, 1968).

		T/(T _P - T _{CR})					
	x(m)	0	100	200	300	400	500
f	t(y)						
0.01	80	0.500	0.079	0.002			
0.1	8 x 10 ²	0.500	0.327	0.186	0.090	0.037	0.013
1	8 x 10 ³	0.421	0.384	0.344	0.303	0.262	0.222
10	8 x 10 ⁴	0.173	0.171	0.169	0.166	0.163	0.160

		T _x	t = 80y				
	x(m)	0	100	200	300	400	500
T _P (°C)	T _R (°C)						
1050	350	700	405	351			
	300	675	359	302			
	250	650	313	252			
950	350	650	397	351			
	300	625	351	301			
	250	600	305	251			
850	350	600	390	351			
	300	575	343	301			
	250	550	297	251			

(continued)

Table I I I.i. (Continued)

		$T_x, \quad t = 8 \times 10^2 \text{ y}$						
		x(m)	0	100	200	300	400	500
$T_P(^{\circ}\text{C})$	$T_R(^{\circ}\text{C})$							
1050	350	700	579	480	413	376	359	
	300	675	545	440	368	328	310	
	250	650	512	399	322	280	260	
950	350	650	546	462	404	372	358	
	300	625	513	421	359	324	308	
	250	600	479	380	313	276	259	
850	350	600	514	443	395	369	357	
	300	575	480	402	350	320	307	
	250	550	446	362	304	272	258	
		$T_x, \quad t = 8 \times 10^3 \text{ y}$						
		x(m)	0	100	200	300	400	500
$T_P(^{\circ}\text{C})$	$T_R(^{\circ}\text{C})$							
1050	350	645	619	591	562	533	505	
	300	616	588	558	527	497	467	
	250	587	557	525	492	460	428	
950	350	603	580	556	532	507	483	
	300	574	550	524	497	470	444	
	250	545	519	491	462	433	405	
850	350	560	542	522	502	481	461	
	300	532	511	489	467	444	422	
	250	503	480	456	432	407	383	
		$T_x, \quad t = 8 \times 10^4 \text{ y}$						
		x(m)	0	100	200	300	400	500
$T_P(^{\circ}\text{C})$	$T_R(^{\circ}\text{C})$							
1050	350	471	470	468	466	464	462	
	300	430	428	427	425	422	420	
	250	388	387	385	383	380	378	
950	350	454	453	451	450	448	446	
	300	412	411	410	408	406	404	
	250	371	370	368	366	364	362	
850	350	437	436	435	433	432	430	
	300	395	394	393	391	390	388	
	250	354	353	351	350	348	346	

Table III.ii. Conduction Model (Similar Thermal Properties)

Maximum temperature attained in country rocks at
distance x from the contact in time t (see Fig. 4.10).

	$x(m)$	0	100	250	500	1000
	f	0	0.500	0.932	1.820	4.330
	$t(y)$	0	4×10^3	7×10^3	1×10^4	3×10^4
	$T/(T_p - T_R)$	0.500	0.407	0.324	0.242	0.161
$T_p (^{\circ}C)$	$T_R (^{\circ}C)$					
1050	350	700	635	577	519	463
	300	675	605	543	482	421
	250	650	576	509	444	379
950	350	650	594	544	495	447
	300	625	565	511	457	405
	250	600	535	477	419	363
850	350	600	554	512	471	431
	300	575	524	478	433	389
	250	550	494	444	395	347

Table III.iii. Conduction Model (Dissimilar Thermal Properties)

Maximum contact temperature (T_c) for varying conductivity (K) and diffusivity (κ) of peridotite (P) and country rock (R) after Lovering (1936) (see Fig. 4.11).

$$\mathcal{K} = \left(\frac{K}{\sqrt{\kappa}} \right)_P \bigg/ \left(\frac{K}{\sqrt{\kappa}} \right)_R$$

$$T_c = \left[(T_p - T_R) \times T/T_o \right] + T_R$$

		1	1.25	1.3	1.4	1.5	1.8	2.0
T/T_o		0.500	0.555	0.560	0.580	0.600	0.640	0.670
$T_p (^{\circ}\text{C})$	$T_R (^{\circ}\text{C})$							
1050	350	700	739	742	756	770	798	819
	300	675	716	720	735	750	780	803
	250	650	694	698	714	730	762	786
950	350	650	683	686	698	710	734	752
	300	625	661	664	677	690	716	736
	250	600	638	642	656	670	698	719
850	350	600	628	630	640	650	670	685
	300	575	605	608	619	630	652	669
	250	550	583	586	598	610	634	652

Table III.iv. Frictional Heating Model.

- (a) Relationship between heat produced at contact (q), rate of motion (u), shear strength (τ), and thermal gradient at contact ($dt/dx_{(x=0)}$) (see Fig. 4.14, 4.18).

$$q = u\tau$$

$$dT/dx_{(x=0)} = \frac{-q}{\rho C_p \kappa}$$

$$\rho = 3.0 \text{ g/cm}^3$$

$$C_p = 0.2 \text{ cal/g}^\circ\text{C}$$

$$\kappa = 10^{-2} \text{ cm}^2/\text{s}$$

$$K = 6 \times 10^{-3} \text{ cal/cm s}^\circ\text{C}$$

(cal/cm ³)	u(cm/s)	q (hfu)	$\frac{dT}{dx}_{(x=0)}$ (°C/km)
25 (1kb)	3×10^{-8} (1 cm/y)	0.8	-13
	2×10^{-7} (5 cm/y)	4.0	-67
	3×10^{-7} (10 cm/y)	8.0	-130
	5×10^{-7} (15 cm/y)	12	-200
	6×10^{-7} (20 cm/y)	16	-270
50 (2kb)	3×10^{-8} (1 cm/y)	1.6	-27
	2×10^{-7} (5 cm/y)	8.0	-130
	3×10^{-7} (10 cm/y)	16	-270
	5×10^{-7} (15 cm/y)	24	-400
	6×10^{-7} (20 cm/y)	32	-530
75 (3kb)	3×10^{-8} (1 cm/y)	2.4	-40
	2×10^{-7} (5 cm/y)	12	-200
	3×10^{-7} (10 cm/y)	24	-400
	5×10^{-7} (15 cm/y)	36	-600
	6×10^{-7} (20 cm/y)	48	-800

- (b) Relationship between heat produced at contact (q), time since beginning of motion (t), and temperature increase of the contact ($\Delta T_{(x=0)}$) (see Fig. 4.13, 4.16).

$$\Delta T_{(x=0)} = \frac{q}{\rho C_p} \left(\frac{t}{\pi \kappa} \right)^{1/2} \quad (^\circ\text{C})$$

t(s)	q(hfu)	1.6	8.0	16	24	32	48
3×10^{10} (10^3 y)	3	13	27	40	53	80	
3×10^{11} (10^4 y)	9	42	84	130	170	250	
3×10^{12} (10^5 y)	27	130	270	400	530	800	
3×10^{13} (10^6 y)	86	420	840	1200	1700	2500	
3×10^{13} (2×10^6 y)	120	600	1200	1800	2400	3600	
2×10^{14} (5×10^6 y)	190	950	1900	2800	3800	5700	
3×10^{14} (10^7 y)	270	1300	2700	4000	5300	8000	

APPENDIX IV. Published papers and a manuscript under review written by the author which have a bearing on the present study.

A suite of alkali basalts and gabbros associated with the Hare Bay Allochthon of western Newfoundland

R. A. JAMIESON

Department of Geology, Memorial University of Newfoundland, St. John's, Nfld., Canada A1C 5S7

Received 14 May 1976

Revision accepted for publication 21 October 1976

The Hare Bay Allochthon of northwestern Newfoundland consists of a series of sedimentary, volcanic, metamorphic, and ultramafic rocks which was emplaced over a Cambro-Ordovician continental margin as several thrust sheets. It probably represents a continental margin sequence overridden by oceanic crust and upper mantle. The Partridge Point gabbro, Cape Onion volcanics, and Ireland Point Volcanics, which now occur in the Maiden Point, Cape Onion, and St. Anthony tectonic slices respectively, appear to be closely related on petrographic and chemical grounds. Olivine, titanite, kaersutite, and plagioclase indicate that these rocks formed as a single suite of hydrous alkali basalts, possibly as part of a seamount near a continental margin. This relationship provides a link between the lower sedimentary and the upper igneous-metamorphic structural slices of the allochthon and implies that most of the transported rocks in the Hare Bay area evolved in close proximity to each other.

L'allochthone de Hare Bay au nord-ouest de Terre-Neuve consiste en une série de roches sédimentaires, volcaniques, métamorphiques et ultramafiques qui ont été mises en place sur une bordure continentale Cambro-Ordovicienne en plusieurs écaillles. Cet allochthone représente probablement une séquence de bordure continentale chevauchée par la croûte océanique et le manteau supérieur. Le gabbro de Partridge Point, les roches volcaniques de Cape Onion, et d'Ireland Point, qui se présentent maintenant dans les écaillles tectoniques de Maiden Point, Cape Onion et St. Anthony respectivement, sont étroitement apparentées aux points de vue pétrographique et chimique. L'olivine, la titanite, la kaersutite et le plagioclase indiquent que ces roches se sont formées comme une suite unique de basaltes alcalins hydratés, possiblement comme partie d'une montagne sous-marine adjacente à une bordure continentale. Cette relation suggère un lien entre les écaillles structurales de l'allochthone dans les roches sédimentaires à la base et les roches ignées et métamorphiques au sommet et implique que la plupart des roches transportées dans la région de Hare Bay ont évolué à proximité les unes des autres.

Can. J. Earth Sci., **14**, 346-356 (1977)

[Traduit par le journal]

Introduction

The Hare Bay Allochthon of northwestern Newfoundland, which may represent a sequence of continental margin sediments overridden by oceanic crust, was emplaced as a series of thrust sheets over autochthonous carbonate and flysch during the early Middle Ordovician. The northern part of the allochthon consists of five separate tectonic slices (Fig. 1), and its stratigraphy has recently been reviewed by Williams (1975). The present study was undertaken in connection with detailed work on the uppermost unit, the St. Anthony Complex, in an attempt to determine its origin and its relationship to the rocks which underlie it.

At the base of the allochthon two mainly sedimentary units occur. The Lower Ordovician Northwest Arm Formation consists of thinly bedded shales and siltstones and is locally chaotically deformed. It is overlain structurally by

the Maiden Point Formation, a thick turbidite sequence of presumed Cambrian age, which also contains minor volcanic and gabbroic rocks. These are separated from the higher structural slices by the extensive Milan Arm Mélange, which contains blocks of both the underlying and overlying lithologies in a matrix of chaotically deformed black shale.

The two upper slices are mainly igneous and metamorphic in character. The Cape Onion Formation consists mostly of mafic pillow lava and dykes, and is associated with black shales containing Tremadocian graptolites. The St. Anthony Complex includes the undeformed Ireland Point Volcanics, mafic pillow lavas and pyroclastic rocks which grade upwards into the strongly deformed Goose Cove Schist and Green Ridge Amphibolite. The metamorphism is probably associated with the emplacement of the White Hills Peridotite (Williams and Smyth

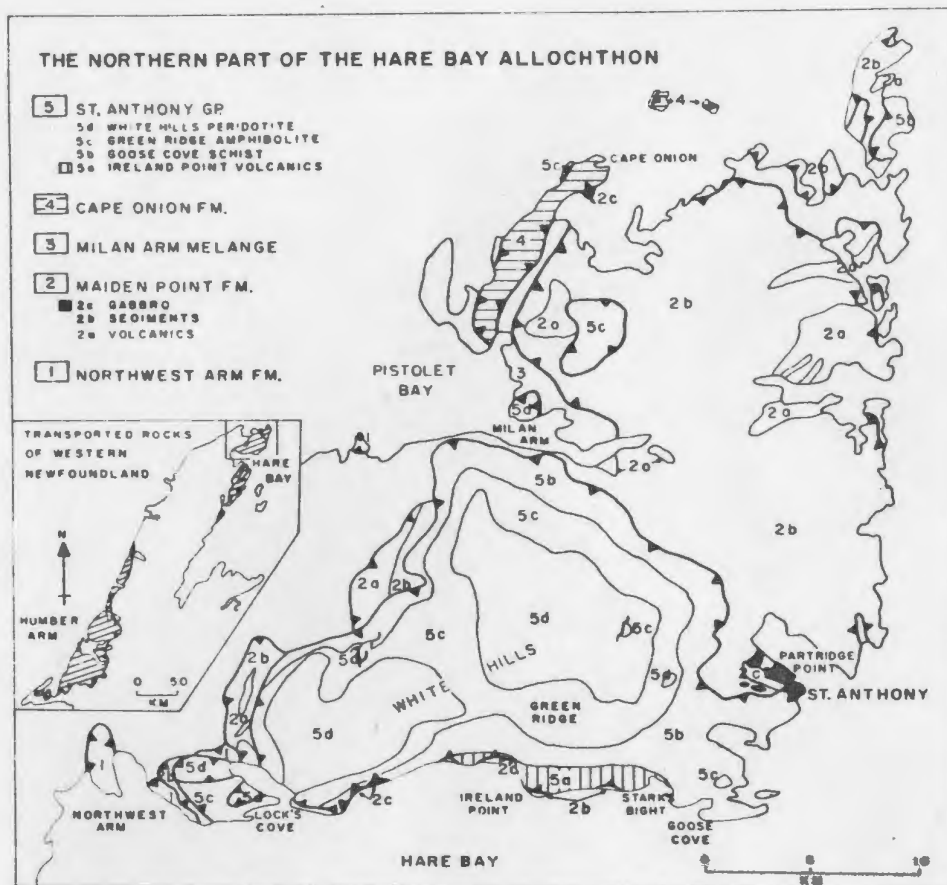


FIG. 1. The northern part of the Hare Bay Allochthon showing the distribution of transported rocks (after Smyth 1973 and Williams 1975). The shaded units are discussed in detail in the text.

1973), a harzburgite-lherzolite massif similar to the basal ultramafic units of the Bay of Islands Complex and other ophiolite suites.

The reconstruction of the pre-tectonic setting of the transported rocks is hampered considerably by the lack of overlapping stratigraphy due to the extensive thrusting and locally intense metamorphism which accompanied the emplacement, and by the scarcity of fossils. No fossils have been found in either the Maiden Point Formation or the St. Anthony Group, the most extensive units in the allochthon. Tremadocian graptolites occur in black shales of the Cape Union Formation, but the current interpretation that these shales are interbedded with the volcanic rocks may not be correct (C. DeLong, personal communication, 1976). An $^{40}\text{Ar}/^{39}\text{Ar}$ age of 480 ± 5 Ma for the metamorphism of the Green Ridge Amphibolite is interpreted as the date of the emplacement of the White Hills Peridotite (Dallmeyer 1976) but is of no use in clarifying the original relationships among the

allochthonous rocks. Owing to the lack of stratigraphic control and the importance of a reconstruction to the understanding of western Newfoundland geology, any evidence bearing on this problem must be regarded as important.

It seems likely that the Maiden Point Formation was deposited at a Cambro-Ordovician continental margin (Smyth 1973), and that the White Hills Peridotite represents the upper oceanic mantle (e.g. Church and Stevens 1971; Williams 1975). However, the affinities of the various volcanic and metamorphic rocks remain problematical. For example, metavolcanic rocks of the Goose Cove Schist which are in part equivalent to the Ireland Point Volcanics occur in some localities with metasediments probably equivalent to the Maiden Point Formation. The Ireland Point volcanics and the Goose Cove Schist protoliths are thus assigned the same tentative Lower Cambrian age as the sediments (Williams 1975).

There is now sufficient petrographic and geo-

chemical evidence to suggest that the gabbros which occur in the upper part of the Maiden Point slice, the Cape Onion volcanics, and the Ireland Point Volcanics formed as a single suite of alkalic igneous rocks, although they now occur in three separate tectonic units. This relationship provides a previously unrecognized link between the sedimentary Maiden Point Formation and the igneous and metamorphic rocks which now overlie it.

Field Relations

Gabbro intrudes the Maiden Point Formation near its structural top at St. Anthony and directly beneath the Hare Bay Thrust along the north shore of Hare Bay (Cooper 1937). It also occurs as blocks within the Milan Arm Mélange. At Partridge Point rhythmic layering with mafic to felsic bands is well-developed, individual layers rarely exceeding 50 cm in thickness. Small pockets of coarse-grained leucocratic material are locally present. For convenience, these intrusives are referred to informally as the 'Partridge Point gabbro' throughout the text.

The Cape Onion volcanics occur above (and/or within) the Milan Arm Mélange. They consist of well-preserved mafic pillow lava, with minor dykes, breccias, and agglomerates. Shales containing Tremadocian graptolites may be interbedded with them. The pillow lavas have a distinctive variolitic appearance, with light-coloured globules appearing a few centimetres within a chilled mafic rim and coalescing towards the core of the pillow.

The Ireland Point Volcanics occur directly above the Hare Bay Thrust at the base of the St. Anthony slice. Pillow lava at Ireland Point bears a striking resemblance to that at Cape Onion, with identical variolitic structures. To the east the pillow lavas take on a massive, vesicular appearance, and breccias, tuffs, and agglomerates become common. The most distinctive lithology in the formation is a plagioclase-porphyrific pillow lava exposed at Stark's Bight, where it is interbedded with and faulted against aphyric, vesicular pillow lava. Along the eastern side of Stark's Bight the volcanics become increasingly deformed and grade upwards into flattened volcanic breccias and phyllites of the Goose Cove Schist.

Petrography

Both the volcanic and the gabbroic rocks have been affected to varying degrees by low grade

metamorphism involving hydration and oxidation of the original assemblages. Olivine has generally been replaced by chlorite and carbonate. Calcic plagioclase is almost invariably altered to albite, epidote, and carbonate, with minor prehnite or pumpellyite. In places the mafic minerals are partially chloritized. However, none of these changes has served to obliterate the original grain boundaries or to obscure entirely the identity of the original minerals.

Virtually all of the rocks are characterized by the assemblage titanite and plagioclase, and are best described as alkali basalts (Wilkinson 1974). Significant variations in the mineralogy occur which are useful in determining the crystallization history of the suite.

The most distinctive feature of the Cape Onion volcanics and some of the Ireland Point Volcanics is the variolitic structure noted above. The devitrified groundmass contains two distinct phases—one, leucocratic and globular, now consists of anhedral albite and carbonate; the other, melanocratic and interstitial to the globules, consists of chlorite. The term 'variolitic' which has been used to describe these lavas is not precisely applicable since the globules lack any sort of regular internal radial or concentric arrangement of minerals (e.g. Phillips 1973), nor is there any evidence that such structures once existed. However, since no more appropriate term appears to be available, 'variolitic' is used for convenience.

All of the variolitic lavas examined contain euhedral olivine phenocrysts in a matrix of radiating, acicular, purple pleochroic clinopyroxene identified by microprobe analysis to be titanite (R. Jamieson, unpublished data). Augite occurs in both the mafic and felsic devitrified phases, commonly growing across the sharp boundaries between the varioles and the matrix. Modal plagioclase is rare in fine-grained samples. Coarser-grained material contains euhedral olivine, titanite, and interstitial plagioclase laths. Rarely, clinopyroxene is rimmed by a brown amphibole with the optical properties of kaersutite. Where amphibole occurs, olivine may be absent or show rounded corners and embayed faces suggesting resorption.

The Partridge Point gabbro and most of the Ireland Point Volcanics are distinguished by the presence of amphibole and the absence of olivine. Mafic bands within the gabbro contain abundant titanite, kaersutite, biotite, euhedral iron-titanium oxide, apatite, and interstitial

TABLE 1. The presumed order of development of the mineral assemblages observed in the Hare Bay alkalic suite

Mineral assemblage*	Locality
OL + cpx	Cape Onion, Ireland Point
OL + cpx + amph	Cape Onion
CPX + amph + plag	Ireland Point, Partridge Point
CPX + amph + bt + plag	Partridge Point, mafic bands
AMPH + plag	Partridge Point, felsic bands
PLAG + cpx	Stark's Bight
PLAG	Stark's Bight, Lock's Cove

*First-formed phases are in capitals; later and groundmass phases are in lower case letters. Iron-titanium oxides and apatite are usually present as accessories. ol = olivine; cpx = clinopyroxene; amph = amphibole; plag = plagioclase; bt = biotite.

plagioclase. The most common assemblage in both the volcanic and gabbroic rocks contains titanite mantled and partially replaced along cracks and cleavages by optically continuous kaersutite. Both phases are euhedral with respect to the surrounding plagioclase and are considered to be magmatic in origin. The kaersutite is usually rimmed by small amounts of a deep blue-green amphibole, and rarely a third, colourless amphibole forms overgrowths on the latter. Accessory apatite and opaque oxides are common. Late felsic veins in the gabbro contain euhedral kaersutite and abundant plagioclase, but not titanite.

At Stark's Bight, the porphyritic pillow cores contain over 50% plagioclase phenocrysts in places, as single crystals or crystal aggregates, in a groundmass of fine-grained plagioclase and brown clinopyroxene. The aphyric vesicular volcanics east of Ireland Point contain plagioclase laths which define a fluidal texture in a devitrified matrix. These are similar in appearance to pillow lavas at Lock's Cove which contain skeletal plagioclase microlites. However, the extensive thrusting obscures the stratigraphic relationship of the latter to the other volcanic rocks in the area.

The sequence of crystallization shown in Table 1 is derived from the above observations. Olivine in the Cape Onion volcanics is probably the earliest-formed phase, since it occurs as phenocrysts with skeletal, apparently quenched clinopyroxene, while plagioclase is absent. The amphibole which mantles the titanite must postdate the appearance of pyroxene, and the resorption textures displayed by olivine where it is present in amphibole-bearing assemblages suggest a reaction relationship between olivine and the melt to produce amphibole. In most rocks

olivine is absent and amphibole is abundant, and in the latest phase of the gabbro, amphibole has replaced titanite as the primary mafic phase. Plagioclase is usually present but it is generally interstitial to the mafic phases and probably crystallized later. At some point it becomes the primary phase in rocks such as the aphyric volcanics at Stark's Bight, but the nature of the accompanying mafic phases cannot be determined in these samples. The implications of this inferred crystallization history are discussed below.

Chemistry

The following discussion assumes that low-grade hydration and oxidation have not significantly affected the major element chemistry. Although this assumption is probably unjustified, particularly for the alkali elements, insufficient data are available at the present time to quantify the possible effects. Pervasive low-grade alteration may increase the apparent alkalinity of basalts (e.g. Vallance 1974); however, the mineralogy supports the chemical data in pointing to an alkalic composition as a primary feature of the Hare Bay gabbros and volcanics.

The analysed samples appear to lie on a common trend, particularly well-displayed by the $\text{FeO}_T\text{-SiO}_2$ variation diagram of Fig. 2a. The variolitic Cape Onion and Ireland Point volcanics plot toward the silica-poor end of the trend and the aphyric plagioclase-rich lavas fall at the silica-rich end, while the layered Partridge Point gabbro spans the whole range. The plagioclase-enriched nature of the porphyritic Stark's Bight pillow lavas is shown on the $\text{Al}_2\text{O}_3\text{-SiO}_2$ diagram (Fig. 2b), where the pillow cores can be seen to lie approximately on a control line from An_{80} to the aphyric rims. On the total alkalis-

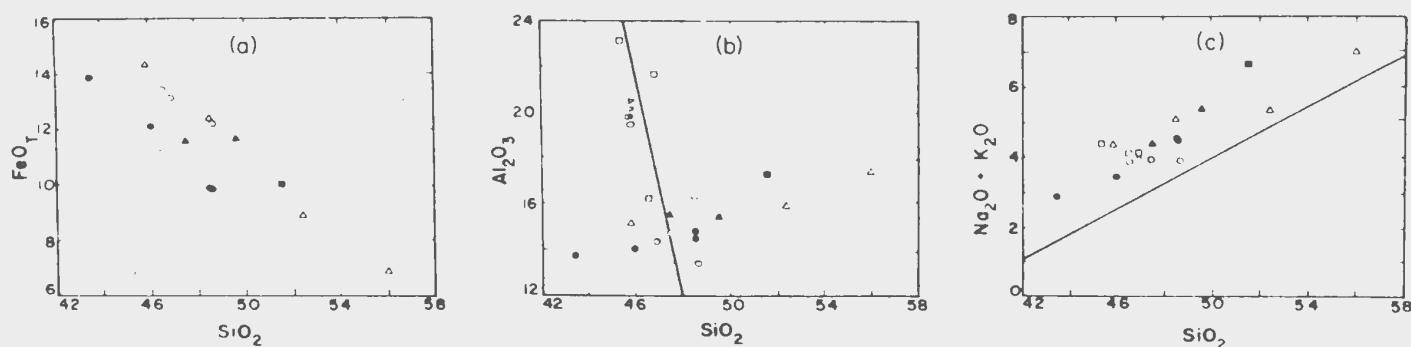


FIG. 2. Silica variation diagrams for the Hare Bay volcanics and gabbros, recalculated to 100% volatile-free. (a) $\text{FeO}_T = \text{FeO} + 0.899 \text{Fe}_2\text{O}_3$ (b) shows a control line from An_{80} to account for the variation in composition from porphyritic pillow cores to an aphyric rim. (c) The dividing line for Hawaiian basalts separates alkalic compositions above it from tholeiitic compositions below it (MacDonald and Katsura 1964). Open circles—Ireland Point Volcanics; closed circles—Cape Onion volcanics; open squares—plagioclase-porphyritic pillow cores and one aphyric rim from Stark's Bight; closed square—Lock's Cove pillow lava; open triangles—Partridge Point gabbro; closed triangles—aphyric pillow lavas between Stark's Bight and Ireland Point.

silica diagram (Fig. 2c) the compositions form a linear trend in the field of alkali to transitional basalts (MacDonald and Katsura 1964). While these data do not in themselves confirm a comagmatic origin for the suite, incompatible trends would rule out consanguinity.

The chemical data may be used to compare the Hare Bay alkali basalts with other potentially correlative rocks of western Newfoundland. A suite of greenschist facies basaltic rocks occurs south of Hare Bay near the base of the Maiden Point slice, about 2 km structurally below the Partridge Point gabbro (Smyth 1973). An AFM diagram (Fig. 3) clearly distinguishes these basalts, which plot in the tholeiitic field, from those described in this study, which plot in the alkalic field. The variation of TiO_2 with FeO_T/MgO was used by Church and Coish (1976) to illustrate the gradation of compositions from east to west within the Newfoundland ophiolites (Fig. 4). The Hare Bay alkali basalts span the gap between the tholeiites of the ophiolite suites and the alkalic Skinner Cove Volcanics (described below), but are distinct from both.

The Skinner Cove Volcanics, which plot at high values of TiO_2 and FeO_T/MgO in Fig. 4, are a suite of ankaramites to trachytes occurring as a slice beneath the Bay of Islands ophiolite complex (Strong 1974). They have been interpreted as having formed away from the axis of an oceanic spreading centre. They are distinctly more alkalic than the Hare Bay suite, particularly with respect to the concentrations of TiO_2 and K_2O . In addition, modal olivine is more

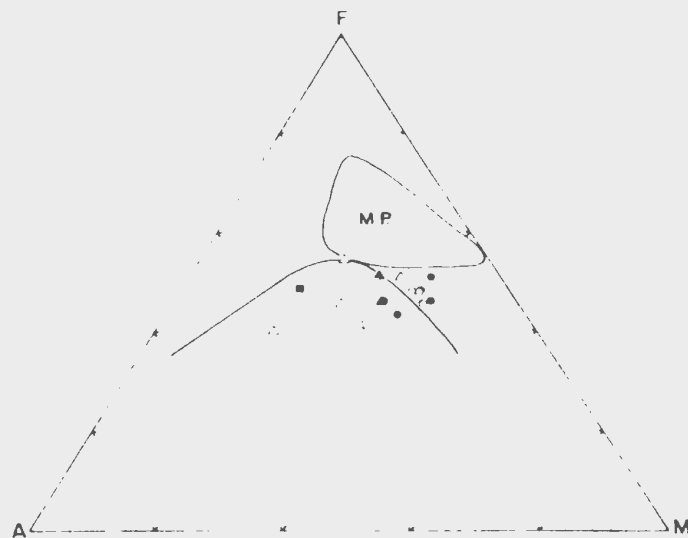


FIG. 3. AFM diagram showing the composition of volcanics and gabbros north of Hare Bay with respect to the line separating alkalic rocks (below) from tholeiitic rocks (above) (Irvine and Baragar 1971). The field of volcanics from the lower part of the Maiden Point Slice is shown for comparison (M.P.). Ornamentation as for Fig. 2. $A = \text{Na}_2\text{O} + \text{K}_2\text{O}$; $F = \text{FeO} + 0.899 \text{Fe}_2\text{O}_3$; $M = \text{MgO}$.

common, and alkali feldspar occurs in the trachytes. Although Lower Ordovician fossiliferous sediments were previously reported to be interbedded with the volcanics (Strong 1974), these are apparently in tectonic contact (D. Baker, personal communication, 1976) and thus the age of the suite is unknown. Although there is no evidence of a genetic relationship, it is worth noting the occurrence of two suites of alkalic volcanic rocks in similar structural positions

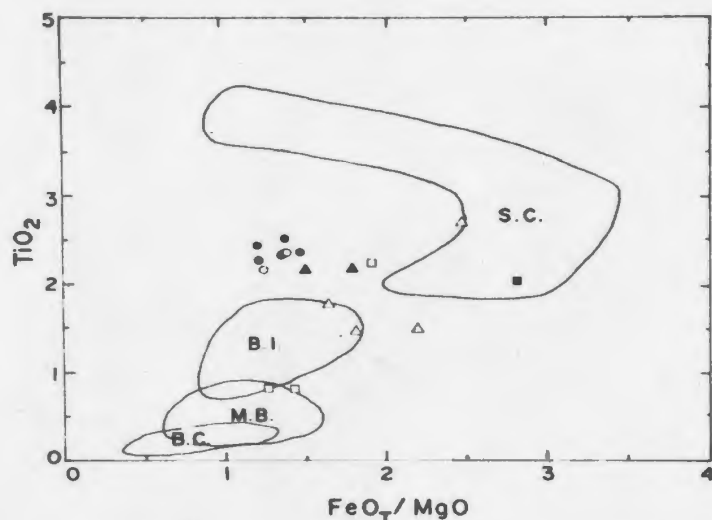


FIG. 4. The distinction between the Hare Bay alkalic suite and other volcanic rocks in western Newfoundland as shown by the variation of TiO_2 with FeO_T/MgO . Data from Church (unpublished diagram). S.C.—Skinner Cove; B.I.—Bay of Islands; M.B.—Ming's Bight; B.C.—Bett's Cove. Ornamentation as for Fig. 2.

beneath the ophiolite massifs of western Newfoundland.

Discussion

The sequence of crystallization determined from the petrography and outlined in Table 1 is similar to that determined experimentally for the crystallization of a range of hydrous basaltic magmas at pressures of 5 kb or less (Yoder and Tilley 1962; Holloway and Burnham 1972; Helz 1973). When the modal proportions observed in these natural examples are compared with the experimental results, it appears that the actual pressure of crystallization was less than 5 kb, stabilizing plagioclase and clinopyroxene at the expense of amphibole (Fig. 5).

In order to examine the phase relationships in further detail, the chemical compositions of the Hare Bay alkali basalts have been projected into the system $\text{CaO-MgO-Al}_2\text{O}_3\text{-SiO}_2\text{-Na}_2\text{O-H}_2\text{O}$ using the method of Cawthorn and O'Hara (1976). Figure 6a shows a projection from Mg_2SiO_4 and H_2O onto the plane $\text{CaSiO}_3\text{-MgSiO}_3\text{-Al}_2\text{O}_3\text{-Na}_2\text{O}$. It is apparent that the data plot very close to the 5 kb hydrous olivine-clinopyroxene-amphibole cotectic determined by Cawthorn (1973) for liquids containing 4%–6% Na_2O , supporting the qualitative arguments presented above that the observed mineralogy and chemistry result from the low-pres-

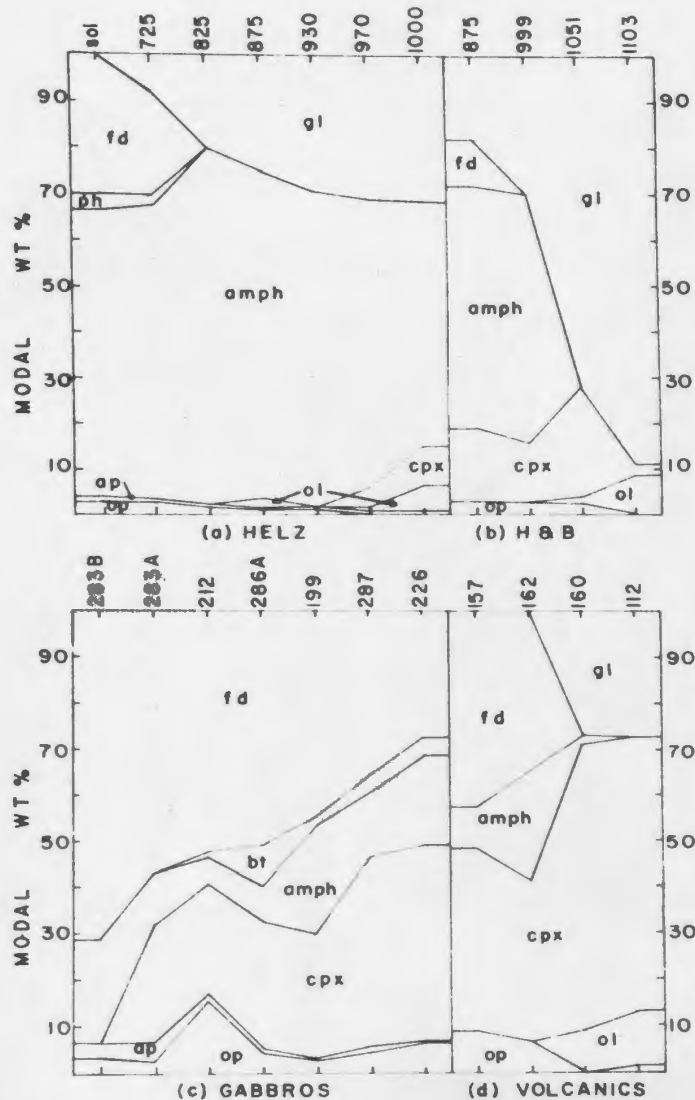


FIG. 5. Modal proportions (plotted in weight %) observed in some experimental work compared with examples from Hare Bay. (a) 1801 Hualalai alkali basalt, QFM buffer, $P_r = 5 \text{ kb} = P_{\text{H}_2\text{O}}$ (Helz 1973). (b) 1921 Kilauea tholeiite, NNO buffer, $P_l = 5 \text{ kb} > P_{\text{H}_2\text{O}}$, $f_{\text{H}_2\text{O}} \approx 0.6$ (Holloway and Burnham 1972). For (a) and (b) the numbers on the horizontal axes refer to the run temperatures. (c) Partridge Point gabbro. (d) Ireland Point (157, 162, 160) and Cape Onion volcanics (112). For (c) and (d) the numbers on the horizontal axes are sample numbers, and the data is plotted with feldspar decreasing from left to right. gl—glass; fd—feldspar; ph—phlogopite; amph—amphibole; cpx—clinopyroxene; bt—biotite; ol—olivine; ap—apatite; op—opaques.

sure crystallization of a hydrous alkaline melt. Figure 6b, which shows the data projected from $\text{CaMgSi}_2\text{O}_6$ and H_2O onto the plane $\text{CaAl}_2\text{O}_4\text{-MgO-SiO}_2$, separates the different stages of crystallization. The olivine-bearing volcanic rocks plot in the olivine primary phase field

TABLE 2. The chemical and normative compositions of the Hare Bay alkalic suite

	1 RJ75-286A	2 RJ75-212	3 RJ75-283A	4 RJ75-283B	5 DFS-115D	6 DFS-115L	7 DFS-115AD	8 DFS-115AL	9 RJ75-157
SiO ₂	42.61	46.38	50.13	53.90	43.40	46.70	42.00	46.70	44.62
TiO ₂	1.85	2.57	1.37	1.44	2.29	1.98	2.40	2.27	1.99
Al ₂ O ₃	14.82	15.66	14.56	16.73	13.20	13.90	13.20	14.20	12.30
Fe ₂ O ₃	2.02	4.71	2.64	2.05	4.55	3.18	4.64	3.21	1.73
FeO	11.62	7.55	6.15	4.78	7.33	6.64	9.22	6.61	9.63
MnO	0.19	0.19	0.17	0.12	0.16	0.14	0.18	0.13	0.15
MgO	9.00	4.97	5.00	3.13	10.00	8.00	9.91	6.77	9.82
CaO	8.06	8.49	9.74	7.37	9.77	10.87	11.87	11.45	7.95
Na ₂ O	2.85	4.21	4.87	6.39	2.66	3.77	0.99	2.77	3.45
K ₂ O	1.33	0.62	0.30	0.35	0.55	0.51	1.74	0.57	0.10
P ₂ O ₅	0.13	0.27	0.43	0.05	0.50	0.40	0.50	0.50	n.d.
L.O.I.	4.26	4.26	3.59	2.21	4.61	4.34	3.97	3.21	6.71
TOTAL	98.74	99.83	98.95	98.52	99.02	100.43	100.62	99.39	98.45
Normative compositions (wt %)									
OR	8.32	3.83	1.86	2.15	3.44	3.14	10.64	3.50	0.64
AB	14.27	34.91	40.25	52.68	23.55	25.53	6.76	25.57	29.77
AN	25.10	23.01	17.81	16.54	23.78	20.29	27.35	20.94	19.38
NE	6.10	1.27	1.60	1.87	0.16	4.15	1.03	4.11	1.11
DI	13.39	15.55	24.34	17.19	19.22	26.54	24.30	27.89	19.16
HY	—	—	—	—	—	—	—	—	—
OL	25.69	8.53	6.35	3.52	17.03	10.67	17.04	7.46	23.08
MT	3.10	7.14	4.01	3.09	6.99	4.80	6.96	4.84	2.73
ILM	3.72	5.10	2.73	2.84	4.61	3.91	4.72	4.48	4.12
AP	0.32	0.66	1.05	0.12	1.23	0.97	1.20	1.21	—

TABLE 2. (Continued)

	10 RJ75-160A	11 RJ75-160B	12 RJ75-160C	13 RJ75-255	14 RJ75-256	15 RJ75-257	16 RJ75-258	17 RJ75-263	18 RJ75-229
SiO ₂	43.51	44.68	44.04	42.29	43.55	44.02	44.30	46.62	46.95
TiO ₂	2.17	2.22	2.25	0.45	0.76	2.20	2.04	2.05	1.84
Al ₂ O ₃	13.20	13.87	14.07	20.97	20.07	15.11	14.41	15.86	15.75
Fe ₂ O ₃	2.71	2.66	1.30	3.10	3.64	3.96	6.26	3.03	2.97
FeO	9.74	9.64	11.36	3.44	2.52	6.92	5.17	7.73	6.41
MnO	0.15	0.16	0.16	0.11	0.09	0.19	0.18	0.16	0.13
MgO	9.65	9.26	10.14	4.89	4.92	6.15	6.44	7.70	3.54
CaO	7.91	8.00	7.72	13.72	13.56	11.30	10.40	6.57	7.47
Na ₂ O	3.10	3.41	2.96	3.01	2.73	3.57	3.48	3.14	5.27
K ₂ O	0.48	0.30	0.63	1.28	1.06	0.10	0.61	1.71	0.79
P ₂ O ₅	0.06	n.d.	0.23	0.01	n.d.	0.24	0.03	0.22	0.01
L.O.I.	5.68	6.10	5.03	6.91	6.43	6.23	4.67	5.13	6.88
TOTAL	98.40	100.30	99.89	100.18	99.33	99.99	97.99	99.92	98.01
Normative compositions (wt %)									
OR	3.05	1.88	3.92	8.11	6.74	0.63	3.86	10.66	5.12
AB	25.42	27.93	23.39	1.95	10.25	24.16	25.97	28.03	37.75
AN	22.59	22.99	24.50	42.81	42.39	26.57	23.47	25.46	18.64
NE	1.54	1.46	1.63	13.73	7.92	4.37	3.02	—	6.00
DI	15.63	15.52	11.67	24.00	23.48	25.41	24.82	5.99	17.99
HY	—	—	—	—	—	—	—	5.36	—
OL	22.93	21.64	27.83	3.63	1.98	7.70	4.91	15.22	5.86
MT	4.23	4.09	1.99	4.82	5.68	6.12	9.73	4.63	4.73
ILM	4.44	4.48	4.50	0.92	1.55	4.46	4.15	4.11	3.83
AP	0.15	—	0.56	0.02	—	0.59	0.07	0.54	0.03

NOTE: (1-4)* Partridge Point Gabbro; (5-8)* Cape Onion volcanics; (9-12)* Ireland Point Volcanics; (13, 14)* Stark's Bight porphyritic pillow cores; (15)* Stark's Bight aphyric pillow rim; (16, 17)* Aphyric pillow lavas between Ireland Point and Stark's Bight; (18)* Lock's Cove pillow lava. *Analyst, R. A. Jamieson. †Analyst, G. Andrews.

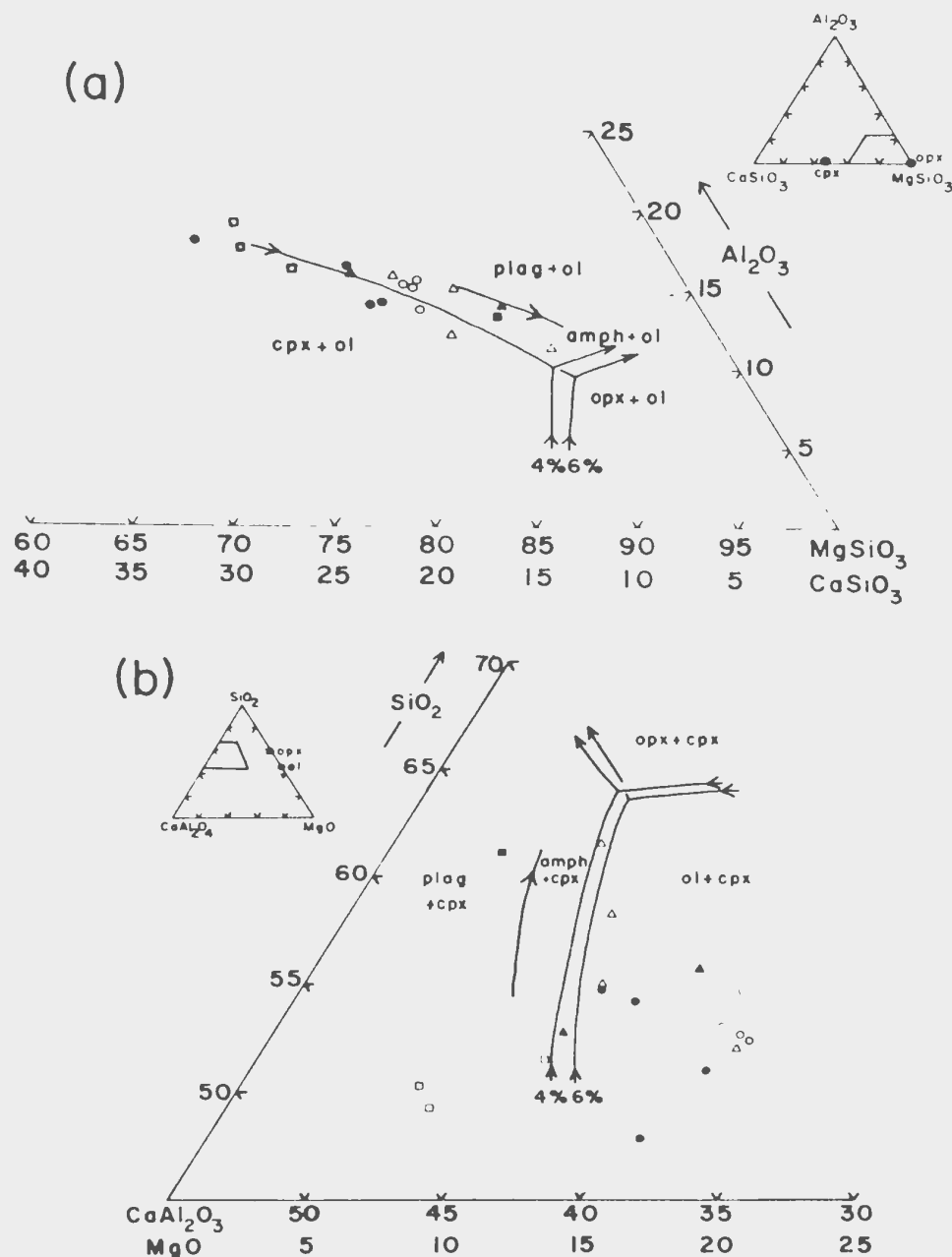


FIG. 6. The system $\text{CaO-MgO-Al}_2\text{O}_3\text{-SiO}_2\text{-Na}_2\text{O-H}_2\text{O}$ at $P_T = P_{H_2O} = 5 \text{ kb}$. (a) Projection from Mg_2SiO_4 and H_2O onto the plane $\text{CaSiO}_3\text{-MgSiO}_3\text{-Al}_2\text{O}_3\text{-Na}_2\text{O}$. (b) Projection from $\text{CaMgSi}_2\text{O}_6$ and H_2O onto the plane $\text{CaAl}_2\text{O}_4\text{-MgO-SiO}_2\text{-Na}_2\text{O}$. Insets show the positions of the enlarged areas with respect to the entire projection planes. 4% and 6% refer to the concentration of Na_2O in the liquids (after Cawthorn and O'Hara 1976). Abbreviations and ornamentation as for previous figures. Details in text.

along with the mafic gabbroic bands, and the trend of the gabbro compositions toward the amphibole field is evident. The plagioclase-porphyrific volcanic rocks at Stark's Bight plot in the plagioclase field, as would be predicted. The second projection is more precisely applicable to the investigated samples than the first, since clinopyroxene is generally present as a crystalline phase.

The hypothesis that the Partridge Point gabbro, the Ireland Point Volcanics, and the Cape Onion volcanics represent a closely related suite of alkali basalts is thus supported by the experimental data, which further suggest that the observed compositions result from low-pressure differentiation under hydrous conditions.

Several points arising from the preceding descriptions have important implications for the

interpretation of the pre-tectonic history of the Hare Bay region. (1) The Partridge Point gabbro intrudes Maiden Point continental margin sediments of presumed Cambrian to Cambro-Ordovician age near their structural top. (2) The alkali basalts and gabbros of the Hare Bay region do not closely resemble other volcanic rocks in the western Newfoundland allochthons (with the possible exception of the Skinner Cove suite). (3) The Cape Onion volcanics, the Ireland Point Volcanics, and the Partridge Point gabbro are alkalic rocks of a very similar type and are probably co-magmatic, although there is no field evidence of consanguinity.

These observations suggest that the Hare Bay alkalic igneous suite is not genetically related to the partial ophiolite with which it is now tectonically associated, although the petrogenesis of the White Hills Peridotite is practically unknown. The tectonic juxtaposition of alkali basalts with ophiolites is known from other parts of the world, notably the Mediterranean area. For example, at Othris, alkalic volcanic rocks occurring beneath a complete ophiolite suite are overlain by continental margin sediments (Hynes 1974). In Cyprus, alkali volcanic rocks are interbedded with subaerial sediments containing plant fossils (LaPierre and Rocci 1976). In these cases it has been concluded that the alkalic rocks were associated with the initial rifting of the continents and were overridden by younger oceanic crust.

This explanation is considered unlikely for the Hare Bay rocks. The Maiden Point Formation is inferred to overlie tholeiitic dykes dated at 605 Ma (Stukas and Reynolds 1974) and includes tholeiitic volcanics near its base, both of which have been interpreted as being related to the earliest stages of the formation of the proto-Atlantic Ocean (Strong and Williams 1972; Smyth 1973). The gabbro occurs at the structural top of the sequence of turbidites typical of mature continental margins. However, the stratigraphy of the Maiden Point Formation is unknown, and if the Tremadocian age for the Cape Onion volcanics is not correct, the stage of evolution of the continental margin at the time of the alkalic igneous activity cannot be precisely known. The amount of sedimentary material overlying the suite is minimal, but much may have been tectonically excluded from the sequence. The available geological evidence, while not conclusive, suggests that the Hare Bay suite formed after the initial rifting of the continent.

Since magmatic amphibole occurs in all three units, it should be possible to obtain independent isotopic ages which could confirm or rule out the proposed relationships.

Alkali basalts may also form parts of oceanic islands or seamounts which sometimes occur near continental margins, closely associated with continentally-derived sediments (*e.g.* Stillman *et al.* 1975; Sheridan 1974). This hypothesis fits the available data somewhat better, although again the evidence is not conclusive. The interpretation of these alkali basalts as a seamount would mean that in geophysical terms they were part of the upper oceanic crust at the time of their formation, as has been suggested for the Cape Onion volcanics by Williams (1975). However, it must be stressed that they cannot be equated with the ridge-formed volcanics in Layers 2 and 3 of the idealized stratigraphy of the oceanic crust (*e.g.* Worzel 1974).

Whatever their ultimate explanation, the recognition of this suite of alkali basalts within the Hare Bay Allochthon provides further information necessary for the reconstruction of the pre-tectonic geology of western Newfoundland.

Acknowledgements

The research was done while the author held a National Research Council of Canada 1967 Science Scholarship. Field support was provided from D. F. Strong's NRC grant. D. F. Strong and R. K. Stevens provided invaluable comment and criticism at all stages of the research and the comments of the referees and other readers have been most helpful. Thanks are also extended to J. Burry for her able assistance in the field and to C. DeLong for access to material collected for his honours thesis.

- CAWTHORN, R. G. 1973. Experimental and petrological studies on amphibole in ultrabasic rocks. Unpublished Ph.D. thesis, Edinburgh University, Edinburgh, Scotland, 70 p.
- CAWTHORN, R. G. and O'HARA, M. J. 1976. Experimental evidence for amphibole fractionation in calc-alkaline magmas. *American Journal of Science*, **276**, pp. 309–329.
- CHURCH, W. R. and COISH, R. 1976. Oceanic versus island arc origin of ophiolites. *Earth and Planetary Science Letters*, **31**, pp. 8–14.
- CHURCH, W. R. and STEVENS, R. K. 1971. Early Paleozoic ophiolite complexes of the Newfoundland Appalachians as mantle-oceanic crust sequences. *Journal of Geophysical Research*, **76**, pp. 1460–1466.
- COOPER, J. R. 1937. Geology and mineral deposits of the Hare Bay area. Newfoundland Department of Natural Resources, Geology Section, Bulletin 9, 36 p.
- DALLMEYER, R. D. 1976. Diachronous ophiolite obduction in western Newfoundland: evidence from $^{40}\text{Ar}/^{39}\text{Ar}$ ages

- of the Hare Bay metamorphic aureole. Unpublished manuscript.
- HEILZ, R. T. 1973. Phase relations of basalts in their melting range at $P_{H_2O} = 5$ kb as a function of oxygen fugacity. Part I. Mafic phases. *Journal of Petrology*, **14**, pp. 249–302.
- HOLLOWAY, J. R. and BURNHAM, C. W. 1972. Melting relations of basalt with equilibrium water pressure less than total pressure. *Journal of Petrology*, **13**, pp. 1–29.
- HYNES, A. J. 1974. Igneous activity at the birth of an ocean basin in eastern Greece. *Canadian Journal of Earth Sciences*, **11**, pp. 842–853.
- IRVINE, T. N. and BARAGAR, W. R. A. 1971. A guide to the chemical classification of the common volcanic rocks. *Canadian Journal of Earth Sciences*, **8**, pp. 522–548.
- LAPIERRE, H. and ROCCI, G. 1976. Le volcanisme alcalin du sud-ouest de Chypre et le probleme de l'ouverture des regions Tethysiennes au Trias. *Tectonophysics*, **30**, pp. 299–313.
- MACDONALD, G. A. and KATSURA, T. 1964. Chemical composition of Hawaiian lavas. *Journal of Petrology*, **5**, pp. 82–133.
- PHILLIPS, W. J. 1973. Interpretation of crystalline spheroidal structures in igneous rocks. *Lithos*, **6**, pp. 235–244.
- SHERIDAN, R. E. 1974. Atlantic continental margin of North America. *In: The Geology of Continental Margins* (C. A. Burke and C. L. Drake *Eds.*), pp. 391–407.
- STILLMAN, C. J., FUSTER, J. M., BENNELL-BAKER, M. J., MUNOZ, M., SMEWING, J. D., and SAGREDO, J. 1975. Basal complex of Fuertaventura (Canary Islands) is an oceanic intrusive complex with rift system affinities. *Nature*, **257**, pp. 469–471.
- SMYTH, W. R. 1973. The stratigraphy and structure of the southern part of the Hare Bay Allochthon, N.W. Newfoundland. Unpublished Ph.D. thesis, Memorial University, St. John's, Nfld., Canada, 172 p.
- STRONG, D. F. 1974. An 'off-axis' alkali volcanic suite associated with the Bay of Islands ophiolite, Newfoundland. *Earth and Planetary Science Letters*, **21**, pp. 301–309.
- STRONG, D. F. and WILLIAMS, H. 1972. Early Paleozoic flood basalts of northwestern Newfoundland: their petrology and tectonic significance. *Proceedings of the Geological Association of Canada*, **24**, pp. 43–54.
- STUKAS, V. and REYNOLDS, P. J. 1974. $^{40}\text{Ar}/^{39}\text{Ar}$ dating of the Long Range dikes, Newfoundland. *Earth and Planetary Science Letters*, **22**, pp. 256–266.
- VALLANCE, T. G. 1974. Spilitic degradation of a tholeiitic basalt. *Journal of Petrology*, **15**, pp. 79–96.
- WILKINSON, J. F. G. 1974. The mineralogy and petrology of alkali basaltic rocks. *In: The Alkaline Rocks* (H. Sørensen, *Ed.*) pp. 67–95.
- WILLIAMS, H. 1971. Mafic-ultramafic complexes in western Newfoundland Appalachians and the evidence for their transportation: a review and interim report. *Proceedings of the Geological Association of Canada*, **24**, pp. 9–25.
- 1975. Structural succession, nomenclature, and interpretation of transported rocks in western Newfoundland. *Canadian Journal of Earth Sciences*, **12**, pp. 1874–1894.
- WILLIAMS, H. and SMYTH, W. R. 1973. Metamorphic aureoles beneath ophiolite suites and alpine peridotites: tectonic implications with west Newfoundland examples. *American Journal of Science*, **273**, pp. 594–621.
- WORZEL, J. L. 1974. Standard oceanic and continental structure. *In: The Geology of Continental Margins* (C. A. Burke and C. L. Drake, *Eds.*) pp. 59–66.
- YODER, H. S. and TILLEY, C. E. 1962. Origin of basalt magmas: an experimental study of natural and synthetic rock systems. *Journal of Petrology*, **3**, pp. 342–532.

The first metamorphic sodic amphibole identified from the Newfoundland Appalachians—its occurrence, composition and possible tectonic implications

MODELS for the emplacement of the western Newfoundland ophiolite suites include obduction over an eastward-dipping subduction zone¹, but no blueschist facies assemblages, considered to form in response to the high P/T gradients associated with subduction, have yet been identified in this area. Magnesioriebeckite and crossite which occur in meta-volcanics from the vicinity of Croque, northwestern Newfoundland, provide the first indication that these conditions may have been approached. This report deals with the petrographic relations, composition and probable conditions of formation of the Newfoundland sodic amphiboles, the latest in a series of occurrences described from Vermont^{2,3}, Quebec⁴ and New Brunswick^{5,6} (Fig. 1).

The host rocks are undeformed metabasalts which occur at the structural base of the Maiden Point Formation, at the bottom of the Hare Bay Allochthon, a sequence of sedimentary, metamorphic and igneous rocks which includes a partial ophiolite at its top⁷. The greenschist facies mineral assemblage albite-epidote-actinolite-chlorite-sphene-stilpnomelane magnetite-quartz-(white mica) replaces the original pyroxene and plagioclase. There is little or no preferred orientation of the minerals, and the outlines of the pre-existing plagioclase phenocrysts are often preserved. Actinolite and brown stilpnomelane appear to post-date all other phases, growing as well developed acicular or sheaflike grains across a fine-grained mat of chlorite, epidote, albite and sphene. Actinolite and stilpnomelane do not appear in the matrix. Rare veinlets of albite, epidote and quartz transect the groundmass.

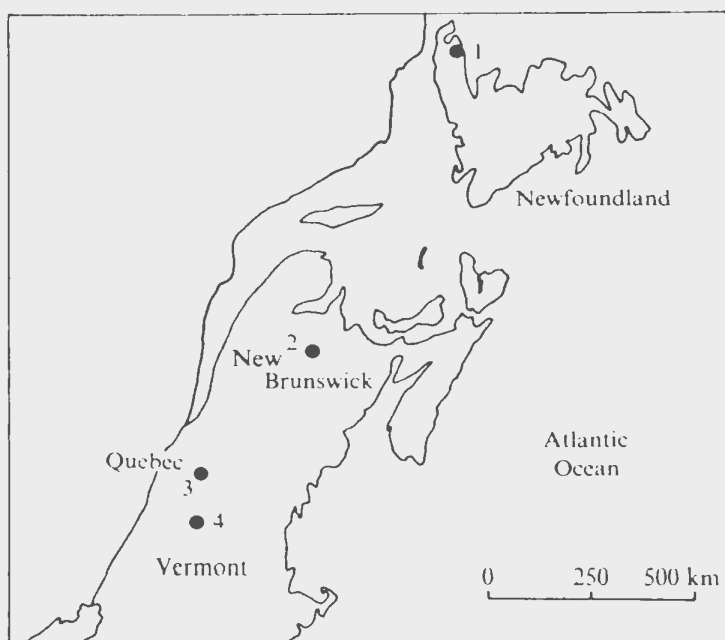


Fig. 1 A geographical location map showing the occurrence of sodic amphibole in the northern Appalachians. 1, Maiden Point Formation volcanics, Croque, Newfoundland (this paper); 2, Tetagouche Group Volcanics, New Brunswick^{5,6}; 3, Tibbet Hill Volcanics, Quebec⁴; 4, Hazen's Notch Formation, Vermont^{2,3}.

Amphibole with the pleochroic scheme X=yellow-green, Y=blue-violet, Z=indigo occurs in three samples from a suite originally collected by Smyth⁷. It rarely forms discrete grains, generally occurring as irregular zones or patches within actinolite crystals. Where a regular relationship can be defined, the blue amphibole tends to occur as cores rimmed by actinolite. No sharp boundaries between the actinolite and the sodic amphibole grains are visible. Where both amphiboles are present, actinolite is always the more abundant phase.

Microprobe analyses show that the amphiboles range continuously from sodic to calcic compositions (Table 1). The calcium-rich amphiboles have the low Al content and nearly ideal M4 site occupancy ($\text{Ca} + \text{Na} = 2.0$) that identify them as actinolites⁸ (Fig. 2). Approximately one-quarter of the analysed actinolites are unusually rich in sodium, with $1.2 < \text{Ca} < 1.5$ formula units, and are transitional into sodic compositions, with $\text{Ca} < 1.2$ units. The sodic amphiboles are best described as magnesioriebeckite (Fig. 3), with one analysed grain containing enough octahedral Al to be classified as crossite. Although the range of compositions between actinolite and magnesioriebeckite appears to be continuous when all the analyses are considered, each of the three samples studied displays a somewhat different set of compositions. RS 78-69 contains no analysed grains with $1.0 < \text{Ca} < 1.4$, RS 71-172 has a complete range between 1.0 and 1.8 Ca formula units, and RS 165-70 contains no amphibole with $\text{Ca} < 1.2$ units.

Studies of amphiboles from blueschist facies terrains have pointed to the existence of a miscibility gap between sodic and calcic compositions⁹⁻¹² and intermediate compositions, while rare, are not unknown (Fig. 2). Klein¹⁰ cites

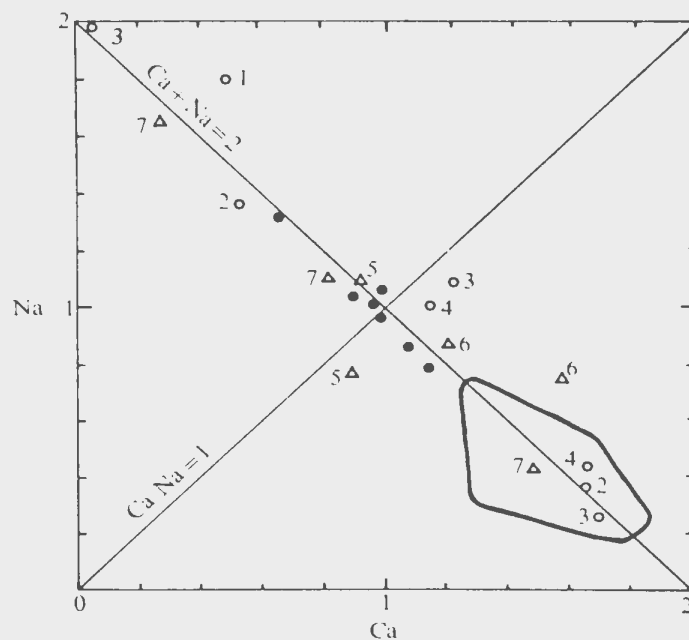


Fig. 2 The compositional range in terms of sodium and calcium content of amphiboles from the Croque metabasalts (●). The outlined field includes all actinolite compositions from the area. Also plotted are amphibole compositions from elsewhere in the Appalachians (◻) and other intermediate sodic-calcic compositions (Δ). 1, New Brunswick (H. Helmstaedt, private communication); 2, Quebec⁴; 3, Vermont (representative analyses of end members from the Tillotson Peak area, J. Laird, private communication); 4, Vermont³; 5, Labrador¹³; 6, Switzerland¹⁰; 7, Washington¹⁴.

Table 1 Representative analyses of amphiboles from the Croque metavolcanics

	Magnesioriebeckite RS 78-69/4-4	Intermediate sodic calcic amphibole RS 71-172/1-3	Actinolite RS 165-70/2-3
SiO ₂	52.59	51.57	54.95
TiO ₂	0.06	0.05	0.02
Al ₂ O ₃	2.57	4.85	1.16
Fe ₂ O ₃ *	7.69	6.66	2.66
FeO	15.52	11.67	11.56
MnO	0.30	0.59	0.31
MgO	9.18	12.17	14.96
CaO	4.09	7.32	9.89
Na ₂ O	4.57	2.82	1.63
K ₂ O	0.05	0.07	0.05
Total	96.62	97.77	97.19
Structural formula on the basis of 23 oxygens			
Si	7.84	7.49	7.93
Al ^{iv}	0.16	0.51	0.07
Al ^{vi}	0.29	0.32	0.12
Ti	0.01	0.01	0.00
Fe ³⁺ *	0.86	0.73	0.29
Fe ²⁺	1.94	1.42	1.39
Mn	0.04	0.07	0.04
Mg	2.04	2.64	3.22
Ca	0.65	1.14	1.53
Na	1.32	0.79	0.46
K	0.01	0.01	0.01

*Ferric iron was estimated according to the method of Papike *et al.*²⁰

one case of coexisting hornblende and sodic actinolite from a metamorphic ophiolite in the Swiss Alps. Because of lack of evidence for equilibrium coexistence and the associated epidote-amphibolite facies mineralogy, this pair was thought to have formed at pressures and temperatures above the proposed miscibility gap. Metamorphic conditions of $P > 6-10$ kbar and $T < 600$ °C were estimated for the formation of intermediate 'riebeckite-tremolite' from a metamorphosed iron formation in Labrador¹¹. Amphiboles from the Shuksan region, Washington, show continuous zoning from crossite to actinolite¹⁴. In this case, Brown concluded that with increasing dT/dP the pair sodic amphibole-calcic amphibole is replaced by a single intermediate amphibole, which in turn is replaced by Na-rich actinolite and iron oxide. If this inferred relationship is correct and applicable to the Croque metavolcanics, sample RS 78-69 would have formed under conditions of relatively low dT/dP , since it is the only sample to show any gap between sodic and calcic compositions and also contains the most sodium-rich amphiboles. Samples RS 71-172, with its intermediate compositions, and RS 165-70, with its sodic actinolites, would have formed under progressively higher T/P gradients.

The presence of sodic amphibole alone is not sufficient to define a blueschist facies assemblage¹⁵, particularly in this case where it is an uncommon phase and has a magnesioriebeckite crossite composition rather than one close to glaucophane. The stability of magnesioriebeckite ranges from authigenic to magmatic conditions⁸, and is probably very sensitive to bulk rock composition and f_2 as well as pressure and temperature. The stability field of crossite has not been experimentally defined, but probably lies between those of glaucophane and magnesioriebeckite. The metamorphic conditions at Croque cannot be deduced from the presence of this phase alone, but must be related to the mineral assemblage as a whole.

Brown¹⁶ has suggested that the reactions chlorite + K-feldspar = stilpnomelane + actinolite and chlorite + K-feldspar + magnetite = muscovite + stilpnomelane + actinolite occur within the chlorite zone of the greenschist facies, at relatively high pressures and over a wide range of temperatures. The reaction curves, with negative slopes,

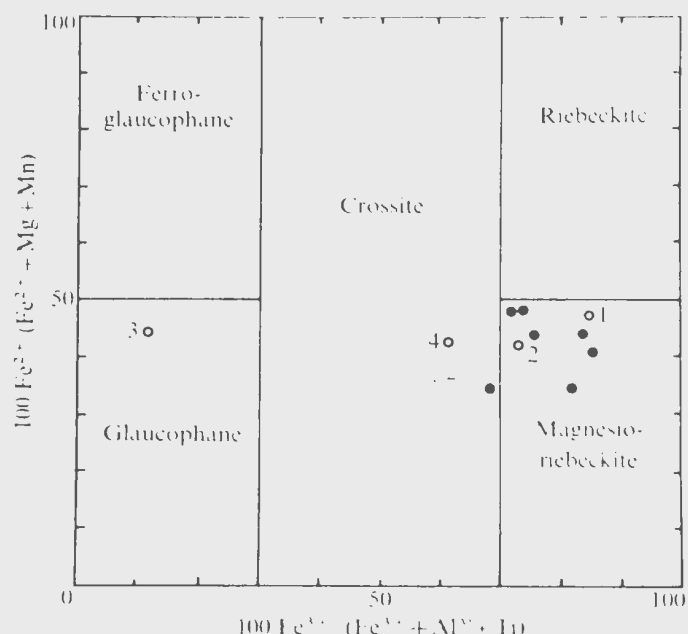


Fig. 3 Compositions of sodic amphiboles from Croque (●) in terms of glaucophane-riebeckite end members. Also plotted are amphibole compositions from elsewhere in the Appalachians (○). Ferric iron was estimated by the method of Papike *et al.*²⁰. 1, New Brunswick (H. Helmstaedt, personal communication); 2, Quebec⁴; 3, Vermont (J. Laird, personal communication); 4, Vermont³.

lie at lower pressures on a schematic diagram than the stability fields of glaucophane and lawsonite, although they may intersect the blueschist facies curves at high pressures and very low temperatures. The mineral assemblages observed in the Croque metavolcanics seem to exemplify the proposed reaction relationships, with stilpnomelane + actinolite overgrowing the earlier chlorite-rich greenschist facies assemblage. White mica replaces feldspar in at least one example. On this basis it seems likely that the assemblages formed within the greenschist facies at rather high pressures, with one sample representing a possible transition to blueschist facies conditions.

Magnesioriebeckite occurs in comparable stratigraphic positions elsewhere in the Canadian Appalachians. Trzcieski⁴ speculated, on the basis of 'crossite' in Tibbet Hill Volcanics of Quebec, that blueschist facies metamorphism had occurred in association with a subduction zone. However, Fig. 3 shows that the sodic amphibole in question is magnesioriebeckite, similar to the Croque amphiboles in composition. The presence of chlorite, stilpnomelane, actinolite and white mica in the assemblage, together with the similar stratigraphic position in volcanics which underlie a Cambro-Ordovician flysch sequence strongly suggest that the metamorphism occurred under conditions very similar to those in western Newfoundland. Magnesioriebeckite has also been observed in similar assemblages in Lower Palaeozoic volcanics in the New Brunswick Appalachians^{5,6}. An amphibole with optical properties very similar to the sodic amphiboles in the Croque assemblage has been observed replacing chlorite in blocks of greywacke from the basal melange of the Humber Arm Allochthon in southwestern Newfoundland (R. K. Stevens, private communication). Glaucophane, barroisite and omphacite associated with Taconic metamorphism in Vermont^{2,3} suggest that a higher P/T gradient was achieved in that region.

The structural position of the Croque metavolcanics and the lack of a tectonic fabric are consistent with metamorphism resulting from deep burial. However, only 3.4 km of overlying material can presently be accounted for in the structural sequence¹⁷, although the mineral assemblages

suggest that pressures of at least 3–4 kbar were involved. Current models for the onset of obduction in western Newfoundland would predict initial deep burial of the continental margin in response to loading by the overriding oceanic plate¹⁸. Later isostatic rebound and collapse of the continental margin sequence into the series of thrust sheets which is now observed would lead to the emplacement of the volcanics and associated greywackes into their present structural position. This model is supported by the presence of eclogitic dykes in the underlying, more deeply buried, Grenville basement to the east¹⁹. It would, however, represent conditions with lower P/T gradients than those reflected in the Franciscan 'subduction melange' of California and similar sequences where complete blueschist facies assemblages are common.

I thank Dr. W. R. Smyth for providing the thin sections and sample localities, and Dr R. K. Stevens, Dr K. D. Collerson, and Dr D. F. Strong for useful discussion and criticism. Dr J. Laird and Dr H. Helmstaedt provided additional information about the Vermont and New Brunswick occurrences, respectively, and Dr A. Thompson assisted with the microprobe analyses.

R. A. JAMIESON

*Department of Geology,
Memorial University of Newfoundland,
St. John's, Newfoundland A1C 5S7*

Received October 26; accepted December 1, 1976

- 1 Strong, D. F., *A.I.M.E. Soc. Mining Eng. Preprint* 73-1-320, 31 pp. (1973).
- 2 Laird, J., and Albee, A. L., *Geol. Soc. Am. Abstr. with Prog.*, 7, 1159 (1975).
- 3 Doolan, B. L., Drake, J. C., and Crocker, D., *Geol. Soc. Am. Abstr. with Prog.*, 5, 157 (1973).
- 4 Trzcinski, W. F., *Can. J. Earth Sci.*, 13, 711–714 (1976).
- 5 Helmstaedt, H., *Geol. Surv. Can. Pap.*, 70, 28 (1971).
- 6 Skinner, R., *Geol. Surv. Can. Mem.*, 371, 113 pp. (1974).
- 7 Smyth, W. R., thesis, Memorial Univ. (unpubl.), 172 pp. (1973).
- 8 Deer, W. A., Howie, R. A., and Zussman, J., *Rock-Forming Minerals*, 2, 333–351 (1963).
- 9 Coleman, R. G., and Papike, J. J., *J. Petrol.*, 9, 105–122 (1968).
- 10 Klein, C., *Am. Mineral.*, 54, 212–237 (1969).
- 11 Himmelberg, G. R., and Papike, J. J., *J. Petrol.*, 10, 102–114 (1969).
- 12 Liou, J. G., Ho, C. O., and Yen, F. P., *J. Petrol.*, 16, 80–109 (1975).
- 13 Klein, C., *J. Petrol.*, 7, 246–305 (1966).
- 14 Brown, E. H., *Bull. Geol. Soc. Am.*, 85, 333–344 (1974).
- 15 Turner, F. J., *Metamorphic Petrology, Mineralogical and Field Aspects*, 289–290 (1968).
- 16 Brown, E. H., *J. Petrol.*, 16, 258–271 (1975).
- 17 Williams, H., *Can. J. Earth Sci.*, 12, 1874–1894 (1975).
- 18 Williams, H., and Stevens, R. K., in *The Geology of Continental Margins* (ed. by C. A. Burk and C. L. Drake) 781–796 (1974).
- 19 De Wit, M. J., and Strong, D. F., *J. Geol.*, 83, 609–627 (1975).
- 20 Papike, J. J., Cameron, K. L., and Baldwin, K., *Geol. Soc. Am. Abstr. with Prog.*, 6, 1053–1054 (1974).

A JACUPIRANGITE - SYENITE ASSOCIATION BENEATH THE
WHITE HILLS PERIDOTITE, NORTHWESTERN NEWFOUNDLAND

R. A. Jamieson and R. W. Talkington
Department of Geology
Memorial University of Newfoundland
St. John's, Newfoundland, Canada
A1B 3X5

ABSTRACT

An association of jacupirangite, alkaline pyroxenite, hornblende gneiss, and syenitic mylonite occurs at the base of the White Hills Peridotite in the St. Anthony Complex of northwestern Newfoundland. The rocks, which have affinities to carbonatites, were deformed during the emplacement of the peridotite and are both orogenic and oceanic in their setting. The jacupirangite and alkaline pyroxenite, which consist of titanaugite, kaersutite, biotite, ilmenite, apatite, and carbonate, are rich in FeO , TiO_2 , and P_2O_5 . The syenitic mylonites consist of sodic plagioclase with minor augite, hornblende, olivine, zircon, and magnetite and are rich in Na_2O , Al_2O_3 , and SiO_2 while the hornblende gneisses, which consist of sodic plagioclase and kaersutite, have intermediate compositions. The geochemistry and petrology of the rocks are best explained by a model involving the separation of an ultramafic and a felsic liquid from an iron-rich magma. The jacupirangite-syenite assemblage may have originated in association with the alkaline basaltic rocks in the area.

INTRODUCTION

A jacupirangite associated with syenite occurs beneath the White Hills Peridotite of northwestern Newfoundland (Fig. 1). The rocks are part of the St. Anthony Complex, the highest structural slice of the Hare Bay Allochthon, which consists of the White Hills Peridotite and its dynamothermal aureole, a suite of amphibolites, greenschists, and volcanics metamorphosed during the emplacement of the peridotite (Williams and Smyth, 1973). The jacupirangite and associated alkaline rocks occur between the peridotite, which is thought to be a slice of upper oceanic mantle which was once the basal part of an ophiolite, and its aureole, which is composed mainly of metavolcanic rocks which formed in an ocean basin (Williams, 1975). The alkaline suite was deformed during the emplacement of the peridotite and is presumed to have originated in an oceanic environment. Although alkaline basaltic rocks are common beneath ophiolite suites (e.g. LaPierre and Rocci, 1976; Jamieson, 1977), alkaline ultrabasic rocks are rare in oceanic and orogenic settings. To the authors' knowledge, the occurrence of jacupirangite with transported oceanic rocks is unique.

The alkaline rocks form a suite including jacupirangite, alkaline pyroxenite, hornblende gneiss, and syenitic mylonite. They have not been previously described, since they were included with the amphibolites during earlier reconnaissance mapping of the St. Anthony Complex. The jacupirangite-syenite suite was recognized by the authors during detailed work on the St. Anthony Complex and the White Hills Peridotite. This paper describes the field relationships, mineralogy, and petrology of the alkaline rocks, and speculates on their

origin in the context of the existing geological models for the St. Anthony Complex.

FIELD RELATIONSHIPS

The jacupirangite-syenite assemblage outcrops beneath peridotite in three stream beds and at one lakeshore locality on the northern and eastern flanks of the eastern massif of the White Hills (Fig. 1). It has not been found on the western massif, nor anywhere in the interior of either ultramafic body. The contact of the jacupirangite with the overlying peridotite is visible in places, but the basal contact with the underlying amphibolites is not exposed. A composite section, based on observations from the four exposures, is described below.

The fine-grained, intensely serpentized peridotite at the upper contact is similar to ultramafics from the basal contact zone elsewhere in the White Hills. A penetrative foliation which runs parallel to the basal contact contains thin amphibole bands and is axial planar to small isoclinal folds. This foliation is associated with the comminution of olivine and orthopyroxene, and appears to overprint the main tectonite fabric in the harzburgites which form most of the White Hills Peridotite. The fabric in the contact zone is thought to have formed during the tectonic emplacement of the peridotite.

The jacupirangite near the contact is a dense, equigranular purple-black rock with no tectonic fabric, in marked contrast to the adjacent peridotite. The contact between the two lithologies is planar. No evidence of cross-cutting relationships, inclusions of one rock type in the other, chilled margins, or contact metamorphism suggesting an

intrusive relationship was seen. Dull purple medium- to coarse-grained clinopyroxene forms most of the rock, with minor shiny black amphibole and mica. The rock is fresh, except for locally abundant diffuse green veins. This massive jacupirangite-alkaline pyroxenite zone is probably not more than 2 to 3 metres thick.

The proportion of amphibole to clinopyroxene increases downwards away from the peridotite contact. The disappearance of pyroxene approximately coincides with the first appearance of leucocratic bands in the assemblage and the development of a penetrative fabric which trends parallel to the base of the peridotite. The proportion of felsic to mafic material increases downwards with the degree of deformation, resulting in a hornblende gneiss unit which may be up to 3 metres thick. It consists of roughly equal proportions of interbanded coarse-grained black amphibole and fine-grained white plagioclase and resembles parts of the underlying amphibolites in the metamorphic aureole.

The base of the sequence consists of fine-grained grey to white syenitic mylonite which contains streaks of mafic minerals and rare zircon porphyroclasts in a plagioclase matrix. Locally an L-S fabric is well developed, with a foliation defined by bands of mafic minerals parallel to the base of the peridotite and the lineation in the plane of the foliation trending northwest-southeast.

Beneath an alkaline pyroxenite band at locality A (Fig. 1) there is a 3- to 4-metre thick zone of black friable hornblendite containing thin bands of virtually pure plagioclase (Fig. 2). A lens of massive alkaline pyroxenite occurs in this zone, with the hornblendite and feldspar bands deflected around it ~~(Fig. 2)~~. A few crystals of black hornblende over 10 cm long occur in the hornblendite bands. The composition

4

banding in this zone is also approximately parallel to the base of the peridotite.

The lower contact of the jacupirangite-syenite sequence is not exposed. It is probably structurally concordant with the upper part of the metamorphic aureole, since the main foliations of both units are parallel to the base of the White Hills Peridotite.

MINERALOGY

The changes in the overall appearance of the rocks in the field correspond to changes in the mineralogy and microscopic texture. The transition from a homogeneous jacupirangite or alkaline pyroxenite to hornblende gneiss and syenitic mylonite can be traced in thin section as amphibole replaces pyroxene as the main mafic mineral and as the proportion of plagioclase rapidly increases with the development of the penetrative fabric. Modal analyses are listed in Table 1 and representative microprobe analyses are given in Table 2.

The massive jacupirangites consist of equigranular, purple-brown, slightly pleochroic titanaugite, with interstitial ilmenite, apatite, biotite, kaersutite, and carbonate. Deep red-brown Ti-rich biotite and kaersutite are interstitial to the clinopyroxene, with the amphibole commonly replacing the pyroxene. Titanaugite and kaersutite together form 70 to 80 per cent of the jacupirangite, with ilmenite and apatite accounting for most of the rest. The titanaugite occurs as subhedral, rounded crystals which lack well-developed angular faces, in a matrix of ilmenite, apatite, and carbonate (Fig. ³ 1). Equigranular carbonate forms 20 per cent of one sample (241, Table 1), and is considered

a primary phase in all cases. Under cathodoluminescence, the apatite has the purple colour characteristic of apatite from carbonatites (Smith and Stenstrom, 1965). Two samples which contain over 80 per cent clinopyroxene or clinopyroxene and amphibole and which are relatively poor in ilmenite and apatite are referred to as "alkaline pyroxenites". Although a penetrative fabric is not developed in the jacupirangite and alkaline pyroxenite, local deformation has resulted in some recrystallization of small polygonal grains of titanaugite from larger homogeneous crystals.

Beneath the massive jacupirangite-alkaline pyroxenite zone, kaersutite replaces titanaugite as the dominant mafic silicate. The amphibole replaces the clinopyroxene along cracks and cleavages and overgrows grain boundaries (Fig. 5). Homogeneous kaersutite crystals 2 to 5 mm across occur, sometimes containing inclusions of ilmenite, apatite, and relict titanaugite. Both the amphibole and the clinopyroxene are characterized by high Ti, Al, and alkalis and low Si throughout the sequence, although the relict titanaugite tends to be poorer in Al and Ti than the clinopyroxene in the jacupirangite and alkaline pyroxenite (Table 2). With the development of a penetrative foliation and the appearance of plagioclase titanaugite virtually disappears, surviving only as small anhedral grains surrounded by amphibole.

The hornblende gneiss consists almost entirely of sodic plagioclase and amphibole nearly identical to that in the undeformed rocks (Table 2). It occurs as augen surrounded and linked by trails of small recrystallized amphiboles of similar composition (Fig. 6). The albite is invariably fine-grained and anhedral, with serrated grain boundaries. Larger feldspars have kinked polysynthetic twinning and show extensive subgrain development.

The basal mylonites contain more than 75 per cent sodic plagioclase and have the overall mineralogy of syenites. The larger feldspars are commonly perthitic, with fine threadlike lamellae of potassium feldspar in albite. The mafic minerals include augite, fayalitic olivine, zircon, hornblende, biotite, and magnetite distributed in granular bands throughout the feldspathic matrix. The clinopyroxene is a green sodium-rich augite (Table 2) which occurs as clusters of isolated grains elongated parallel to the foliation or as augen surrounded by pressure shadows of magnetite and biotite (Fig. 7). Pale yellow iron-rich olivine (Table 2) is associated with magnetite in fine-grained bands (Fig. 8). The rare zircon porphyroclasts reach 5-10 mm in size, and frequently contain biotite inclusions (Fig. 9). The banded texture, augened porphyroclasts, and the fine-grained anhedral matrix of albite with interlocking grain boundaries and a strong preferred orientation serve to classify these rocks as mylonites according to the terminology of Bell and Etheridge (1973).

Two types of secondary mineral assemblages are present. One consists of diffuse veins and patches of green diopside, green hornblende, plagioclase, and carbonate in massive alkaline pyroxenite. The diopside has the appearance of bleached zones in the titanaugite surrounding the other secondary minerals. It is much poorer in Ti, Al, Na, and Fe than the titanaugite it replaces, while the green hornblende is poorer in Ti, Al, Fe, and Ca than the kaersutite (Table 2). Trails of tiny inclusions, which are independent of existing grain boundaries, cleavages, or fractures, cross the pyroxenite between the large patches of altered clinopyroxene (Fig. 10). Similar bubble trails can also be seen in other samples associated with the amphibolitization of clinopyroxene (e.g. Fig. 5).

The other secondary mineral assemblage is a greenschist facies alteration which produced thin veins of chlorite and epidote which cross-cut all the pre-existing textures. Blue-green hastingsite (Table 2) replaces kaersutite adjacent to these veins. Clinopyroxene may be partly replaced by green fibrous amphibole, and in the syenitic mylonites sodic amphibole associated with augite and magnetite, and epidote, chlorite and sericite patches are probably related to this stage of alteration.

GEOCHEMISTRY

Fourteen samples representing all the lithologies from jacupirangite to syenitic mylonite have been analyzed for major and trace elements (Table 3). The entire suite is undersaturated with the exception of the two most siliceous syenites.

The geochemical data must be interpreted with caution, since the behaviour of the mobile components during the deformation cannot be quantified. One essentially unaltered jacupirangite (RJ76-491, Table 3) can be used as a reliable guide to the original composition of these rocks, but there is no pristine equivalent of the syenitic mylonites. Comparison of RJ76-491 with amphibolitized equivalents adjacent to it (RJ76-492, 490) shows considerable depletion of Rb and Ba in the altered samples, suggesting that the amphibolitization was accompanied by changes in the trace element composition even in the undeformed rocks. A jacupirangite adjacent to the peridotite (RJ76-492, Table 3) is particularly low in Zr, Sr, Ba, and Nb. These trace elements are enriched in peridotite close to the contact (Table 4) which suggests that some metasomatism has occurred across the contact. The syenitic mylonites, which seem to have

retained their original mineralogy and which have undergone similar degrees of deformation, may preserve their original relationships to each other.

Given the limitations of the geochemical data, some features of the bulk rock compositions are remarkable. The jacupirangites have very high concentrations of TiO_2 , P_2O_5 , and total FeO , while the syenitic mylonites have low concentrations of these components and very high Al_2O_3 and Na_2O (Table 3). The hornblende gneisses have intermediate compositions. The high CaO and low TiO_2 and P_2O_5 compositions of the alkaline pyroxenites reflect a mineralogy rich in titanaugite and poor in ilmenite and apatite.

The trace element concentrations of the ultrabasic rocks show enrichment in Ba, Nb, Sr, Rb, and Zr (Table 3), elements usually concentrated in more siliceous differentiated rocks. High concentrations of these elements are characteristic of carbonatites (Deans and Powell, 1968) and this affinity is further suggested by the presence of carbonate in the matrix of the jacupirangites and by the purple cathodoluminescence of the apatite. The syenitic mylonites, on the other hand, are relatively poor in these elements which decrease with increasing SiO_2 within the group.

Both alkaline pyroxenite analyses show anomalously high concentrations of MgO , Cr , and Ni and low concentrations of Ba, Sr, Al_2O_3 , and alkalis even when their pyroxene-rich mineralogy is taken into account. In both cases the samples show extensive development of the secondary diopside-hornblende-plagioclase-carbonate assemblage. The unusual compositions of these pyroxenites may result from the passage of high temperature fluids enriched in Cr , Ni , MgO , and CO_2 , which leached Na_2O , TiO_2 , and Al_2O_3 from the titanaugite and formed diopside, hornblende,

plagioclase, and carbonate. Similar alteration of a primary pyroxene assemblage in ultramafic xenoliths has been described by Francis (1976).

PETROGENESIS

A complete petrological description of the alkalic rock suite should be able to account for the carbonatitic affinities of the jacupirangite, the relationships among the jacupirangite, alkaline pyroxenite, syenite, and hornblende gneiss, the distribution of the major and trace elements, and the relationship of the entire sequence to the other rocks in the area. Unfortunately, some key pieces of evidence are missing. The deformation has obliterated the original contact relationships and the primary textures in the gneisses and the mylonites, and large parts of the sequence have probably been removed by tectonic disruption. The probable redistribution of mobile chemical components has already been noted. For these reasons, most of the petrogenetic problems can be dealt with only in terms of the relative merits of alternative hypotheses.

The jacupirangite and alkaline pyroxenite are the only parts of the sequence in which an igneous paragenesis is preserved. Titanaugite crystallized first, with biotite and kaersutite later. The replacement of titanaugite by kaersutite was probably in response to an increase in the concentrations of volatiles and alkalis in the interstitial melt. The non-silicate matrix phases apparently crystallized contemporaneously with the clinopyroxene, since the pyroxene contains matrix inclusions and the matrix contains pyroxene inclusions. The similarity of the alkaline pyroxenite bulk compositions (Table 3) to titanaugite analyses (Table 2) suggests that these rocks are cumulates.

The role of CO_2 in the melting and crystallization behaviour of ultrabasic rocks has been the subject of much recent work (e.g. Wyllie, 1966; Mysen and Boettcher, 1975; Koster van Groos, 1975; Boettcher et al., 1975). Experiments have shown that CO_2 -saturated melts are more alkalic and undersaturated than H_2O -rich melts at similar temperatures and pressures. Apparently the high activity of CO_2 in the melt raises the liquidus temperature (Eggler, 1975). Mysen and Boettcher (1975) found that for vapour compositions with a mole fraction of $\text{CO}_2 \geq 0.5$, the melts produced by partial melting of natural peridotite were nepheline normative. Similar results have been obtained in synthetic systems (Boettcher et al., 1975; Eggler, 1975). The presence of carbonate in the matrix of the jacupirangite suggests that the melt from which the rocks crystallized was rich in CO_2 . With increasing pressure at a constant temperature and mole fraction of CO_2 , Mysen and Boettcher (1975) found an increase in the FeO/MgO ratio. It is conceivable that the iron-rich jacupirangite and alkaline pyroxenite crystallized from a melt derived directly by high-pressure anatexis of peridotite in the presence of a CO_2 -rich vapour. However, olivine is usually a liquidus phase in basic and ultrabasic undersaturated alkaline systems (Edgar, 1974), and olivine is common in alkaline pyroxenites and the rocks associated with them (Upton, 1967). The absence of olivine and the low concentrations of Cr, Ni, and MgO suggests that olivine fractionation may have played a role in the development of the very iron-rich magmas from which the jacupirangite and alkaline pyroxenite crystallized.

A major petrogenetic problem centres on the origin of the leucocratic rocks now represented by the syenitic mylonites. Possible relationships between the ultrabasic and feldspathic rocks include the following:

(1) The two lithologies are unrelated and were juxtaposed as the result of deformation.

(2) The syenites were produced by fenitization associated with the alkaline ultrabasic rocks.

(3) The syenites were produced by partial melting of the ultrabasic rocks during the metamorphism.

(4) The syenite and jacupirangite were part of the same igneous system and were related by (i) crystal fractionation, or (ii) liquid immiscibility.

The first two possibilities can be quickly dismissed. Tectonic interleaving of unrelated rocks on the scale displayed by the hornblende gneisses and the banded hornblendite-syenite zone (Fig. 2, 3) is virtually inconceivable. Even in basic rocks fenitization usually involves desilication (Verwoerd, 1966), while considerable SiO_2 would have to have been added to the surrounding peridotites and amphibolites to produce a syenitic composition. The mineralogical similarity of the syenitic mylonites to fenites is superficial, since no aegirine or acmite occurs, and the sodic amphibole is clearly post-tectonic.

Since upper amphibolite facies conditions were reached in the metamorphic aureole surrounding the peridotite (Williams and Smyth, 1973), it is reasonable to consider partial melting during metamorphism as a means of producing the syenites. In support of this hypothesis is the restriction of the leucocratic rocks to the deformed parts of the sequence, and their increasing proportion with the increasing intensity of the deformation. However, the chemistry of the syenitic mylonites and their high volume in proportion to the ultrabasic rocks suggest that partial melting was not responsible. Partial melts in amphibolites of

the aureole amount to less than 5 per cent of the rock, while the syenitic rocks are roughly equal in volume to the ultrabasic ones. The geochemistry of the syenites is characterized by decreasing abundances of most trace elements with increasing silica, a feature which cannot be attributed to the degree of deformation or structural position of the syenitic mylonites. This pattern would not be predicted by a simple partial melting model involving crystal-liquid equilibria, which would have "incompatible" elements concentrated in the early, silica-rich melts (e.g. Carmichael et al., 1974, p. 632).

The remaining possibility is that the syenitic mylonites were originally part of an igneous sequence including the jacupirangites, and were related to them through either crystal fractionation or liquid immiscibility. In the first case, a trend from ultrabasic to syenitic compositions would be expected, which could be related to the removal of one or more of the observed phases. In Fig. 11, where CaO is plotted against SiO₂ as an example of the major element distributions, the compositions of the jacupirangites, alkaline pyroxenites, hornblende gneisses, and syenitic mylonites form separate clusters, which would not be predicted from a simple crystal fractionation model. This diagram also illustrates that fractionation of titanaugite, the major mafic phase, could not produce the observed trend. More remarkable is the $\text{FeO}_T/(\text{FeO}_T + \text{MgO})$ ratio, which normally increases with differentiation, but in this case shows virtually no change and even decreases slightly over an SiO₂ interval of nearly 40 per cent (Fig. 12). In addition, the trace element geochemistry within the syenites is the opposite to that which would be predicted from crystal-melt equilibria (e.g. Carmichael et al., p. 73-74), since Ba, Sr, Rb,

and Nb all decrease with increasing silica (Table 3). The hornblende gneisses, with their basaltic compositions, represent possible intermediate members of a continuous sequence. However, their mineralogy, albite and kaersutite, is unsuitable for basaltic rocks under amphibolite facies compositions where calcic plagioclase is stable, and is more likely to represent an original mixture of two different bulk compositions which did not equilibrate during metamorphism. All these features suggest that crystal fractionation was not responsible for the coexisting jacupirangite and syenite.

This leaves liquid immiscibility as the remaining possible differentiation mechanism. Considerable petrological work has been done recently on the role of liquid immiscibility in the origin of ocellar alkaline ultramafic rocks and lunar basalts (e.g. Roedder and Wieblen, 1971; Hess et al., 1975; Naslund, 1976; Irvine, 1976; Philpotts, 1976; Hess, 1977). These studies have shown that many synthetic and natural systems have fields of stable or metastable liquid immiscibility in which a liquid rich in SiO_2 , Al_2O_3 , Na_2O , and K_2O separates from a liquid rich in FeO , MgO , and CaO . Partitioning of minor and trace elements such as TiO_2 , P_2O_5 , MnO , Zr , Sr , Cr , Ba , and the rare earth elements into the mafic melt is favoured, with particularly high partition coefficients for TiO_2 and P_2O_5 (Watson, 1976).

Figure 13 shows TiO_2 and P_2O_5 plotted against $(\text{Na}_2\text{O} + \text{K}_2\text{O} + \text{Al}_2\text{O}_3)/(\text{FeO}_T + \text{MgO} + \text{MnO} + \text{CaO})$ to emphasize the extent of the partition of these components into the mafic or felsic phase. The extreme TiO_2 and P_2O_5 enrichment in the jacupirangites shown in these plots is difficult to explain by any means other than liquid immiscibility. The distribution of the trace elements is less clear due to the variations in mineralogy

and deformation, but the freshest jacupirangite (RJ76-491, Table 3) shows high concentrations of incompatible elements. In an AFM diagram (Fig. 14) the jacupirangites and syenites plot on opposite sides of the miscibility gap outlined by Philpotts (1976) for natural rocks. The jacupirangites also plot near the composition at which fractionated lunar KREEP basalts split into two liquid phases (Hess et al., 1975). The close coincidence of the end member compositions with documented natural examples of immiscible liquids strongly supports the liquid immiscibility model. The AFM plot also clearly shows the clustering of compositions, supporting the immiscibility rather than the crystal fractionation hypothesis. Rigorous application of the model to the jacupirangite-syenite suite would require good textural evidence (Philpotts, 1977) and reliable geochemical data, but both are impossible due to the deformation. In spite of this, it is concluded that the liquid immiscibility hypothesis fits the available data better than the other models considered.

DISCUSSION

The field, petrographic, and geochemical data support the following model for the development of the jacupirangite-syenite assemblage. An alkaline ultrabasic liquid was generated in the upper mantle by partial melting in the presence of a CO_2 -rich vapour phase. An iron-rich magma evolved as a result of the high pressure of anatexis or early olivine fractionation. When the necessary degree of iron enrichment was achieved, two liquid phases separated from the magma. The mafic liquid was enriched in FeO, MgO, CaO, TiO_2 , P_2O_5 and many trace elements, while the felsic phase concentrated Na_2O , K_2O , Al_2O_3 , and SiO_2 . The two liquids crystallized separately. Titanite accumulating from the

ultrabasic liquid formed the alkaline pyroxenites. The extreme enrichment of this liquid in TiO_2 and P_2O_5 may have led to the further separation of an immiscible ilmenite-apatite liquid (Philpotts, 1967), which is suggested by the globular shapes of clinopyroxenes in ilmenite and ilmenite in clinopyroxene. The proportion of ilmenite to apatite in the jacupirangites is roughly 2 to 1 (Table 1), the same as that of the eutectic composition for the immiscible TiO_2 - P_2O_5 liquids described by Philpotts (1967). A similar model has been proposed for jacupirangites from southern Norway (Bergstøl, 1972).

The suite of alkaline rocks was deformed during the displacement of the White Hills Peridotite. The peridotite sheet probably overrode the magma chamber in which the rocks crystallized, and at this stage the locus of motion must have shifted downwards slightly so that the strain during further motion of the thrust sheet was concentrated in the syenites, which recrystallized into mylonites. Virtually complete replacement of titanaugite by kaersutite accompanied the deformation.

The identification of yet another example of alkaline ultrabasic rocks for which a case can be made for liquid immiscibility is interesting, but it is the geological setting of these rocks which is particularly unusual. Over 90 per cent of known carbonatites and alkaline ultrabasic rocks are in cratonic areas, usually associated with rifting (Gittins, 1966). Oceanic and orogenic occurrences are rare, so that the association of jacupirangite with transported upper oceanic mantle requires further discussion.

Alkaline basaltic rocks are relatively common beneath ophiolite suites. La Pierre and Rocci (1976) describe trachytes from Cyprus, Hynes (1974) has documented examples from Othris, and similar associations

are known from Oman (Glennie et al., 1974) and Syria (Smewing, pers. comm.). In western Newfoundland the association is represented by the Skinner Cove Volcanics beneath the Bay of Islands Complex (Strong, 1974; Baker, in prep.) and the Ireland Point Volcanics in the St. Anthony Complex (Jamieson, 1977). None of these sequences includes alkaline ultrabasic rocks of the type described in this paper.

The jacupirangite-syenite assemblage probably fits into the regional setting of alkaline magmatism near a continental margin which characterizes the upper part of the Hare Bay Allochthon (Jamieson, 1977). It may have been part of a plutonic complex associated with the Ireland Point alkali basalts. Possibly analogous situations are Fuertaventura in the Canary Islands, where carbonatites and alkaline gabbros occur as part of the Betancuria Massif (Gastesi, 1969; Munoz, 1969), or the Cape Verde Islands where carbonatites are also known (Dillon and Sougy, 1974). The proximity of these islands to continental margins enhances their similarity to the Ireland Point Volcanics, and may have a bearing on their origin. In modern orogenic environments, alkaline ultrabasic rocks with affinities to kimberlite and alnöite occur in the Solomon Islands of the southwest Pacific (Allen and Deans, 1965). In ancient rocks, the synorogenic emplacement of alkaline pyroxenite in the Seiland province of Norway during the late stages of the Caledonian orogeny (Robins, 1974) may be analogous.

The rarity and small volume of orogenic and oceanic carbonatites and alkaline ultrabasic rocks, and the resulting high odds against their emplacement and preservation probably explains why they have not been previously reported in association with ophiolite. Since the St. Anthony jacupirangite-syenite assemblage falls within the general pattern of

alkalic magmatism in the area and does not require a special set of conditions to explain its origin, its occurrence may help broaden our understanding of igneous processes in the oceanic environment.

ACKNOWLEDGEMENTS

The authors thank Mr. D. Press and Mrs. G. Andrews for help with the chemical analyses, Dr. A. W. Thompson for assistance with the microprobe analyses, and Ms. G. Campbell for the drafting. C. A. Gallagher and N. Noel provided excellent assistance in the field. Special thanks go to Dr. D. F. Strong and Dr. T. J. Calon for helpful comments and criticisms during the preparation of the manuscript, and Dr. W. R. Smyth who provided the original thin sections and sample locations. R. A. Jamieson acknowledges the National Research Council of Canada for financial support through a 1967 Science Scholarship and operating grants awarded to D. F. Strong in 1976 and 1977. R. W. Talkington was supported by a Memorial University Fellowship and an NRC operating grant awarded to J. G. Malpas.

REFERENCES

- ALLEN, J. B., DEANS, T.: Ultrabasic eruptives with alnöitic-kimberlitic affinities from Malaita, Solomon Islands. *Min. Mag.* 34, 16-34 (1965).
- BAKER, D.: Geology and geochemistry of the Skinner Cove Formation: Humber Arm Allochthon, western Newfoundland. M.Sc. thesis, Memorial University, in preparation (1978).
- BELL, T. H., ETHERIDGE, M.A.: Microstructure of mylonites and their descriptive terminology. *Lithos* 6, 337-348 (1973).
- BERGSTØL, S.: The jacupirangite at Kodal, Vestfold, Norway. *Mineral. Dep.* 7, 233-246 (1972).
- BOETTCHER, A. L., MYSEN, B. O., MODRESKI, P. J.: Melting in the mantle: Phase relationships in natural and synthetic peridotite-H₂O and peridotite-H₂O-CO₂ systems at high pressures. *Phys. Chem. Earth* 9, 855-867 (1975).
- CARMICHAEL, I.S.E., TURNER, F. J., VERHOOGEN, J.: *Igneous Petrology*. 739 p. McGraw-Hill (1974).
- DEANS, T., POWELL, J. L.: Trace elements and strontium isotopes in carbonatites, fluorites, and limestones from India and Pakistan. *Nature* 218, 750-752 (1968).
- DILLON, W.P., SOUGY, J.M.A.: Geology of west Africa and the Canary and Cape Verde Islands. In: *The Ocean Basins and Margins* (A.E.M. Nairn and F. G. Stehli, eds.), pp. 315-390. Plenum, New York (1974).
- EDGAR, A. D.: Experimental studies. In: *The Alkaline Rocks* (H. Sorensen, ed.), pp. 355-389. John Wiley and Sons (1974).
- EGGLER, D.H.: CO₂ as a volatile component of the mantle: the system Mg₂SiO₄-SiO₂-H₂O-CO₂. *Phys. Chem. Earth* 9, 869-881 (1975).
- FRANCIS, D. M.: The origin of amphibole in lherzolite xenoliths from Nunivak Island, Alaska. *Jour. Petrol.* 17, 357-378 (1976).
- GASTESI, P.: Petrology of the ultramafic and basic rocks of Betancuria Massif, Fuertaventura Island (Canarian Archipelago). *Bull. Volc.* 33, 1008-1038 (1969).
- GITTINS, J.: Summaries and bibliographies of carbonatite complexes. In: *Carbonatites* (O. J. Tuttle and J. Gittins, eds.), pp. 417-541. Interscience Publishers (1966).
- GLENNIE, K. W., BOEUF, M. G. A., HUGHES CLARKE, M. W., MOODY-STUART, M., PILAAR, W. F. H., REINHARDT, B. M.: *Geology of the Oman Mountains*. 423 pp. Royal Dutch Geological and Mining Society Publication (1974).

- HESS, P. C.: Structure of silicate melts. *Can. Mineral.* 15, 162-178 (1977).
- HESS, P. C., RUTHERFORD, M. J., GUILLEMETTE, R.N., RYERSON, F.J., TUCHFIELD, H.A.: Residual products of fractional crystallization of lunar magmas: an experimental study. *Proc. Sixth Lunar Science Conf.* 1, 895-909 (1975).
- HYNES, A. J.: Igneous activity at the birth of an ocean basin in eastern Greece. *Can. Jour. Earth Sci.*, 11, 842-853 (1974).
- IRVINE, T. N.: Metastable liquid immiscibility and MgO-FeO-SiO_2 fractionation patterns in the system $\text{Mg}_2\text{SiO}_4\text{-Fe}_2\text{SiO}_4\text{-CaAl}_2\text{Si}_2\text{O}_8\text{-KAlSi}_3\text{O}_8\text{-SiO}_2$. *Carnegie Inst. Wash. Yb.* 75, 597-611 (1976).
- JAMIESON, R. A.: A suite of alkali basalts and gabbros associated with the Hare Bay Allochthon of western Newfoundland. *Can. Jour. Earth Sci.*, 14, 346-356 (1977).
- KOSTER VAN GROOS, A. F.: The effect of high CO_2 pressures on alkalic rocks and its bearing on the formation of alkalic ultrabasic rocks and the associated carbonatites. *Amer. Jour. Sci.* 275, 163-185 (1975).
- LAPIERRE, H., ROCCI, G.: Le volcanism alcalin du sud-ouest de Chypre et le probleme de l'ouverture des regions Tethysiennes au Trias. *Tectonophysics* 30, 299-313 (1976).
- MUNOZ, M.: Ring complexes of Pajara in Fuertaventura Island. *Bull. Volc.* 33, 840-861 (1969).
- MYSEN, B. O., ARCULUS, R.J., EGGLE, D.H.: Solubility of carbon dioxide in melts of andesite, tholeiite, and olivine nephelinite composition to 30 kb pressure. *Contrib. Mineral. Petrol.* 53, 227-240 (1975).
- MYSEN, B. O., BOETTCHER, A. L.: Melting of a hydrous mantle: II. Geochemistry of crystals and liquids formed by anatexis of mantle peridotite at high pressures and high temperatures as a function of controlled activities of H_2O , H_2 , and CO_2 . *Jour. Petrol.* 16, 549-593 (1975).
- NASLUND, H. R.: Liquid immiscibility in the system $\text{KAlSi}_3\text{O}_8\text{-NaAlSi}_3\text{O}_8\text{-FeO-Fe}_2\text{O}_3\text{-SiO}_2$ and its applications to natural magmas. *Carnegie Inst. Wash. Yb.* 75, 592-597 (1976).
- PHILPOTTS, A. R.: Origin of certain iron-titanium oxide and apatite rocks. *Econ. Geol.* 62, 303-315 (1967).
- PHILPOTTS, A. R.: Silicate liquid immiscibility: its probable extent and petrogenetic significance. *Amer. Jour. Sci.* 276, 1147-1177 (1976).
- PHILPOTTS, A. R.: Archean variolites - quenched immiscible liquids: Discussion. *Can. Jour. Earth Sci.* 14, 139-144 (1977).

- ROBINS, B.: Synorogenic alkaline pyroxenite dykes on Seiland, northern Norway. Norsk Geolog. Tids. 54, 247-268 (1974).
- ROEDDER, E., WEIBLEN, P. W.: Petrology of silicate melt inclusions, Apollo 11 and Apollo 12 and terrestrial equivalents. In: Proc. Second Lunar Sci. Conf., Geochim. Cosmochim. Acta, Suppl. 2, Vol. 1, pp. 507-528. Cambridge: The M.I.T. Press (1971).
- SMITH, J. V., STENSTROM, R. C.: Electron-excited luminescence as a petrologic tool. Jour. Geol. 73, 627-635 (1965).
- STRONG, D. F.: An "off-axis" alkali volcanic suite associated with the Bay of Islands ophiolite, Newfoundland. Earth Planet. Sci. Lett. 21, 301-309 (1974).
- UPTON, B.G.J.: Alkaline pyroxenites. In: Ultramafic and Related Rocks (P. J. Wyllie, ed.), pp. 281-288. John Wiley and Sons (1967).
- VERWOERD, W. J.: Fenitization of basic igneous rocks. In: Carbonatites (O. J. Tuttle and J. Gittins, eds.), pp. 295-308. Interscience Publishers (1966).
- WATSON, B. E.: Two-liquid partition coefficients: experimental data and geochemical implications. Contrib. Mineral. Petrol. 56, 119-134 (1976).
- WILLIAMS, H.: Structural succession, nomenclature, and interpretation of transported rocks in western Newfoundland. Can. Jour. Earth Sci. 12, 1874-1894 (1975).
- WILLIAMS, H., SMYTH, W. R.: Metamorphic aureoles beneath ophiolite suites and alpine peridotites: tectonic implications with west Newfoundland examples. Amer. Jour. Sci. 273, 594-621 (1973).
- WYLLIE, P. J.: Experimental studies of carbonatite problems: the origin and differentiation of carbonatite magmas. In: Carbonatites (O. J. Tuttle and J. Gittins, eds.), pp. 311-352. Interscience Publishers (1966).





THE ST. ANTHONY COMPLEX,
NORTHWESTERN NEWFOUNDLAND:
A PETROLOGICAL STUDY OF THE RELATIONSHIP
BETWEEN A PERIDOTITE SHEET AND ITS
DYNOMOTHERMAL AUREOLE

CENTRE FOR **PART 2** STUDIES

**TOTAL OF 10 PAGES ONLY
MAY BE XEROXED**

(Without Author's Permission)

REBECCA ANNE JAMIESON

THE ST. ANTHONY COMPLEX, NORTHWESTERN NEWFOUNDLAND:
A PETROLOGICAL STUDY OF THE RELATIONSHIP BETWEEN
A PERIDOTITE SHEET AND ITS DYNAMOTHERMAL AUREOLE

VOLUME 2

Figures and Tables

Rebecca Anne Jamieson, B.Sc.



Department of Geology
Memorial University of Newfoundland
St. John's, Newfoundland

ABSTRACT

The St. Anthony Complex consists of a suite of alkaline basaltic rocks (the Ireland Point Volcanics), greenschist and epidote amphibolite facies metasedimentary and metabasic rocks (the Goose Cove Schist), amphibolite to transitional granulite facies metabasites (the Green Ridge Amphibolite), an assemblage of dunite, troctolite, gabbro, and anorthosite (the Long Ridge Metagabbro), and a lherzolite-harzburgite massif (the White Hills Peridotite). These rocks are interpreted as a partial ophiolite and an underlying dynamothermal aureole formed during its tectonic emplacement.

The overall metamorphic grade increases from the base of the St. Anthony Complex to the peridotite contact. Lithological and structural discontinuities occur within the aureole, with the epidote amphibolite to amphibolite facies transition marked by a metasomatic mylonite zone. Temperatures of 850°C to 950°C have been calculated for the amphibolites and peridotites in the contact zone, while the transition from greenschists to undeformed volcanics corresponds to temperatures of 300°C to 350°C. This indicates an overall thermal gradient of 750° to 800°C/km. Pressure estimates range from 7 to 10 kb near the peridotite contact to 2 kb or less at the greenschist-volcanic transition.

The lithological evidence and the pressure and temperature estimates suggest that the aureole is composite, formed by the juxtaposition of progressively shallower units during the dynamothermal metamorphism which accompanied the tectonic emplacement of the peridotite.

Thermal models indicate that heating by conduction and friction contributed to the high contact temperatures. The evidence is consistent with a model involving westward transportation of oceanic lithosphere over tholeiitic gabbros, alkaline basalts, and turbidites to form the St. Anthony Complex, before final emplacement along late thrust faults as part of the Hare Bay Allochthon.

Comparison of the St. Anthony Complex with other peridotite-aureole complexes shows general similarities in geological setting, lithology, and metamorphic grade. It is concluded that the formation of dynamothermal aureoles beneath transported peridotite is a normal process accompanying the early stages of tectonic peridotite emplacement.

TABLE OF CONTENTS

VOLUME 1

Abstract	i
List of Figures	v
List of Tables	ix
CHAPTER 1. INTRODUCTION	1
1.1. The Ophiolite Aureole Problem	1
1.2. Regional Setting	4
1.2.1. The Newfoundland Appalachians	4
1.2.2. The Humber Zone	4
1.2.3. The Hare Bay Allochthon	7
1.3. Previous Work	9
1.4. Purpose and Scope of Study	12
1.5. Acknowledgements	13
CHAPTER 2. THE GEOLOGY OF THE ST. ANTHONY COMPLEX	15
2.1. The Ireland Point Volcanics and Related Rocks	15
2.1.1. Gabbro	15
2.1.2. Variolitic Pillow Lava	17
2.1.3. Pillow Breccia	19
2.1.4. Vesicular Pillow Lava	19
2.1.5. Porphyritic Pillow Lava	20
2.2. The Goose Cove Schist	21
2.2.1. Metasediments	22
2.2.2. Banded Metavolcanics	23
2.2.3. Spotted Metavolcanics	24
2.2.4. Epidote Amphibolite	25
2.3. The Green Ridge Amphibolite	25
2.3.1. Biotite Amphibolite	26
2.3.2. Quartz Amphibolite	27
2.3.3. Plagioclase Amphibolite	29
2.4. The Long Ridge Metagabbro	30
2.5. The White Hills Peridotite	31
2.5.1. Jacupirangite and Syenite	31
2.5.2. Peridotite	32
2.6. Post-tectonic Dykes	34
2.7. Structure	34
2.8. Discussion	38
CHAPTER 3. PETROLOGY AND GEOCHEMISTRY	41
3.1. The Ireland Point Volcanics and Related Rocks	41
3.1.1. Petrography	41
3.1.2. Geochemistry	43
3.1.3. Mineral Chemistry	47
3.1.4. Petrogenesis	49
3.2. The Goose Cove Schist	57
3.2.1. Petrography	57
3.2.2. Geochemistry	60
3.2.3. Mineral Chemistry	62
3.2.4. Petrogenesis	67

3.3. The Green Ridge Amphibolite	74
3.3.1. Petrography	74
3.3.2. Geochemistry	79
3.3.3. Mineral Chemistry	82
3.3.4. Petrogenesis	86
3.4. The Long Ridge Metagabbro	93
3.4.1. Petrography	93
3.4.2. Geochemistry	95
3.4.3. Mineral Chemistry	95
3.4.4. Petrogenesis	97
3.5. The Jacupirangite - Syenite Association	99
3.6. The White Hills Peridotite	101
3.6.1. Petrography	101
3.6.2. Geochemistry	103
3.6.3. Mineral Chemistry	105
3.6.4. Petrogenesis	110
3.7. Discussion	113
CHAPTER 4. THE THERMAL STRUCTURE OF THE ST. ANTHONY COMPLEX	115
4.1. Geothermometry and Geobarometry	115
4.1.1. The Ireland Point Volcanics	116
4.1.2. The Goose Cove Schist	117
4.1.3. The Green Ridge Amphibolite	119
4.1.4. The Long Ridge Metagabbro	123
4.1.5. The White Hills Peridotite	124
4.2. Metamorphic Profiles	125
4.3. Thermal Models	130
4.3.1. Introduction	130
4.3.2. The Conduction Model	132
4.3.3. The Friction Model	136
4.3.4. Combined Conduction and Friction Models	141
4.3.5. The Effects of Reactions on Heat Production	143
4.3.6. Limitations and Implications of the Thermal Models	144
CHAPTER 5. THE GEOLOGICAL HISTORY OF THE ST. ANTHONY COMPLEX	149
5.1. Pre-tectonic History	149
5.2. Syntectonic History	153
5.3. Post-tectonic History	158
5.4. Regional Implications	158
5.4.1. The Hare Bay Allochthon	158
5.4.2. Other Areas in Western Newfoundland	159
CHAPTER 6. THE OPHIOLITE AUREOLE PROBLEM	162
6.1. Geological Setting	162
6.2. Relationships of Peridotites to their Aureoles	163
6.3. Metamorphism	164
6.4. Discussion	168
6.5. Summary and Conclusions	172
REFERENCES	174

APPENDIX I. ROCK ANALYSES	196
i. Sample Preparation	196
ii. Major Element Analyses	196
iii. Trace Element Analyses	198
APPENDIX II. MINERAL ANALYSES	200
i. Analytical Method	200
ii. Amphibole	201
iii. Pyroxene	206
iv. Feldspar	207
v. Olivine	207
vi. Epidote	207
vii. Chlorite	207
viii. Mica	207
ix. Oxides	208
APPENDIX III. THERMAL MODELS	209
APPENDIX IV. PUBLICATIONS AND MANUSCRIPTS RELATING TO STUDY	215

LIST OF FIGURES

VOLUME 1

FIGURE II.i. Nomenclature of calcic and sub-calcic amphiboles	202
II.ii. Amphibole substitutions	205

VOLUME 2

FIGURE 1.1. Alpine peridotite emplacement and associated metamorphism	1
1.2. Model for the development of Humber Zone geology	2
1.3. Geology of the Humber Arm and Hare Bay Allochthons	3
FIGURE 2.1. Rhythmic layering in gabbro, Partridge Point	5
2.2. Variolitic pillow lava, Ireland Point	5
2.3. Map of Ouirpon Harbour area	6
2.4. Variolitic pillow lava overlying black shale, east of Ireland Point	7
2.5. Pillow breccia, Ireland Point	7
2.6. Vesicular pillow lava, Ireland Bight	8
2.7. Porphyritic pillow lava, Stark's Bight	8
2.8 (a-d). Transition from the Ireland Point Volcanics to the Goose Cove Schist	9
2.9. Deformed pillow breccia, Stark's Bight	11
2.10. Folded marble and chert, Fischot Island	11
2.11. Semi-pelitic schist with quartz aggregates, Three Mountain Harbour	12
2.12. Psammite, Lobster Point	12
2.13. Pelite, Goose Cove West	13
2.14. Finely laminated cherty horizon, east of Goose Cove	13

FIGURE 2.15.	Massive, coarse-grained greenschist, Duck Point	14
2.16.	Banded greenschist, Goose Cove	14
2.17 (a, b).	Variable deformation in banded greenschist	15
2.18 (a, b).	Variable deformation in spotted greenschist	16
2.19.	Deformed pillows in spotted greenschist, Cremaillere Harbour	17
2.20.	Banding in spotted greenschists, Savage Point	17
2.21.	Epidote amphibolite	18
2.22.	Map of the Howe Harbour area	19
2.23.	Biotite amphibolite with epidote amphibolite inclusion	20
2.24.	Biotite amphibolite with melted quartz amphibolite inclusion, Northeast Island	20
2.25.	Relict igneous layering in metagabbro, Wild Cove	21
2.26.	Folded marble band, Northeast Island	21
2.27.	Partially melted quartz amphibolite, Northeast Island	22
2.28.	Compositional layering in quartz amphibolite, Three Mountain Summit	22
2.29.	Quartz amphibolite with band of very coarse-grained quartz and feldspar	23
2.30.	Inhomogeneously deformed metagabbro, Long Ridge	23
2.31.	Interlayered dunite, troctolite, and gabbro, Long Ridge	24
2.32.	Interlayered syenite, alkaline pyroxenite, and hornblende gneiss	24
2.33.	Lens of alkaline pyroxenite surrounded by interlayered syenite and hornblendite, Northern Long Pond	25
2.34.	Rectangular jointing in harzburgite, White Hills	25
2.35.	Fold in peridotite contact zone, Western Long Pond	26
2.36.	Ultramafic mylonite, Milan Arm Melange	26
2.37.	Post-tectonic diabase dyke, Lobster Point	27
2.38.	Brecciated metasedimentary schist, Goose Cove West	27
2.39.	Folded calc-silicate layer in amphibolite, Northeast Island	28
2.40.	F ₃ fold in epidote amphibolite, Three Mountain Summit	28
2.41.	Hare Bay thrust fault, Ireland Point	29
FIGURE 3.1 (a, b).	Variolitic pillow lava	32
3.2.	Kaersutite microlites, massive flow	33
3.3.	Plagioclase microlites, vesicular pillow lava	33
3.4.	Vesicular glass shard, pillow breccia	34
3.5 (a, b).	Porphyritic pillow lava	35
3.6.	Gabbro	36
3.7.	Diorite	36
3.8.	Effects of alteration on the geochemistry of the Ireland Point Volcanics	37
3.9.	Immobile element geochemistry of the Ireland Point Volcanics	38
3.10.	Immobile element geochemistry of the Ireland Point Volcanics	39
3.11.	Immobile element geochemistry of the Cape Onion and Maiden Point volcanics	40
3.12.	Immobile element geochemistry of the Cape Onion and Maiden Point volcanics	41
3.13.	Geochemistry of volcanic rocks in relation to tectonic setting	42
3.14.	Pyroxene quadrilateral, volcanic rocks	43
3.15.	Pyroxene variation diagrams, volcanic rocks	44
3.16.	Amphibole compositions, Ireland Point Volcanics	45

FIGURE 3.17. Compositions of the Ireland Point Volcanics in the basalt tetrahedron	46
3.18. Experimental phase relations, hydrous basaltic systems	48
3.19. Phase relations in the system $\text{CaO} - \text{MgO} - \text{Al}_2\text{O}_3 - \text{SiO}_2 - \text{Na}_2\text{O} - \text{H}_2\text{O}$, 5 kb	49
3.20. Variolitic pillow lava with olivine growth across boundary	50
3.21. Quartz aggregate in psammite	50
3.22. Semi-pelitic schist with folded muscovite	52
3.23. Rotated garnets in ferruginous metachert	52
3.24. Massive greenschist with relict diabasic texture	54
3.25. Spotted greenschist with deformed aggregates after plagioclase porphyroclasts	54
3.26. Banded greenschist showing S_1 and F_2	55
3.27. Epidote amphibolite with amphibole intergrowth	55
3.28. Geochemistry of the Goose Cove Schist	56
3.29. Geochemical comparison of the Goose Cove Schist and the Ireland Point Volcanics	57
3.30. Co-existing chlorite and amphibole compositions	58
3.31. Feldspar compositions, Goose Cove Schist and Green Ridge Amphibolite	59
3.32. Amphibole compositions, Goose Cove Schist	60
3.33. Metamorphic mineral assemblages, Goose Cove Schist and Green Ridge Amphibolite	61
3.34. ACF diagram, Goose Cove Schist	62
3.35. Experimental phase relations, greenschist facies	63
3.36 (a, b). Biotite amphibolite	65
3.37. Quartz amphibolite	66
3.38. Two-pyroxene amphibolite	66
3.39. Plagioclase amphibolite	67
3.40. Geochemistry of quartz and plagioclase amphibolites	68
3.41. Composition - volume diagram, biotite amphibolite	71
3.42. Geochemistry of biotite amphibolite	72
3.43. Immobile element geochemistry, Green Ridge Amphibolite, and comparison with greenschists and volcanics	73
3.44. Amphibole compositions, Green Ridge Amphibolite	74
3.45. Pyroxene quadrilateral, Green Ridge Amphibolite and Long Ridge Metagabbro	75
3.46. ACF diagram, Green Ridge Amphibolite	76
3.47. Melt compositions, Green Ridge Amphibolite	77
3.48. Experimental amphibolite - garnulite phase relations	78
3.49. Deformed dunite, Long Ridge	80
3.50 (a, b). Coronitic metagabbro	80
3.51. Relict igneous clinopyroxene in metagabbro	81
3.52. Geochemistry of the Long Ridge Metagabbro	82
3.53. Amphibole compositions, Long Ridge Metagabbro	83
3.54 (a-c). Jacupirangite - syenite assemblage	85
3.55. Geochemistry of the jacupirangite - syenite assemblage	87
3.56. AFM diagram, jacupirangite - syenite assemblage	88
3.57 (a, b). Basal mylonite, White Hills Peridotite	90
3.58. Plagioclase exsolution from orthopyroxene	91
3.59. Amphibole lherzolite, base of White Hills Peridotite	91
3.60. Geochemistry of the White Hills Peridotite	92

FIGURE 3.61.	Peridotite compositions in the system $\text{CaO} - \text{MgO} - \text{Al}_2\text{O}_3 - \text{SiO}_2$	93
3.62.	Orthopyroxene compositions, White Hills and other peridotites	94
3.63.	Pyroxene quadrilateral, White Hills and other peridotites	95
3.64.	Spinel prism, White Hills Peridotite	96
3.65.	Amphibole compositions, White Hills Peridotite	97
3.66.	Plagioclase to spinel lherzolite transition	98
FIGURE 4.1.	Phase relations relating to sub-greenschist facies conditions	99
4.2.	Garnet - biotite geothermometry, biotite amphibolites	100
4.3.	Compositions of the Long Ridge Metagabbro in the system $\text{CaO} - \text{MgO} - \text{Al}_2\text{O}_3 - \text{SiO}_2 - \text{H}_2\text{O}$	104
4.4.	Olivine - spinel compositions, White Hills Peridotite	105
4.5.	Metamorphic section, Fischot Islands	106
4.6.	Metamorphic section, Three Mountain Summit	107
4.7.	Metamorphic section, Brimstone Pond	108
4.8.	Composite thermal gradient through the St. Anthony Complex	109
4.9.	Temperature distribution as a function of time, T_p , and T_R for the conduction model	111
4.10.	Maximum temperatures reached through aureole, regardless of time, by conduction	112
4.11.	Contact temperatures for different thermal properties	114
4.12.	Contact temperatures as a function of time for the case where $T_p = 950^\circ\text{C}$, $T_R = 300^\circ\text{C}$, for the conduction model	115
4.13.	Relationship between heat production, shear strength, and rate of motion for frictional heating model	117
4.14.	Relationship between temperature increase at contact, time, and heat production for the frictional heating model	118
4.15.	Decrease in heat production with a linear decrease in shear strength	119
4.16.	Contact temperature as a function of time for $T_R = 300^\circ\text{C}$, frictional heating model	120
4.17.	Contact temperature as a function of time, frictional heating model with decreasing shear strength	121
4.18.	Thermal gradient as a function of heat produced at the contact, frictional heating model	122
4.19.	Combined friction and conduction models for $T_p = 950^\circ\text{C}$, $T_R = 300^\circ\text{C}$, and decreasing shear strength	123
4.20.	Alternative model for the formation of narrow, inverted metamorphic sequences	125
FIGURE 5.1.	Pre-emplacement development of the St. Anthony Complex	127
5.2.	Syn-emplacement development of the St. Anthony Complex	127
5.3.	Late syn-emplacement development of the St. Anthony Complex	127
FIGURE 6.1.	Pyroxene compositions, various peridotite - aureole complexes	131
6.2.	Garnet compositions, various peridotite - aureole complexes	133
6.3 (a, b).	Amphibole compositions, various peridotite - aureole complexes	134

PLATE 1.	Position of the St. Anthony Complex in the Appalachian Orogen	back pocket
2.	Geological map of the northern part of the Hare Bay Allochthon	"
3.	Lithological map of the southeastern part of the St. Anthony Complex	"
4.	Structural map of the southeastern part of the St. Anthony Complex	"

LIST OF TABLES

VOLUME 1

TABLE I.i.	Precision and accuracy of major element analyses	197
I.ii.	Precision and accuracy of trace element analyses	199
TABLE II.i (a).	Sample calculation of ferric iron content of amphibole	203
TABLE III.i.	Conduction model, similar thermal properties	210
III.ii.	Maximum temperatures attained in country rocks by conduction for similar thermal properties	212
III.iii.	Maximum contact temperatures for conduction model with dissimilar thermal properties	213
III.iv.	Contact temperatures, frictional heating model	214

VOLUME 2

TABLE 1.1.	Correlation between the Hare Bay and Humber Arm Allochthons	4
TABLE 3.1.	Abbreviations of mineral names	30
3.2.	Petrography of the Ireland Point Volcanics	31
3.3.	Crystallization sequence of the Ireland Point Volcanics	47
3.4.	Petrography of the Goose Cove Schist metasediments	51
3.5.	Petrography of the Goose Cove Schist metabasites	53
3.6.	Petrography of the Green Ridge Amphibolite	64
3.7.	Average compositions of epidote, biotite, and quartz amphibolites	69
3.8.	Calculated chemical changes for metasomatic transformation of epidote and quartz amphibolite into biotite amphibolite	70
3.9.	Petrography of the Long Ridge Metagabbro	79
3.10.	Petrography of the jacupirangite - syenite assemblage	84
3.11.	Petrography of the White Hills Peridotite	89
TABLE 4.1.	Garnet - biotite geothermometry, biotite amphibolite	101
4.2.	Calcite - dolomite geothermometry, marble	102
4.3.	Orthopyroxene - clinopyroxene geothermometry, amphibolite and peridotite	103
4.4.	Parameters and data sources for thermal models	110
4.5.	Effect of variable thermal properties on contact temperatures produced by conduction	113
4.6.	Initial country rock temperatures required to produce observed contact temperatures by conduction	116
4.7.	Heat produced by dehydration reactions	124

TABLE 5.1.	Lower and Middle Ordovician tectonic and depositional events in western Newfoundland	126
TABLE 6.1.	Geological settings of various peridotite - aureole complexes	128
6.2.	Peridotite - aureole geology, various ophiolite - aureole complexes	129
6.3.	Mineral assemblages, various ophiolite - aureole complexes	130
6.4.	Two-pyroxene temperature estimates for the Lizard compared to those from the St. Anthony Complex	132
6.5.	Garnet - clinopyroxene temperature estimates for various ophiolite - aureole complexes	132
TABLE I.iii.	Rock analyses, Ireland Point Volcanics	136
I.iv.	Rock analyses, Goose Cove Schist	137
I.v.	Rock analyses, Green Ridge Amphibolite	138
I.vi.	Rock analyses, Long Ridge Metagabbro	139
I.vii.	Rock analyses, White Hills Peridotite	140
I.viii.	Rock analyses, other rocks	141
TABLE II.i(b).	Amphibole analyses	142
II.ii.	Pyroxene analyses	143
II.iii.	Feldspar analyses	144
II.iv.	Olivine analyses	145
II.v.	Epidote analyses	146
II.vi.	Chlorite analyses	147
II.vii.	Mica analyses	148
II.viii.	Oxide analyses	149
II.ix.	Garnet analyses	150

FIGURE 1.1: Metamorphism and the emplacement of ophiolites and Alpine peridotites.

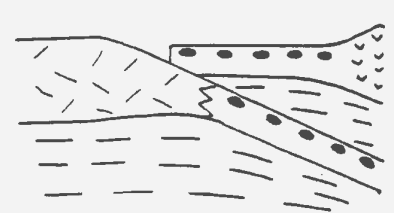
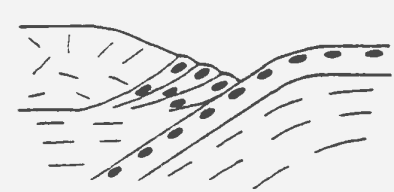

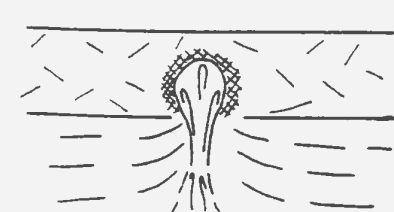
MEANS OF EMPLACEMENT	FORM OF PERIDOTITE	ASSOCIATED METAMORPHIC ROCKS	EXAMPLES
<p>a)</p>  <p>thrusting of oceanic crust over continental margin (obduction)</p>	ophiolite nappe	basal aureole of amphibolite and greenschist	western Newfoundland (Williams and Smyth, 1973)
<p>b)</p>  <p>accidental incorporation into accretionary melange</p>	fragmented blocks of ophiolite in melange	greenschist, blueschist, eclogite	Franciscan terrain (Ernst, 1970)
<p>c)</p>  <p>continental collision</p>	slivers of peridotite in nappes of intracontinental suture zones	granulite, eclogite	western Alps (Nicolas and Jackson, 1972)
<p>d)</p>  <p>diapiric intrusion</p>	steep-sided, isolated peridotite body	thermal aureoles of high-grade amphibolites	the Ronda Peridotite (?) (Loomis, 1972)

FIGURE 1.2: Geological evolution of western Newfoundland (Humber Zone) (after Strong *et al.*, 1974; Williams and Stevens, 1974; Malpas and Strong, 1975; Malpas, 1976; Williams *et al.*, 1977)

a) CAMBRIAN (pre-tectonic)

CONTINENTAL SHELF

carbonate bank
shallow water sediments
plateau lavas
Precambrian basement

OCEANIC CRUST AND MANTLE

deep water sediments
pillow lavas
sheeted dykes
gabbro
peridotite



CONTINENTAL SLOPE AND RISE

limestone breccia
turbidites
shales

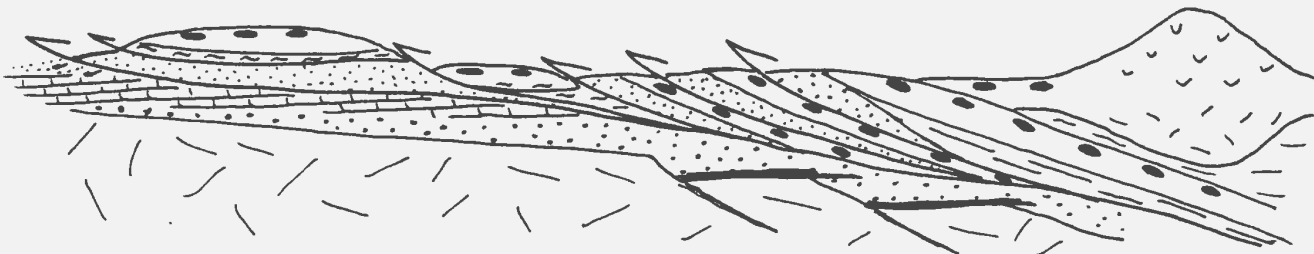
b) EARLY TO MIDDLE ORDOVICIAN (Taconic orogeny)

HUMBER ARM, HARE BAY ALLOCHTHONS

ophiolites
melange
easterly-derived flysch
continental slope and rise flysch

NOTRE DAME BAY

volcanic arc and
related sediments



BURLINGTON PENINSULA

intensely deformed ophiolites,
melange, flysch

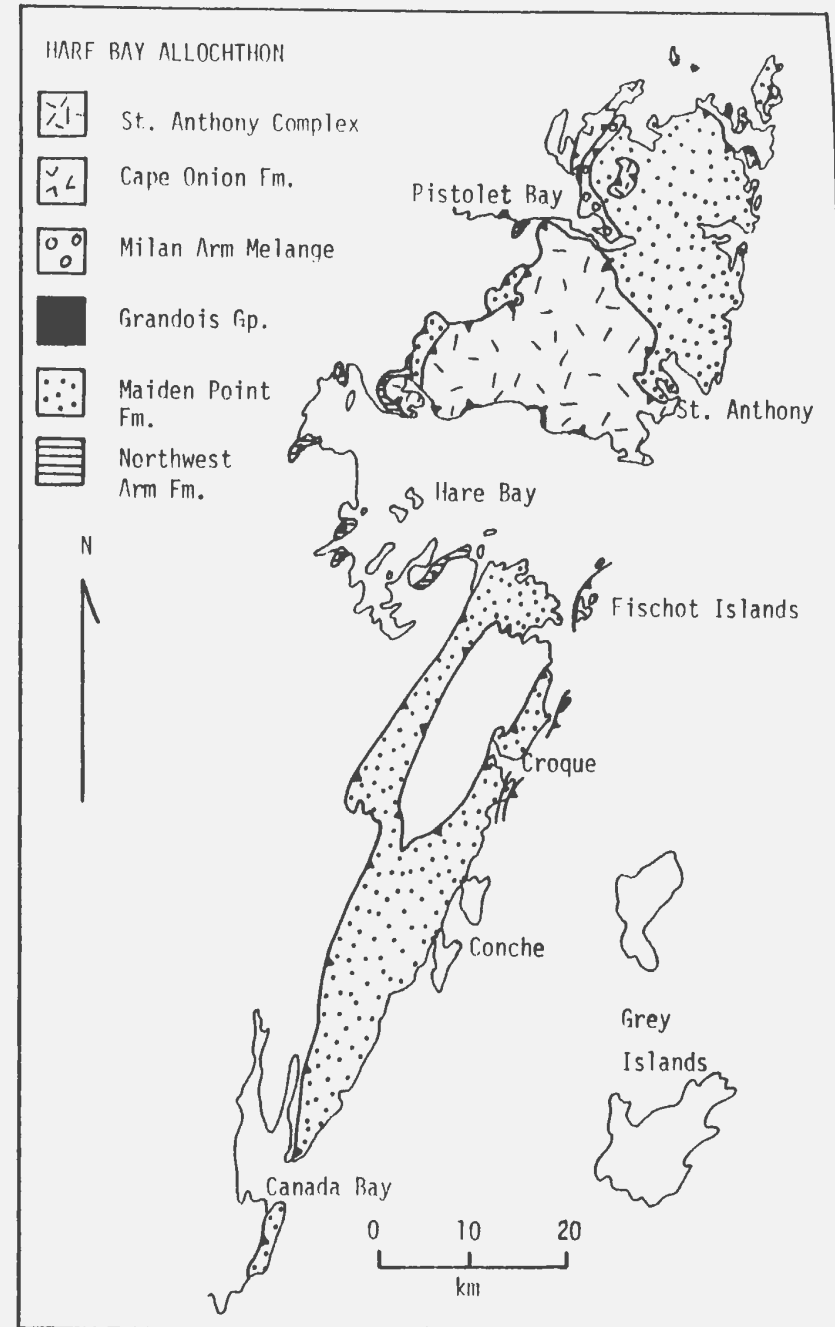
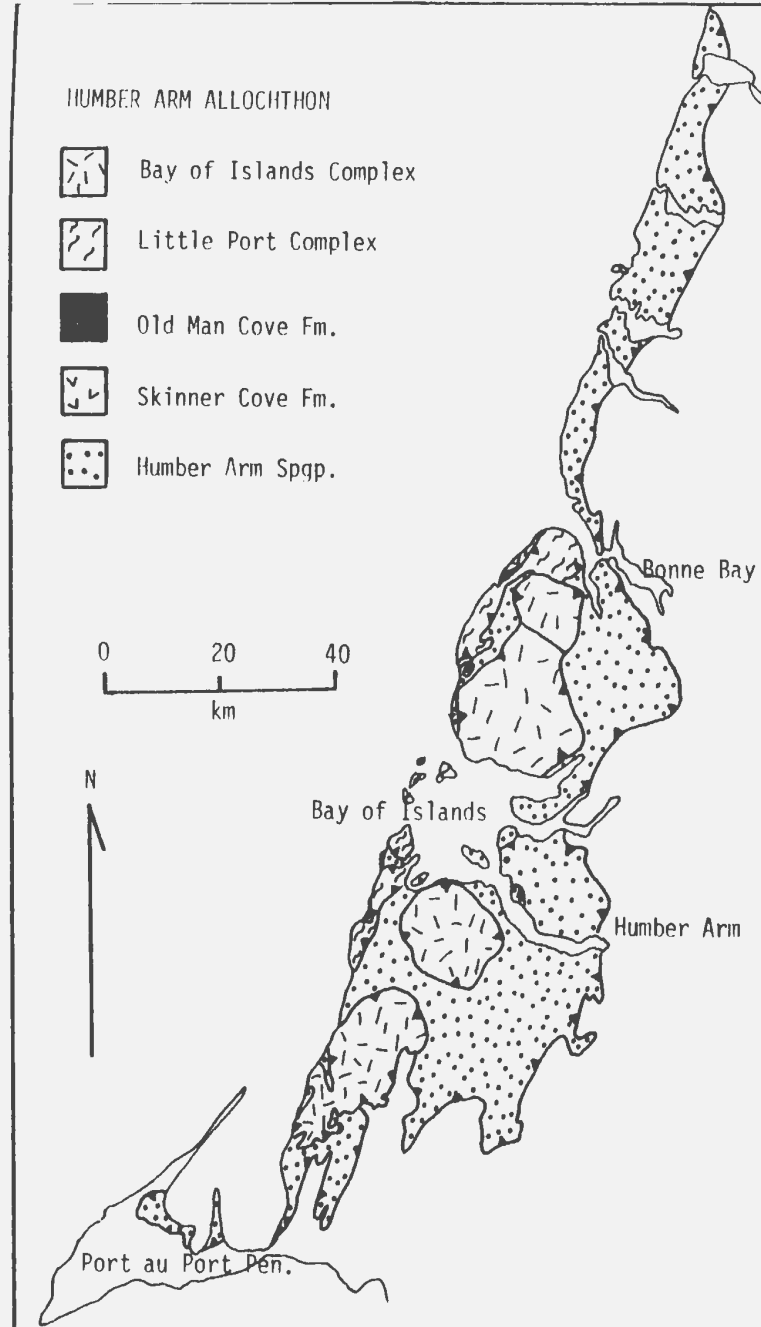


FIGURE 1.3: Geology of the Hare Bay and Humber Arm Allochthons (after Williams, 1975) (cf. Table 1.1, Plate 2).

(after Williams, 1975) (* fossil ages)

NUMBER AND ALLOCATIONS

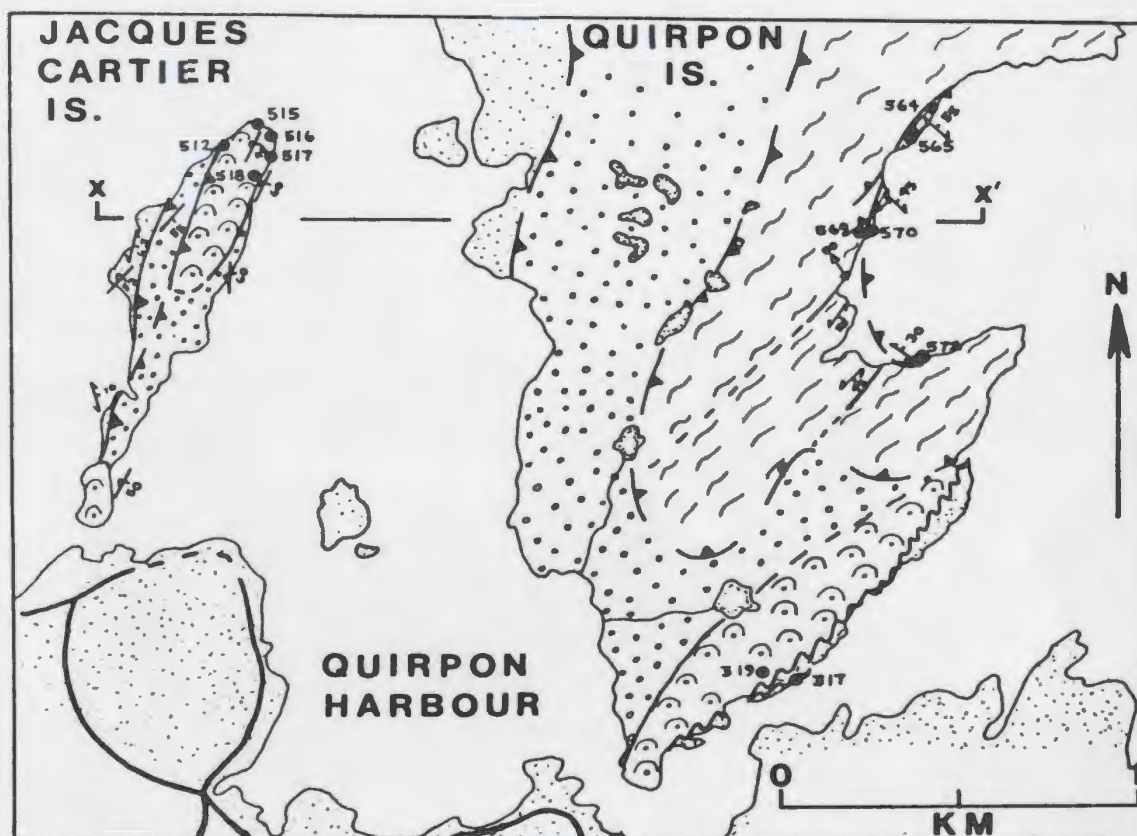


FIGURE 2.1: Rhythmic layering in gabbro at Partridge Point. Hammer handle is 30 cm long.



FIGURE 2.2: Variolitic pillow lava at Ireland Point. Lens cap is 5 cm in diameter.

FIGURE 2.3: Geology of the Quirpon Harbour area.



ST ANTHONY COMPLEX

 GREEN RIDGE
AMPHIBOLITE

 GOOSE COVE
SCHIST

MAIDEN POINT FORMATION

 VOLCANICS

 SEDIMENTS

GOOSE TICKLE FORMATION





FIGURE 2.4: Variolitic pillow lava overlying black shale, one-half kilometre east of Ireland Point.



FIGURE 2.5: Pillow breccia, Ireland Point.



FIGURE 2.6: Vesicular pillow lava in boulder, north of Ireland Point.



FIGURE 2.7: Porphyritic pillow lava, Stark's Bight (cf. Fig. 2.19).

FIGURE 2.8: Transition from the Ireland Point Volcanics to the Goose Cove Schist.



2.8a: Slightly deformed purple vesicular pillow lava, west side of Stark's Bight.



2.8b: Strongly sheared, but still recognizable, purple vesicular pillow lava, head of Stark's Bight.

FIGURE 2.8 (continued)



2.8c: Interleaved schistose purple vesicular pillow lava and carbonate, with volcanic structures virtually obliterated, east side of Stark's Bight. Hammer head at lower left is 18 cm long.



2.8d: Green carbonate-rich schist derived from vesicular pillow lava, east side of Stark's Bight. Volcanic structures have been obliterated and actinolite occurs in the metamorphic assemblage.



FIGURE 2.9: Deformed pillow breccia near the transition from the Ireland Point Volcanics to the Goose Cove Schist. Note the alteration of the breccia clasts which predates the deformation.



FIGURE 2.10: Marble (white), chert (black), and pelite (grey), defining F_2 fold, southeast coast of Fischot Island.



FIGURE 2.11: Semi-pelitic schist with quartz aggregates, south side of Three Mountain Harbour.



FIGURE 2.12: Psammite, showing primary compositional layering, Lobster Point.



FIGURE 2.13: Pelite with thin marble layers showing S_1 folded by F_2 , Goose Cove West.

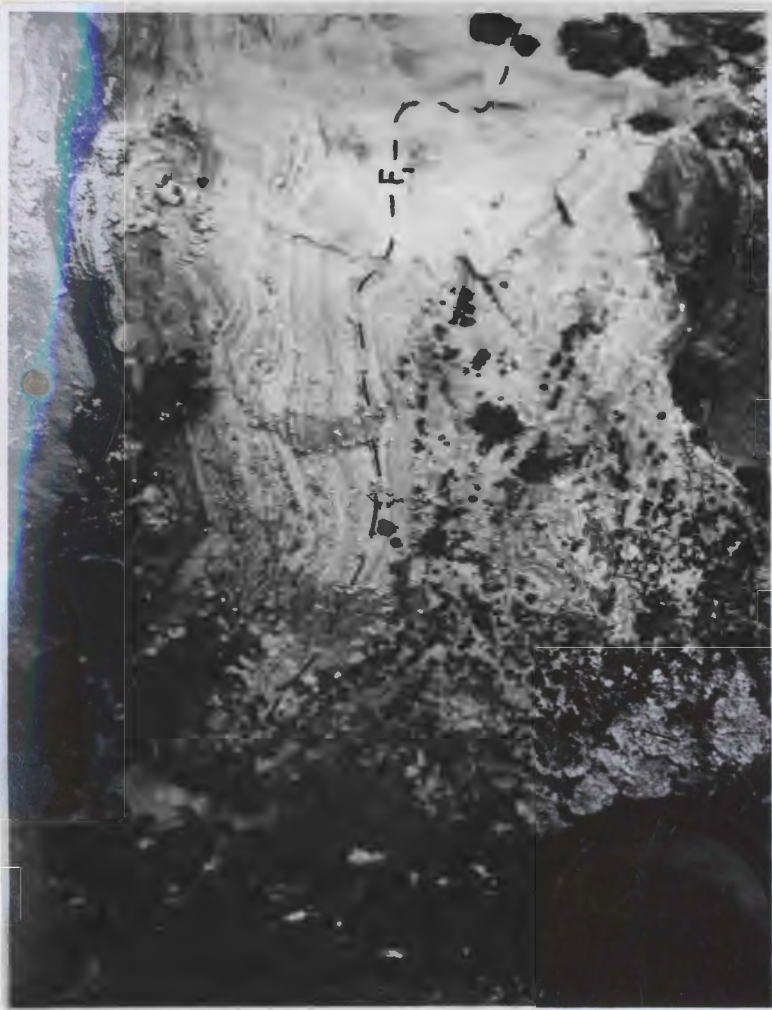


FIGURE 2.14: Finely laminated, cherty metasediment showing F_1 fold, east of Brimstone Pond, Goose Cove. Note lens cap in lower right for scale.



FIGURE 2.15: Massive, coarse-grained greenschist, probably a pre-tectonic sill, Duck Point.



FIGURE 2.16: Banded greenschist, Goose Cove.

FIGURE 2.17: Variable deformation in banded greenschists.

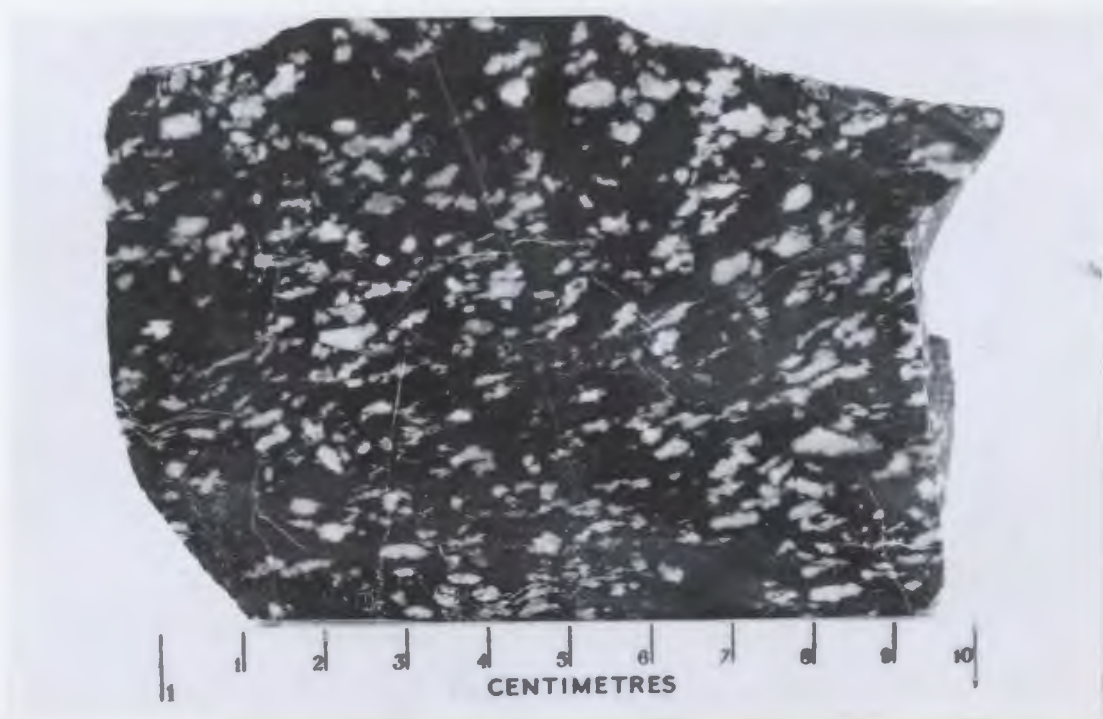


2.17a: Alternating epidote-rich and epidote-poor layers in strongly foliated, banded greenschist with no apparent F_2 folds, south side of Three Mountain Harbour.

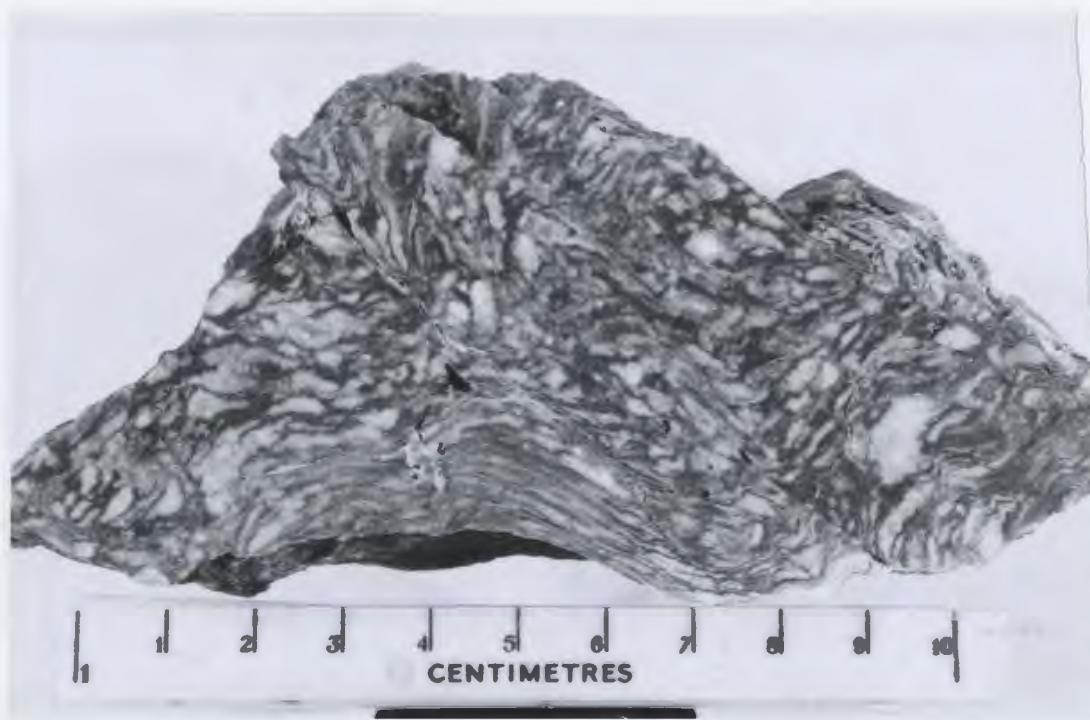


2.17b: Small-scale F_2 folds, banded greenschist, Goose Cove Road.

FIGURE 2.18: Variable deformation in spotted greenschists.



2.18a: RJ75-007, mildly deformed spotted greenschist, Goose Cove Road.



2.18b: RJ75-113, strongly deformed spotted greenschist, St. Anthony Hill.



FIGURE 2.19: Deformed pillows in spotted greenschist, southwest side of Cremaillere Harbour (cf. Fig. 2.7).

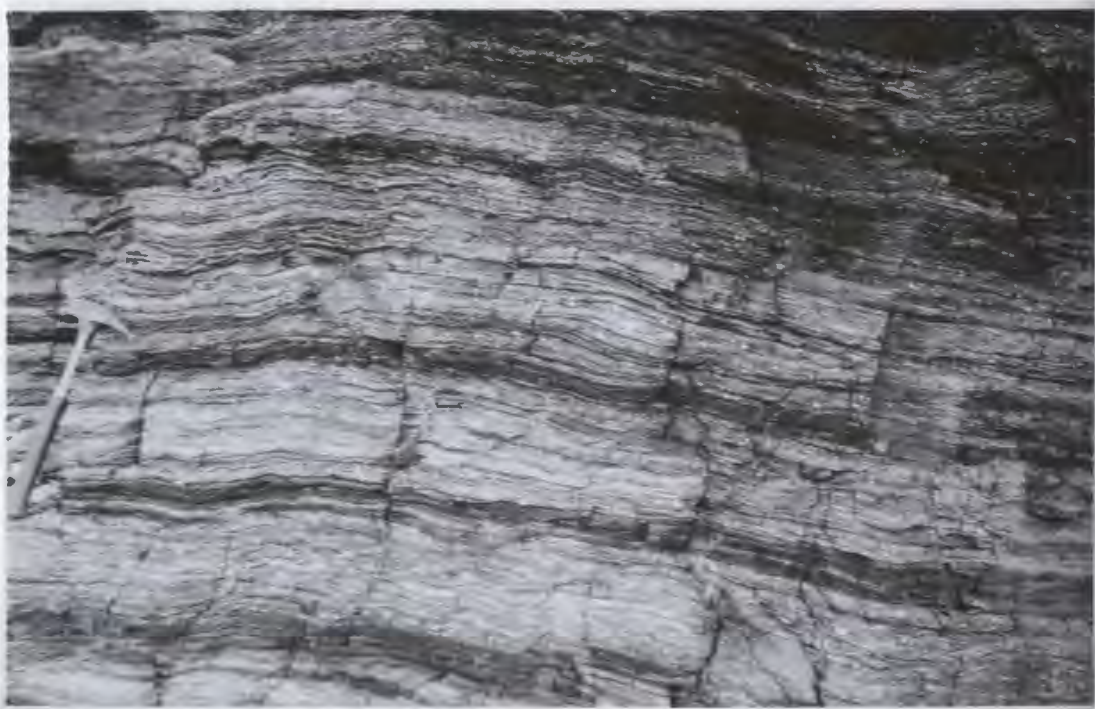
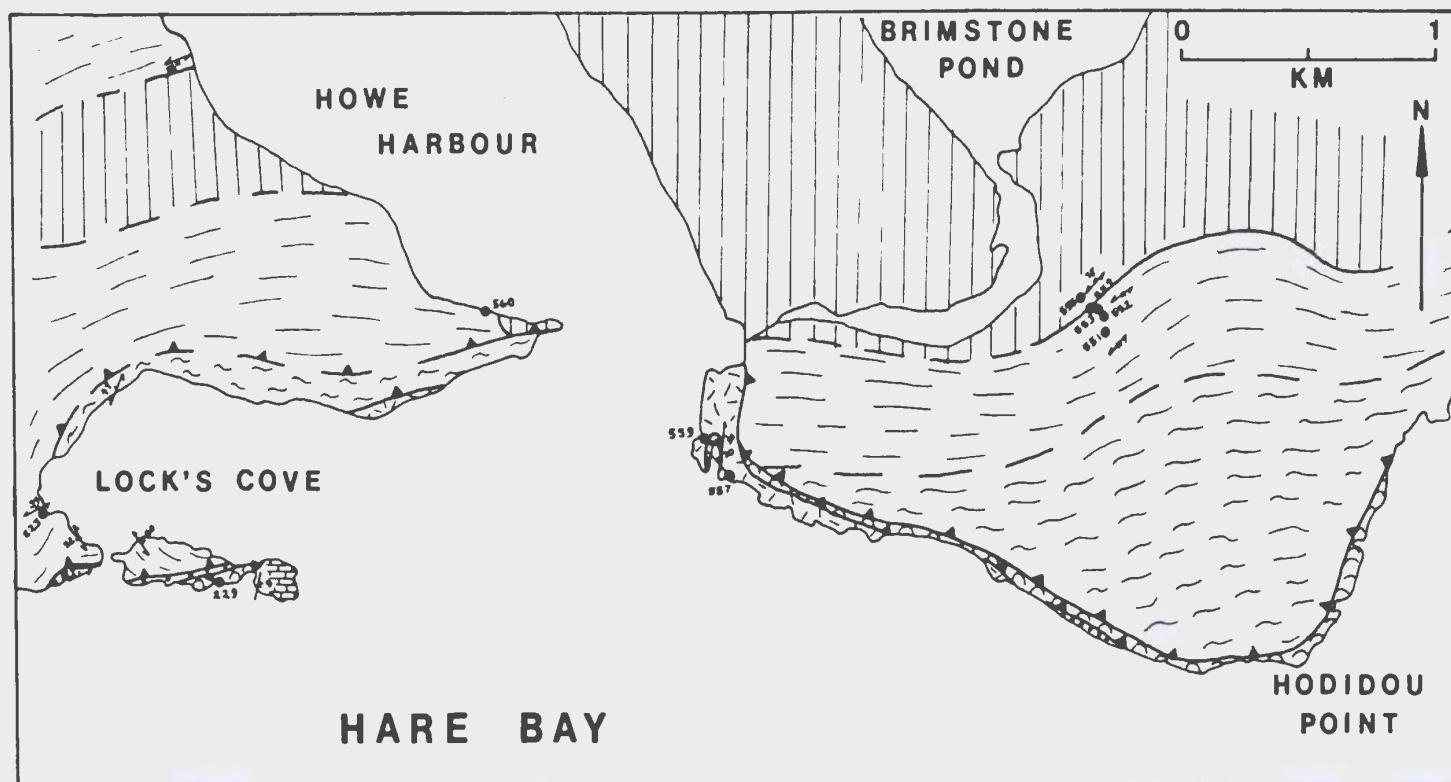


FIGURE 2.20: Banding in spotted greenschists, possibly derived from crystal tuffs, Savage Point.







FIGURE 2.21: DFS-73-122, epidote amphibolite with F_2 fold, Three Mountain Summit.

FIGURE 2.22: Geology of the Howe Harbour area.



ST. ANTHONY COMPLEX

-  WHITE HILLS PERIDOTITE
-  GREEN RIDGE AMPHIBOLITE
-  GOOSE COVE SCHIST
-  IRELAND POINT VOLCANICS

MAIDEN POINT FORMATION



-  GABBRO
-  SEDIMENTS
-  TABLE HEAD FORMATION



FIGURE 2,23: RJ75-138, biotite amphibolite containing epidote amphibolite inclusions, Three Mountain Summit.



FIGURE 2.24: Biotite amphibolite containing inclusion of partially melted quartz amphibolite, south side of Northeast Island.



FIGURE 2.25: Relict igneous layering in metagabbro at Wild Cove, southwest side of Fischot Island.



FIGURE 2.26: Marble band showing F_2 and F_3 folds, Northeast Island.



FIGURE 2.27: Partially melted quartz amphibolite, east side of Northeast Island.



FIGURE 2.28: Compositional layering in quartz amphibolite defined by variable proportions of plagioclase, Three Mountain Summit. Portion of hammer head shown is 4 cm long.

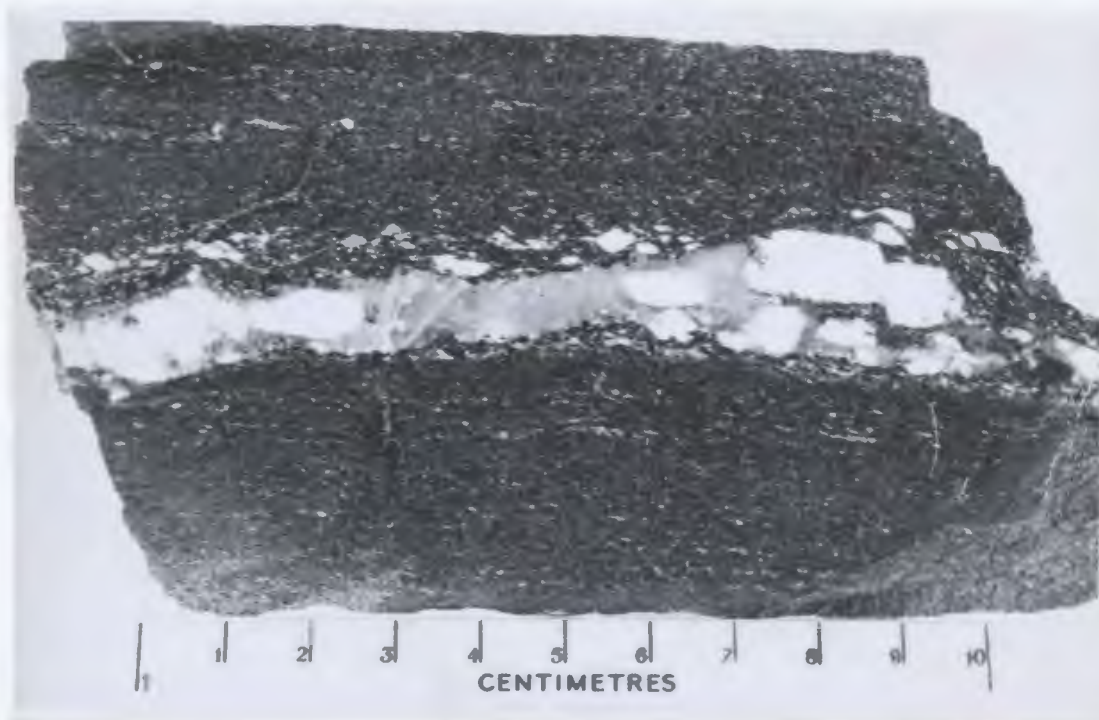


FIGURE 2.29: RJ75-Q80, quartz amphibolite containing band of coarse-grained plagioclase and quartz, Three Mountain Summit.

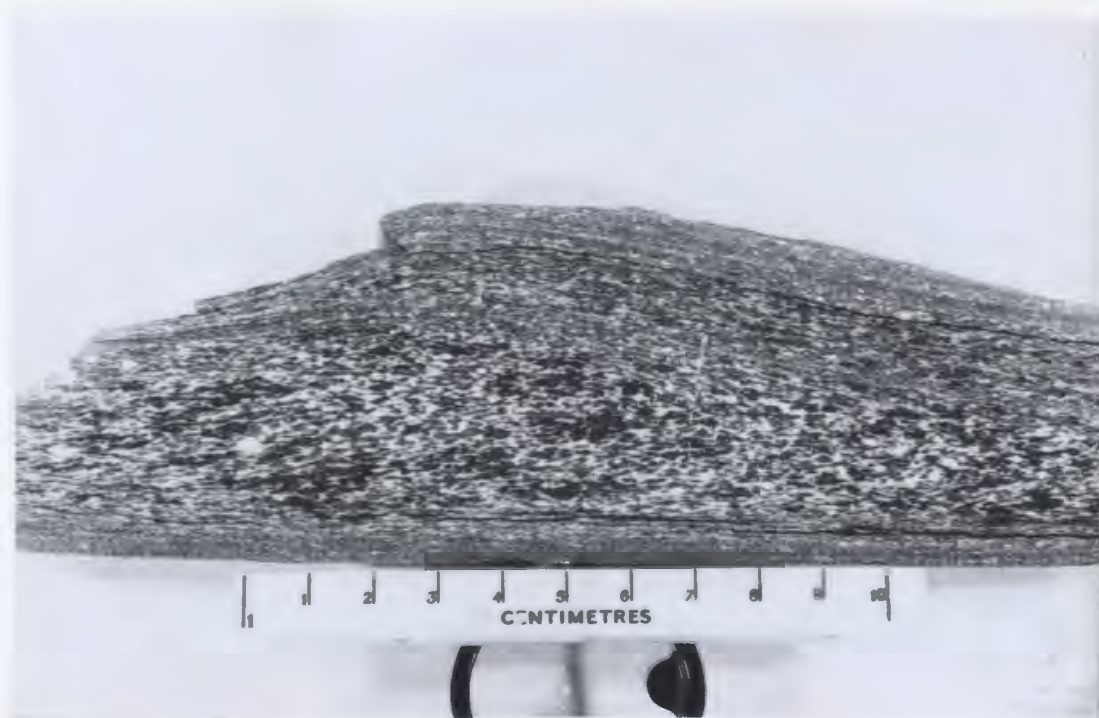


FIGURE 2.30: LRC-77-1, inhomogeneously deformed metagabbro, Long Ridge.



FIGURE 2.31: Interlayered dunite (medium grey at top and bottom of picture), troctolite (dark grey), and gabbro (light grey), Long Ridge. Portion of hammer head shown is 7 cm long.

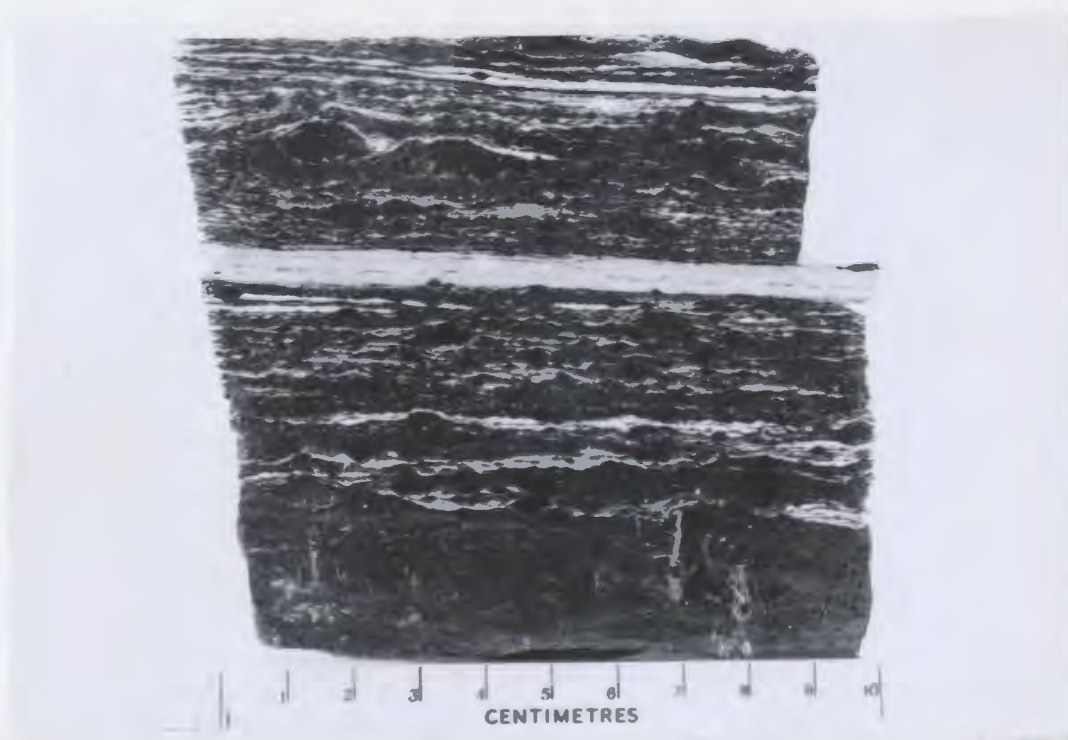


FIGURE 2.32: DFS-73-200, interlayered syenite (white), alkaline pyroxenite (black), and hornblende gneiss (striped), from boulder.



FIGURE 2.33: Lens of alkaline pyroxenite surrounded by interlayered syenite (white) and hornblendite (black), Northern Long Pond.



FIGURE 2.34: Rectangular jointing in harzburgite, showing lineation defined by elongated orthopyroxene crystals, near Deer Park in the White Hills.



FIGURE 2.35: Fold in basal contact zone, White Hills Peridotite, Western Long Pond.



FIGURE 2.36: Ultramafic mylonite, Milan Arm Melange. The light layers consist of serpentinitized peridotite, the dark layers consist mainly of amphibole.



FIGURE 2.37: Post-tectonic diabase dyke, Lobster Point.



FIGURE 2.38: Brecciated metasedimentary schist, Goose Cove West. Portion of hammer head shown in upper left is 11 cm long.



FIGURE 2.39: Epidote-rich layer in quartz amphibolite defining F_2 fold, south side of Northeast Island.



FIGURE 2.40: F_3 fold in epidote amphibolites, looking southeast, Three Mountain Summit.



FIGURE 2.41: Hare Bay thrust separating folded Maiden Point sandstones (bottom) and undeformed variolitic pillow lavas (top), Ireland Point. Cliff is 20 m high.

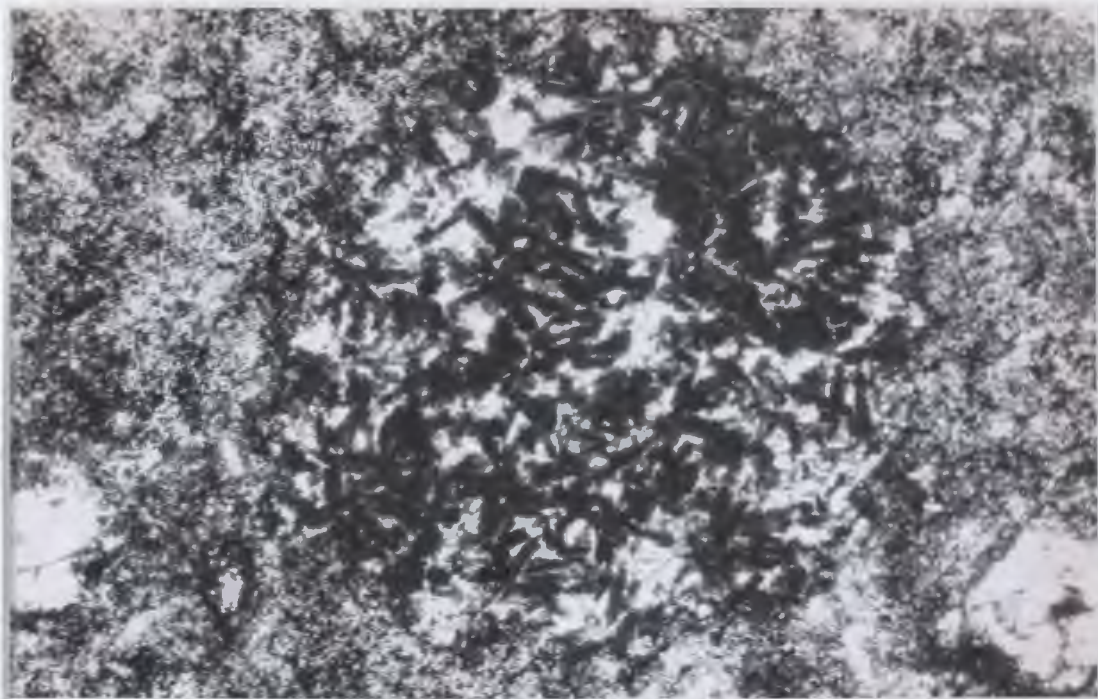
Table 3.1. Mineral abbreviations used throughout this work.

amph	= amphibole, composition unspecified
act	= actinolite
hast	= hastingsite
hb	= hornblende
kaer	= kaersutite
parg	= pargasite
trem	= tremolite
ap	= apatite
carb	= carbonate, composition unspecified
cc	= calcite
dol	= dolomite
chl	= chlorite
cor	= corundum
ep	= epidote
cz	= clinozoisite
zo	= zoisite
fd	= feldspar, composition unspecified
ab	= albite
an	= anorthite
Ksp	= potassium feldspar, type unspecified
plag	= plagioclase, type unspecified
gnt	= garnet, composition unspecified
alm	= almandine
gross	= grossular
py	= pyrope
spess	= spessartine
mica	= composition unspecified
bt	= biotite
mus	= muscovite
phl	= phlogopite
ser	= sericite
ol	= olivine, composition unspecified
fa	= fayalite
fo	= forsterite
ox	= oxides, composition unspecified
chr	= chromite
hem	= hematite
ilm	= ilmenite
mt	= magnetite
sp	= spinel, type unspecified
pr	= prehnite
pump	= pumpellyite
px	= pyroxene, composition unspecified
aug	= augite
cpx	= clinopyroxene, composition unspecified
di	= diopside
en	= enstatite
fs	= ferrosilite
hy	= hypersthene
opx	= orthopyroxene, composition unspecified
tiaug	= titanaugite
qz	= quartz
sauss	= sausserite
serp	= serpentine
sph	= sphene
tour	= tourmaline
zlr	= zircon

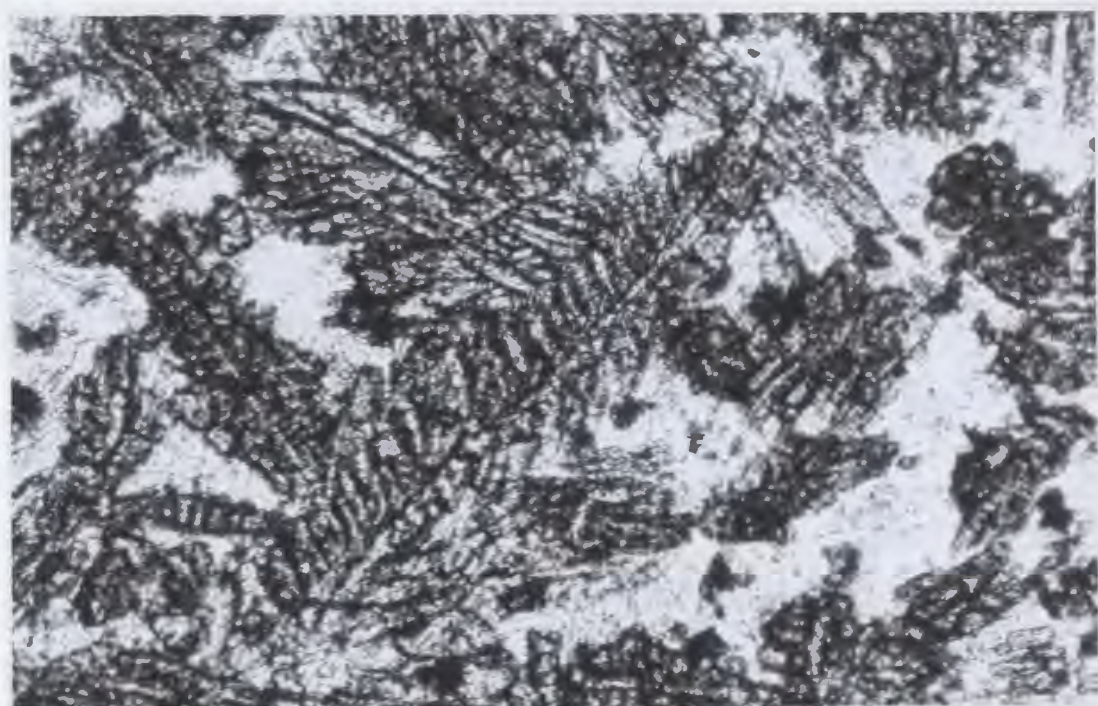
Table 3.2. Petrography of the Ireland Point Volcanics.

LITHOLOGY	MINERALOGY	TEXTURE
1a) VARIOLITIC PILLOW LAVA 160, 319 ^a , 512 ^a , 515, 516, 517, 518, 526 ^a , 527, 538, 542, 543, 546, 550 ^a , 599 FIG. 3.1, 3.10.	Phenocrysts: ol (5-15%) (\rightarrow chl, carb) Groundmass: tlaug (40-60%) (fresh \rightarrow chl, sph); kaer + hb (0-10%) "glass" (30-50%) (\rightarrow chl, ab, cc) kaer pleochroism: X = light yellow brown, Y = reddish brown, Z = dark reddish brown	variolitic (see text, p.) euhedral ol, dendritic to acicular tlaug mantled by kaer (\rightarrow hb) in devitrified matrix
1b) MASSIVE FLOWS 157, 162, 547 ^a , 549 FIG. 3.2.	Phenocrysts: absent Groundmass: tlaug (30-40%) (\rightarrow chl, sph, cc, chl); plag (40-50%) (\rightarrow ab); kaer + hb (0-25%) (fresh \rightarrow chl); "glass" (< 10%) (\rightarrow chl, ab, cc) kaer pleochroism: as above hb pleochroism: X = yellow-green, Y = deep green- blue, Z = dark green	supophitic intergrown tlaug, plag laths, commonly radiating; kaer replacing tlaug or forms euhedral crystals, partly replaced by hb; interstitial devitrified glass
2a) VESICULAR PILLOW LAVA 229 ^a , 257, 258, 263, 468, 534, 535 ^a , 544, 603 FIG. 3.3.	Phenocrysts: plag (0-5%) (\rightarrow ab) Groundmass: plag (70-90%) (\rightarrow ab); "glass" (50-80%) (\rightarrow chl, ab, cc, hm, sph)	vesicular to amygdaloidal (cc, chl) rare euhedral plag phenocrysts; generally microlitic plag laths with trachytic texture
2b) PILLOW BRECCIA 532 ^a , 537 ^a , 548 ^a FIG. 3.4.	Pillow fragments (548): plag (50%) (\rightarrow ab, cc); "glass" (50%) (\rightarrow cc, hm, chl) Matrix (532, 537): glass (\rightarrow hm, chl, cc, sph); cc; chl	vesicular pillow fragments with trachytic texture in matrix of pumiceous glass fragments, cc, chl
2c) FLATTENED VESICULAR PILLOW LAVA INTERLEAVED WITH CALCITE 260 ^a , 470 ^a , 471 ^a	Relict volcanics: plag (\rightarrow ab); glass (\rightarrow hm, chl, cc) Matrix: cc, chl, hm, ep, ab chl \rightarrow act at transition from Ireland Point Volcanics to Goose Cove Schist	bands with relict trachytic texture in fine- grained, schistose, chl- and cc-rich matrix
3) PORPHYRITIC PILLOW LAVA 255 ^a , 256 ^a , 463, 464, 465, 466, 467 ^a , 469 FIG. 3.5.	Phenocrysts: plag (20-55%) (\rightarrow cc, chl, ep, ab, ? pump); cpx (0-10%) (\rightarrow cc, chl, ep, ? pump); ol (0-5%) (\rightarrow cc, chl) Groundmass: plag (15-30%) (\rightarrow ab, ep); cpx (30-40%) (\rightarrow chl, sph)	glomeroporphyritic; amygdaloidal cc, chl, ep, large (up to 2 cm) zoned plag phenocrysts associated with smaller (< 5 mm) euhedral ol, cpx in groundmass of felted cpx, plag
4a) GABBRO 167, 200, 207, 209 ^a , 210, 212, 213, 281, 282, 283A, 284, 286, 286A, 317 ^a , 430, 529, 541, 557, 559 ^a FIG. 3.6.	tlaug (20-40%) (\rightarrow chl); plag (30-60%) (\rightarrow ab, ep); kaer + hb (5-25%); bt (0-10%) (\rightarrow chl, stilp); ilm? (2-10%) (\rightarrow mt, sph); ap (0-2%) Pleochroism: kaer (see above); hb (see above)	euhedral, patchily zoned tlaug (1-10 mm) mantled by kaer, (which is partly replaced by hb), with interstitial tabular plag, euhedral Fe-Ti ox (ilm?) completely replaced by lamellar mt-sph intergrowths, associated with bt (? primary); ap poikilitically enclosed in tlaug; ilm
4b) DIORITE 283B, 429 ^a , 431, 432 FIG. 3.7.	plag (75-90%) (\rightarrow ab, ep); kaer + hb (10-25%) (\rightarrow chl); ilm? (0-2%) (\rightarrow mt, sph); ap (0-2%) Pleochroism: see above	euhedral, acicular kaer (1-5 mm) poikilitically enclosing ap, and partly replaced by hb; rare cubic ilm; in matrix of tabular plag
a = highly altered		(\rightarrow chl, ab) = completely altered to chlorite, albite (\rightarrow chl, ab) = partly altered to chlorite, albite

FIGURE 3.1: Variolitic pillow lava



3.1a: RJ76-516. Variole in altered pillow lava, showing titanaugite crystals (dark) in leucocratic variole, sharp boundaries, and lack of radiating structure within the variole. Titanaugite outside the variole has been replaced by chlorite. Diameter of variole is 1.5 mm.



3.1b: RJ76-563. Dendritic titanaugite microlite, variolitic pillow lava. Length of crystal is about 0.1 mm.



FIGURE 3.2: RJ75-162: Kaersutite microlites in massive flow intergrown with plagioclase laths. Large euhedral crystal at centre is about 0.5 mm across.

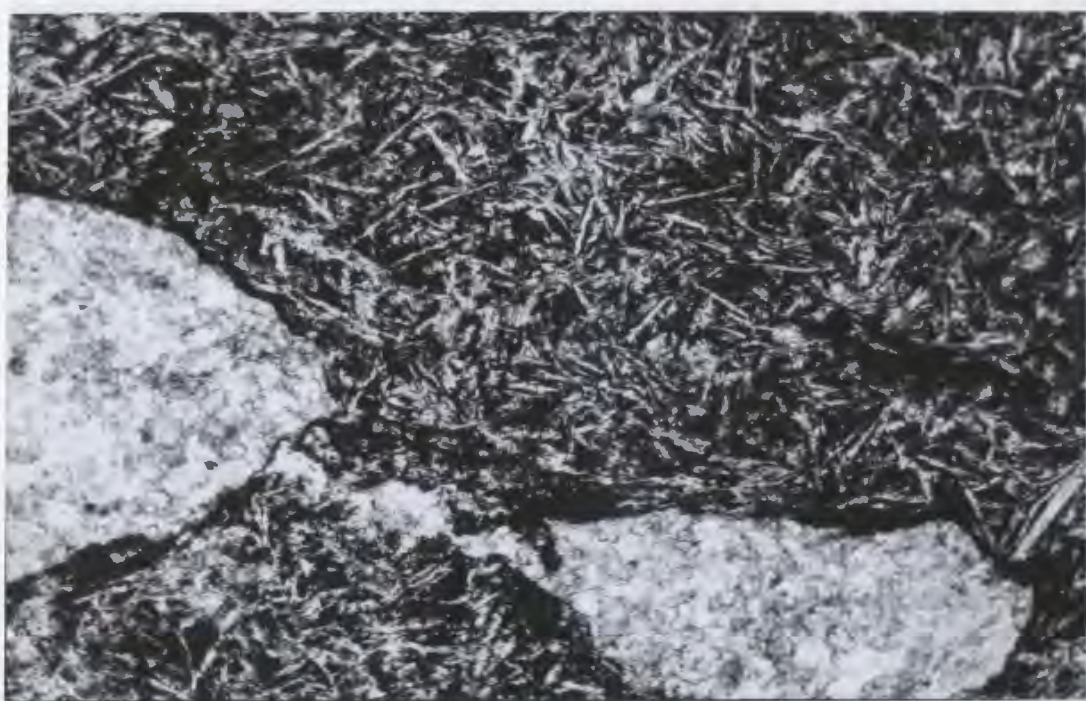


FIGURE 3.3: RJ75-070: Vesicular pillow lava showing plagioclase microlites in hematized, devitrified groundmass and amygdaloidal calcite. Vesicle at lower right is 1 mm across.

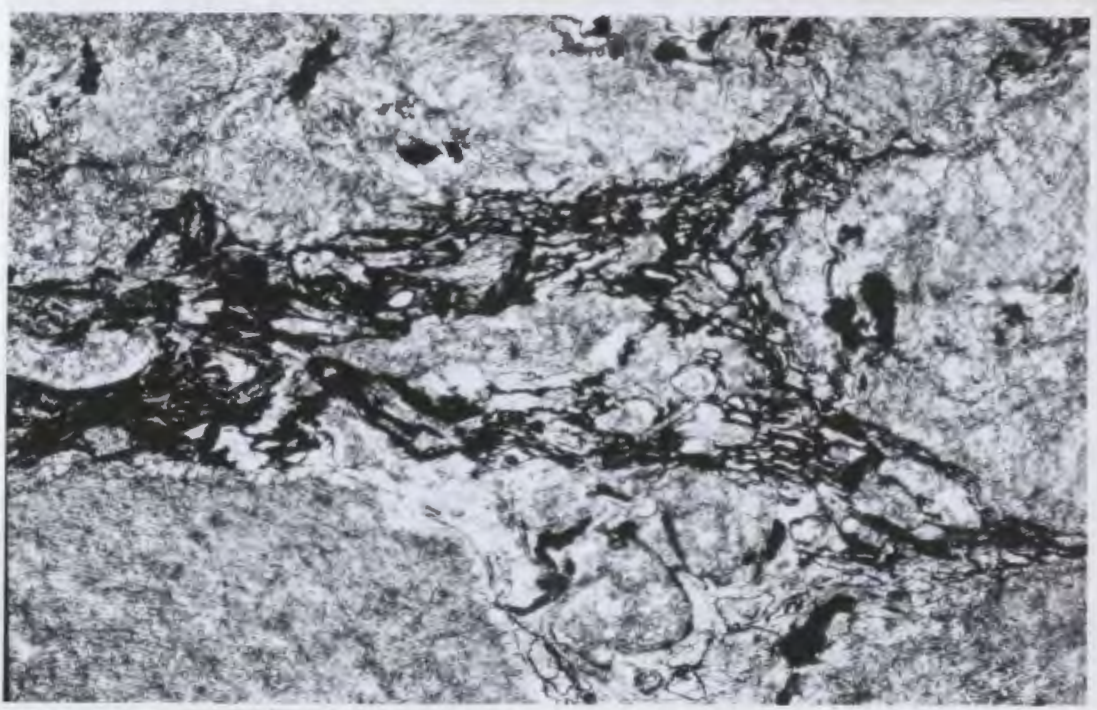
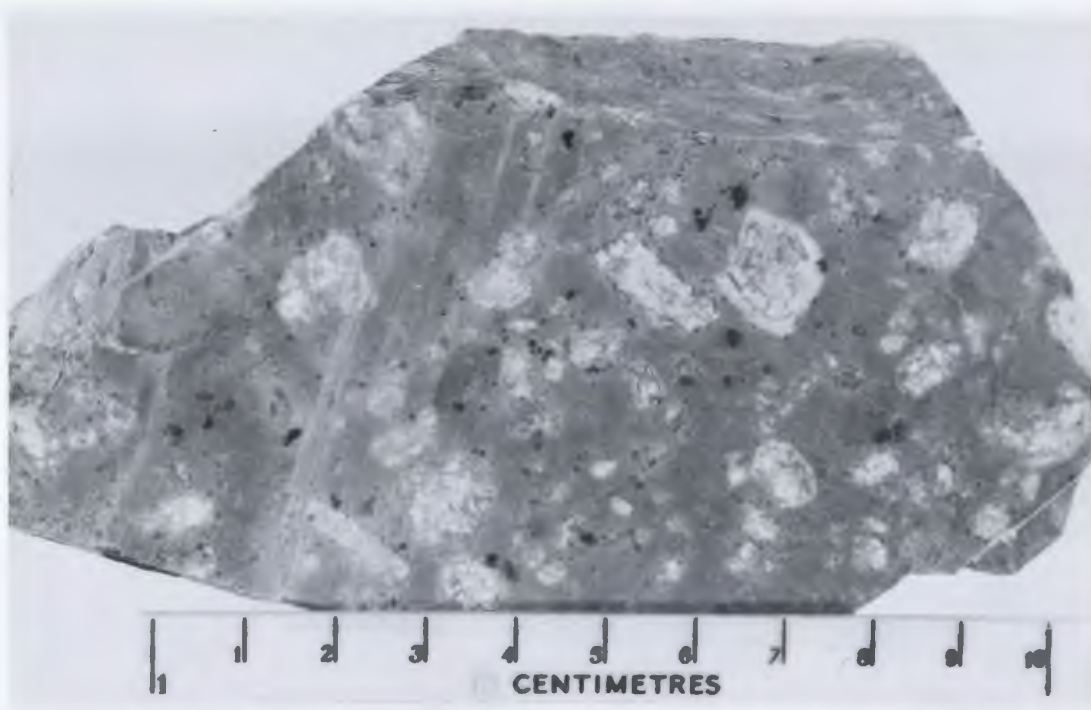
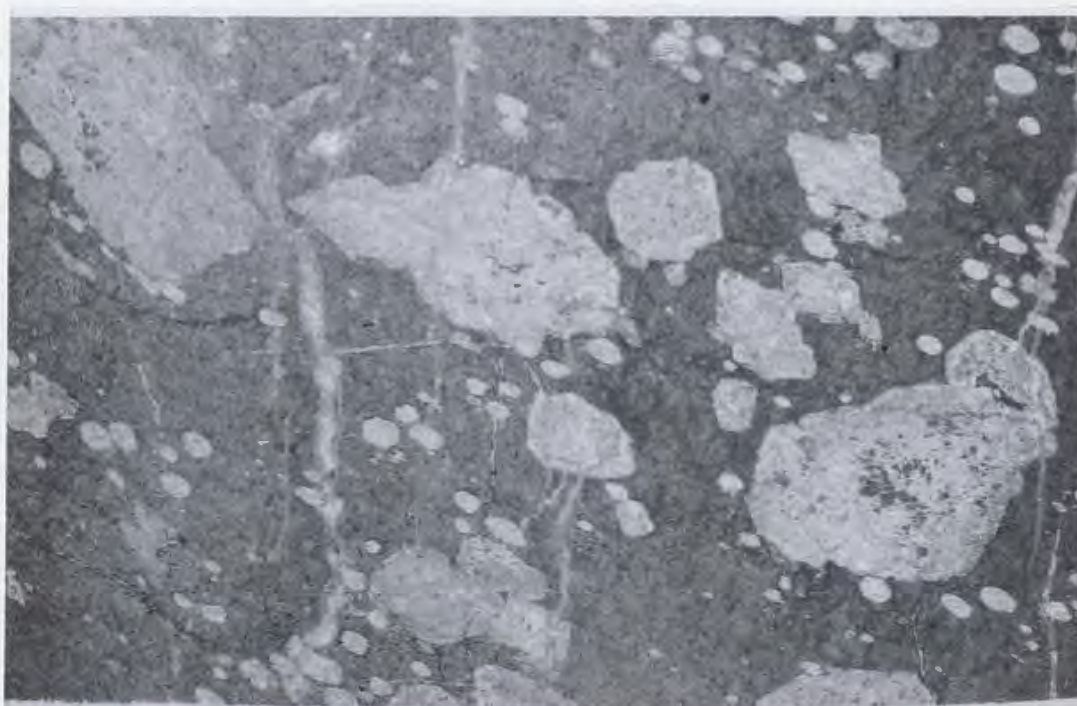


FIGURE 3.4: RJ76-532. Vesicular glass shard in a calcite-rich matrix, pillow breccia. Width of field is 3 mm.

FIGURE 3.5: Porphyritic pillow lava.



3.5a: RJ76-466. Porphyritic pillow lava showing altered plagioclase phenocrysts (white) and chloritized clinopyroxene and olivine crystals (dark).



3.5b: RJ75-255: Thin section of porphyritic pillow lava showing altered plagioclase phenocrysts and abundant calcite amygdalae. Width of section is 3.5 cm.



FIGURE 3.6: RJ75-286. Gabbro, showing fresh pyroxene (right), amphibole rimming pyroxene (medium to dark grey, centre), and chloritized biotite (left). Width of field is about 3 mm.

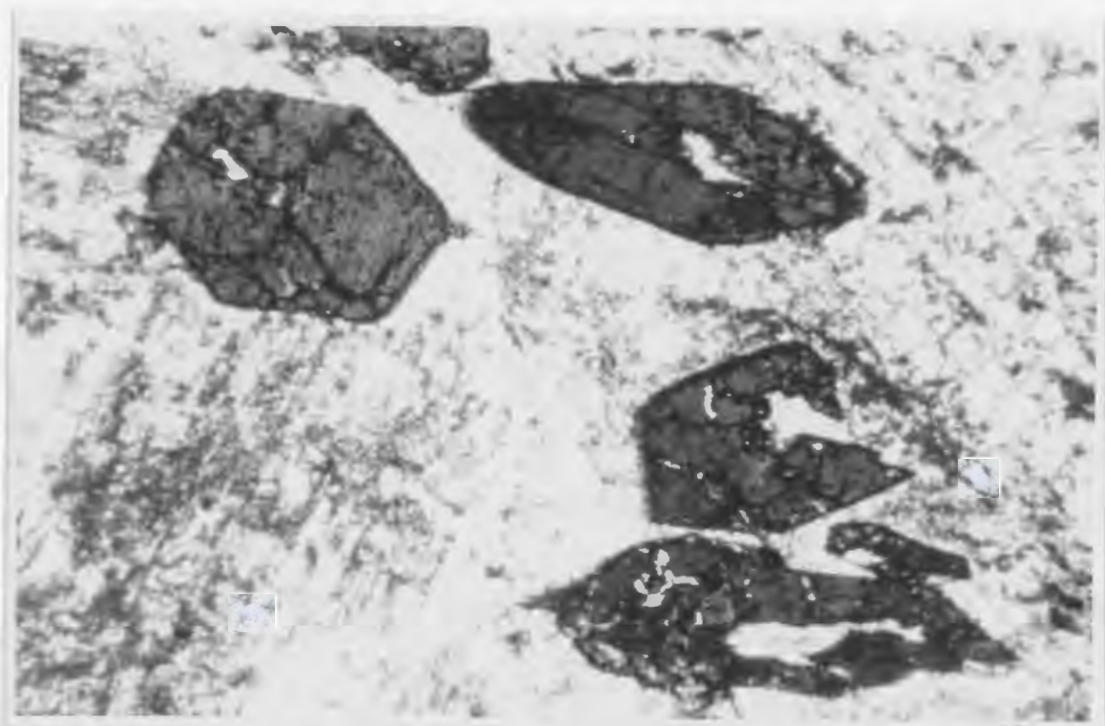


FIGURE 3.7: RJ75-283B. Euhedral kaersutite in diorite, surrounded by altered plagioclase laths. Crystal at upper left is 0.5 mm across.

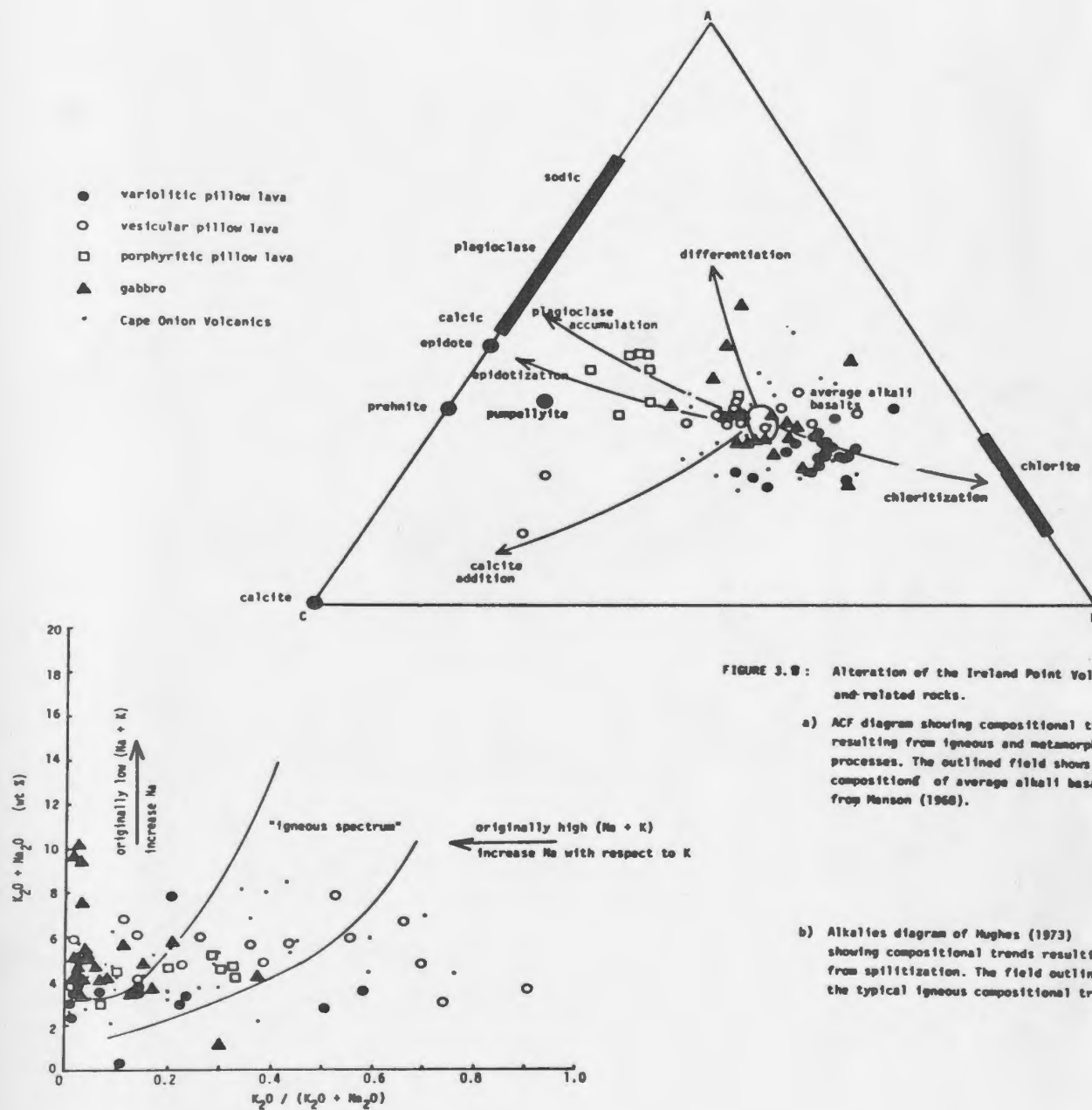


FIGURE 3.8: Alteration of the Ireland Point Volcanics and related rocks.

a) ACF diagram showing compositional trends resulting from igneous and metamorphic processes. The outlined field shows the composition of average alkali basalts from Manson (1968).

b) Alkalies diagram of Hughes (1973) showing compositional trends resulting from spilittization. The field outlines the typical igneous compositional trend.

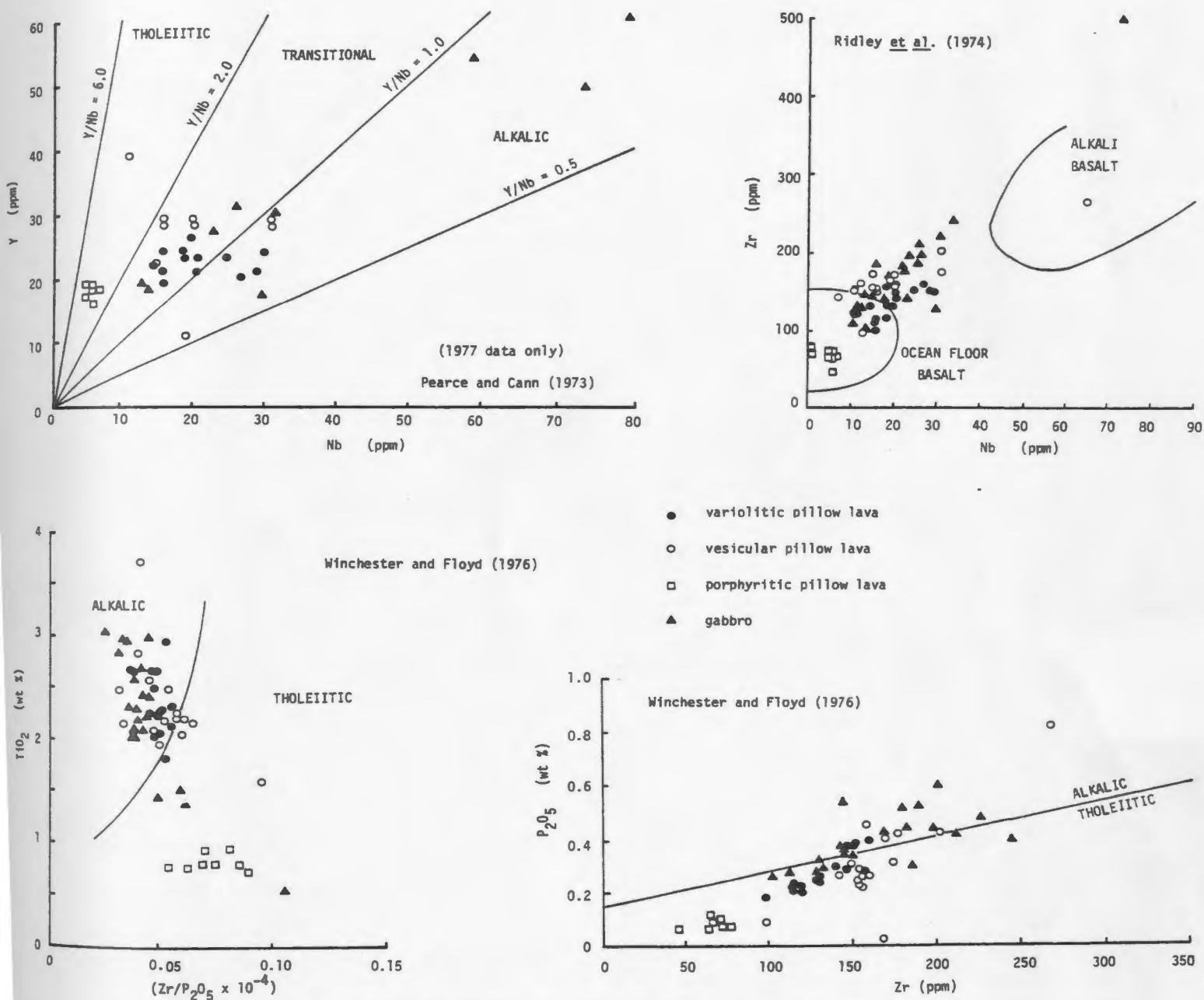
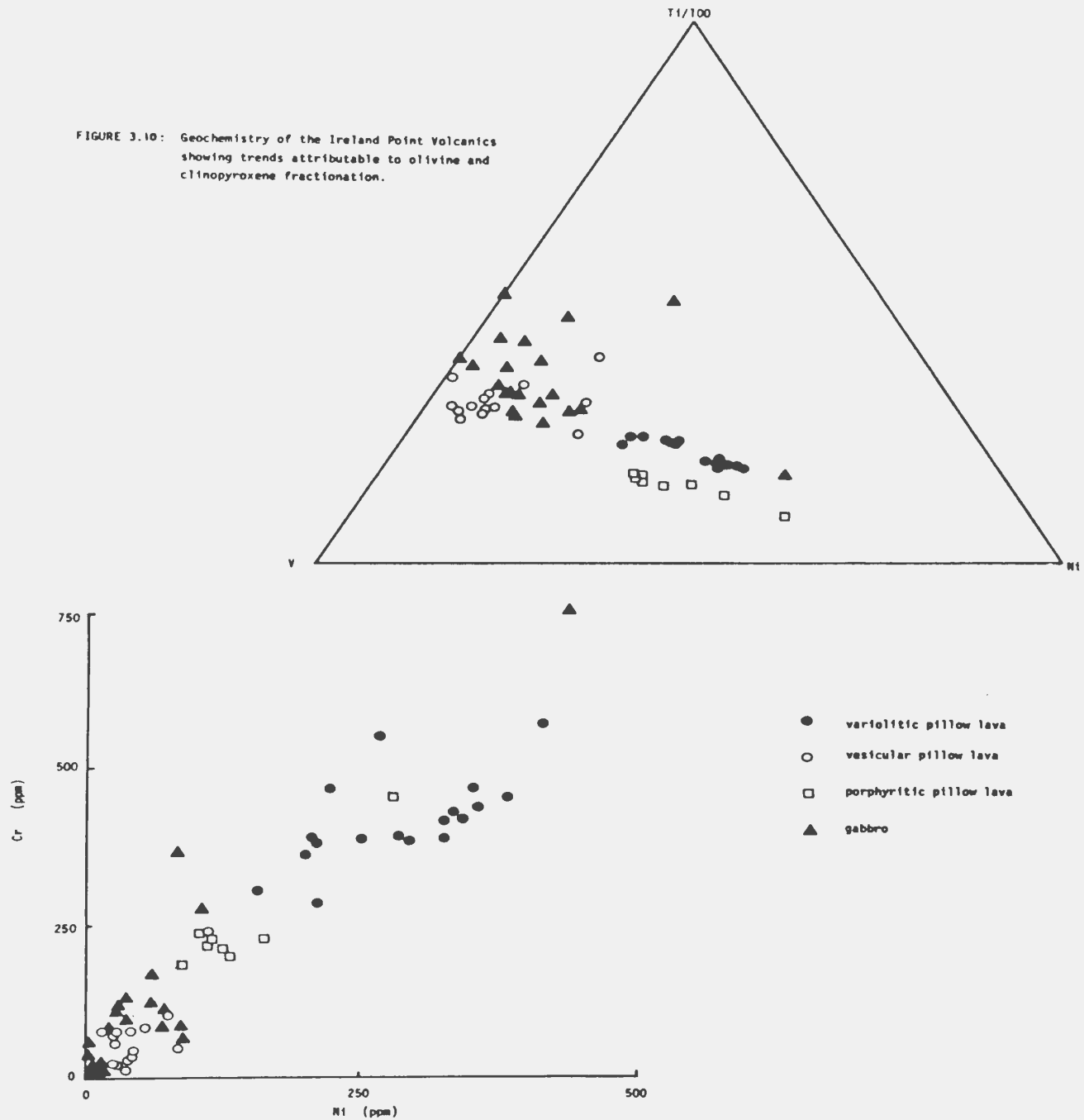


FIGURE 3.9: Immobible element geochemistry of the Ireland Point Volcanics. Disregarding the compositions of the porphyritic pillow lavas (cumulates) and the gabbros (differentiated), the basalts can be classified as alkaline to transitional.

FIGURE 3.10: Geochemistry of the Ireland Point Volcanics showing trends attributable to olivine and clinopyroxene fractionation.



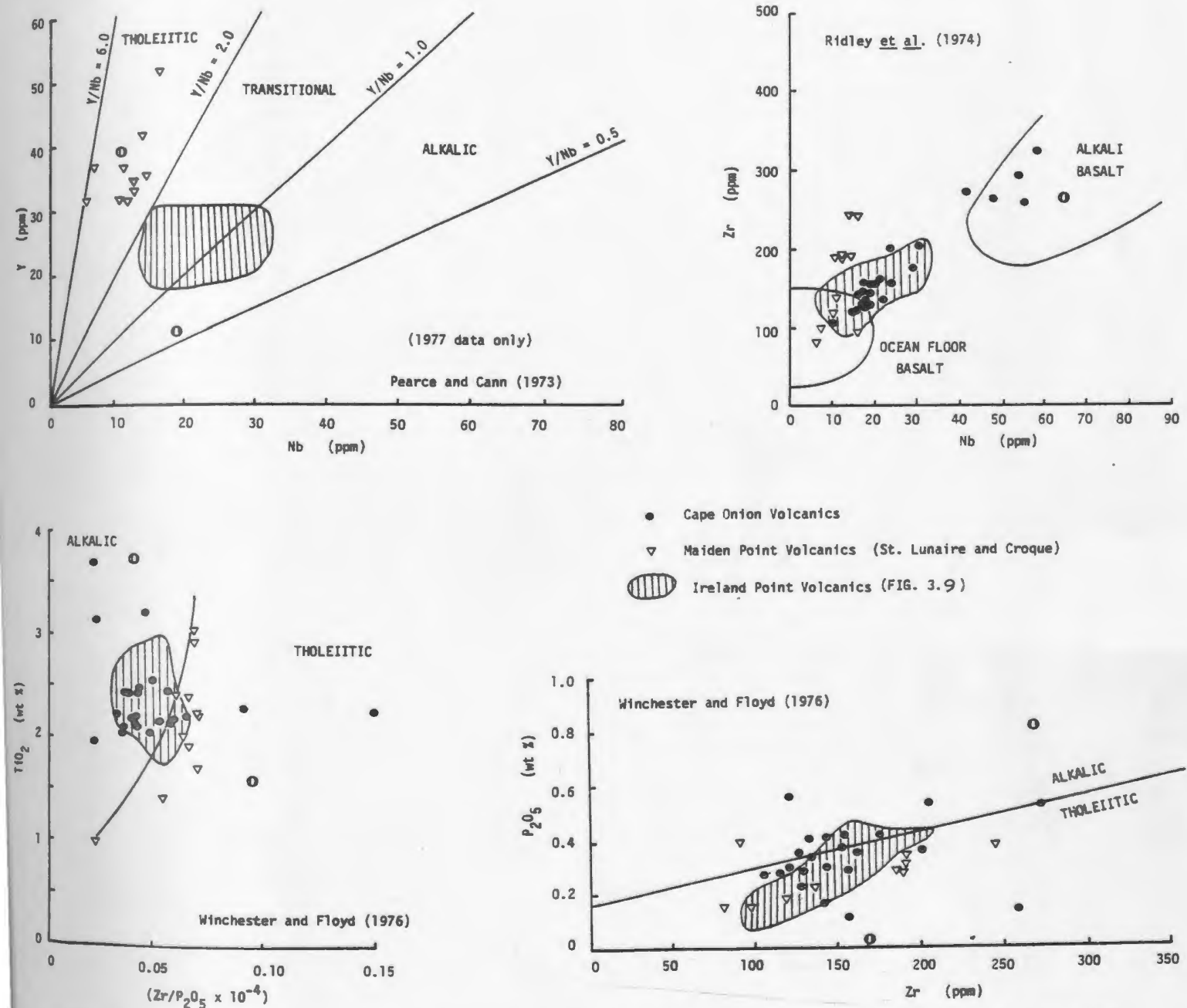
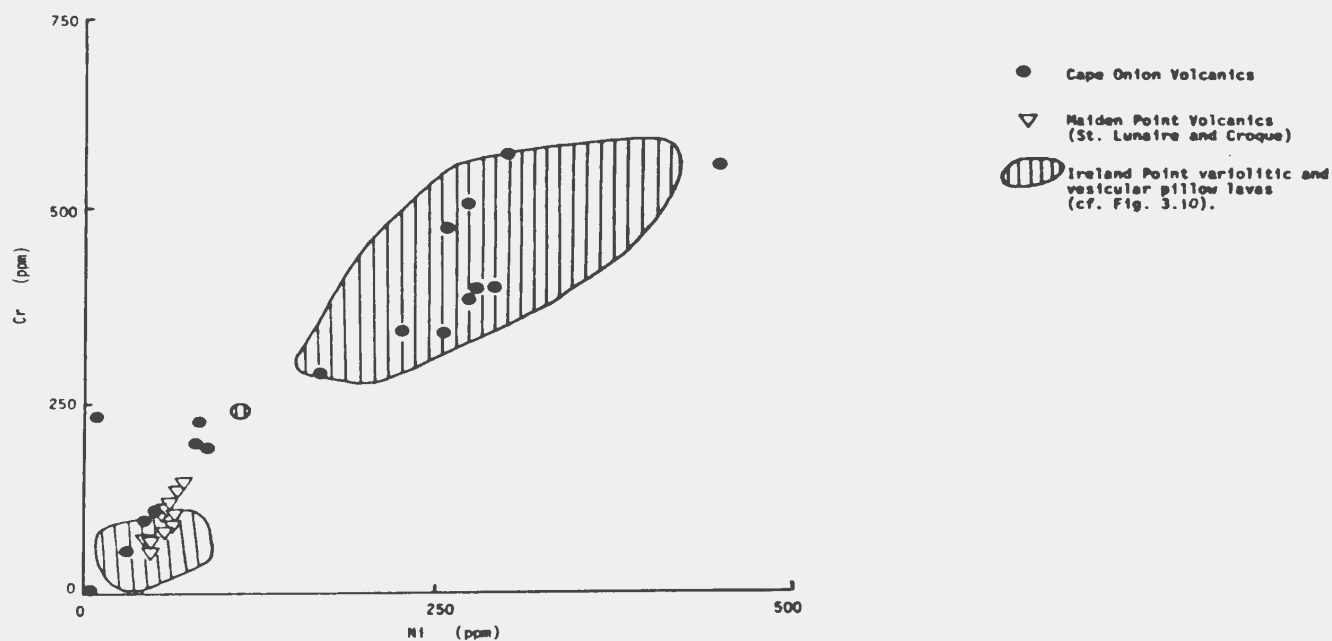
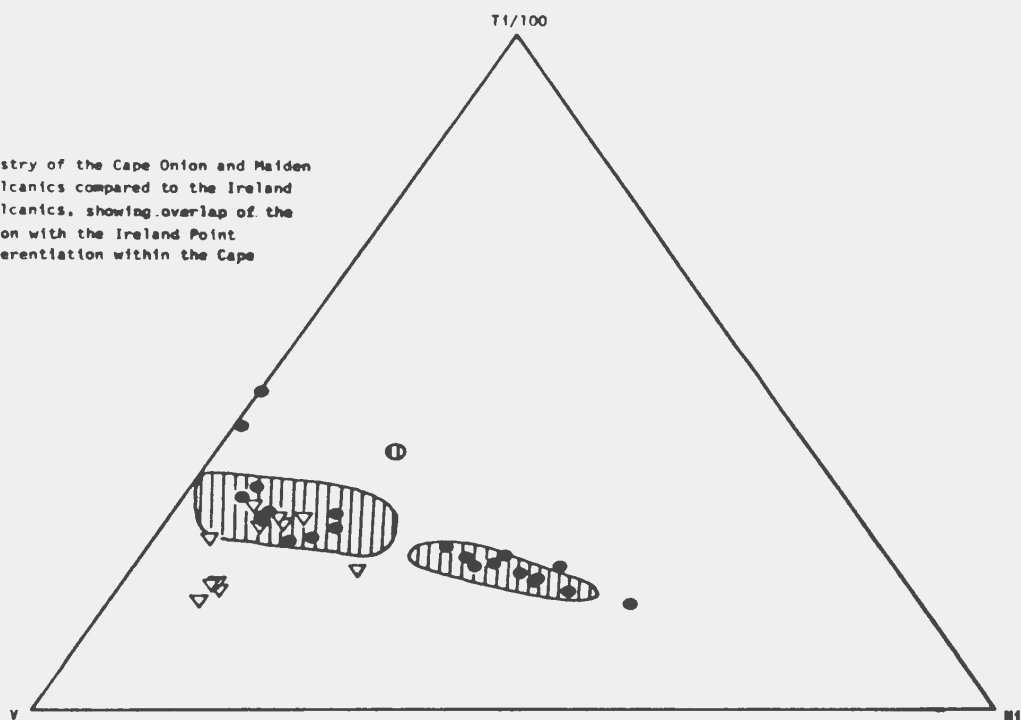


FIGURE 3.11: Immobile element geochemistry of the Cape Onion Volcanics and the volcanic rocks from near the base of the Maiden Point Slice, compared to that of the Ireland Point pillow lavas (cf. FIG. 3.9). Note the overlap between the Cape Onion and Ireland Point compositions, and the slight but consistent differences between the Maiden Point and Ireland Point volcanics. TiO_2 and P_2O_5 data for the Cape Onion Volcanics from DeLong, 1976.

FIGURE 3.12: Geochemistry of the Cape Onion and Maiden Point volcanics compared to the Ireland Point Volcanics, showing overlap of the Cape Onion with the Ireland Point and differentiation within the Cape Onion.



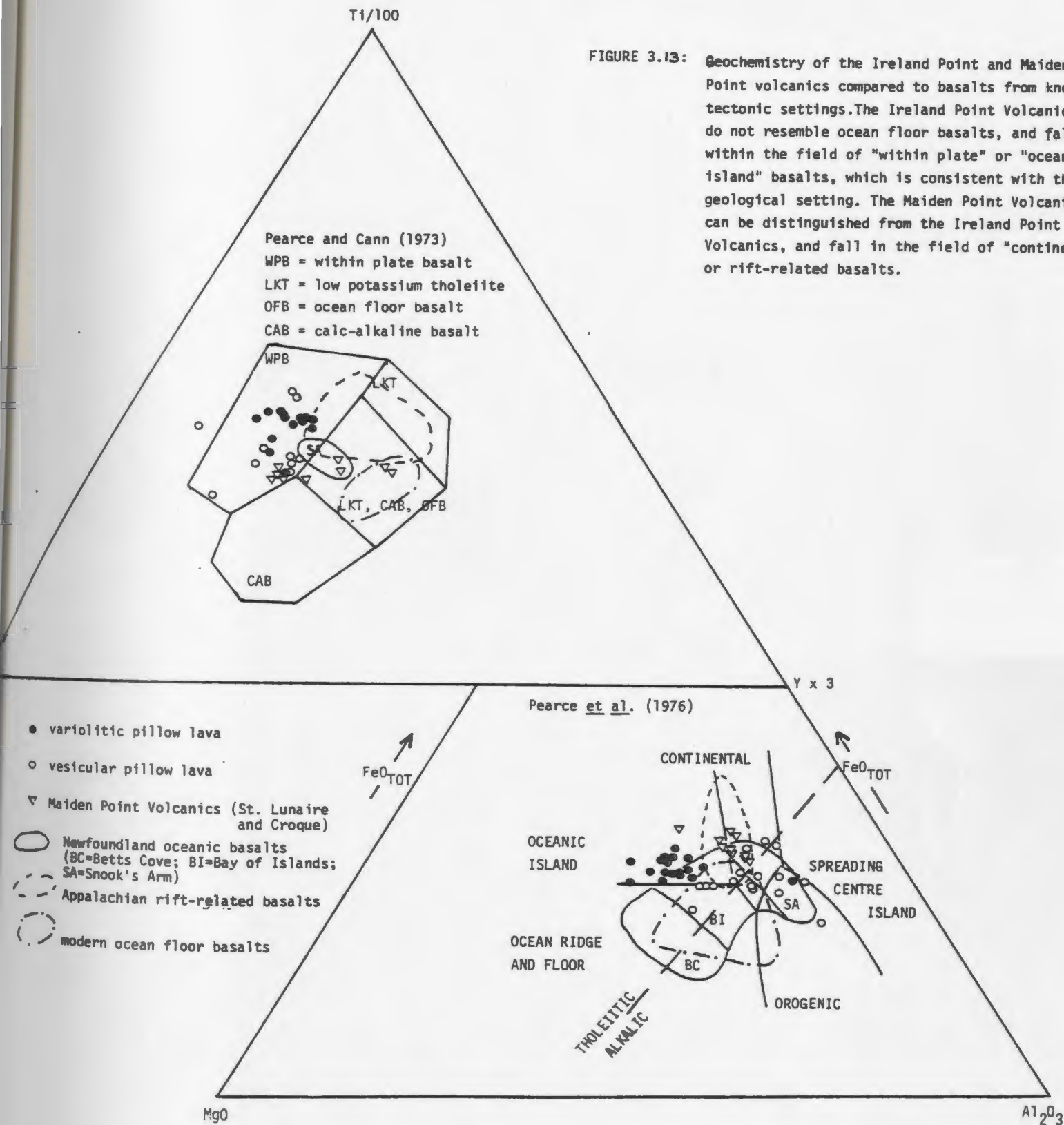
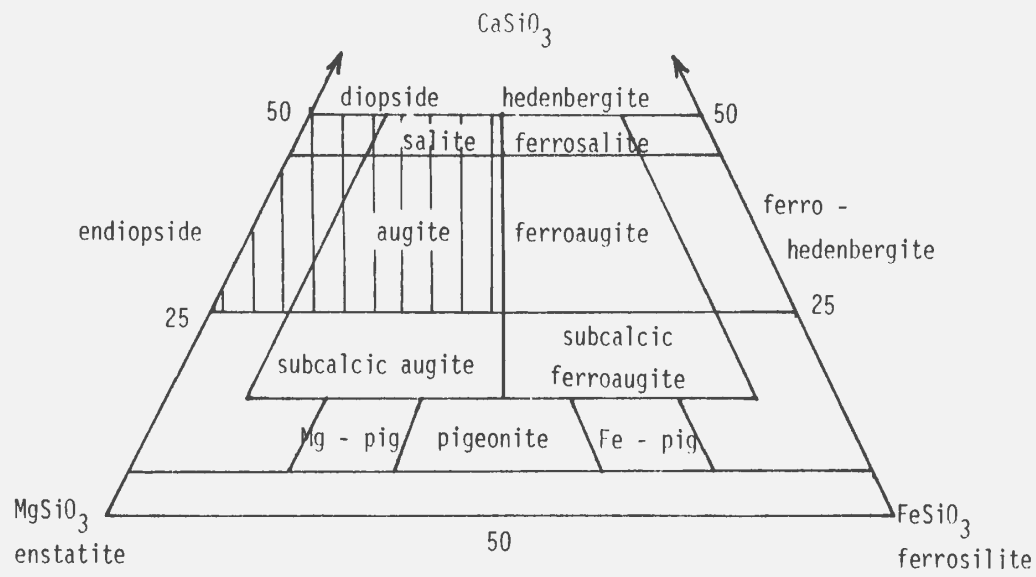
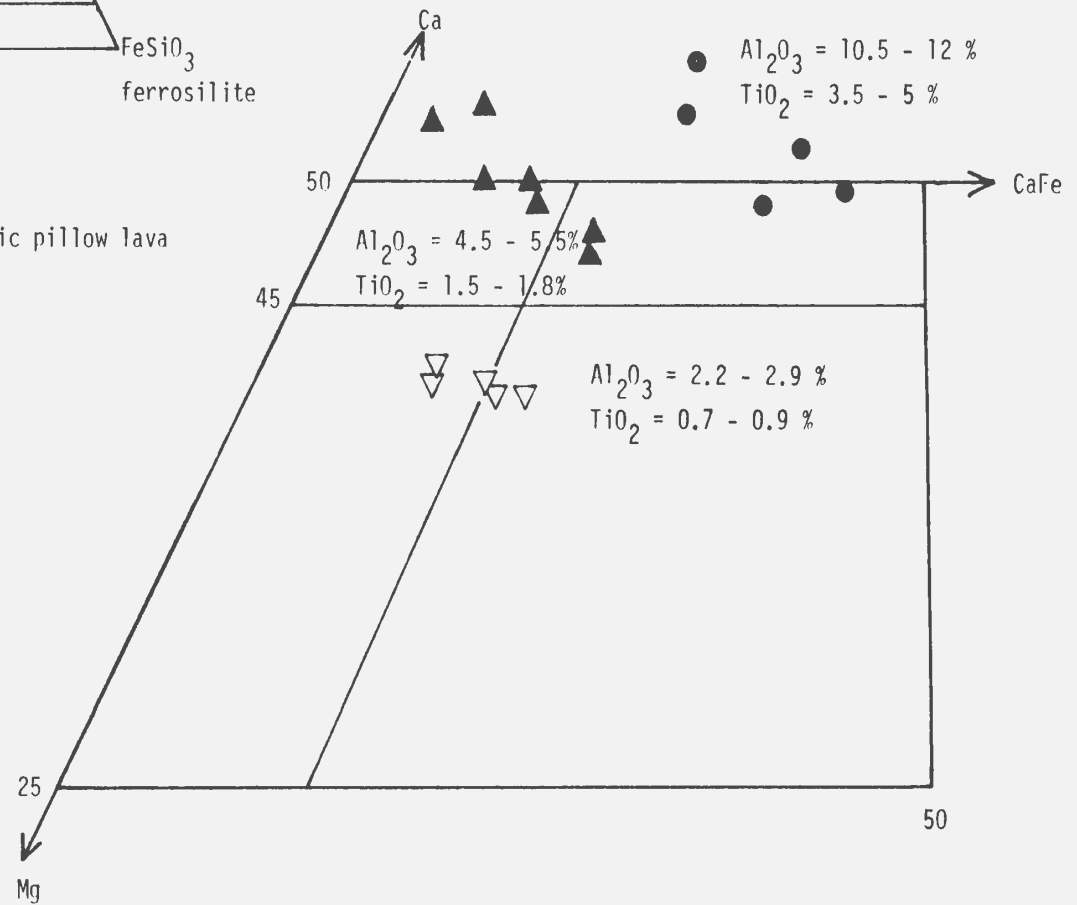


FIGURE 3.13: Geochemistry of the Ireland Point and Maiden Point volcanics compared to basalts from known tectonic settings. The Ireland Point Volcanics do not resemble ocean floor basalts, and fall within the field of "within plate" or "oceanic island" basalts, which is consistent with their geological setting. The Maiden Point Volcanics can be distinguished from the Ireland Point Volcanics, and fall in the field of "continental" or rift-related basalts.



- Ireland Point and Cape Onion variolitic pillow lava
- ▲ Partridge Point gabbro
- ▽ Croque Harbour volcanics

FIGURE 3.14: Clinopyroxene compositions from the Ireland Point Volcanics and related rocks compared to those from the Croque Harbour volcanics, near the base of the Maiden Point Slice.



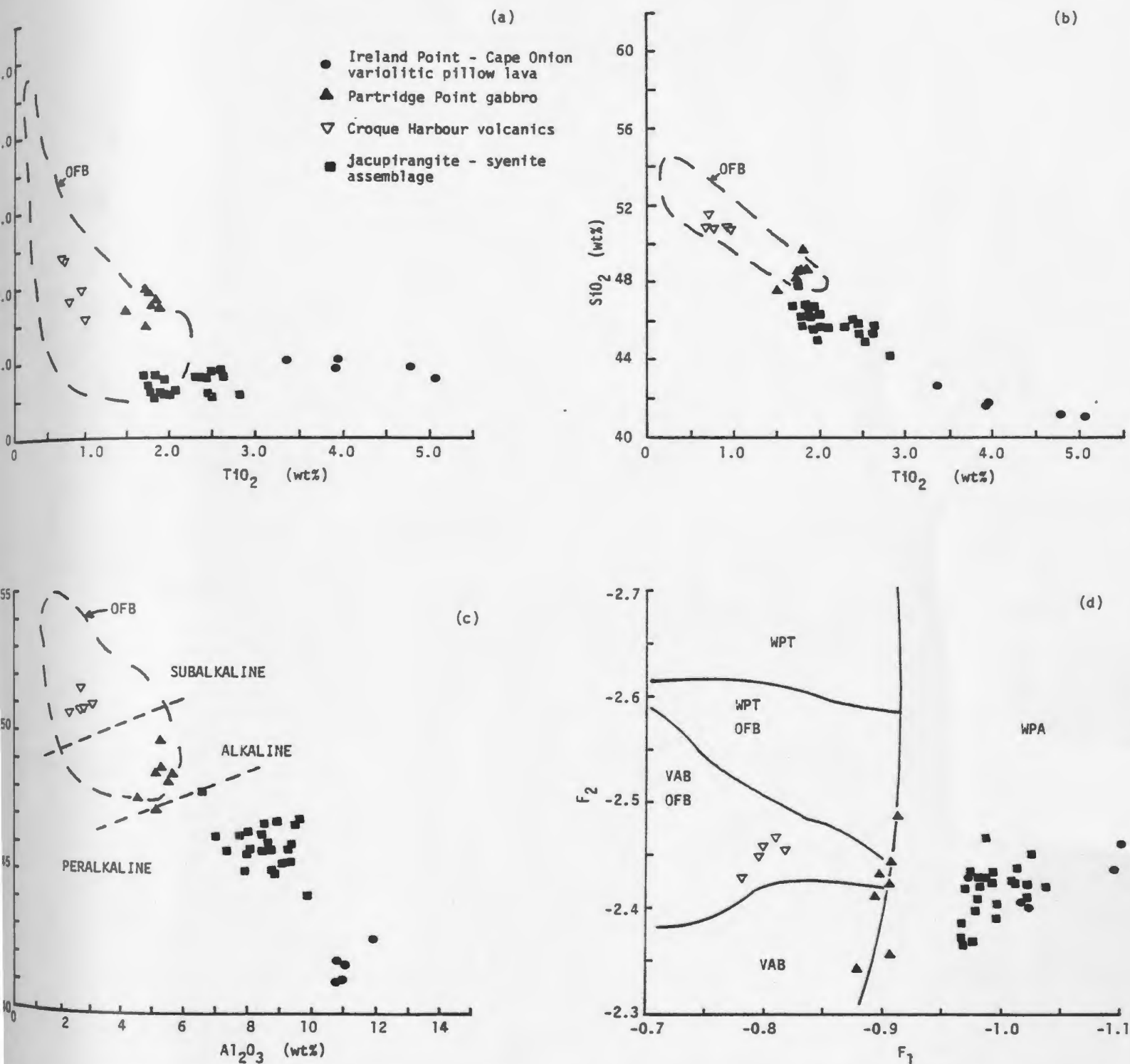


FIGURE 3.15: Compositions of clinopyroxenes from the variolitic pillow lavas, related gabbros, alkaline ultramafic rocks of the Jacupirangite - syenite assemblage, and the Croque Harbour volcanics from the base of the Maiden Point Slice plotted in the variation diagrams of LeBas (1962) (c) and Nisbet and Pearce (1977) (a,b,d).

OFB = ocean floor basalt; WPA = within plate alkaline; WPT = within plate tholeiite; VAB = volcanic arc basalt

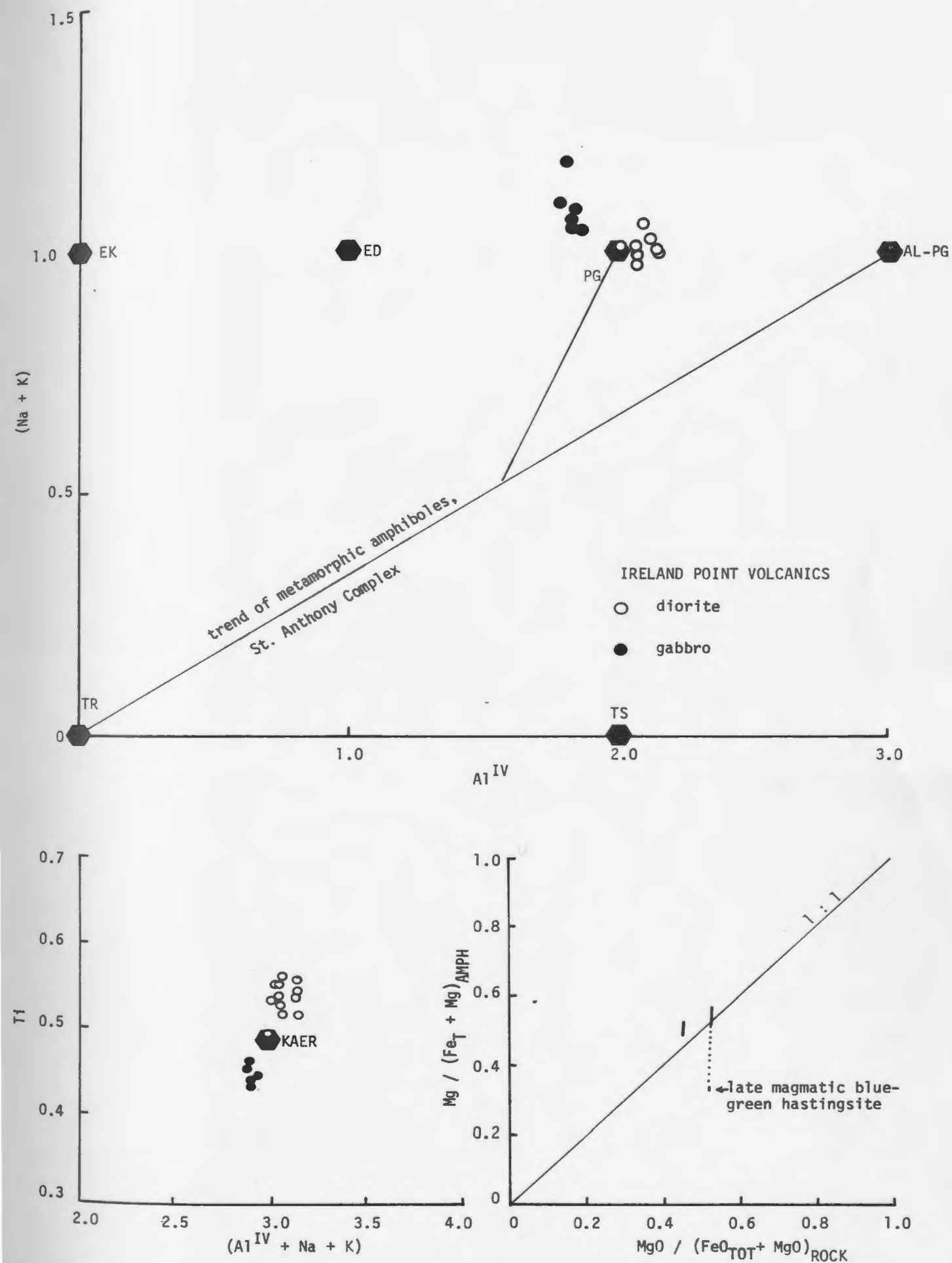


FIGURE 3.16: Amphibole chemistry of the Ireland Point Volcanics, showing enrichment in Ti, Al, Na, and K in the magmatic kaersutites compared to the trend of metamorphic amphiboles in the St. Anthony Complex.

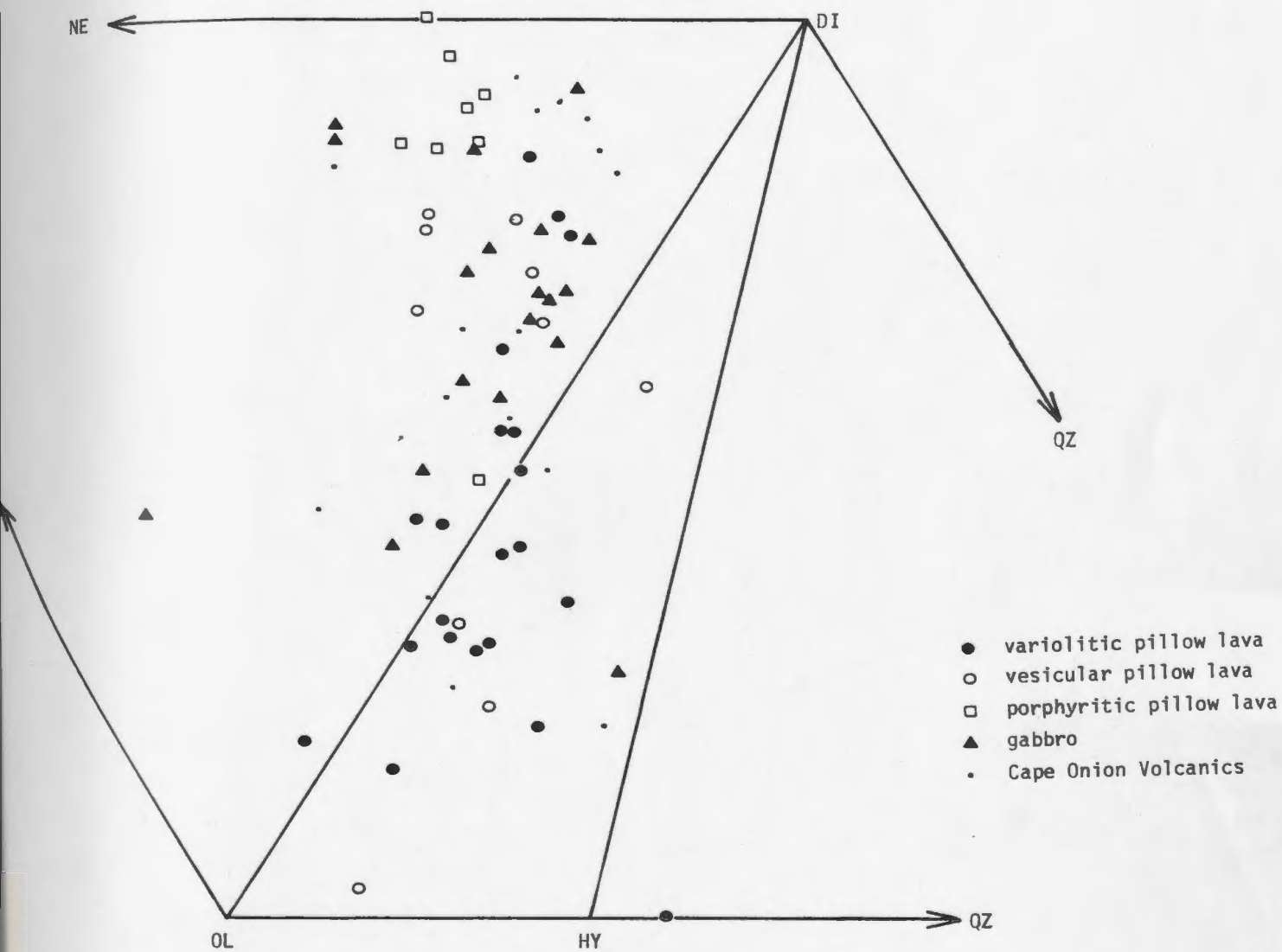


FIGURE 3.17: Compositions of the Ireland Point Volcanics and related rocks projected from plagioclase in the basalt tetrahedron (Fe_2O_3 reduced to 1.5%).

Table 3.3. Crystallization sequence in the Ireland Point Volcanics. Earliest-formed phases are in capitals; apatite is a common accessory.

Variolitic pillow lavas	OL + tiaug OL + tiaug + kaer
Massive flows	TIAUG + kaer + plag
Gabbros	ILM(?) + TIAUG + kaer + plag KAER + plag
Vesicular pillow lavas	PLAG
Porphyritic pillow lavas (cumulates)	PLAG + cpx + ol

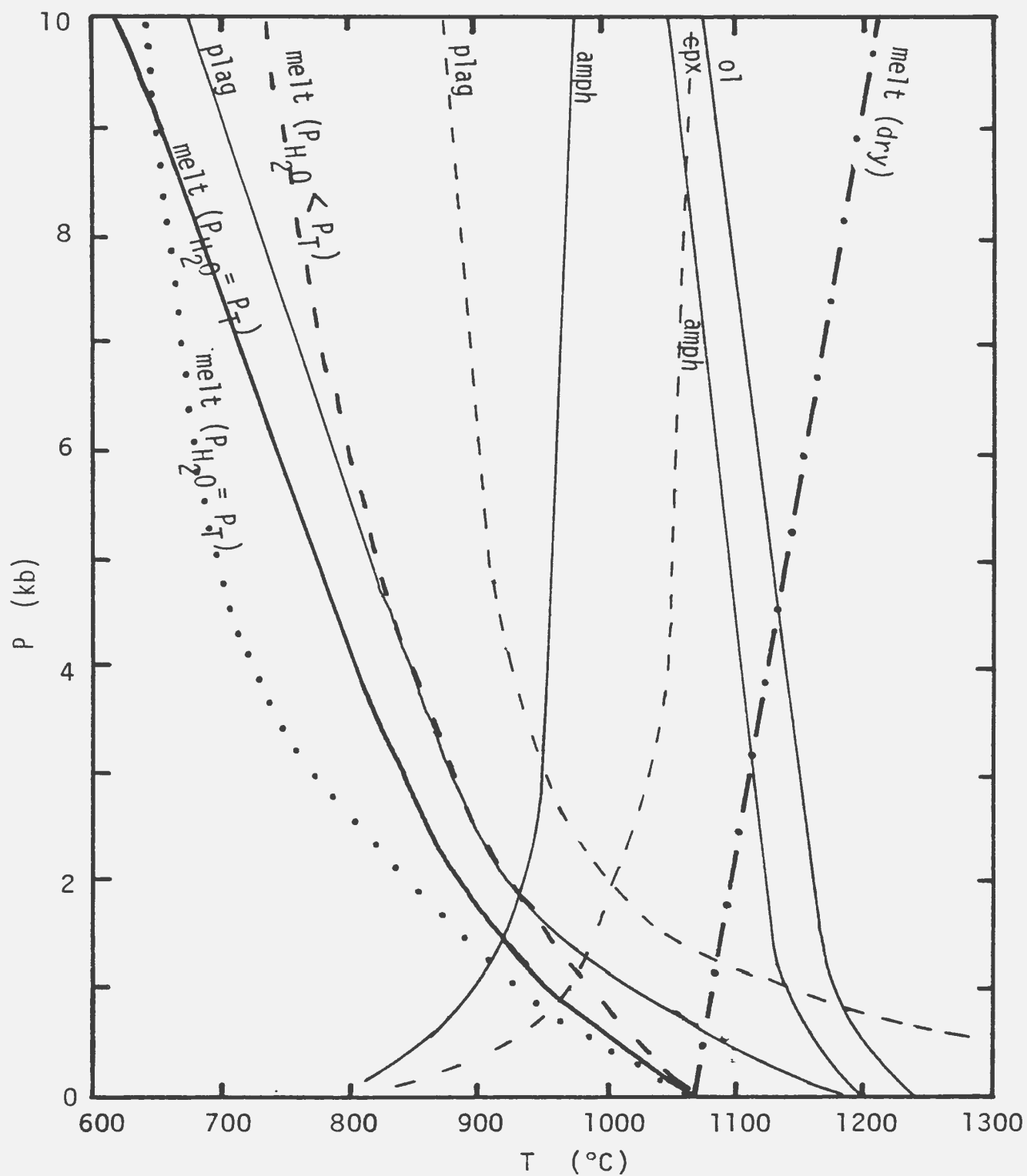


FIGURE 3.18: Phase relations in the system basalt - H₂O. Solid lines from Yoder and Tilley (1962). Dashed lines from Holloway and Burnham (1972). Dotted line from Tuthill (1968).

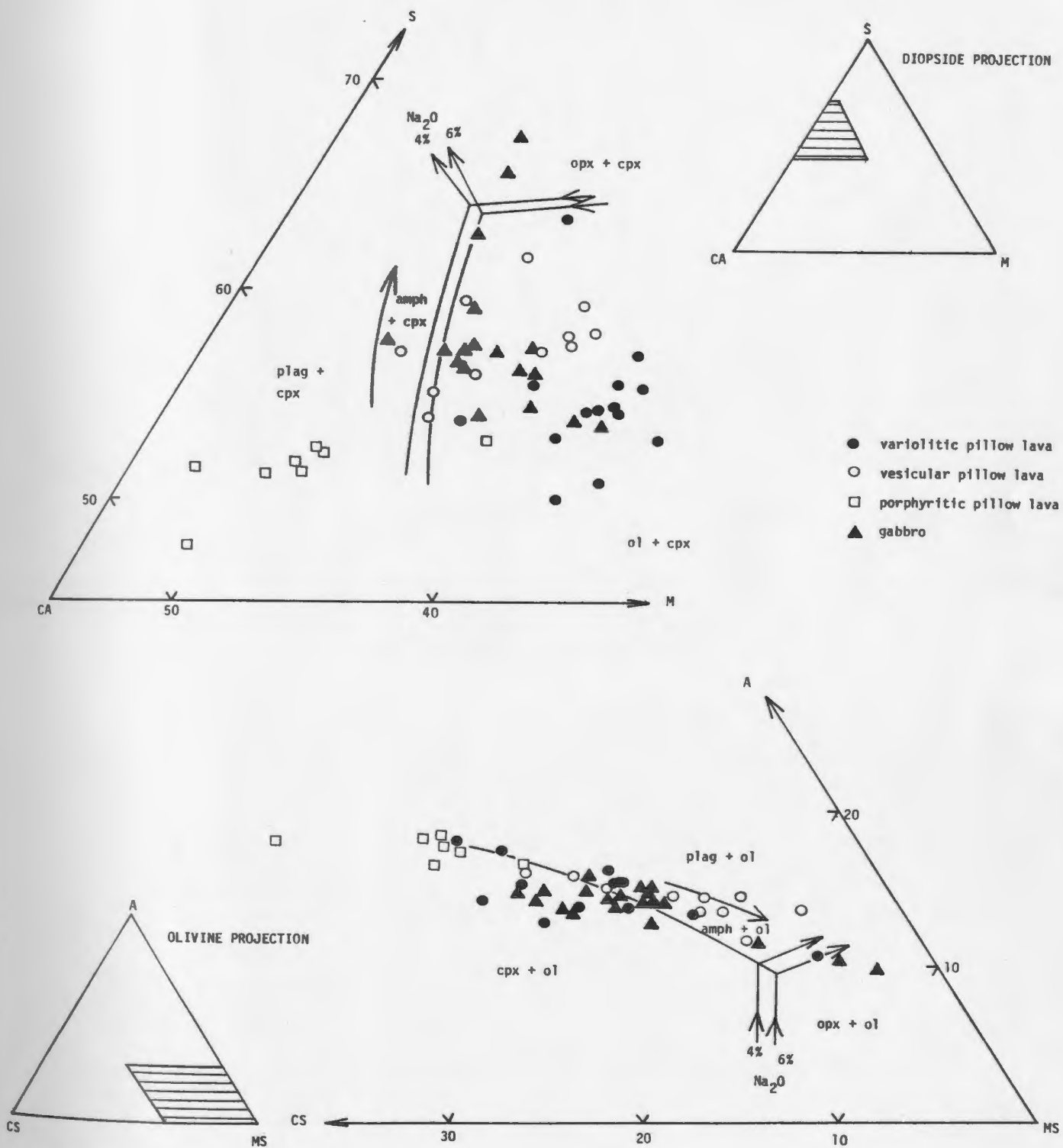


FIGURE 3.19: Projections into the system $\text{CaO} - \text{MgO} - \text{Al}_2\text{O}_3 - \text{SiO}_2 - \text{Na}_2\text{O} - \text{H}_2\text{O}$ from Na_2O , H_2O , olivine, and diopside, showing the phase relations for 5 kb $P_{\text{H}_2\text{O}}$ (after Cawthorn and O'Hara, 1976) and the compositions of the Ireland Point Volcanics.

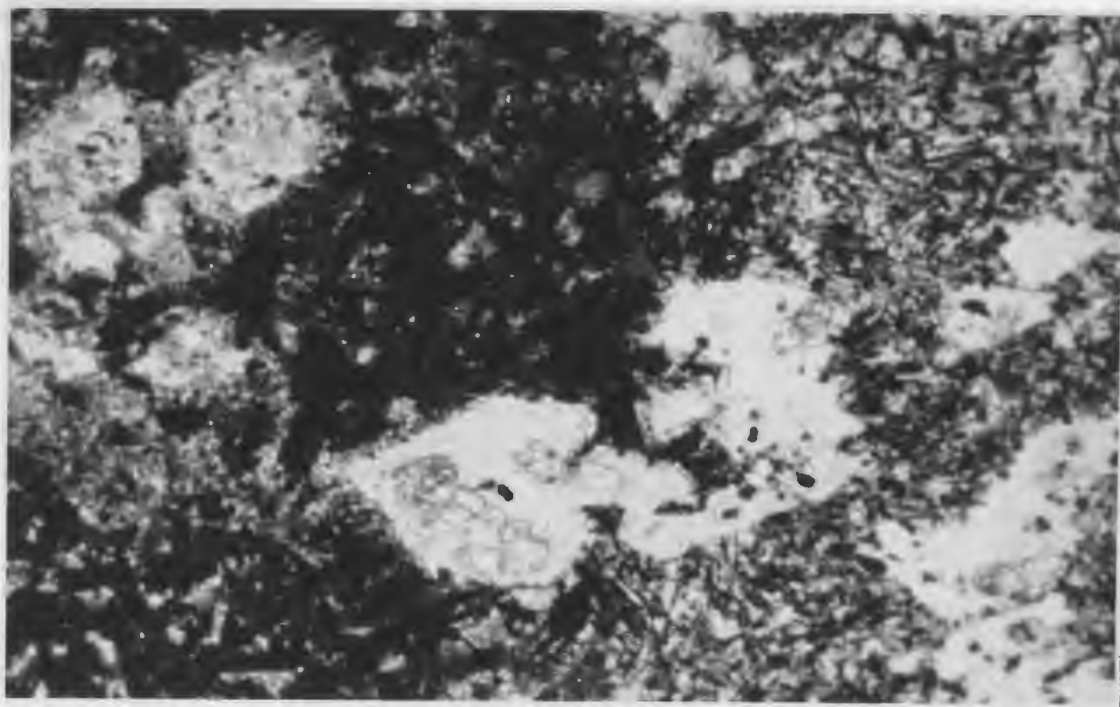


FIGURE 3.20: RJ76-542: Variolitic pillow lava showing penetration of olivine crystal from matrix into variole without obvious effect on the variole boundary. Olivine crystal at centre is 1 mm long.

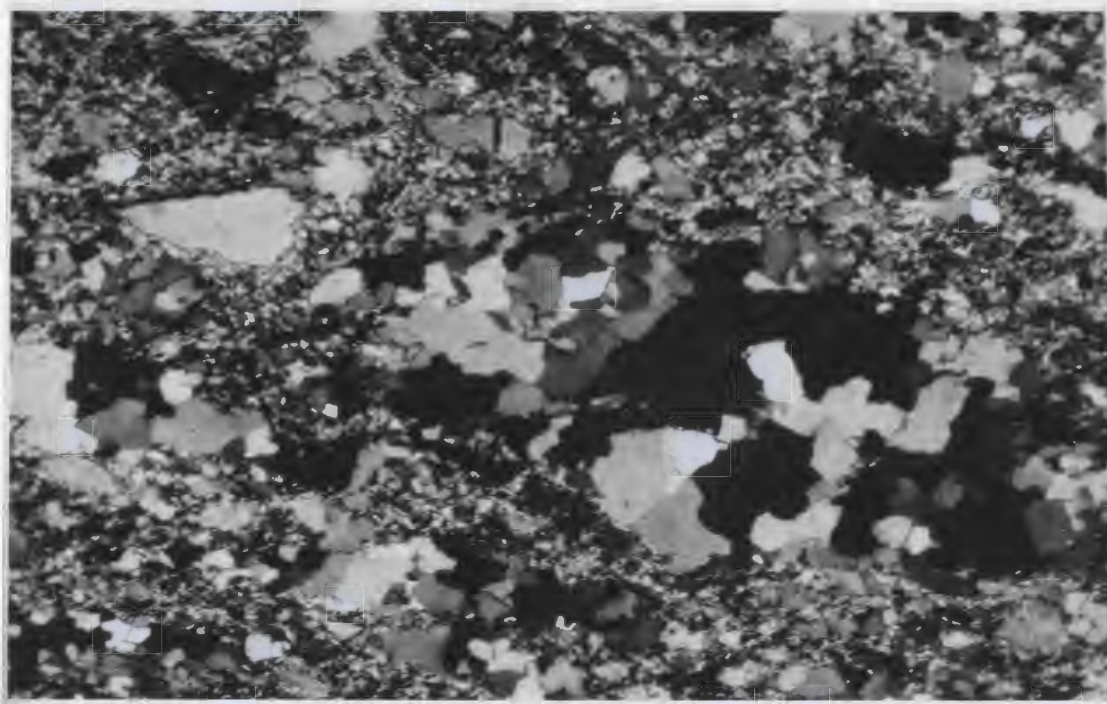


FIGURE 3.21: RJ75-221. Quartz aggregate after detrital quartz grain, psammite. Width of field is about 2 mm.

Table 3.4. Petrography of Goose Cove Schist Metasediments.

LITHOLOGY	MINERALOGY	FABRIC
1) METASEDIMENTS		
1a) Psammite and semi-pelite 472 FIG. 3.21, 3.22	qz (25-50%); plag (10-25%); mus (5-25%); bt (0-25%); chl (3-20%); gnt (0-2%); ox (1-10%); ep (0-15%) chl + ms → bt + gnt	S ₁ approximately parallel to compositional layering; isoclinal; F ₁ rarely visible in semi-pelites; compositional layering (qz/mus/ep + chl) detrital qz → lensoidal aggregates of smaller, sutured grains → more regular grains with undulose Xn.
1b) Pelite 066, 433	qz (15-30%); plag (0-10%); mus (45-55%); chl (5-20%); bt (0-15%); op (5-10%); ep (0-10%); Ksp? (0-5%); gnt (0-2%) chl + ms → bt + gnt	compositional layering (qz/mica/chl) S ₁ (mica/chl/flattened qz, fd aggregates / op needles) axial planar to isoclinal F ₁ which folds compositional layering; resulting S ₁ nearly parallel to compositional layering; S ₁ crenulated. qz-small grains, sutured grain boundaries, may be strongly flattened in fold limbs. gnt-small, euhedral, centred on mt.
1c) Garnetiferous Chert 441, 443 FIG. 3.23.	qz (40%); mt (30%); spess (5-15%); mus (0-15%); ab (4-10%); cc (0-10%); chl (0-15%)	compositional layering (mt+gnt+chl/qz + fd); isoclinally folded by F ₁ ; S ₁ (chl + ms / elongated qz-fd aggregates) nearly parallel to layering gnt-euhedral; round, sigmoidal spiral straight inclusion trails; qz - highly sutured grain boundaries → straighter at higher grades.
1d) Calc-silicate	cc (20-50%); ep (30-60%); qz (5-20%); mus (5-20%); act (0-10%); chl (5-15%)	compositional layering (cc/ep/qz) S ₁ (mus, act, chl) may be tightly folded (F ₁). small, euhedral, zoned ep in cc-rich matrix. ep locally grows perpendicular to margins of folded layers.

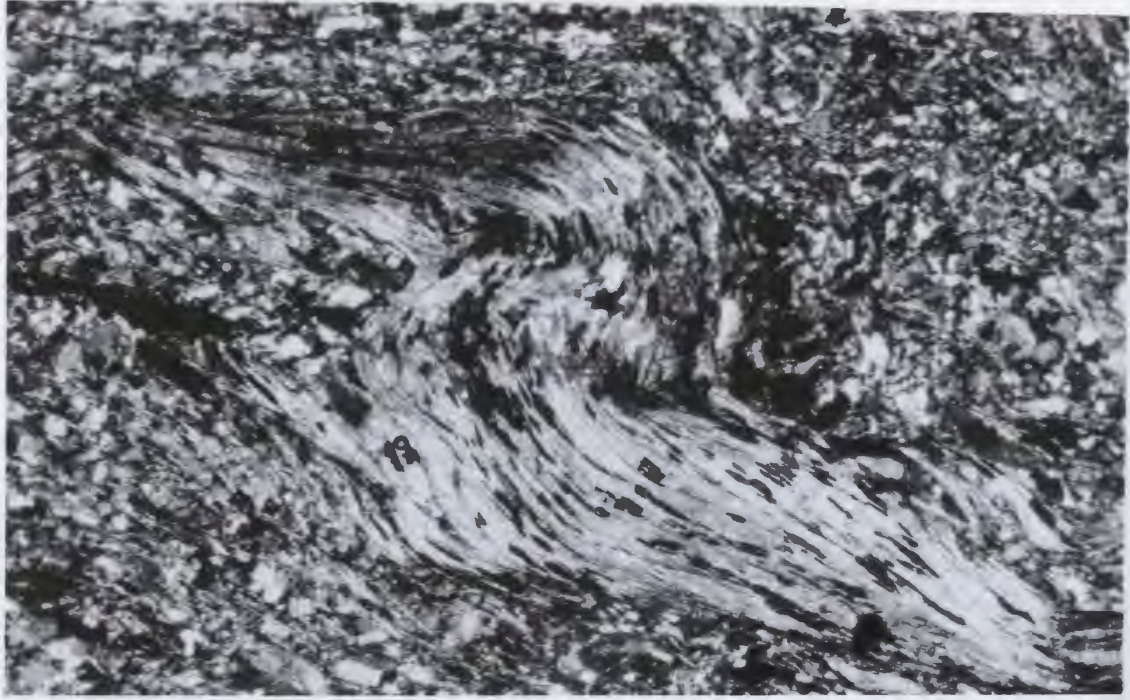


FIGURE 3.22: RJ75-097. Small F_2 fold defined by muscovite in semi-pelitic schist, Goose Cove. Width of field is 2.5 mm.

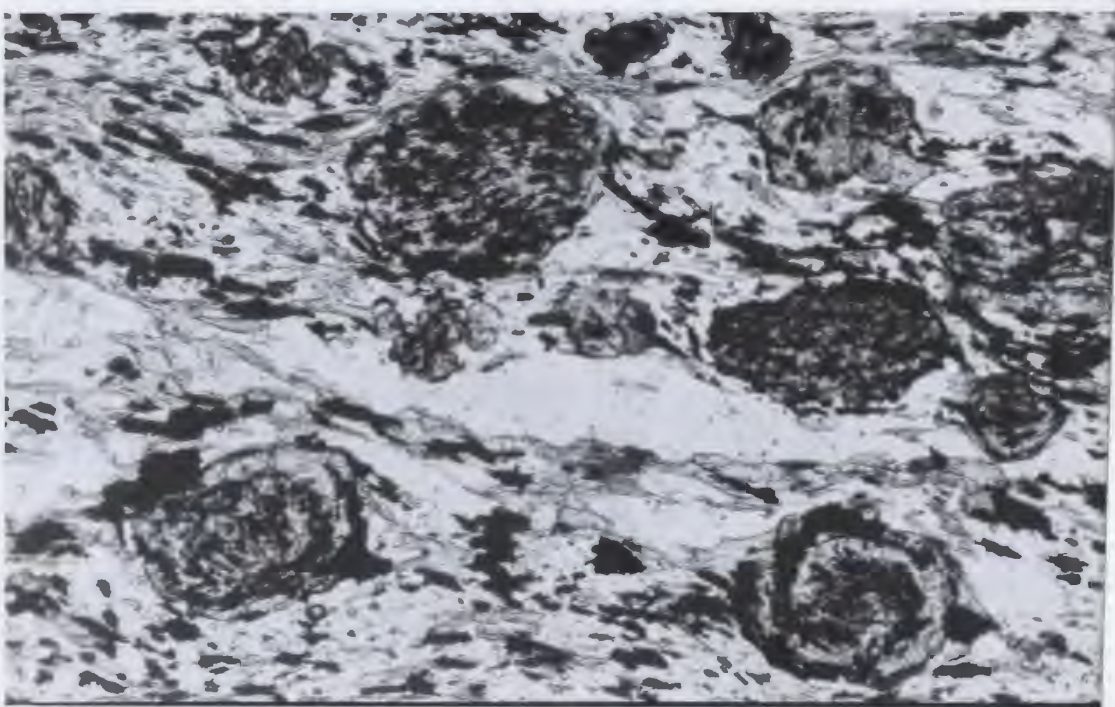


FIGURE 3.23: RJ76-443. Rotated garnets in ferruginous metachert, Fischot Islands. Largest garnet is about 0.1 mm in diameter.

Table 3.5. Petrography of the Goose Cove Schist metabasites.

LITHOLOGY	MINERALOGY	TEXTURE
2) METABASITES		
2a) Massive 004, 042, 060, 062, 063, 179, 222, 292, 435 FIG. 3.24.	amph (35-50%); ab (10-25%); chl (2-20%); ep (15-30%); qz (< 2%); mus (0-3%); sph (0-3%); ox (0-1%) <u>Pleochroism:</u> <u>amph</u> X = pale yellow; Y = pale green; Z = pale blue-green; chl → hb	S ₁ (amph, chl) weak coarse-grained amphib, patchily zoned, with acicular overgrowths (of same composition) (after cpx?) interstitial granular ab, chl, ep, acicular amphib relict diabasic texture: amphib (after cpx?) intergrown with ab + sauss (after plag)
2b) Banded 009, 026, 029, 103, 108, 112, 151, 171, 186, 298, 300, 414, 417, 439 FIG. 3.26.	act + hb (45-65%); ep (5-35%); plag (10-30%); chl (2-15%); cc (0-2%); qz (0-2%); op (0-1%); sph (0-1%) <u>Pleochroism:</u> <u>hb</u> X = yellow; Y = Z = blue-green act + chl → hb	compositional layering (metamorphic) (ep/amph) S ₁ strong, parallel layering; F ₂ sub-similar, strongly asymmetrical; S ₂ rarely developed by transposition of S ₁ in F ₂ axial planes; very fine grained
2c) Spotted 007, 020, 033, 100, 164, 184, 196, 296, 436, 530 FIG. 3.25.	<u>Matrix:</u> act + hb (35-50%); sodic plag (5-20%); ep (25-40%); cc (1-10%); chl (2-20%); mus (0-2%); sph (0-2%); ox (0-1%) <u>"Porphyroclasts"</u> (10-50% of rock): cc, ab, mus, ep	S ₁ weak to strong (act/chl/elongated porphyro- clasts); porphyroclasts - originally plag phenocrysts, now fine-grained aggregates of secondary minerals, broken, rotated, and flattened in plane of S ₁ ; elongations of 20:1; in schistose, fine-grained matrix
2d) Epidote Amphibolite 085, 088, 089, 090, 133, 143, 440, 475, 569 FIG. 3.27.	hb (50-70%); plag (10-25%); ep (10-25%); bt (0-5%); qz (2-10%); sph (0-3%); ox (0-2%); mus (0-1%); ep + act + ab ⇌ hb + Ca-plag <u>Pleochroism:</u> <u>hb</u> X = yellow; Y = dark green; Z = dark green to blue-green	compositional layering - coarse-grained bands containing ep + act + ab in medium-grained matrix of hb + plag + qz + ep. S ₁ strong, parallel layering. F ₂ tight recumbent to isoclinal, folding S ₁ , layering. Mb contains abundant inclusions of qz, sph.



FIGURE 3.24: RJ75-042. Massive greenschist showing relict diabasic texture, with saussuritized plagioclase (dark laths) surrounded by actinolitic hornblende (after clinopyroxene). Width of field is 2 mm.



FIGURE 3.25: RJ75-117. Spotted greenschist showing elongated aggregates of epidote, calcite, and albite after plagioclase porphyroclasts, in a matrix of actinolitic hornblende. Width of field is 3.8 cm.



FIGURE 3.26: RJ75-010. Banded greenschist, with alternating epidote-rich and actinolite-rich bands defining S_1 , folded by F_2 . Width of field is 4 cm.

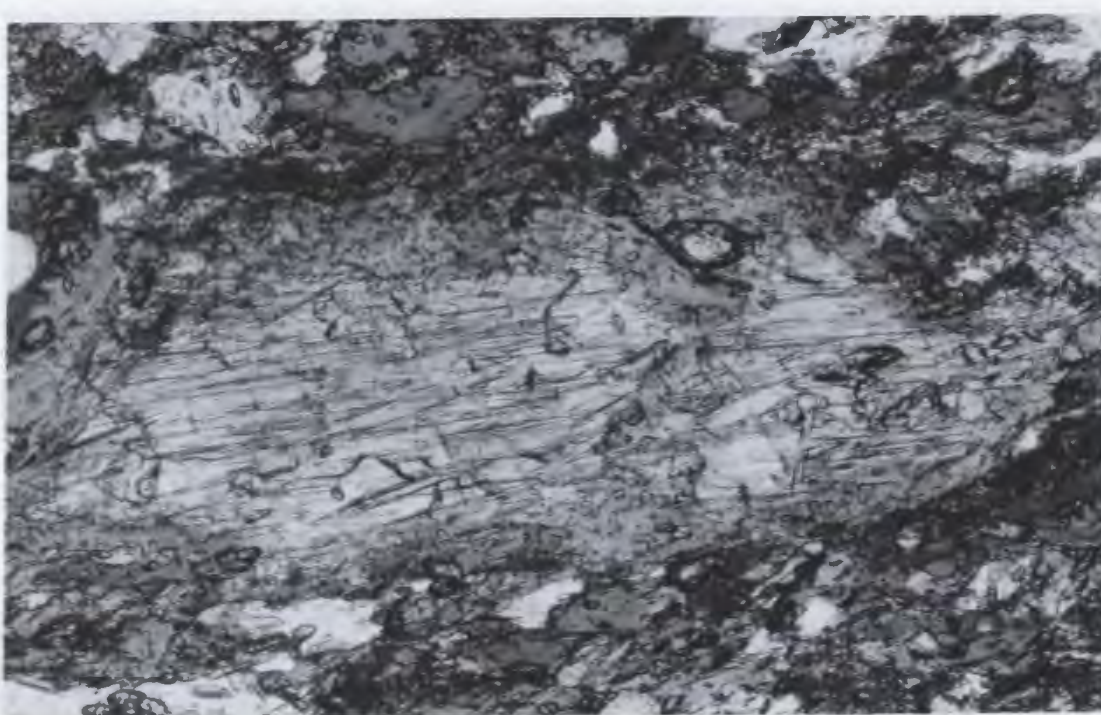


FIGURE 3.27: RJ75-086. Intergrowth of actinolite, epidote, and sodic plagioclase surrounded by green hornblende, in a matrix of hornblende, epidote, sphene, and oligoclase. Width of field is 0.8 mm.

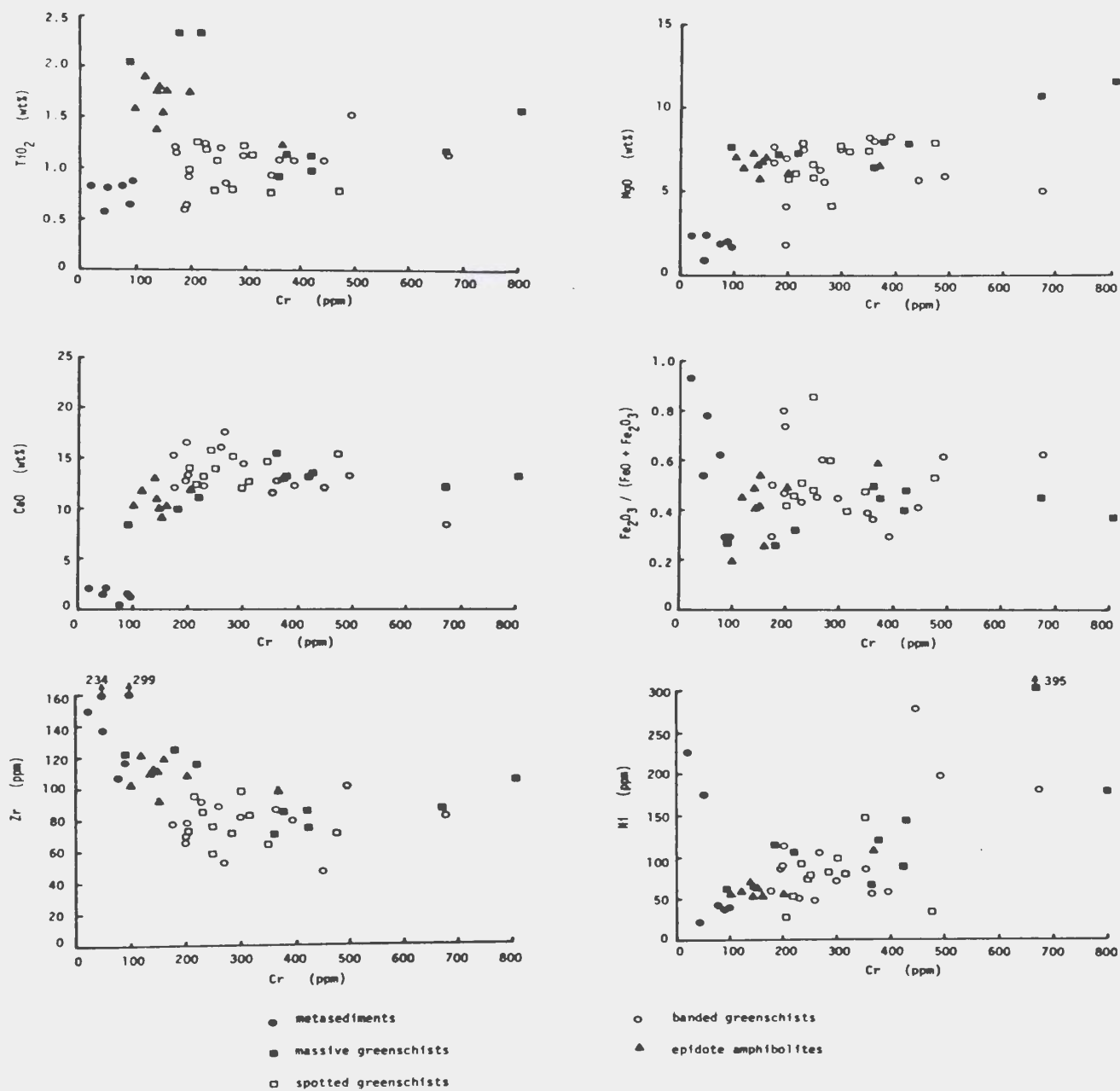


FIGURE 3.28: Geochemistry of the Goose Cove Schist, showing overall similarity of various types, with the exception of metasediments and epidote amphibolites (see also FIG. 3.29).

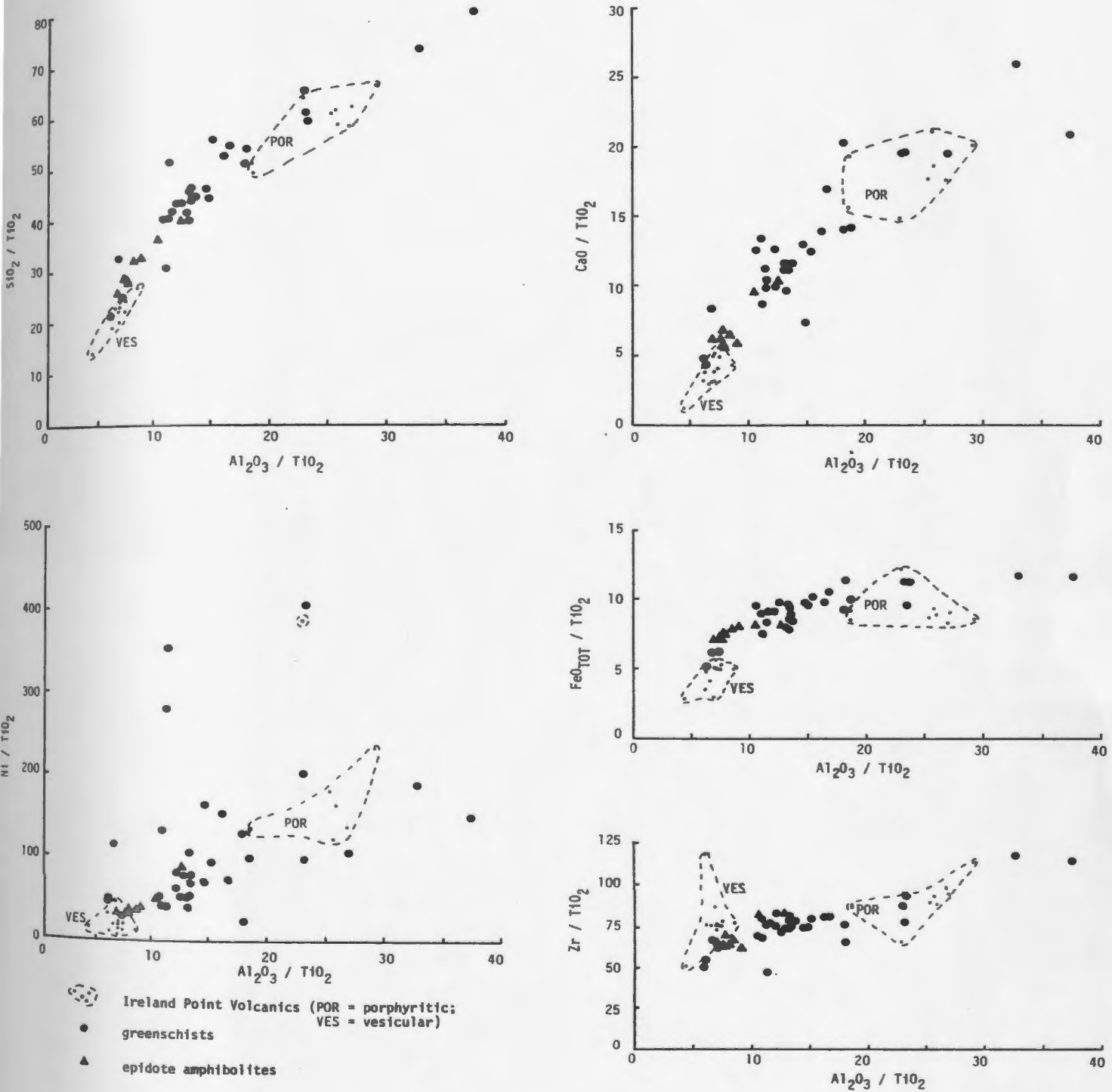


FIGURE 3.29: Geochemistry of the Goose Cove Schist in comparison to its probable protoliths, the vesicular and porphyritic pillow lavas of the Ireland Point Volcanics.

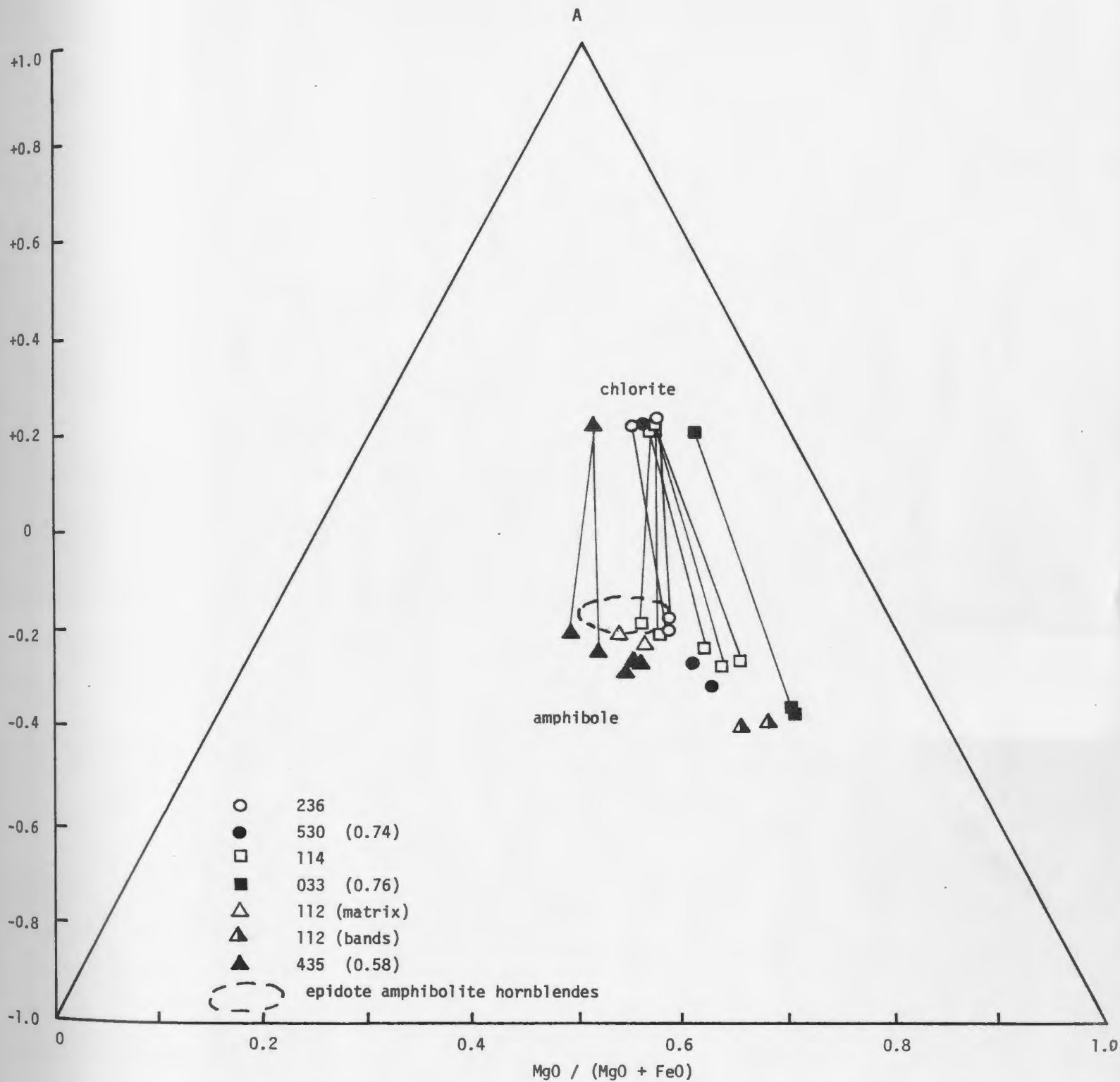
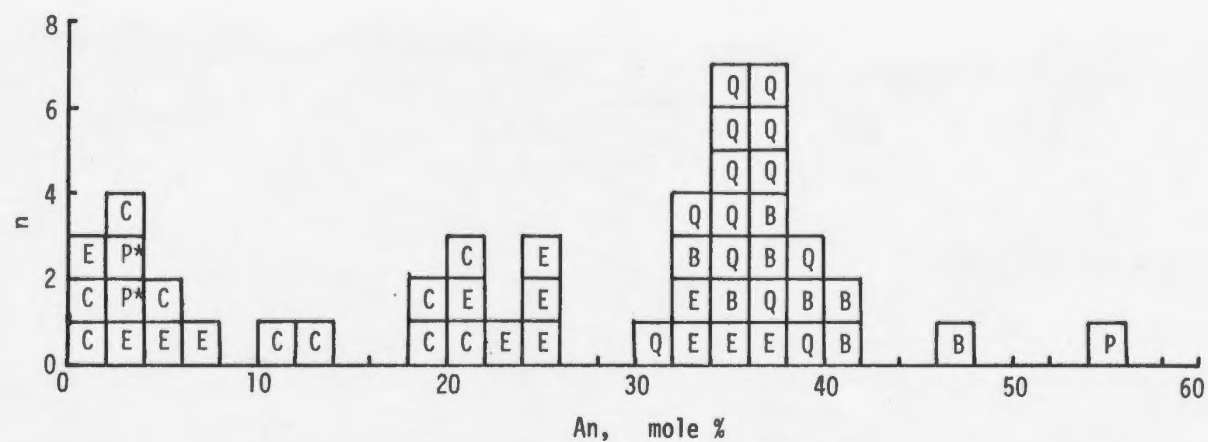


FIGURE 3.30: AFM projection from epidote (after Harte and Graham, 1975) showing trend of amphibole and chlorite compositions in the Goose Cove Schist. Numbers in brackets after sample numbers indicate whole rock $\text{MgO} / (\text{MgO} + \text{FeO})$, where known. Tie-lines join coexisting phases.

FIGURE 3.31: Plagioclase compositions from the Goose Cove Schist and Green Ridge Amphibolite.



C amph + plag + chl + ep
(435, 033, 530, 114, 236)

E hb + plag + ep
(086, 087, 089, 090, 133)

B hb + plag + bt + gnt
(083, 131, 477)

Q hb + plag + qz
(085, 130, 080, 451, 458)

P hb + plag (* retrograde)
(128, 504)

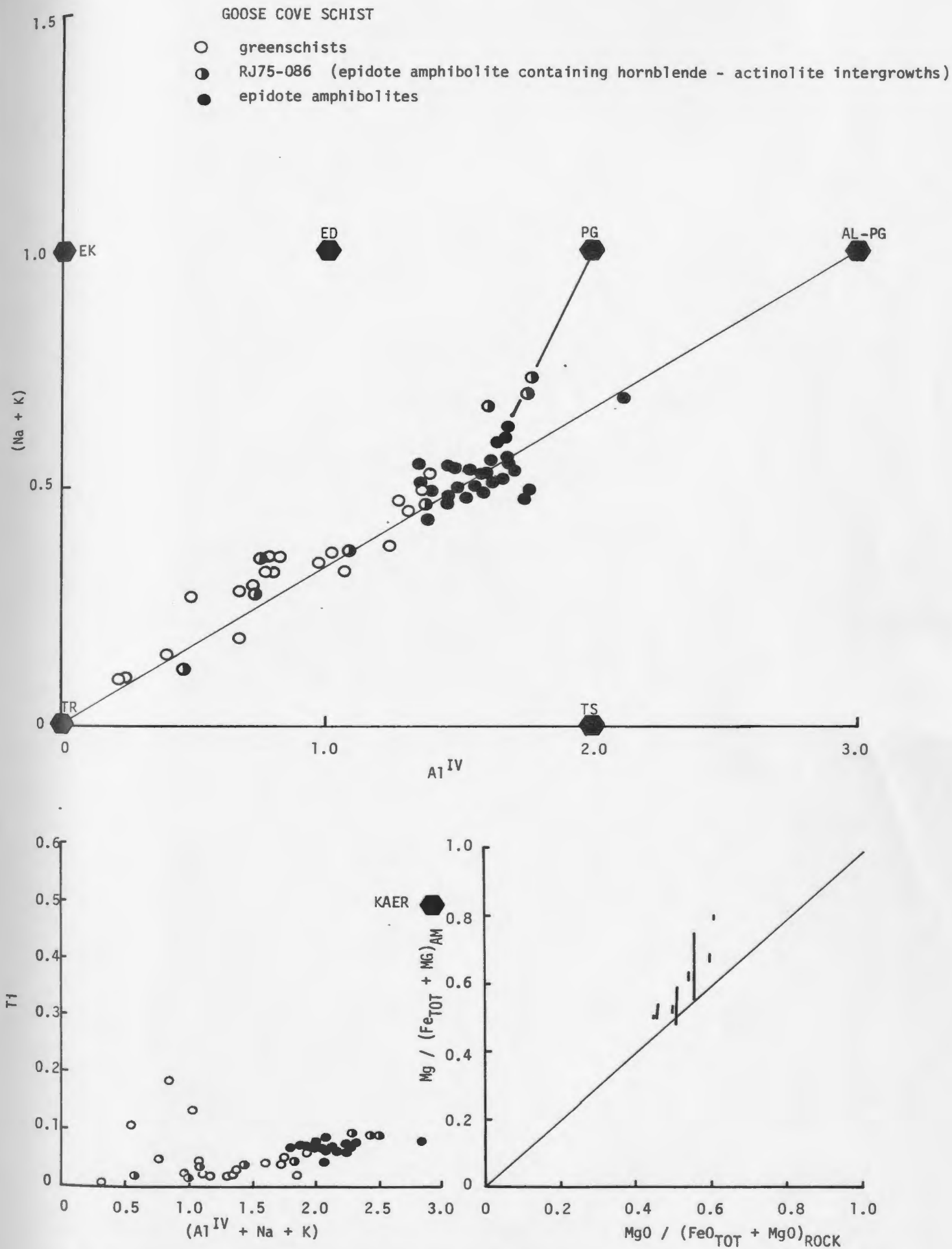


FIGURE 3.32: Compositions of amphiboles from the Goose Cove Schist, showing trend from actinolite to Al-pargasite, and generally low Ti.

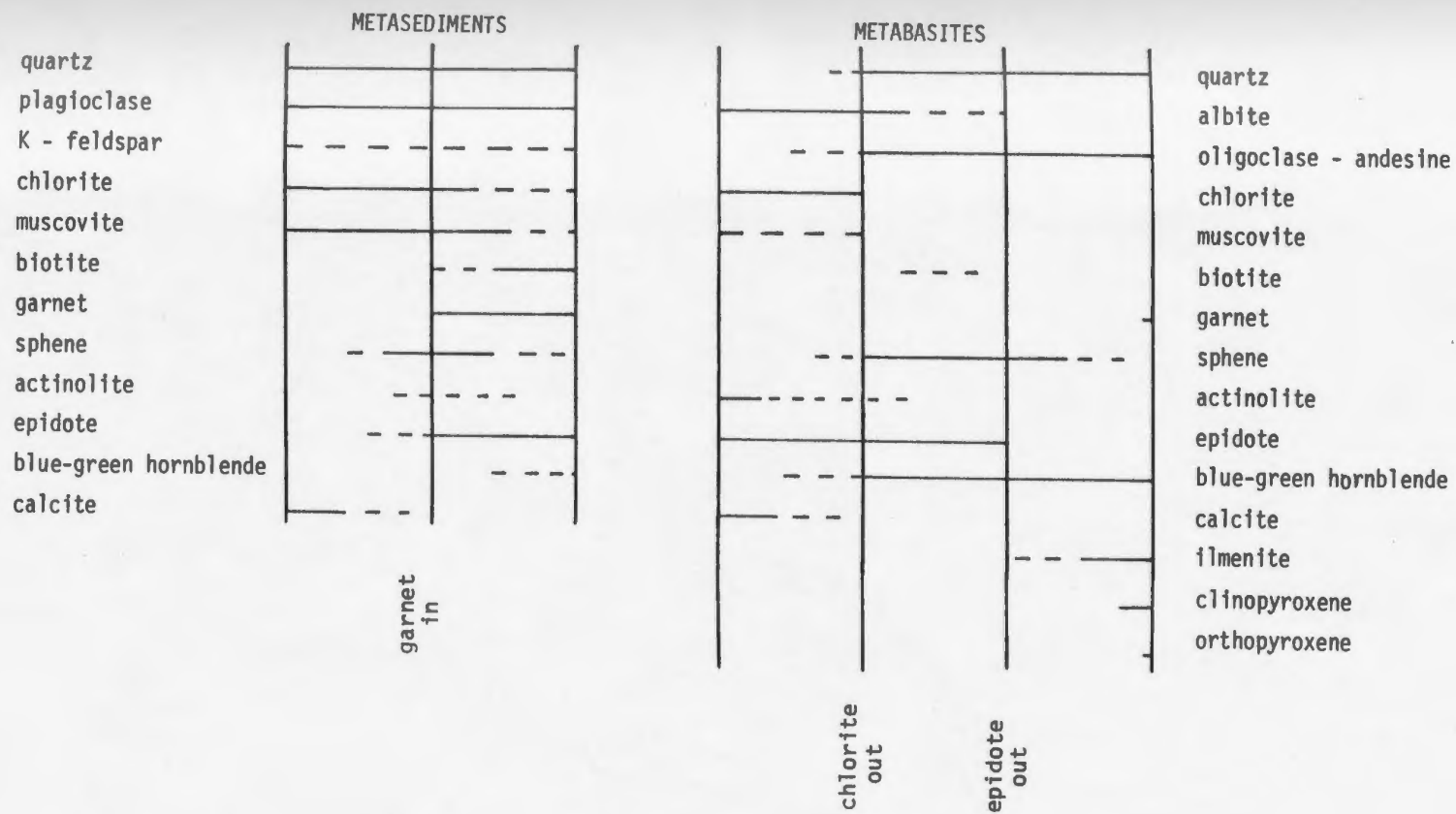


FIGURE 3.33: Mineral assemblages in the Goose Cove Schist and Green Ridge Amphibolite.

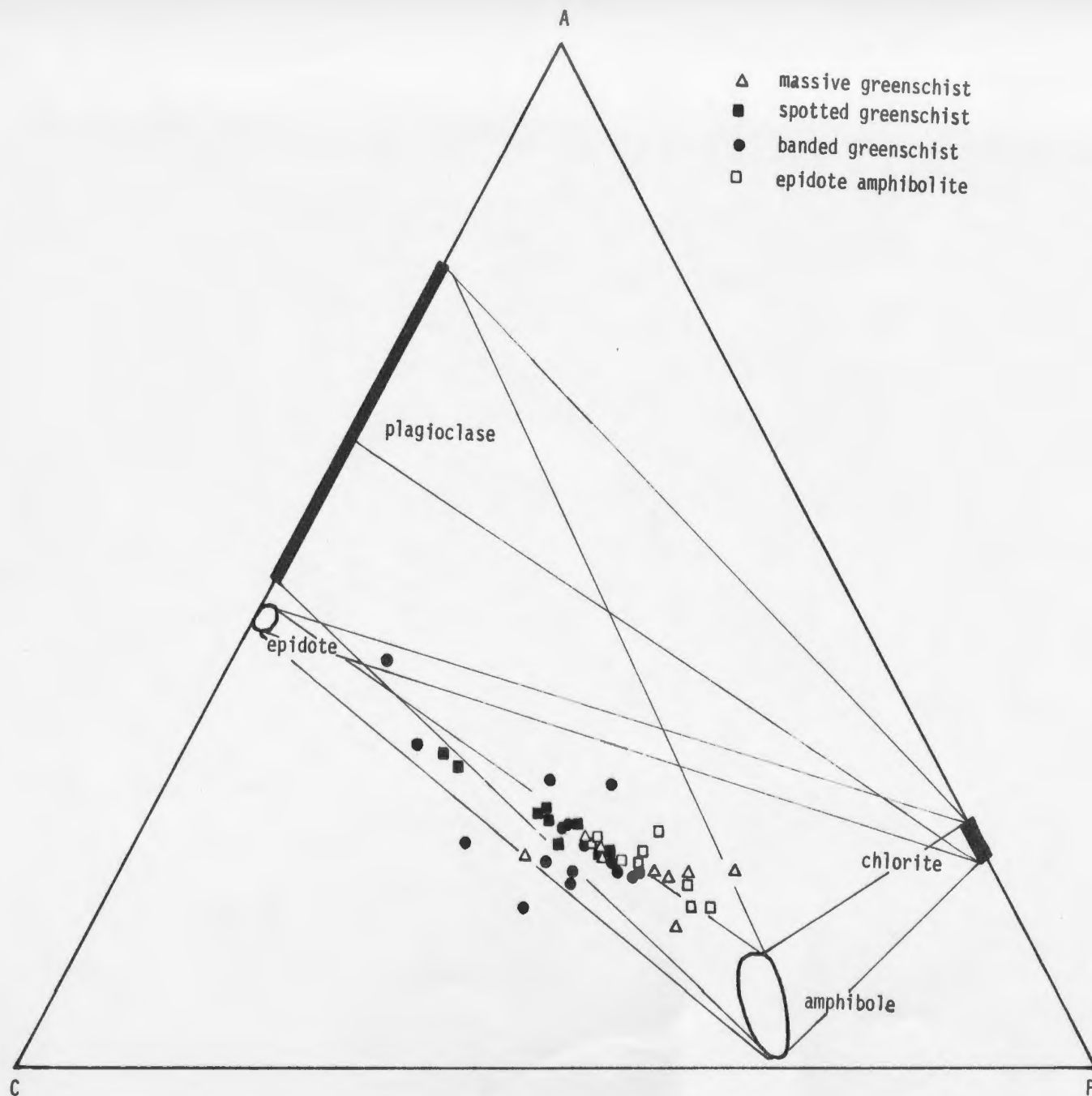


FIGURE 3.34: ACF diagram for the Goose Cove Schist, showing whole rock compositions and fields for analysed minerals.

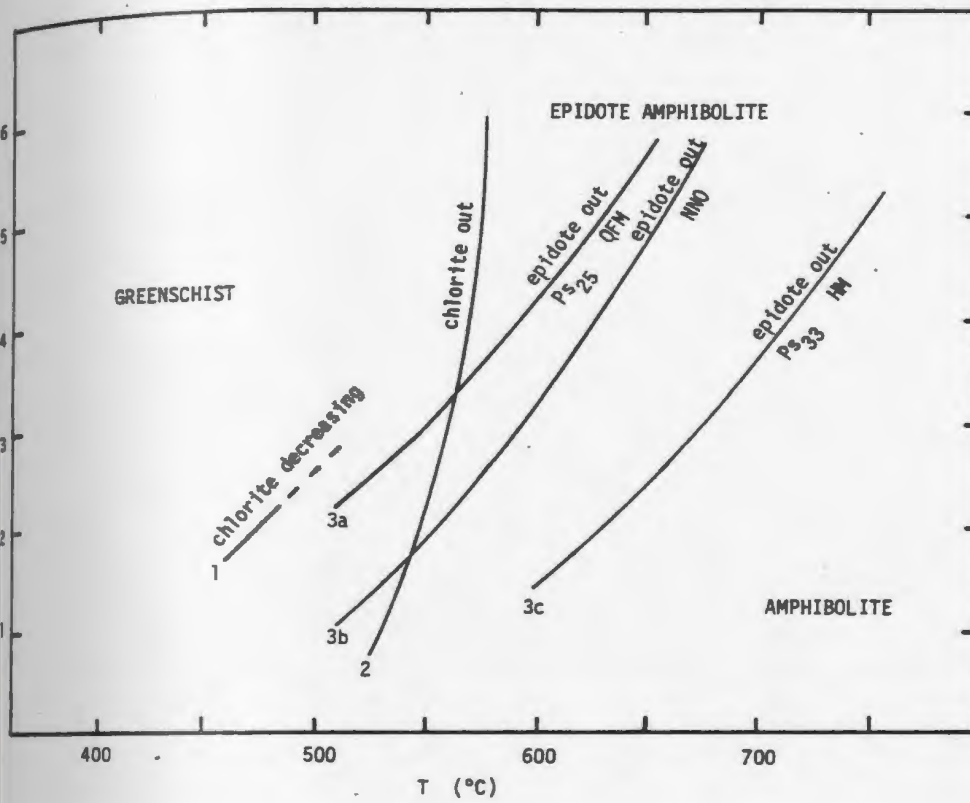


FIGURE 3.35a: Pressure-temperature relations for the greenschist to epidote amphibolite to amphibolite facies transition for different oxygen fugacities (after Liou, 1973; Liou *et al.*, 1974).

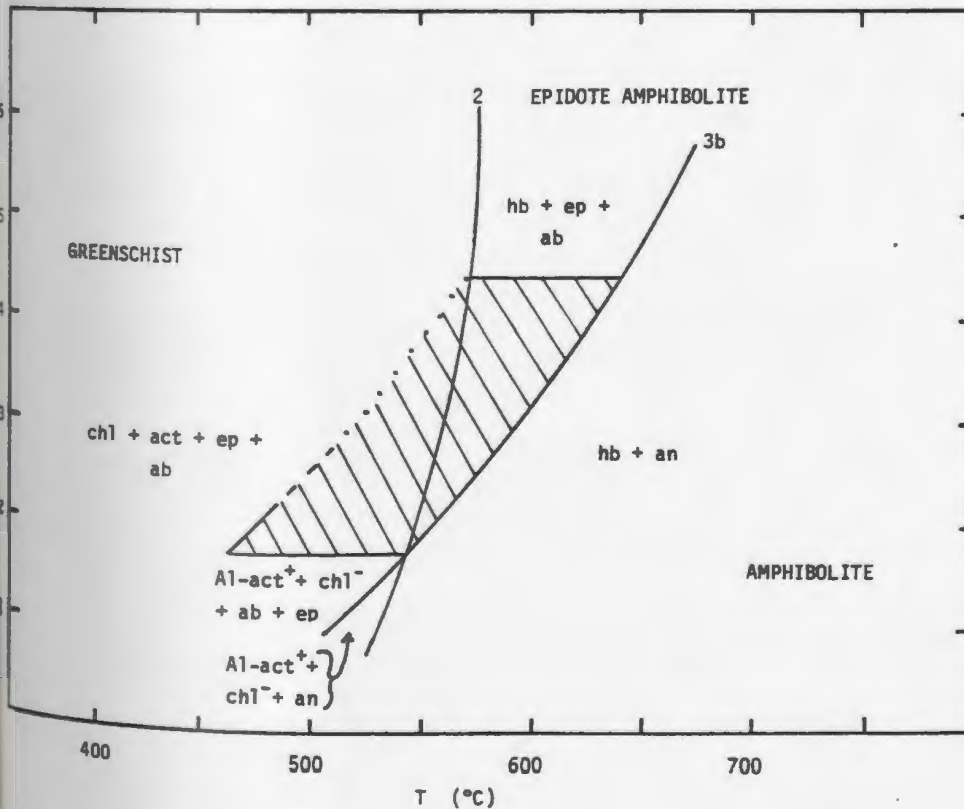


FIGURE 3.35b: Mineral assemblages in greenschist, epidote amphibolite, and amphibolite facies metabasites, for the NNO buffer. Shaded area indicates stability field of the Goose Cove Schist.

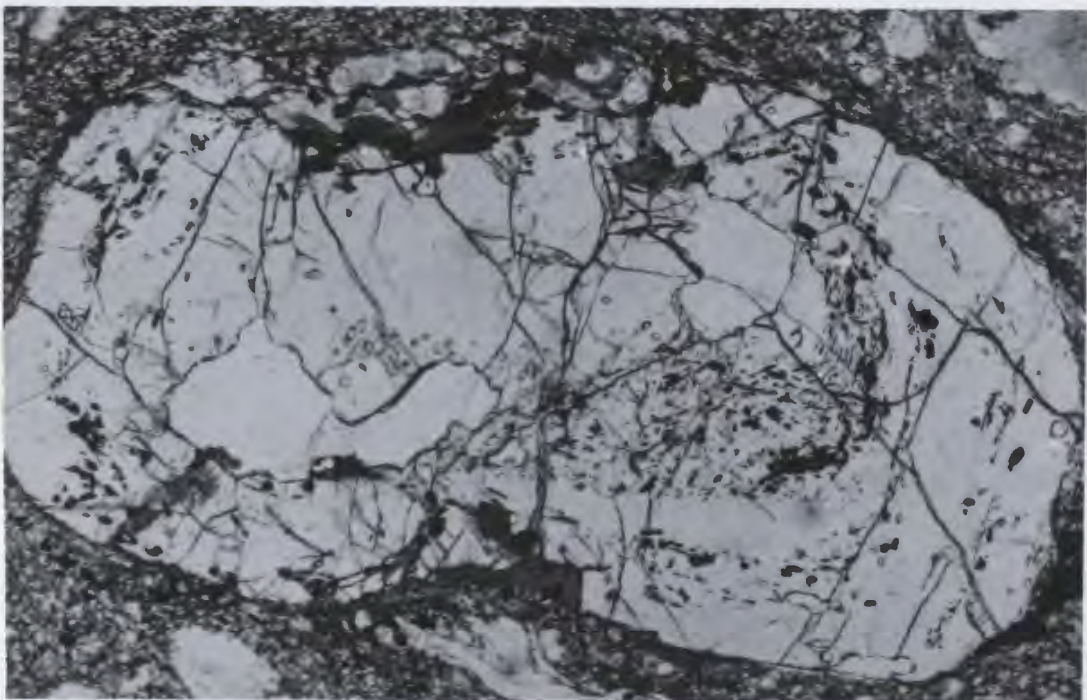
Table 3.6. Petrography of the Green Ridge Amphibolite

LITHOLOGY	MINERALOGY	FABRIC
1) BIOTITE AMPHIBOLITE 082, 083, S131, 189, 272, 273, 274, 460, 473, 477, 478 FIG. 3.36.	hb (0-60%); bt (3-50%); gnt (2-10%); plag (10-35%); qz (5-25%); sph (1-5%); ox (1-10%); cc (< 1%) <u>Pleochroism</u> : hb: X = yellow, Y = green; Z = green/ blue-green (commonly zoned) hb → bt + gnt + qz <u>Retrograde</u> : ep, ser, chl	mylonitic S ₂ (bt) compositional layering (bt/hb) parallel to S ₂ → progressive disruption (folding, boudinage, shearing) → porphyroclastic gnt, plag, hb in fine-grained bt-rich matrix; bt replaces hb along grain boundaries and cleavages; gnt con- tains circular to linear inclusion trails, not continuous with matrix; hb zoned from green cores to dark blue-green rims; plag sericitized
2a) QUARTZ AMPHIBOLITE 071, 076, 080, 129, 130, 131, 136, 187, 268B, 269, 279, 446, 448, 455, 456, 458, 459, 503, 551, 565, 572 FIG. 3.37.	hb (35-70%); pl (20-40%); qz (5-20%); sph (0-5%); ilm (1-6%); cpx (0-20%); ap (1-2%); rt (1%); <u>Hb Pleochroism</u> : X = yellow; Y = green, Z = green, blue-green, sph ↔ ilm <u>Retrograde</u> : chl, sauss, ep, sph	S ₂ strong (hb); L ₂ commonly well-developed (hb); compositional layering (hb/plag) parallel S ₂ ; medium-coarse grained subidiomorphic hb (1-5mm); matrix qz and fd anhedral, sutured to straight grain boundaries, commonly show undulose Xn.
2b) HORNBLENDE GRANULITE 552, 553 FIG. 3.38.	hb (30-40%); plag (30-40%); qz (5%); cpx (20%); hy (0-2%); ilm (5-10%); gnt (1%; one sample only). <u>Hb Pleochroism</u> : X = yellow, Y = brown, Z = brown, red-brown. cpx → hb <u>Retrograde</u> (locally pervasive): act, sauss, ep, sph, serp	S ₂ strong (hb, cpx), hb (010) in plane of S ₂ compositional layering (cpx/hb) parallel S ₂ ; hb replaces cpx, cpx approaching granoblastic but somewhat elongated parallel to S ₂
3) PLAGIOCLASE AMPHIBOLITE 128, 138, 267, 268A, 270, 315, 502, 504, 554, 560, 564, 570 FIG. 3.39.	hb (40-50%); plag (40-60%); cpx (0-17%); sph (0-2%) <u>Hb Pleochroism</u> : X = pale yellow, Y = Z = pale green cpx → hb <u>Retrograde</u> (locally pervasive): chl, sauss, hm, ep, pr	S ₂ strong to inhomogeneous (hb, plag aggregates) compositional layering (modified primary) in Wild Cove metagabbro only; shape preferred orientation of hb, fd aggregates; cpx replaced by hb.

FIGURE 3.36: Biotite amphibolite.



3.36a: RJ75-082. Biotite amphibolite showing disrupted hornblende-rich layers and garnet, feldspar, and hornblende porphyroclasts in a fine-grained biotite- and quartz-rich matrix. Width of field is 3.8 cm.



3.36b: DFS-73-131. Garnet porphyroclast with rounded edges containing inclusions of ilmenite, quartz, biotite, and hornblende. Width of field is 3 mm.

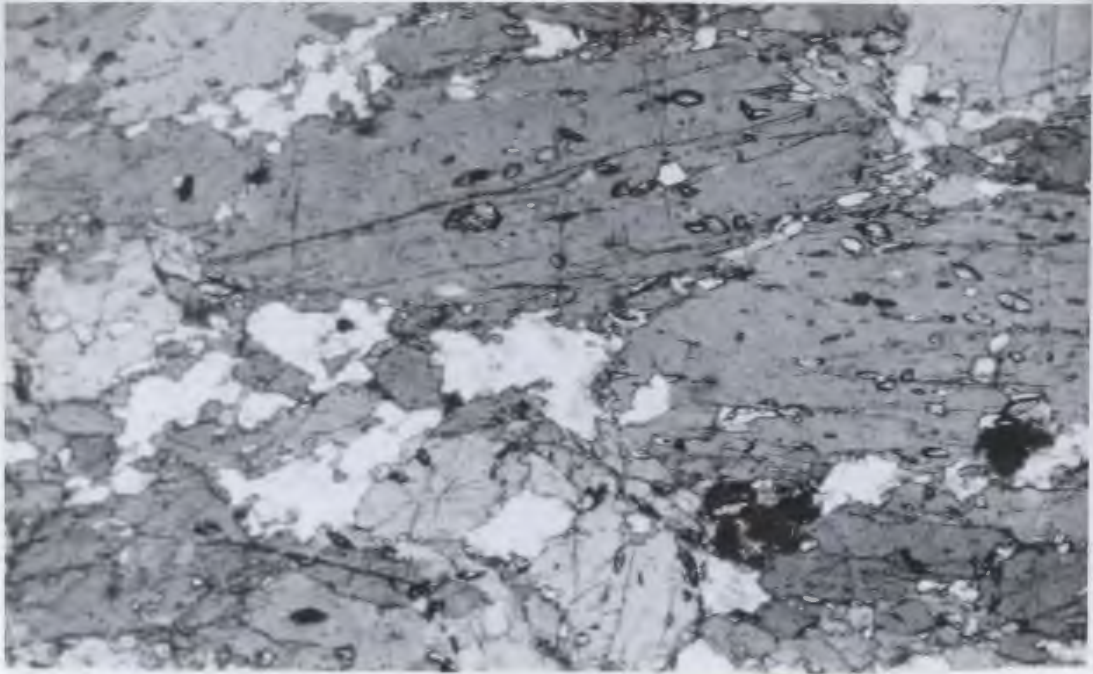


FIGURE 3.37: RJ75-080: Quartz amphibolite, showing hornblende crystals (grey) containing sphene inclusions (lens-shaped with high relief), with interstitial quartz and feldspar (clear). Width of field is 2 mm.

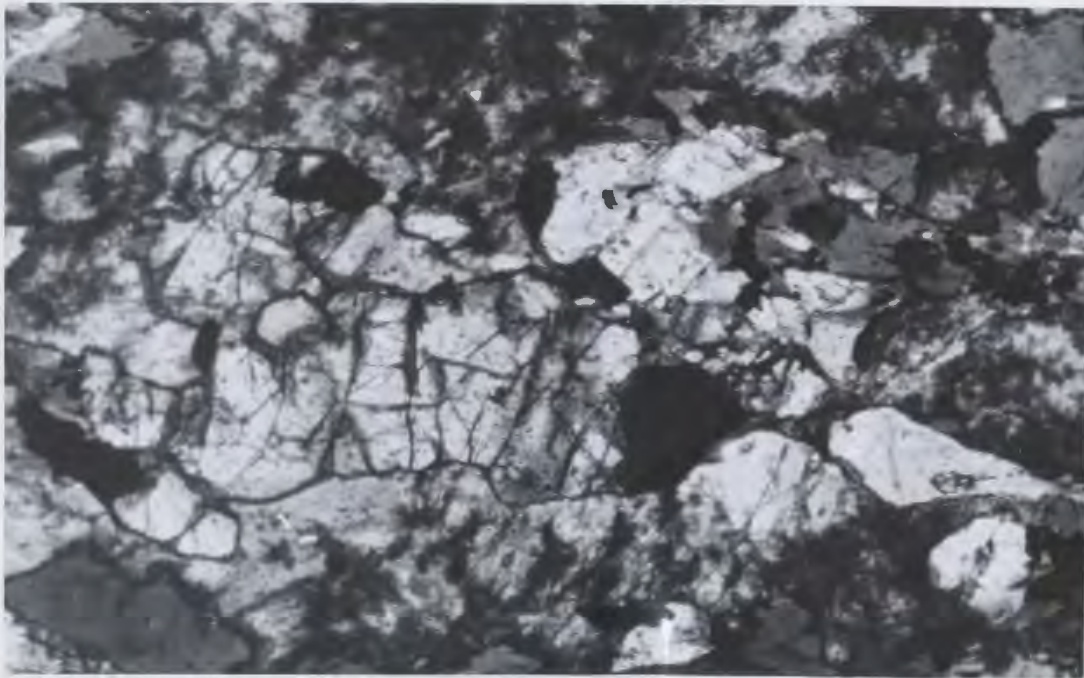


FIGURE 3.38: RJ76-552. Hypersthene (centre, high relief), augite (light grey, low relief), brown hornblende (dark grey), ilmenite, and saussuritized plagioclase, two-pyroxene amphibolite, Brimstone Pond. Hypersthene crystal is 1 mm long.

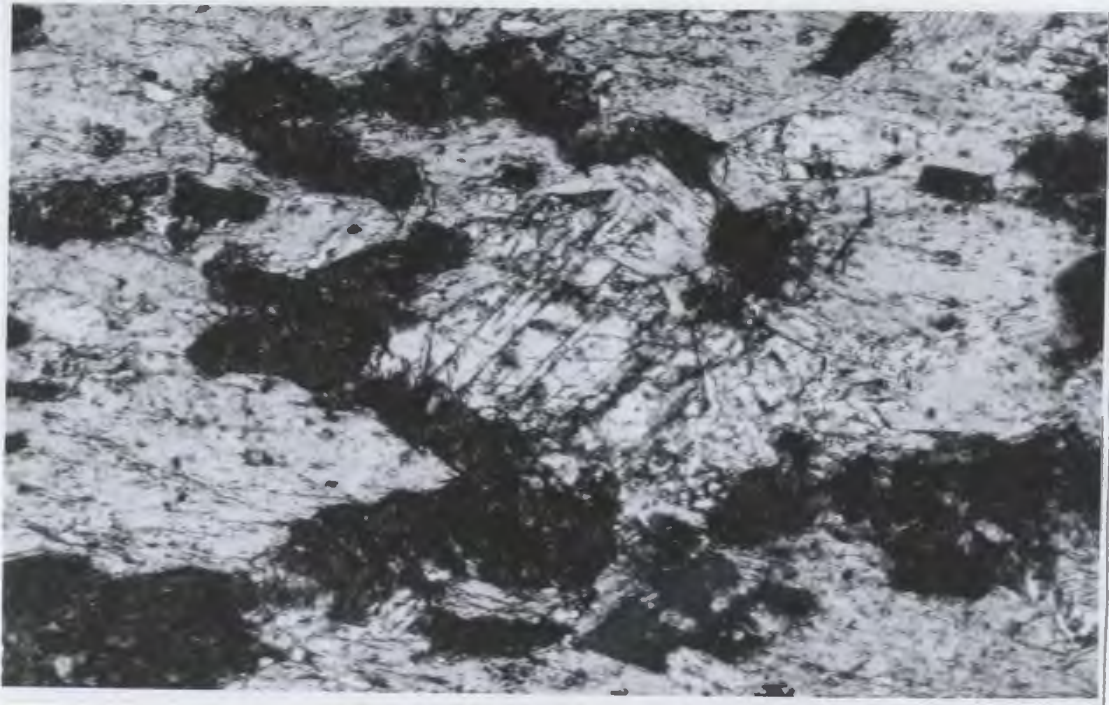


FIGURE 3.39: RJ75-128. Plagioclase amphibolite, showing clinopyroxene (centre, high relief), saussuritized plagioclase (dark grey), and pale green hornblende (light grey). Width of field is about 3 mm.

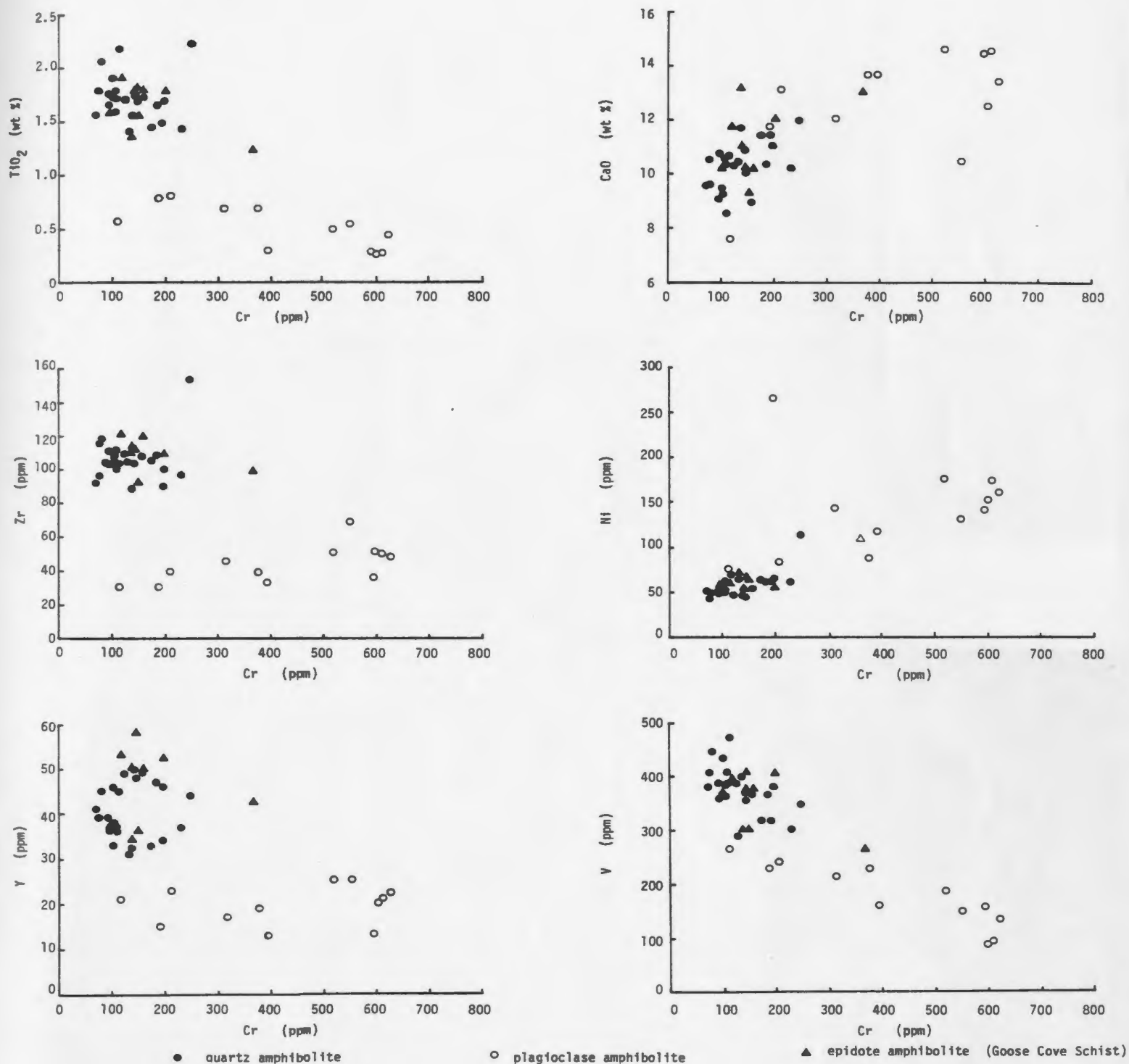


FIGURE 3.40: Compositions of the Green Ridge Amphibolite, showing differences between quartz and plagioclase amphibolites. The composition of the epidote amphibolite unit of the Goose Cove Schist is shown for comparison - note the almost complete overlap with the quartz amphibolites (see also FIG. 3.43).

Table 3.7. Average Compositions, epidote amphibolite (EA), quartz amphibolite (QA) and biotite amphibolite (BA)

	EA	QA	BA
SiO ₂	49.55	49.57	56.77
TiO ₂	1.65	1.71	1.72
Al ₂ O ₃	13.99	14.20	15.53
FeO _T	12.40	12.66	10.26
MnO	0.22	0.22	0.21
MgO	6.61	7.48	4.33
CaO	11.16	10.27	5.99
Na ₂ O	2.89	2.88	2.37
K ₂ O	0.76	0.48	2.24
P ₂ O ₅	0.15	0.15	0.33
Zr	108	106	173
Sr	174	202	213
Rb	13	8	54
Zn	124	122	123
Cu	111	68	115
Ba	129	131	414
Y	36	38	30
Ni	64	57	74
Cr	172	158	156
V	351	372	256
Ga	20	19	21
Nb	5	7	20
Fe ₂ O ₃ /FeO+Fe ₂ O ₃	0.421	0.279	0.193
L.O.I.	2.12	2.50	3.30
<i>p</i>	3.07	3.06	2.91

Table 3.8. Calculations for the reaction $A + X \rightarrow B$.(a) ISO-CHEMICAL REACTION ($\Delta X = 0$)

Component n	f_v	EA \rightarrow BA	f_v	QA \rightarrow BA
SiO ₂		0.92		0.92
TiO ₂		1.01		1.04
Al ₂ O ₃		0.95		0.96
FeO		1.27		1.30
MnO		1.10		1.10
MgO		1.60		1.81
CaO		1.96		1.80
Na ₂ O		1.28		1.28
K ₂ O		0.36		0.23
P ₂ O ₅		0.48		0.48

(b) ISOVOLUMETRIC REACTION ($f_v = 1$)

	ΔX_n	EA \rightarrow BA	ΔX_n	QA \rightarrow BA
SiO ₂		+4.38		+4.36
TiO ₂		-0.02		-0.08
Al ₂ O ₃		+0.76		+0.55
FeO		-2.65		-2.91
MnO		-0.02		-0.02
MgO		-2.50		-3.37
CaO		-5.47		-4.58
Na ₂ O		-0.64		-0.63
K ₂ O		+1.37		+1.65
P ₂ O ₅		+0.16		+0.16

(c) CONSTANT Al₂O₃ ($f_v = 0.955$)

SiO ₂	+1.95	+1.93
TiO ₂	-0.09	-0.15
FeO	-3.09	-3.35
MnO	-0.03	-0.03
MgO	-2.68	-3.35
CaO	-5.73	-4.84
Na ₂ O	-0.74	-0.73
K ₂ O	+1.27	+1.55
P ₂ O ₅	+0.15	+0.15

(d) TRACE ELEMENTS ($f_v = 1$) or f_v where $\Delta X = 0$.

	X	f_v	X	f_v
Zr	+56	0.66	+58	0.64
Sr	+28	0.86	+ 0.4	1.00
Rb	+38	0.25	+43	0.16
Zn	-7	1.06	-5	1.04
Cu	-2	1.01	+41	0.62
Ba	+264	0.32	+262	0.33
Nb	+14	0.26	+12	0.37
Y	-8	1.26	-10	1.33
Ni	+6	0.91	+13	0.81
Cr	-24	1.16	+10	0.93
V	-108	1.44	-29	1.53
Ga	-0.1	1.00	+1	0.95

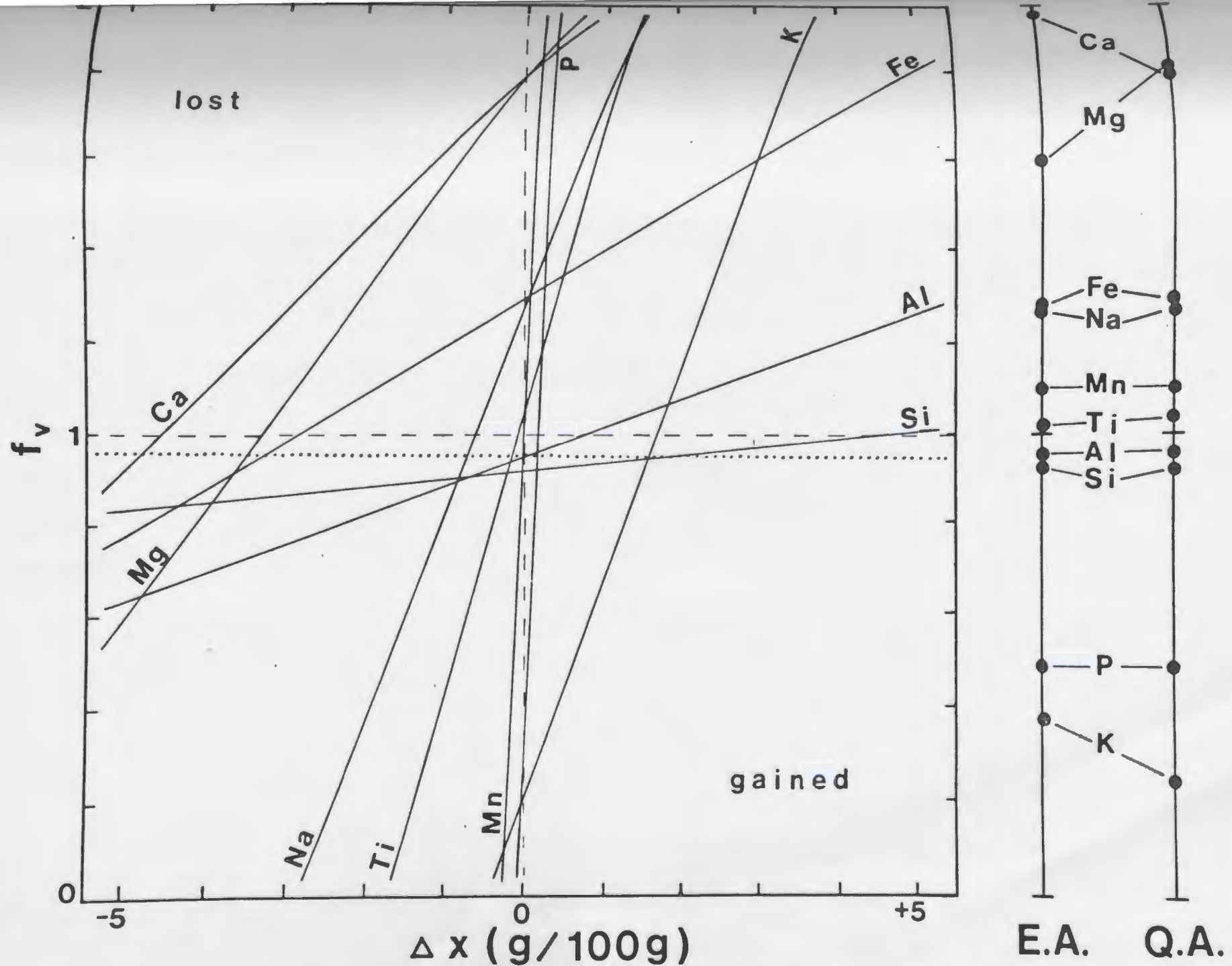


FIGURE 3.41: Composition-volume diagram for metasomatic formation of biotite amphibolite from quartz and epidote amphibolite (after Gresens, 1967). At right of diagram, elements falling above $f_v = 1.0$ have been lost from the system, while those below this axis have been added to it.

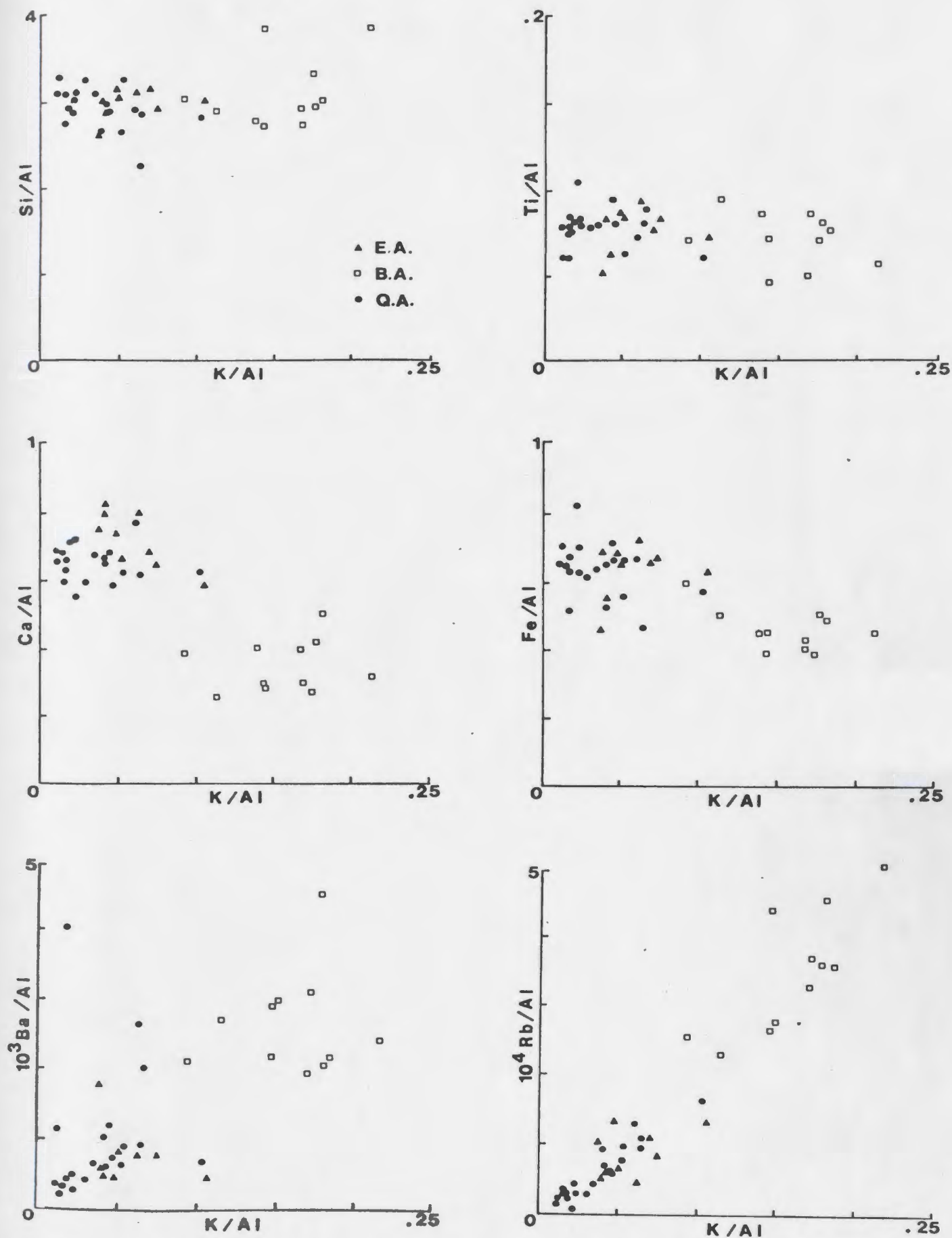
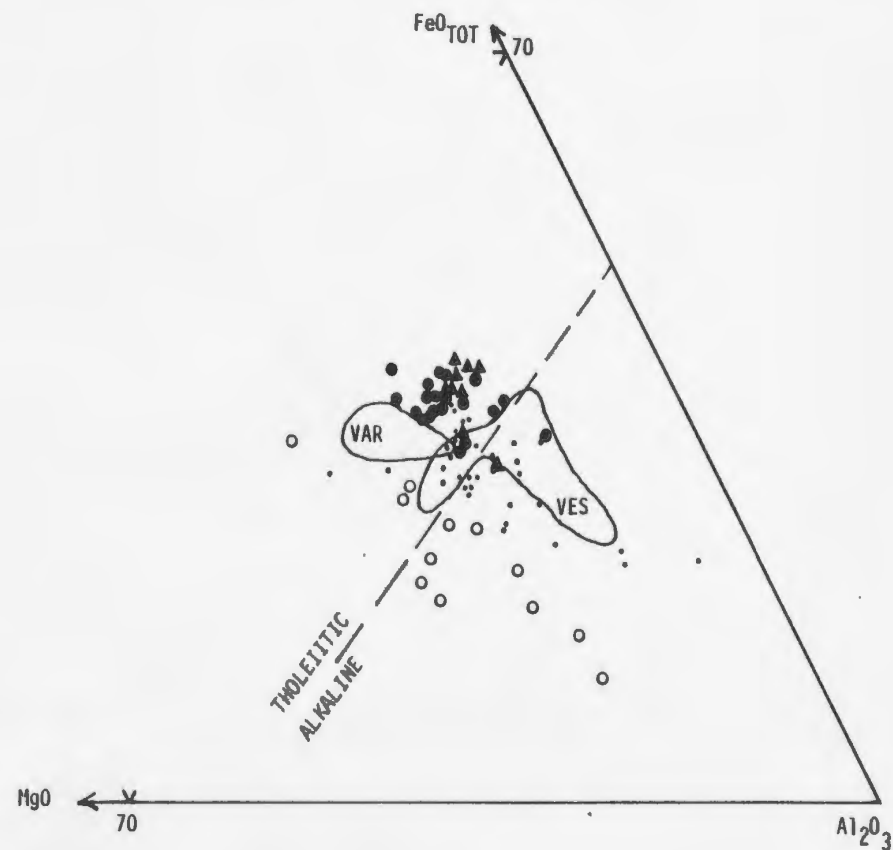
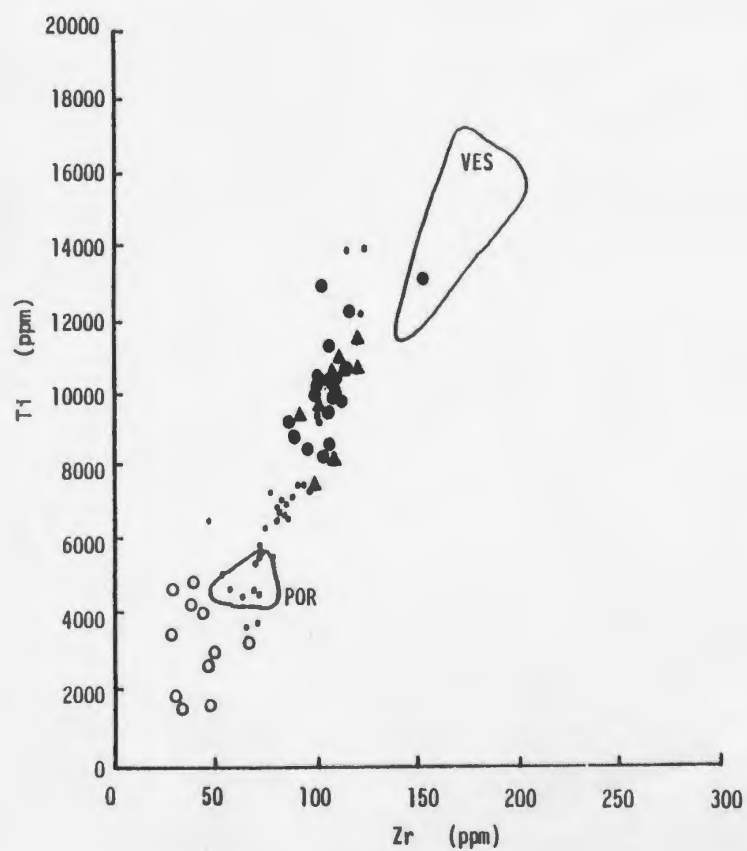
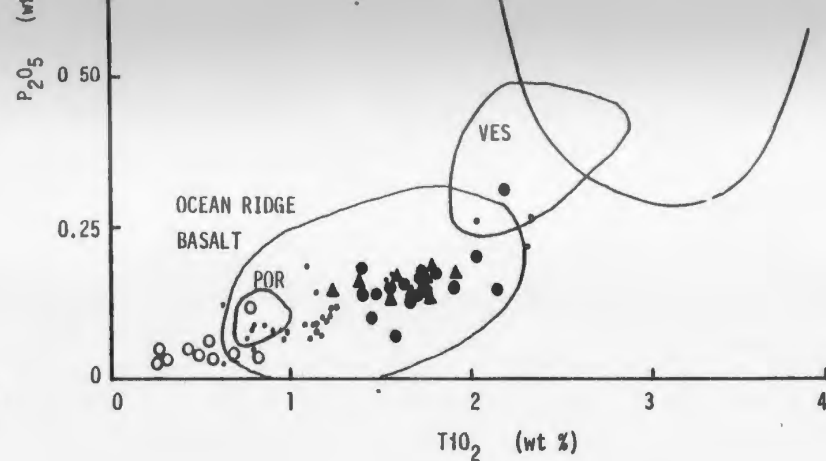
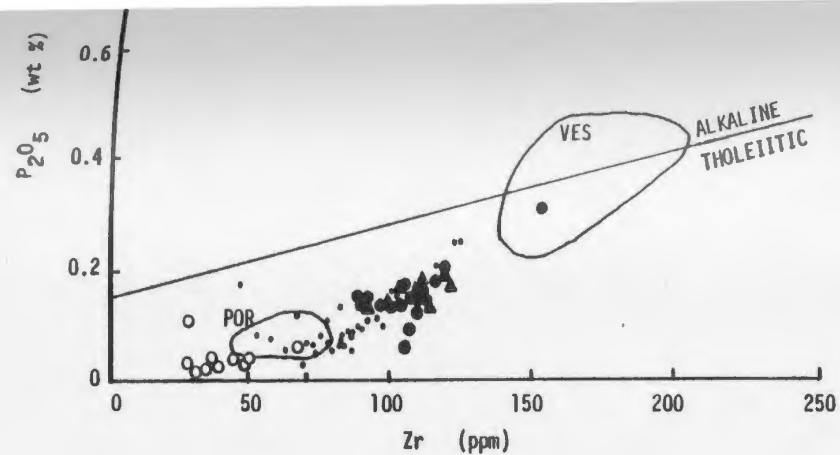


FIGURE 3.42: Geochemistry of biotite amphibolite with respect to quartz and epidote amphibolites, showing general similarity of Si and Ti, enrichment in K, Ba, and Rb, and depletion in Ca and Fe.



• greenschist (Goose Cove Schist)

▲ epidote amphibolite (Goose Cove Schist)

● quartz amphibolite (Green Ridge Amphibolite)

○ plagioclase amphibolite (Green Ridge Amphibolite)

FIGURE 3.43: Geochemical comparison between the Green Ridge Amphibolite, Goose Cove Schist, and the Ireland Point Volcanics.

(VES = vesicular pillow lava; POR = porphyritic pillow lava; VAR = variolitic pillow lava) (cf. FIG. 3.40).

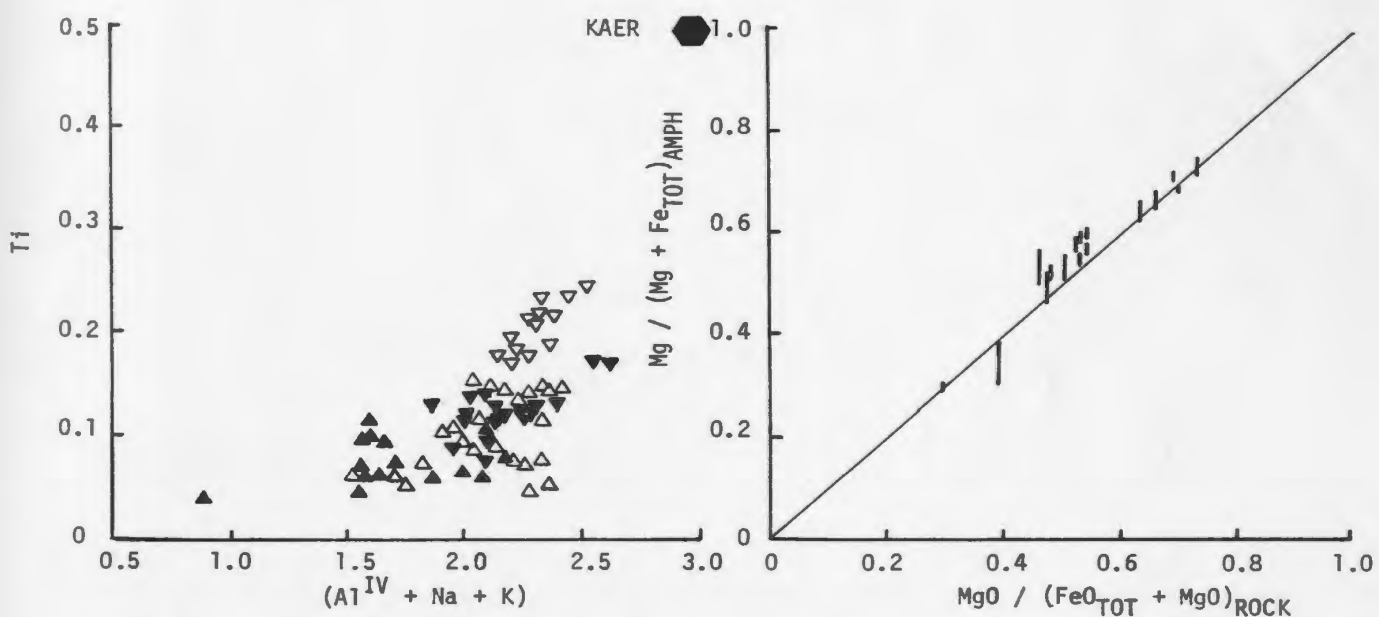
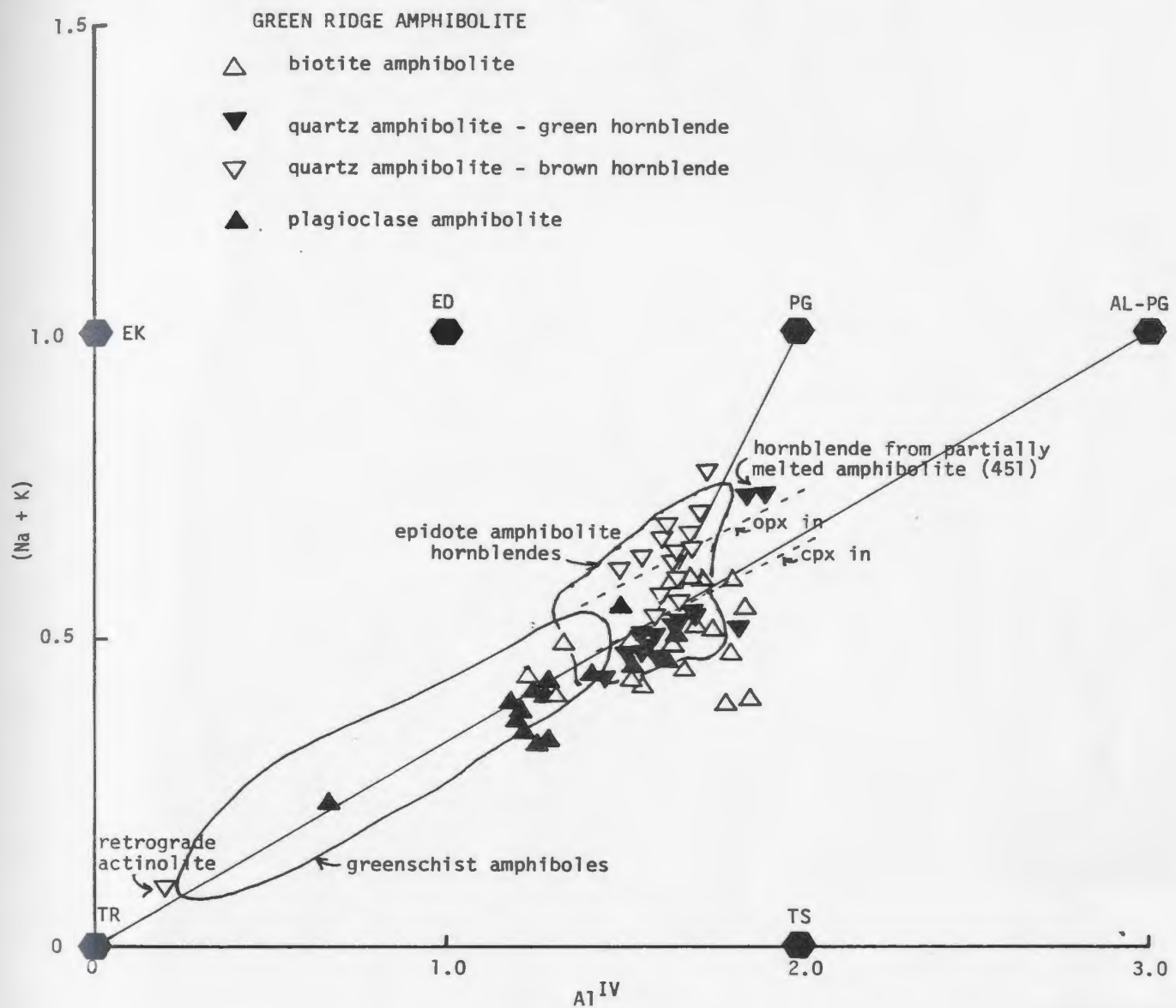


FIGURE 3.44: Compositions of amphiboles from the Green Ridge Amphibolite, showing trend of brown hornblendes toward pargasite with the appearance of orthopyroxene, enrichment of brown hornblendes in Ti, and dependence of Mg/Fe on host rock composition.

FIGURE 3.45a: Compositions of pyroxenes from the Green Ridge Amphibolite and the Long Ridge Metagabbro. Tie lines join coexisting hypersthene and augite from the Brimstone Pond two-pyroxene amphibolites. The field is that shown enlarged in Fig. 3.45b.

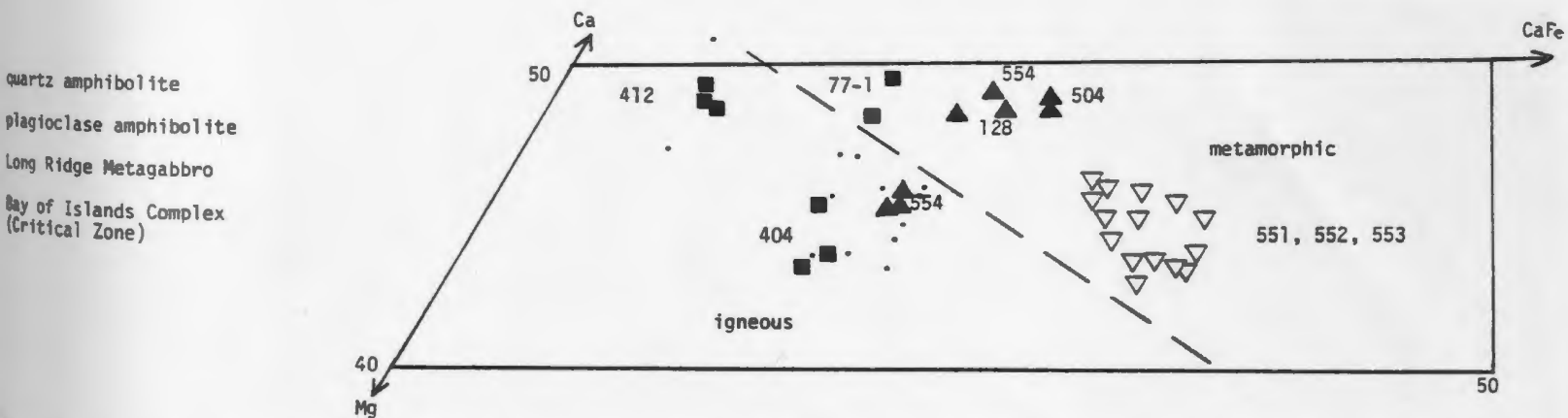
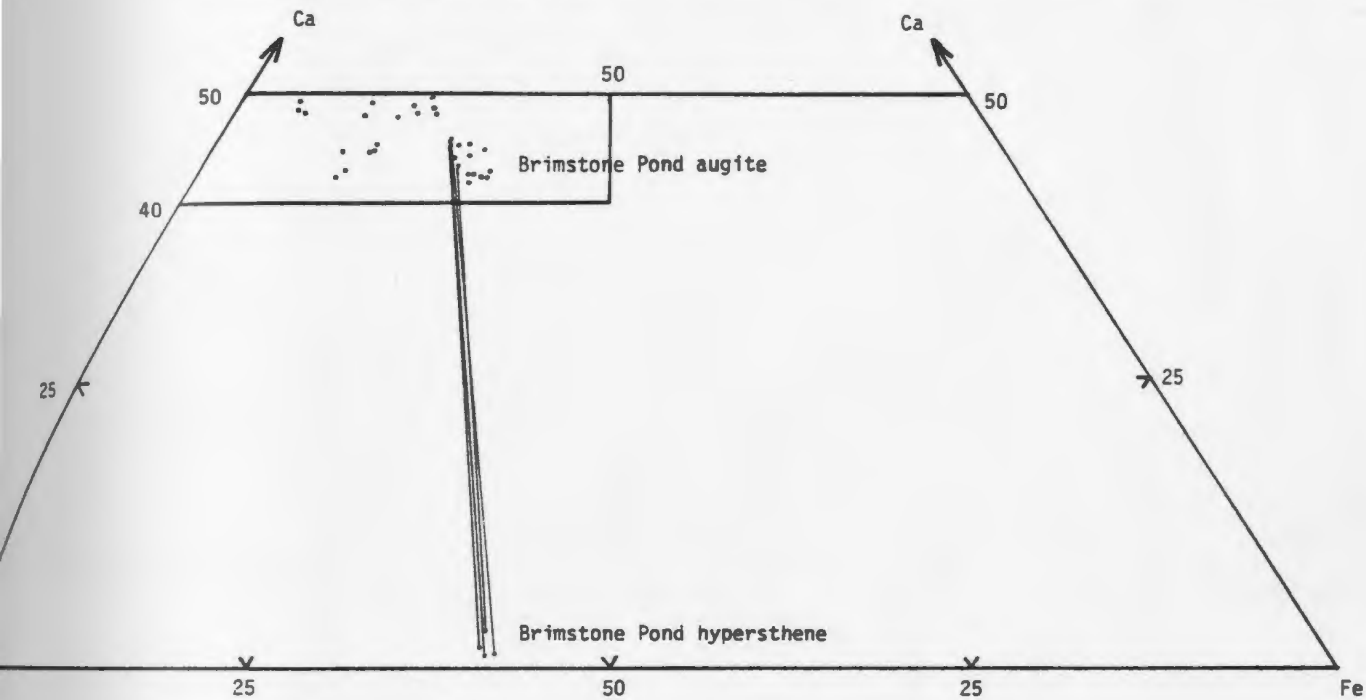


FIGURE 3.45b: Clinopyroxene compositions from the Green Ridge Amphibolite and the Long Ridge Metagabbro compared to those from the Critical Zone of the Bay of Islands Complex (Malpas, 1976). The dividing line between igneous and metamorphic pyroxenes is based on textural grounds and mineral parageneses.

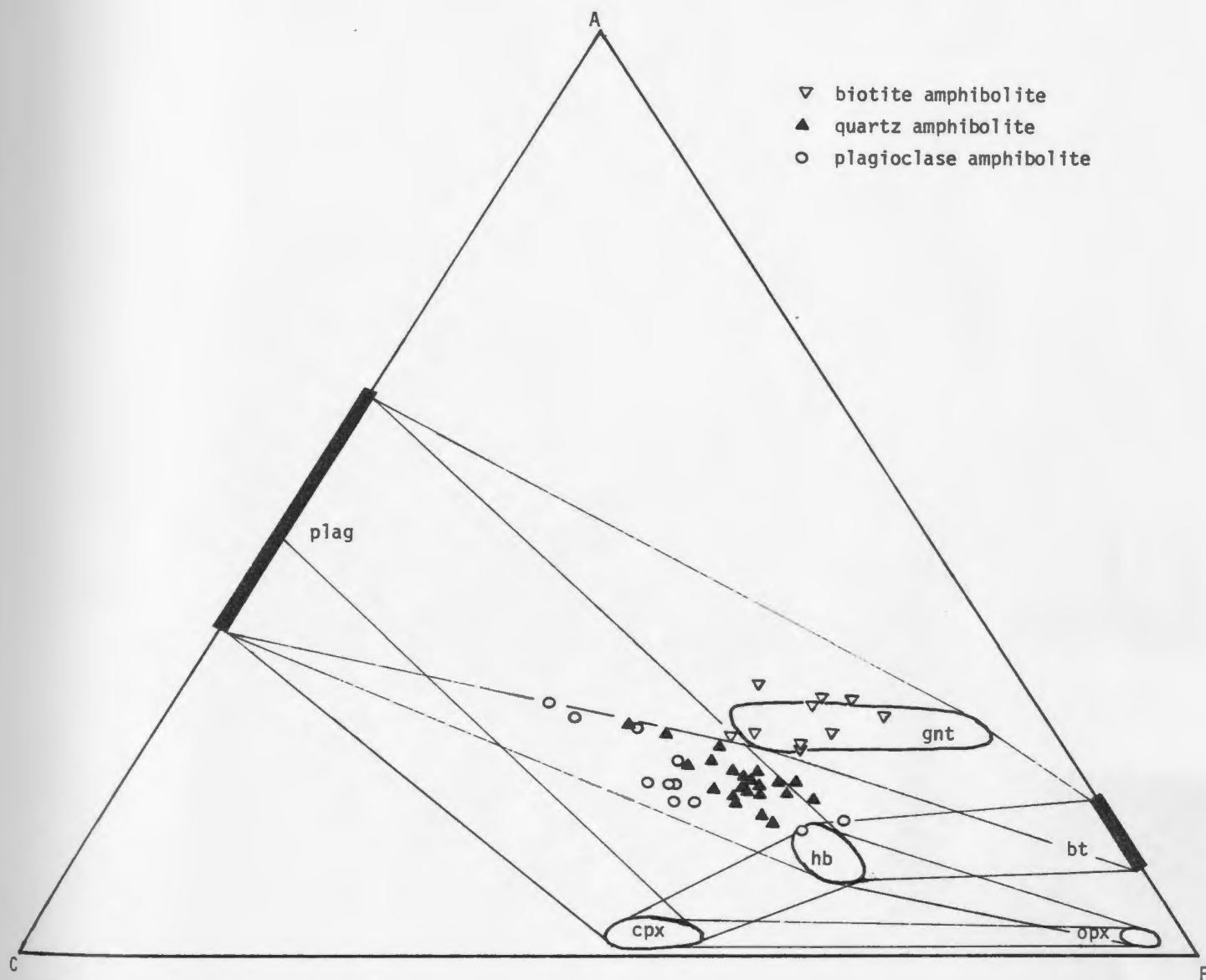


FIGURE 3.46: ACF diagram for the Green Ridge Amphibolite showing whole rock compositions and the compositional fields of the analysed minerals.

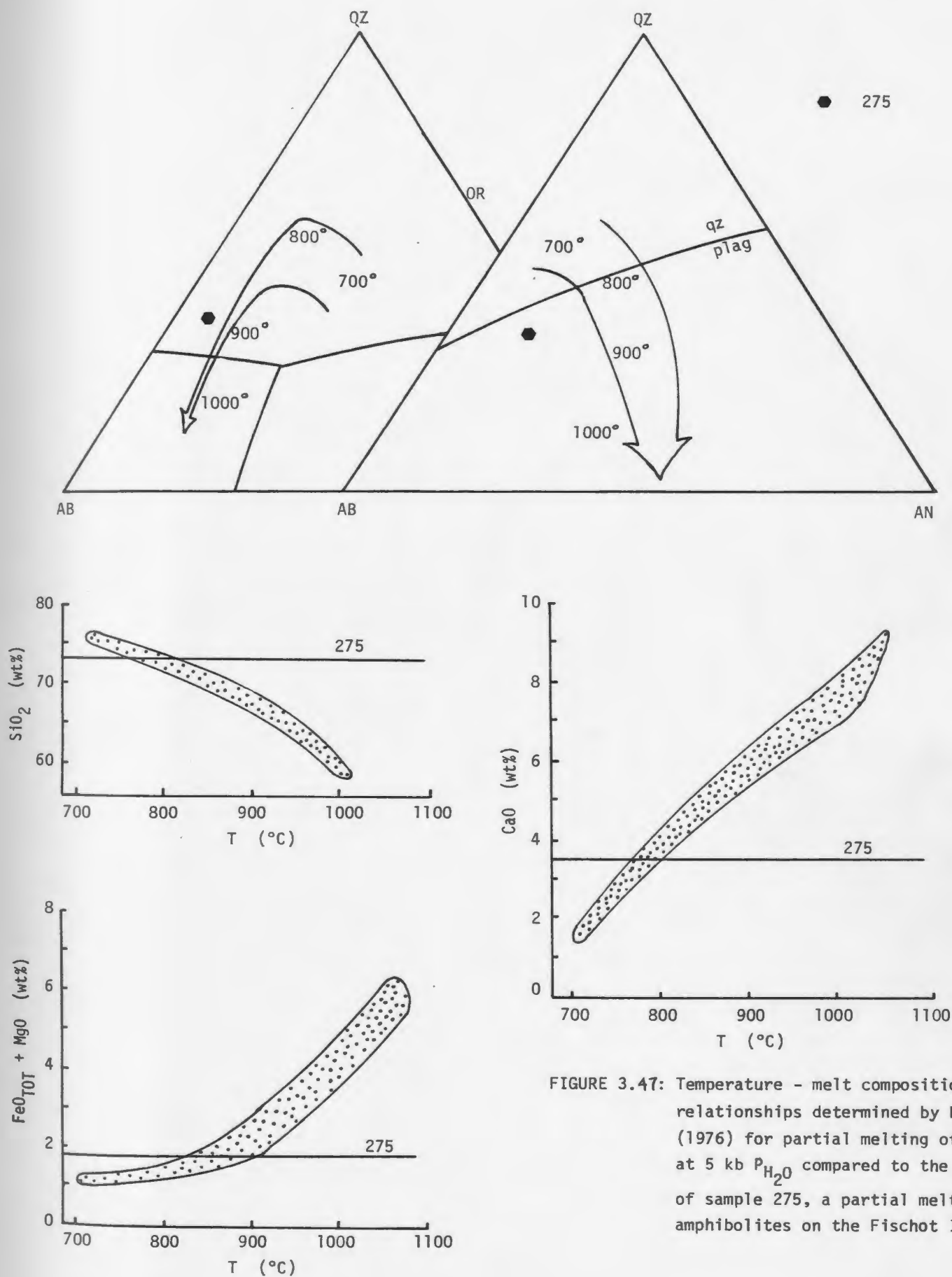


FIGURE 3.47: Temperature - melt composition relationships determined by Helz (1976) for partial melting of basalt at 5 kb P_{H_2O} compared to the composition of sample 275, a partial melt from the amphibolites on the Fischot Islands.

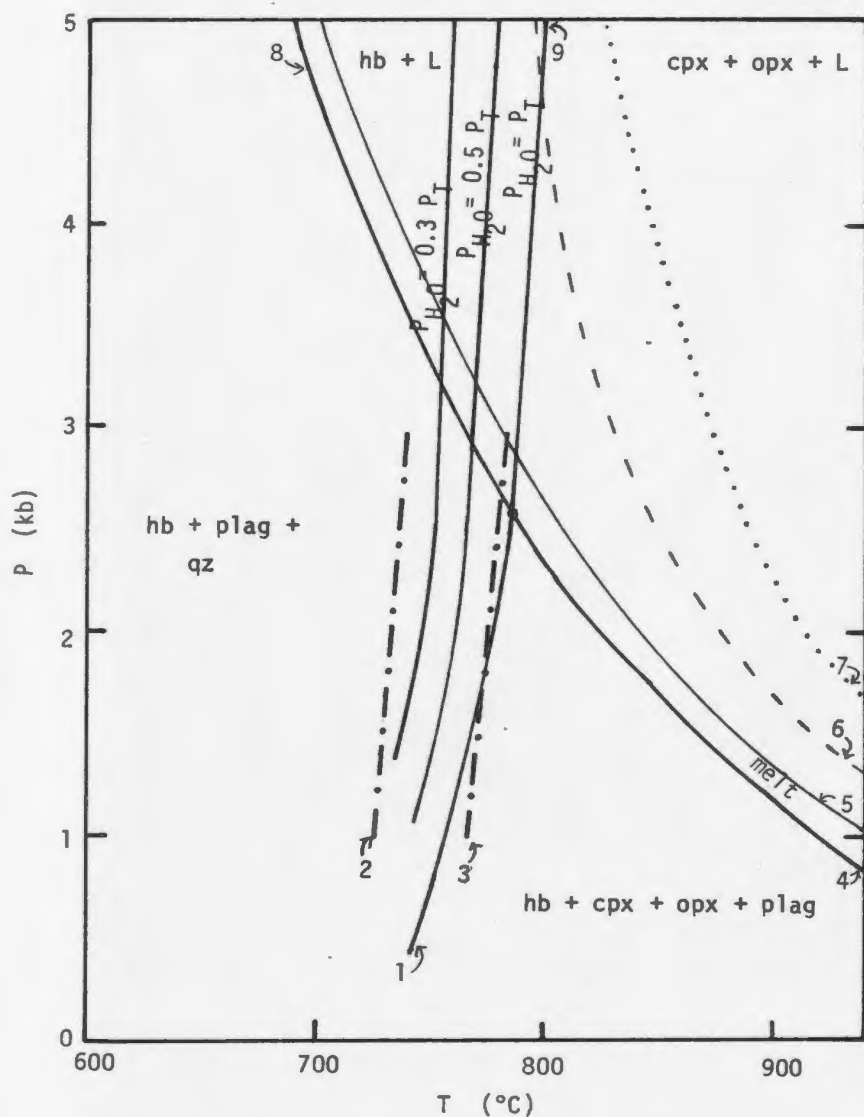


FIGURE 3.48: Phase relations for the amphibolite facies to granulite facies transition.

- (1) $hb + plag + qz \rightleftharpoons hb + cpx + opx + plag + H_2O$ (Binns, 1968, 1969)
- (2) $hb + plag + ox + sph + qz \rightleftharpoons hb + plag + cpx + ox + sph + qz$ (HM; Spear, 1976)
- (3) $hb + plag + ilm + sph \rightleftharpoons hb + cpx + opx + plag + ilm + sph$ (QFM; Spear, 1976)
- (4) $hb + cpx + opx + plag \rightleftharpoons cpx + opx + L$ (Binns, 1968, 1969)
- (5) basalt melting curve, $P_{H_2O} = P_T$ (Tuthill, 1968)
- (6) basalt melting curve, $P_{H_2O} = P_T$ (Yoder and Tilley, 1962)
- (7) basalt melting curve, $P_{H_2O} = 0.6 P_T$ (Holloway and Burnham, 1972)
- (8) $hb + plag + qz \rightleftharpoons hb + L$ (Binns, 1968, 1969)
- (9) $hb + L \rightleftharpoons cpx + opx + L$ (Binns, 1968, 1969).

Table 3.9. Petrography of the Long Ridge Metagabbro

LITHOLOGY	MINERALOGY	FABRIC
1) DUNITE 401, 411 ^a FIG. 3.49.	ol (→ serp, mt) (95-99%); chr (1-5%)	relict cumulate ol (1-3 mm) with kink bands, transected by bands of granoblastic ol (nearly strain-free, some with undulose Xn or kink bands); chr defines relict igneous layering; S ₁ defined by recrystallized ol
2) TROCTOLITE 412	ol (60-80%) (→ serp, mt); plag (20-35%) (⇒ sauss); chr (0-2%); coronas (plag, ol); cpx (→ amph) ± sp (< 5%)	coronitic, undeformed; concentric zones of amph growing radially out from plag and ol cores/ or, fresh cpx rims on ol/ or, amph - sp vermicular intergrowths; amph - granoblastic to fibrous
3) GABBRO 402, 405, 406, 408 FIG. 3.50, 3.51.	plag (⇒ sauss) (40-60%); cpx (→ amph) (30-50%); ol (⇒ serp, chl, carb) (0-10%); cpx ⇒ amph tour, cor (small amounts in one sample only) ? metasomatic	undeformed → strong foliation (amph) variable over a few cm. tabular, twinned, cpx → aggregates of subidiomorphic amph; in matrix of sauss plag; some vermicular sp-amph coronas
4) ANORTHOSITE 409, 410	plag (⇒ sodic plag + cz) (100%)	tabular plag → elongated, deformation twins, subgrain development → recrystallized granular plag; interstitial cz strongly zoned.

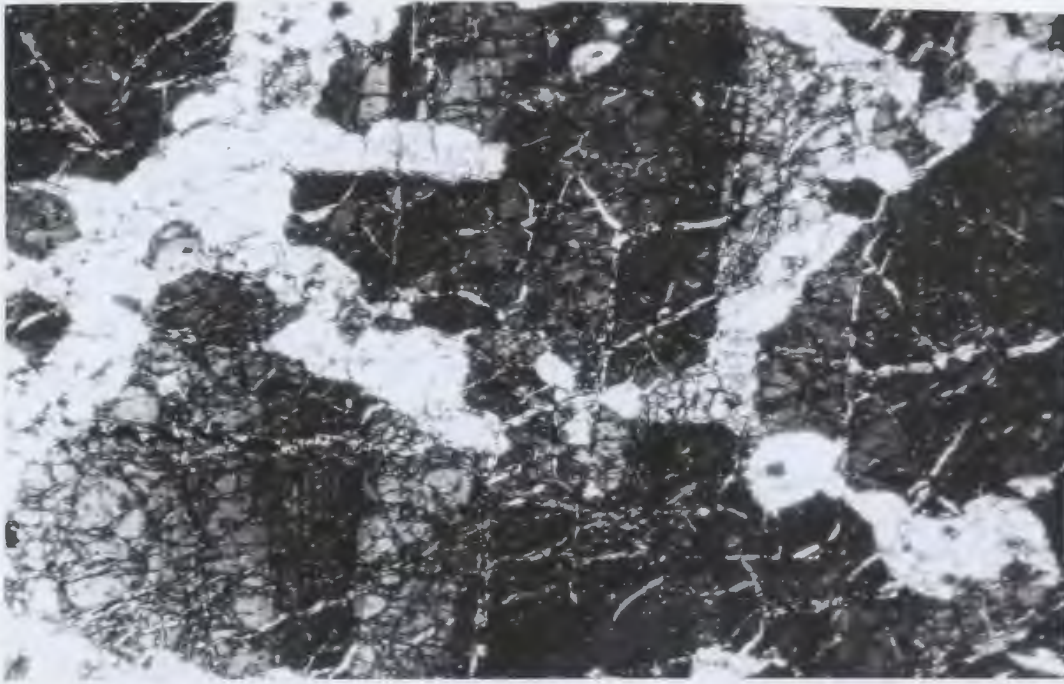


FIGURE 3.49: RJ76-401. Dunite from Long Ridge showing large olivine crystal (primary?) with deformation lamellae and smaller recrystallized olivine grains (Crossed Nicols). Width of field is about 2 mm.

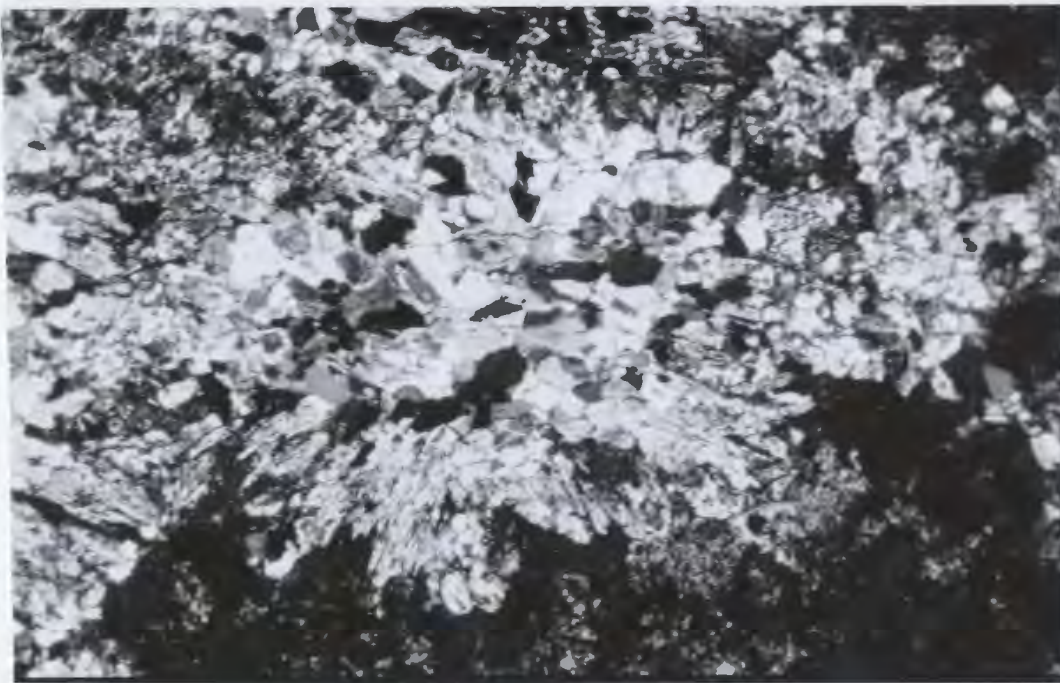


FIGURE 3.50a: RJ75-132. Coronitic metagabbro showing mosaic of amphibole after olivine or clinopyroxene, surrounded by saussuritized plagioclase (dark) with intervening corona of amphibole and spinel (Crossed Nicols). Width of field is about 2 mm.

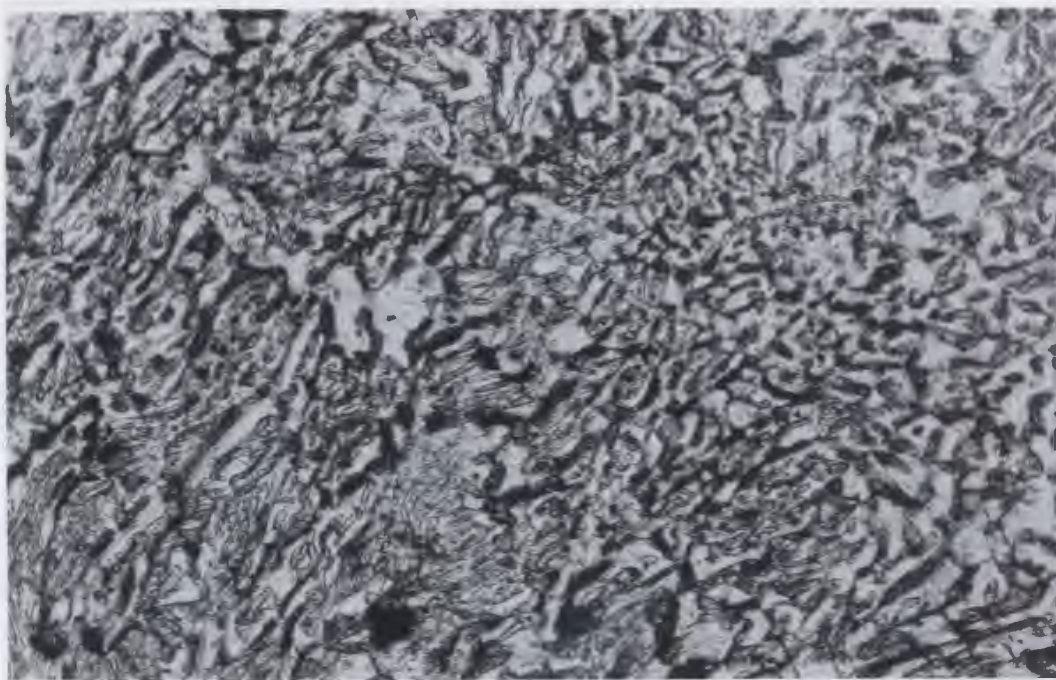


FIGURE 3.50b: RJ75-132. Detail of 3.50a, showing vermicular spinel (high relief) intergrown with amphibole (Plane polarized light). Width of field is about 0.05 mm.



FIGURE 3.51: RJ76-404. Relict, twinned, primary clinopyroxene being replaced by amphibole, Long Ridge Metagabbro (Crossed Nicols). Width of field is about 4 mm.

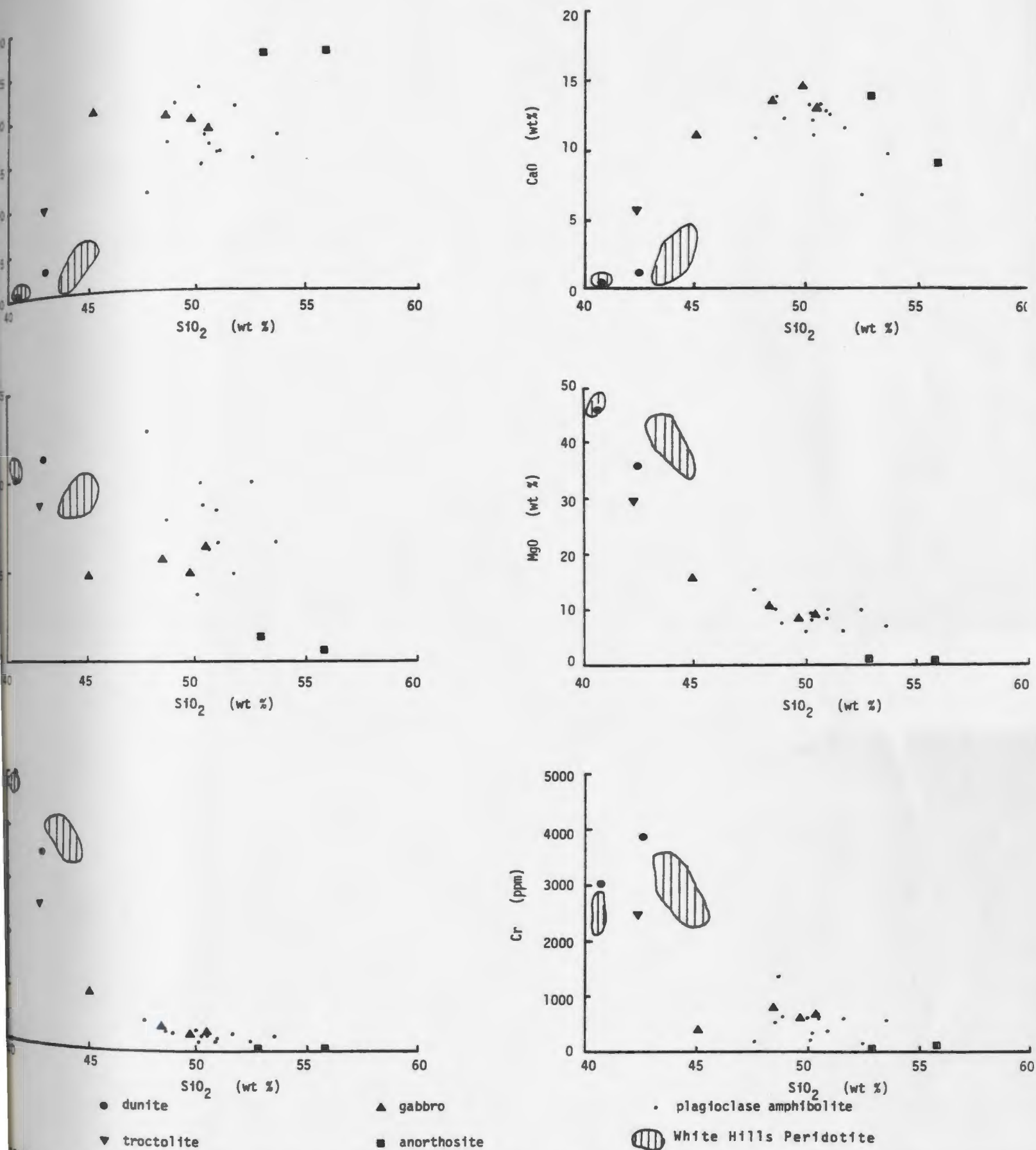


FIGURE 3.52: SiO_2 variation diagrams for the Long Ridge Metagabbro showing a differentiation trend from dunite to anorthosite, presumably controlled mainly by olivine, clinopyroxene, and plagioclase. Also plotted are the compositions of the plagioclase amphibolite unit of the Green Ridge Amphibolite, showing overlap with the field of the gabbros.

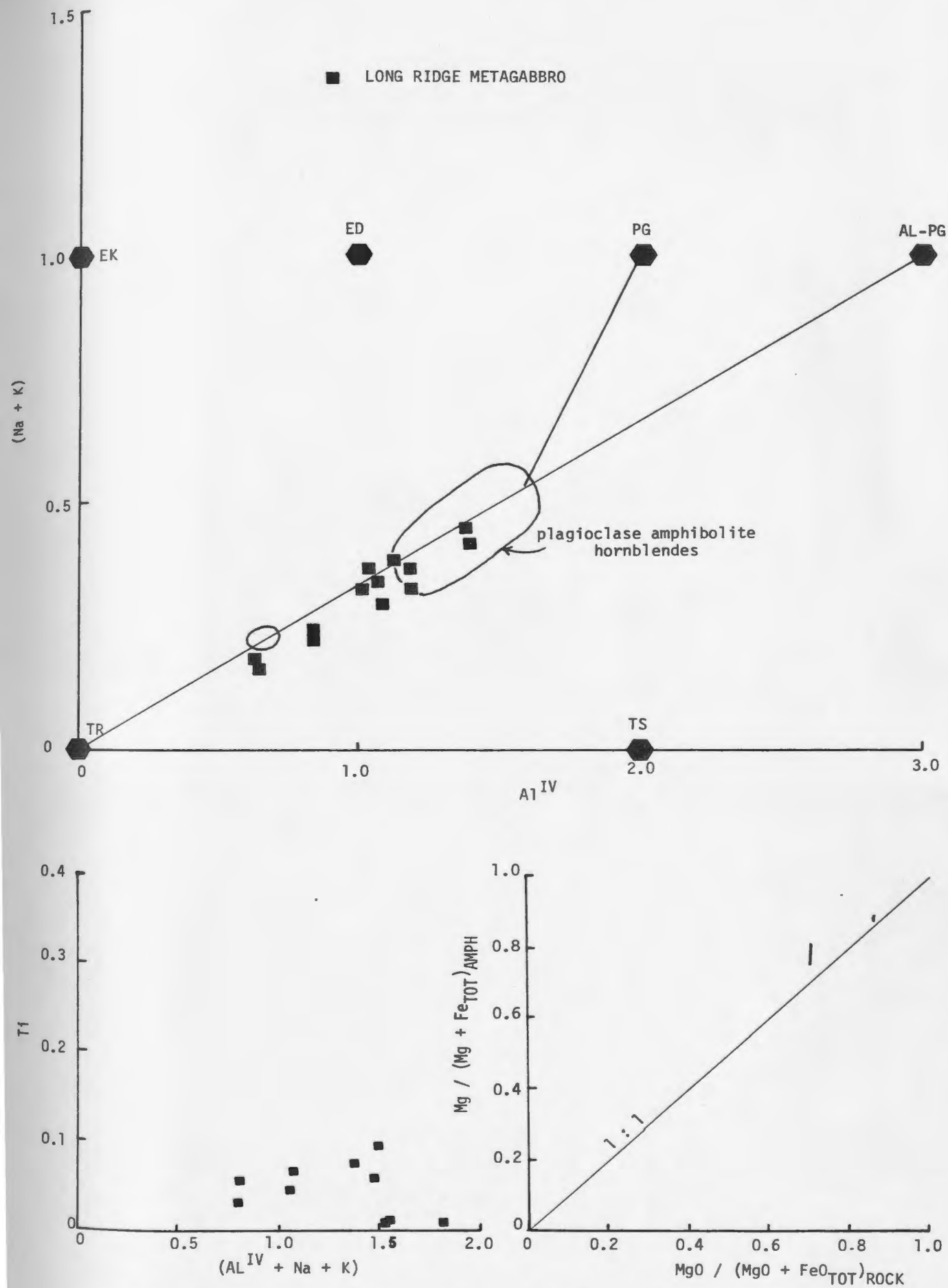


FIGURE 3.53: Composition of amphiboles from the Long Ridge Metagabbro compared to the trend of metamorphic amphiboles from the Green Ridge Amphibolite and the Goose Cove Schist, showing overlap with the compositional field of hornblendes from the plagioclase amphibolites, and low Al^{IV} , Ti, and alkalis.

Table 3.10. Petrography of jacupirangite-syenite assemblage.

LITHOLOGY	MINERALOGY	TEXTURE
1) JACUPIRANGITE 490, 491, 492 FIG. 3.54a	tiaug (15-60%); kaer (13-50%); bt (0.2-10%); ilm (12-18%); ap (4-9%); cc (0.3-20%) kaer pleochroism: X = yellow to pale brown Y = Z = deep red brown tiaug slightly pleochroic: pink-red tiaug \rightleftharpoons kaer	medium to coarse grained, equigranular, subhedral tiaug; interstitial ilm, ap, bt, kaer, cc amphibole commonly overgrows and replaces pyroxene mild deformation \rightarrow polygonization of cpx
2) ALKALINE PYROXENITE 489	tiaug (20-65%); kaer (2-65%); ap (0-1%); cc (0-1%); ox (0.1-1%); ab (0-5%) tiaug \rightleftharpoons kaer secondary salite, hb	medium to coarse grained, equigranular, subhedral tiaug, locally mainly altered to kaer; Locally extensive development of secondary cpx and amph associated with fractures
3) HORNBLENDE GNEISS 486, 487, 488 FIG. 3.54b.	tiaug (0.5-2%); hb (30-55%); bt (0-1%); ox (0.5-4%); ap (1-3%); ab (40-70%) tiaug \rightleftharpoons hb	augen of hb surrounded by smaller, recrystallized hb in bands separated by layers of fine-grained, anhedral, ab; gneissic to mylonitic fabric (equivalent to S_{p2} in peridotites)
4) SYENITIC MYLONITE 496, 497, 651, 654 FIG. 3.54c.	cpx (1-5%); amph (1-6%); bt (2-8%); ox (3-5%); ap (0-3%); ab (75-90%); ol (0-4%); zir (0-1%)	mainly ab (locally perthitic)- fine-grained with serrated grain boundaries; aug, ol, zir (porphyroclasts), bt, hb concentrated in bands; commonly augened, elongated parallel to foliation; mylonitic fabric (equivalent to S_{p2} in peridotites).

FIGURE 3.54: Jacupirangite - syenite assemblage.



3.54a: RJ76-491: Undeformed jacupirangite with titanaugite (bright colours) and interstitial biotite and kaersutite (brown), ilmenite (black), and apatite (white). (Partly crossed Nicols). Width of field is 3.2 cm.



3.54b: RJ76-488. Hornblende gneiss, showing kaersutite augen (brown), relict titanaugite (blue), and interstitial fine-grained albite (grey and white). (Partly crossed Nicols). Width of field is 3.2 cm.

FIGURE 3.54 (continued)



3.54c: RJ76-497. Syenitic mylonite showing augite augen (green) with opaque pressure shadows, and layers of fine-grained fayalitic olivine and hornblende in a matrix of fine-grained albite. (Partly crossed Nicols). Width of field is 3.3 cm.

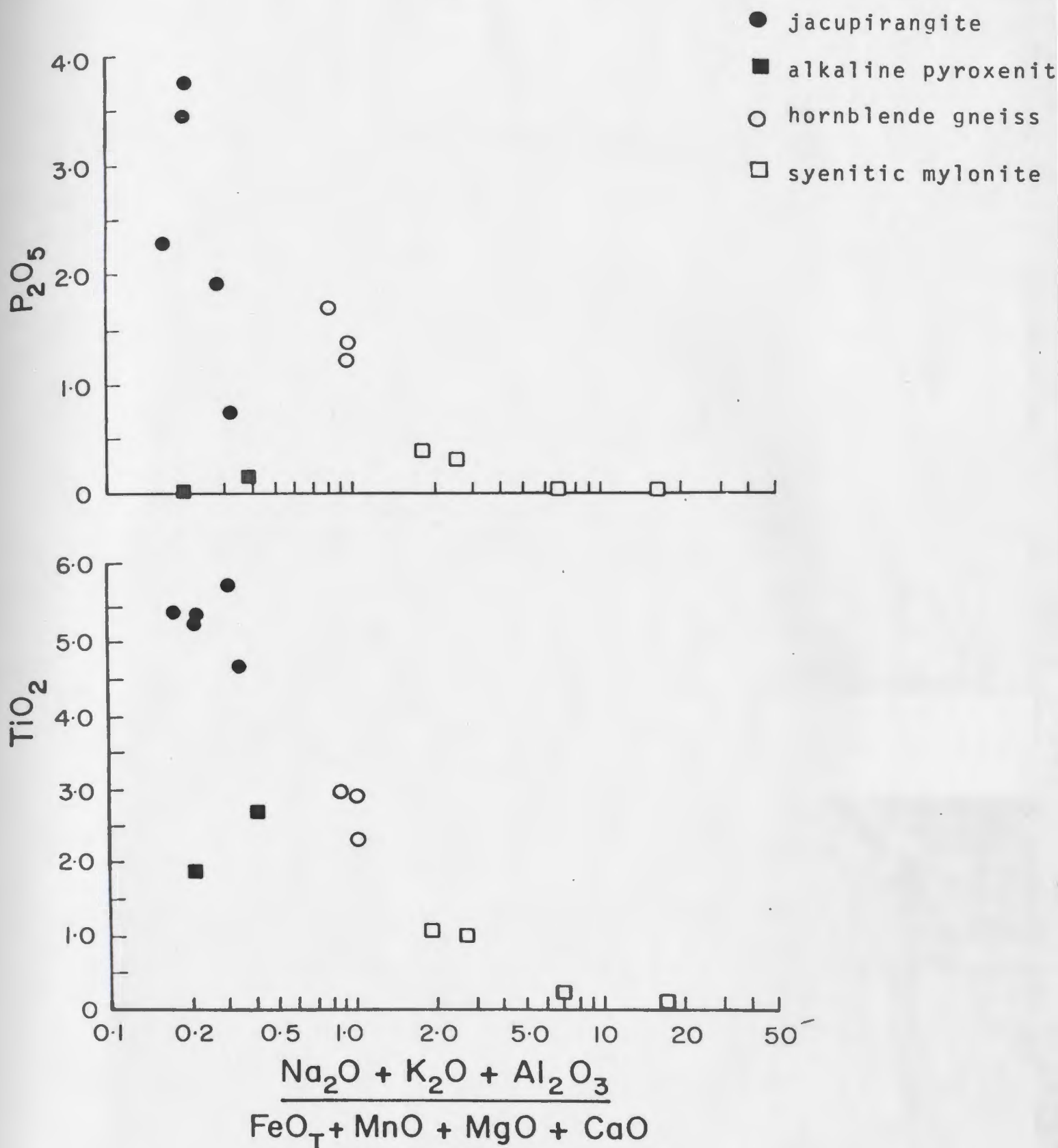
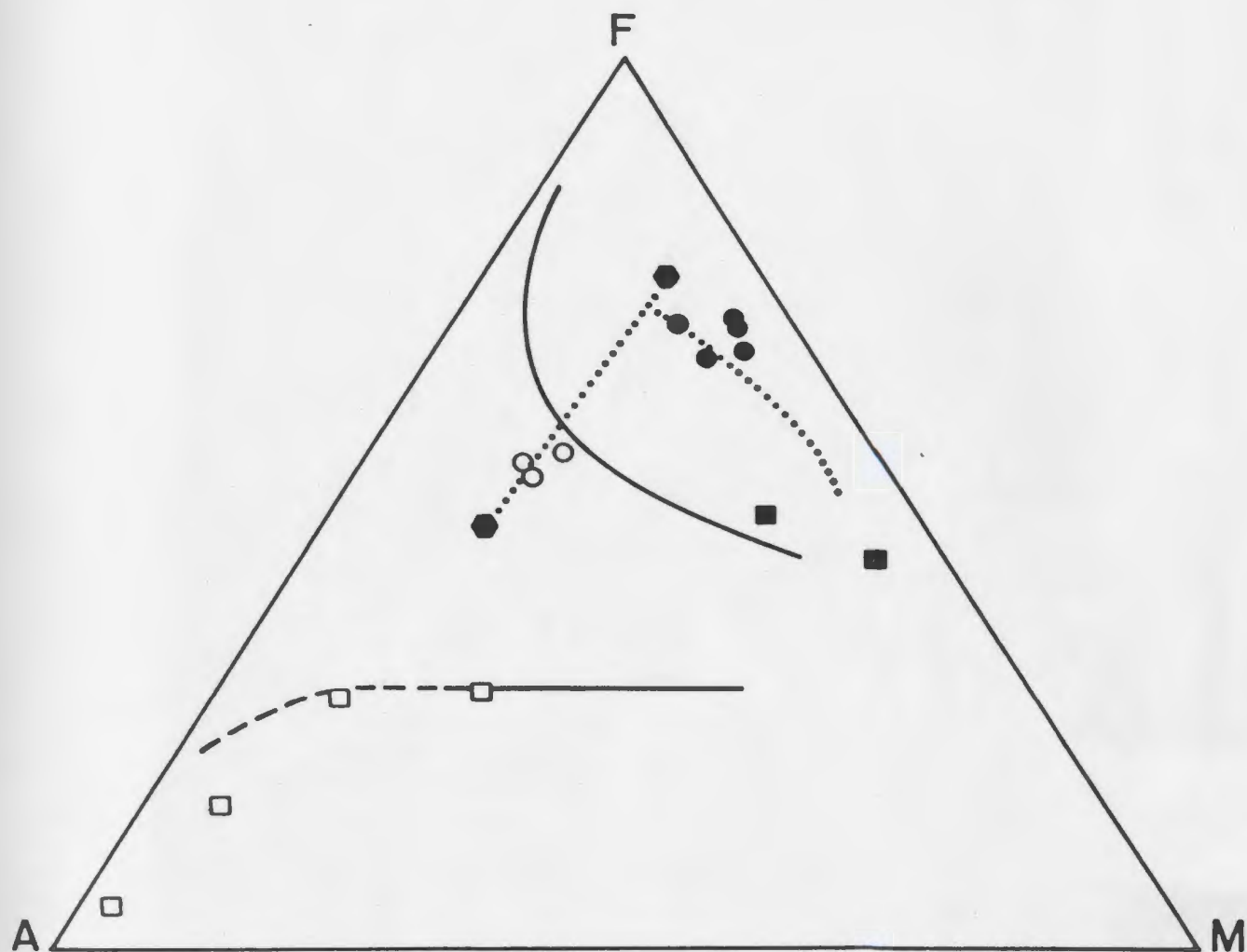


FIGURE 3.55: Compositions of jacupirangite - syenite assemblage rocks emphasizing partitioning of TiO_2 , P_2O_5 , FeO , MnO , MgO , and CaO into mafic rocks and Na_2O , K_2O , and Al_2O_3 into felsic rocks.



● jacupirangite

○ hornblende gneiss

■ alkaline pyroxenite

□ syenitic mylonite

● immiscible liquid compositions (Hess et al, 1975)

FIGURE 3.56: Compositions of jacupirangite - syenite assemblage rocks compared to experimentally determined liquid immiscibility fields. Solid and dashed lines from Philpotts (1976), dotted lines from Hess et al, (1975).

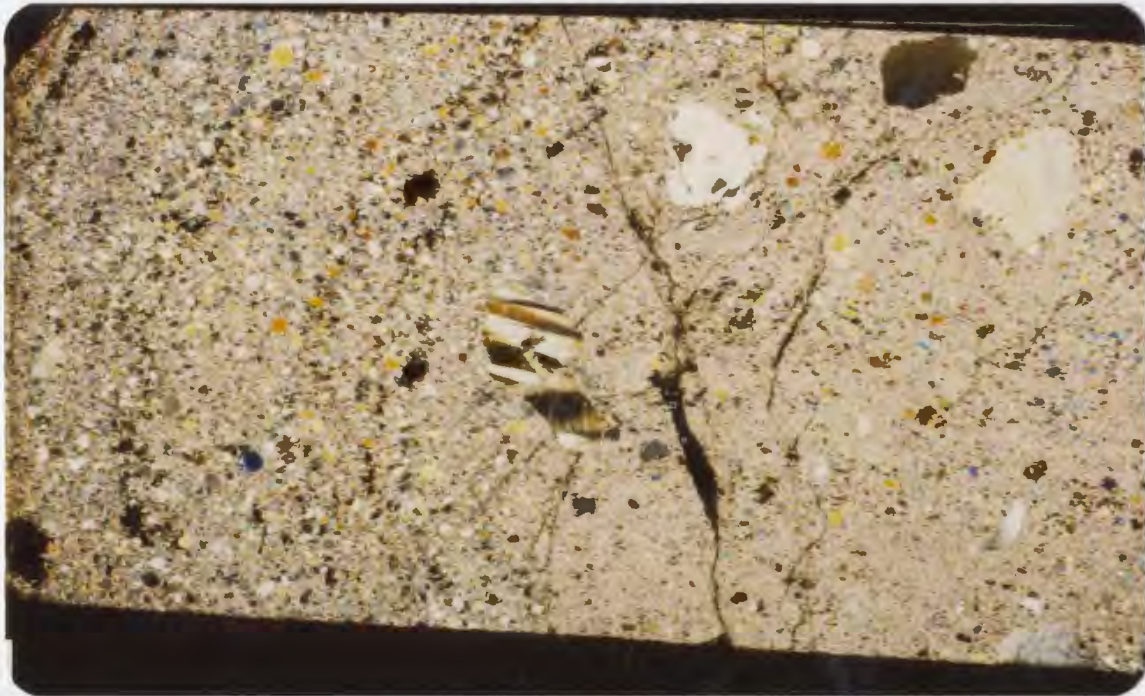
Table 3.11. Petrography of the White Hills Peridotite.

LITHOLOGY	MINERALOGY	FABRIC
1) HARZBURGITE 121, 125, 127, 483 509, 555 FIG. 3.57b.	ol (\rightarrow serp) (60-80%); opx (\rightarrow talc, tremolite) (20-35%) sp (\rightarrow chl, mt) (1-5%); parg (0-1%) opx exsolving cpx // (100)	S _{p1} - porphyroclastic opx, ol in matrix of ol, opx, sp S _{p2} - mylonitic; opx porphyroclasts elongated along (100) (5mm to 2cm) in very fine-grained matrix ($\sim 50\mu$) of ol, opx, sp
2) LHERZOLITE 124, 493, 498, 662 FIG. 3.57a, 3.58, 3.59.	ol (\rightarrow serp) (60-80%); opx (\rightarrow trem, talc) (20-30%); cpx (1-10%); plag (< 1%); parg (0-10%); phl (< 1%); sp (1-3%) Parg pleochroism; X = yellow; Y = Z = orange brown opx exsolving cpx \rightarrow parg / brown and green-brown spinel cpx, plag // (100) opx \rightarrow ol	S _{p1} - porphyroclastic opx, ol, cpx; holly leaf sp S _{p2} - mylonitic; opx porphyroclasts elongated along (100) (see above); pargasite bands parallel to S _{p2} ; elongated sp aggregates;
3) PYROXENITE 484	cpx (50-70%); opx (50-30%); sp (1-5%) ol (0-10%) cpx, opx mutual exsolution	S _{p1} - coarse-grained cpx, opx (1-5 mm); bent; undulose Xn; recrystallized along grain boundaries
4) DUNITE 126, 500, 507	ol (\rightarrow serp, mt) (90-99%); chr (\rightarrow mt) (1-10%)	S _{p1} elongated ol with kink bands in matrix of fine grained, recrystallized ol, chr S _{p2} - decrease in grain size (< 50 μ);
5) GABBRO G12, 509 FIG. 3.57b.	cpx (40-60%); opx (0-20%); parg (0-30%); plag (10-20%); sp (2-10%) cpx \rightarrow parg plag + opx \rightarrow gr sp	S _{p2} - locally mylonitic cpx, opx, showing undulose Xn, recrystallized along grain boundaries bright green spinel elongated parallel to S _{p2} , concentrated in layers, sometimes with pargasite

FIGURE 3.57: Basal mylonite, White Hills Peridotite.



3.57a: RJ76-498. Plagioclase-bearing mylonite, showing greatly elongated orthopyroxene crystals in a fine-grained matrix consisting mainly of olivine. Plagioclase is associated with the orthopyroxene crystals in the upper left. (Crossed Nicols). Width of field is 3.8 cm.



3.57b: RJ76-509. Folded gabbroic band (left) in harzburgite. Gabbro consists of spinel, plagioclase, and pyroxene; harzburgite contains orthopyroxene porphyroclasts in olivine matrix. Note kinked orthopyroxene in fold hinge. Width of field is 3.6 cm.

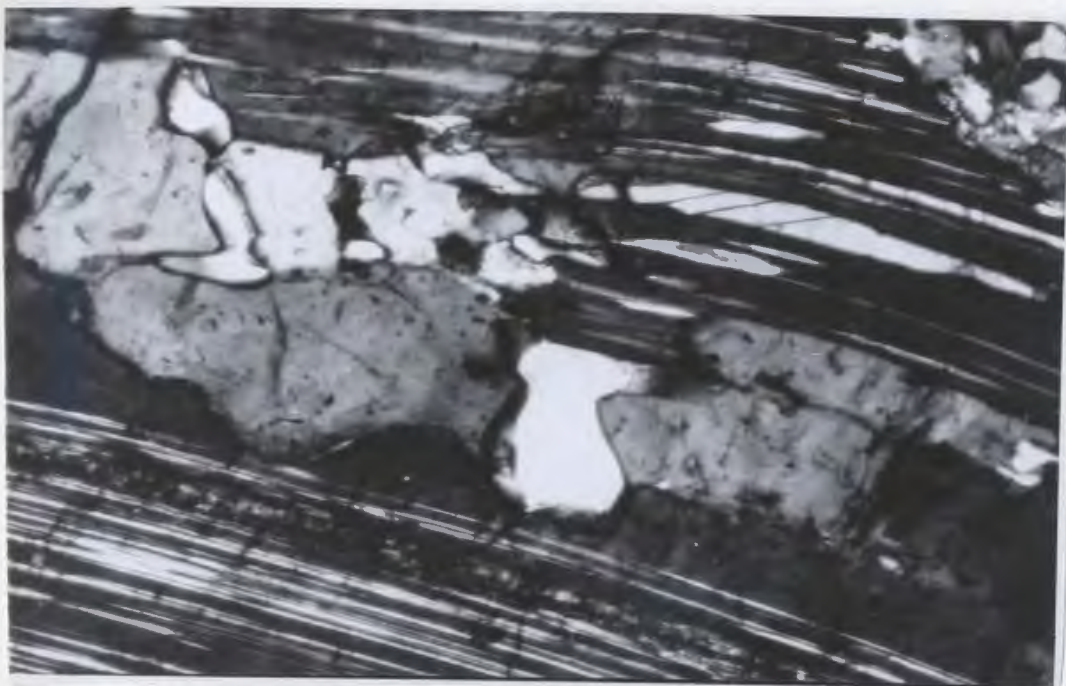


FIGURE 3.58: RJ76-498. Plagioclase (clear) exsolving from orthopyroxene. Note twinning in plagioclase at high angle to (100) in pyroxene. Width of field is about 0.1 mm.

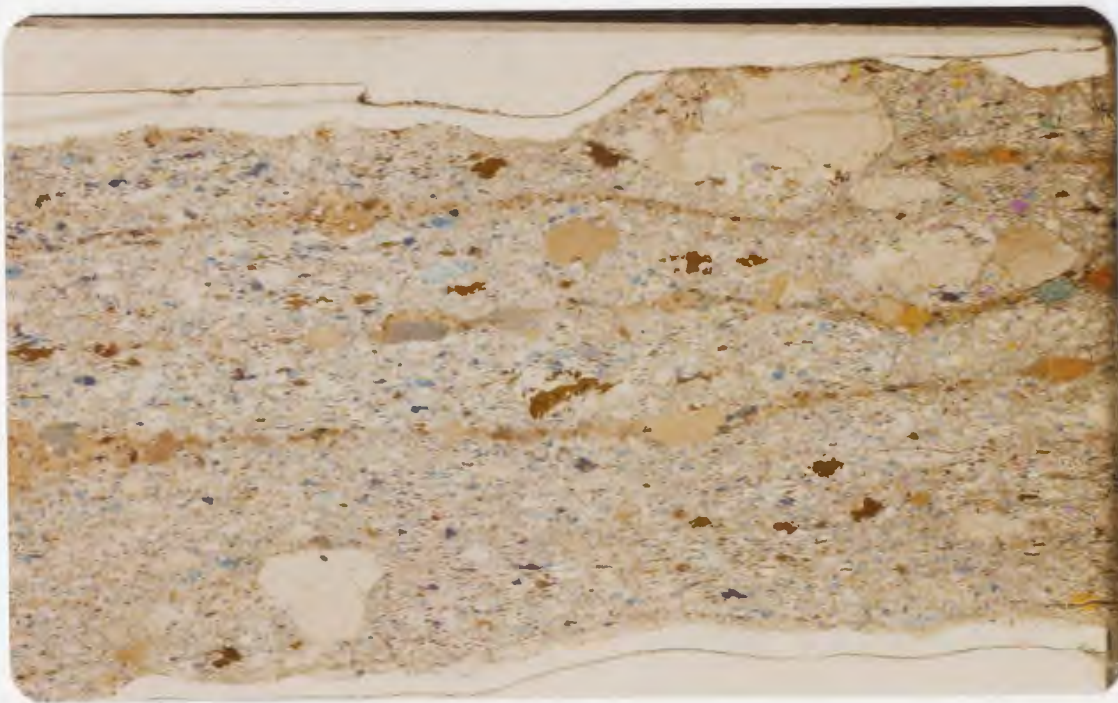


FIGURE 3.59: RJ77-662A. Amphibole lherzolite from base of peridotite. Pargasite bands (orange-brown) and enstatite porphyroclasts (buff) occur in a matrix of fine-grained olivine, pyroxene, and spinel (brown). (Partly crossed Nicols). Width of field is 3.5 cm.

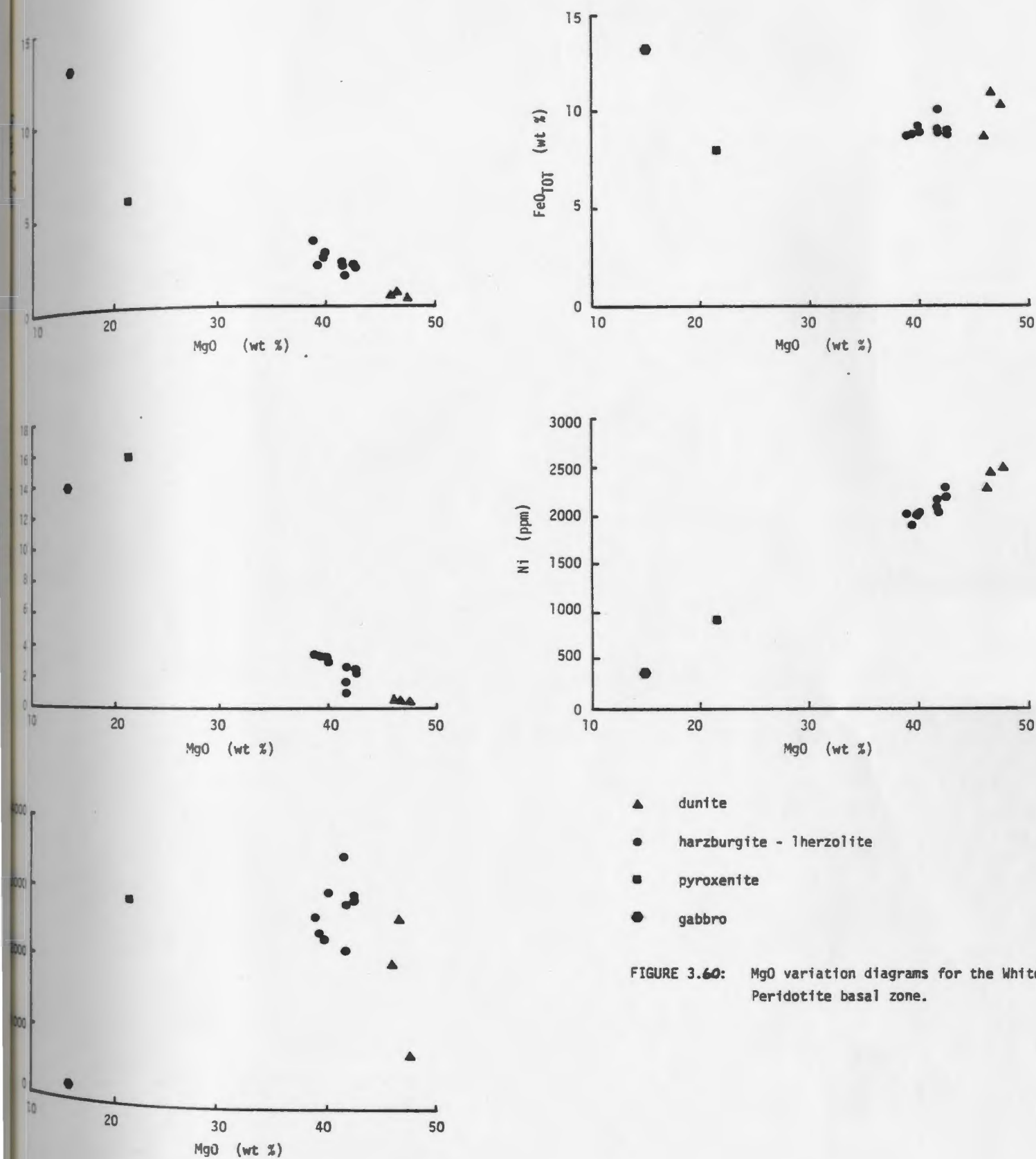


FIGURE 3.60: MgO variation diagrams for the White Hills Peridotite basal zone.

- harzburgite
- lherzolite
- ▲ dunite - serpentinized
- △ dunite - fresh
- basal zone lherzolite
- amphibole lherzolite
- pyroxenite

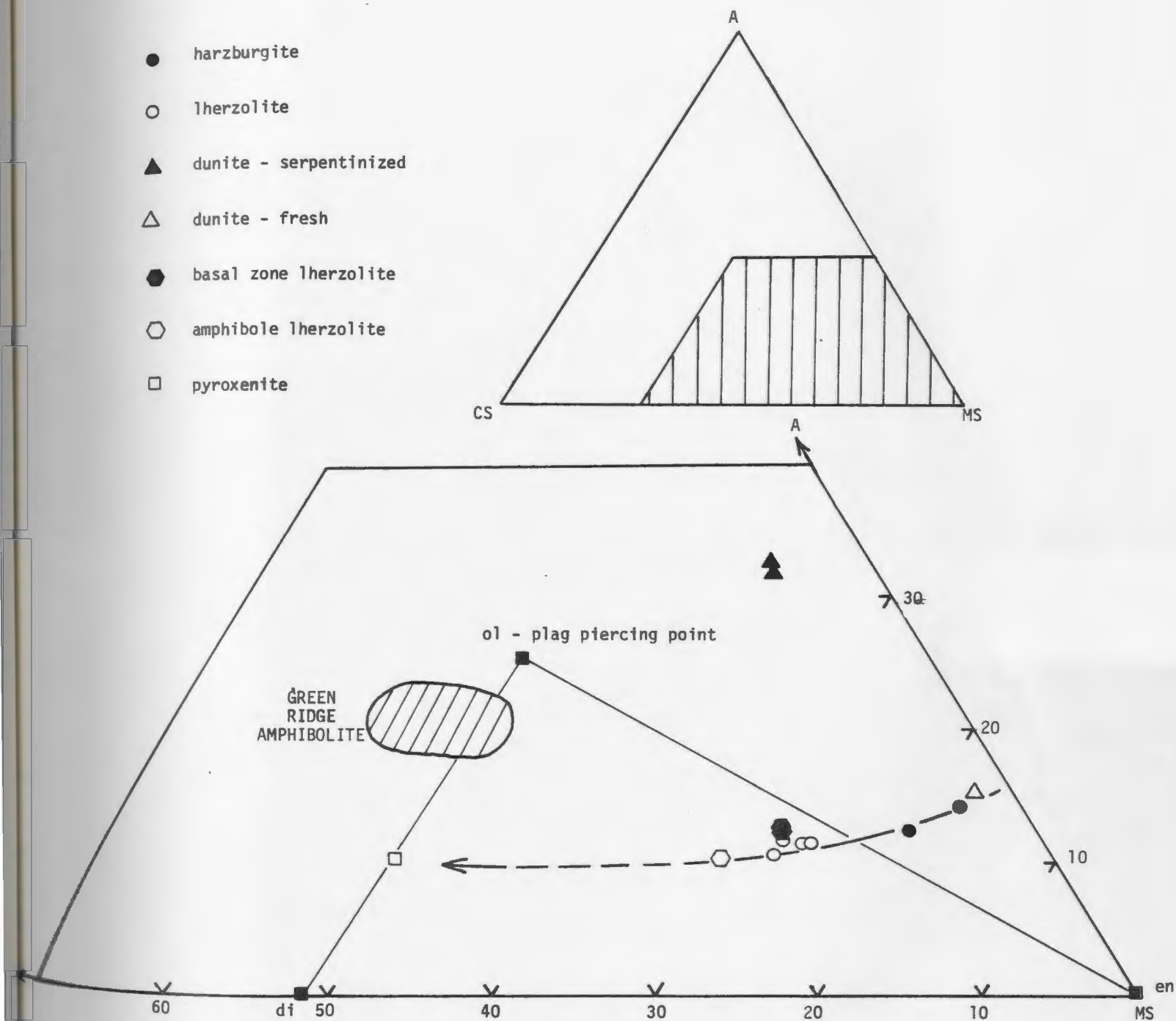


FIGURE 3.61: Compositions of the White Hills Peridotite projected onto the plane $\text{CaSiO}_3 - \text{MgSiO}_3 - \text{Al}_2\text{O}_3$ from olivine (after O'Hara, 1968), showing the trend of amphibole lherzolite toward pyroxenite rather than amphibolite.

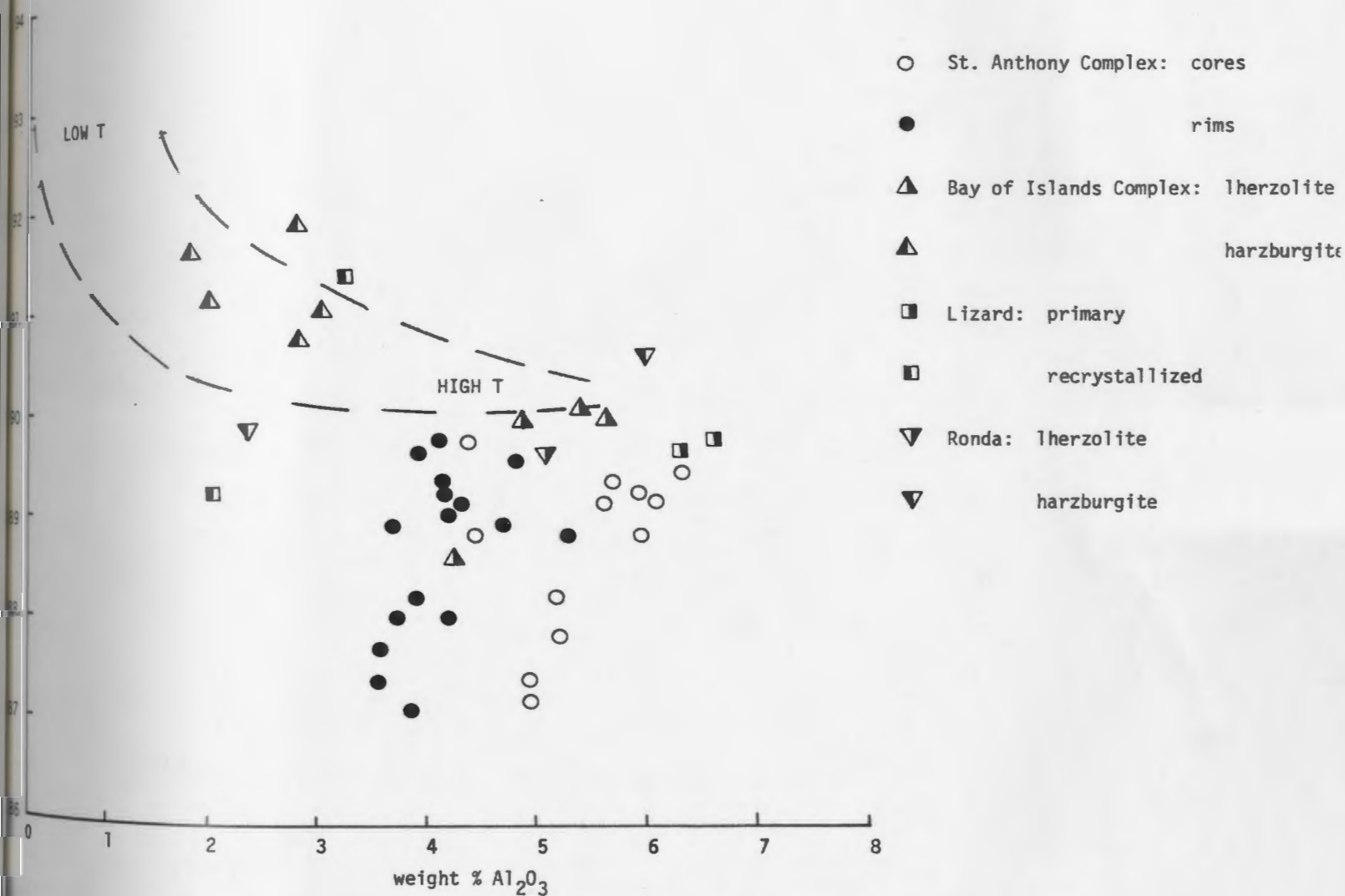
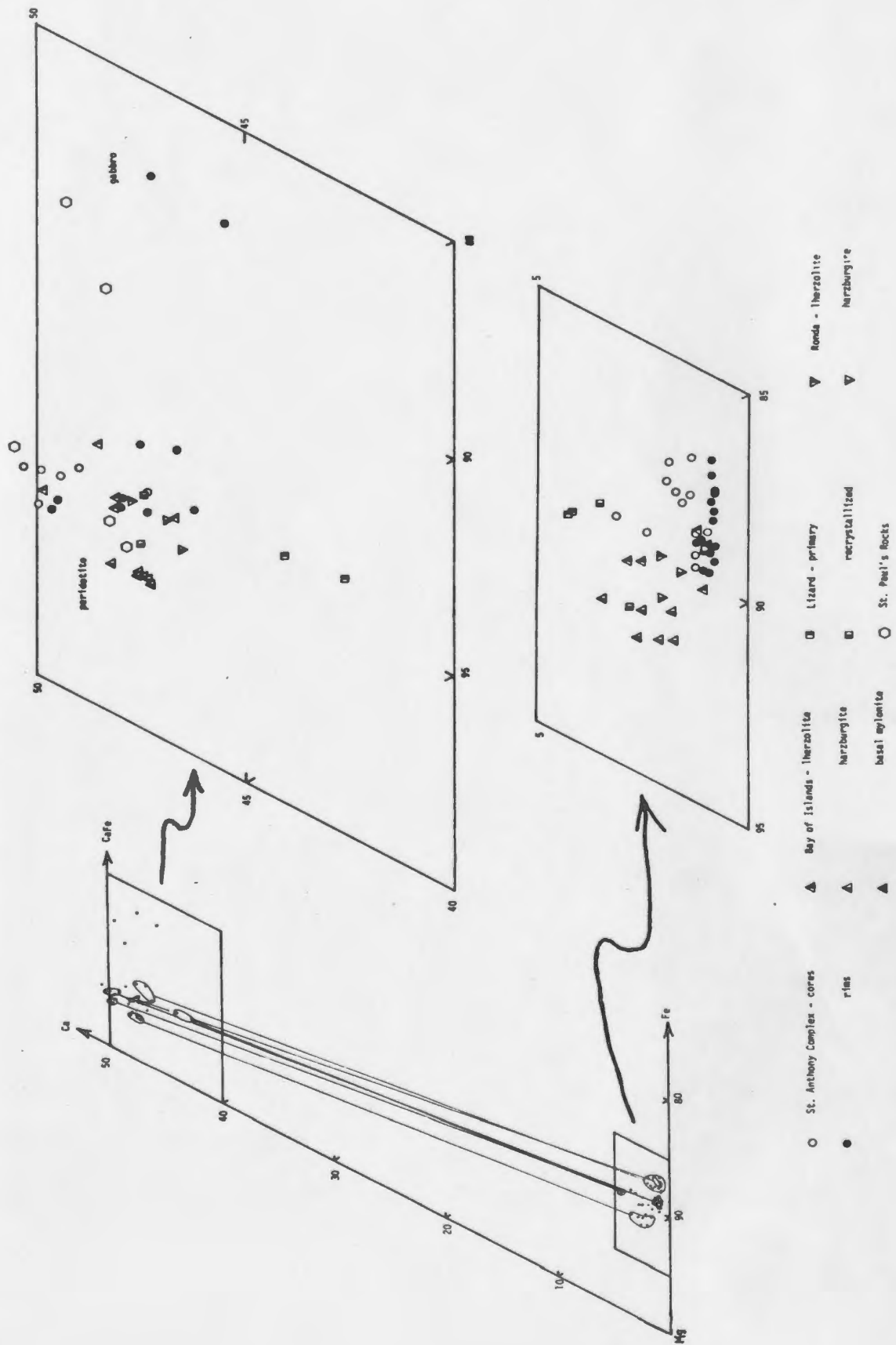


FIGURE 3.62: Orthopyroxene compositions from the White Hills Peridotite compared to those from other peridotites with dynamothermal aureoles. The high temperature - low temperature trend is taken from Dick (1977).

FIGURE 3.65: Compositions of pyroxenes from the White Hills Peridotite compared to those from other peridotites with dynamothermal histories. Tie lines join coexisting pyroxenes.



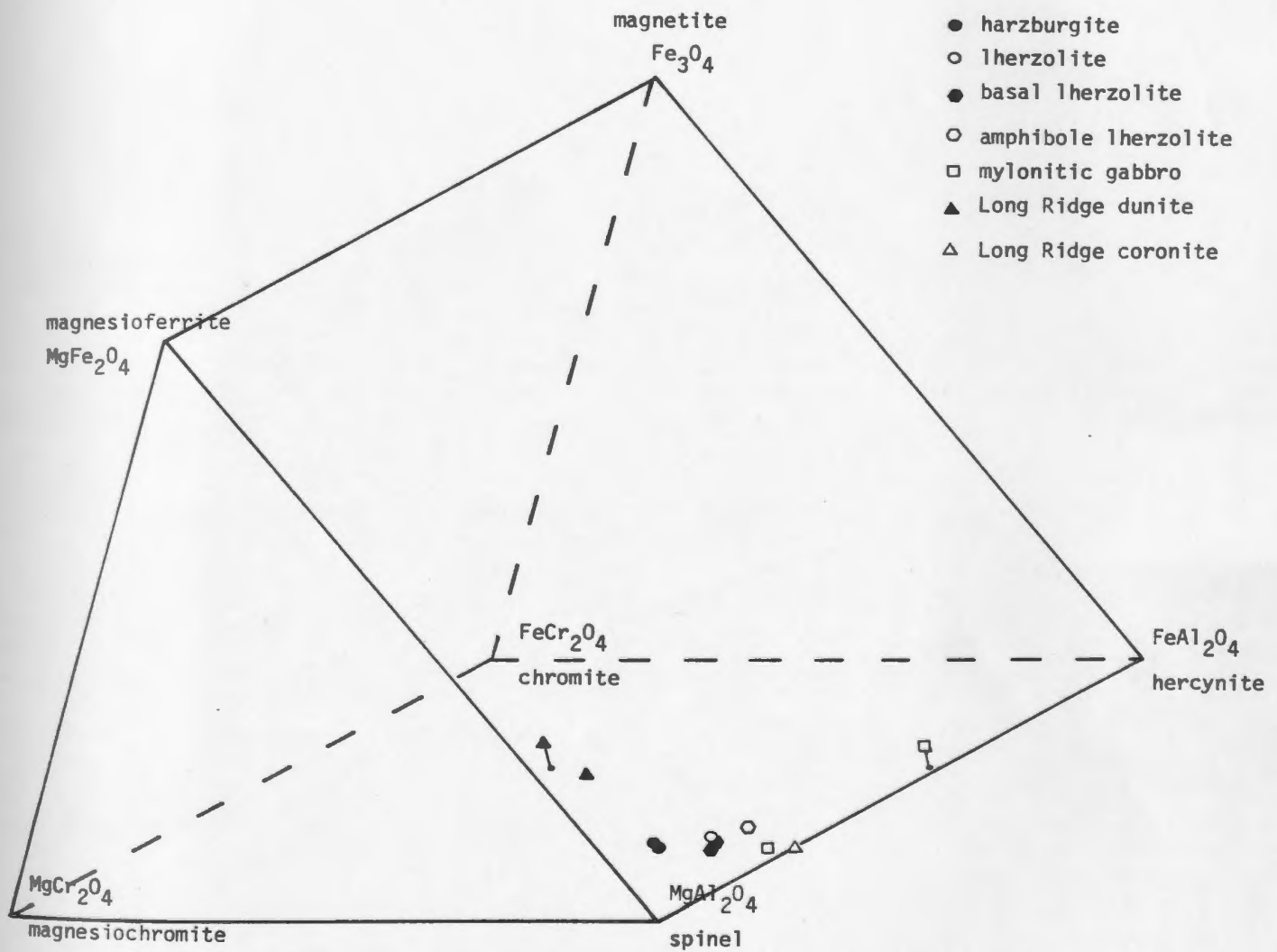


FIGURE 3.64: Spinel compositions from the White Hills Peridotite and the Long Ridge Metagabbro shown in the spinel prism of Irvine (1965).

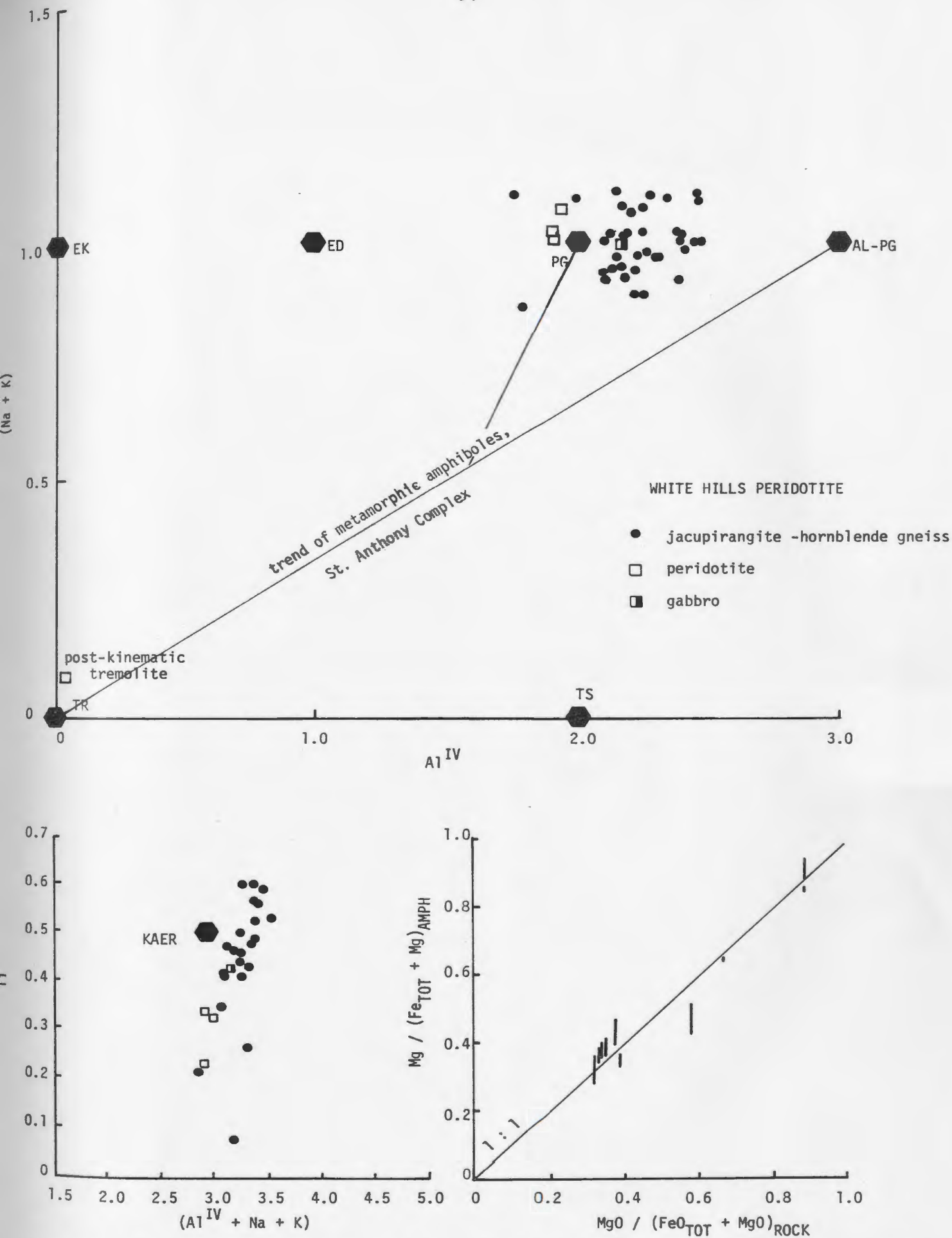


FIGURE 3.65: Amphibole chemistry of the White Hills Peridotite and associated rocks, showing enrichment in Al, Na, K, and Ti, particularly in the kaersutites from the jacupirangite - syenite assemblage, and the overall dependence of Mg/Fe on bulk rock composition.

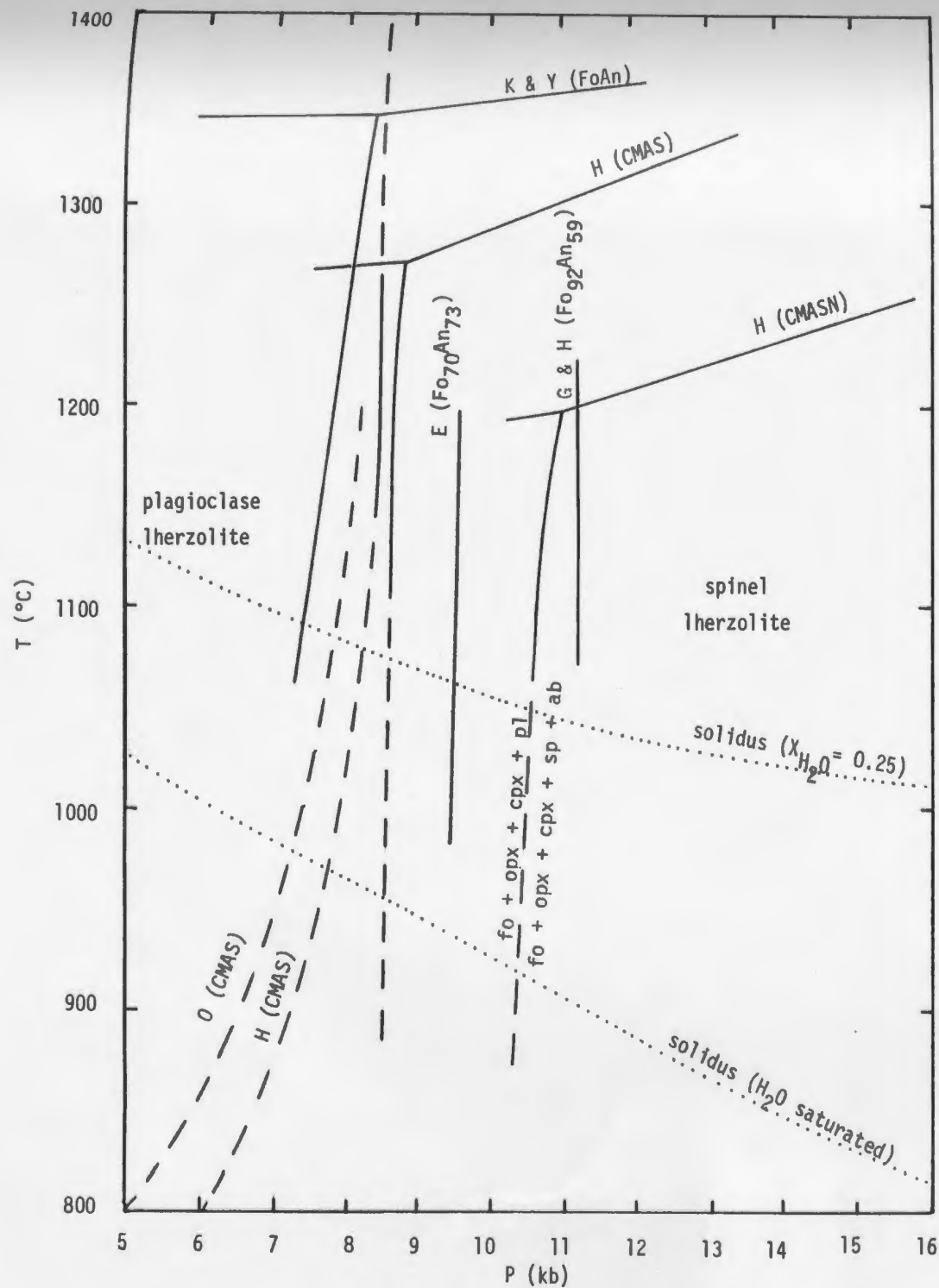


FIGURE 3.66: Pressure - temperature relationships for the transition from plagioclase peridotite to spinel peridotite for different bulk compositions. Solid lines indicate experimentally calibrated curves; dashed lines indicate calculated or extrapolated curves.

K & Y = Kushiro and Yoder (1966)

H = Herzberg (1976a,b; 1978)

E = Emslie (1971)

G & H = Green and Hibberson (1971)

O = Obata (1976)

Solidus lines from Boettcher *et al.*, (1975)

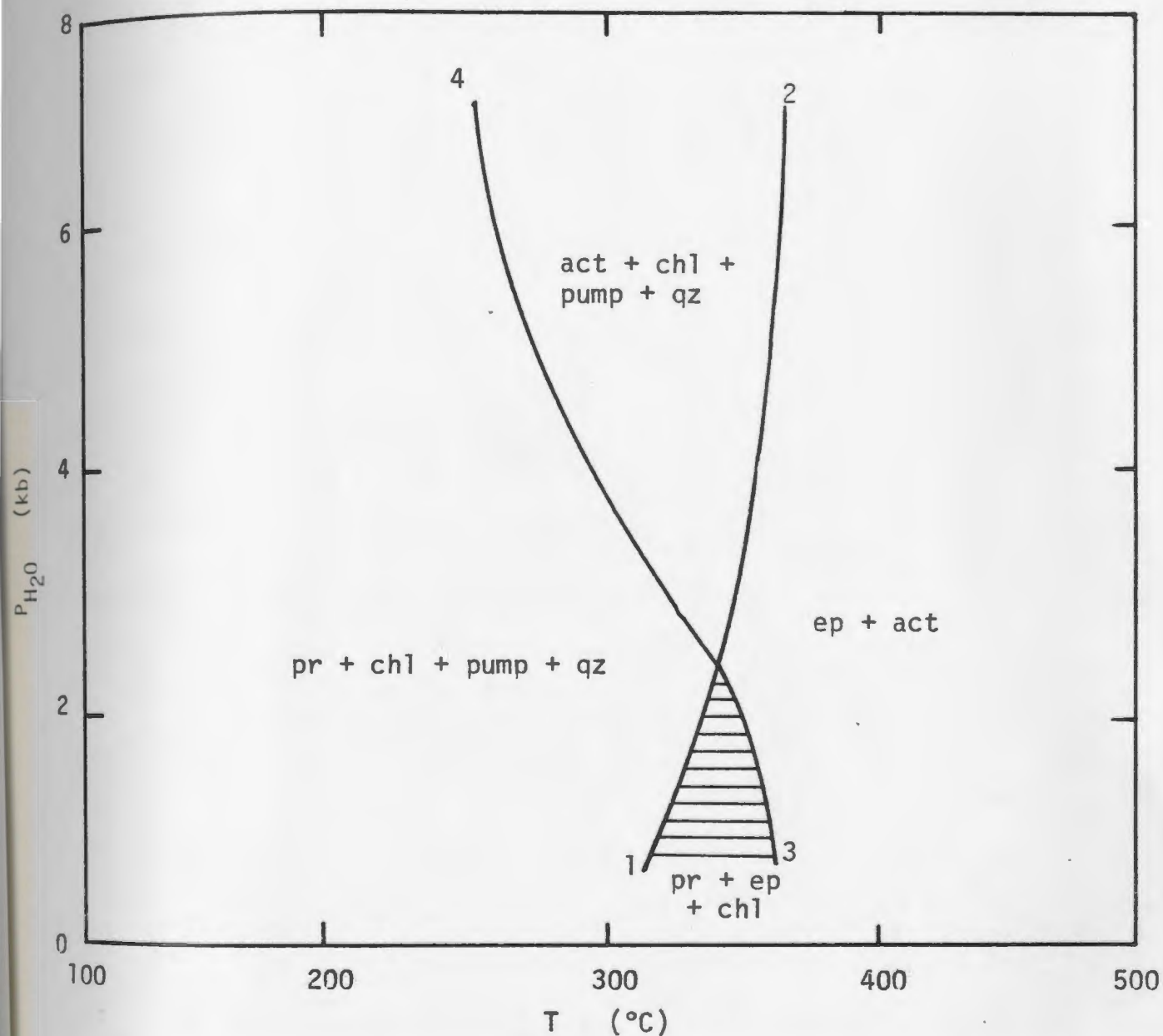
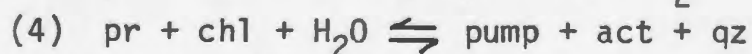
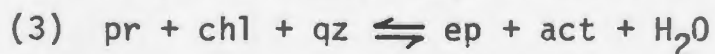
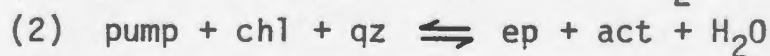
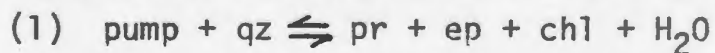


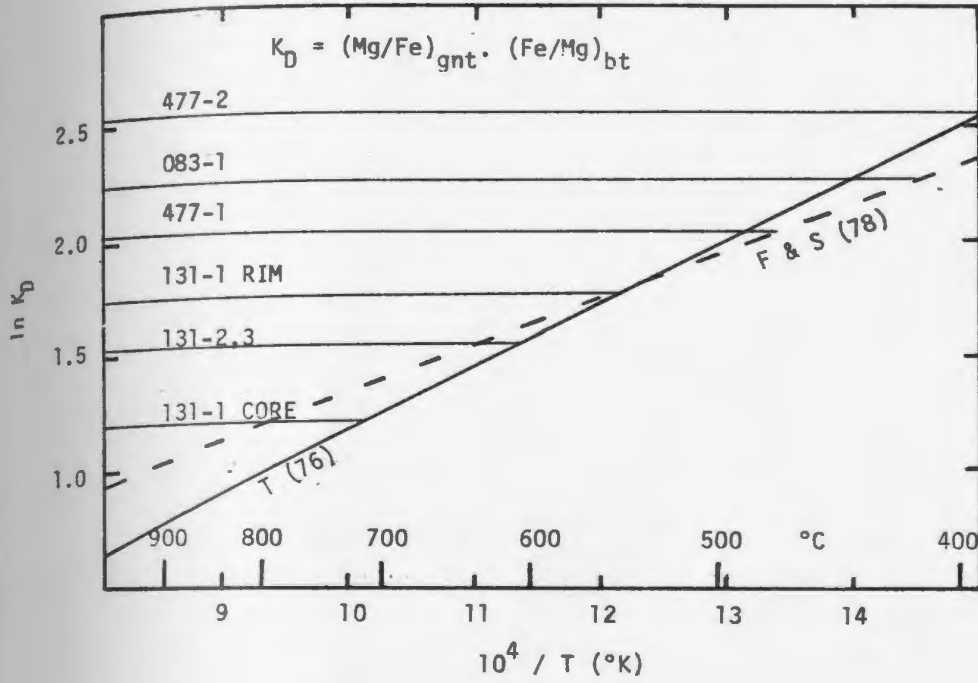
FIGURE 4.1: Phase relationships for low-grade metamorphism of basic rocks.



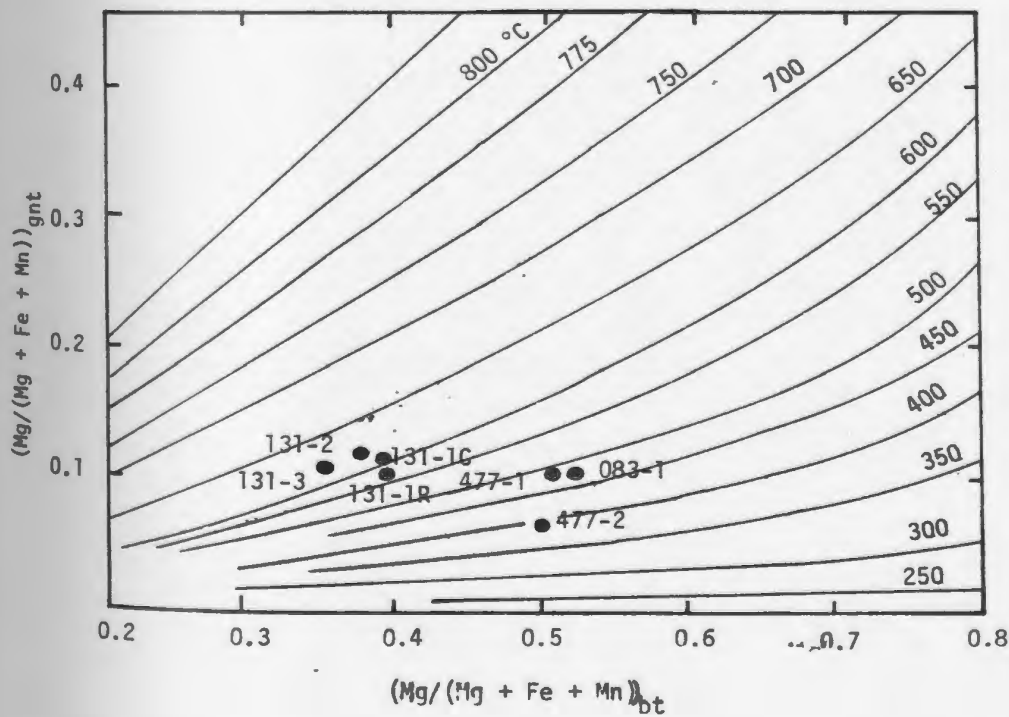
(after Nitsch, 1971)

Shaded area shows stability of secondary mineral assemblage in the Ireland Point Volcanics.

FIGURE 4.2: Biotite - garnet thermometry of biotite amphibolites, Three Mountain Summit (cf. Table 4.1).



a) Calibrations of Thompson (1976) (solid line) and Ferry and Spear (1978) (dashed line).



b) Calibration of Perchuk (1970).

Table 4.1. Temperature estimates for biotite-garnet pairs in the biotite amphibolite mylonite zone (see Fig. 4.2).

	T°C			
Sample	Perchuk (1970)	Thompson (1976)	Ferry & Spear (1978)	Average
small, matrix garnets				
131 - 2, 3	620	620	635	625
large porphyroclast				
131 - 1, CORE	610	717	791	610*
131 - 1 RIM	575	563	570	571
euhedral matrix garnets				
477 - 1	480	496	469	482
477 - 2	390	394	360	381
euhedral garnet with hornblende, biotite				
083 - 1	475	444	427	449

* difference attributable to high Mn, not compensated for by equations of Thompson (1976) or Ferry & Spear (1978).

Table 4.2. Temperature estimates for the Northeast Island marble.

$$T (^{\circ}\text{K}) = \frac{-1690}{\log X_{\text{MgCO}_3}^{\text{cc}} - 0.795} \quad (\text{Rice, 1977})$$

SAMPLE	X calcite MgCO ₃	T(°C)
1-1	.121	714
1-2	.037	486
1-AVE	.071	596
2-1	.190	842
2-2	.112	695
2-3	.058	559
2-AVE	.126	724
3-1	.168	804
3-2	.069	591
3-AVE	.107	684
CAL-AVE	.106	682

Table 4.3. Two-pyroxene geothermometry of the St. Anthony Complex using the equation of Wells (1977):

$$T(^{\circ}\text{K}) = \frac{7341}{3.355 + 2.44 X_{\text{Fe}}^{\text{opx}} - \ln K}$$

$$K = \frac{a_{\text{Mg}_2\text{Si}_2\text{O}_6}^{\text{cpx}}}{a_{\text{Mg}_2\text{Si}_2\text{O}_6}^{\text{opx}}}$$

SAMPLE	TEMPERATURE (°C)		
<hr/>			
hornblende granulite	average		
RJ76-552			
552-1		863	
552-2		849	
552-3		860	
552-AVE		869	
<hr/>			
basal	cores	rims	matrix
basal amphibole lherzolite			
RJ77-662			
662-1		942	935
662-5		958	
<hr/>			
plagioclase-bearing basal peridotite			
RJ76-498			
498-1	879	909	911
	904	904	
498-2	845	944	937
<hr/>			
pyroxenite band, interior of massif			
RJ75-124			
124-1	875		853
124-3	874		836
<hr/>			
folded fine-grained plag-spinel band, near base			
509-2			919
509-3	973		

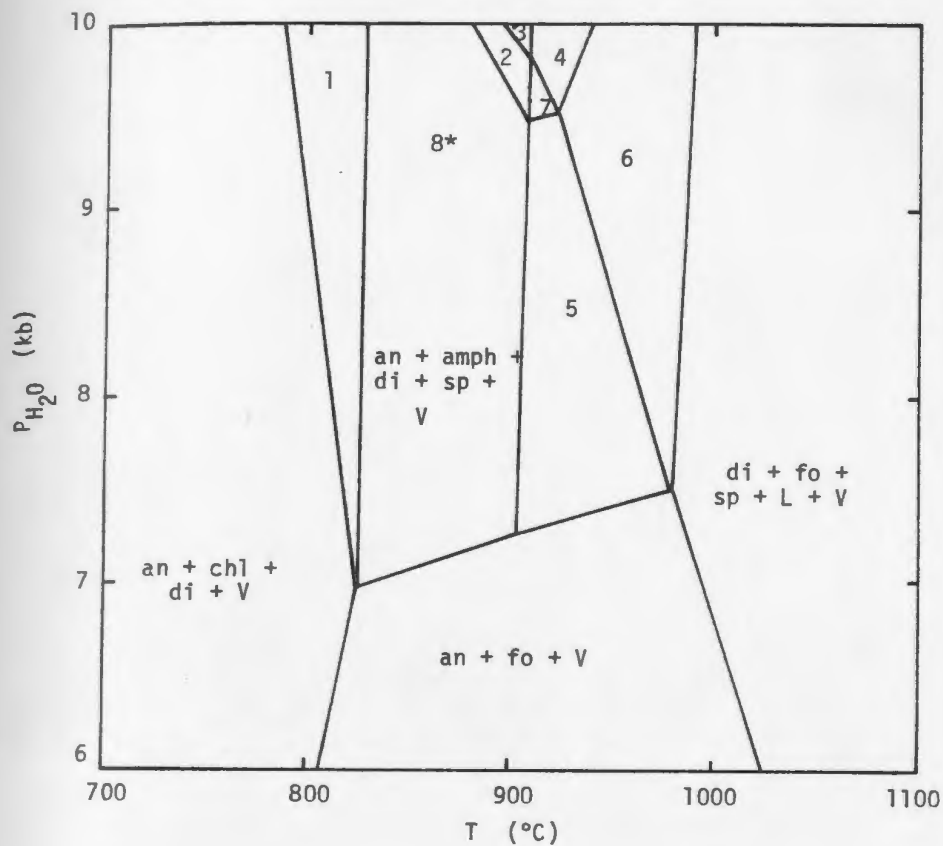


FIGURE 4.3a: Phase relations in the system $\text{CaO} - \text{MgO} - \text{Al}_2\text{O}_3 - \text{SiO}_2 - \text{H}_2\text{O}$ (Ford, 1972).

* Long Ridge Metagabbro coronites

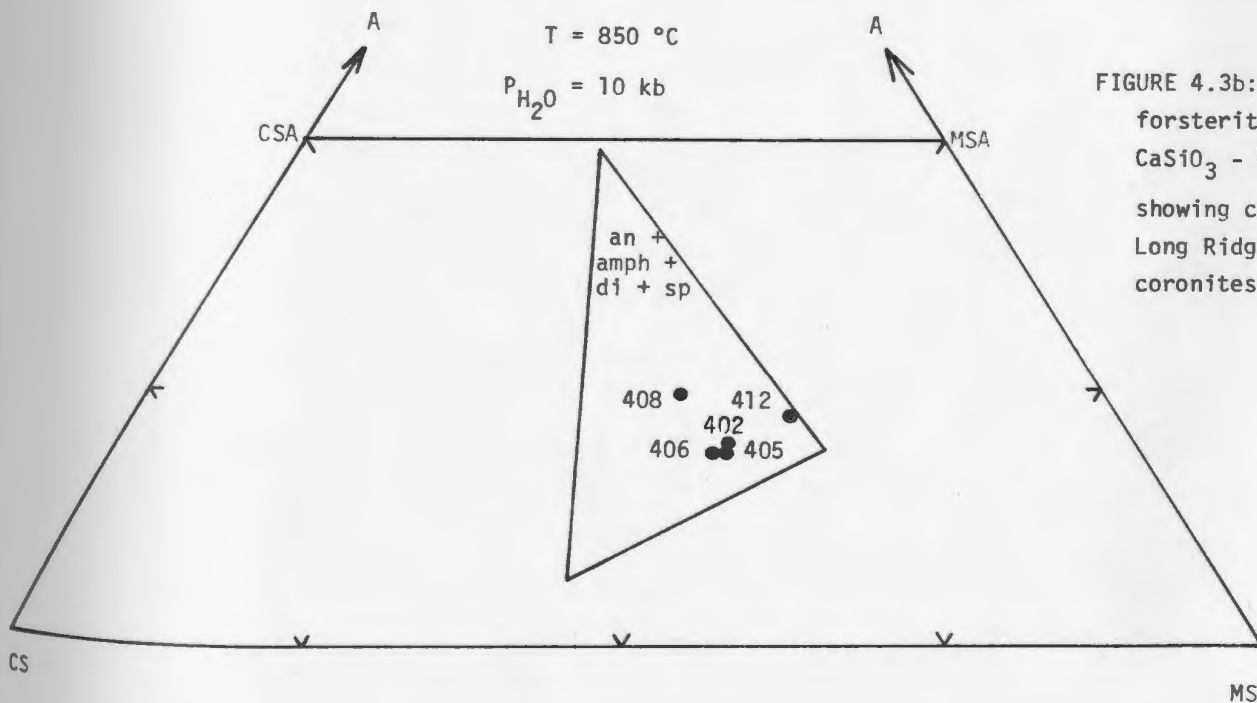


FIGURE 4.3b: Projection from forsterite onto the plane $\text{CaSiO}_3 - \text{MgSiO}_3 - \text{Al}_2\text{O}_3$ showing compositions of Long Ridge Metagabbro coronites (after Ford, 1972).

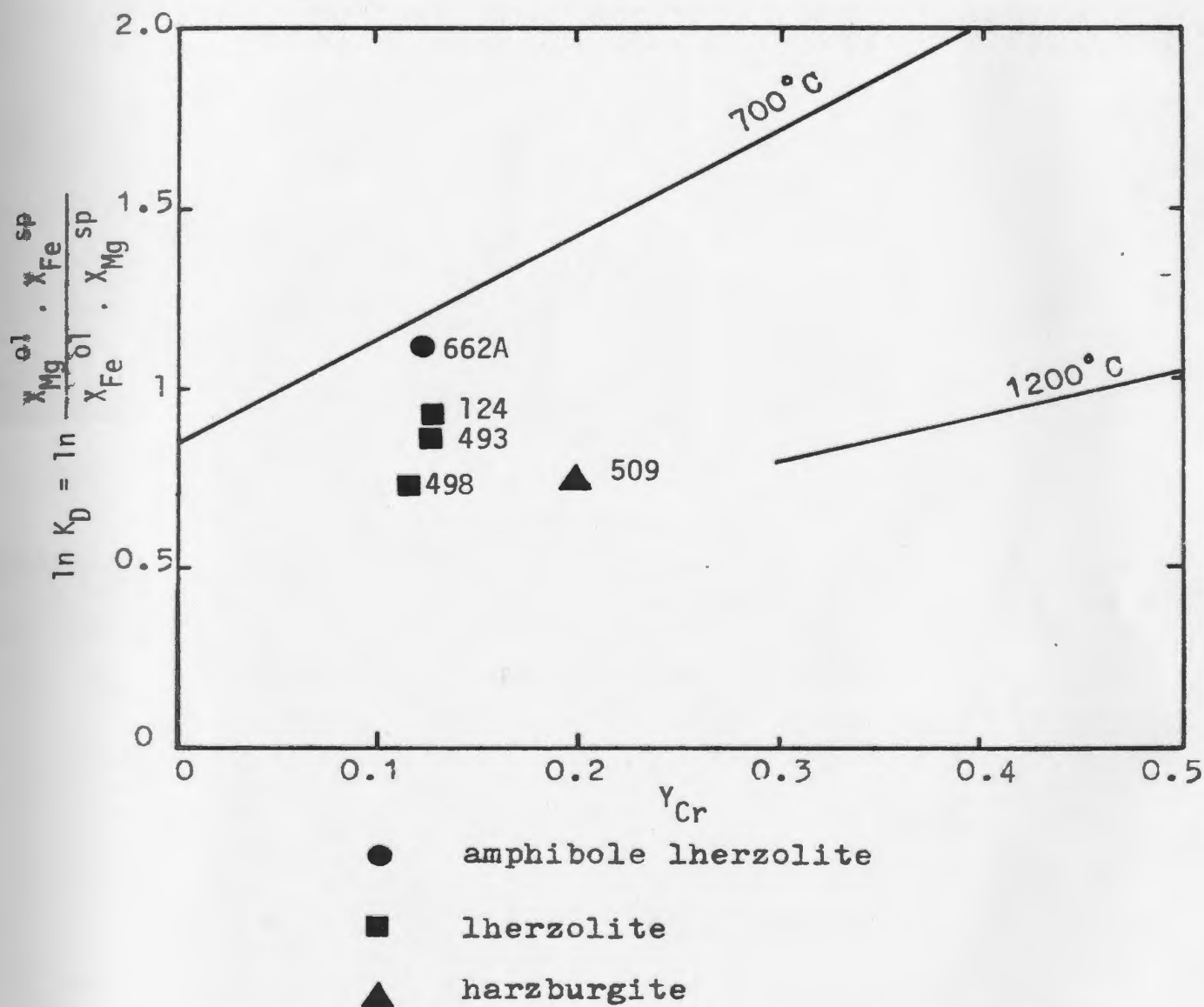
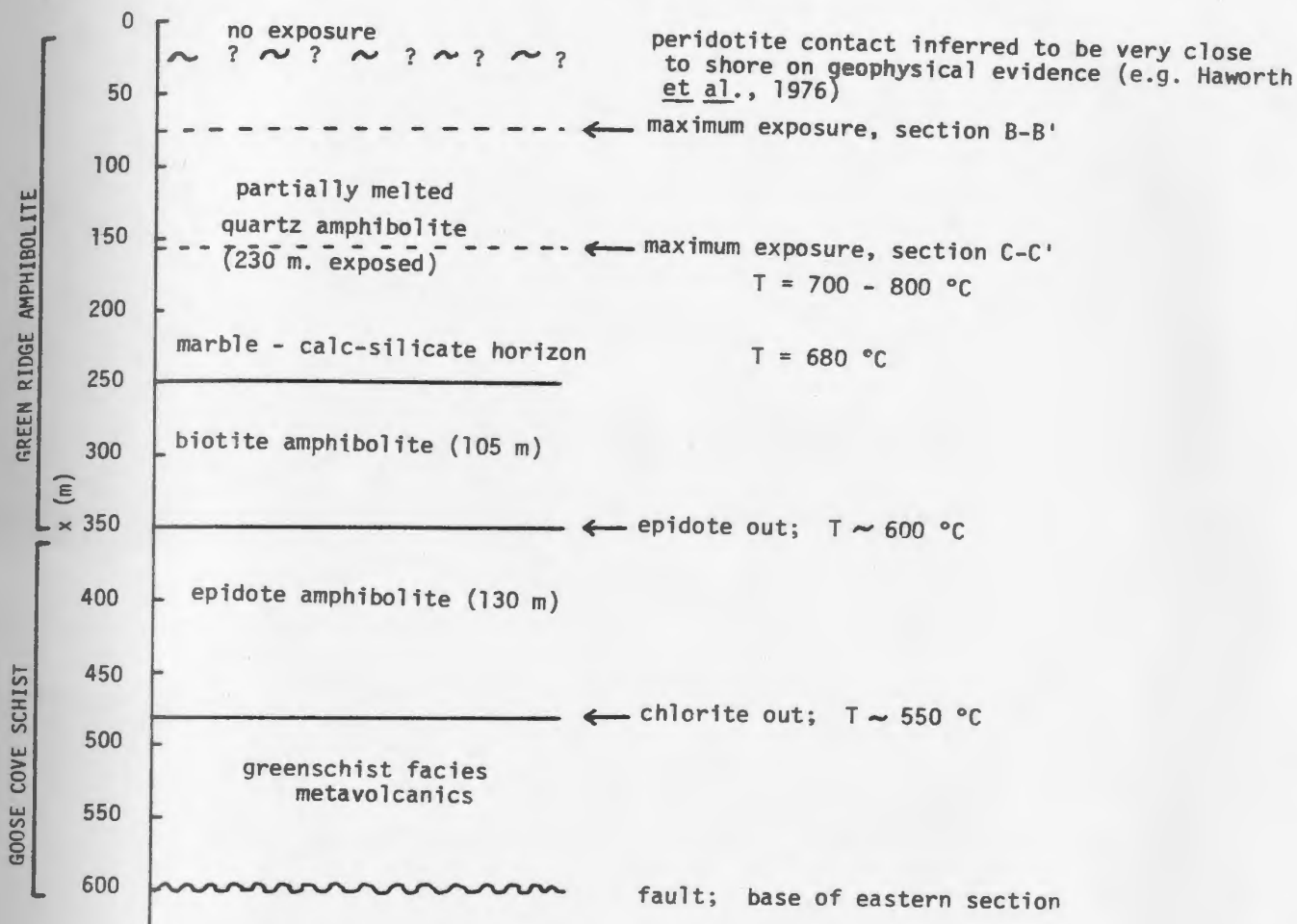


FIGURE 4.4: Compositions of spinels from basal zone of the White Hills Peridotite in relation to the approximate isotherms of Evans and Frost (1975)

FIGURE 4.5: Metamorphic section, Fischot Islands

a) Northeast Island and eastern Fischot Island



b) western Fischot Island

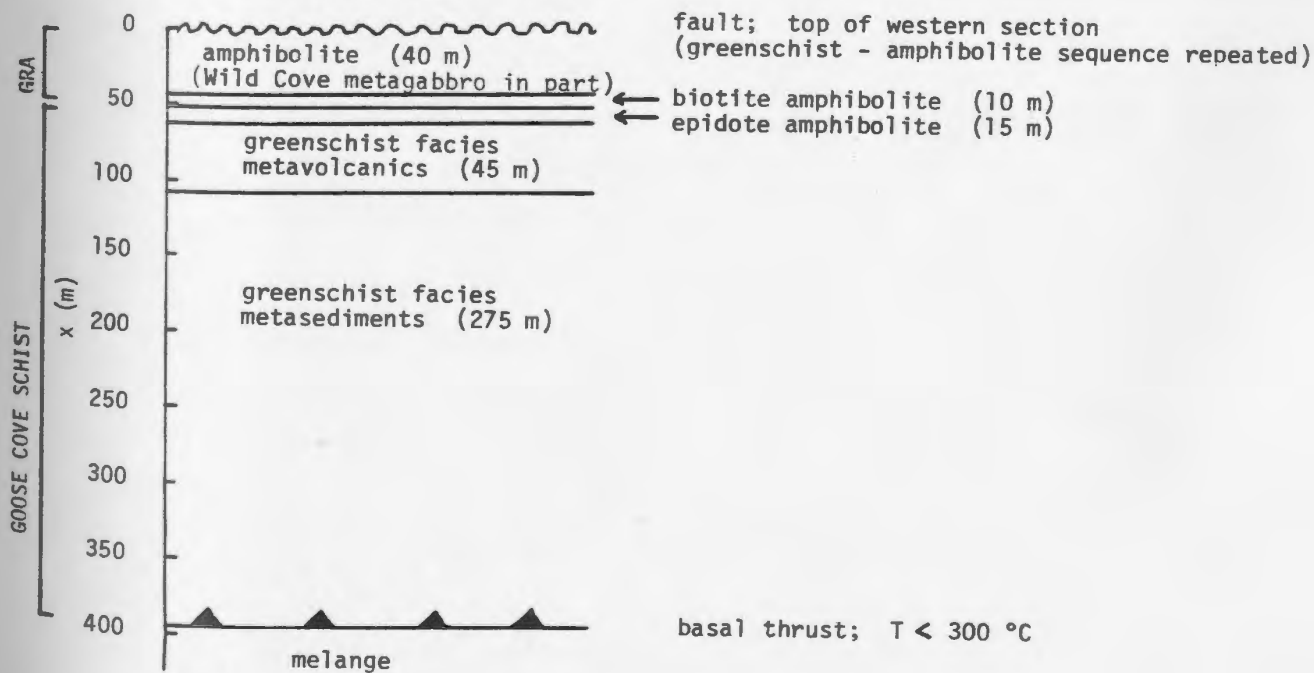


FIGURE 4.6: Metamorphic section, Three Mountain Summit

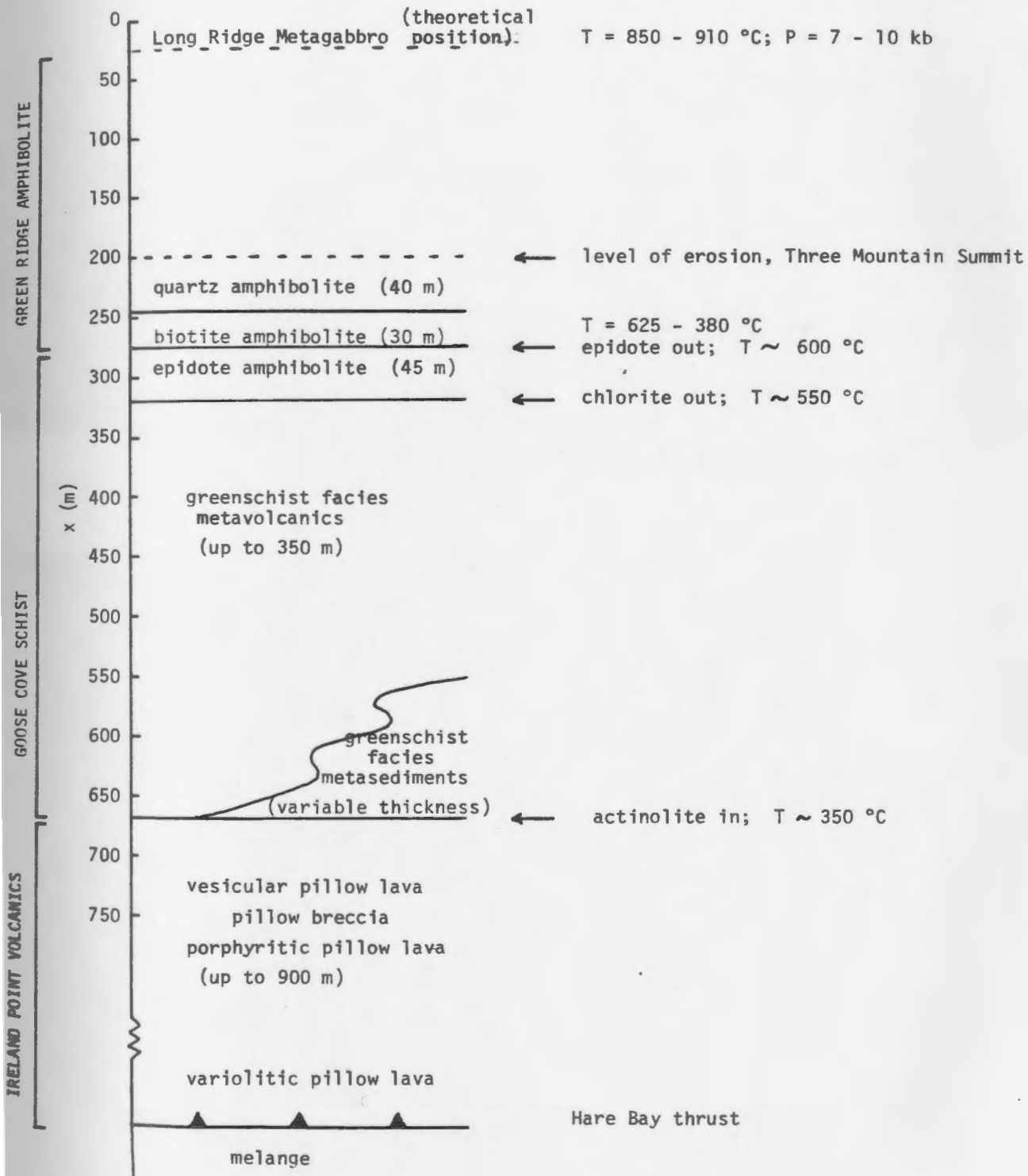
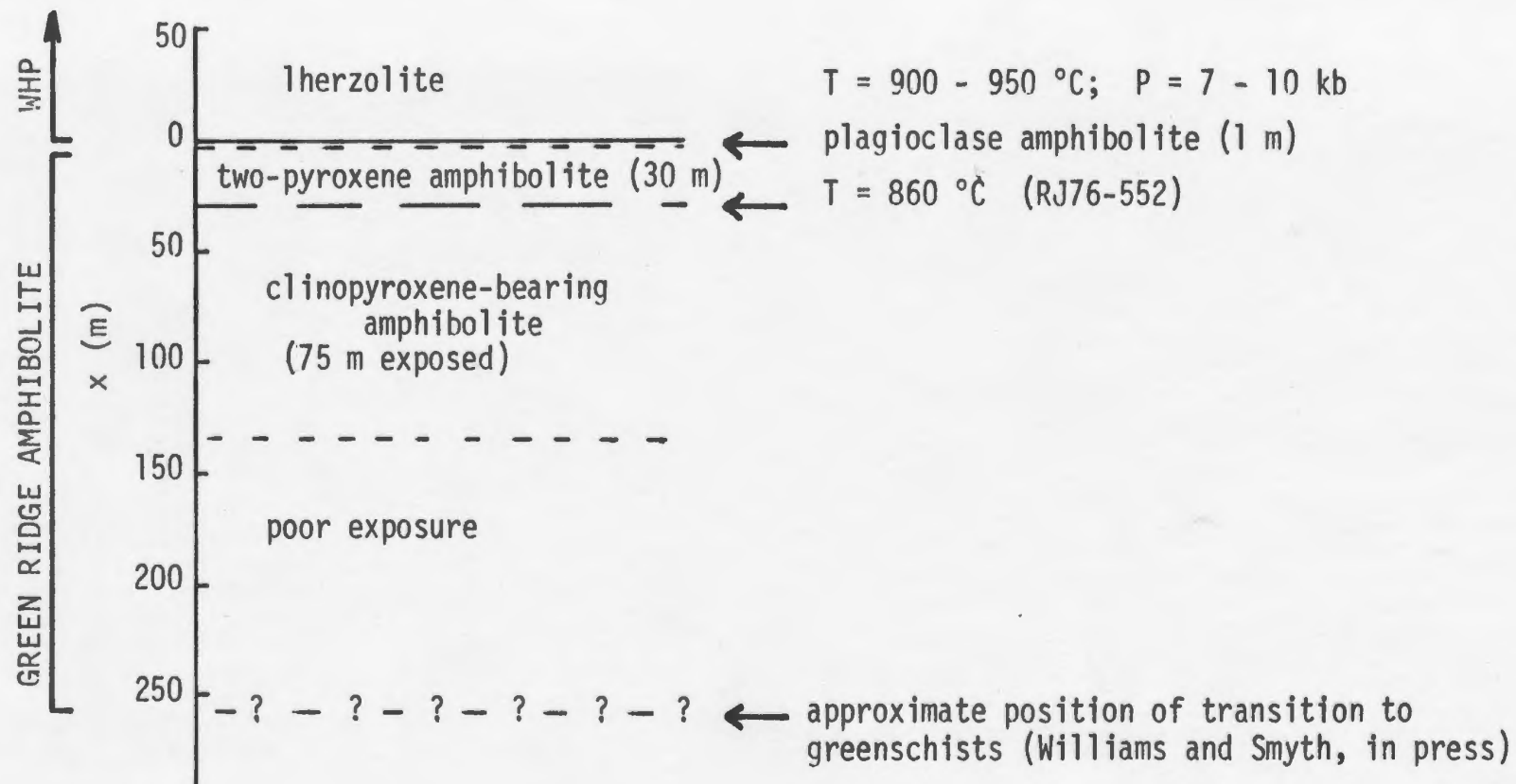


FIGURE 4.7: Metamorphic section, Brimstone Pond



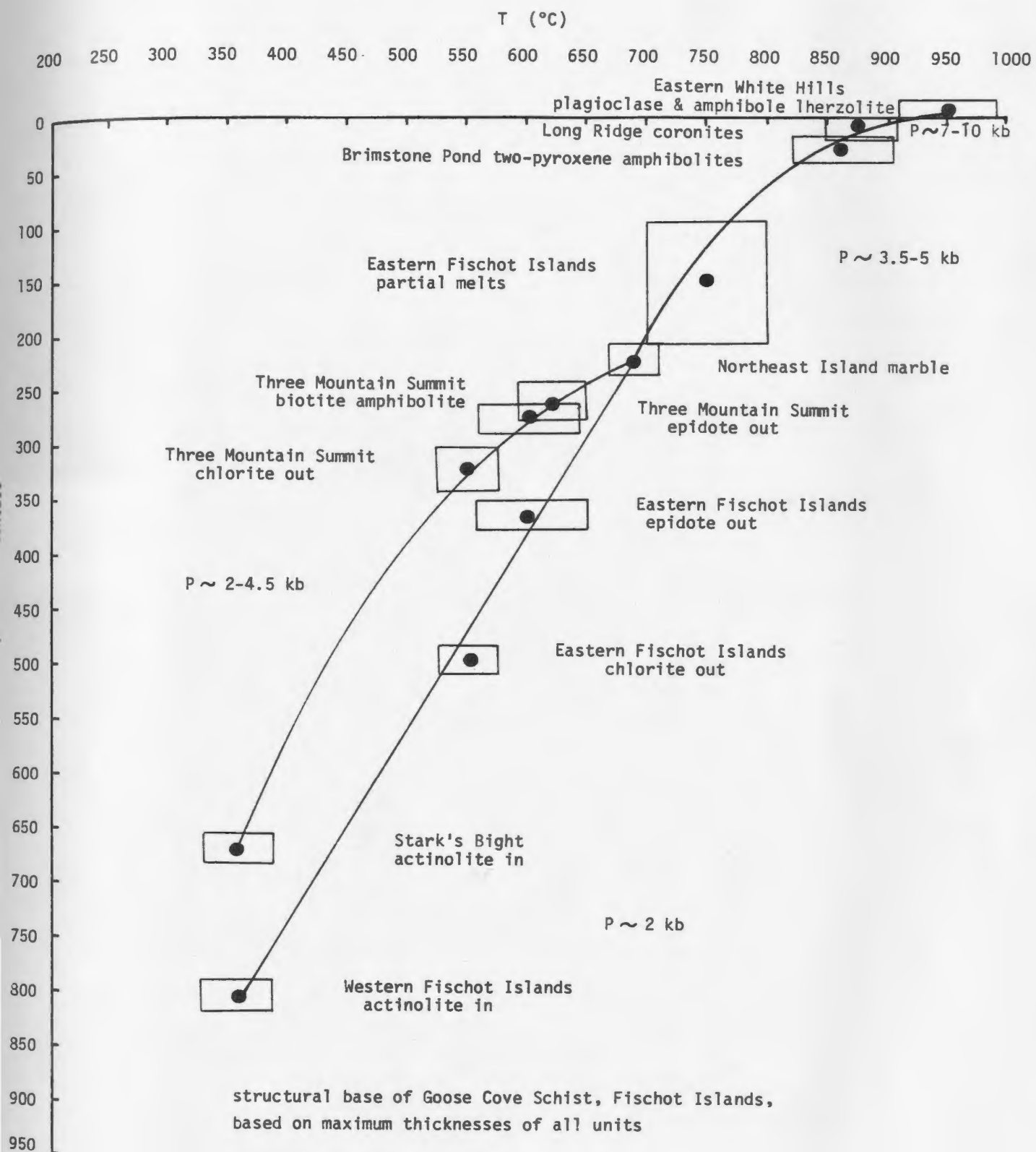


FIGURE 4.8: Composite pressure - temperature profile through the Goose Cove Schist and the Green Ridge Amphibolite, based on Fig. 4.5 - 4.7.

Table 4.4. Parameters used in thermal models

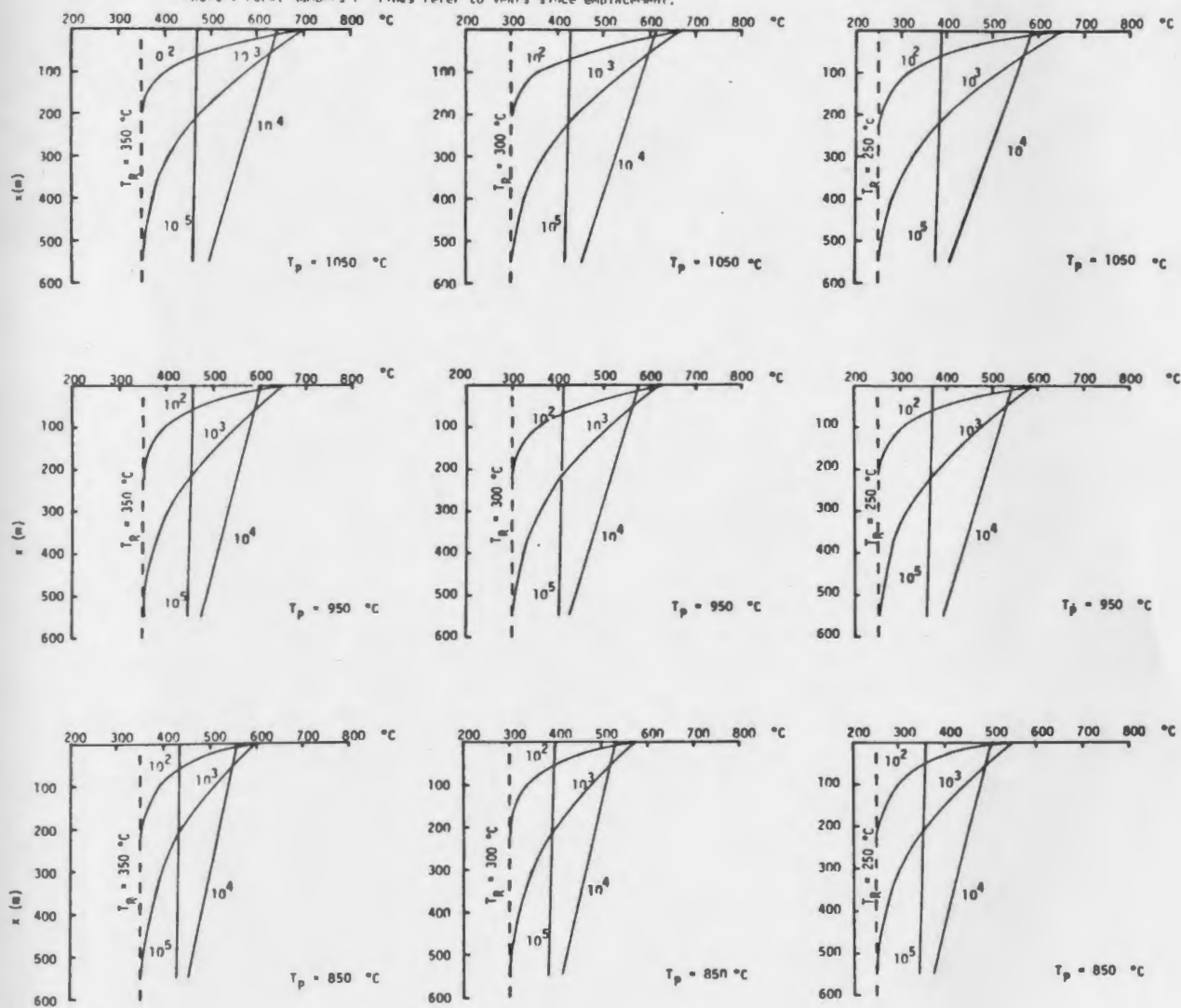
T_p, T_R, T_C	=	temperatures of peridotite, country rock, and contact ($^{\circ}\text{C}$)
dT/dx	=	thermal gradient in country rock from contact to x metres from contact
t	=	time elapsed since emplacement of peridotite (s)
f	=	dimensionless time factor for conduction models (\mathcal{T} of Jaeger, 1968) ($f = \kappa t/a^2$)
a	=	1/2 thickness of peridotite sheet (cm)
K_p, K_R	=	conductivity of peridotite, country rock ($\text{cal/cm s } ^{\circ}\text{C}$); for models $K_p = K_R = 6 \times 10^{-3}$ (Clark, 1966)
κ_p, κ_R	=	diffusivity of peridotite, country rock (cm^2/s ; $\kappa = K/\rho C_p$); for models, $\kappa_p = \kappa_R = 10^{-2}$ (e.g. MacGregor, 1964; Oxburgh & Turcotte, 1974; Graham and England, 1975).
K	=	$(K/\sqrt{\kappa})_p / (K/\sqrt{\kappa})_R$ ratio for models involving different thermal properties for country rock and peridotite (Lovering, 1936).
ρ	=	density (g/cm^3); for models, $\rho = 3.0$
C_p	=	specific heat ($\text{cal/gm}^{\circ}\text{C}$); for models, $C_p = 0.2$ (estimated from $\kappa = K/\rho C_p$).
q	=	amount of heat generated by friction at contact (hfu = heat flow units) ($q = u \mathcal{T}$)
u	=	velocity (cm/s)
\mathcal{T}	=	shear strength (bars or cal/cm^3) (Griggs <u>et al.</u> , 1960)
C	=	temperature at which \mathcal{T} begins to decrease in a linear fashion ($^{\circ}\text{C}$) (T_c of Graham and England, 1975)
B	=	temperature interval over which \mathcal{T} decreases ($^{\circ}\text{C}$) (Graham and England, 1975).

CONVERSION FACTORS:

$$\begin{aligned}
 1 \text{ year} &= 3 \times 10^7 \text{ s} \\
 1 \text{ cal/cm}^3 &= 41.8 \text{ bar}
 \end{aligned}$$

$$\begin{aligned}
 1 \text{ hfu} &= 10^{-6} \text{ cal/cm}^2 \text{ s} \\
 1 \text{ cm/y} &= 3 \times 10^{-8} \text{ cm/s}
 \end{aligned}$$

FIGURE 4.9: Temperature in country rocks a distance x metres from the peridotite contact as a function of time since emplacement, if heating is by conduction only, for different starting temperatures for the peridotite and country rock. Numbers on lines refer to years since emplacement.



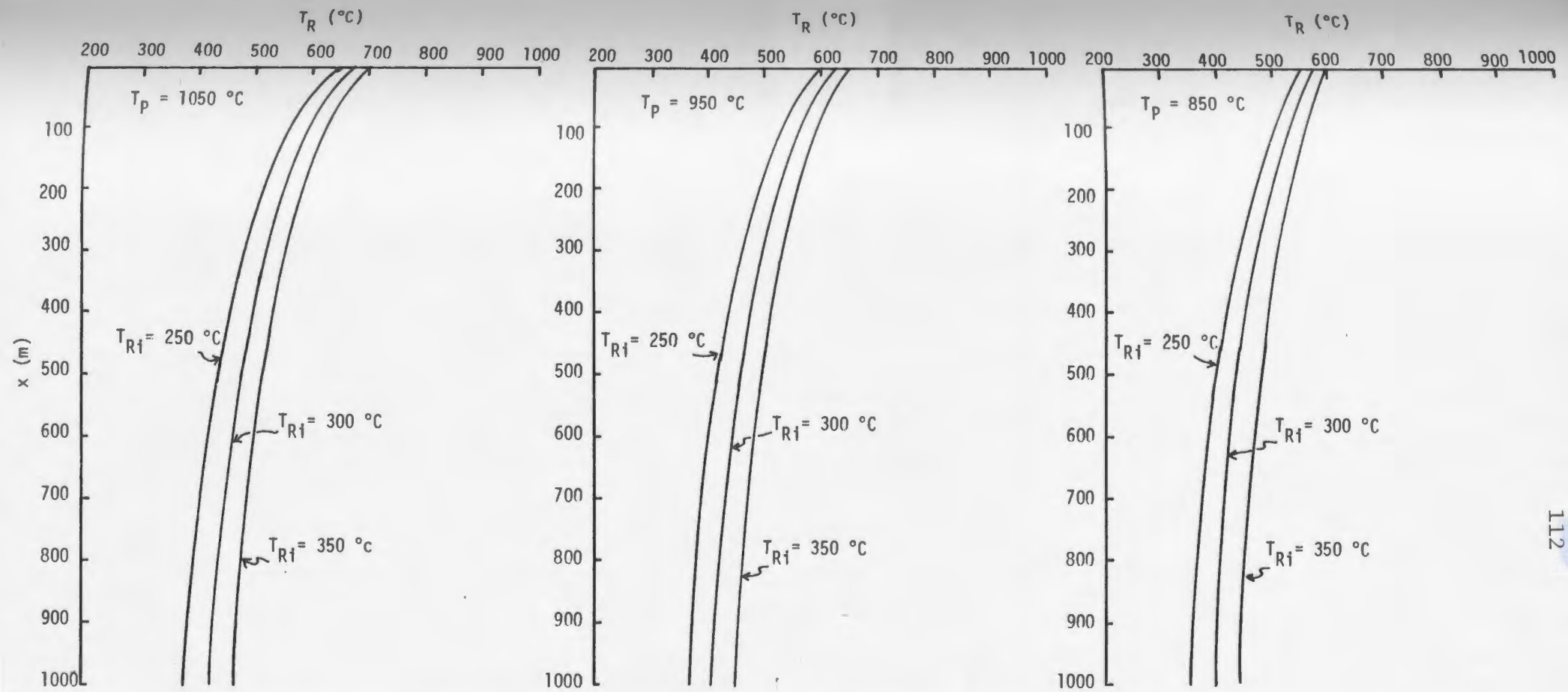


FIGURE 4.10: Maximum temperature reached in country rock at distance x from peridotite contact, regardless of time, for different initial temperatures of peridotite (T_P) and country rock (T_{Ri}).

Table 4.5(a). Effect of variable conductivity (K) and diffusivity (κ) on maximum contact temperature for $T_p = 950^\circ\text{C}$, $T_R = 300^\circ\text{C}$. (conduction model)

K_p	κ_p	K_R	κ_R	K	T_c
6×10^{-3}	10^{-2}	6×10^{-3}	10^{-2}	1	625°C
7×10^{-3}	10^{-2}	5×10^{-3}	10^{-2}	1.4	677°C
			9×10^{-3}	1.3	664°C
			8×10^{-3}	1.25	661°C
			9×10^{-3}	1.3	664°C
8×10^{-3}	10^{-2}	4.7×10^{-3}	8×10^{-3}	1.5	690°C
		4×10^{-3}	10^{-2}	2.0	736°C
		4×10^{-3}	9×10^{-2}	1.8	716°C

Table 4.5(b). Maximum contact temperatures reached immediately after emplacement for conduction model with different starting conditions.

T_p ($^\circ\text{C}$)	K		T_R ($^\circ\text{C}$)
	1	1.3	
1050	350	700	742
	300	675	720
	250	650	698
950	350	650	686
	300	625	664
	250	600	642
850	350	600	636
	300	575	608
	250	550	586

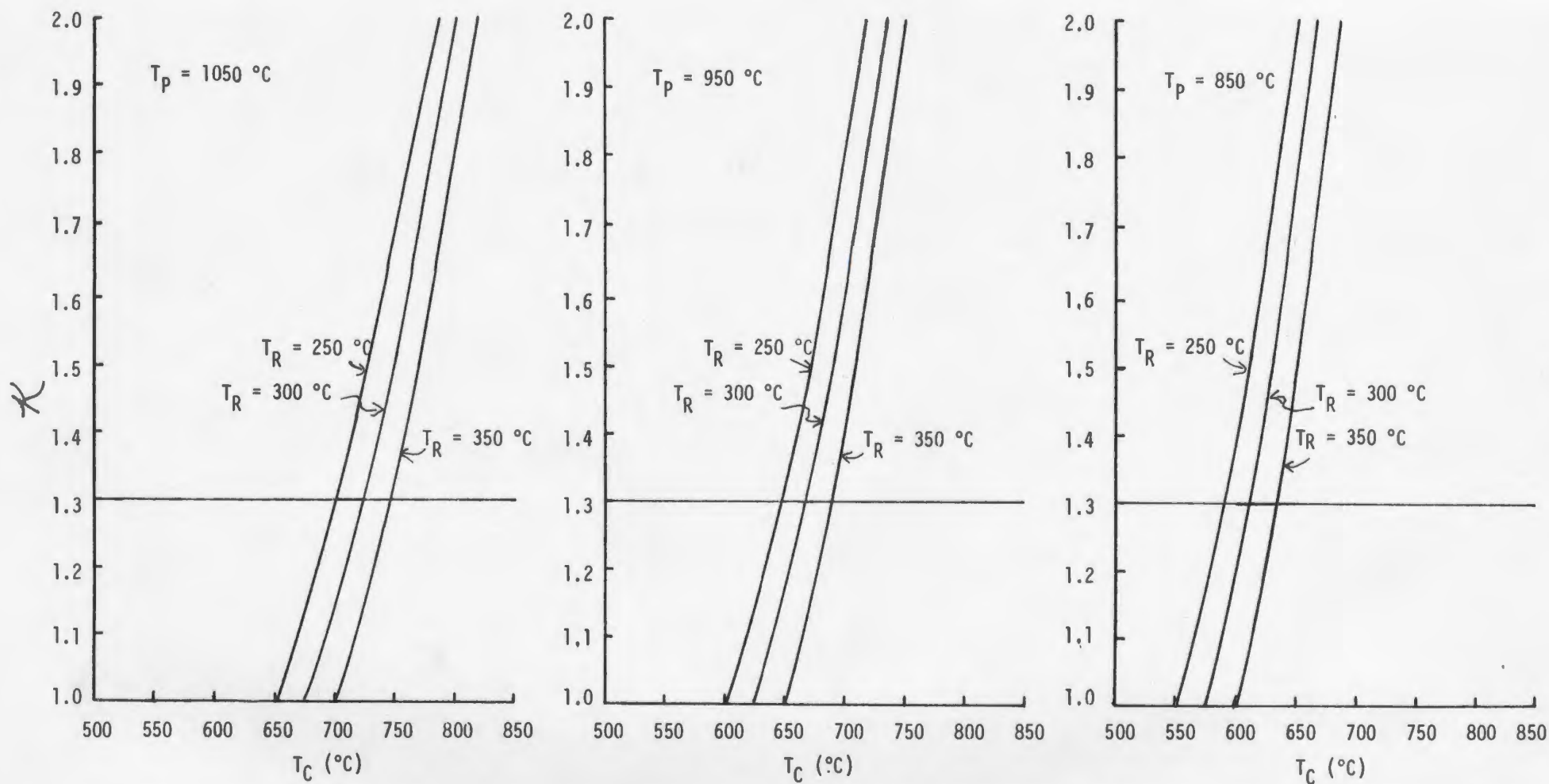


FIGURE 4.11: Maximum contact temperature achieved, if heating is by conduction only, for varying thermal properties for the peridotite and the country rock. $K = 1.3$ is considered likely on the basis of literature values for K , κ (after Lovering, 1936).

$$K = (K/\sqrt{\kappa})_P / (K/\sqrt{\kappa})_R$$

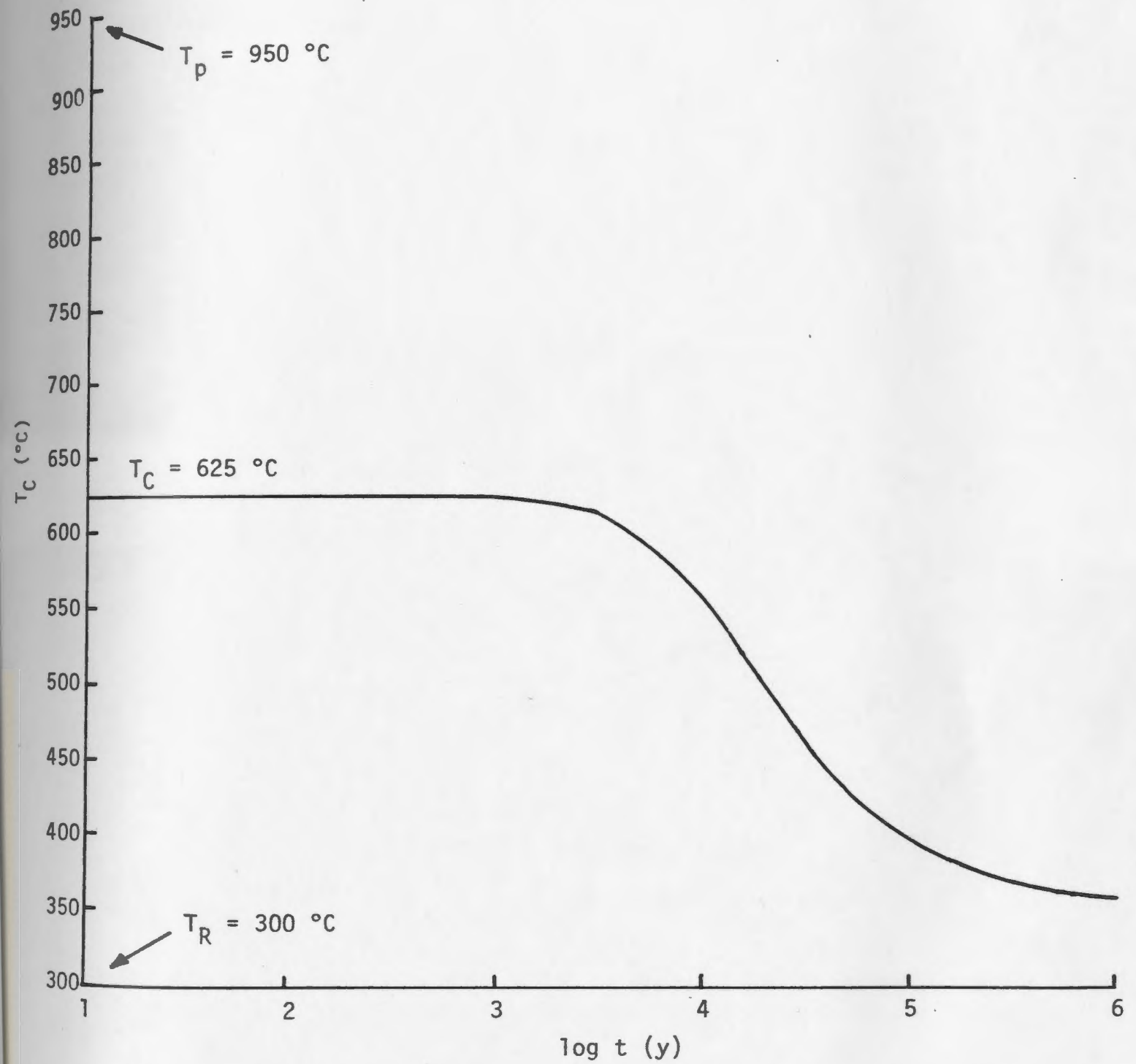


FIGURE 4.12: Variation in contact temperature with time after emplacement of peridotite, conduction model.

Table 4.6. Initial temperatures for peridotite and country rock required in order for the contact temperature to reach 850°C by conduction.

$$T_c = 850^{\circ}\text{C}$$

K	$T_p (^{\circ}\text{C})$	$T_R (^{\circ}\text{C})$
1.0	1050	650
	950	750
	850	850
1.3	1050	600
	950	725
	850	849
1.5	1050	550
	950	700
	850	849
2.0	1050	445
	950	648
	850	849

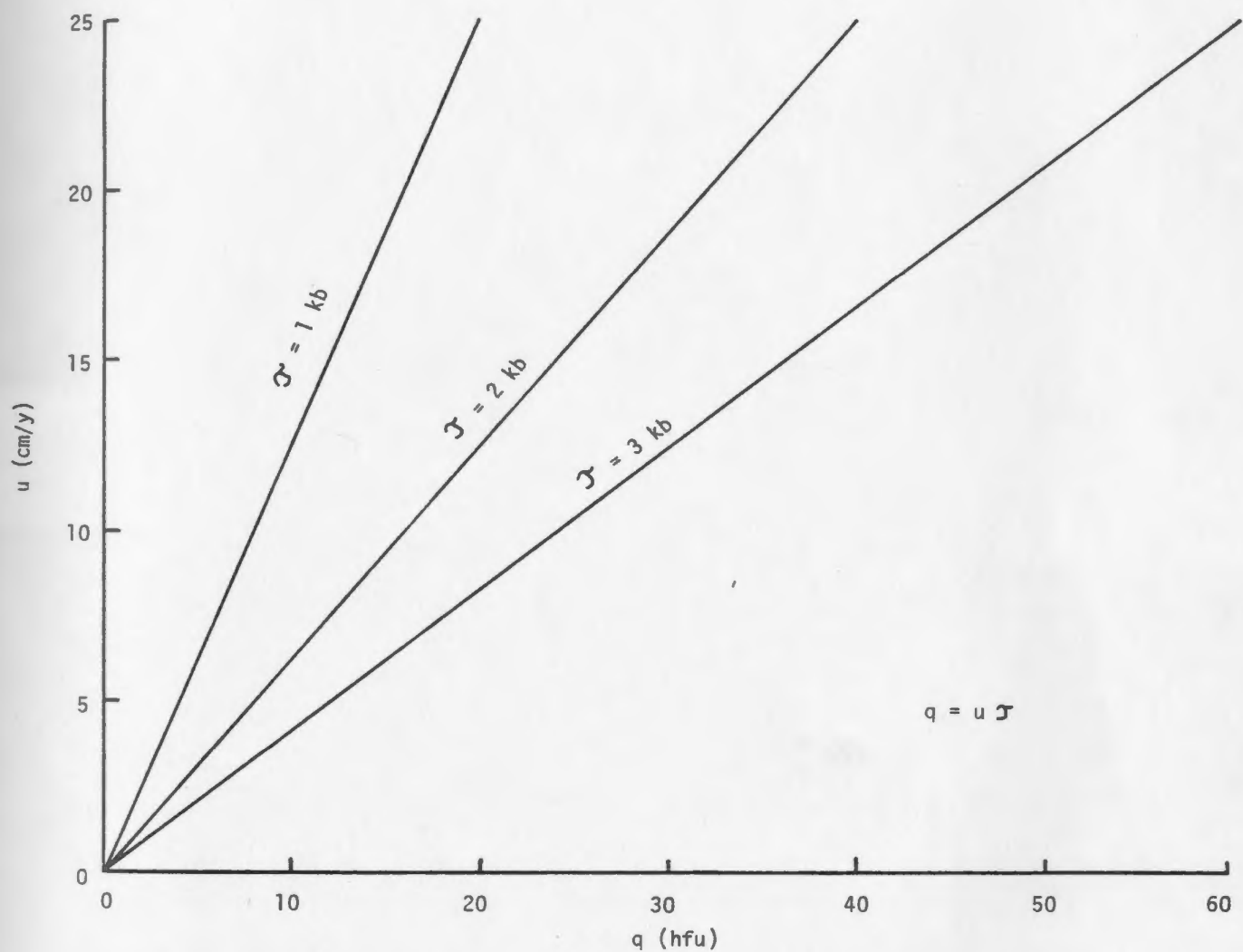


FIGURE 4.13: Relationship between velocity of motion (u), shear strength (τ), and heat produced at the contact (q), for frictional heating model, assuming τ not a function of T .

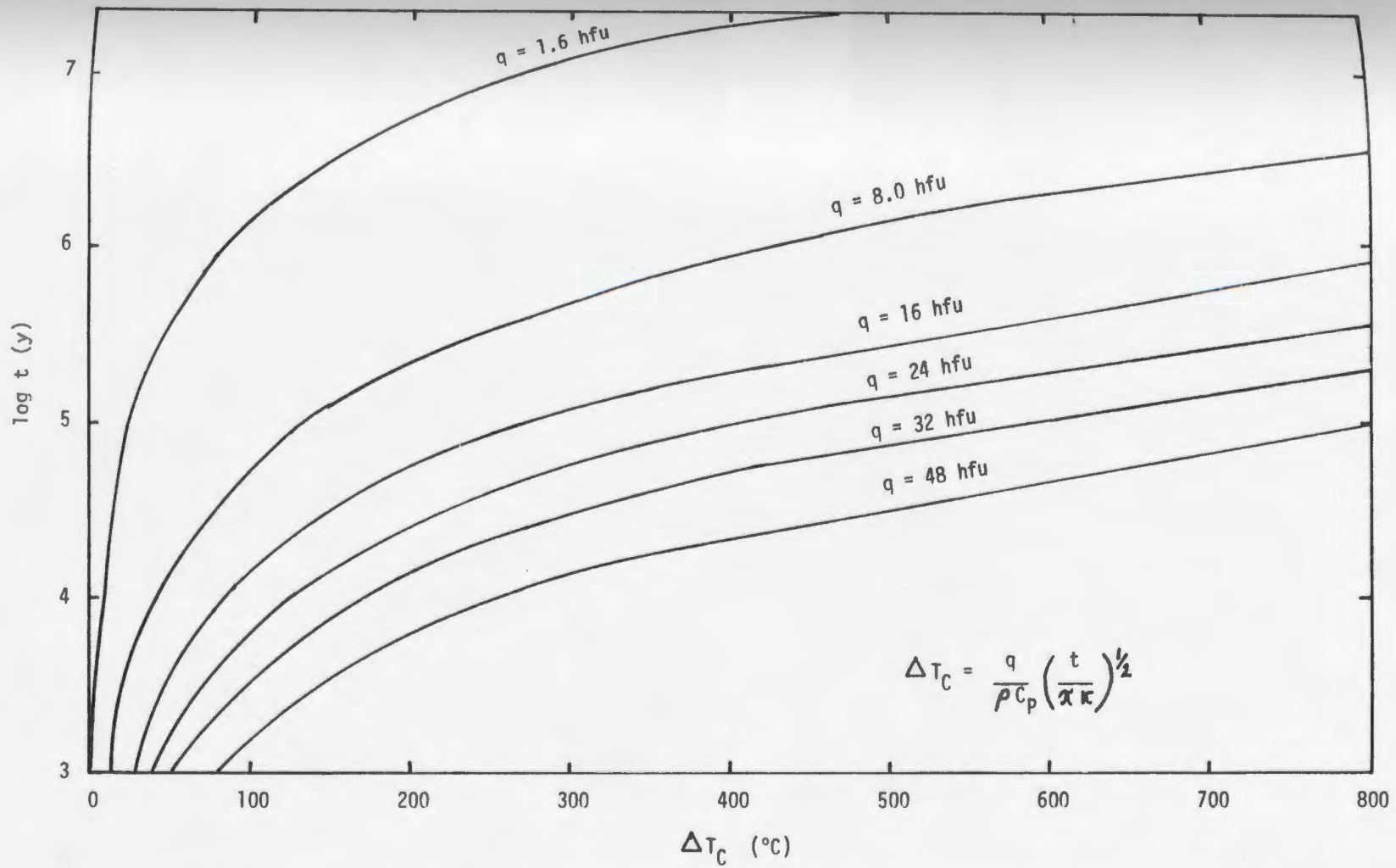


FIGURE 4.14: Increase in contact temperature with time since the beginning of motion for the frictional heating model, showing dependence on heat flow(q) at the contact.

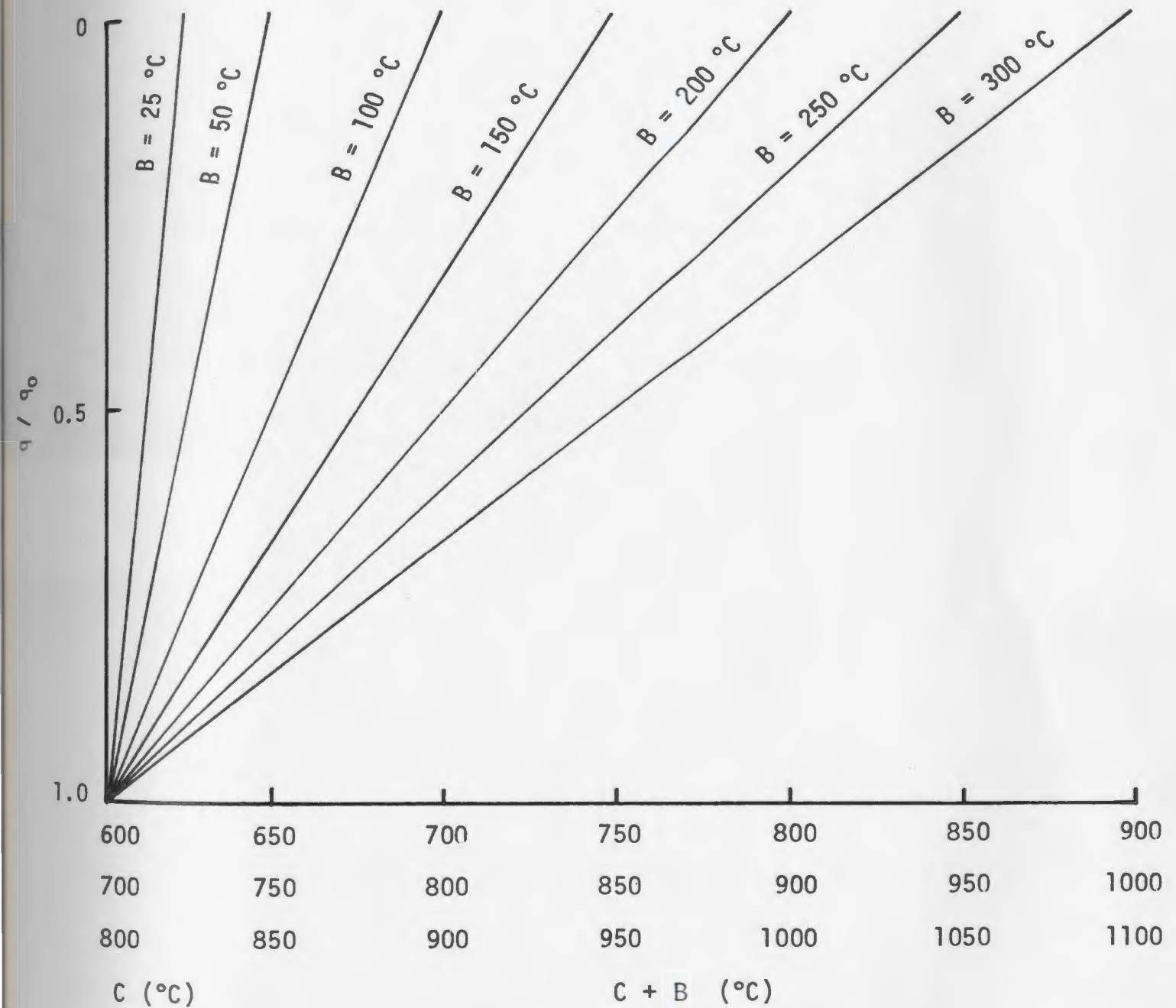


FIGURE 4.15: Relationship between maximum temperature reached at contact ($C + B$) and interval over which the heat produced at the contact falls to zero (B) as shear strength decreases from temperature C to temperature $C + B$.

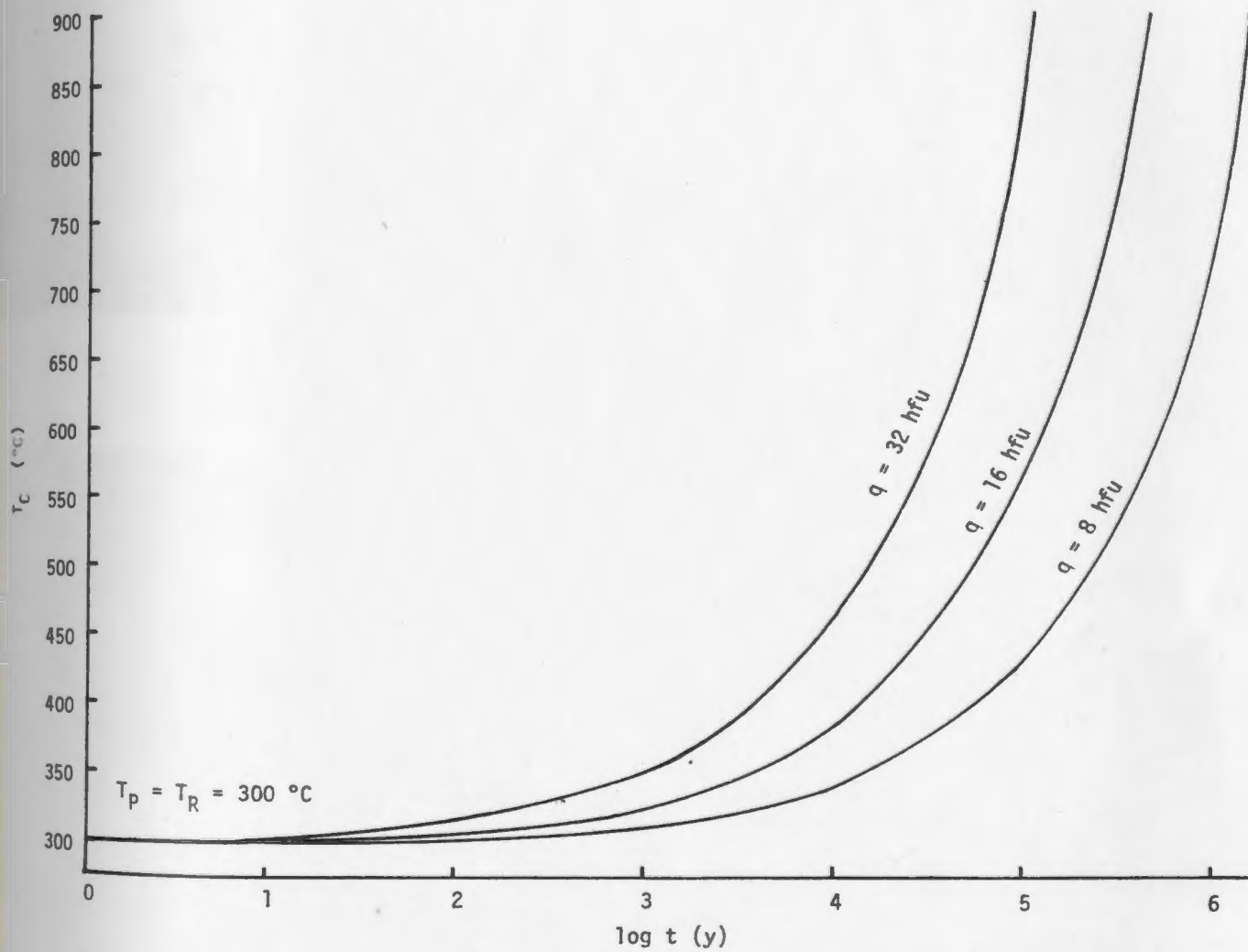
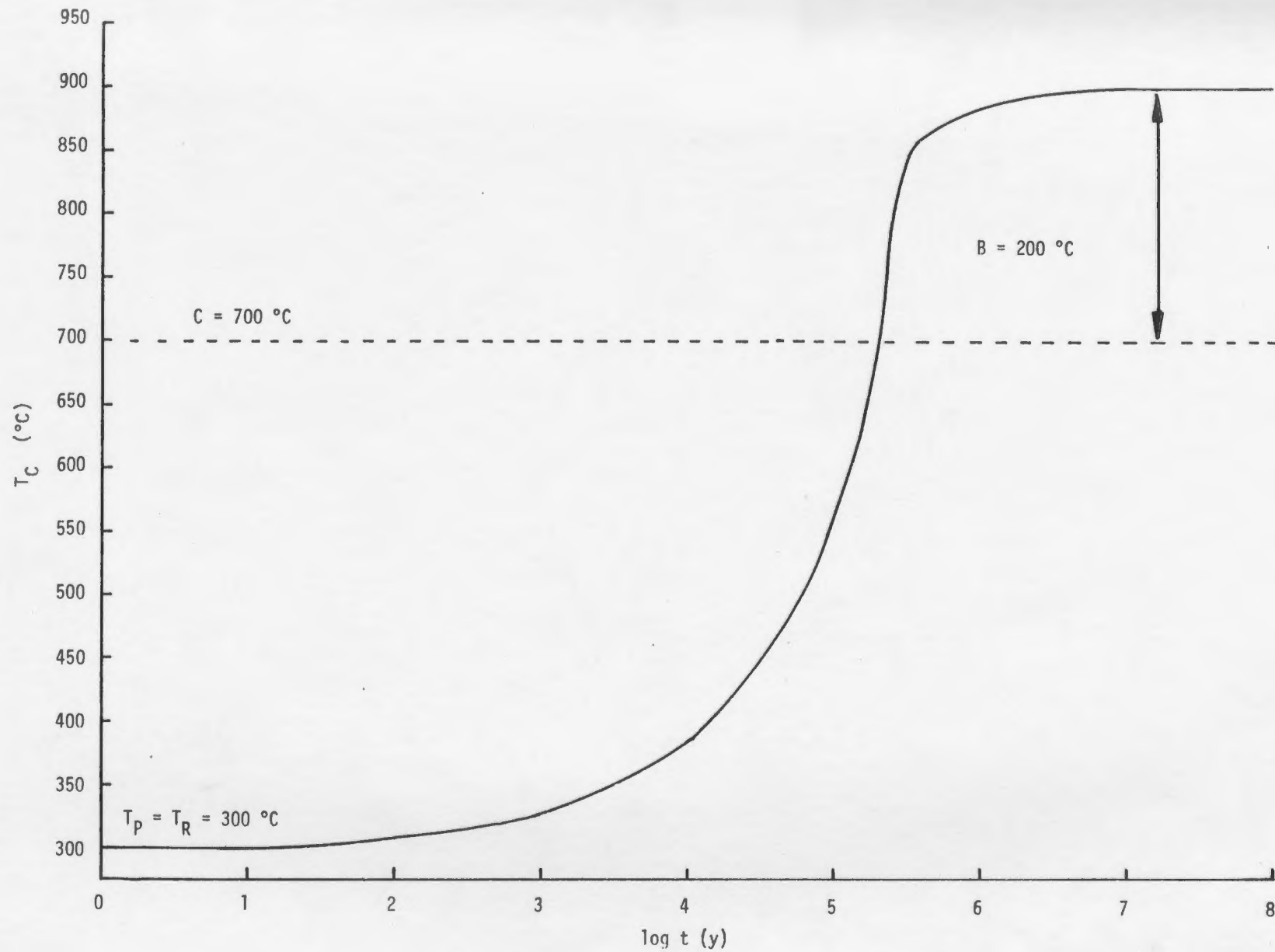


FIGURE 4.16: Variation in contact temperature with time after the beginning of motion, for different values of q , assuming \mathcal{T} constant, frictional heating model.

FIGURE 4.17: Frictional heating model for the case where $T_R = 300^\circ\text{C}$ and shear strength drops to zero over the interval 700° to 900°C .



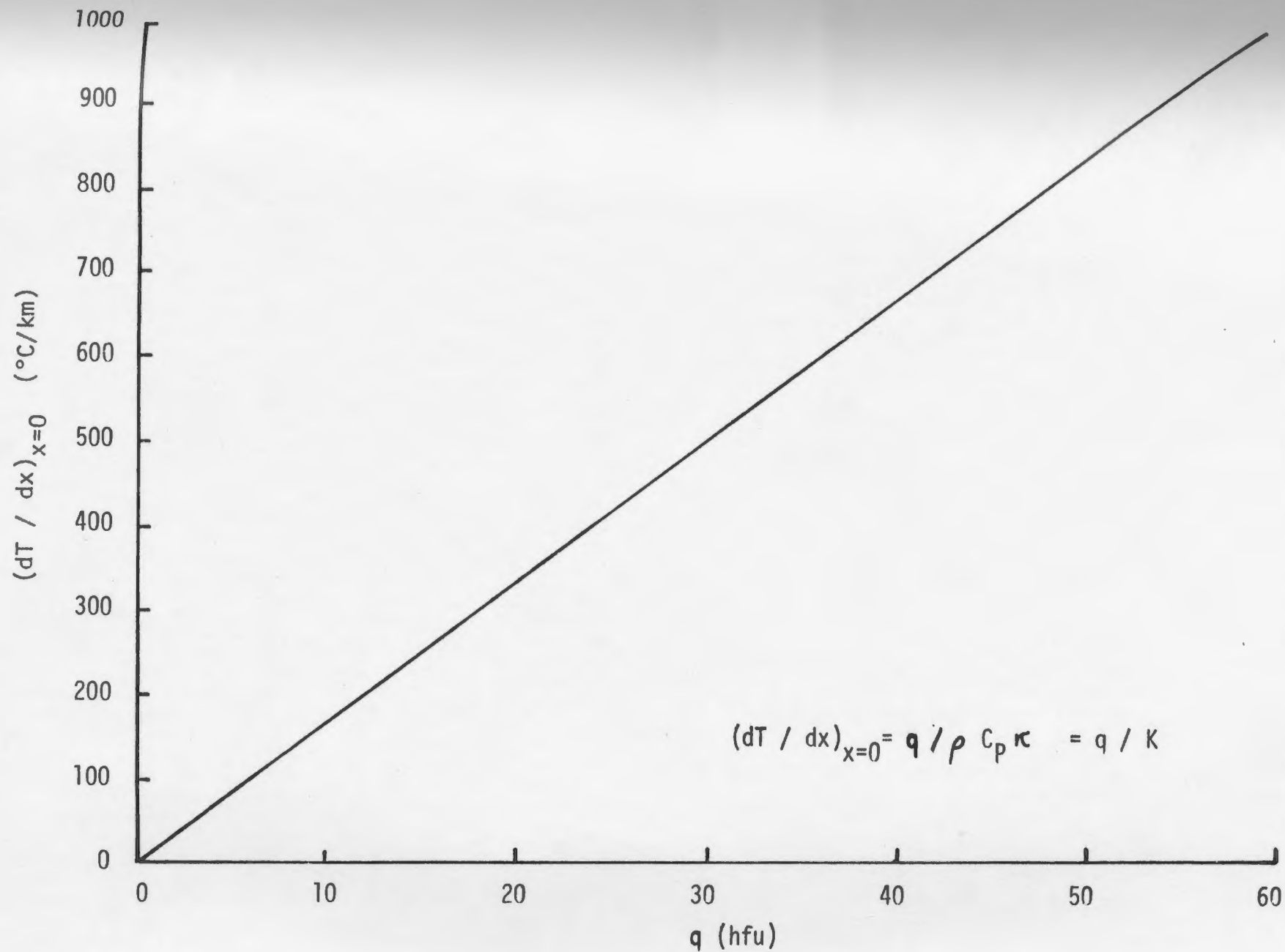


FIGURE 4.18: Relationship between the thermal gradient at the contact and the amount of heat generated by friction at the contact.

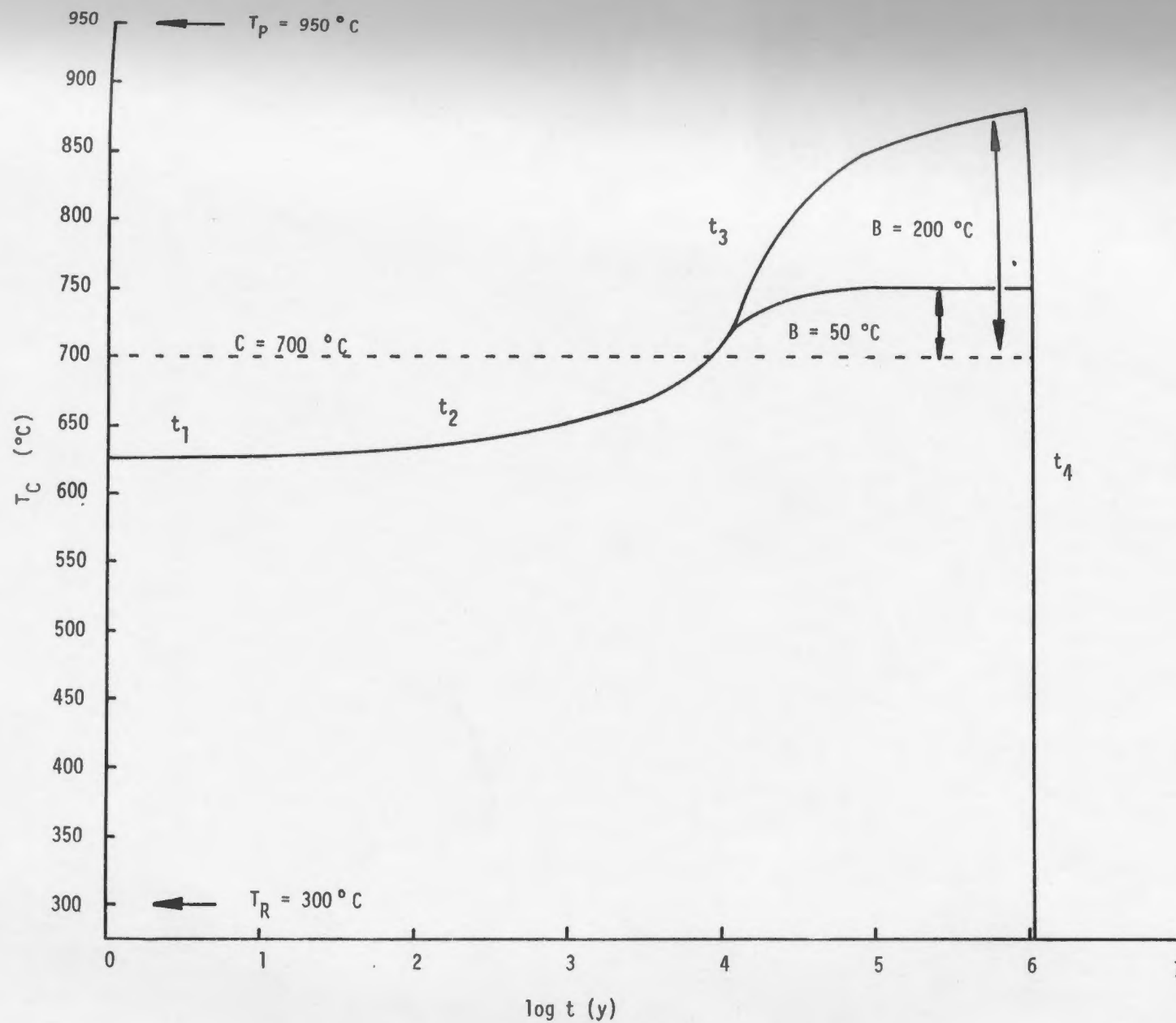
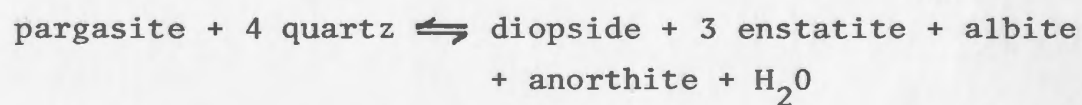


FIGURE 4.19: Combined friction and conduction models for the case where $T_P = 950^\circ\text{C}$, $T_R = 300^\circ\text{C}$, and for shear strengths which drop off over 200° and 50°C (see text).

Table 4.7. Thermodynamic parameters for dehydration of pargasite (Robie and Waldbaum, 1968).

Mineral	$\Delta H_f/\text{gfw}$ (1000°K) (Kcal/mole)
pargasite*	- 3021
diopside	- 767
enstatite	- 371
albite	- 937
anorthite	- 1011
quartz	- 218
H ₂ O	- 59.2

* data at 298°K (J. R. Holloway, pers. comm. to D. F. Strong, 1978).

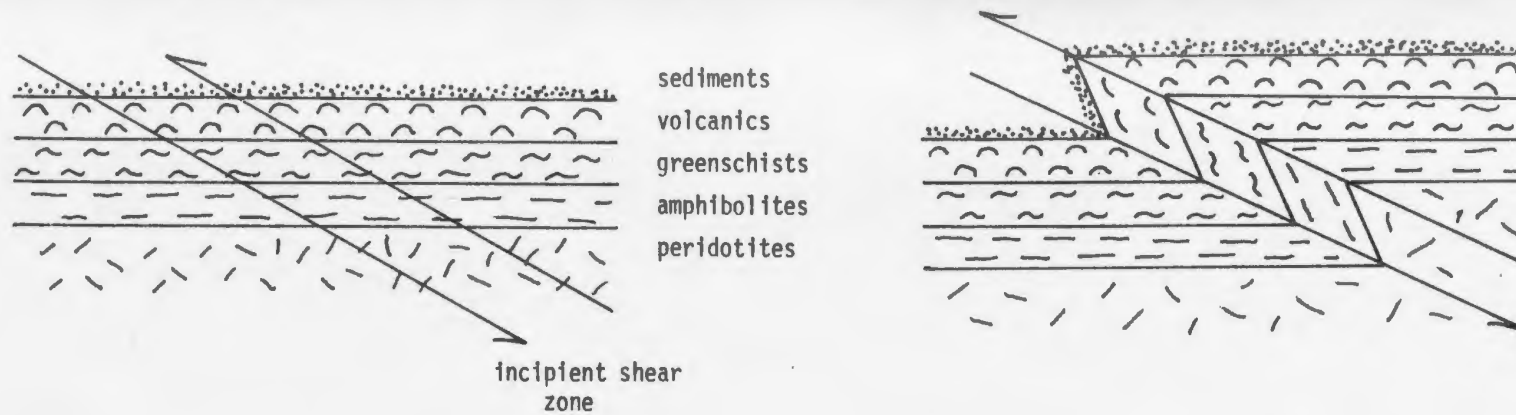


$$\Delta H_r = -5 \text{ Kcal/mole pargasite}$$

$$1 \text{ mole pargasite} = 280 \text{ cc}$$

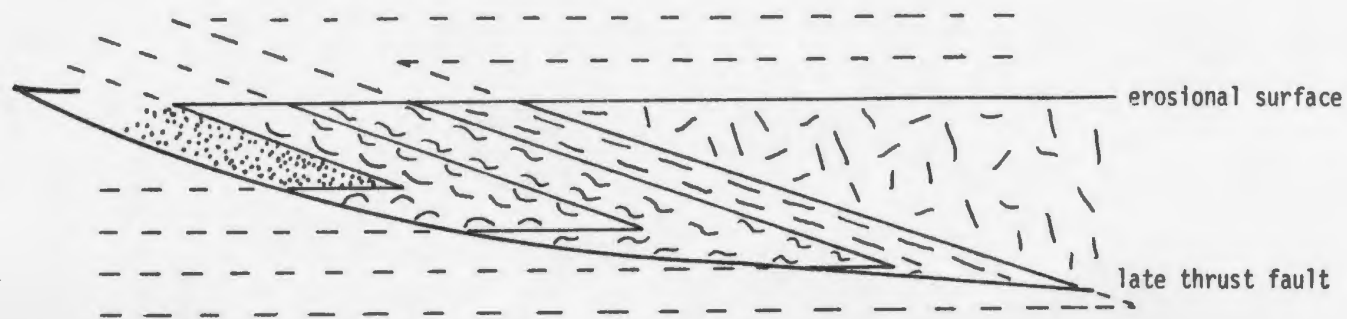
$$\Delta H_r = -18 \text{ cal/cc}$$

FIGURE 4.20: Alternative model for development of St. Anthony Complex by inversion and thinning of a pre-existing oceanic metamorphic sequence in a large shear zone (after Zwart, 1974).



a) pre-tectonic sequence - metamorphically zoned oceanic crust

b) early stage of shear zone development



c) shear zone development and effects of later thrusting and erosion

Table S.1. Timing of depositional and tectonic events in the Lower and Middle Ordovician of western Newfoundland relating to the emplacement of the St. Anthony Complex. (H.A.A. = Humber Arm Allochthon, H.B.A. = Hare Bay Allochthon)

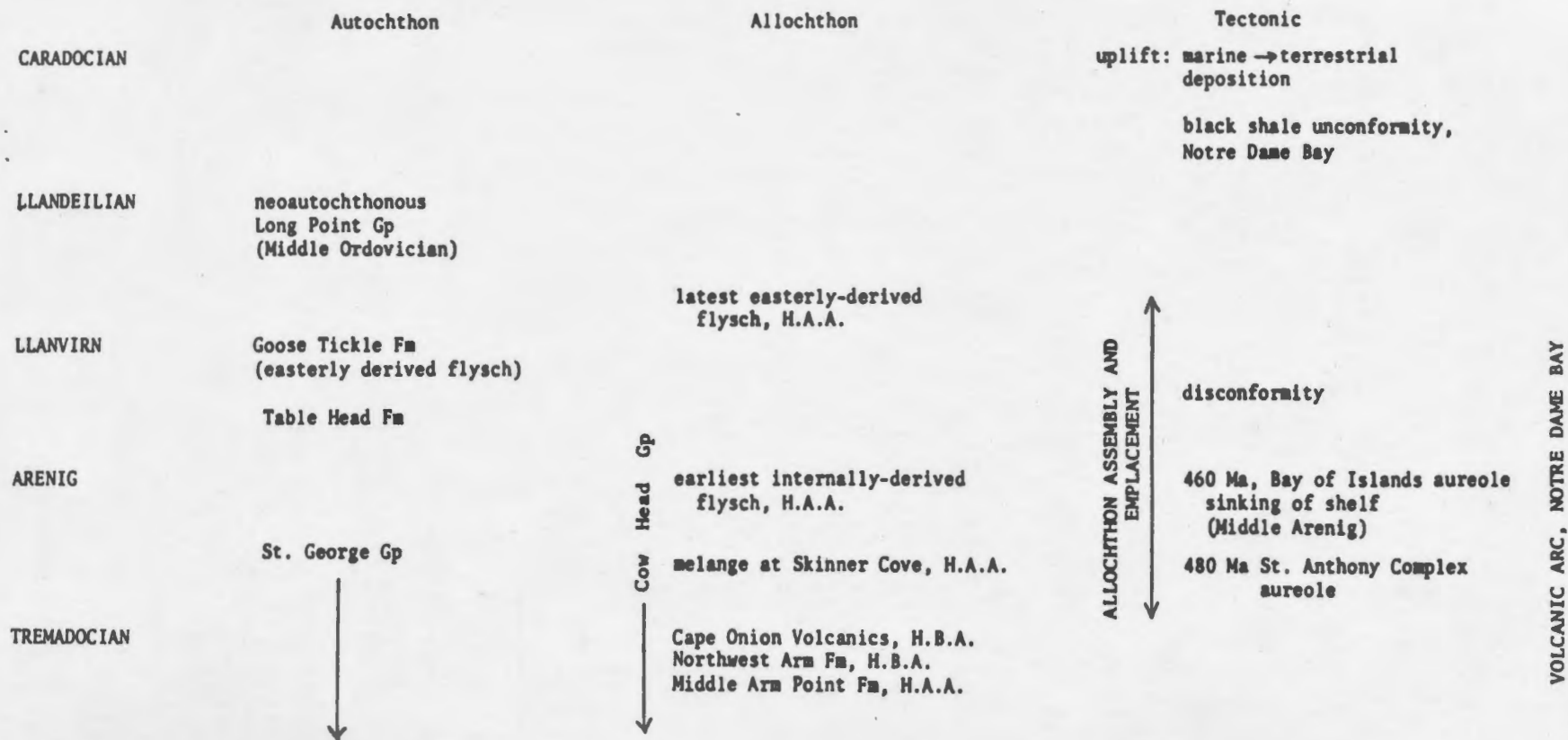


FIGURE 5.1: Pre-tectonic view of western Newfoundland, Tremadocian (not to scale)

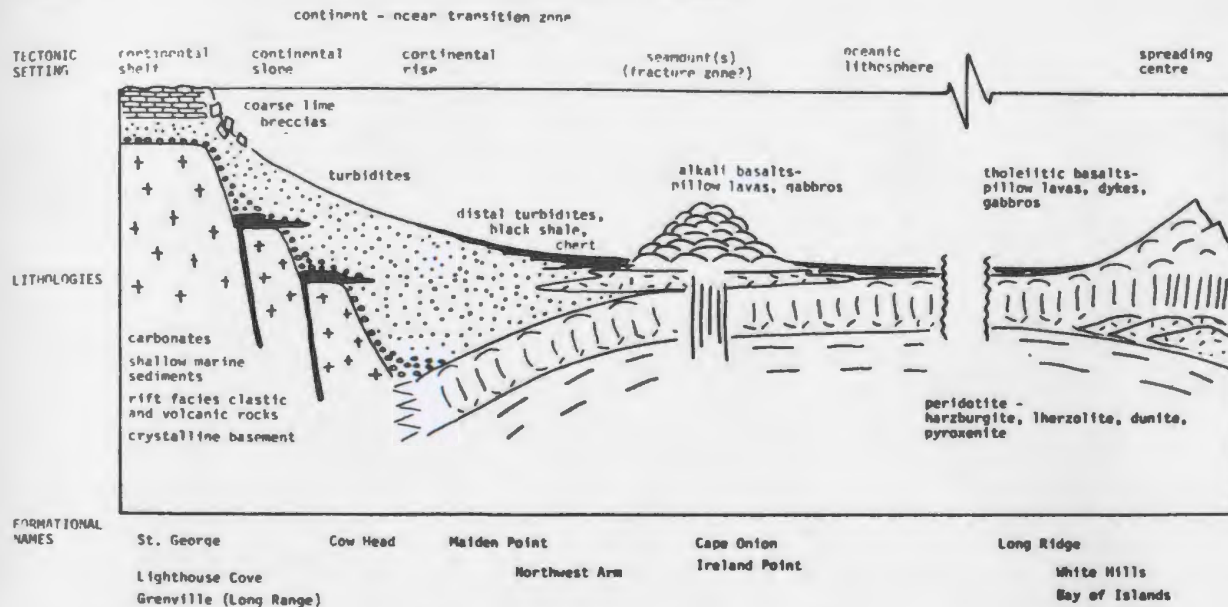


FIGURE 5.2: Formation of the St. Anthony Complex, 480 Ma.

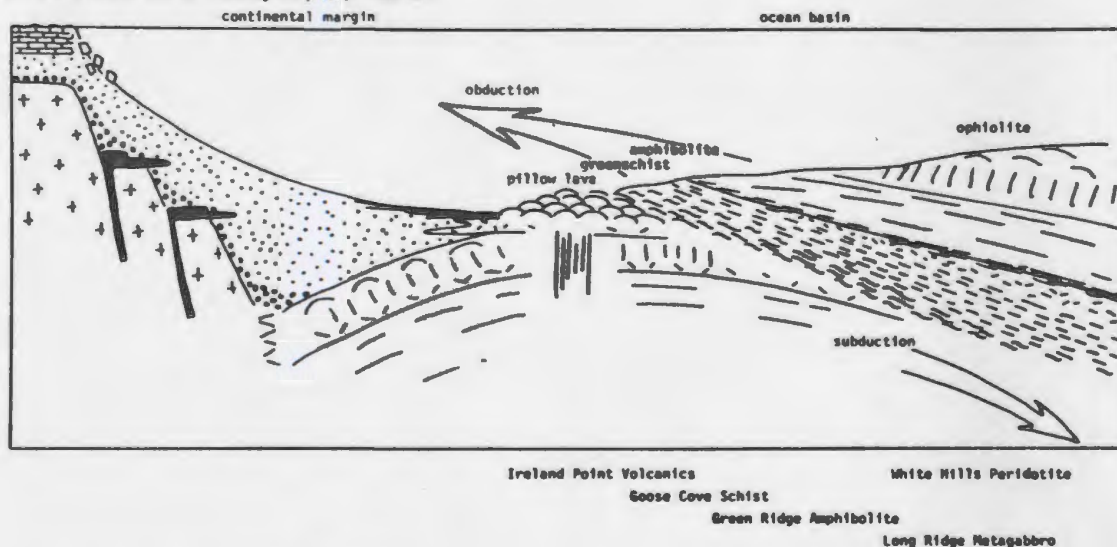


FIGURE 5.3: Emplacement of St. Anthony Complex, post-480 Ma.

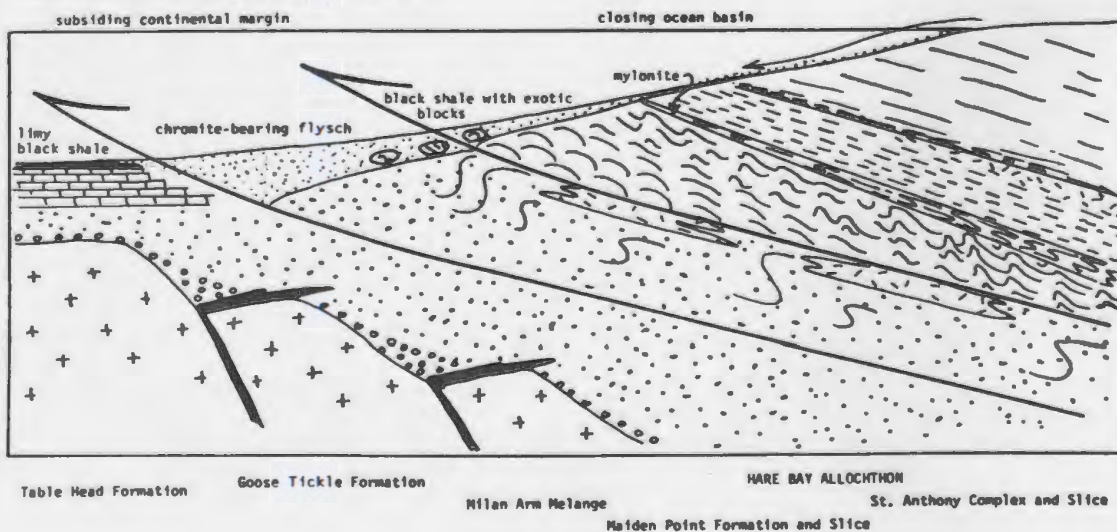


Table 6.1. Geological setting of selected ophiolite-aureole associations.

LOCALITY	TECTONIC SETTING AND AGE OF METAMORPHISM	PERIDOTITE TYPE	REFERENCES
ST. ANTHONY COMPLEX	Humber Zone of Newfoundland Appalachians, Hare Bay Allochthon (see Chapter 1). Taconic (480 \pm 5 Ma; $^{40}\text{Ar}/^{39}\text{Ar}$)	harzburgite-lherzolite massif with minor dunite, pyroxenite, and gabbro	See Chapters 1 to 5
BAY OF ISLANDS	Humber Zone of Newfoundland Appalachians, Humber Arm Allochthon (see Chapter 1). Taconic (460 \pm 5 Ma; $^{40}\text{Ar}/^{39}\text{Ar}$)	complete ophiolite suite with underlying aureole	Smith (1958); Williams and Smyth (1973); Dallmeyer and Williams (1975); Malpas (1976)
MOUNT ALBERT	Quebec Appalachians Taconic (495 Ma, K/Ar)	harzburgite massif with minor pyroxenite, dunite, chromite	MacGregor (1964); MacGregor and Basu (1976)
LIZARD	Cornwall (349-492 Ma, K/Ar)	harzburgite-lherzolite with associated troctolite, gabbro, diabase dykes; underlying aureole	Flett (1946); Sanders (1955); Green (1964a, b, c); Strong et al. (1975); Badham and Kirby (1976)
TINAKUILLO	Coastal Ranges, Venezuela (Cretaceous?)	harzburgite-lherzolite with pyroxenite, dunite and associated gabbro; sheet between underlying and overlying aureole rocks	MacKenzie (1960, 1961); Thayer and Brown (1961)
RED HILLS	Dun Mountain ophiolite belt, New Zealand (Permian)	harzburgite, dunite sheet; underlying aureole rocks	Challis (1965a, b); Coombs et al. (1976)
BREZOVICA	Vardar Zone, Inner Yugoslavian Dinarides (Jurassic)	harzburgite, dunite sheet overlying aureole	Karamata (1968; 1974)
KRIVAJA	Central ophiolite zone, Yugoslavian Dinarides. Jurassic (160-170 Ma; K/Ar)	lherzolite with minor harzburgite associated with gabbro, spilite, locally ophiolitic melange	Pamić (1971; 1977); Pamić et al. (1973); Lamphere et al. (1975)
RONDA	Betic Cordillera, southeastern Spain Oligocene (23-35 Ma; K/Ar)	lherzolite with harzburgite, abundant gabbro & pyroxenite layers; sheet between underlying and overlying aureole rocks	Dickey (1970); Loomis (1972a, b); Obata and Dickey (1975); Obata (1977); Lundeen (1978); Westerhof (1977)

Table 6.2. Geology of Aureoles

LOCALITY	PERIDOTITE-AUREOLE CONTACT ZONE	AUREOLE LITHOLOGIES	AUREOLE-COUNTRY ROCKS CONTACT ZONE	THICKNESS OF AUREOLE
ST. ANTHONY COMPLEX	mylonitic peridotite, locally amphibole- rich/inhomogeneously deformed plagioclase amphibolite or, rarely, jacupirangite; foliated parallel to contact.	basic amphibolites → biotite-rich mylonite → basic greenschists → psammites and pelites	Goose Cove Schist gradational into undeformed volcanics	600-750 m
BAY OF ISLANDS	mylonitic peridotite/basic hornfels or banded amphibolite strongly foliated parallel to contact	basic hornfels → amphibolite → greenschist → phyllitic meta- sediments	generally faulted; locally gradational phyllite → argillite	180-450 m
MOUNT ALBERT	mylonitic peridotite/garnet amphibolite strongly foliated parallel to contact	basic amphibolite → epidote amphi- bolite with minor metasedimentary layers	gradational into greenschist facies volcanics and sediments	1500 m
LIZARD	mylonitic peridotite/granulite or metagabbro or acid-basic gneiss; peridotite locally interbanded with granulite parallel to contact; locally acid-basic gneisses cut peridotite contact	basic granulite, amphibolite (Traboe Schist) or acid-basic schist (Kennack Gneiss) → amphibolite, epidote amphibolite (Landsevednack Hornblende Schist) → biotite-andalusite grade metasediments with minor meta- volcanic layers (Old Lizard Head Series)	faulted where exposed	minimum 500 m
TINAKUILLO	mylonitic peridotite/garnet amphibolite	garnet amphibolite → amphibolite	gradational into green- schist facies metabasites	up to 2000 m
RED HILLS	peridotite/relatively homogeneous amphibolite rodingite common	basic amphibolite → greenschist foliated parallel to contact	gradational into undeformed, lower greenschist facies spilite, tuff, argillite	700 m
BREZOVIKA	peridotite/garnet amphibolite inter- banded over 30 m; brecciation common foliation parallel to contact	garnet amphibolite → epidote amphibolite → greenschist	gradational into undeformed spilites, psammites, argillites	300-500 m
KRIVAJA	interbanded peridotite/eclogite or garnet amphibolite over 100 m	eclogite or garnet amphibolite → amphibolite → epidote amphibolite peridotite and amphibolite structurally conformable; isoclinal folding, foliation parallel to contact	tectonic contact with melange	500-1000 m
RONDA	peridotite/gneissic hornfels; peridotite locally brecciated; contains meta- sedimentary inclusions	Casares unit (overlying) - meta- sedimentary gneisses, kinsigites Blanca unit (underlying) - cordierite hornfels, blastomylonite; foliation parallel to contact	Casares unit gradational into undeformed meta- sediments	Casares - 4000-5000 m Blanca - 800 m

Table 6.3. Mineralogy of Contact Zones.

LOCALITY	PERIDOTITE	AUREOLE	P-T
ST. ANTHONY COMPLEX	ol + en + di + br-gr sp \pm parg \pm plag	br hb + cpx \pm opx + plag + ilm	peridotite: 900-950°C 7-10 kb aureole: 850-900°C 4-10 kb
BAY OF ISLANDS	bands of parg + gnt + phlog + gr sp + cpx alternating with en + ol + sp local rodingite	br hb + plag (An ₇₂) + di + gnt \pm opx	720-850°C (aureole) 1000°C (peridotite)
MOUNT ALBERT	not described	gnt + cpx + plag + br hb	700-800°C, 6 kb (aureole) 950-1200°C (peridotite)
LIZARD	recrystallized anhydrous: di + plag + br hb + en + ol \pm sp recrystallized hydrous: ol + parg + en + br sp	opx + cpx + br hb + plag	945-975°C (aureole), < 5 kb 900-1200°C (peridotite)
TINAQUILLO	not described	gnt + plag + br hb + cpx \pm opx	600-800°C (aureole)
RED HILLS	not described	cpx + opx + plag + br hb	700-800°C (aureole)
BREZOVICA	not described	opx + gnt + plag + hb	700°C (aureole)
KRIVAJA	not described	parg + an + cor + gnt + cpx / hb + gnt + cpx / gnt + di + hb + plag	1000°C, 10-20 kb (aureole)
RONDA	not described	Casares: gnt + cord + bt + sill + graph + ky + and Blanca: cord + bt + sill + ksp + plag + qz	Casares: 8.5-9 kb, 725°C Blanca: 3.5 kb, 725°C. Peridotite: originally 1100-1200°C, 20-35 kb; re-equilibrated at 800-1000°C, 5-13 kb.

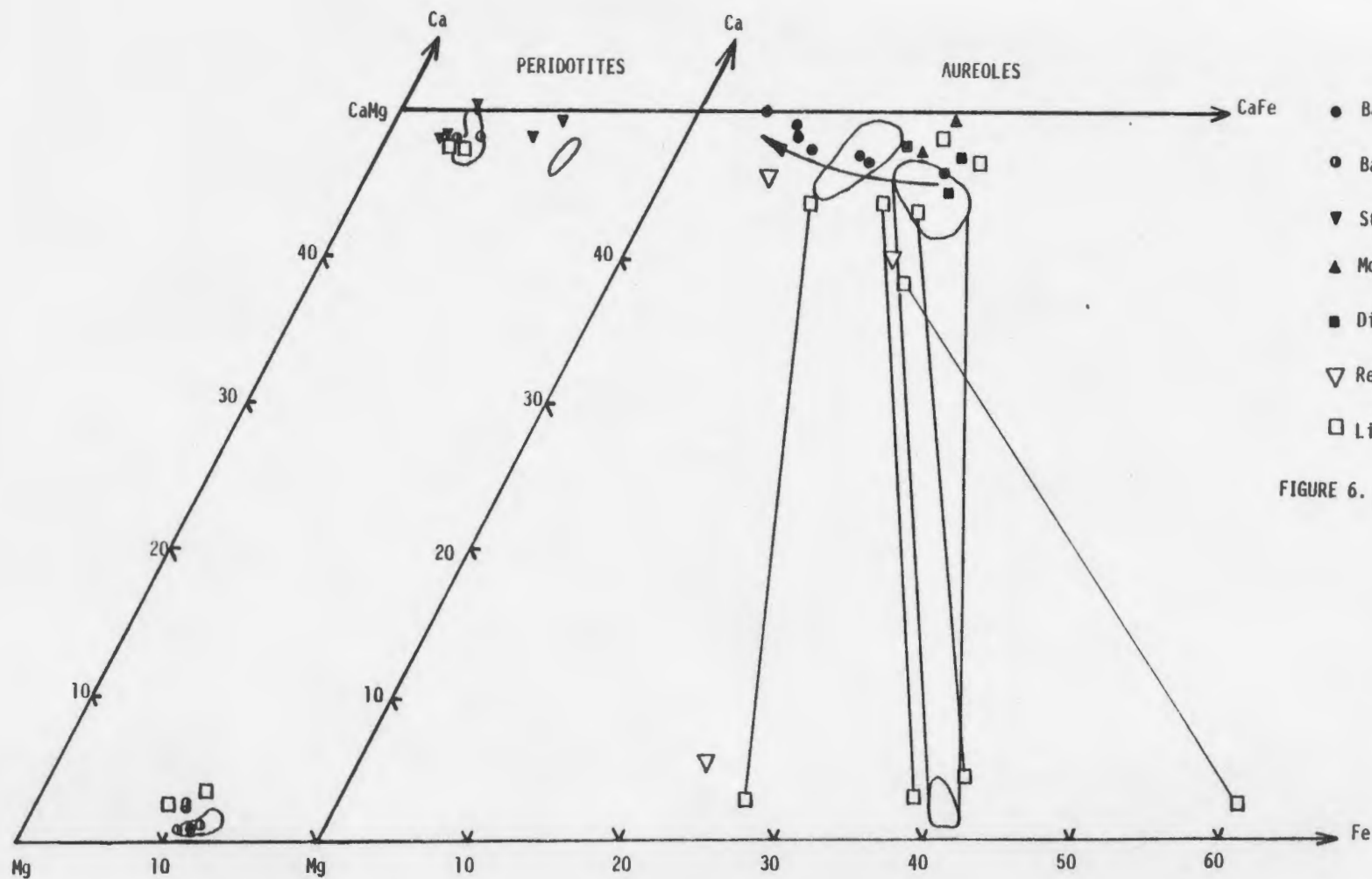


FIGURE 6. 1: Compositions of pyroxenes from various peridotite - aureole complexes compared to data from the St. Anthony Complex (outlined fields). Tie-lines join coexisting clino- and ortho-pyroxene. The arrow shows the trend of the Bay of Islands clinopyroxenes toward the peridotite contact.

Table 6.4. Two-pyroxene temperatures for contact zone rocks calculated by the method of Wells (1977).

Rock Type	Lizard*	T(°C)
		St. Anthony Complex**
Recrystallized anhydrous Peridotite		
90686	872	
90689	883	904-958
Two-pyroxene basic hornblende granulite		
90703	976	
90697	946	849-869

* Data and sample numbers from Green, 1964a, b.

** Table 4.3.

Table 6.5. Ranges of temperatures for given pressures for cpx-gnt assemblages in various aureoles, using calibration of Råheim and Green (1974).

Location	P (assumed) (kb)	$K_D = \frac{(\text{FeO/MgO})_{\text{gnt}}}{(\text{FeO/MgO})_{\text{cpx}}}$	T (°C)
Mount Albert (MacGregor, 1964)	5	3.6 - 4.7	725-775
Bay of Islands (Malpas, 1976)	10	2.7 - 4.6	750-950
Central Dinarides (Pamić et al., 1973)	15	3.1 - 5.3	730-875

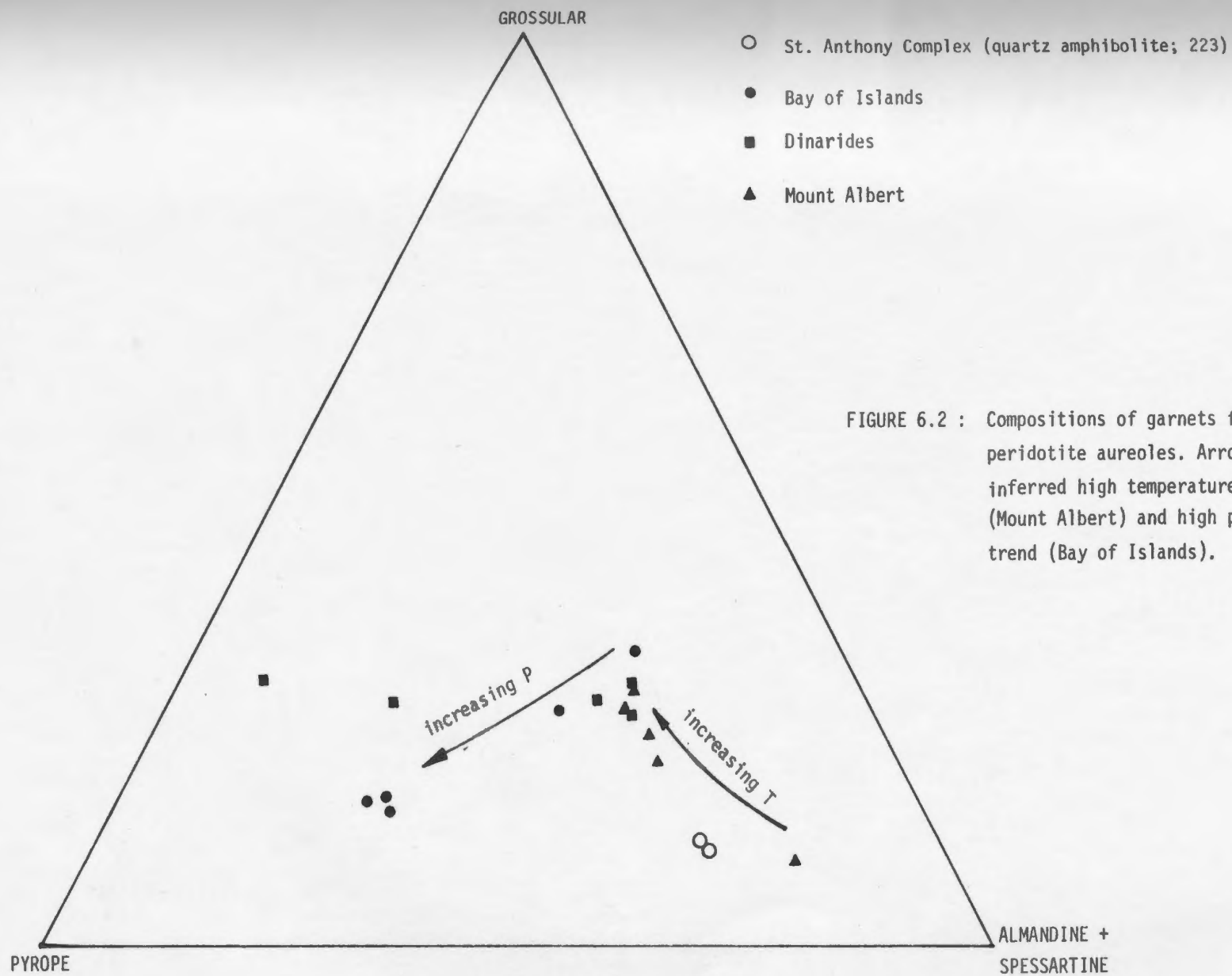
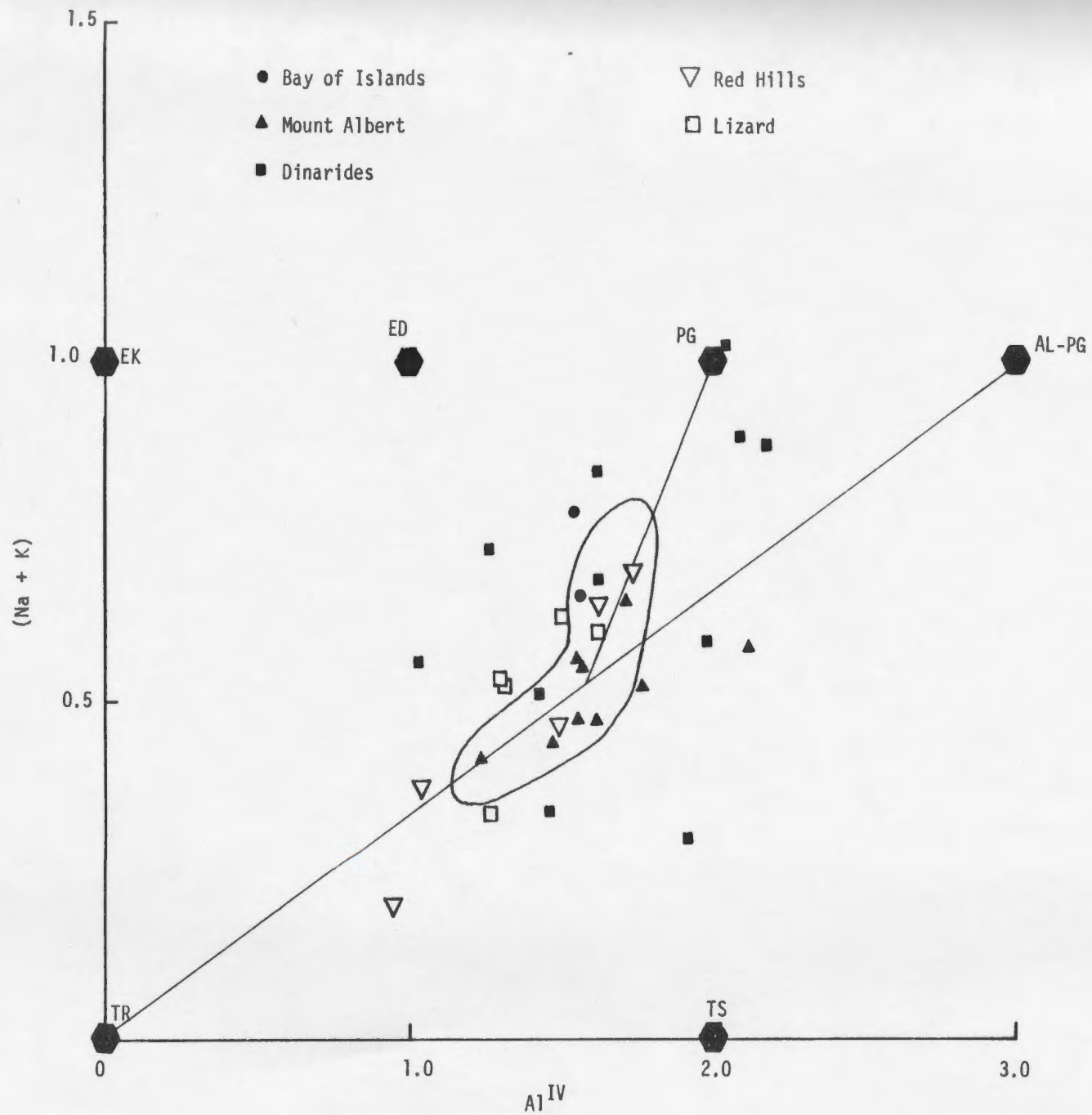


FIGURE 6.2 : Compositions of garnets from various peridotite aureoles. Arrows show inferred high temperature trend (Mount Albert) and high pressure trend (Bay of Islands).

FIGURE 6.3a: Compositions of aureole amphiboles compared to those from the Green Ridge Amphibolite (outlined field). Lines show overall St. Anthony Complex trends (Chapter 3).



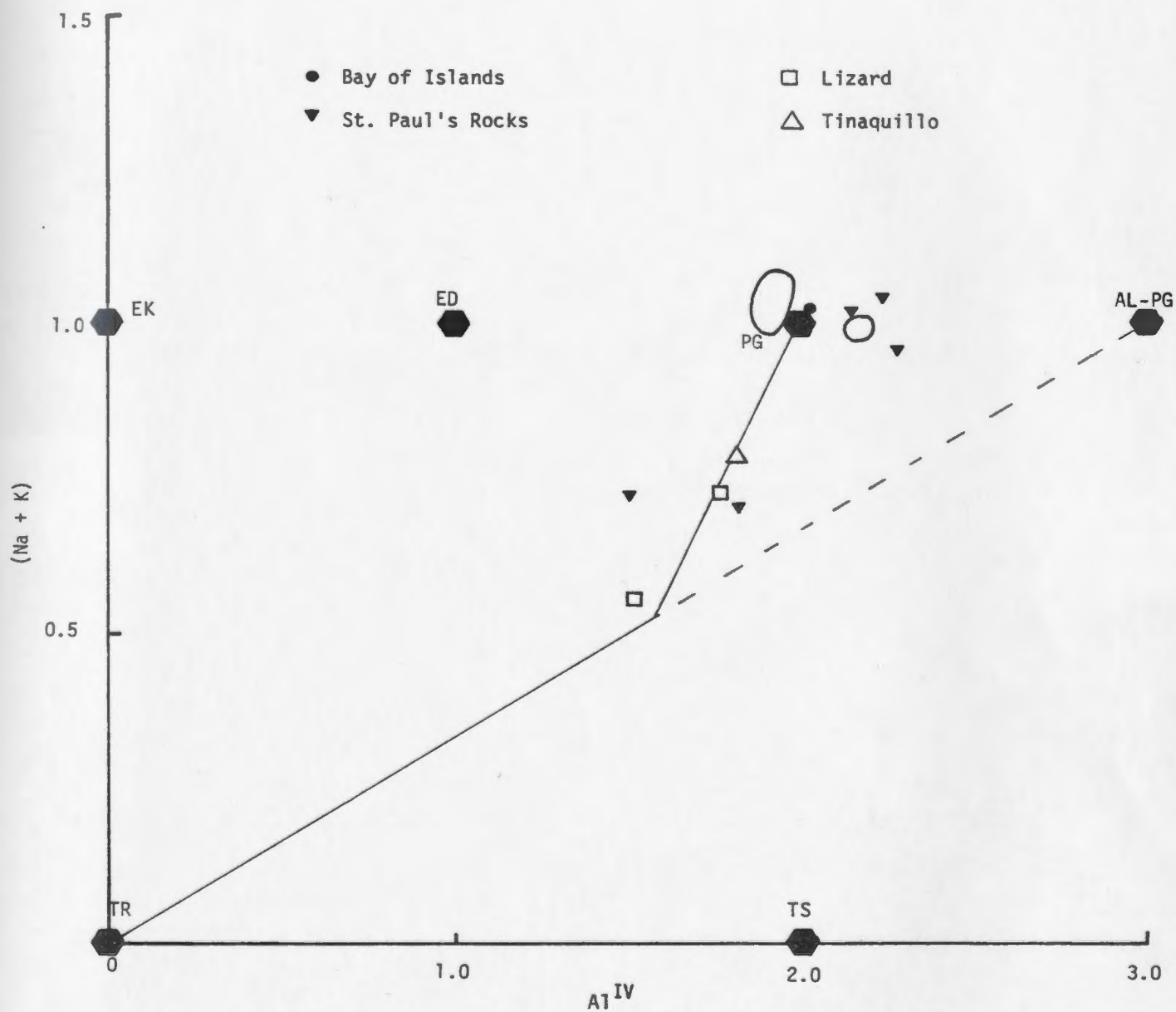


FIGURE 6.3b: Compositions of peridotite amphiboles compared to those from the White Hills Peridotite (outlined fields). Lines show overall St. Anthony Complex trends.

TABLE I.iii. Major elements, trace elements, and CIPW norms of the Ireland Point Volcanics and related rocks.

IPV = Ireland Point Volcanics
QHV = Quirpon Harbour Volcanics
PPG = Partridge Point Gabbro
COV = Cape Onion Volcanics
SLV = St. Lunaire Volcanics
CHV = Croque Harbour Volcanics

SI02	*	45.49	*	44.82	*	44.81	*	44.69	*	46.90	*	38.91	*	46.78	*
TI02	*	1.97	*	2.12	*	2.12	*	2.19	*	2.67	*	2.58	*	1.69	*
AL203	*	12.52	*	13.87	*	14.40	*	14.13	*	16.12	*	11.81	*	11.25	*
FE203	*	1.93	*	2.42	*	2.06	*	1.36	*	0.55	*	0.20	*	1.04	*
FEO	*	9.63	*	9.74	*	9.64	*	10.77	*	10.42	*	12.71	*	9.53	*
MNO	*	0.16	*	0.16	*	0.15	*	0.15	*	0.14	*	0.17	*	0.13	*
MGO	*	9.59	*	9.51	*	9.06	*	9.69	*	5.85	*	11.71	*	11.06	*
CAO	*	8.13	*	7.98	*	8.15	*	7.75	*	5.66	*	9.03	*	7.68	*
NA2O	*	3.21	*	2.80	*	3.07	*	2.90	*	4.15	*	0.25	*	3.36	*
K2O	*	0.06	*	0.45	*	0.22	*	0.57	*	1.47	*	0.03	*	0.10	*
P2O5	*	0.19	*	0.22	*	0.22	*	0.20	*	0.39	*	0.25	*	0.17	*
LOI	*	6.71	*	5.68	*	6.10	*	4.96	*	4.25	*	12.51	*	6.24	*
TOTAL	*	99.59	*	99.77	*	100.00	*	99.36	*	98.57	*	100.16	*	99.03	*

ZR	*	116	*	120	*	119	*	120	*	169	*	155	*	98	*
SR	*	240	*	190	*	195	*	171	*	487	*	410	*	141	*
RB	*	2	*	7	*	4	*	9	*	8	*	1	*	5	*
ZN	*	113	*	111	*	119	*	113	*	136	*	222	*	85	*
CU	*	91	*	71	*	86	*	85	*	131	*	119	*	69	*
BA	*	62	*	181	*	124	*	207	*	575	*	53	*	38	*
NB	*	11	*	11	*	12	*	12	*	20	*	18	*	16	*
Y	*	31	*	32	*	33	*	33	*	35	*	33	*	19	*
PB	*	7	*	8	*	8	*	6	*	8	*	9	*	2	*
NI	*	291	*	332	*	339	*	354	*	6	*	412	*	301	*
CR	*	380	*	426	*	416	*	433	*	59	*	571	*	463	*
V	*	263	*	278	*	273	*	276	*	319	*	301	*	232	*
GA	*	25	*	26	*	25	*	27	*	26	*	30	*	17	*

AN	*	21.00	*	25.43	*	26.45	*	25.25	*	22.27	*	35.34	*	16.51	*
NE	*	0.0	*	0.0	*	0.0	*	0.0	*	1.47	*	0.0	*	0.0	*
LC	*	0.0	*	0.0	*	0.0	*	0.0	*	0.0	*	0.0	*	0.0	*
COR	*	0.0	*	0.0	*	0.0	*	0.0	*	0.0	*	0.0	*	0.0	*
WD	*	0.0	*	0.0	*	0.0	*	0.0	*	0.0	*	0.0	*	0.0	*
DI	*	17.13	*	12.33	*	12.30	*	11.56	*	4.22	*	11.45	*	18.93	*
WO	*	8.81	*	6.35	*	6.32	*	5.92	*	2.13	*	5.86	*	9.76	*
EN	*	5.37	*	3.90	*	3.82	*	3.45	*	1.05	*	3.37	*	6.07	*
FS	*	2.94	*	2.08	*	2.16	*	2.18	*	1.04	*	2.22	*	3.11	*
HY	*	6.48	*	7.22	*	4.32	*	1.17	*	0.0	*	28.89	*	6.90	*
EN	*	4.19	*	4.71	*	2.76	*	0.71	*	0.0	*	17.43	*	4.56	*
FS	*	2.29	*	2.51	*	1.56	*	0.45	*	0.0	*	11.45	*	2.33	*
OL	*	18.13	*	18.40	*	19.80	*	25.41	*	21.16	*	15.00	*	20.88	*
FO	*	11.30	*	11.59	*	12.21	*	14.98	*	10.08	*	8.70	*	13.35	*
FA	*	6.82	*	6.81	*	7.59	*	10.44	*	11.08	*	6.30	*	7.53	*
LA	*	0.0	*	0.0	*	0.0	*	0.0	*	0.0	*	0.0	*	0.0	*
MT	*	3.01	*	3.73	*	3.18	*	2.09	*	0.84	*	0.33	*	1.62	*
ILM	*	4.02	*	4.28	*	4.28	*	4.40	*	5.37	*	5.58	*	3.46	*
AP	*	0.47	*	0.54	*	0.54	*	0.49	*	0.96	*	0.66	*	0.43	*
HM	*	0.0	*	0.0	*	0.0	*	0.0	*	0.0	*	0.0	*	0.0	*

RJ75-157 IPV (VARIOLITIC) MASSIVE FLOW IRELAND POINT
 RJ75160A IPV (VARIOLITIC) PILLOW LAVA (CORE+RIM) IRELAND POINT
 RJ75160B IPV (VARIOLITIC) PILLOW LAVA (CORE) IRELAND PCINT
 RJ75160C IPV (VARIOLITIC) PILLOW LAVA (RIM) IRELAND POINT
 RJ75-162 IPV (VARIOLITIC) PILLOWED FLOW IRELAND POINT
 RJ75-319 QHV (VARIOLITIC) ALTERED PILLOW LAVA QUIRPON ISLAND
 RJ76-512 QHV (VARIOLITIC) ALTERED FLOW JACQUES CARTIER ISLAND

TI02	*	1.90	*	2.11	*	2.07	*	1.96	*	1.95	*	2.45	*	2.40	*
AL203	*	13.55	*	14.24	*	13.89	*	14.47	*	10.69	*	10.75	*	12.09	*
FE2O3	*	1.98	*	2.23	*	0.62	*	1.14	*	1.81	*	2.19	*	2.22	*
FEO	*	9.69	*	10.99	*	12.96	*	7.78	*	9.22	*	8.25	*	8.08	*
MNO	*	0.15	*	0.16	*	0.17	*	0.10	*	0.19	*	0.15	*	0.14	*
MGO	*	8.74	*	9.09	*	10.05	*	3.86	*	7.48	*	8.07	*	6.97	*
CAO	*	10.36	*	10.31	*	7.16	*	4.89	*	12.32	*	11.00	*	12.39	*
NA2O	*	2.37	*	1.25	*	2.12	*	5.91	*	2.53	*	3.63	*	3.84	*
K2O	*	0.73	*	1.26	*	0.60	*	1.52	*	0.03	*	0.06	*	0.09	*
P2O5	*	0.22	*	0.23	*	0.21	*	0.36	*	0.26	*	0.36	*	0.37	*
LOI	*	5.17	*	5.42	*	5.93	*	3.33	*	13.03	*	6.23	*	6.85	*
TOTAL	*	98.84	*	98.14	*	98.27	*	98.18	*	99.69	*	98.14	*	99.50	*

ZR	*	115	*	130	*	114	*	150	*	139	*	151	*	159	*
SR	*	390	*	475	*	232	*	186	*	735	*	335	*	338	*
RB	*	26	*	40	*	24	*	26	*	2	*	0	*	1	*
ZN	*	100	*	114	*	122	*	86	*	85	*	75	*	107	*
CU	*	70	*	62	*	41	*	61	*	56	*	56	*	85	*
BA	*	294	*	662	*	240	*	840	*	57	*	62	*	52	*
NB	*	16	*	19	*	19	*	25	*	21	*	29	*	27	*
Y	*	19	*	23	*	24	*	23	*	21	*	21	*	20	*
PB	*	1	*	0	*	4	*	0	*	1	*	0	*	0	*
NI	*	324	*	380	*	349	*	208	*	219	*	264	*	197	*
CR	*	413	*	452	*	465	*	279	*	463	*	551	*	358	*
V	*	238	*	267	*	292	*	230	*	255	*	289	*	276	*
GA	*	27	*	27	*	26	*	18	*	17	*	16	*	24	*

SAMPLE	* RJ76-515 *	* RJ76-516 *	* RJ76-517 *	* RJ76-518 *	* RJ76-526 *	* RJ76-527 *	* RJ76-535 *
QZ	0.0	0.0	0.0	0.0	0.0	0.0	0.0
OR	4.61	8.03	3.84	9.47	0.20	0.39	0.57
AB	19.21	9.65	19.43	51.40	13.98	26.64	19.19
AN	25.81	31.84	28.82	8.93	20.45	13.99	16.71
NE	1.19	0.95	0.0	0.72	5.81	3.67	8.60
LC	0.0	0.0	0.0	0.0	0.0	0.0	0.0
COR	0.0	0.0	0.0	0.0	0.0	0.0	0.0
WD	0.0	0.0	0.0	0.0	0.0	0.0	0.0
DI	22.43	17.74	6.72	11.77	39.32	34.64	38.16
WO	11.50	9.07	3.41	5.93	20.10	17.89	19.64
EN	6.78	5.19	1.83	2.82	11.48	11.35	12.06
FS	4.14	3.48	1.47	3.02	7.74	5.41	6.46
HY	0.0	0.0	7.43	0.0	0.0	0.0	0.0
EN	0.0	0.0	4.11	0.0	0.0	0.0	0.0
FS	0.0	0.0	3.32	0.0	0.0	0.0	0.0
OL	19.29	23.40	28.01	11.17	12.24	11.24	7.44
FO	11.53	13.47	14.83	5.12	7.02	7.37	4.68
FA	7.76	9.94	13.18	6.05	5.22	3.87	2.76
LA	0.0	0.0	0.0	0.0	0.0	0.0	0.0
MT	3.06	3.49	0.97	1.74	3.03	3.45	3.47
ILM	3.85	4.32	4.26	3.92	4.27	5.06	4.92
AP	0.55	0.58	0.53	0.88	0.70	0.91	0.93
HM	0.0	0.0	0.0	0.0	0.0	0.0	0.0

RJ76-515 QHV (VARIOLITIC) PILLOW LAVA JACQUES CARTIER ISLAND
 RJ76-516 QHV (VARIOLITIC) PILLOW LAVA JACQUES CARTIER ISLAND
 RJ76-517 QHV (VARIOLITIC) PILLOW LAVA JACQUES CARTIER ISLAND
 RJ76-518 QHV (VARIOLITIC) PILLOW LAVA JACQUES CARTIER ISLAND
 PJ76-526 IPV (VARIOLITIC) ALTERED PILLOW LAVA BLOCK AT RALEIGH TURNOFF
 RJ76-527 IPV (VARIOLITIC) PILLOW LAVA BLOCK AT RALEIGH TURNOFF
 RJ76-538 IPV (VARIOLITIC) PILLOW LAVA (RIM) IRELAND BIGHT

SAMPLE		KJ76-532		KJ76-533		KJ76-539		KJ76-536		KJ76-539		KJ76-550		KJ76-559	
SI02	*	46.43	*	47.92	*	41.19	*	45.38	*	49.29	*	42.46	*	44.99	*
TI02	*	2.32	*	3.44	*	2.47	*	1.93	*	2.45	*	1.94	*	2.46	*
AL203	*	12.75	*	15.16	*	13.20	*	12.08	*	14.56	*	11.63	*	12.86	*
FE203	*	1.24	*	0.57	*	1.79	*	2.04	*	0.66	*	1.22	*	0.80	*
FEO	*	10.01	*	9.46	*	11.34	*	9.45	*	10.24	*	10.29	*	10.42	*
MNO	*	0.15	*	0.10	*	0.18	*	0.15	*	0.14	*	0.15	*	0.16	*
MGO	*	9.35	*	6.09	*	9.99	*	10.19	*	8.67	*	9.18	*	10.05	*
CAO	*	6.72	*	4.08	*	9.37	*	9.32	*	2.91	*	8.37	*	7.37	*
NA2O	*	3.64	*	5.40	*	1.36	*	2.78	*	3.25	*	2.03	*	2.90	*
K2O	*	0.12	*	0.10	*	1.87	*	0.46	*	0.06	*	0.03	*	0.48	*
P2O5	*	0.25	*	0.39	*	0.28	*	0.20	*	0.24	*	0.20	*	0.35	*
LOI	*	5.26	*	5.40	*	5.85	*	4.86	*	7.92	*	10.69	*	5.66	*
TOTAL	*	98.24	*	98.11	*	98.88	*	98.84	*	100.39	*	98.19	*	98.50	*

ZR	*	130	*	176	*	146	*	110	*	129	*	114	*	148	*
SR	*	239	*	193	*	214	*	174	*	342	*	315	*	146	*
RB	*	2	*	2	*	29	*	8	*	3	*	0	*	8	*
ZN	*	88	*	110	*	120	*	92	*	104	*	97	*	108	*
CU	*	77	*	79	*	79	*	76	*	94	*	76	*	80	*
BA	*	72	*	78	*	470	*	121	*	70	*	44	*	279	*
NB	*	20	*	31	*	21	*	16	*	15	*	16	*	30	*
Y	*	26	*	29	*	23	*	21	*	22	*	24	*	24	*
PB	*	0	*	0	*	0	*	0	*	2	*	0	*	4	*
NI	*	203	*	54	*	247	*	283	*	154	*	323	*	207	*
CR	*	386	*	80	*	382	*	387	*	300	*	382	*	376	*
V	*	328	*	434	*	292	*	233	*	351	*	269	*	316	*
GA	*	22	*	25	*	25	*	20	*	22	*	21	*	21	*

SAMPLE	RJ76-542	RJ76-544	RJ76-545	RJ76-546	RJ76-549	RJ76-550	RJ76-559
OR	0.0	3.75	0.0	0.0	5.49	0.0	0.0
AB	0.76	3.28	11.88	2.89	0.38	0.20	0.0
AN	33.12	2.47	7.72	25.03	29.74	19.63	3.06
NE	19.46	16.47	26.22	20.35	13.93	25.75	25.43
LC	0.0	9.01	2.52	0.0	0.0	0.0	22.25
COR	0.0	7.47	0.0	0.0	0.0	0.0	0.0
WO	0.0	0.0	0.0	0.0	4.79	0.0	0.0
DI	11.92	0.89	17.77	22.25	0.0	16.51	0.0
WD	6.12	7.05	9.10	11.47	0.0	8.44	11.95
EN	3.64	0.98	5.33	7.17	0.0	4.87	6.14
FS	2.16	0.0	3.34	3.61	0.0	3.19	3.66
HY	9.69	0.0	0.0	1.25	39.00	20.34	2.15
EN	6.08	0.64	0.0	0.83	23.35	12.29	8.30
FS	3.60	49.28	0.0	0.42	15.65	8.05	5.23
OL	17.75	18.15	25.38	20.69	0.0	10.81	3.07
FO	10.73	0.0	15.01	13.31	0.0	6.28	20.85
FA	7.01	0.0	10.38	7.38	0.0	4.53	12.66
LA	0.0	0.0	0.0	0.0	0.0	0.0	8.20
MT	1.93	0.78	2.77	3.15	1.03	2.02	0.0
ILM	4.74	0.40	5.04	3.90	5.03	4.21	1.25
AP	0.62	0.22	0.70	0.49	0.60	0.53	5.03
HM	0.0	0.16	0.0	0.0	0.0	0.0	0.88

RJ76-542 IPV (VARIOLITIC) PILLOW LAVA IRELAND BIGHT
 RJ76-544 IPV (VARIOLITIC) PILLOW LAVA ABOVE BLACK SHALE EAST OF IRELAND POINT
 RJ76-545 IPV (VARIOLITIC) PILLOW LAVA EAST OF IRELAND POINT
 RJ76-546 IPV (VARIOLITIC) PILLOW LAVA EAST OF IRELAND POINT
 RJ76-549 IPV (VESICULAR) MASSIVE FLOW WEST OF STARK'S BIGHT
 RJ76-550 IPV (VARIOLITIC) ALTERED PILLOW LAVA WEST OF STARK'S BIGHT
 RJ76-599 IPV (VARIOLITIC) PILLOW LAVA GRIQUET

SAMPLE	* RJ70-532 *	* RJ70-545 *	* RJ75-229 *	* RJ75-257 *	* RJ75-258 *	* RJ75-260 *	* RJ75-263 *
SI02	* 31.83 *	* 38.00 *	* 48.47 *	* 44.86 *	* 46.30 *	* 47.48 *	* 47.37 *
TI02	* 1.25 *	* 1.87 *	* 1.83 *	* 2.04 *	* 2.10 *	* 2.01 *	* 2.07 *
AL203	* 7.24 *	* 11.75 *	* 15.74 *	* 15.19 *	* 14.58 *	* 14.11 *	* 14.57 *
FE203	* 2.20 *	* 9.32 *	* 3.08 *	* 3.79 *	* 6.18 *	* 4.45 *	* 3.17 *
FEO	* 5.23 *	* 1.64 *	* 6.41 *	* 6.71 *	* 5.17 *	* 6.28 *	* 7.57 *
MNO	* 0.15 *	* 0.10 *	* 0.13 *	* 0.19 *	* 0.17 *	* 0.14 *	* 0.15 *
MGO	* 2.29 *	* 3.20 *	* 3.57 *	* 5.93 *	* 6.26 *	* 7.91 *	* 7.84 *
CAO	* 25.34 *	* 16.04 *	* 7.97 *	* 11.39 *	* 10.52 *	* 7.73 *	* 6.61 *
NA2O	* 0.27 *	* 1.98 *	* 5.64 *	* 3.46 *	* 3.35 *	* 0.75 *	* 2.78 *
K2O	* 2.53 *	* 3.82 *	* 0.73 *	* 0.05 *	* 0.55 *	* 2.11 *	* 1.74 *
P2O5	* 0.08 *	* 0.40 *	* 0.26 *	* 0.27 *	* 0.26 *	* 0.22 *	* 0.23 *
LOI	* 22.29 *	* 13.07 *	* 6.88 *	* 6.11 *	* 4.55 *	* 6.70 *	* 5.11 *
TOTAL	* 100.70 *	* 100.19 *	* 100.71 *	* 99.99 *	* 99.99 *	* 99.89 *	* 99.21 *

ZR	* 97 *	* 157 *	* 141 *	* 153 *	* 159 *	* 154 *	* 151 *
SR	* 261 *	* 159 *	* 406 *	* 285 *	* 307 *	* 373 *	* 261 *
RB	* 33 *	* 37 *	* 25 *	* 1 *	* 6 *	* 23 *	* 20 *
ZN	* 55 *	* 58 *	* 84 *	* 103 *	* 109 *	* 90 *	* 114 *
CU	* 30 *	* 46 *	* 110 *	* 83 *	* 110 *	* 65 *	* 126 *
BA	* 164 *	* 145 *	* 428 *	* 51 *	* 107 *	* 124 *	* 246 *
NB	* 13 *	* 20 *	* 7 *	* 11 *	* 12 *	* 15 *	* 11 *
Y	* 14 *	* 29 *	* 47 *	* 42 *	* 43 *	* 22 *	* 39 *
PB	* 0 *	* 0 *	* 6 *	* 8 *	* 7 *	* 0 *	* 7 *
NI	* 38 *	* 31 *	* 27 *	* 26 *	* 18 *	* 44 *	* 29 *
CR	* 10 *	* 19 *	* 55 *	* 69 *	* 74 *	* 41 *	* 73 *
V	* 40 *	* 266 *	* 294 *	* 303 *	* 308 *	* 217 *	* 294 *
GA	* 12 *	* 14 *	* 19 *	* 21 *	* 21 *	* 23 *	* 21 *

SAMPLE	RJ75-532	RJ75-548	RJ75-229	RJ75-257	RJ75-258	RJ75-259	RJ75-263
QZ	0.0	0.0	0.0	0.0	0.0	0.0	0.0
OR	0.0	2.38	0.0	0.31	3.40	7.35	9.0
AB	0.0	0.0	0.0	26.91	29.69	13.38	10.02
AN	17.27	13.65	4.88	27.44	24.22	6.81	24.99
NE	1.93	10.42	2.71	2.31	0.0	31.01	23.52
LC	18.29	18.45	2.16	0.0	0.0	0.0	0.0
COR	0.0	0.0	0.0	0.0	0.0	0.0	0.0
WO	0.0	20.61	0.0	0.0	0.0	0.0	0.0
DI	27.97	19.73	4.76	24.96	22.61	6.85	7.96
WO	14.09	10.58	3.70	12.93	12.03	3.59	4.12
EN	6.76	9.15	0.64	8.48	9.81	2.62	2.71
FS	7.12	0.0	0.0	3.54	0.77	0.64	1.13
HY	0.0	0.0	0.0	0.0	3.08	23.02	16.30
EN	0.0	0.0	4.59	0.0	2.86	18.52	11.51
FS	0.0	0.0	38.60	0.0	0.22	4.51	4.79
QL	25.57	0.0	16.49	7.41	2.79	0.0	6.67
FO	1.50	0.0	6.63	5.07	2.57	0.0	4.57
FA	1.74	0.0	0.0	2.34	0.22	0.0	2.10
LA	22.34	0.0	0.0	0.0	0.0	0.0	0.0
MT	4.98	0.22	19.70	5.85	9.38	6.92	4.88
ILM	3.70	4.08	10.05	4.13	4.18	4.10	4.18
AP	0.29	1.07	5.60	0.67	0.63	0.55	0.57
HM	0.0	9.40	4.06	0.0	0.0	0.0	0.0

RJ76-532 IPV (PILLOW BRECCIA) CALCITE-RICH MATRIX IRELAND BIGHT
 RJ76-548 IPV (PILLOW BRECCIA) VESICULAR PILLOW FRAGMENT EAST OF IRELAND POINT
 RJ75-229 IPV (VESICULAR) PILLOW LAVA LOCK'S COVE
 RJ75-257 IPV (VESICULAR) PILLOW LAVA STARK'S BIGHT
 RJ75-258 IPV (VESICULAR) PILLOW LAVA STARK'S BIGHT
 RJ75-260 IPV (VESICULAR) FLATTENED PILLOW LAVA INTERLEAVED WITH CALCITE S.B.
 RJ75-263 IPV (VESICULAR) PILLOW LAVA STARK'S BIGHT

SAMPLE	* RJ75-468 *	* RJ75-470 *	* RJ75-534 *	* RJ75-535 *	* RJ75-537 *	* RJ75-547 *	* RJ75-553 *
SI02	* 46.80 *	* 42.60 *	* 46.07 *	* 46.52 *	* 51.74 *	* 46.68 *	* 48.90 *
TI02	* 1.97 *	* 2.27 *	* 2.04 *	* 2.33 *	* 2.09 *	* 1.95 *	* 2.25 *
AL203	* 13.94 *	* 14.08 *	* 13.39 *	* 16.03 *	* 14.84 *	* 14.63 *	* 13.76 *
FE203	* 7.28 *	* 7.15 *	* 2.30 *	* 1.42 *	* 1.69 *	* 4.76 *	* 1.04 *
FEO	* 4.56 *	* 5.05 *	* 6.52 *	* 5.64 *	* 7.91 *	* 6.00 *	* 7.00 *
MNO	* 0.12 *	* 0.14 *	* 0.15 *	* 0.09 *	* 0.12 *	* 0.19 *	* 0.15 *
MGO	* 4.21 *	* 5.23 *	* 8.56 *	* 3.64 *	* 4.38 *	* 6.52 *	* 4.33 *
CAO	* 10.24 *	* 8.85 *	* 6.11 *	* 7.32 *	* 5.58 *	* 9.58 *	* 7.26 *
NA2O	* 3.43 *	* 2.41 *	* 2.90 *	* 3.38 *	* 1.35 *	* 3.51 *	* 4.77 *
K2O	* 1.92 *	* 3.01 *	* 2.24 *	* 3.75 *	* 3.09 *	* 1.01 *	* 0.78 *
P2O5	* 0.29 *	* 0.29 *	* 0.24 *	* 0.39 *	* 0.03 *	* 0.24 *	* 0.75 *
LOI	* 5.13 *	* 7.63 *	* 7.98 *	* 7.54 *	* 7.77 *	* 3.71 *	* 8.53 *
TOTAL	* 99.89 *	* 98.71 *	* 98.50 *	* 98.05 *	* 100.59 *	* 98.78 *	* 99.52 *

ZR	* 148 *	* 173 *	* 154 *	* 201 *	* 167 *	* 152 *	* 266 *
SR	* 257 *	* 265 *	* 266 *	* 213 *	* 211 *	* 575 *	* 335 *
RB	* 23 *	* 30 *	* 24 *	* 44 *	* 48 *	* 9 *	* 23 *
ZN	* 77 *	* 90 *	* 74 *	* 62 *	* 83 *	* 90 *	* 79 *
CU	* 51 *	* 65 *	* 36 *	* 27 *	* 64 *	* 94 *	* 32 *
BA	* 163 *	* 149 *	* 131 *	* 330 *	* 210 *	* 142 *	* 204 *
NB	* 16 *	* 15 *	* 20 *	* 31 *	* 19 *	* 16 *	* 65 *
Y	* 29 *	* 32 *	* 28 *	* 28 *	* 11 *	* 28 *	* 27 *
PB	* 4 *	* 0 *	* 0 *	* 7 *	* 5 *	* 1 *	* 0 *
NI	* 39 *	* 28 *	* 41 *	* 110 *	* 84 *	* 41 *	* 74 *
CR	* 29 *	* 23 *	* 75 *	* 236 *	* 47 *	* 33 *	* 100 *
V	* 287 *	* 355 *	* 298 *	* 252 *	* 68 *	* 262 *	* 167 *
GA	* 16 *	* 22 *	* 18 *	* 16 *	* 21 *	* 19 *	* 23 *

SAMPLE	RJ76-468	RJ76-470	RJ76-534	RJ76-535	RJ76-537	RJ76-547	RJ76-593
OR	11.97	19.53	14.52	24.48	19.67	6.28	5.07
AB	28.31	16.46	27.11	21.24	12.31	29.85	44.35
AN	17.91	20.54	18.67	19.33	27.27	22.28	15.20
NE	1.26	3.21	0.0	5.61	0.0	0.75	0.0
LC	0.0	0.0	0.0	0.0	0.0	0.0	0.0
COR	0.0	0.0	0.0	0.0	0.0	0.0	0.0
WD	1.28	0.0	0.0	0.0	0.0	0.0	0.0
DI	23.86	19.93	10.49	14.66	1.94	20.79	15.64
WO	12.80	10.69	5.47	7.52	0.98	10.89	7.95
EN	11.06	9.24	3.78	4.44	0.50	7.86	4.29
FS	0.0	0.0	1.24	2.70	0.46	2.04	3.40
HY	0.0	0.0	5.95	0.0	21.46	0.0	5.76
EN	0.0	0.0	4.48	0.0	11.25	0.0	3.21
FS	0.0	0.0	1.47	0.0	10.21	0.0	2.55
OL	0.0	3.55	14.58	6.51	0.0	8.31	5.72
FO	0.0	3.55	10.71	3.90	0.0	6.46	3.05
FA	0.0	0.0	3.87	2.61	0.0	1.85	2.67
LA	0.0	0.0	0.0	0.0	0.0	0.0	0.0
MT	9.90	11.15	3.68	2.27	2.64	7.26	1.66
LM	3.95	4.73	4.28	4.89	4.28	3.90	4.70
AP	0.71	0.74	0.62	1.00	0.08	0.59	1.92
HM	0.86	0.16	0.0	0.0	0.0	0.0	0.0

RJ76-468 IPV (VESICULAR) PILLOW LAVA STARK'S BIGHT
 RJ76-470 IPV (VESICULAR) FLATTENED PILLOW LAVA INTERLEAVED WITH CALCITE S.B.
 RJ76-534 IPV (VESICULAR) MASSIVE FLOW IRELAND POINT
 RJ76-535 IPV (VESICULAR) ALTERED MASSIVE FLOW IRELAND POINT
 RJ76-537 IPV (VESICULAR) MASSIVE FLOW IRELAND BIGHT
 RJ76-547 IPV (VESICULAR) PILLOW LAVA EAST OF IRELAND POINT
 RJ76-603 IPV (VESICULAR) PILLOW LAVA BLOCK ON RALEIGH ROAD

SAMPLE	* RJ75-255 *	* RJ75-256 *	* RJ75-453 *	* RJ75-454 *	* RJ75-455 *	* RJ75-456 *	* RJ75-457 *
SiO2	* 43.00 *	* 44.27 *	* 42.83 *	* 40.19 *	* 43.61 *	* 43.81 *	* 42.84 *
TiO2	* 0.75 *	* 0.68 *	* 0.85 *	* 0.83 *	* 0.73 *	* 0.76 *	* 0.71 *
AL2O3	* 20.12 *	* 19.82 *	* 15.82 *	* 15.46 *	* 18.51 *	* 19.69 *	* 18.23 *
FE2O3	* 3.54 *	* 3.73 *	* 4.56 *	* 5.15 *	* 4.35 *	* 4.78 *	* 5.39 *
FeO	* 3.08 *	* 2.52 *	* 3.11 *	* 2.99 *	* 2.48 *	* 2.47 *	* 1.79 *
MNO	* 0.12 *	* 0.10 *	* 0.11 *	* 0.12 *	* 0.10 *	* 0.12 *	* 0.10 *
MGO	* 4.61 *	* 4.89 *	* 5.43 *	* 4.98 *	* 5.37 *	* 4.25 *	* 3.03 *
CAO	* 13.26 *	* 13.73 *	* 13.40 *	* 16.14 *	* 12.98 *	* 14.21 *	* 14.99 *
NA2O	* 2.96 *	* 2.66 *	* 3.34 *	* 3.54 *	* 2.93 *	* 2.66 *	* 3.44 *
K2O	* 1.26 *	* 1.12 *	* 0.81 *	* 0.39 *	* 1.39 *	* 1.31 *	* 1.34 *
P2O5	* 0.09 *	* 0.08 *	* 0.08 *	* 0.09 *	* 0.07 *	* 0.09 *	* 0.11 *
LOI	* 6.87 *	* 6.43 *	* 7.46 *	* 8.73 *	* 6.25 *	* 5.70 *	* 7.09 *
TOTAL	* 99.66 *	* 100.03 *	* 97.80 *	* 98.61 *	* 98.77 *	* 99.85 *	* 99.06 *

ZR	* 73 *	* 77 *	* 73 *	* 72 *	* 65 *	* 67 *	* 66 *
SR	* 231 *	* 358 *	* 292 *	* 259 *	* 316 *	* 271 *	* 311 *
RB	* 12 *	* 10 *	* 8 *	* 7 *	* 16 *	* 16 *	* 16 *
ZN	* 111 *	* 82 *	* 52 *	* 59 *	* 52 *	* 52 *	* 48 *
CU	* 114 *	* 113 *	* 65 *	* 102 *	* 47 *	* 57 *	* 47 *
EA	* 98 *	* 98 *	* 67 *	* 36 *	* 110 *	* 82 *	* 61 *
NB	* 1 *	* 1 *	* 6 *	* 5 *	* 6 *	* 7 *	* 5 *
Y	* 27 *	* 26 *	* 19 *	* 17 *	* 16 *	* 18 *	* 19 *
PB	* 7 *	* 7 *	* 0 *	* 0 *	* 2 *	* 0 *	* 3 *
NI	* 104 *	* 159 *	* 114 *	* 112 *	* 132 *	* 125 *	* 88 *
CR	* 231 *	* 224 *	* 224 *	* 212 *	* 195 *	* 207 *	* 183 *
V	* 146 *	* 132 *	* 158 *	* 159 *	* 133 *	* 149 *	* 127 *
GA	* 15 *	* 18 *	* 15 *	* 14 *	* 17 *	* 15 *	* 15 *

SAMPLE	* RJ75-255 *	* RJ75-256 *	* RJ75-463 *	* RJ75-464 *	* RJ75-465 *	* RJ75-466 *	* RJ75-467 *
OZ	0.0	0.0	0.0	0.0	0.0	0.0	0.0
DR	8.02	7.07	5.30	2.56	8.88	8.22	8.01
AB	7.93	11.44	12.09	4.30	10.14	9.30	9.64
AN	40.81	41.46	28.54	27.97	35.94	40.27	32.99
NE	10.32	6.82	10.40	15.72	9.02	7.91	11.92
LC	0.0	0.0	0.0	0.0	0.0	0.0	0.0
COR	0.0	0.0	0.0	0.0	0.0	0.0	0.0
WD	0.0	0.0	0.53	9.20	0.0	1.18	10.17
DI	23.31	24.14	33.84	29.95	25.82	24.25	17.70
WO	12.32	12.88	18.04	16.05	13.85	13.01	9.49
EN	9.58	10.74	14.97	13.80	11.97	11.24	8.20
FS	1.41	0.51	0.82	0.10	0.0	0.0	0.0
HY	0.0	0.0	0.0	0.0	0.0	0.0	0.0
EN	0.0	0.0	0.0	0.0	0.0	0.0	0.0
FS	0.0	0.0	0.0	0.0	0.0	0.0	0.0
OL	2.27	1.66	0.0	0.0	1.74	0.0	0.0
FO	1.95	1.58	0.0	0.0	1.74	0.0	0.0
FA	0.32	0.08	0.0	0.0	0.0	0.0	0.0
LA	0.0	0.0	0.0	0.0	0.0	0.0	0.0
MT	5.53	5.77	7.32	8.31	6.70	6.53	4.39
ILM	1.53	1.38	1.79	1.75	1.50	1.53	1.47
AP	0.23	0.20	0.21	0.23	0.18	0.22	0.28
HM	0.0	0.0	0.0	0.0	0.08	0.57	2.83

RJ75-255 IPV (PORPHYRITIC) ALTERED PILLOW LAVA STARK'S BIGHT
 RJ75-256 IPV (PORPHYRITIC) PILLOW LAVA STARK'S BIGHT
 RJ76-463 IPV (PORPHYRITIC) PILLOW LAVA (RIM) STARK'S BIGHT
 RJ76-464 IPV (PORPHYRITIC) PILLOW LAVA (RIM+CORE) STARK'S BIGHT
 RJ76-465 IPV (PORPHYRITIC) PILLOW LAVA (CORE) STARK'S BIGHT
 RJ76-466 IPV (PORPHYRITIC) PILLOW LAVA (CORE) STARK'S BIGHT
 RJ76-467 IPV (PORPHYRITIC) ALTERED PILLOW LAVA (CORE) STARK'S BIGHT

SAMPLE	* RJ75-469 *	* RJ75-167 *	* RJ75-200 *	* RJ75-207 *	* RJ75-209 *	* RJ75-210 *	* RJ75-212 *
SI02	* 45.15 *	* 45.68 *	* 47.46 *	* 45.39 *	* 48.20 *	* 46.48 *	* 46.67 *
TI02	* 0.72 *	* 2.16 *	* 2.32 *	* 2.16 *	* 2.84 *	* 2.43 *	* 2.83 *
AL203	* 16.50 *	* 14.63 *	* 14.41 *	* 15.19 *	* 13.75 *	* 13.99 *	* 15.14 *
FE203	* 4.37 *	* 1.80 *	* 1.93 *	* 1.88 *	* 3.04 *	* 2.47 *	* 4.69 *
FE0	* 4.97 *	* 9.29 *	* 9.27 *	* 9.08 *	* 9.35 *	* 9.54 *	* 7.55 *
MNO	* 0.14 *	* 0.15 *	* 0.16 *	* 0.18 *	* 0.17 *	* 0.19 *	* 0.18 *
MGO	* 8.80 *	* 6.33 *	* 5.36 *	* 6.55 *	* 4.23 *	* 5.69 *	* 3.66 *
CA0	* 10.78 *	* 9.99 *	* 9.95 *	* 8.30 *	* 8.95 *	* 8.24 *	* 8.94 *
NA20	* 2.62 *	* 3.68 *	* 4.17 *	* 4.17 *	* 4.73 *	* 4.68 *	* 4.74 *
K20	* 0.20 *	* 0.13 *	* 0.24 *	* 0.10 *	* 0.21 *	* 0.10 *	* 0.59 *
P205	* 0.07 *	* 0.34 *	* 0.42 *	* 0.35 *	* 0.50 *	* 0.40 *	* 0.49 *
LOI	* 4.34 *	* 3.93 *	* 3.32 *	* 4.73 *	* 3.84 *	* 3.89 *	* 4.26 *
TOTAL	* 98.66 *	* 98.11 *	* 99.01 *	* 98.08 *	* 99.81 *	* 98.10 *	* 99.74 *

ZR	* 47 *	* 147 *	* 198 *	* 144 *	* 189 *	* 168 *	* 180 *
SR	* 202 *	* 1071 *	* 857 *	* 827 *	* 551 *	* 665 *	* 870 *
RB	* 1 *	* 3 *	* 11 *	* 2 *	* 4 *	* 2 *	* 17 *
ZN	* 64 *	* 125 *	* 114 *	* 207 *	* 218 *	* 228 *	* 127 *
CU	* 60 *	* 158 *	* 73 *	* 169 *	* 178 *	* 158 *	* 58 *
BA	* 5 *	* 210 *	* 379 *	* 139 *	* 464 *	* 228 *	* 419 *
NB	* 6 *	* 13 *	* 24 *	* 15 *	* 26 *	* 19 *	* 22 *
Y	* 18 *	* 32 *	* 37 *	* 32 *	* 41 *	* 35 *	* 36 *
PB	* 0 *	* 8 *	* 6 *	* 9 *	* 8 *	* 8 *	* 8 *
NI	* 278 *	* 71 *	* 36 *	* 103 *	* 0 *	* 58 *	* 0 *
CR	* 449 *	* 107 *	* 127 *	* 271 *	* 39 *	* 167 *	* 35 *
V	* 161 *	* 258 *	* 264 *	* 246 *	* 327 *	* 286 *	* 293 *
GA	* 17 *	* 25 *	* 18 *	* 27 *	* 23 *	* 27 *	* 26 *

SAMPLE	FJ75-469	FJ75-167	FJ75-200	FJ75-207	FJ75-209	FJ75-210	FJ75-212
OZ	0.0	0.0	0.0	0.0	0.0	0.0	0.0
OR	1.25	0.91	1.45	0.63	1.29	0.63	0.65
AB	23.50	22.12	32.77	33.20	40.02	36.53	36.01
AN	34.64	24.41	20.77	24.01	16.31	17.89	19.14
NE	0.0	2.12	2.21	2.47	0.89	2.96	3.23
LC	0.0	0.0	0.0	0.0	0.0	0.0	0.0
COF	0.0	0.0	0.0	0.0	0.0	0.0	0.0
WD	0.0	0.0	0.0	0.0	0.0	0.0	0.0
DI	17.14	21.52	23.32	14.69	22.18	18.91	19.32
NO	9.01	10.95	11.31	7.49	11.20	9.60	10.16
EN	6.72	5.94	6.09	4.17	5.56	5.08	5.97
FS	1.41	4.63	5.42	3.03	5.42	4.23	3.70
HY	3.03	0.0	0.0	0.0	0.0	0.0	0.0
EN	2.55	0.0	0.0	0.0	0.0	0.0	0.0
FS	0.53	0.0	0.0	0.0	0.0	0.0	0.0
OL	12.04	14.03	10.89	15.76	7.37	13.37	4.21
FO	9.79	7.55	5.30	9.31	3.79	6.97	2.50
FA	2.26	6.48	5.39	7.46	4.08	6.40	1.71
LA	0.0	0.0	0.0	0.0	0.0	0.0	0.0
MT	5.72	2.77	5.93	2.92	4.59	3.80	7.12
ILM	1.45	4.35	4.60	4.39	5.62	4.89	5.62
AP	0.17	0.34	1.02	0.87	1.21	0.99	1.19
HM	0.0	0.0	0.0	0.0	0.0	0.0	0.0

FJ75-469 IPV (PORPHYRITIC) PILLOW LAVA (RIM) STARK'S BIGHT
 FJ75-167 PPG IRELAND BIGHT
 FJ75-200 PPG FISHING PCINT
 FJ75-207 PPG FISHING POINT
 FJ75-209 PPG ALTERED FISHING POINT
 FJ75-210 PPG FISHING PCINT
 FJ75-212 PPG MAFIC FISHING PCINT

SAMPLE	* RJ75-213 *	* RJ75-281 *	* RJ75-282 *	* RJ75-283A *	* RJ75-283B *	* RJ75-284 *	* RJ75-285 *
SiO2	47.29	47.28	49.81	50.26	53.66	45.95	44.15
TiO2	1.98	2.10	1.47	1.40	1.34	2.14	2.54
AL2O3	15.67	13.87	16.19	15.35	16.94	12.96	12.45
FE2O3	2.78	2.57	2.89	2.90	1.88	2.16	1.32
FeO	6.30	8.68	4.80	6.39	4.78	10.18	12.03
MNO	0.13	0.17	0.11	0.17	0.12	0.18	0.21
MGO	5.35	5.63	4.62	4.86	3.00	7.56	7.92
CAO	10.08	11.45	12.30	9.90	7.37	10.98	10.03
NA2O	3.84	3.65	4.82	5.10	7.12	2.92	2.86
K2O	0.68	0.32	0.11	0.20	0.22	0.45	0.56
P2O5	0.32	0.42	0.30	0.41	0.38	0.28	0.32
LOI	3.73	3.08	2.71	3.62	2.21	3.85	4.19
TOTAL	98.65	99.22	100.13	100.56	99.02	99.61	98.58

ZR	151	182	185	212	244	133	146
SR	738	782	1045	807	929	674	488
FB	13	5	2	3	3	9	16
ZN	188	136	176	112	103	197	238
CU	164	120	154	61	75	157	204
BA	405	318	172	343	374	315	238
NB	14	22	16	26	34	12	18
Y	31	40	36	44	45	31	35
PB	8	9	8	8	8	9	8
NI	33	28	20	27	1	61	85
CR	91	113	76	104	54	101	79
V	236	206	193	120	84	286	280
GA	23	25	27	28	28	25	27

	RJ75-213	RJ75-281	RJ75-282	RJ75-283A	RJ75-283B	RJ75-284	RJ75-286
OR	0.0	0.0	0.0	0.0	0.0	0.0	0.0
AB	4.23	1.97	0.67	1.22	1.34	2.77	3.50
AN	30.39	28.38	31.30	38.61	51.67	23.68	20.85
NE	24.75	21.32	22.78	18.97	14.05	21.84	20.63
LC	1.79	2.01	5.70	3.18	5.69	1.14	2.58
COR	0.0	0.0	0.0	0.0	0.0	0.0	0.0
WD	0.0	0.0	0.0	0.0	0.0	0.0	0.0
DI	21.14	28.87	30.66	23.82	17.61	27.35	24.78
WD	10.88	14.70	15.94	12.22	8.99	13.95	12.56
EN	6.68	8.05	10.79	7.23	5.07	7.76	6.53
FS	3.58	6.12	3.93	4.38	3.55	5.64	5.69
HY	0.0	0.0	0.0	0.0	0.0	0.0	0.0
EN	0.0	0.0	0.0	0.0	0.0	0.0	0.0
FS	0.0	0.0	0.0	0.0	0.0	0.0	0.0
OL	8.19	8.39	0.99	6.13	3.28	15.01	19.72
FO	5.15	4.57	0.71	3.68	1.85	8.33	10.06
FA	3.05	3.82	0.28	2.45	1.43	6.68	9.66
LA	0.0	0.0	0.0	0.0	0.0	0.0	0.0
MT	4.24	3.87	4.30	4.33	2.81	3.27	2.03
ILM	3.96	4.14	2.86	2.74	2.63	4.24	5.11
AP	0.78	1.01	0.71	0.98	0.91	0.68	0.79
HM	0.0	0.0	0.0	0.0	0.0	0.0	0.0

RJ75-213	PPG	FISHING POINT
RJ75-281	PPG	PARTRIDGE POINT
RJ75-282	PPG	PARTRIDGE POINT
RJ75283A	PPG	PARTRIDGE POINT
RJ75283B	PPG	LEUCOCRATIC PARTRIDGE POINT
RJ75-284	PPG	PARTRIDGE POINT
RJ75-286	PPG	MAFIC PARTRIDGE PCINT

SAMPLE	* RJ75-250A *	* RJ75-317 *	* RJ75-329 *	* RJ75-430 *	* RJ75-431 *	* RJ75-432 *	* RJ75-529 *
SiO2	* 43.59 *	* 45.12 *	* 57.29 *	* 46.94 *	* 56.34 *	* 60.64 *	* 46.85 *
TiO2	* 1.91 *	* 1.96 *	* 0.50 *	* 2.85 *	* 0.53 *	* 0.56 *	* 2.70 *
AL2O3	* 13.88 *	* 8.79 *	* 17.98 *	* 14.32 *	* 17.84 *	* 18.51 *	* 14.89 *
FE2O3	* 2.29 *	* 3.50 *	* 0.0 *	* 3.13 *	* 1.60 *	* 1.16 *	* 3.49 *
FeO	* 11.22 *	* 8.88 *	* 8.74 *	* 9.03 *	* 4.98 *	* 3.93 *	* 8.46 *
MNO	* 0.19 *	* 0.17 *	* 0.13 *	* 0.17 *	* 0.11 *	* 0.08 *	* 0.16 *
MGO	* 8.88 *	* 13.89 *	* 0.88 *	* 4.15 *	* 0.92 *	* 0.80 *	* 4.01 *
CAO	* 8.34 *	* 8.36 *	* 2.16 *	* 9.18 *	* 4.87 *	* 3.23 *	* 9.20 *
NA2O	* 2.47 *	* 0.74 *	* 9.25 *	* 4.37 *	* 8.83 *	* 9.83 *	* 4.49 *
K2O	* 1.46 *	* 0.31 *	* 0.12 *	* 1.12 *	* 0.30 *	* 0.20 *	* 0.18 *
P2O5	* 0.26 *	* 0.30 *	* 0.15 *	* 0.46 *	* 0.47 *	* 0.10 *	* 0.57 *
LOI	* 4.21 *	* 6.77 *	* 2.70 *	* 2.87 *	* 2.04 *	* 1.66 *	* 3.69 *
TOTAL	* 98.70 *	* 99.79 *	* 99.90 *	* 98.59 *	* 98.83 *	* 100.70 *	* 98.69 *

ZR	* 112 *	* 130 *	* 679 *	* 225 *	* 513 *	* 532 *	* 201 *
SR	* 347 *	* 160 *	* 664 *	* 1009 *	* 1542 *	* 1050 *	* 752 *
RB	* 44 *	* 13 *	* 2 *	* 39 *	* 8 *	* 6 *	* 7 *
ZN	* 128 *	* 100 *	* 164 *	* 133 *	* 118 *	* 98 *	* 125 *
CU	* 98 *	* 50 *	* 17 *	* 36 *	* 17 *	* 16 *	* 35 *
BA	* 335 *	* 103 *	* 311 *	* 536 *	* 314 *	* 547 *	* 680 *
NB	* 11 *	* 30 *	* 80 *	* 31 *	* 59 *	* 73 *	* 26 *
Y	* 28 *	* 17 *	* 60 *	* 30 *	* 54 *	* 49 *	* 31 *
PB	* 9 *	* 3 *	* 55 *	* 0 *	* 20 *	* 15 *	* 7 *
NI	* 86 *	* 435 *	* 15 *	* 18 *	* 6 *	* 8 *	* 13 *
CR	* 64 *	* 901 *	* 23 *	* 13 *	* 14 *	* 9 *	* 0 *
V	* 227 *	* 231 *	* 18 *	* 237 *	* 42 *	* 33 *	* 287 *
GA	* 26 *	* 19 *	* 27 *	* 29 *	* 25 *	* 27 *	* 22 *

SAMPLE	RJ75286A	RJ75-317	RJ76-429	RJ76-430	RJ76-431	RJ76-432	RJ76-529
QZ	0.0	2.52	0.0	0.0	0.0	0.0	0.0
DR	9.13	1.97	0.73	6.91	1.83	1.19	1.12
AB	17.61	6.73	69.11	30.46	63.19	73.50	38.55
AN	23.77	21.23	7.39	16.87	8.43	5.85	20.99
NE	2.44	0.0	5.19	4.42	7.58	5.68	0.78
LC	0.0	0.0	0.0	0.0	0.0	0.0	0.0
COR	0.0	0.0	0.0	0.0	0.0	0.0	0.0
WO	0.0	0.0	0.0	0.0	0.0	0.0	0.0
DI	15.06	17.01	2.30	22.78	11.49	8.27	19.07
WO	7.68	8.88	1.10	11.52	5.59	4.04	9.67
EN	4.29	6.24	0.15	5.83	1.43	1.13	5.08
FS	3.09	1.89	1.05	5.42	4.47	3.11	4.32
HY	0.0	40.34	0.0	0.0	0.0	0.0	0.0
EN	0.0	30.95	0.0	0.0	0.0	0.0	0.0
FS	0.0	9.39	0.0	0.0	0.0	0.0	0.0
OL	23.99	0.0	12.95	7.04	2.91	2.50	7.38
FO	13.38	0.0	1.48	3.48	0.66	0.62	3.81
FA	10.61	0.0	11.47	3.56	2.25	1.88	3.57
LA	0.0	0.0	0.0	0.0	0.0	0.0	0.0
MT	3.51	5.45	0.0	4.74	2.40	1.70	5.33
ILM	3.84	4.00	0.98	5.65	1.04	1.07	5.40
AP	0.64	0.75	0.36	1.12	1.13	0.23	1.39
HM	0.0	0.0	0.0	0.0	0.0	0.0	0.0

RJ75286A PPG MAFIC PARTRIDGE POINT
 RJ75-317 PPG ALTERED QUIRPON ISLAND
 RJ76-429 PPG ALTERED LEUCOCRATIC ST.ANTHONY BIGHT
 RJ76-430 PPG ST.ANTHONY BIGHT
 RJ76-431 PPG LEUCOCRATIC ST.ANTHONY BIGHT
 RJ76-432 PPG LEUCOCRATIC ST.ANTHONY BIGHT
 RJ76-529 PPG ST.ANTHONY BIGHT

SAMPLE	* NJ75-341 *	* NJ75-357 *	* NJ75-359 *	* CD 75005 *	* CD 75015 *	* CD 75015 *	* CD 75017 *
SI02	* 45.23 *	* 46.41 *	* 40.20 *	* 46.67 *	* 40.38 *	* 44.13 *	* 40.90 *
TI02	* 2.28 *	* 1.89 *	* 2.71 *	* 2.11 *	* 1.94 *	* 2.05 *	* 3.04 *
AL203	* 13.17 *	* 15.15 *	* 14.73 *	* 12.53 *	* 15.00 *	* 11.63 *	* 16.23 *
FE2O3	* 3.12 *	* 1.95 *	* 2.68 *	* 4.62 *	* 1.45 *	* 2.79 *	* 3.00 *
FEO	* 8.69 *	* 7.88 *	* 9.77 *	* 4.69 *	* 8.93 *	* 9.91 *	* 10.10 *
MNO	* 0.15 *	* 0.21 *	* 0.46 *	* 0.13 *	* 0.33 *	* 0.15 *	* 0.13 *
MGO	* 6.94 *	* 6.37 *	* 5.65 *	* 6.38 *	* 4.00 *	* 14.87 *	* 7.89 *
CAO	* 11.47 *	* 9.06 *	* 7.68 *	* 12.97 *	* 9.80 *	* 8.12 *	* 9.20 *
NA2O	* 2.99 *	* 3.54 *	* 4.48 *	* 4.16 *	* 5.00 *	* 1.82 *	* 1.70 *
K2O	* 0.09 *	* 0.25 *	* 0.07 *	* 0.36 *	* 0.50 *	* 0.18 *	* 2.45 *
P2O5	* 0.26 *	* 0.24 *	* 0.48 *	* 0.37 *	* 0.43 *	* 0.24 *	* 0.32 *
LOI	* 4.65 *	* 5.44 *	* 10.20 *	* 4.37 *	* 9.59 *	* 5.01 *	* 4.87 *
TOTAL	* 99.04 *	* 98.89 *	* 99.31 *	* 99.36 *	* 97.35 *	* 100.90 *	* 99.83 *

ZR	* 130 *	* 103 *	* 145 *	* 134 *	* 323 *	* 106 *	* 160 *
SR	* 961 *	* 393 *	* 404 *	* 357 *	* 250 *	* 122 *	* 292 *
RB	* 2 *	* 5 *	* 6 *	* 3 *	* 10 *	* 2 *	* 45 *
ZN	* 100 *	* 108 *	* 155 *	* 151 *	* 189 *	* 162 *	* 189 *
CU	* 116 *	* 96 *	* 50 *	* 58 *	* 260 *	* 51 *	* 70 *
BA	* 159 *	* 415 *	* 170 *	* 303 *	* 153 *	* 93 *	* 354 *
NB	* 13 *	* 14 *	* 23 *	* 22 *	* 58 *	* 10 *	* 21 *
Y	* 19 *	* 18 *	* 27 *	* 32 *	* 48 *	* 31 *	* 32 *
PB	* 1 *	* 7 *	* 12 *	* 7 *	* 7 *	* 7 *	* 7 *
NI	* 70 *	* 82 *	* 58 *	* 218 *	* 26 *	* 446 *	* 298 *
CR	* 78 *	* 360 *	* 119 *	* 328 *	* 87 *	* 555 *	* 568 *
V	* 320 *	* 267 *	* 335 *	* 230 *	* 263 *	* 246 *	* 379 *
GA	* 20 *	* 21 *	* 26 *	* 20 *	* 22 *	* 26 *	* 25 *

SAMPLE	RJ76-541	RJ76-557	RJ76-559	CD 75005	CD 75014	CD 75016	CD 75017
OZ	0.0	0.0	0.0	0.0	0.0	0.0	0.0
OR	0.56	1.58	0.46	2.24	3.37	1.11	15.21
AB	26.28	32.05	26.92	24.14	15.49	16.06	5.71
AN	23.57	26.44	22.30	15.22	19.38	24.02	30.98
NE	0.28	0.0	8.46	7.00	17.72	0.0	5.11
LC	0.0	0.0	0.0	0.0	0.0	0.0	0.0
COR	0.0	0.0	0.0	0.0	0.0	0.0	0.0
WD	0.0	0.0	0.0	0.09	0.0	0.0	0.0
DI	23.39	16.27	13.97	39.15	27.39	13.13	12.11
WO	14.58	8.35	7.08	20.79	13.71	6.84	6.22
EN	8.78	4.97	3.70	16.72	6.04	4.68	3.74
FS	5.03	2.94	3.18	1.63	7.64	1.62	2.15
HY	0.0	2.78	0.0	0.0	0.0	14.21	0.0
EN	0.0	1.75	0.0	0.0	0.0	10.56	0.0
FS	0.0	1.03	0.0	0.0	0.0	3.65	0.0
OL	10.89	13.42	16.50	0.0	8.92	22.62	19.40
FO	6.68	8.12	8.47	0.0	3.72	16.38	11.88
FA	4.21	5.30	8.03	0.0	5.19	6.23	7.52
LA	0.0	0.0	0.0	0.0	0.0	0.0	0.0
MT	4.79	3.03	4.36	7.05	2.40	4.22	4.58
ILM	4.59	3.84	5.77	4.22	4.20	4.06	6.08
AP	0.64	0.60	1.25	0.91	1.14	0.58	0.78
HM	0.0	0.0	0.0	0.0	0.0	0.0	0.0

RJ76-541 PPG IRELAND BIGHT
 RJ76-557 PPG HOWE HARBOUR
 RJ76-559 PPG ALTERED HOWE HARBOUR
 CD-75005 COV MASSIVE FLOW
 CD-75014 COV VESICULAR VOLCANIC ELOCK
 CD-75016 COV PILLOW LAVA
 CD-75017 COV PILLOW LAVA (RIM+CORE)

SAMPLE	* CD 75029 *	* CD 75036 *	* CD 75041 *	* CD 75042 *	* CD 75044 *	* CD 75045 *	* CD 75046 *
SI02	* 45.20 *	* 49.76 *	* 46.58 *	* 44.50 *	* 48.29 *	* 45.71 *	* 44.13 *
TI02	* 1.96 *	* 3.53 *	* 1.81 *	* 2.10 *	* 2.10 *	* 2.05 *	* 2.17 *
AL203	* 12.29 *	* 17.14 *	* 11.94 *	* 12.00 *	* 14.06 *	* 13.38 *	* 12.00 *
FE203	* 3.61 *	* 1.58 *	* 0.25 *	* 4.50 *	* 2.00 *	* 3.28 *	* 1.80 *
FEO	* 9.55 *	* 8.17 *	* 7.70 *	* 8.12 *	* 6.95 *	* 6.36 *	* 9.17 *
MNO	* 0.13 *	* 0.10 *	* 0.15 *	* 0.15 *	* 0.11 *	* 0.14 *	* 0.16 *
MGO	* 9.32 *	* 2.98 *	* 6.11 *	* 9.00 *	* 5.53 *	* 6.00 *	* 8.34 *
CAO	* 9.33 *	* 3.27 *	* 12.89 *	* 11.16 *	* 11.54 *	* 12.86 *	* 14.29 *
NA2O	* 3.59 *	* 4.63 *	* 4.00 *	* 2.67 *	* 4.01 *	* 4.00 *	* 1.00 *
K2O	* 0.40 *	* 3.48 *	* 0.27 *	* 0.67 *	* 0.69 *	* 0.40 *	* 3.16 *
P2O5	* 0.25 *	* 1.24 *	* 0.50 *	* 0.27 *	* 0.31 *	* 0.20 *	* 0.10 *
LOI	* 3.78 *	* 3.92 *	* 7.31 *	* 4.89 *	* 4.68 *	* 5.51 *	* 5.78 *
TOTAL	* 99.41 *	* 99.80 *	* 99.51 *	* 100.03 *	* 100.27 *	* 99.89 *	* 102.10 *

ZR	* 130 *	* 293 *	* 121 *	* 120 *	* 133 *	* 128 *	* 155 *
SR	* 252 *	* 207 *	* 340 *	* 285 *	* 528 *	* 483 *	* 691 *
RB	* 5 *	* 48 *	* 2 *	* 11 *	* 10 *	* 4 *	* 36 *
ZN	* 158 *	* 196 *	* 161 *	* 169 *	* 155 *	* 160 *	* 158 *
CU	* 54 *	* 19 *	* 53 *	* 64 *	* 72 *	* 80 *	* 67 *
BA	* 388 *	* 619 *	* 131 *	* 317 *	* 740 *	* 623 *	* 5800 *
NB	* 17 *	* 54 *	* 16 *	* 15 *	* 18 *	* 19 *	* 24 *
Y	* 31 *	* 57 *	* 31 *	* 30 *	* 35 *	* 30 *	* 31 *
PB	* 6 *	* 8 *	* 8 *	* 7 *	* 6 *	* 5 *	* 6 *
NI	* 271 *	* 4 *	* 252 *	* 276 *	* 224 *	* 165 *	* 269 *
CR	* 504 *	* 72 *	* 335 *	* 393 *	* 337 *	* 283 *	* 379 *
V	* 242 *	* 299 *	* 202 *	* 216 *	* 252 *	* 240 *	* 259 *
GA	* 24 *	* 24 *	* 20 *	* 21 *	* 20 *	* 20 *	* 17 *

SAMPLE	CD 75029	CD 75036	CD 75041	CD 75042	CD 75044	CD 75045	CD 75046
OZ	0.0	0.0	0.0	0.0	0.0	0.0	0.0
OR	2.47	21.44	1.73	4.16	4.27	2.50	1.75
AB	24.88	40.35	22.53	20.25	27.59	19.64	0.0
AN	16.98	8.55	15.00	19.74	17.17	18.41	19.64
NE	3.73	0.0	7.68	1.89	4.28	8.79	4.76
LC	0.0	0.0	0.0	0.0	0.0	0.0	13.83
COR	0.0	2.87	0.0	0.0	0.0	0.0	0.0
WO	0.0	0.0	0.0	0.0	0.0	0.0	0.0
DI	24.07	0.0	41.65	29.39	31.39	38.47	43.33
WO	12.41	0.0	21.23	15.29	16.13	19.97	22.25
EN	7.78	0.0	11.75	10.39	9.72	13.30	13.33
FS	3.37	0.0	8.67	3.71	5.54	5.20	7.75
HY	0.0	7.60	0.0	0.0	0.0	0.0	0.0
EN	0.0	3.65	0.0	0.0	0.0	0.0	0.0
FS	0.0	3.96	0.0	0.0	0.0	0.0	0.0
JL	17.90	6.30	6.03	12.86	5.34	2.54	9.46
FO	11.56	2.87	3.33	9.23	3.28	1.77	5.77
FA	6.34	3.43	2.70	3.63	2.06	0.76	3.69
LA	0.0	0.0	0.0	0.0	0.0	0.0	0.0
MT	5.47	2.39	0.39	6.86	3.03	5.04	2.71
ILM	3.89	6.99	3.73	4.19	4.17	4.13	4.28
AP	0.61	3.00	1.26	0.66	0.75	0.49	0.24
HM	0.0	0.0	0.0	0.0	0.0	0.0	0.0

CD-75029 COV PILLOW LAVA (CORE)
 CD-75036 COV VOLCANIC BLOCK
 CD-75041 COV PILLOW LAVA (CORE)
 CD-75042 COV PILLOW LAVA
 CD-75044 COV PILLOW LAVA
 CD-75045 COV PILLOW LAVA
 CD-75046 COV PILLOW LAVA (RIM)

SAMPLE	* CD 75049 *	* CD 75050 *	* CD 75051 *	* CD 75001 *	* CD 75010 *	* CD 75027 *	* CD 75030 *
SI02	* 44.27 *	* 44.49 *	* 44.70 *	* 46.96 *	* 44.83 *	* 44.63 *	* 45.59 *
TI02	* 2.00 *	* 1.99 *	* 2.26 *	* 2.39 *	* 1.92 *	* 2.00 *	* 2.37 *
AL203	* 12.77 *	* 11.31 *	* 12.47 *	* 14.37 *	* 14.89 *	* 14.69 *	* 15.93 *
FE203	* 2.85 *	* 3.42 *	* 1.37 *	* 5.65 *	* 2.83 *	* 7.60 *	* 3.37 *
FEO	* 10.03 *	* 9.43 *	* 10.53 *	* 5.38 *	* 7.97 *	* 3.67 *	* 8.66 *
MNO	* 0.17 *	* 0.19 *	* 0.13 *	* 0.14 *	* 0.17 *	* 0.13 *	* 0.17 *
MGO	* 10.95 *	* 12.00 *	* 7.65 *	* 7.56 *	* 7.95 *	* 6.40 *	* 5.20 *
CAO	* 8.20 *	* 11.33 *	* 7.04 *	* 9.33 *	* 5.53 *	* 11.41 *	* 10.19 *
NA2O	* 2.91 *	* 1.33 *	* 2.35 *	* 4.16 *	* 3.92 *	* 2.44 *	* 2.88 *
K2O	* 0.15 *	* 0.80 *	* 0.10 *	* 0.86 *	* 0.98 *	* 1.03 *	* 2.24 *
P2O5	* 0.25 *	* 0.33 *	* 0.25 *	* 0.38 *	* 0.36 *	* 0.25 *	* 0.33 *
LOI	* 4.95 *	* 5.34 *	* 7.35 *	* 2.99 *	* 7.16 *	* 3.02 *	* 3.21 *
TOTAL	* 99.50 *	* 101.96 *	* 96.20 *	* 100.17 *	* 98.51 *	* 97.27 *	* 100.14 *

ZR	* 115 *	* 126 *	* 142 *	* 174 *	* 143 *	* 156 *	* 199 *
SR	* 248 *	* 433 *	* 365 *	* 624 *	* 442 *	* 767 *	* 1473 *
RB	* 1 *	* 15 *	* 1 *	* 8 *	* 13 *	* 9 *	* 12 *
ZN	* 173 *	* 169 *	* 183 *	* 166 *	* 154 *	* 155 *	* 181 *
CU	* 75 *	* 47 *	* 51 *	* 78 *	* 62 *	* 97 *	* 68 *
BA	* 71 *	* 288 *	* 54 *	* 782 *	* 891 *	* 975 *	* 562 *
NB	* 10 *	* 18 *	* 19 *	* 29 *	* 17 *	* 17 *	* 24 *
Y	* 32 *	* 31 *	* 30 *	* 34 *	* 35 *	* 36 *	* 36 *
PB	* 6 *	* 8 *	* 8 *	* 7 *	* 7 *	* 7 *	* 6 *
NI	* 287 *	* 333 *	* 254 *	* 100 *	* 79 *	* 42 *	* 31 *
CR	* 394 *	* 466 *	* 472 *	* 225 *	* 217 *	* 91 *	* 52 *
V	* 260 *	* 252 *	* 314 *	* 303 *	* 287 *	* 278 *	* 269 *
GA	* 28 *	* 24 *	* 31 *	* 25 *	* 26 *	* 23 *	* 25 *

SAMPLE	CD 75049	CD 75050	CD 75051	CD 75052	CD 75053	CD 75054	CD 75055	CD 75056	CD 75057	CD 75058	CD 75059
OZ	0.0	0.0	0.0	0.0	0.0	0.0	0.0	0.0	0.0	0.0	0.0
OR	0.94	4.89	0.67	5.23	5.34	5.46	5.46	5.46	5.46	5.46	5.46
AB	25.04	11.65	22.39	30.26	36.05	21.90	27.68	27.68	27.68	27.68	27.68
AN	22.57	23.31	26.09	19.52	22.05	21.90	27.68	27.68	27.68	27.68	27.68
NE	0.0	0.0	0.0	3.23	0.14	0.0	0.0	0.0	0.0	0.0	0.0
LC	0.0	0.0	0.0	0.0	0.0	0.0	0.0	0.0	0.0	0.0	0.0
COR	0.0	0.0	0.0	0.0	0.0	0.0	0.0	0.0	0.0	0.0	0.0
WO	0.0	0.0	0.0	0.0	0.0	0.0	0.0	0.0	0.0	0.0	0.0
DI	15.16	26.26	9.35	20.86	4.40	23.87	23.87	23.87	23.87	23.87	23.87
WO	7.93	13.63	4.76	11.10	2.27	12.80	12.80	12.80	12.80	12.80	12.80
EN	4.96	9.10	2.59	9.03	1.44	11.07	11.07	11.07	11.07	11.07	11.07
FS	2.38	3.52	2.00	0.73	0.69	0.0	0.0	0.0	0.0	0.0	0.0
HY	2.57	8.03	33.41	0.0	0.0	3.88	3.88	3.88	3.88	3.88	3.88
EN	1.74	5.79	18.85	0.0	0.0	3.88	3.88	3.88	3.88	3.88	3.88
FS	0.33	2.24	14.56	0.0	0.0	0.0	0.0	0.0	0.0	0.0	0.0
OL	23.72	16.03	0.0	7.89	21.63	1.38	1.38	1.38	1.38	1.38	1.38
FO	15.52	11.24	0.0	7.24	14.18	1.38	1.38	1.38	1.38	1.38	1.38
FA	8.20	4.79	0.0	0.65	7.45	0.0	0.0	0.0	0.0	0.0	0.0
LA	0.0	0.0	0.0	0.0	0.0	0.0	0.0	0.0	0.0	0.0	0.0
MT	4.37	5.13	2.24	8.63	4.49	6.85	6.85	6.85	6.85	6.85	6.85
ILM	4.02	3.91	4.83	4.67	3.99	4.03	4.03	4.03	4.03	4.03	4.03
AP	0.61	0.79	0.65	0.91	0.92	0.62	0.62	0.62	0.62	0.62	0.62
HM	0.0	0.0	0.0	0.0	0.0	3.34	3.34	3.34	3.34	3.34	3.34

CD-75049 CCV PILLOW LAVA (CORE)
 CD-75050 QHV VARIOLITIC PILLOW LAVA
 CD-75051 QHV VARIOLITIC PILLOW LAVA
 CD-75001 COV FINE GRAINED DYKE
 CD-75010 COV DYKE
 CD-75027 COV DYKE
 CD-75030 CCV DYKE

SAMPLE	* CD 75030 *	* CD 75013 *	* CD 75015 *	* CD 75022 *	* CD 75023 *	* CD 75034 *	* CD 75035 *
SI02	* 46.20 *	* 51.87 *	* 46.40 *	* 44.26 *	* 47.62 *	* 48.00 *	* 45.27 *
TI02	* 2.25 *	* 2.07 *	* 2.31 *	* 2.30 *	* 1.86 *	* 2.36 *	* 3.00 *
AL203	* 15.00 *	* 16.41 *	* 13.61 *	* 14.40 *	* 16.92 *	* 15.67 *	* 16.08 *
FE203	* 13.09 *	* 6.43 *	* 7.05 *	* 7.02 *	* 5.97 *	* 6.31 *	* 7.10 *
FED	* 0.0 *	* 2.83 *	* 5.58 *	* 6.10 *	* 5.32 *	* 5.67 *	* 7.06 *
MNO	* 0.13 *	* 0.17 *	* 0.23 *	* 0.16 *	* 0.18 *	* 0.15 *	* 0.28 *
MGO	* 7.39 *	* 4.88 *	* 7.89 *	* 7.44 *	* 3.03 *	* 5.58 *	* 3.43 *
CAO	* 8.51 *	* 2.80 *	* 7.92 *	* 8.39 *	* 5.33 *	* 7.89 *	* 6.08 *
NA2O	* 2.39 *	* 4.69 *	* 3.85 *	* 3.23 *	* 5.05 *	* 3.10 *	* 4.22 *
K2O	* 3.47 *	* 2.96 *	* 0.19 *	* 1.30 *	* 2.61 *	* 2.55 *	* 2.35 *
P2O5	* 0.15 *	* 0.48 *	* 0.38 *	* 0.33 *	* 0.11 *	* 0.50 *	* 1.05 *
LOI	* 3.40 *	* 3.39 *	* 4.21 *	* 3.80 *	* 3.64 *	* 3.27 *	* 4.60 *
TOTAL	* 101.98 *	* 98.98 *	* 99.62 *	* 98.73 *	* 97.64 *	* 101.05 *	* 100.52 *

ZR	* 140 *	* 271 *	* 154 *	* 153 *	* 257 *	* 203 *	* 263 *
SR	* 250 *	* 486 *	* 290 *	* 491 *	* 824 *	* 771 *	* 808 *
RB	* 10 *	* 44 *	* 3 *	* 11 *	* 42 *	* 26 *	* 26 *
ZN	* 167 *	* 176 *	* 242 *	* 170 *	* 227 *	* 184 *	* 226 *
CU	* 90 *	* 26 *	* 106 *	* 82 *	* 35 *	* 36 *	* 21 *
BA	* 939 *	* 1360 *	* 185 *	* 360 *	* 1415 *	* 1483 *	* 926 *
NB	* 16 *	* 41 *	* 20 *	* 19 *	* 55 *	* 30 *	* 48 *
Y	* 30 *	* 45 *	* 36 *	* 33 *	* 41 *	* 37 *	* 47 *
PB	* 7 *	* 10 *	* 15 *	* 8 *	* 13 *	* 10 *	* 9 *
NI	* 78 *	* 0 *	* 87 *	* 51 *	* 0 *	* 48 *	* 0 *
CR	* 190 *	* 30 *	* 184 *	* 104 *	* 30 *	* 78 *	* 38 *
V	* 334 *	* 168 *	* 272 *	* 321 *	* 132 *	* 299 *	* 195 *
GA	* 22 *	* 28 *	* 28 *	* 29 *	* 26 *	* 27 *	* 36 *

SAMPLE	CD 75039	CD 75013	CD 75015	CD 75022	CD 75023	CD 75034	CD 75035
QZ	0.0	1.39	0.0	0.0	0.0	0.0	0.0
OR	20.80	18.30	1.18	8.09	15.41	15.41	14.47
AB	20.51	41.51	34.14	27.55	34.96	26.82	35.06
AN	20.24	11.28	20.22	22.07	16.80	21.79	18.76
NE	0.0	0.0	0.0	0.67	5.69	0.0	1.17
LC	0.0	0.0	0.0	0.0	0.0	0.0	0.0
COR	0.0	1.51	0.0	0.0	0.0	0.0	0.0
WO	0.0	0.0	0.0	0.0	0.0	0.0	0.0
DI	11.03	0.0	14.39	15.36	8.44	11.75	4.49
WO	5.92	0.0	7.67	8.15	4.41	6.23	2.34
EN	5.11	0.0	6.38	6.54	3.15	4.96	1.63
FS	0.0	0.0	0.34	0.67	0.88	0.56	0.51
HY	0.0	12.71	11.15	0.0	4.47	6.15	6.84
EN	0.0	12.71	10.59	0.0	3.42	5.25	5.09
FS	0.0	0.0	0.56	0.0	1.05	0.63	1.75
OL	9.50	0.0	2.68	10.13	0.0	2.94	0.0
FO	9.50	0.0	2.54	9.10	0.0	2.62	0.0
FA	0.0	0.0	0.15	1.03	0.0	0.33	0.0
LA	0.0	0.0	0.0	0.0	0.0	0.0	0.0
MT	0.0	3.85	10.71	10.72	9.21	9.36	10.73
ILM	0.28	4.11	4.60	4.60	3.76	4.58	5.94
AP	0.35	1.17	0.93	0.81	0.27	1.19	2.54
HM	13.28	4.07	0.0	0.0	0.0	0.0	0.0

CD-75039 COV DYKE
 CD-75013 COV GABBRO
 CD-75015 COV GABBRO
 CD-75022 COV GABBRO
 CD-75023 COV GABBRO
 CD-75034 COV GABBRO
 CD-75035 COV GABBRO

SI02	*	46.32	*	52.49	*	49.27	*	49.20	*	48.42	*	48.85	*	47.67	*
TI 02	*	0.92	*	1.36	*	1.65	*	1.76	*	1.89	*	2.12	*	2.09	*
AL203	*	24.27	*	10.49	*	13.92	*	13.36	*	14.03	*	13.71	*	13.67	*
FE203	*	0.25	*	1.64	*	2.78	*	0.87	*	0.84	*	1.83	*	3.04	*
FE0	*	7.28	*	10.42	*	10.19	*	11.79	*	11.71	*	8.74	*	8.05	*
MNO	*	0.08	*	0.16	*	0.23	*	0.20	*	0.20	*	0.15	*	0.18	*
MGO	*	3.44	*	7.03	*	5.64	*	6.42	*	6.63	*	5.44	*	5.31	*
CAO	*	1.08	*	7.95	*	8.06	*	4.75	*	5.70	*	10.30	*	11.02	*
NA2O	*	0.26	*	3.25	*	3.69	*	2.40	*	4.48	*	3.08	*	2.59	*
K2O	*	6.83	*	0.56	*	0.31	*	0.02	*	0.10	*	0.32	*	0.90	*
P2O5	*	0.35	*	0.14	*	0.13	*	0.16	*	0.20	*	0.25	*	0.25	*
LOI	*	5.84	*	3.78	*	4.04	*	8.02	*	4.35	*	3.80	*	3.46	*
TOTAL	*	97.52	*	99.27	*	99.91	*	98.95	*	98.55	*	98.59	*	98.23	*

ZR	*	91	*	80	*	97	*	117	*	134	*	185	*	188	*
SR	*	54	*	118	*	384	*	85	*	117	*	233	*	407	*
RB	*	207	*	9	*	6	*	3	*	5	*	5	*	17	*
ZN	*	48	*	101	*	107	*	109	*	111	*	100	*	102	*
CU	*	10	*	53	*	90	*	51	*	20	*	137	*	132	*
BA	*	1775	*	829	*	537	*	33	*	217	*	180	*	564	*
NB	*	16	*	6	*	7	*	10	*	11	*	12	*	11	*
Y	*	49	*	31	*	36	*	31	*	36	*	33	*	31	*
PB	*	0	*	0	*	4	*	2	*	3	*	0	*	1	*
NI	*	68	*	47	*	58	*	61	*	66	*	57	*	64	*
CR	*	142	*	66	*	107	*	114	*	130	*	78	*	87	*
V	*	163	*	393	*	406	*	454	*	456	*	286	*	267	*
GA	*	34	*	13	*	16	*	16	*	17	*	23	*	21	*

SAMPLE	RJ76-521	RJ76-522	RJ76-523	RJ76-575	RJ76-577	RJ76-585	RJ76-586
OZ	3.11	2.89	0.0	0.23	0.0	0.92	0.65
OR	44.02	3.47	1.91	0.13	0.63	1.99	5.61
AB	2.40	28.80	32.57	22.33	40.24	27.49	23.12
AN	3.37	12.97	21.39	24.78	18.98	23.88	24.29
NE	0.0	0.0	0.0	0.0	0.0	0.0	0.0
LC	0.0	0.0	0.0	0.0	0.0	0.0	0.0
COR	15.70	0.0	0.0	1.25	0.0	0.0	0.0
WO	0.0	0.0	0.0	0.0	0.0	0.0	0.0
DI	0.0	22.58	16.09	0.0	8.02	23.29	25.91
WO	0.0	11.44	8.12	0.0	4.04	11.82	13.23
EN	0.0	5.85	3.98	0.0	1.90	6.25	7.49
FS	0.0	5.29	4.00	0.0	2.08	5.22	5.19
HY	22.20	23.76	17.05	37.81	9.13	14.76	10.93
EN	9.34	12.48	8.50	17.58	4.36	8.04	6.46
FS	12.86	11.28	8.55	20.23	4.77	6.72	4.47
OL	0.0	0.0	3.21	0.0	17.41	0.0	0.0
FO	0.0	0.0	1.52	0.0	7.89	0.0	0.0
FA	0.0	0.0	1.69	0.0	9.51	0.0	0.0
LA	0.0	0.0	0.0	0.0	0.0	0.0	0.0
MT	0.40	2.49	4.20	1.39	1.29	2.80	4.65
ILM	1.91	2.70	3.27	3.68	3.81	4.25	4.19
AP	0.89	0.34	0.32	0.41	0.49	0.61	0.61
HM	0.0	0.0	0.0	0.0	0.0	0.0	0.0

RJ76-521 SLV TUFF ST.LUNAIRE
 RJ76-522 SLV ALTERED MASSIVE FLOW ST.LUNAIRE
 RJ76-523 SLV ALTERED MASSIVE FLOW ST.LUNAIRE
 RJ76-575 CHV ALTERED BASALT CROQUE ROAD
 RJ76-577 CHV BASALT CROQUE ROAD
 RJ76-585 CHV MASSIVE BASALT CROQUE HARBOUR
 RJ76-586 CHV PORPHYRITIC BASALT CROQUE HARBOUR

SAMPLE	* RJ76-588		* RJ76-561		* RJ76-592		* RJ7-595	
SI02	*	47.60	*	46.81	*	49.55	*	48.81
TI02	*	2.74	*	2.26	*	2.26	*	2.84
AL203	*	12.86	*	14.34	*	13.28	*	14.26
FE203	*	2.22	*	2.28	*	1.24	*	2.70
FEO	*	10.19	*	9.19	*	9.88	*	9.98
MNO	*	0.21	*	0.18	*	0.18	*	0.15
MGO	*	5.43	*	5.58	*	5.80	*	6.42
CAO	*	9.49	*	9.28	*	6.09	*	5.38
NA2O	*	2.41	*	3.38	*	5.21	*	3.49
K2O	*	0.59	*	0.59	*	0.13	*	1.46
P2O5	*	0.33	*	0.27	*	0.29	*	0.33
LOI	*	4.59	*	4.45	*	3.84	*	4.61
TOTAL	*	98.66	*	98.61	*	97.75	*	98.43

ZR	*	242	*	189	*	189	*	241
SR	*	228	*	101	*	92	*	148
RB	*	12	*	13	*	0	*	41
ZN	*	117	*	112	*	97	*	129
CU	*	173	*	102	*	114	*	179
BA	*	397	*	539	*	138	*	551
NB	*	14	*	12	*	14	*	16
Y	*	40	*	32	*	35	*	51
PB	*	3	*	7	*	0	*	7
NI	*	48	*	65	*	55	*	43
CR	*	49	*	98	*	102	*	67
V	*	359	*	312	*	334	*	479
GA	*	19	*	21	*	17	*	26

DR	*	3.71	*	3.70	*	0.0	*	0.0	*
AB	*	21.68	*	30.37	*	0.82	*	9.20	*
AN	*	23.95	*	23.59	*	46.94	*	31.47	*
NE	*	0.0	*	0.0	*	13.27	*	20.18	*
LC	*	0.0	*	0.0	*	0.0	*	0.0	*
CDR	*	0.0	*	0.0	*	0.0	*	0.0	*
WD	*	0.0	*	0.0	*	0.0	*	0.0	*
DI	*	19.68	*	19.28	*	13.96	*	4.91	*
WO	*	9.95	*	9.79	*	7.06	*	2.50	*
EN	*	5.01	*	5.18	*	3.54	*	1.39	*
FS	*	4.72	*	4.32	*	3.36	*	1.02	*
HY	*	18.19	*	5.35	*	3.11	*	13.77	*
EN	*	9.37	*	2.92	*	1.60	*	7.96	*
FS	*	8.83	*	2.43	*	1.52	*	5.81	*
OL	*	0.0	*	8.96	*	14.69	*	9.73	*
FO	*	0.0	*	4.67	*	7.18	*	5.39	*
FA	*	0.0	*	4.29	*	7.51	*	4.34	*
LA	*	0.0	*	0.0	*	0.0	*	0.0	*
MT	*	3.42	*	3.51	*	1.91	*	4.17	*
ILM	*	5.53	*	4.56	*	4.57	*	5.75	*
AP	*	0.82	*	0.67	*	0.72	*	0.82	*
HM	*	0.0	*	0.0	*	0.0	*	0.0	*

RJ76-588	CHV	SHEARED EASALT	CROQUE HARBOUR
RJ76-591	CHV	NODULE-BEARING BASALT	CROQUE HARBOUR
RJ76-592	CHV	NODULE-BEARING BASALT	CROQUE HARBOUR
RJ76-595	CHV	CROSSITE-BEARING BASALT	CROQUE HARBOUR

Table I.iv. Major and trace element analyses and CIPW norms, Goose Cove Schist.

SI02	*	64.55	*	60.02	*	54.18	*	53.88	*	77.91	*	45.85	*	47.75	*
TI02	*	0.82	*	0.79	*	0.78	*	0.76	*	0.56	*	0.86	*	1.09	*
AL203	*	15.59	*	19.72	*	12.46	*	13.54	*	9.34	*	14.43	*	15.05	*
FE203	*	1.83	*	4.83	*	15.09	*	13.42	*	2.09	*	4.66	*	3.78	*
FEO	*	4.48	*	2.98	*	1.23	*	3.85	*	1.84	*	4.85	*	5.84	*
MNO	*	0.08	*	0.12	*	2.71	*	2.36	*	0.06	*	0.16	*	0.17	*
MGO	*	1.54	*	1.76	*	2.19	*	2.29	*	0.76	*	6.17	*	7.69	*
CAO	*	0.94	*	0.35	*	1.88	*	1.94	*	1.28	*	14.63	*	12.69	*
NA2O	*	1.57	*	1.01	*	5.54	*	2.17	*	1.84	*	2.74	*	2.76	*
K2O	*	3.75	*	5.08	*	0.07	*	1.61	*	2.82	*	0.35	*	0.25	*
P2O5	*	0.13	*	0.11	*	0.16	*	0.17	*	0.08	*	0.07	*	0.08	*
LOI	*	3.20	*	3.71	*	2.00	*	2.79	*	1.93	*	4.46	*	2.88	*
TOTAL	*	98.48	*	100.48	*	98.29	*	98.78	*	100.51	*	99.23	*	100.04	*

ZR	*	234	*	106	*	149	*	136	*	299	*	70	*	85	*
SR	*	99	*	80	*	296	*	133	*	150	*	120	*	172	*
RB	*	136	*	154	*	3	*	53	*	64	*	5	*	3	*
ZN	*	141	*	60	*	112	*	132	*	48	*	120	*	103	*
CU	*	170	*	45	*	16	*	162	*	23	*	216	*	200	*
BA	*	787	*	688	*	669	*	845	*	773	*	40	*	51	*
NB	*	10	*	17	*	18	*	16	*	11	*	0	*	0	*
Y	*	33	*	32	*	43	*	33	*	21	*	40	*	39	*
PB	*	21	*	28	*	52	*	45	*	16	*	6	*	7	*
NI	*	38	*	41	*	225	*	175	*	20	*	65	*	88	*
CR	*	98	*	77	*	23	*	52	*	46	*	361	*	422	*
V	*	100	*	111	*	100	*	197	*	59	*	259	*	273	*
GA	*	22	*	26	*	17	*	20	*	15	*	16	*	19	*

DR	*	23.25	*	31.02	*	15.41	*	29.16	*	53.13	*	0.0	*	0.0	*
AB	*	13.93	*	8.83	*	48.67	*	9.91	*	16.91	*	2.18	*	1.52	*
AN	*	4.21	*	1.06	*	8.61	*	19.12	*	15.79	*	17.32	*	24.92	*
NE	*	0.0	*	0.0	*	0.0	*	8.88	*	5.92	*	27.48	*	28.73	*
LC	*	0.0	*	0.0	*	0.0	*	0.0	*	0.0	*	3.87	*	0.0	*
COR	*	7.84	*	12.59	*	0.24	*	5.31	*	1.14	*	0.0	*	0.0	*
WO	*	0.0	*	0.0	*	0.0	*	0.0	*	0.0	*	0.0	*	0.0	*
DI	*	0.0	*	0.0	*	0.0	*	0.0	*	0.0	*	38.75	*	28.45	*
WO	*	0.0	*	0.0	*	0.0	*	0.0	*	0.0	*	20.30	*	14.84	*
EN	*	0.0	*	0.0	*	0.0	*	0.0	*	0.0	*	14.69	*	10.34	*
FS	*	0.0	*	0.0	*	0.0	*	0.0	*	0.0	*	3.76	*	3.27	*
HY	*	9.78	*	4.94	*	5.66	*	5.94	*	2.77	*	0.0	*	1.35	*
EN	*	4.02	*	4.53	*	5.66	*	5.94	*	1.92	*	0.0	*	1.03	*
FS	*	5.77	*	0.41	*	0.0	*	0.0	*	0.85	*	0.0	*	0.33	*
OL	*	0.0	*	0.0	*	0.0	*	0.0	*	0.0	*	1.37	*	7.87	*
FO	*	0.0	*	0.0	*	0.0	*	0.0	*	0.0	*	1.07	*	5.84	*
FA	*	0.0	*	0.0	*	0.0	*	0.0	*	0.0	*	0.30	*	2.04	*
LA	*	0.0	*	0.0	*	0.0	*	0.0	*	0.0	*	0.0	*	0.0	*
MT	*	2.78	*	7.24	*	10.95	*	18.65	*	3.07	*	7.13	*	5.64	*
ILM	*	1.63	*	1.55	*	1.54	*	1.50	*	1.08	*	1.72	*	2.13	*
AP	*	0.32	*	0.26	*	0.39	*	0.41	*	0.19	*	0.17	*	0.19	*
HM	*	0.0	*	0.0	*	8.11	*	1.11	*	0.0	*	0.0	*	0.0	*

RJ75-066 GCS HETASEDIMENT STARK'S BIGHT
 RJ76-433 GCS METASEDIMENT LOBSTER POINT
 RJ76-441 GCS METACHERT FISCHCT ISLAND
 RJ76-443 GCS METACHERT FISCHOT ISLAND
 RJ76-472 GCS METASEDIMENT THREE MOUNTAIN SUMMIT
 RJ75-004 GCS COARSE GRAINED GREENSCHIST GOOSE COVE ROAD
 RJ75-042 GCS COARSE GRAINED GREENSCHIST OBSERVATION PCINT

SAMPLE	* RJ75-060	* RJ75-062	* RJ75-063	* RJ75-179	* RJ75-222	* RJ75-292	* RJ75-435
SiO2	* 47.65	* 48.47	* 47.05	* 45.85	* 47.64	* 47.29	* 47.45
TiO2	* 2.24	* 1.51	* 1.09	* 1.12	* 2.23	* 0.92	* 1.95
AL2O3	* 13.80	* 10.36	* 14.70	* 13.12	* 13.86	* 15.05	* 14.25
FE2O3	* 3.52	* 3.45	* 4.54	* 4.83	* 2.95	* 4.49	* 3.23
FeO	* 7.69	* 6.15	* 5.63	* 5.95	* 8.62	* 4.91	* 9.27
MNO	* 0.19	* 0.17	* 0.18	* 0.19	* 0.15	* 0.17	* 0.19
MGO	* 7.01	* 11.16	* 7.75	* 10.31	* 6.81	* 7.64	* 7.25
CAO	* 10.72	* 12.59	* 12.70	* 11.68	* 9.51	* 12.84	* 8.03
NA2O	* 2.66	* 1.46	* 2.47	* 2.14	* 2.54	* 2.35	* 3.23
K2O	* 0.71	* 0.87	* 0.31	* 0.37	* 1.01	* 0.15	* 0.59
P2O5	* 0.20	* 0.16	* 0.07	* 0.09	* 0.24	* 0.06	* 0.24
LOI	* 3.05	* 3.62	* 2.48	* 3.34	* 3.88	* 2.94	* 3.06
TOTAL	* 99.44	* 99.97	* 98.97	* 98.99	* 99.44	* 98.81	* 98.74

ZR	* 115	* 101	* 84	* 86	* 124	* 74	* 122
SR	* 446	* 218	* 180	* 151	* 344	* 125	* 456
RB	* 12	* 13	* 5	* 5	* 25	* 2	* 12
ZN	* 136	* 100	* 112	* 114	* 215	* 96	* 102
CU	* 185	* 78	* 233	* 115	* 235	* 88	* 62
BA	* 214	* 247	* 56	* 62	* 387	* 33	* 314
NB	* 15	* 12	* 0	* 0	* 18	* 1	* 20
Y	* 32	* 34	* 40	* 37	* 35	* 36	* 27
PB	* 9	* 9	* 9	* 9	* 8	* 7	* 3
NI	* 104	* 175	* 117	* 395	* 114	* 143	* 60
CR	* 220	* 814	* 377	* 670	* 181	* 424	* 92
V	* 268	* 269	* 278	* 264	* 262	* 234	* 271
GA	* 22	* 21	* 20	* 18	* 22	* 18	* 23

OR	*	0.0	*	0.0	*	0.0	*	0.0	*	0.0	*	0.0	*
AB	*	4.35	*	5.33	*	1.90	*	2.28	*	6.24	*	0.92	*
AN	*	23.33	*	12.80	*	21.64	*	18.91	*	22.48	*	20.73	*
NE	*	24.48	*	19.84	*	29.11	*	26.21	*	24.51	*	31.35	*
LC	*	0.0	*	0.0	*	0.0	*	0.0	*	0.0	*	0.0	*
CDR	*	0.0	*	0.0	*	0.0	*	0.0	*	0.0	*	0.0	*
WO	*	0.0	*	0.0	*	0.0	*	0.0	*	0.0	*	0.0	*
DI	*	23.81	*	34.92	*	28.50	*	26.80	*	19.04	*	27.55	*
WO	*	12.32	*	18.35	*	14.92	*	14.09	*	9.77	*	14.48	*
EN	*	7.93	*	13.57	*	10.75	*	10.51	*	5.84	*	10.77	*
FS	*	3.56	*	3.01	*	2.83	*	2.19	*	3.43	*	2.29	*
HY	*	11.34	*	17.82	*	4.52	*	6.44	*	16.42	*	9.66	*
EN	*	7.82	*	14.58	*	3.58	*	5.33	*	10.34	*	7.96	*
FS	*	3.51	*	3.23	*	0.94	*	1.11	*	6.08	*	1.70	*
OL	*	2.45	*	0.57	*	5.11	*	9.45	*	1.80	*	0.95	*
FO	*	1.64	*	0.45	*	3.96	*	7.69	*	1.09	*	0.77	*
FA	*	0.81	*	0.11	*	1.15	*	1.77	*	0.71	*	0.18	*
LA	*	0.0	*	0.0	*	0.0	*	0.0	*	0.0	*	0.0	*
MT	*	5.29	*	5.18	*	6.82	*	7.31	*	4.47	*	6.79	*
ILM	*	4.41	*	2.97	*	2.14	*	2.22	*	4.43	*	1.82	*
AP	*	0.48	*	0.39	*	0.17	*	0.22	*	0.58	*	0.15	*
HM	*	0.0	*	0.0	*	0.0	*	0.0	*	0.0	*	0.0	*

RJ75-060	GCS	COARSE	GRAINED	GREENSCHIST	DUCK POINT
RJ75-062	GCS	COARSE	GRAINED	GREENSCHIST	DUCK POINT
RJ75-063	GCS	COARSE	GRAINED	GREENSCHIST	DUCK POINT
RJ75-179	GCS	COARSE	GRAINED	GREENSCHIST	FISCHOT ISLAND
RJ75-222	GCS	COARSE	GRAINED	GREENSCHIST	LOBSTER POINT
RJ75-292	GCS	COARSE	GRAINED	GREENSCHIST	SUGARLOAF HILL
RJ76-435	GCS	COARSE	GRAINED	GREENSCHIST	LOBSTER POINT

SAMPLE	* R375-00 *	* R375-020 *	* R375-033 *	* R375-100 *	* R375-104 *	* R375-184 *	* R375-190 *
SI02	* 47.49 *	* 45.78 *	* 42.91 *	* 47.70 *	* 46.93 *	* 45.99 *	* 47.57 *
TI02	* 0.95 *	* 1.01 *	* 0.74 *	* 1.09 *	* 1.17 *	* 0.72 *	* 1.21 *
AL203	* 17.19 *	* 14.83 *	* 17.29 *	* 14.78 *	* 14.59 *	* 16.63 *	* 16.10 *
FE203	* 3.75 *	* 4.94 *	* 4.60 *	* 3.81 *	* 4.41 *	* 4.04 *	* 4.55 *
FEO	* 5.32 *	* 5.38 *	* 4.16 *	* 5.86 *	* 5.39 *	* 4.48 *	* 5.48 *
MNO	* 0.15 *	* 0.18 *	* 0.15 *	* 0.16 *	* 0.18 *	* 0.15 *	* 0.22 *
MGO	* 5.76 *	* 6.27 *	* 7.44 *	* 7.08 *	* 7.36 *	* 7.08 *	* 5.83 *
CAO	* 13.42 *	* 13.15 *	* 14.55 *	* 12.14 *	* 11.66 *	* 14.13 *	* 11.75 *
NA2O	* 2.57 *	* 2.89 *	* 1.94 *	* 2.59 *	* 2.79 *	* 2.09 *	* 3.30 *
K2O	* 0.39 *	* 0.32 *	* 0.16 *	* 0.53 *	* 0.68 *	* 0.32 *	* 0.40 *
P2O5	* 0.07 *	* 0.08 *	* 0.04 *	* 0.08 *	* 0.10 *	* 0.06 *	* 0.11 *
LOI	* 3.00 *	* 2.95 *	* 4.12 *	* 2.54 *	* 3.16 *	* 2.72 *	* 2.36 *
TOTAL	* 100.06 *	* 97.68 *	* 98.10 *	* 98.36 *	* 98.42 *	* 98.41 *	* 98.88 *

ZR	* 72 *	* 75 *	* 69 *	* 82 *	* 97 *	* 63 *	* 94 *
SR	* 131 *	* 121 *	* 155 *	* 124 *	* 160 *	* 149 *	* 197 *
RB	* 5 *	* 4 *	* 2 *	* 6 *	* 6 *	* 6 *	* 4 *
ZN	* 75 *	* 110 *	* 96 *	* 85 *	* 111 *	* 107 *	* 101 *
CU	* 119 *	* 169 *	* 128 *	* 82 *	* 155 *	* 176 *	* 270 *
BA	* 36 *	* 40 *	* 40 *	* 38 *	* 64 *	* 27 *	* 54 *
NB	* 1 *	* 0 *	* 0 *	* 1 *	* 1 *	* 0 *	* 1 *
Y	* 37 *	* 39 *	* 32 *	* 38 *	* 36 *	* 32 *	* 42 *
PB	* 7 *	* 7 *	* 7 *	* 9 *	* 7 *	* 7 *	* 7 *
NI	* 25 *	* 73 *	* 300 *	* 79 *	* 97 *	* 146 *	* 52 *
CR	* 205 *	* 251 *	* 476 *	* 315 *	* 300 *	* 351 *	* 217 *
V	* 247 *	* 272 *	* 197 *	* 260 *	* 276 *	* 195 *	* 276 *
GA	* 17 *	* 17 *	* 16 *	* 19 *	* 18 *	* 17 *	* 20 *

OR	*	2.37	*	1.99	*	1.01	*	3.27	*	4.22	*	1.97	*	2.45	*
AB	*	22.40	*	21.66	*	11.42	*	22.86	*	24.77	*	18.47	*	28.32	*
AN	*	35.24	*	27.98	*	40.40	*	28.31	*	26.52	*	36.61	*	28.93	*
NE	*	0.0	*	2.23	*	3.27	*	0.0	*	0.0	*	0.0	*	0.32	*
LC	*	0.0	*	0.0	*	0.0	*	0.0	*	0.0	*	0.0	*	0.0	*
COR	*	0.0	*	0.0	*	0.0	*	0.0	*	0.0	*	0.0	*	0.0	*
WO	*	0.0	*	0.0	*	0.0	*	0.0	*	0.0	*	0.0	*	0.0	*
OI	*	26.44	*	32.17	*	28.55	*	27.28	*	26.73	*	28.82	*	24.64	*
WO	*	13.74	*	16.82	*	15.09	*	14.21	*	14.01	*	15.14	*	12.85	*
EN	*	9.25	*	11.95	*	11.68	*	9.73	*	10.16	*	11.18	*	8.92	*
FS	*	3.45	*	3.39	*	1.79	*	3.35	*	2.56	*	2.50	*	2.88	*
HY	*	1.48	*	0.0	*	0.0	*	6.15	*	1.03	*	0.18	*	0.0	*
EN	*	1.08	*	0.0	*	0.0	*	4.58	*	0.82	*	0.15	*	0.0	*
FS	*	0.40	*	0.0	*	0.0	*	1.58	*	0.21	*	0.03	*	0.0	*
QL	*	4.40	*	4.14	*	6.57	*	3.95	*	7.38	*	6.18	*	5.81	*
FO	*	3.11	*	3.16	*	5.62	*	2.86	*	5.78	*	4.96	*	4.29	*
FA	*	1.28	*	0.99	*	0.95	*	1.09	*	1.60	*	1.22	*	1.53	*
LA	*	0.0	*	0.0	*	0.0	*	0.0	*	0.0	*	0.0	*	0.0	*
MT	*	5.60	*	7.55	*	7.09	*	5.76	*	6.71	*	6.12	*	6.83	*
ILM	*	1.86	*	2.02	*	1.49	*	2.16	*	2.33	*	1.43	*	2.38	*
AP	*	0.17	*	0.20	*	0.10	*	0.19	*	0.24	*	0.15	*	0.26	*
HM	*	0.0	*	0.0	*	0.0	*	0.0	*	0.0	*	0.0	*	0.0	*

RJ75-007	GCS	SPOTTED	GREENSCHIST	GOOSE COVE ROAD
RJ75-020	GCS	SPOTTED	GREENSCHIST	GOOSE COVE ROAD
RJ75-033	GCS	SPOTTED	GREENSCHIST	CREMAILLERE ROAD
RJ75-100	GCS	SPOTTED	GREENSCHIST	THREE MOUNTAIN HARBOUR
RJ75-164	GCS	SPOTTED	GREENSCHIST	IRELAND BROOK
RJ75-184	GCS	SPOTTED	GREENSCHIST	FISCHOT ISLAND
RJ75-196	GCS	SPOTTED	GREENSCHIST	CREMAILLERE HILL

SAMPLE		RJ75-296		RJ76-436		RJ76-530		RJ76-629		RJ76-108		RJ76-186		RJ76-300
SI02	*	45.76	*	45.05	*	46.46	*	45.74	*	43.17	*	45.94	*	44.62
TI02	*	0.75	*	0.75	*	1.14	*	0.89	*	0.60	*	0.58	*	1.13
AL2O3	*	20.28	*	17.49	*	14.88	*	16.61	*	19.73	*	21.76	*	12.55
FE2O3	*	4.35	*	6.73	*	4.79	*	4.32	*	5.58	*	5.84	*	4.74
FEO	*	2.93	*	1.15	*	4.78	*	4.90	*	2.00	*	1.46	*	5.75
MNO	*	0.13	*	0.13	*	0.18	*	0.18	*	0.14	*	0.14	*	0.18
MGO	*	4.01	*	5.57	*	7.50	*	6.69	*	3.88	*	1.75	*	5.91
CAO	*	14.71	*	14.77	*	12.62	*	12.71	*	15.59	*	12.11	*	15.16
NA2O	*	3.02	*	2.52	*	2.49	*	2.64	*	1.93	*	2.80	*	3.42
K2O	*	0.33	*	0.46	*	0.44	*	0.65	*	1.17	*	2.21	*	0.36
P2O5	*	0.07	*	0.08	*	0.09	*	0.07	*	0.02	*	0.11	*	0.09
LOI	*	3.26	*	3.72	*	3.85	*	3.19	*	4.59	*	2.97	*	6.32
TOTAL	*	99.60	*	98.42	*	99.22	*	98.59	*	98.40	*	97.67	*	100.23

ZR	*	71	*	58	*	84	*	78	*	70	*	66	*	89
SR	*	209	*	215	*	169	*	243	*	402	*	239	*	197
RB	*	3	*	8	*	3	*	8	*	14	*	39	*	3
ZN	*	94	*	55	*	76	*	88	*	72	*	60	*	123
CU	*	162	*	77	*	65	*	134	*	128	*	29	*	226
BA	*	35	*	115	*	49	*	59	*	108	*	191	*	47
NB	*	1	*	4	*	7	*	0	*	0	*	0	*	0
Y	*	31	*	17	*	27	*	37	*	32	*	26	*	39
PB	*	5	*	0	*	0	*	7	*	7	*	6	*	5
NI	*	81	*	75	*	91	*	90	*	113	*	87	*	49
CR	*	284	*	252	*	232	*	201	*	201	*	199	*	261
V	*	181	*	171	*	245	*	226	*	138	*	134	*	274
GA	*	16	*	15	*	18	*	17	*	15	*	17	*	19

OZ	*	0.0	*	0.0	*	0.0	*	0.0	*	0.0	*	0.0	*	0.0	*
OR	*	2.02	*	2.87	*	2.73	*	4.02	*	7.37	*	13.78	*	2.26	*
AB	*	17.72	*	15.89	*	22.09	*	19.34	*	8.01	*	18.19	*	12.78	*
AN	*	42.33	*	37.02	*	29.49	*	33.06	*	44.44	*	42.51	*	18.98	*
NE	*	4.76	*	3.59	*	0.0	*	2.20	*	5.08	*	3.69	*	9.76	*
LC	*	0.0	*	0.0	*	0.0	*	0.0	*	0.0	*	0.0	*	0.0	*
COR	*	0.0	*	0.0	*	0.0	*	0.0	*	0.0	*	0.0	*	0.0	*
WO	*	1.10	*	0.0	*	0.0	*	0.0	*	3.95	*	3.14	*	2.39	*
DI	*	23.81	*	30.99	*	28.14	*	26.00	*	22.20	*	9.92	*	43.95	*
WO	*	12.67	*	16.62	*	14.84	*	13.62	*	11.91	*	5.32	*	22.88	*
EN	*	10.36	*	14.37	*	11.32	*	9.85	*	10.29	*	4.60	*	15.66	*
FS	*	0.78	*	0.0	*	1.98	*	2.52	*	0.0	*	0.0	*	5.40	*
HY	*	0.0	*	0.0	*	3.00	*	0.0	*	0.0	*	0.0	*	0.0	*
EN	*	0.0	*	0.0	*	2.55	*	0.0	*	0.0	*	0.0	*	0.0	*
FS	*	0.0	*	0.0	*	0.45	*	0.0	*	0.0	*	0.0	*	0.0	*
OL	*	0.0	*	0.20	*	4.78	*	6.83	*	0.0	*	0.0	*	0.0	*
FO	*	0.0	*	0.20	*	4.00	*	5.33	*	0.0	*	0.0	*	0.0	*
FA	*	0.0	*	0.0	*	0.77	*	1.50	*	0.0	*	0.0	*	0.0	*
LA	*	0.0	*	0.0	*	0.0	*	0.0	*	0.0	*	0.0	*	0.0	*
MT	*	6.54	*	2.07	*	7.28	*	6.56	*	5.45	*	3.63	*	7.31	*
ILM	*	1.48	*	1.50	*	2.27	*	1.77	*	1.21	*	1.16	*	2.28	*
AP	*	0.17	*	0.20	*	0.22	*	0.17	*	0.05	*	0.27	*	0.22	*
HM	*	0.0	*	5.68	*	0.0	*	0.0	*	2.18	*	3.66	*	0.0	*

RJ75-296	GCS	SPOTTED GREENSCHIST	SAVAGE HILL
RJ76-436	GCS	SPOTTED GREENSCHIST	SAVAGE POINT
RJ76-530	GCS	SPOTTED GREENSCHIST	IRELAND BROOK
RJ75-029	GCS	BANDED GREENSCHIST	GOOSE COVE WEST
RJ75-108	GCS	BANDED GREENSCHIST	THREE MOUNTAIN HARBOUR
RJ75-186	GCS	BANDED GREENSCHIST	FISCHOT ISLAND
RJ75-300	GCS	BANDED GREENSCHIST	SAVAGE HILL

SI02	*	48.09	*	48.25	*	47.89	*	46.26	*	49.14	*	47.74	*	47.49	*
TI02	*	1.06	*	1.13	*	1.10	*	1.09	*	0.90	*	1.20	*	1.06	*
AL203	*	14.21	*	14.31	*	16.37	*	13.35	*	13.80	*	13.84	*	14.04	*
FE203	*	3.01	*	3.33	*	7.01	*	4.69	*	3.70	*	4.54	*	3.81	*
FEO	*	7.21	*	7.97	*	4.22	*	5.73	*	5.82	*	5.99	*	6.66	*
MNO	*	0.19	*	0.21	*	0.19	*	0.18	*	0.17	*	0.18	*	0.17	*
MGO	*	8.09	*	7.50	*	4.85	*	7.21	*	8.01	*	7.26	*	7.78	*
CAO	*	12.02	*	11.86	*	8.16	*	13.83	*	11.34	*	11.83	*	12.37	*
NA2O	*	2.52	*	2.73	*	4.15	*	2.36	*	3.01	*	2.54	*	2.60	*
K2O	*	0.23	*	0.16	*	1.53	*	0.51	*	0.24	*	0.86	*	0.10	*
P2O5	*	0.06	*	0.07	*	0.13	*	0.07	*	0.07	*	0.11	*	0.06	*
LOI	*	2.38	*	2.32	*	3.17	*	2.87	*	2.43	*	2.10	*	2.93	*
TOTAL	*	99.07	*	99.84	*	98.77	*	98.15	*	98.63	*	98.19	*	99.07	*

ZR	*	79	*	81	*	82	*	82	*	72	*	91	*	86	*
SR	*	142	*	165	*	218	*	180	*	141	*	196	*	305	*
RB	*	2	*	2	*	28	*	7	*	4	*	11	*	2	*
ZN	*	112	*	124	*	115	*	97	*	104	*	105	*	185	*
CU	*	180	*	179	*	241	*	124	*	129	*	126	*	188	*
BA	*	75	*	59	*	100	*	80	*	107	*	153	*	51	*
NB	*	0	*	0	*	0	*	1	*	1	*	0	*	0	*
Y	*	39	*	43	*	35	*	39	*	36	*	40	*	39	*
PB	*	6	*	7	*	7	*	6	*	6	*	6	*	7	*
NI	*	58	*	61	*	181	*	71	*	86	*	51	*	56	*
CR	*	394	*	177	*	676	*	301	*	356	*	231	*	365	*
V	*	293	*	316	*	224	*	271	*	252	*	300	*	274	*
GA	*	19	*	20	*	19	*	18	*	18	*	18	*	18	*

02	*	0.0	*	0.0	*	0.0	*	0.0	*	0.0	*	0.0	*	0.0	*
OR	*	1.40	*	0.97	*	9.45	*	3.16	*	1.47	*	5.29	*	0.61	*
AB	*	22.04	*	23.68	*	34.39	*	19.35	*	26.46	*	22.35	*	22.87	*
AN	*	27.68	*	26.98	*	22.48	*	25.52	*	24.34	*	24.78	*	27.38	*
NE	*	0.0	*	0.0	*	1.25	*	0.86	*	0.0	*	0.0	*	0.0	*
LC	*	0.0	*	0.0	*	0.0	*	0.0	*	0.0	*	0.0	*	0.0	*
COR	*	0.0	*	0.0	*	0.0	*	0.0	*	0.0	*	0.0	*	0.0	*
WO	*	0.0	*	0.0	*	0.0	*	0.0	*	0.0	*	0.0	*	0.0	*
DI	*	27.15	*	26.75	*	14.86	*	36.78	*	26.98	*	28.50	*	29.05	*
WO	*	14.03	*	13.75	*	7.94	*	19.23	*	14.07	*	14.87	*	15.08	*
EN	*	8.97	*	8.35	*	6.69	*	13.64	*	9.77	*	10.41	*	10.04	*
FS	*	4.15	*	4.64	*	0.23	*	3.91	*	3.14	*	3.21	*	3.94	*
HY	*	8.59	*	7.58	*	0.0	*	0.0	*	9.77	*	5.92	*	6.78	*
EN	*	5.87	*	4.87	*	0.0	*	0.0	*	7.39	*	4.53	*	4.87	*
FS	*	2.71	*	2.71	*	0.0	*	0.0	*	2.38	*	1.40	*	1.91	*
OL	*	6.32	*	6.69	*	4.31	*	4.78	*	3.38	*	3.63	*	5.25	*
FO	*	4.19	*	4.15	*	4.15	*	3.64	*	2.49	*	2.71	*	3.67	*
FA	*	2.13	*	2.54	*	0.15	*	1.15	*	0.88	*	0.92	*	1.59	*
LA	*	0.0	*	0.0	*	0.0	*	0.0	*	0.0	*	0.0	*	0.0	*
MT	*	4.51	*	4.95	*	10.62	*	7.13	*	5.57	*	6.85	*	5.74	*
ILM	*	2.08	*	2.20	*	2.18	*	2.17	*	1.78	*	2.37	*	2.09	*
AP	*	0.14	*	0.17	*	0.32	*	0.17	*	0.17	*	0.27	*	0.14	*
HM	*	0.0	*	0.0	*	0.0	*	0.0	*	0.0	*	0.0	*	0.0	*

RJ75-009	GCS	BANDED	GREENSCHIST	GOOSE COVE ROAD
RJ75-026	GCS	BANDED	GREENSCHIST	GOOSE COVE ROAD
RJ75-103	GCS	BANDED	GREENSCHIST	VIERGE COVE
RJ75-112	GCS	BANDED	GREENSCHIST	GOOSE COVE
RJ75-151	GCS	BANDED	GREENSCHIST	GREENWOOD COVE
RJ75-171	GCS	BANDED	GREENSCHIST	PUMPHOUSE POND
RJ75-298	GCS	BANDED	GREENSCHIST	SAVAGE POINT

5102	44.37	42.70	44.39	42.79	48.78	47.89	47.43
TI02	1.11	0.81	1.48	0.99	1.74	1.75	1.71
AL2O3	11.88	14.71	16.45	11.40	13.46	13.74	13.23
FE2O3	5.56	5.84	7.30	3.50	3.19	5.57	6.57
FeO	5.51	3.92	4.48	5.02	9.46	7.92	6.87
MNO	0.22	0.17	0.28	0.21	0.24	0.21	0.19
MGO	6.12	5.25	5.84	5.26	6.86	5.58	5.91
CAO	13.97	16.49	12.84	11.09	9.89	9.81	11.62
NA2O	1.96	2.82	1.99	2.47	2.83	3.22	2.57
K2O	0.03	0.25	0.79	0.77	0.64	0.95	0.49
P2O5	0.10	0.08	0.15	0.16	0.17	0.16	0.15
LOI	9.71	6.63	3.52	9.56	1.94	1.97	1.89
TOTAL	100.54	99.73	99.51	100.22	99.20	98.48	98.63

ZR	77	53	101	47	119	111	108
SR	251	147	193	202	134	175	140
RB	3	8	16	1	9	12	7
ZN	108	65	86	64	183	155	147
CU	122	77	26	60	202	119	96
BA	33	10	67	5	117	113	84
NB	6	5	5	6	4	2	2
Y	32	24	36	23	50	58	52
PB	6	9	11	0	9	8	8
NI	60	106	198	278	52	64	55
CR	177	270	495	449	163	150	203
V	268	207	245	161	373	373	402
GA	15	14	20	17	22	21	20

OR	*	0.15	*	0.01	*	0.10	*	0.03	*	0.0	*	0.0	*	0.0	*
AB	*	19.26	*	10.69	*	17.54	*	23.05	*	24.61	*	28.22	*	22.47	*
AN	*	25.90	*	28.72	*	35.02	*	19.57	*	22.75	*	20.96	*	23.89	*
NE	*	0.0	*	8.09	*	0.0	*	0.0	*	0.0	*	0.0	*	0.0	*
LC	*	0.0	*	0.0	*	0.0	*	0.0	*	0.0	*	0.0	*	0.0	*
COR	*	0.0	*	0.0	*	0.0	*	0.0	*	0.0	*	0.0	*	0.0	*
WO	*	0.0	*	6.94	*	0.0	*	0.0	*	0.0	*	0.0	*	0.0	*
DI	*	39.63	*	33.02	*	23.65	*	32.15	*	21.79	*	23.09	*	27.81	*
WO	*	20.75	*	17.53	*	12.66	*	16.69	*	11.11	*	11.18	*	14.50	*
EN	*	14.88	*	14.04	*	10.79	*	11.14	*	6.21	*	7.30	*	10.09	*
FS	*	4.00	*	1.45	*	0.20	*	4.32	*	4.47	*	3.90	*	3.22	*
HY	*	2.41	*	0.0	*	4.44	*	4.60	*	15.29	*	6.58	*	6.75	*
EN	*	1.90	*	0.0	*	4.36	*	3.31	*	8.89	*	4.29	*	5.12	*
FS	*	0.51	*	0.0	*	0.08	*	1.28	*	6.40	*	2.29	*	1.63	*
OL	*	0.0	*	0.0	*	0.0	*	0.0	*	3.08	*	3.12	*	0.0	*
FO	*	0.0	*	0.0	*	0.0	*	0.0	*	1.72	*	1.96	*	0.0	*
FA	*	0.0	*	0.0	*	0.0	*	0.0	*	1.36	*	1.16	*	0.0	*
LA	*	0.0	*	0.0	*	0.0	*	0.0	*	0.0	*	0.0	*	0.0	*
MT	*	3.87	*	9.09	*	11.03	*	5.60	*	4.75	*	8.36	*	9.84	*
ILM	*	2.32	*	1.65	*	2.93	*	2.07	*	3.40	*	3.44	*	3.36	*
AP	*	0.26	*	0.20	*	0.36	*	0.41	*	0.41	*	0.39	*	0.36	*
HM	*	0.0	*	0.0	*	0.0	*	0.0	*	0.0	*	0.0	*	0.0	*

RJ76-414 GCS BANDED GREENSCHIST ST. ANTHONY HILL
 RJ76-417 GCS BANDED GREENSCHIST ST. ANTHONY HILL
 RJ76-439 GCS BANDED GREENSCHIST FISCHOT ISLAND
 RJ76-471 IPV (VESICULAR) FLATTENED PILLOW LAVA INTERBANDED WITH CALCITE S.B.
 RJ75-085 GCS EPIDOTE AMPHIBOLITE THREE MOUNTAIN SUMMIT
 RJ75-088 GCS EPIDOTE AMPHIBOLITE THREE MOUNTAIN SUMMIT
 RJ75-089 GCS EPIDOTE AMPHIBOLITE THREE MOUNTAIN SUMMIT

SAMPLE	* RJ75-010 *	* RJ75-133 *	* RJ75-143 *	* J75-440 *	* RJ75-475 *	* RJ75-559 *
SiO2	* 47.56 *	* 46.68 *	* 48.21 *	* 47.81 *	* 48.50 *	* 48.83 *
TiO2	* 1.87 *	* 1.19 *	* 1.71 *	* 1.34 *	* 1.50 *	* 1.54 *
AL2O3	* 12.89 *	* 15.01 *	* 12.88 *	* 14.01 *	* 13.56 *	* 13.04 *
FE2O3	* 6.21 *	* 6.01 *	* 5.21 *	* 5.56 *	* 6.77 *	* 2.37 *
FEO	* 7.50 *	* 4.27 *	* 7.67 *	* 5.87 *	* 5.88 *	* 9.91 *
MNO	* 0.24 *	* 0.19 *	* 0.21 *	* 0.18 *	* 0.24 *	* 0.18 *
MGO	* 6.22 *	* 6.31 *	* 6.29 *	* 7.01 *	* 6.56 *	* 6.81 *
CAO	* 11.40 *	* 12.41 *	* 10.53 *	* 12.80 *	* 8.81 *	* 9.89 *
NA2O	* 2.70 *	* 3.11 *	* 2.92 *	* 2.21 *	* 2.80 *	* 2.83 *
K2O	* 0.75 *	* 0.52 *	* 0.58 *	* 0.54 *	* 1.33 *	* 0.85 *
P2O5	* 0.16 *	* 0.13 *	* 0.12 *	* 0.15 *	* 0.12 *	* 0.15 *
LOI	* 1.96 *	* 2.26 *	* 1.81 *	* 2.87 *	* 2.13 *	* 2.23 *
TOTAL	* 99.46 *	* 98.09 *	* 98.14 *	* 100.35 *	* 98.20 *	* 98.63 *

ZR	* 121 *	* 98 *	* 113 *	* 109 *	* 92 *	* 102 *
SR	* 152 *	* 268 *	* 115 *	* 179 *	* 166 *	* 285 *
RB	* 6 *	* 7 *	* 10 *	* 8 *	* 19 *	* 15 *
ZN	* 143 *	* 109 *	* 140 *	* 86 *	* 99 *	* 57 *
CU	* 167 *	* 162 *	* 126 *	* 84 *	* 26 *	* 14 *
BA	* 105 *	* 281 *	* 63 *	* 69 *	* 63 *	* 2275 *
NB	* 1 *	* 2 *	* 2 *	* 15 *	* 6 *	* 8 *
Y	* 53 *	* 42 *	* 50 *	* 34 *	* 36 *	* 37 *
PB	* 8 *	* 7 *	* 8 *	* 0 *	* 0 *	* 1 *
NI	* 59 *	* 108 *	* 53 *	* 70 *	* 62 *	* 56 *
CR	* 121 *	* 370 *	* 145 *	* 139 *	* 154 *	* 103 *
V	* 391 *	* 257 *	* 406 *	* 295 *	* 299 *	* 367 *
GA	* 21 *	* 19 *	* 21 *	* 22 *	* 18 *	* 20 *

SAMPLE	RJ75-090	RJ75-133	RJ75-143	RJ76-440	RJ76-475	RJ76-569
QZ	4.84	3.80	3.81	1.27	2.25	0.00
OR	23.42	25.50	25.64	19.18	24.66	8.21
AB	21.36	26.55	21.09	27.40	21.34	24.84
AN	0.0	1.05	0.0	0.0	0.0	21.13
NE	0.0	0.0	0.0	0.0	0.0	0.0
LC	0.0	0.0	0.0	0.0	0.0	0.0
COR	0.0	0.0	0.0	0.0	0.0	0.0
WD	0.0	0.0	0.0	0.0	0.0	0.0
DI	28.65	28.97	26.16	29.26	18.51	23.65
WO	14.88	15.41	13.51	15.34	9.75	12.01
EN	9.94	12.58	8.61	11.16	7.34	6.37
FS	3.84	0.97	4.03	2.75	1.43	5.27
HY	8.24	0.0	11.22	8.41	11.54	11.91
EN	5.94	0.0	7.64	6.74	9.66	6.52
FS	2.30	0.0	3.58	1.66	1.88	5.39
OL	0.0	2.89	0.0	0.0	0.0	6.30
FO	0.0	2.66	0.0	0.0	0.0	3.30
FA	0.0	0.23	0.0	0.0	0.0	3.01
LA	0.0	0.0	0.0	0.0	0.0	0.0
MT	9.23	9.08	7.84	8.27	10.22	3.56
ILM	3.64	2.36	3.37	2.61	2.97	3.03
AP	0.38	0.31	0.29	0.36	0.29	0.36
HM	0.0	0.0	0.0	0.0	0.0	0.0

RJ75-090	GCS	EPIDOTE AMPHIBOLITE	THREE MOUNTAIN SUMMIT
RJ75-133	GCS	EPIDOTE AMPHIBOLITE	GRAVEL PIT GOOSE COVE ROAD
RJ75-143	GCS	EPIDOTE AMPHIBOLITE	THREE MOUNTAIN SUMMIT
RJ76-440	GCS	EPIDOTE AMPHIBOLITE	FISCHOT ISLAND
RJ76-475	GCS	EGS EPIDOTE AMPHIBOLITE	WHALE GROTTO MOUNTAIN
RJ76-569	GCS	EPIDOTE AMPHIBOLITE	QUIRPON ISLAND

Table I.v. Major and trace element analyses and CIPW norms, Green Ridge Amphibolite.

SAMPLE	* RJ75-081 *	* RJ75-083 *	* RJ75-180 *	* RJ75-272 *	* RJ75-273 *	* RJ75-274 *	* RJ75-400 *
SiO2	* 54.05 *	* 51.75 *	* 54.38 *	* 52.82 *	* 52.17 *	* 51.99 *	* 52.73 *
TiO2	* 2.22 *	* 1.85 *	* 1.17 *	* 2.25 *	* 1.79 *	* 1.56 *	* 0.95 *
AL2O3	* 16.66 *	* 14.80 *	* 15.44 *	* 15.35 *	* 16.16 *	* 14.40 *	* 13.73 *
FE2O3	* 0.23 *	* 1.70 *	* 2.62 *	* 1.64 *	* 2.30 *	* 3.45 *	* 1.99 *
FeO	* 9.42 *	* 9.05 *	* 7.09 *	* 9.34 *	* 8.24 *	* 9.06 *	* 5.78 *
MNO	* 0.19 *	* 0.19 *	* 0.19 *	* 0.24 *	* 0.25 *	* 0.26 *	* 0.16 *
MGO	* 2.79 *	* 5.55 *	* 4.12 *	* 3.79 *	* 4.86 *	* 5.02 *	* 3.02 *
CAO	* 5.49 *	* 6.87 *	* 6.83 *	* 4.35 *	* 5.19 *	* 6.17 *	* 4.45 *
NA2O	* 2.29 *	* 1.51 *	* 2.86 *	* 2.96 *	* 1.83 *	* 2.89 *	* 2.12 *
K2O	* 2.62 *	* 2.45 *	* 2.42 *	* 1.61 *	* 2.17 *	* 1.23 *	* 1.84 *
P2O5	* 0.51 *	* 0.31 *	* 0.19 *	* 0.51 *	* 0.30 *	* 0.17 *	* 0.12 *
LOI	* 1.79 *	* 3.48 *	* 2.72 *	* 4.18 *	* 4.04 *	* 3.35 *	* 3.35 *
TOTAL	* 98.26 *	* 99.51 *	* 100.03 *	* 99.04 *	* 99.30 *	* 99.55 *	* 100.25 *

ZR	* 262 *	* 165 *	* 133 *	* 222 *	* 165 *	* 131 *	* 123 *
SR	* 396 *	* 166 *	* 154 *	* 233 *	* 126 *	* 140 *	* 138 *
RB	* 67 *	* 70 *	* 53 *	* 36 *	* 73 *	* 37 *	* 38 *
ZN	* 144 *	* 157 *	* 125 *	* 113 *	* 182 *	* 1249 *	* 88 *
CU	* 151 *	* 184 *	* 145 *	* 120 *	* 197 *	* 577 *	* 41 *
BA	* 568 *	* 319 *	* 313 *	* 427 *	* 362 *	* 314 *	* 415 *
NB	* 38 *	* 18 *	* 4 *	* 33 *	* 21 *	* 7 *	* 10 *
Y	* 39 *	* 39 *	* 36 *	* 32 *	* 39 *	* 50 *	* 27 *
PB	* 13 *	* 15 *	* 14 *	* 12 *	* 15 *	* 14 *	* 11 *
NI	* 63 *	* 128 *	* 86 *	* 69 *	* 113 *	* 38 *	* 52 *
CR	* 145 *	* 263 *	* 226 *	* 126 *	* 225 *	* 131 *	* 91 *
V	* 243 *	* 285 *	* 238 *	* 284 *	* 258 *	* 283 *	* 204 *
GA	* 22 *	* 19 *	* 20 *	* 18 *	* 25 *	* 24 *	* 22 *

SAMPLE		RJ75-082		RJ75-083		RJ75-189		RJ75-272		RJ75-273		RJ75-274		RJ75-275	
GR	*	10.13	*	7.27	*	5.44	*	10.74	*	11.29	*	0.52	*	26.99	*
AB	*	16.04	*	15.07	*	14.69	*	10.03	*	13.45	*	7.55	*	11.22	*
AN	*	20.07	*	13.30	*	24.85	*	26.40	*	16.24	*	25.41	*	18.51	*
NE	*	25.04	*	27.44	*	22.74	*	19.27	*	25.09	*	23.57	*	21.98	*
LC	*	0.0	*	0.0	*	0.0	*	0.0	*	0.0	*	0.0	*	0.0	*
COR	*	0.0	*	0.0	*	0.0	*	0.0	*	0.0	*	0.0	*	0.0	*
WO	*	1.24	*	0.0	*	0.0	*	2.15	*	2.13	*	0.0	*	0.46	*
DI	*	0.0	*	0.0	*	0.0	*	0.0	*	0.0	*	0.0	*	0.0	*
WD	*	0.0	*	5.00	*	8.99	*	0.0	*	0.0	*	5.94	*	0.0	*
EN	*	0.0	*	2.53	*	4.55	*	0.0	*	0.0	*	3.01	*	0.0	*
FS	*	0.0	*	1.30	*	2.34	*	0.0	*	0.0	*	1.52	*	0.0	*
HY	*	0.0	*	1.17	*	2.10	*	0.0	*	0.0	*	1.42	*	0.0	*
EN	*	21.47	*	24.90	*	15.59	*	23.15	*	23.93	*	22.18	*	15.69	*
FS	*	7.20	*	13.09	*	8.20	*	9.95	*	12.70	*	11.47	*	7.76	*
OL	*	14.27	*	11.82	*	7.39	*	13.20	*	11.24	*	10.71	*	7.93	*
FO	*	0.0	*	0.0	*	0.0	*	0.0	*	0.0	*	0.0	*	0.0	*
FA	*	0.0	*	0.0	*	0.0	*	0.0	*	0.0	*	0.0	*	0.0	*
LA	*	0.0	*	0.0	*	0.0	*	0.0	*	0.0	*	0.0	*	0.0	*
MT	*	0.0	*	0.0	*	0.0	*	0.0	*	0.0	*	0.0	*	0.0	*
ILM	*	0.35	*	2.56	*	3.90	*	2.51	*	3.50	*	5.20	*	2.98	*
AP	*	4.37	*	3.66	*	2.28	*	4.50	*	3.57	*	3.08	*	1.88	*
HM	*	1.23	*	0.75	*	0.45	*	1.25	*	0.73	*	0.41	*	0.29	*
	*	0.0	*	0.0	*	0.0	*	0.0	*	0.0	*	0.0	*	0.0	*

RJ75-082	GRA	BIOTITE	AMPHIBOLITE	THREE MOUNTAIN SUMMIT
RJ75-083	GRA	BIOTITE	AMPHIBOLITE	THREE MOUNTAIN SUMMIT
RJ75-189	GRA	BIOTITE	AMPHIBOLITE	WILD COVE FISCHOT ISLAND
RJ75-272	GRA	BIOTITE	AMPHIBOLITE	NORTHEAST ISLAND
RJ75-273	GRA	BIOTITE	AMPHIBOLITE	NORTHEAST ISLAND
RJ75-274	GRA	BIOTITE	AMPHIBOLITE	NORTHEAST ISLAND
RJ76-460	GRA	BIOTITE	AMPHIBOLITE	NORTHEAST ISLAND

SAMPLE	* RJ76-41	* RJ76-477	* RJ76-478	* PS -131	* RJ76-071	* RJ76-072	* RJ76-080
SiO2	* 56.87	* 51.73	* 60.62	* 52.98	* 48.52	* 49.25	* 47.48
TiO2	* 1.55	* 1.69	* 1.14	* 2.07	* 1.59	* 1.65	* 1.71
AL2O3	* 14.39	* 14.46	* 13.22	* 16.04	* 13.16	* 13.40	* 13.20
FE2O3	* 2.05	* 2.07	* 1.34	* 1.99	* 4.01	* 3.11	* 4.62
FeO	* 7.78	* 8.09	* 7.20	* 8.39	* 8.49	* 9.19	* 8.82
MNO	* 0.22	* 0.23	* 0.13	* 0.20	* 0.19	* 0.21	* 0.25
MGO	* 4.10	* 4.87	* 3.90	* 3.87	* 7.78	* 7.03	* 7.73
CAO	* 4.31	* 8.05	* 4.66	* 7.16	* 9.98	* 9.99	* 10.43
NA2O	* 1.77	* 2.20	* 1.77	* 2.95	* 2.58	* 2.71	* 2.62
K2O	* 2.34	* 2.44	* 2.61	* 2.07	* 0.14	* 0.43	* 0.28
P2O5	* 0.37	* 0.28	* 0.34	* 0.39	* 0.14	* 0.14	* 0.13
LOI	* 4.24	* 3.84	* 3.37	* 1.92	* 2.04	* 2.25	* 2.03
TOTAL	* 99.99	* 99.95	* 100.30	* 100.03	* 98.62	* 99.36	* 99.30

ZR	* 162	* 152	* 129	* 0	* 108	* 109	* 103
SR	* 204	* 220	* 156	* 0	* 113	* 140	* 91
RB	* 53	* 53	* 71	* 0	* 2	* 6	* 6
ZN	* 109	* 98	* 114	* 0	* 104	* 143	* 121
CU	* 84	* 65	* 89	* 0	* 62	* 97	* 24
BA	* 671	* 322	* 332	* 0	* 49	* 90	* 38
NB	* 22	* 15	* 15	* 0	* 4	* 4	* 9
Y	* 29	* 30	* 34	* 0	* 47	* 49	* 39
PB	* 6	* 15	* 12	* 0	* 7	* 10	* 0
NI	* 67	* 49	* 64	* 0	* 61	* 46	* 51
CR	* 142	* 73	* 134	* 0	* 187	* 125	* 96
V	* 279	* 235	* 283	* 0	* 362	* 387	* 385
GA	* 19	* 20	* 18	* 0	* 21	* 22	* 19

SAMPLE	* RJ76-473 *	* RJ76-477 *	* RJ76-478 *	* DFS-131 *	* RJ75-071 *	* RJ75-075 *	* RJ75-080 *
QZ	19.37	4.53	21.48	4.94	1.20	0.41	0.0
OR	14.44	15.00	15.91	12.47	0.86	2.62	1.70
AB	15.64	19.37	15.45	25.44	22.59	23.61	22.79
AN	19.83	23.28	21.06	24.88	24.75	23.81	24.09
NE	0.0	0.0	0.0	0.0	0.0	0.0	0.0
LC	0.0	0.0	0.0	0.0	0.0	0.0	0.0
COR	2.07	0.0	0.0	0.0	0.0	0.0	0.0
WO	0.0	0.0	0.0	0.0	0.0	0.0	0.0
DI	0.0	13.51	0.43	7.27	20.75	21.53	22.89
WO	0.0	6.84	0.22	3.65	10.69	11.00	11.79
EN	0.0	3.53	0.10	1.71	6.64	6.26	7.30
FS	0.0	3.14	0.11	1.90	3.42	4.27	3.80
HY	21.57	17.17	20.61	17.13	20.33	19.80	15.36
EN	10.66	9.09	9.92	8.11	13.41	11.77	10.10
FS	10.90	8.08	10.69	9.02	6.91	8.04	5.26
OL	0.0	0.0	0.0	0.0	0.0	0.0	2.63
FO	0.0	0.0	0.0	0.0	0.0	0.0	1.67
FA	0.0	0.0	0.0	0.0	0.0	0.0	0.96
LA	0.0	0.0	0.0	0.0	0.0	0.0	0.0
MT	3.10	3.12	2.00	2.94	6.02	4.64	6.89
ILM	3.07	3.34	2.23	4.01	3.13	3.23	3.34
AP	0.90	0.68	0.82	0.92	0.31	0.33	0.31
HM	0.0	0.0	0.0	0.0	0.0	0.0	0.0

RJ76-473	GRA	BIOTITE	AMPHIBOLITE	THREE MOUNTAIN SUMMIT
RJ76-477	GRA	BIOTITE	AMPHIBOLITE	WHALE GROTTO MOUNTAIN
RJ76-478	GRA	BIOTITE	AMPHIBOLITE	WHALE GROTTO MOUNTAIN
DFS73131	GRA	BIOTITE	AMPHIBOLITE	THREE MOUNTAIN SUMMIT
RJ75-071	GRA	QUARTZ	AMPHIBOLITE	THREE MOUNTAIN SUMMIT
RJ75-076	GRA	QUARTZ	AMPHIBOLITE	THREE MOUNTAIN SUMMIT
RJ75-080	GRA	QUARTZ	AMPHIBOLITE	THREE MOUNTAIN SUMMIT

SAMPLE	* RJ75-129 *	* RJ75-130 *	* RJ75-131 *	* RJ75-132 *	* RJ75-137 *	* RJ75-138 *	* RJ75-139 *
ST02	* 48.19 *	* 47.68 *	* 45.03 *	* 49.05 *	* 48.90 *	* 46.88 *	* 47.44 *
TI02	* 1.37 *	* 1.54 *	* 2.11 *	* 1.62 *	* 1.65 *	* 1.61 *	* 1.68 *
AL203	* 14.80 *	* 13.53 *	* 16.88 *	* 13.34 *	* 13.25 *	* 13.44 *	* 13.37 *
FE2O3	* 3.53 *	* 3.63 *	* 4.34 *	* 3.27 *	* 3.42 *	* 1.71 *	* 3.17 *
FE0	* 7.56 *	* 9.01 *	* 7.14 *	* 8.91 *	* 9.32 *	* 10.34 *	* 9.00 *
MNO	* 0.17 *	* 0.21 *	* 0.21 *	* 0.22 *	* 0.21 *	* 0.20 *	* 0.19 *
MGO	* 7.59 *	* 8.50 *	* 4.55 *	* 7.91 *	* 7.19 *	* 8.13 *	* 7.37 *
CAO	* 9.78 *	* 10.17 *	* 11.48 *	* 9.71 *	* 8.54 *	* 10.59 *	* 10.47 *
NA2O	* 3.19 *	* 2.39 *	* 3.05 *	* 2.48 *	* 2.78 *	* 2.92 *	* 3.29 *
K2O	* 0.22 *	* 0.18 *	* 1.00 *	* 0.21 *	* 0.57 *	* 0.22 *	* 0.24 *
P2O5	* 0.13 *	* 0.06 *	* 0.29 *	* 0.12 *	* 0.15 *	* 0.13 *	* 0.16 *
LOI	* 2.51 *	* 2.43 *	* 2.34 *	* 1.84 *	* 2.71 *	* 3.23 *	* 2.46 *
TOTAL	* 99.04 *	* 99.33 *	* 98.42 *	* 98.68 *	* 98.69 *	* 99.40 *	* 98.84 *

ZR	* 96 *	* 104 *	* 153 *	* 109 *	* 108 *	* 99 *	* 104 *
SR	* 180 *	* 117 *	* 379 *	* 111 *	* 105 *	* 107 *	* 126 *
RB	* 5 *	* 4 *	* 17 *	* 4 *	* 8 *	* 4 *	* 3 *
ZN	* 71 *	* 105 *	* 91 *	* 142 *	* 209 *	* 109 *	* 89 *
CU	* 26 *	* 43 *	* 18 *	* 91 *	* 212 *	* 134 *	* 100 *
BA	* 47 *	* 29 *	* 165 *	* 48 *	* 102 *	* 57 *	* 64 *
NB	* 5 *	* 8 *	* 18 *	* 3 *	* 2 *	* 2 *	* 4 *
Y	* 37 *	* 33 *	* 44 *	* 48 *	* 49 *	* 46 *	* 50 *
PB	* 6 *	* 2 *	* 1 *	* 7 *	* 8 *	* 7 *	* 7 *
NI	* 61 *	* 62 *	* 113 *	* 44 *	* 53 *	* 64 *	* 45 *
CR	* 232 *	* 108 *	* 249 *	* 148 *	* 160 *	* 200 *	* 144 *
V	* 300 *	* 363 *	* 347 *	* 354 *	* 365 *	* 379 *	* 367 *
GA	* 13 *	* 20 *	* 21 *	* 19 *	* 23 *	* 21 *	* 20 *

SAMPLE	RJ75-129	RJ75-130	RJ75-131	RJ75-132	RJ75-133	RJ75-134	RJ75-135	RJ75-136	RJ75-137	RJ75-138	RJ75-139	RJ75-140
QZ	0.0	0.0	0.0	0.0	0.0	0.0	0.0	0.0	0.0	0.0	0.0	0.0
QR	1.35	1.10	6.15	1.28	3.51	1.35	1.47	1.35	1.35	1.35	1.35	1.35
AB	27.96	20.87	21.38	21.66	24.50	25.68	25.87	25.87	25.87	25.87	25.87	25.87
AN	26.33	26.48	30.61	25.44	22.90	23.82	21.79	21.79	21.79	21.79	21.79	21.79
NE	0.0	0.0	2.97	0.0	0.0	0.0	0.0	0.0	0.0	0.0	0.0	0.0
LC	0.0	0.0	0.0	0.0	0.0	0.0	0.0	0.0	0.0	0.0	0.0	0.0
COR	0.0	0.0	0.0	0.0	0.0	0.0	0.0	0.0	0.0	0.0	0.0	0.0
WD	0.0	0.0	0.0	0.0	0.0	0.0	0.0	0.0	0.0	0.0	0.0	0.0
DI	18.65	20.44	21.70	19.13	16.55	24.56	25.32	25.32	25.32	25.32	25.32	25.32
WO	9.63	10.52	11.15	9.82	8.46	12.51	12.97	12.97	12.97	12.97	12.97	12.97
EN	6.11	6.45	6.73	5.90	4.85	6.87	7.60	7.60	7.60	7.60	7.60	7.60
FS	2.91	3.47	3.82	3.41	3.23	5.18	4.75	4.75	4.75	4.75	4.75	4.75
HY	10.85	19.45	0.0	22.77	22.99	1.09	1.92	1.92	1.92	1.92	1.92	1.92
EN	7.34	12.65	0.0	14.43	13.80	0.62	1.18	1.18	1.18	1.18	1.18	1.18
FS	3.50	6.81	0.0	8.34	9.20	0.47	0.74	0.74	0.74	0.74	0.74	0.74
OL	6.56	3.07	5.77	0.0	0.0	17.39	12.14	12.14	12.14	12.14	12.14	12.14
FO	4.30	1.93	3.55	0.0	0.0	9.50	7.19	7.19	7.19	7.19	7.19	7.19
FA	2.26	1.14	2.22	0.0	0.0	7.89	4.95	4.95	4.95	4.95	4.95	4.95
LA	0.0	0.0	0.0	0.0	0.0	0.0	0.0	0.0	0.0	0.0	0.0	0.0
MT	5.30	5.43	6.55	4.89	5.16	2.58	4.77	4.77	4.77	4.77	4.77	4.77
ILM	2.70	3.02	4.17	3.18	3.26	3.18	3.31	3.31	3.31	3.31	3.31	3.31
AP	0.31	0.14	0.70	0.29	0.36	0.31	0.39	0.39	0.39	0.39	0.39	0.39
HM	0.0	0.0	0.0	0.0	0.0	0.0	0.0	0.0	0.0	0.0	0.0	0.0

RJ75-129	GRA	QUARTZ	AMPHIBOLITE	LONG RIDGE
RJ75-130	GRA	QUARTZ	AMPHIBOLITE	LONG RIDGE
RJ75-131	GRA	QUARTZ	AMPHIBOLITE	LONG RIDGE
RJ75-136	GRA	QUARTZ	AMPHIBOLITE	THREE MOUNTAIN SUMMIT
RJ75-187	GRA	QUARTZ	AMPHIBOLITE	WILD COVE FISCHOT ISLAND
RJ75268B	GRA	QUARTZ	AMPHIBOLITE	WILD COVE METAGABBRO FISCHOT ISLAND
RJ75-269	GRA	QUARTZ	AMPHIBOLITE	WILD COVE METAGABBRO FISCHOT ISLAND

SAMPLE	* RJ75-279 *	* RJ70-446 *	* RJ70-448 *	* RJ70-453 *	* RJ70-455 *	* RJ70-458 *	* RJ70-459 *
SiO2	* 49.67 *	* 49.28 *	* 47.20 *	* 49.89 *	* 48.43 *	* 51.38 *	* 43.50 *
TiO2	* 1.65 *	* 1.36 *	* 1.43 *	* 1.67 *	* 1.71 *	* 1.60 *	* 2.06 *
AL2O3	* 13.41 *	* 14.71 *	* 15.05 *	* 12.92 *	* 13.71 *	* 13.30 *	* 12.66 *
FE2O3	* 3.53 *	* 5.54 *	* 3.32 *	* 4.43 *	* 4.39 *	* 3.50 *	* 4.34 *
FeO	* 8.66 *	* 6.81 *	* 8.79 *	* 8.10 *	* 8.62 *	* 8.31 *	* 10.75 *
MNO	* 0.33 *	* 0.20 *	* 0.20 *	* 0.21 *	* 0.21 *	* 0.21 *	* 0.25 *
MGO	* 8.00 *	* 5.25 *	* 5.83 *	* 7.08 *	* 5.79 *	* 6.27 *	* 9.25 *
CAO	* 8.20 *	* 10.12 *	* 11.00 *	* 8.87 *	* 9.89 *	* 8.74 *	* 10.14 *
NA2O	* 2.84 *	* 2.35 *	* 2.66 *	* 2.67 *	* 2.59 *	* 3.21 *	* 1.96 *
K2O	* 0.29 *	* 1.40 *	* 0.72 *	* 0.64 *	* 0.53 *	* 0.36 *	* 0.25 *
P2O5	* 0.13 *	* 0.17 *	* 0.13 *	* 0.14 *	* 0.15 *	* 0.14 *	* 0.13 *
LOI	* 2.56 *	* 2.38 *	* 2.96 *	* 2.64 *	* 2.59 *	* 2.66 *	* 2.17 *
TOTAL	* 99.27 *	* 99.57 *	* 99.29 *	* 99.26 *	* 98.61 *	* 99.68 *	* 97.46 *

ZR	* 99 *	* 104 *	* 89 *	* 109 *	* 111 *	* 111 *	* 102 *
SR	* 94 *	* 236 *	* 155 *	* 185 *	* 213 *	* 220 *	* 102 *
RB	* 4 *	* 25 *	* 12 *	* 13 *	* 10 *	* 4 *	* 1 *
ZN	* 178 *	* 130 *	* 118 *	* 115 *	* 114 *	* 211 *	* 157 *
CU	* 57 *	* 44 *	* 51 *	* 74 *	* 18 *	* 78 *	* 83 *
BA	* 69 *	* 104 *	* 99 *	* 124 *	* 90 *	* 58 *	* 66 *
NB	* 9 *	* 9 *	* 9 *	* 9 *	* 9 *	* 10 *	* 9 *
Y	* 37 *	* 31 *	* 34 *	* 38 *	* 36 *	* 36 *	* 45 *
PB	* 0 *	* 3 *	* 5 *	* 0 *	* 1 *	* 0 *	* 0 *
NI	* 50 *	* 63 *	* 62 *	* 48 *	* 52 *	* 49 *	* 68 *
CR	* 111 *	* 133 *	* 196 *	* 106 *	* 109 *	* 97 *	* 117 *
V	* 405 *	* 286 *	* 316 *	* 380 *	* 384 *	* 354 *	* 469 *
GA	* 19 *	* 20 *	* 19 *	* 17 *	* 20 *	* 20 *	* 21 *

SAMPLE	RJ75-279	RJ75-280	RJ75-281	RJ75-282	RJ75-283	RJ75-284	RJ75-285	RJ75-286	RJ75-287	RJ75-288
OZ	1.55	3.57	0.0	3.52	2.75	3.83	0.0	0.0	0.0	0.0
OR	1.77	8.51	4.42	3.91	3.26	2.19	1.55	0.0	0.0	0.0
AB	24.85	20.46	23.36	23.38	22.82	28.00	17.40	0.0	0.0	0.0
AN	23.77	25.19	29.03	22.13	25.22	21.46	25.24	0.0	0.0	0.0
NE	0.0	0.0	0.0	0.0	0.0	0.0	0.0	0.0	0.0	0.0
LC	0.0	0.0	0.0	0.0	0.0	0.0	0.0	0.0	0.0	0.0
COR	0.0	0.0	0.0	0.0	0.0	0.0	0.0	0.0	0.0	0.0
WD	0.0	0.0	0.0	0.0	0.0	0.0	0.0	0.0	0.0	0.0
DI	14.14	19.16	22.78	18.20	20.31	18.19	20.86	0.0	0.0	0.0
WO	7.28	10.16	11.59	9.39	10.38	9.31	10.72	0.0	0.0	0.0
EN	4.44	6.49	6.27	5.87	5.92	5.39	6.45	0.0	0.0	0.0
FS	2.43	3.01	4.92	2.95	4.01	3.49	3.70	0.0	0.0	0.0
HY	24.98	10.18	6.61	18.59	15.26	17.64	9.66	0.0	0.0	0.0
EN	16.16	6.96	3.70	12.38	9.10	10.70	6.14	0.0	0.0	0.0
FS	8.82	3.22	2.91	6.21	6.16	6.93	3.52	0.0	0.0	0.0
OL	0.0	0.0	6.67	0.0	0.0	0.0	13.26	0.0	0.0	0.0
FO	0.0	0.0	3.57	0.0	0.0	0.0	8.12	0.0	0.0	0.0
FA	0.0	0.0	3.10	0.0	0.0	0.0	5.14	0.0	0.0	0.0
LA	0.0	0.0	0.0	0.0	0.0	0.0	0.0	0.0	0.0	0.0
MT	5.29	8.26	5.00	6.65	6.63	5.23	6.60	0.0	0.0	0.0
ILM	3.24	2.66	2.82	3.28	3.38	3.13	4.11	0.0	0.0	0.0
AP	0.31	0.41	0.31	0.34	0.36	0.34	0.32	0.0	0.0	0.0
HM	0.0	0.0	0.0	0.0	0.0	0.0	0.0	0.0	0.0	0.0

RJ75-279	GRA	QUARTZ	AMPHIBOLITE	NORTHEAST ISLAND
RJ76-446	GRA	QUARTZ	AMPHIBOLITE	FISCHOT ISLAND
RJ76-448	GRA	QUARTZ	AMPHIBOLITE	NORTHEAST ISLAND
RJ76-455	GRA	QUARTZ	AMPHIBOLITE	NORTHEAST ISLAND
RJ76-456	GRA	QUARTZ	AMPHIBOLITE	NORTHEAST ISLAND
RJ76-458	GRA	QUARTZ	AMPHIBOLITE	NORTHEAST ISLAND
RJ76-459	GRA	QUARTZ	AMPHIBOLITE	NORTHEAST ISLAND

SAMPLE	* RJ76-303 *	* RJ76-351 *	* RJ76-352 *	* RJ76-353 *	* RJ76-355 *	* RJ76-372 *	* RJ76-126 *
SI02	* 46.18 *	* 44.90 *	* 46.08 *	* 46.66 *	* 49.74 *	* 48.76 *	* 46.72 *
TI02	* 1.97 *	* 1.81 *	* 1.49 *	* 1.38 *	* 1.51 *	* 1.72 *	* 0.47 *
AL203	* 13.47 *	* 13.20 *	* 13.33 *	* 14.72 *	* 12.81 *	* 13.34 *	* 15.60 *
FE203	* 3.20 *	* 3.36 *	* 3.40 *	* 2.50 *	* 2.49 *	* 1.97 *	* 1.50 *
FE0	* 10.65 *	* 10.36 *	* 9.51 *	* 8.65 *	* 10.46 *	* 10.91 *	* 5.93 *
MNO	* 0.22 *	* 0.25 *	* 0.22 *	* 0.17 *	* 0.19 *	* 0.22 *	* 0.14 *
MGO	* 7.16 *	* 9.36 *	* 7.94 *	* 7.12 *	* 6.63 *	* 6.43 *	* 9.83 *
CAO	* 10.11 *	* 8.98 *	* 11.26 *	* 10.88 *	* 9.24 *	* 9.27 *	* 14.00 *
NA2O	* 2.73 *	* 2.20 *	* 2.43 *	* 3.05 *	* 3.76 *	* 3.58 *	* 1.81 *
K2O	* 0.55 *	* 0.79 *	* 0.75 *	* 0.55 *	* 0.15 *	* 0.21 *	* 0.08 *
P2O5	* 0.19 *	* 0.14 *	* 0.14 *	* 0.09 *	* 0.14 *	* 0.17 *	* 0.03 *
LOI	* 2.70 *	* 3.05 *	* 2.63 *	* 3.17 *	* 2.05 *	* 2.18 *	* 2.71 *
TOTAL	* 99.13 *	* 98.40 *	* 99.18 *	* 98.94 *	* 99.17 *	* 98.76 *	* 98.82 *

ZR	* 117 *	* 106 *	* 88 *	* 105 *	* 91 *	* 115 *	* 49 *
SR	* 248 *	* 379 *	* 579 *	* 361 *	* 121 *	* 229 *	* 176 *
RB	* 9 *	* 18 *	* 19 *	* 14 *	* 3 *	* 5 *	* 2 *
ZN	* 60 *	* 182 *	* 88 *	* 63 *	* 86 *	* 109 *	* 81 *
CU	* 24 *	* 106 *	* 48 *	* 48 *	* 61 *	* 68 *	* 72 *
BA	* 170 *	* 280 *	* 369 *	* 158 *	* 154 *	* 574 *	* 49 *
NB	* 7 *	* 9 *	* 4 *	* 8 *	* 8 *	* 9 *	* 0 *
Y	* 45 *	* 46 *	* 32 *	* 33 *	* 41 *	* 39 *	* 25 *
PB	* 0 *	* 0 *	* 0 *	* 1 *	* 0 *	* 9 *	* 6 *
NI	* 47 *	* 58 *	* 70 *	* 63 *	* 49 *	* 41 *	* 173 *
CR	* 82 *	* 105 *	* 140 *	* 176 *	* 72 *	* 77 *	* 523 *
V	* 442 *	* 431 *	* 394 *	* 314 *	* 378 *	* 404 *	* 182 *
GA	* 17 *	* 17 *	* 21 *	* 18 *	* 19 *	* 21 *	* 17 *

OR	*	3.37	*	4.90	*	4.59	*	3.39	*	0.91	*	1.28	*	0.49	*
AB	*	23.95	*	19.52	*	21.23	*	24.27	*	32.76	*	31.36	*	15.94	*
AN	*	23.72	*	24.97	*	24.08	*	25.95	*	18.16	*	20.41	*	35.59	*
NE	*	0.0	*	0.0	*	0.03	*	1.45	*	0.0	*	0.0	*	0.0	*
LC	*	0.0	*	0.0	*	0.0	*	0.0	*	0.0	*	0.0	*	0.0	*
COR	*	0.0	*	0.0	*	0.0	*	0.0	*	0.0	*	0.0	*	0.0	*
WO	*	0.0	*	0.0	*	0.0	*	0.0	*	0.0	*	0.0	*	0.0	*
DI	*	22.18	*	16.92	*	26.78	*	24.34	*	23.18	*	21.57	*	29.31	*
WO	*	11.28	*	8.69	*	13.71	*	12.44	*	11.74	*	10.88	*	15.23	*
EN	*	6.09	*	5.18	*	7.98	*	7.13	*	6.00	*	5.35	*	10.25	*
FS	*	4.81	*	3.05	*	5.09	*	4.77	*	6.45	*	5.34	*	3.83	*
HY	*	5.17	*	8.72	*	0.0	*	0.0	*	9.61	*	7.98	*	1.29	*
EN	*	2.89	*	5.49	*	0.0	*	0.0	*	5.03	*	3.99	*	0.94	*
FS	*	2.28	*	3.23	*	0.0	*	0.0	*	4.57	*	3.99	*	0.35	*
OL	*	12.46	*	15.91	*	14.91	*	13.86	*	8.38	*	10.65	*	14.12	*
FO	*	6.66	*	9.65	*	8.76	*	7.98	*	4.19	*	5.07	*	10.01	*
FA	*	5.79	*	6.26	*	6.15	*	5.88	*	4.19	*	5.58	*	4.11	*
LA	*	0.0	*	0.0	*	0.0	*	0.0	*	0.0	*	0.0	*	0.0	*
MT	*	4.81	*	5.11	*	5.11	*	3.78	*	3.72	*	2.96	*	2.26	*
ILM	*	3.88	*	3.61	*	2.93	*	2.74	*	2.95	*	3.38	*	0.93	*
AP	*	0.46	*	0.34	*	0.34	*	0.22	*	0.33	*	0.41	*	0.07	*
HM	*	0.0	*	0.0	*	0.0	*	0.0	*	0.0	*	0.0	*	0.0	*

RJ76-503 GRA QUARTZ AMPHIBOLITE DEER PARK
 RJ76-551 GRA QUARTZ AMPHIBOLITE BRIMSTONE POND
 RJ76-552 GRA QUARTZ AMPHIBOLITE BRIMSTONE POND
 RJ76-553 GRA QUARTZ AMPHIBOLITE BRIMSTONE POND
 RJ76-565 GRA QUARTZ AMPHIBOLITE QUIRPON ISLAND
 RJ76-572 GRA QUARTZ AMPHIBOLITE QUIRPON ISLAND
 RJ75-128 GRA PLAGIOCLASE AMPHIBOLITE LONG RIDGE

SAMPLE	* RJ75-138 *	* RJ75-207 *	* RJ75268A *	* RJ75-270 *	* RJ75-312 *	* RJ75-302 *	* RJ75-506 *
SI02	* 47.16 *	* 49.17 *	* 51.51 *	* 46.34 *	* 49.73 *	* 47.86 *	* 48.10 *
TI02	* 0.25 *	* 0.25 *	* 0.53 *	* 0.41 *	* 0.55 *	* 0.25 *	* 0.79 *
AL203	* 20.78 *	* 19.06 *	* 16.34 *	* 19.31 *	* 13.72 *	* 15.00 *	* 13.26 *
FE203	* 0.52 *	* 1.98 *	* 1.21 *	* 0.88 *	* 1.62 *	* 1.38 *	* 2.83 *
FE0	* 2.91 *	* 2.69 *	* 5.09 *	* 5.07 *	* 7.70 *	* 4.42 *	* 6.60 *
MNO	* 0.09 *	* 0.08 *	* 0.13 *	* 0.11 *	* 0.18 *	* 0.12 *	* 0.17 *
MGO	* 6.02 *	* 5.94 *	* 6.62 *	* 7.50 *	* 9.72 *	* 9.38 *	* 9.14 *
CAO	* 13.66 *	* 11.87 *	* 10.02 *	* 12.65 *	* 7.14 *	* 13.63 *	* 12.50 *
NA2O	* 2.66 *	* 3.31 *	* 4.28 *	* 2.19 *	* 3.13 *	* 2.27 *	* 2.32 *
K2O	* 0.19 *	* 0.78 *	* 0.39 *	* 0.23 *	* 1.24 *	* 0.41 *	* 0.15 *
P2O5	* 0.04 *	* 0.04 *	* 0.06 *	* 0.04 *	* 0.03 *	* 0.02 *	* 0.03 *
LOI	* 4.10 *	* 3.00 *	* 2.65 *	* 4.04 *	* 4.10 *	* 2.91 *	* 2.72 *
TOTAL	* 98.38 *	* 98.17 *	* 98.83 *	* 98.77 *	* 98.86 *	* 97.65 *	* 98.61 *

ZR	* 49 *	* 50 *	* 68 *	* 47 *	* 29 *	* 35 *	* 39 *
SR	* 166 *	* 197 *	* 212 *	* 164 *	* 150 *	* 366 *	* 183 *
RB	* 3 *	* 13 *	* 6 *	* 3 *	* 23 *	* 9 *	* 3 *
ZN	* 141 *	* 77 *	* 78 *	* 76 *	* 64 *	* 41 *	* 60 *
CU	* 94 *	* 76 *	* 86 *	* 105 *	* 68 *	* 101 *	* 43 *
BA	* 33 *	* 90 *	* 55 *	* 36 *	* 1615 *	* 222 *	* 46 *
NB	* 1 *	* 0 *	* 0 *	* 1 *	* 5 *	* 5 *	* 6 *
Y	* 21 *	* 20 *	* 25 *	* 22 *	* 21 *	* 13 *	* 23 *
PB	* 7 *	* 7 *	* 7 *	* 8 *	* 0 *	* 0 *	* 7 *
NI	* 171 *	* 149 *	* 128 *	* 159 *	* 73 *	* 140 *	* 82 *
CR	* 613 *	* 605 *	* 554 *	* 627 *	* 117 *	* 598 *	* 213 *
V	* 89 *	* 85 *	* 147 *	* 127 *	* 262 *	* 154 *	* 237 *
GA	* 19 *	* 17 *	* 19 *	* 20 *	* 14 *	* 11 *	* 17 *

GR	*	0.0	*	0.0	*	0.0	*	0.0	*	0.0	*	0.0	*	0.0	*
AB	*	1.19	*	4.84	*	2.39	*	1.43	*	7.73	*	2.56	*	0.92	*
AN	*	20.99	*	27.21	*	37.22	*	19.54	*	27.95	*	19.12	*	20.47	*
NE	*	46.83	*	36.58	*	25.16	*	44.48	*	20.82	*	31.17	*	26.41	*
LC	*	1.55	*	1.18	*	0.21	*	0.0	*	0.0	*	0.63	*	0.0	*
COR	*	0.0	*	0.0	*	0.0	*	0.0	*	0.0	*	0.0	*	0.0	*
WO	*	0.0	*	0.0	*	0.0	*	0.0	*	0.0	*	0.0	*	0.0	*
DI	*	19.80	*	19.87	*	21.13	*	17.33	*	13.25	*	32.01	*	30.61	*
WO	*	10.34	*	10.46	*	10.92	*	8.97	*	6.83	*	16.73	*	15.89	*
EN	*	7.25	*	7.84	*	6.98	*	5.84	*	4.26	*	11.84	*	10.61	*
FS	*	2.22	*	1.57	*	3.23	*	2.51	*	2.15	*	3.44	*	4.10	*
HY	*	0.0	*	0.0	*	0.0	*	1.83	*	12.29	*	0.0	*	9.17	*
EN	*	0.0	*	0.0	*	0.0	*	1.28	*	8.17	*	0.0	*	6.61	*
FS	*	0.0	*	0.0	*	0.0	*	0.55	*	4.13	*	0.0	*	2.55	*
OL	*	8.10	*	6.57	*	10.74	*	12.99	*	14.30	*	11.85	*	6.50	*
FO	*	6.05	*	5.38	*	7.11	*	8.81	*	9.19	*	8.98	*	4.56	*
FA	*	2.04	*	1.19	*	3.63	*	4.18	*	5.11	*	2.88	*	1.94	*
LA	*	0.0	*	0.0	*	0.0	*	0.0	*	0.0	*	0.0	*	0.0	*
MT	*	0.80	*	3.01	*	1.82	*	1.35	*	2.48	*	2.11	*	4.28	*
ILM	*	0.50	*	0.50	*	1.05	*	0.82	*	1.10	*	0.50	*	1.56	*
AP	*	0.10	*	0.10	*	0.14	*	0.10	*	0.07	*	0.05	*	0.07	*
HM	*	0.0	*	0.0	*	0.0	*	0.0	*	0.0	*	0.0	*	0.0	*

RJ75-188	GRA	PLAGIOCLASE	AMPHIBOLITE	WILD COVE	METAGABBRO	FISCHOT ISLAND
RJ75-267	GRA	PLAGIOCLASE	AMPHIBOLITE	WILD COVE	METAGABBRO	FISCHOT ISLAND
RJ75268A	GRA	PLAGIOCLASE	AMPHIBOLITE	WILD COVE	METAGABBRO	FISCHOT ISLAND
RJ75-270	GRA	PLAGIOCLASE	AMPHIBOLITE	WILD COVE	METAGABBRO	FISCHOT ISLAND
RJ75-315	GRA	PLAGIOCLASE	AMPHIBOLITE	MILAN ARM	MELANGE	
RJ76-502	GRA	PLAGIOCLASE	AMPHIBOLITE	DEER PARK		
RJ76-504	GRA	PLAGIOCLASE	AMPHIBOLITE	DEER PARK		

SAMPLE	* RJ70-554 *	RJ75-560 *	RJ75-564 *	RJ75-570 *	RJ75050L *	RJ75130L *	RJ75-575 *
SI02	* 48.28 *	46.00	* 47.97 *	49.11	* 75.13 *	79.05	* 71.79 *
TI02	* 0.28 *	0.76	* 0.65 *	0.68	* 0.18 *	0.50	* 0.16 *
AL203	* 14.34 *	10.46	* 15.14 *	14.54	* 12.62 *	9.60	* 14.22 *
FE203	* 1.59 *	4.30	* 2.34 *	2.67	* 0.76 *	1.25	* 0.32 *
FEO	* 4.57 *	8.07	* 5.90 *	5.41	* 0.99 *	1.75	* 0.77 *
MNO	* 0.13 *	0.20	* 0.13 *	0.14	* 0.03 *	0.04	* 0.02 *
MGO	* 9.75 *	13.44	* 7.90 *	8.18	* 0.75 *	1.18	* 0.62 *
CAO	* 12.93 *	11.29	* 11.46 *	13.14	* 4.68 *	3.87	* 3.45 *
NA2O	* 2.22 *	1.58	* 2.65 *	2.27	* 3.84 *	2.81	* 5.33 *
K2O	* 0.60 *	0.24	* 0.29 *	0.33	* 0.14 *	0.12	* 0.81 *
P2O5	* 0.02 *	0.11	* 0.04 *	0.04	* 0.03 *	0.03	* 0.01 *
LOI	* 3.58 *	3.25	* 2.87 *	2.31	* 1.53 *	1.22	* 1.63 *
TOTAL	* 98.29 *	99.70	* 98.34 *	98.82	* 100.68 *	101.42	* 99.13 *

ZR	* 32 *	29	* 45 *	38	* 43 *	31	* 52 *
SR	* 412 *	102	* 308 *	271	* 163 *	163	* 230 *
RB	* 22 *	7	* 10 *	10	* 2 *	4	* 23 *
ZN	* 39 *	76	* 64 *	52	* 21 *	24	* 25 *
CU	* 35 *	11	* 112 *	101	* 15 *	20	* 27 *
BA	* 323 *	215	* 285 *	268	* 39 *	34	* 124 *
NB	* 2 *	7	* 8 *	4	* 6 *	7	* 5 *
Y	* 13 *	15	* 17 *	19	* 13 *	13	* 5 *
PB	* 0 *	3	* 1 *	1	* 0 *	0	* 3 *
NI	* 115 *	276	* 141 *	85	* 3 *	7	* 1 *
CR	* 397 *	192	* 318 *	380	* 17 *	25	* 8 *
V	* 154 *	224	* 209 *	225	* 42 *	72	* 30 *
GA	* 12 *	13	* 16 *	16	* 12 *	10	* 12 *

SAMPLE	RJ76-554	RJ76-560	RJ76-564	RJ76-570	RJ75080L	RJ75130L	RJ75-275
QZ	0.0	0.0	0.0	0.0	0.0	0.0	0.0
OR	3.74	1.47	1.80	2.02	0.83	0.71	4.91
AB	19.83	13.86	23.49	19.90	32.77	23.73	46.26
AN	28.92	21.50	32.77	29.54	16.93	13.20	12.81
NE	0.0	0.0	0.0	0.0	0.0	0.0	0.0
LC	0.0	0.0	0.0	0.0	0.0	0.0	0.0
COR	0.0	0.0	0.0	0.0	0.0	0.0	0.0
WO	0.0	0.0	0.0	0.0	0.0	0.0	0.0
DI	30.88	28.67	21.35	30.25	5.10	4.67	3.81
WO	16.15	14.96	11.07	15.76	2.63	2.41	1.96
EN	11.49	10.46	7.29	10.84	1.64	1.52	1.16
FS	3.24	3.25	2.99	3.65	0.83	0.74	0.69
HY	2.03	12.33	7.55	10.57	0.37	2.10	0.67
EN	1.58	9.41	5.35	7.91	0.25	1.41	0.42
FS	0.45	2.92	2.20	2.67	0.13	0.69	0.25
OL	11.55	13.95	8.10	2.27	0.0	0.0	0.0
FO	8.81	10.39	5.58	1.65	0.0	0.0	0.0
FA	2.74	3.55	2.52	0.61	0.0	0.0	0.0
LA	0.0	0.0	0.0	0.0	0.0	0.0	0.0
MT	2.43	6.46	3.55	4.01	1.11	1.81	0.48
ILM	0.56	1.50	1.29	1.34	0.34	0.95	0.31
AP	0.05	0.27	0.10	0.10	0.07	0.07	0.02
HM	0.0	0.0	0.0	0.0	0.0	0.0	0.0

RJ76-554	GRA	PLAGIOCLASE AMPHIBOLITE	BRIMSTONE POND
RJ76-560	GRA	PLAGIOCLASE AMPHIBOLITE	HOWE HARBOUR
RJ76-564	GRA	PLAGIOCLASE AMPHIBOLITE	QUIRPON ISLAND
RJ76-570	GRA	PLAGIOCLASE AMPHIBOLITE	QUIRPON ISLAND
RJ75080L	GRA	QUARTZOFELDSPATHIC BAND	THREE MOUNTAIN SUMMIT
RJ75130L	GRA	QUARTZOFELDSPATHIC BAND	LONG RIDGE
RJ75-275	GRA	PARTIAL MELT	NORTHEAST ISLAND

SI02	*	62.45	*	51.11	*
TI02	*	0.07	*	1.68	*
AL2O3	*	18.35	*	17.82	*
FE2O3	*	0.69	*	2.15	*
FeO	*	0.72	*	6.29	*
MNO	*	0.03	*	0.14	*
MGO	*	1.16	*	1.94	*
CAO	*	1.05	*	5.34	*
NA2O	*	9.68	*	2.97	*
K2O	*	1.83	*	5.65	*
P2O5	*	0.04	*	0.64	*
LOI	*	1.66	*	2.15	*
TOTAL	*	98.23	*	97.88	*

ZR	*	30	*	506	*
SR	*	242	*	573	*
RB	*	30	*	66	*
ZN	*	21	*	85	*
CU	*	10	*	65	*
BA	*	4880	*	1560	*
NB	*	5	*	50	*
Y	*	10	*	27	*
PB	*	3	*	12	*
NI	*	9	*	19	*
CR	*	22	*	22	*
V	*	32	*	112	*
GA	*	12	*	19	*

CR	*	11.20	*	34.87	*
AB	*	76.31	*	25.93	*
AN	*	2.67	*	19.43	*
NE	*	4.61	*	0.17	*
LC	*	0.0	*	0.0	*
COR	*	0.0	*	0.0	*
WO	*	0.0	*	0.0	*
DI	*	1.95	*	3.28	*
WO	*	1.02	*	1.63	*
EN	*	0.75	*	0.66	*
FS	*	0.18	*	0.99	*
HY	*	0.0	*	0.0	*
EN	*	0.0	*	0.0	*
FS	*	0.0	*	0.0	*
OL	*	1.99	*	8.17	*
FO	*	1.57	*	3.07	*
FA	*	0.42	*	5.09	*
LA	*	0.0	*	0.0	*
MT	*	1.04	*	3.26	*
ILM	*	0.14	*	3.33	*
AP	*	0.10	*	1.55	*
HM	*	0.0	*	0.0	*

RJ75315L	GRA	PARTIAL	MELT	MILAN ARM	MELANGE
RJ76-451	GRA	PARTIAL	MELT	NORTHEAST	ISLAND

Table I.vi. Major and trace element analyses and CIPW norms, Long Ridge Metagabbro.

SI02	*	52.93	*	51.37	*	46.00	*	48.07	*	47.07	*	41.91	*	38.06	*
TI02	*	0.04	*	0.03	*	0.20	*	0.27	*	0.20	*	0.05	*	0.03	*
AL203	*	24.30	*	24.68	*	18.11	*	16.42	*	17.59	*	18.45	*	8.29	*
FE203	*	0.45	*	1.24	*	0.66	*	1.33	*	1.02	*	1.11	*	4.53	*
FEO	*	0.01	*	0.0	*	4.52	*	4.63	*	3.49	*	3.23	*	3.54	*
MNO	*	0.02	*	0.02	*	0.10	*	0.11	*	0.10	*	0.08	*	0.15	*
MGO	*	0.22	*	0.06	*	9.87	*	8.83	*	8.35	*	15.28	*	29.27	*
CAO	*	9.32	*	14.00	*	13.75	*	13.37	*	15.04	*	11.35	*	5.93	*
NA2O	*	5.80	*	5.59	*	1.58	*	2.23	*	1.67	*	1.36	*	0.11	*
K2O	*	1.69	*	0.06	*	0.07	*	0.05	*	0.20	*	0.21	*	0.03	*
P2O5	*	0.07	*	0.06	*	0.02	*	0.02	*	0.01	*	0.02	*	0.01	*
LOI	*	2.17	*	1.39	*	3.16	*	2.68	*	2.57	*	5.03	*	9.60	*
TOTAL	*	97.02	*	98.50	*	98.04	*	98.01	*	97.31	*	98.08	*	99.55	*

ZR	*	105	*	76	*	15	*	19	*	17	*	13	*	10	*
SR	*	418	*	234	*	108	*	175	*	105	*	105	*	44	*
RB	*	23	*	2	*	3	*	4	*	4	*	7	*	2	*
ZN	*	15	*	15	*	40	*	48	*	35	*	37	*	44	*
CU	*	7	*	8	*	43	*	54	*	16	*	86	*	66	*
BA	*	227	*	21	*	0	*	18	*	16	*	25	*	0	*
NB	*	3	*	5	*	4	*	4	*	6	*	5	*	4	*
Y	*	6	*	8	*	11	*	15	*	11	*	7	*	6	*
PB	*	0	*	0	*	4	*	0	*	0	*	4	*	3	*
NI	*	3	*	0	*	193	*	151	*	127	*	508	*	1272	*
CR	*	7	*	9	*	722	*	581	*	537	*	353	*	2409	*
V	*	17	*	25	*	117	*	146	*	104	*	16	*	25	*
GA	*	16	*	18	*	16	*	17	*	14	*	14	*	6	*

OR	*	10.53	*	0.37	*	0.44	*	0.31	*	1.25	*	1.33	*	0.20	*
AB	*	39.99	*	36.43	*	14.06	*	19.79	*	14.92	*	7.07	*	1.03	*
AN	*	37.20	*	43.33	*	44.39	*	36.34	*	42.13	*	46.88	*	24.50	*
NE	*	6.37	*	6.65	*	0.0	*	0.0	*	0.0	*	2.87	*	0.0	*
LC	*	0.0	*	0.0	*	0.0	*	0.0	*	0.0	*	0.0	*	0.0	*
COR	*	0.0	*	0.0	*	0.0	*	0.0	*	0.0	*	0.0	*	0.0	*
WO	*	3.95	*	11.42	*	0.0	*	0.0	*	0.0	*	0.0	*	0.0	*
DI	*	1.25	*	0.33	*	21.90	*	26.51	*	29.15	*	10.65	*	6.36	*
WO	*	0.37	*	0.18	*	11.43	*	13.82	*	15.27	*	5.64	*	3.40	*
EN	*	0.58	*	0.15	*	7.99	*	9.57	*	11.01	*	4.42	*	2.85	*
FS	*	0.0	*	0.0	*	2.48	*	3.12	*	2.87	*	0.59	*	0.12	*
HY	*	0.0	*	0.0	*	3.16	*	5.61	*	2.49	*	0.0	*	10.97	*
EN	*	0.0	*	0.0	*	2.42	*	4.24	*	1.98	*	0.0	*	10.54	*
FS	*	0.0	*	0.0	*	0.75	*	1.38	*	0.52	*	0.0	*	0.43	*
DL	*	0.0	*	0.0	*	14.56	*	8.82	*	8.08	*	29.32	*	49.55	*
FO	*	0.0	*	0.0	*	10.86	*	6.49	*	6.28	*	25.56	*	47.41	*
FA	*	0.0	*	0.0	*	3.71	*	2.33	*	1.80	*	3.79	*	2.14	*
LA	*	0.0	*	0.0	*	0.0	*	0.0	*	0.0	*	0.0	*	0.0	*
MT	*	0.0	*	0.0	*	1.01	*	2.02	*	1.56	*	1.73	*	7.30	*
ILM	*	0.07	*	0.04	*	0.40	*	0.54	*	0.40	*	0.10	*	0.06	*
AP	*	0.17	*	0.14	*	0.05	*	0.05	*	0.02	*	0.05	*	0.03	*
HM	*	0.47	*	1.28	*	0.0	*	0.0	*	0.0	*	0.0	*	0.0	*

RJ76-409 LRC ANORTHOSITE
 RJ76-410 LRC ANORTHOSITE
 RJ76-402 LRC METAGABBRO
 RJ76-405 LRC METAGABBRO
 RJ76-406 LRC METAGABBRO
 RJ76-408 LRC METAGABBRO
 RJ76-412 LRC TROCTOLITE

SAMPLE		RJ75-401		RJ75-411	
SiO2	*	38.49	*	37.02	*
TI O2	*	0.01	*	0.06	*
AL2O3	*	0.28	*	2.46	*
FE2O3	*	3.32	*	8.23	*
FEO	*	6.56	*	2.21	*
MNO	*	0.14	*	0.15	*
MGO	*	45.55	*	35.66	*
CAO	*	0.18	*	1.13	*
NA2O	*	0.03	*	0.15	*
K2O	*	0.02	*	0.02	*
P2O5	*	0.0	*	0.0	*
LOI	*	5.32	*	12.64	*
TOTAL	*	99.90	*	99.73	*

ZR	*	7	*	6	*
SR	*	0	*	3	*
RB	*	0	*	2	*
ZN	*	53	*	39	*
CU	*	22	*	52	*
BA	*	0	*	0	*
NB	*	5	*	4	*
Y	*	7	*	6	*
PB	*	0	*	0	*
NI	*	2459	*	1752	*
CR	*	2964	*	3846	*
V	*	12	*	56	*
GA	*	2	*	2	*

DR	*	0.12	*	0.14	*
AB	*	0.27	*	1.46	*
AN	*	0.50	*	5.44	*
NE	*	0.0	*	0.0	*
LC	*	0.0	*	0.0	*
COR	*	0.0	*	0.16	*
WO	*	0.0	*	0.0	*
DI	*	0.27	*	0.0	*
WO	*	0.14	*	0.0	*
EN	*	0.12	*	0.0	*
FS	*	0.01	*	0.0	*
HY	*	6.38	*	27.16	*
EN	*	5.88	*	27.16	*
FS	*	0.50	*	0.0	*
OL	*	87.25	*	52.43	*
FO	*	79.84	*	52.43	*
FA	*	7.41	*	0.0	*
LA	*	0.0	*	0.0	*
MT	*	5.09	*	8.54	*
ILM	*	0.02	*	0.13	*
AP	*	0.0	*	0.0	*
HM	*	0.0	*	3.56	*

RJ76-401
RJ76-411

LRC
LRC

DUNITE
DUNITE

Table I.vii. Major and trace element analyses and CIPW norms, White Hills
Peridotite.

SiO2	*	34.46	*	36.18	*	34.08	*	43.35	*	43.87	*	46.23	*	46.09	*
TiO2	*	5.14	*	4.40	*	5.45	*	2.63	*	2.83	*	2.79	*	2.26	*
AL2O3	*	6.58	*	10.28	*	8.97	*	11.03	*	16.20	*	16.52	*	16.86	*
FE2O3	*	6.85	*	2.12	*	2.35	*	2.81	*	2.23	*	2.22	*	2.12	*
FEO	*	13.65	*	17.01	*	17.13	*	9.54	*	9.32	*	8.80	*	8.95	*
MNO	*	0.31	*	0.38	*	0.36	*	0.22	*	0.17	*	0.26	*	0.24	*
MGO	*	6.67	*	6.71	*	5.30	*	9.32	*	3.44	*	2.79	*	3.11	*
CAO	*	17.92	*	13.63	*	15.59	*	14.84	*	10.55	*	8.86	*	9.07	*
NA2O	*	1.26	*	0.97	*	1.80	*	2.20	*	4.45	*	5.16	*	5.31	*
K2O	*	0.18	*	1.81	*	1.03	*	0.93	*	1.16	*	1.12	*	1.14	*
P2O5	*	2.16	*	0.68	*	1.78	*	0.15	*	1.60	*	1.16	*	1.29	*
LOI	*	2.43	*	3.67	*	3.76	*	2.42	*	2.08	*	2.18	*	2.09	*
TOTAL	*	97.61	*	97.84	*	97.60	*	99.44	*	97.90	*	98.09	*	98.53	*

ZR	*	238	*	275	*	295	*	143	*	118	*	187	*	154	*
SR	*	949	*	1463	*	1653	*	661	*	2854	*	2651	*	2446	*
RB	*	1	*	48	*	5	*	12	*	9	*	10	*	10	*
ZN	*	163	*	193	*	201	*	94	*	91	*	117	*	98	*
CU	*	44	*	23	*	63	*	57	*	23	*	33	*	18	*
BA	*	140	*	2259	*	539	*	752	*	1386	*	1752	*	950	*
NB	*	24	*	102	*	142	*	23	*	17	*	85	*	34	*
Y	*	37	*	37	*	79	*	29	*	29	*	50	*	31	*
PB	*	1	*	5	*	2	*	0	*	0	*	2	*	1	*
NI	*	10	*	30	*	11	*	163	*	10	*	10	*	7	*
CR	*	1	*	54	*	0	*	290	*	6	*	0	*	5	*
V	*	362	*	250	*	270	*	286	*	165	*	136	*	124	*
GA	*	22	*	29	*	23	*	18	*	20	*	19	*	16	*

AB	*	0.0	*	0.0	*	0.0	*	5.66	*	7.13	*	6.88	*	6.97	*
AN	*	12.51	*	19.94	*	14.63	*	17.99	*	21.61	*	30.24	*	27.75	*
NE	*	6.14	*	4.83	*	9.04	*	9.80	*	9.52	*	8.21	*	10.14	*
LC	*	0.89	*	9.12	*	5.23	*	0.0	*	0.0	*	0.0	*	0.0	*
COR	*	0.0	*	0.0	*	0.0	*	0.0	*	0.0	*	0.0	*	0.0	*
WO	*	0.0	*	0.0	*	0.0	*	0.0	*	0.0	*	0.0	*	0.0	*
DI	*	48.40	*	27.73	*	32.77	*	46.25	*	19.42	*	16.60	*	16.32	*
WO	*	24.72	*	13.84	*	16.27	*	23.87	*	9.72	*	8.27	*	8.13	*
EN	*	13.99	*	5.86	*	6.33	*	15.08	*	4.27	*	3.37	*	3.31	*
FS	*	9.68	*	8.03	*	10.16	*	7.30	*	5.44	*	4.95	*	4.88	*
HY	*	0.0	*	0.0	*	0.0	*	0.0	*	0.0	*	0.0	*	0.0	*
EN	*	0.0	*	0.0	*	0.0	*	0.0	*	0.0	*	0.0	*	0.0	*
FS	*	0.0	*	0.0	*	0.0	*	0.0	*	0.0	*	0.0	*	0.0	*
OL	*	5.80	*	24.23	*	18.74	*	9.47	*	7.83	*	7.06	*	8.63	*
FO	*	2.56	*	8.62	*	5.69	*	6.17	*	3.26	*	2.70	*	3.29	*
FA	*	1.96	*	13.03	*	10.07	*	3.29	*	4.57	*	4.37	*	5.34	*
LA	*	1.28	*	2.57	*	2.97	*	0.0	*	0.0	*	0.0	*	0.0	*
MT	*	10.56	*	3.34	*	3.73	*	4.19	*	3.36	*	3.35	*	3.18	*
LM	*	10.38	*	9.08	*	11.34	*	5.14	*	5.59	*	5.51	*	4.44	*
AP	*	5.34	*	1.72	*	4.53	*	0.36	*	3.87	*	2.80	*	3.10	*
HM	*	0.0	*	0.0	*	0.0	*	0.0	*	0.0	*	0.0	*	0.0	*

RJ76-492	WHP	JACUPIRANGITE	EASTERN LONG POND
RJ76-491	WHP	JACUPIRANGITE	EASTERN LONG POND
RJ76-490	WHP	JACUPIRANGITE	EASTERN LONG POND
RJ76-489	WHP	HORNBLLENDE GNEISS	EASTERN LONG POND
RJ76-488	WHP	HORNBLLENDE GNEISS	EASTERN LONG POND
RJ76-487	WHP	HORNBLLENDE GNEISS	EASTERN LONG POND
RJ76-486	WHP	HORNBLLENDE GNEISS	EASTERN LONG POND

T102	*	1.04	*	0.98	*	0.27	*	0.10	*	0.04	*	0.06	*	0.05	*
AL203	*	17.53	*	18.42	*	18.80	*	19.50	*	2.00	*	2.40	*	1.94	*
FE203	*	1.89	*	1.59	*	0.0	*	0.0	*	2.69	*	2.79	*	1.33	*
FE0	*	3.23	*	3.06	*	2.16	*	0.60	*	6.11	*	6.31	*	7.48	*
MNO	*	0.13	*	0.11	*	0.03	*	0.01	*	0.12	*	0.13	*	0.13	*
MGO	*	3.94	*	1.76	*	0.93	*	0.30	*	39.80	*	38.63	*	41.45	*
CAO	*	3.89	*	3.97	*	1.19	*	0.82	*	2.35	*	3.02	*	2.21	*
NA2O	*	6.56	*	7.20	*	9.20	*	10.55	*	0.03	*	0.06	*	0.05	*
K2O	*	1.48	*	2.32	*	1.30	*	0.16	*	0.02	*	0.02	*	0.02	*
P2O5	*	0.34	*	0.29	*	0.0	*	0.0	*	0.0	*	0.0	*	0.0	*
LOI	*	3.21	*	1.70	*	0.74	*	0.49	*	4.29	*	3.40	*	1.58	*
TOTAL	*	97.87	*	98.87	*	98.42	*	98.23	*	99.92	*	100.33	*	98.99	*

ZR	*	151	*	489	*	744	*	105	*	6	*	4	*	8	*
SR	*	1645	*	1992	*	869	*	1140	*	3	*	0	*	2	*
RB	*	33	*	23	*	20	*	1	*	1	*	1	*	0	*
ZN	*	63	*	63	*	29	*	18	*	54	*	50	*	54	*
CU	*	13	*	13	*	11	*	12	*	36	*	22	*	23	*
BA	*	1485	*	1653	*	416	*	273	*	0	*	0	*	0	*
NB	*	18	*	19	*	7	*	3	*	5	*	5	*	5	*
Y	*	19	*	17	*	8	*	7	*	10	*	8	*	7	*
PB	*	6	*	1	*	0	*	0	*	0	*	0	*	0	*
NI	*	6	*	2	*	12	*	9	*	2135	*	1965	*	2257	*
CR	*	0	*	10	*	9	*	12	*	3484	*	2322	*	2858	*
V	*	47	*	44	*	12	*	0	*	66	*	77	*	60	*
GA	*	18	*	16	*	23	*	20	*	4	*	5	*	5	*

DR	*	9.22	*	14.08	*	7.86	*	0.92	*	0.0	*	0.0	*	0.0	*
AB	*	58.28	*	56.87	*	79.64	*	1.26	*	0.27	*	0.52	*	0.43	*
AN	*	14.73	*	11.39	*	6.31	*	4.59	*	5.50	*	6.42	*	5.14	*
NE	*	0.13	*	3.09	*	0.0	*	0.0	*	0.0	*	0.0	*	0.0	*
LC	*	0.0	*	0.0	*	0.0	*	0.0	*	0.0	*	0.0	*	0.0	*
CDR	*	0.0	*	0.0	*	0.0	*	0.34	*	0.0	*	0.0	*	0.0	*
WD	*	0.0	*	0.0	*	0.0	*	0.0	*	0.0	*	0.0	*	0.0	*
DI	*	3.29	*	6.45	*	0.09	*	0.0	*	5.26	*	7.11	*	4.82	*
WO	*	1.72	*	3.30	*	0.04	*	0.0	*	2.79	*	3.77	*	2.55	*
EN	*	1.21	*	1.90	*	0.02	*	0.0	*	2.25	*	3.04	*	2.02	*
FS	*	0.36	*	1.25	*	0.03	*	0.0	*	0.21	*	0.30	*	0.25	*
HY	*	0.0	*	0.0	*	4.43	*	1.74	*	21.87	*	23.35	*	15.82	*
EN	*	0.0	*	0.0	*	1.94	*	0.76	*	20.02	*	21.26	*	14.07	*
FS	*	0.0	*	0.0	*	2.69	*	0.97	*	1.85	*	2.08	*	1.74	*
CL	*	8.48	*	3.15	*	1.16	*	0.0	*	62.82	*	58.19	*	71.59	*
FO	*	6.40	*	1.82	*	0.43	*	0.0	*	57.02	*	52.52	*	62.99	*
FA	*	2.08	*	1.33	*	0.73	*	0.0	*	5.80	*	5.67	*	8.60	*
LA	*	0.0	*	0.0	*	0.0	*	0.0	*	0.0	*	0.0	*	0.0	*
MT	*	2.89	*	2.37	*	0.0	*	0.0	*	4.08	*	4.17	*	1.98	*
ILM	*	2.08	*	1.91	*	0.52	*	0.19	*	0.08	*	0.12	*	0.10	*
AP	*	0.83	*	0.69	*	0.0	*	0.0	*	0.0	*	0.0	*	0.0	*
HM	*	0.0	*	0.0	*	0.0	*	0.0	*	0.0	*	0.0	*	0.0	*

RJ76-496	WHP	SYENITIC MYLONITE	EASTERN LONG POND
RJ76-497	WHP	SYENITIC MYLONITE	EASTERN LONG POND
RJ77-651	WHP	SYENITIC MYLONITE	NORTHERN LONG POND
RJ77-654	WHP	SYENITIC MYLONITE	NORTHERN LONG POND
RJ75-121	WHP	HARZBURGITE	
RJ75-124	WHP	LHERZOLITE	
RJ75-125	WHP	HARZBURGITE	

TIO2	*	0.01	*	0.03	*	0.02	*	0.02	*	0.09	*	0.12	*	0.0	*
AL2O3	*	0.25	*	1.86	*	1.31	*	5.55	*	2.58	*	3.22	*	0.45	*
FE2O3	*	5.90	*	4.24	*	6.72	*	2.45	*	2.34	*	1.96	*	5.65	*
FEO	*	3.51	*	4.28	*	2.75	*	5.52	*	6.22	*	6.62	*	2.52	*
MNO	*	0.13	*	0.13	*	0.13	*	0.16	*	0.12	*	0.13	*	0.11	*
MGO	*	41.20	*	38.30	*	36.62	*	21.07	*	37.75	*	37.44	*	40.57	*
CAO	*	0.21	*	1.42	*	0.76	*	15.27	*	2.71	*	3.14	*	0.35	*
NA2O	*	0.10	*	0.06	*	0.03	*	0.32	*	0.11	*	0.10	*	0.01	*
K2O	*	0.02	*	0.02	*	0.01	*	0.02	*	0.06	*	0.03	*	0.01	*
P2O5	*	0.01	*	0.01	*	0.0	*	0.01	*	0.0	*	0.01	*	0.0	*
LOI	*	14.59	*	7.96	*	13.07	*	0.87	*	5.41	*	2.37	*	13.27	*
TOTAL	*	101.18	*	99.84	*	100.89	*	99.01	*	99.58	*	98.52	*	101.45	*

ZR	*	7	*	6	*	6	*	22	*	11	*	9	*	7	*
SR	*	1	*	2	*	0	*	16	*	15	*	18	*	0	*
RB	*	2	*	1	*	2	*	3	*	3	*	2	*	3	*
ZN	*	48	*	47	*	48	*	40	*	54	*	58	*	41	*
CU	*	9	*	22	*	21	*	240	*	18	*	28	*	6	*
BA	*	0	*	0	*	4	*	4	*	2	*	1	*	0	*
NB	*	4	*	5	*	5	*	6	*	5	*	5	*	5	*
Y	*	6	*	7	*	7	*	19	*	7	*	8	*	8	*
PB	*	0	*	0	*	0	*	0	*	0	*	0	*	0	*
NI	*	2450	*	2032	*	2006	*	873	*	1997	*	1986	*	2257	*
CR	*	687	*	2802	*	2180	*	2859	*	2968	*	2635	*	1965	*
V	*	6	*	58	*	53	*	231	*	75	*	82	*	16	*
GA	*	1	*	3	*	2	*	8	*	6	*	5	*	0	*

OR	*	0.14	*	0.13	*	0.07	*	0.12	*	0.08	*	0.18	*	0.07	*
AB	*	0.98	*	0.55	*	0.29	*	0.76	*	0.99	*	0.88	*	0.10	*
AN	*	0.20	*	5.17	*	3.88	*	13.91	*	6.76	*	8.58	*	1.31	*
NE	*	0.0	*	0.0	*	0.0	*	0.0	*	0.0	*	0.0	*	0.0	*
LC	*	0.0	*	0.0	*	0.0	*	0.0	*	0.0	*	0.0	*	0.0	*
COR	*	0.0	*	0.0	*	0.0	*	0.0	*	0.0	*	0.0	*	0.0	*
WO	*	0.0	*	0.0	*	0.0	*	0.0	*	0.0	*	0.0	*	0.0	*
DI	*	0.72	*	1.90	*	0.32	*	49.92	*	5.91	*	5.95	*	0.51	*
WO	*	0.39	*	1.01	*	0.17	*	26.40	*	3.14	*	3.15	*	0.28	*
EN	*	0.33	*	0.85	*	0.15	*	20.55	*	2.52	*	2.51	*	0.24	*
FS	*	0.01	*	0.04	*	0.0	*	2.98	*	0.26	*	0.28	*	0.0	*
HY	*	12.19	*	32.19	*	39.50	*	6.75	*	21.66	*	23.01	*	28.28	*
EN	*	11.98	*	30.73	*	39.50	*	5.89	*	19.66	*	20.66	*	28.23	*
FS	*	0.21	*	1.47	*	0.0	*	0.86	*	2.00	*	2.34	*	0.05	*
OL	*	75.84	*	53.28	*	44.99	*	21.97	*	60.52	*	58.18	*	60.45	*
FO	*	74.40	*	50.62	*	44.99	*	18.94	*	54.41	*	51.71	*	60.34	*
FA	*	1.44	*	2.66	*	0.0	*	3.03	*	6.10	*	6.47	*	0.11	*
LA	*	0.0	*	0.0	*	0.0	*	0.0	*	0.0	*	0.0	*	0.0	*
MT	*	9.88	*	6.69	*	10.51	*	3.62	*	3.60	*	2.96	*	9.29	*
ILM	*	0.02	*	0.06	*	0.04	*	0.93	*	0.18	*	0.24	*	0.0	*
AP	*	0.03	*	0.03	*	0.0	*	0.02	*	0.0	*	0.02	*	0.0	*
HM	*	0.0	*	0.0	*	0.04	*	0.0	*	0.0	*	0.0	*	0.0	*

RJ75-126 WHP DUNITE
RJ75-127 WHP HARZBURGITE
RJ7L-483 WHP HARZBURGITE
RJ76-484 WHP PYROXENITE
RJ76-493 WHP BASAL ZONE LHERZOLITE
RJ76-498 WHP BASAL ZONE PLAGIOCLASE LHERZOLITE
RJ76-500 WHP DUNITE

TI02	*	0.03	*	0.04	*	0.27	*	0.88	*
AL203	*	0.63	*	1.95	*	2.08	*	1.58	*
FE203	*	6.02	*	1.97	*	1.18	*	12.45	*
FEO	*	4.26	*	6.51	*	7.42	*	0.0	*
MNO	*	0.13	*	0.13	*	0.14	*	12.82	*
MGO	*	41.35	*	40.52	*	38.20	*	0.16	*
CAO	*	0.29	*	2.07	*	3.11	*	14.48	*
NA2O	*	0.07	*	0.05	*	0.31	*	13.39	*
K2O	*	0.04	*	0.03	*	0.18	*	1.58	*
P2O5	*	0.0	*	0.0	*	0.03	*	0.34	*
LOI	*	12.18	*	3.27	*	1.60	*	0.03	*
TOTAL	*	101.01	*	98.61	*	98.82	*	0.98	*
								98.69	*

ZR	*	5	*	6	*	13	*	57	*
SR	*	6	*	5	*	27	*	155	*
RB	*	1	*	1	*	6	*	5	*
ZN	*	54	*	56	*	67	*	120	*
CU	*	7	*	25	*	33	*	93	*
BA	*	0	*	0	*	0	*	128	*
NB	*	4	*	5	*	4	*	9	*
Y	*	6	*	7	*	5	*	17	*
PB	*	0	*	1	*	4	*	0	*
NI	*	2427	*	2163	*	1847	*	348	*
CR	*	2609	*	2925	*	2407	*	181	*
V	*	21	*	59	*	94	*	377	*
GA	*	4	*	4	*	9	*	24	*

CK	*	0.27	*	0.19	*	1.09	*	0.0	*
AB	*	0.67	*	0.44	*	2.70	*	0.0	*
AN	*	1.45	*	5.25	*	3.86	*	27.06	*
NE	*	0.0	*	0.0	*	0.0	*	7.57	*
LC	*	0.0	*	0.0	*	0.0	*	1.65	*
COR	*	0.0	*	0.0	*	0.0	*	0.0	*
WO	*	0.0	*	0.0	*	0.0	*	0.0	*
DI	*	0.13	*	4.34	*	9.32	*	22.80	*
WO	*	0.07	*	2.30	*	4.93	*	11.70	*
EN	*	0.06	*	1.85	*	3.88	*	6.99	*
FS	*	0.0	*	0.19	*	0.51	*	4.11	*
HY	*	12.65	*	18.69	*	18.25	*	0.0	*
EN	*	12.29	*	16.92	*	16.14	*	0.0	*
FS	*	0.36	*	1.76	*	2.11	*	0.0	*
OL	*	74.94	*	68.01	*	62.42	*	37.70	*
FO	*	72.58	*	61.02	*	54.54	*	21.53	*
FA	*	2.36	*	7.00	*	7.88	*	13.97	*
LA	*	0.0	*	0.0	*	0.0	*	2.19	*
MT	*	9.83	*	3.00	*	1.76	*	0.0	*
ILM	*	0.06	*	0.08	*	0.53	*	3.14	*
AP	*	0.0	*	0.0	*	0.07	*	0.07	*
HM	*	0.0	*	0.0	*	0.0	*	0.0	*

RJ76-507	WHP	DUNITE
RJ76-555	WHP	HARZBURGITE
RJ77662A	WHP	BASAL ZONE AMPHIBOLE LHERZOLITE
RJ77-G12	WHP	BASAL ZONE AMPHIBOLE METAGABBRO

Table I.viii. Major and trace element analyses and CIPW norms, other rocks, including four post-tectonic dykes and one Maiden Point Formation sandstone.

AL203	*	12.28	*	12.31	*	15.50	*	12.45	*	10.02	*
FE203	*	2.12	*	1.35	*	2.15	*	3.54	*	1.33	*
FEO	*	4.42	*	8.25	*	7.64	*	9.65	*	3.34	*
MNO	*	0.09	*	0.21	*	0.15	*	0.27	*	0.08	*
MGO	*	8.40	*	9.42	*	7.84	*	5.16	*	1.92	*
CAO	*	5.69	*	4.61	*	9.45	*	7.82	*	1.47	*
NA2O	*	1.49	*	2.13	*	2.29	*	3.33	*	4.70	*
K2O	*	7.90	*	0.14	*	1.34	*	1.54	*	0.11	*
P2O5	*	0.55	*	0.24	*	0.22	*	0.99	*	0.17	*
LOI	*	2.47	*	8.53	*	3.83	*	2.77	*	2.66	*
TOTAL	*	98.53	*	99.12	*	99.33	*	97.91	*	100.87	*

ZR	*	579	*	118	*	141	*	247	*	116	*
SR	*	782	*	248	*	336	*	309	*	141	*
RB	*	156	*	5	*	35	*	35	*	3	*
ZN	*	98	*	120	*	209	*	157	*	45	*
CU	*	122	*	72	*	189	*	141	*	21	*
BA	*	2903	*	64	*	249	*	1135	*	16	*
NB	*	13	*	2	*	2	*	7	*	9	*
Y	*	20	*	36	*	37	*	62	*	38	*
PB	*	20	*	10	*	7	*	11	*	10	*
NI	*	336	*	122	*	134	*	9	*	36	*
CR	*	359	*	624	*	210	*	74	*	90	*
V	*	137	*	278	*	214	*	370	*	140	*
GA	*	21	*	24	*	20	*	23	*	13	*

OR	*	48.48	*	0.91	*	8.29	*	9.56	*	40.48	*
AB	*	6.56	*	19.87	*	20.28	*	29.59	*	40.48	*
AN	*	3.62	*	23.60	*	29.36	*	15.20	*	6.03	*
NE	*	3.54	*	0.0	*	0.0	*	0.0	*	0.0	*
LC	*	0.0	*	0.0	*	0.0	*	0.0	*	0.0	*
COR	*	0.0	*	0.0	*	0.0	*	0.0	*	0.0	*
WD	*	0.0	*	0.0	*	0.0	*	0.0	*	0.0	*
DI	*	18.17	*	0.0	*	14.89	*	15.71	*	0.27	*
WO	*	9.55	*	0.0	*	7.67	*	8.00	*	0.14	*
EN	*	7.08	*	0.0	*	4.76	*	4.37	*	0.07	*
FS	*	1.55	*	0.0	*	2.45	*	3.35	*	0.06	*
HY	*	0.0	*	39.86	*	11.61	*	14.03	*	8.96	*
EN	*	0.0	*	25.86	*	7.66	*	7.94	*	4.80	*
FS	*	0.0	*	13.99	*	3.95	*	6.09	*	4.16	*
OL	*	12.74	*	0.0	*	8.80	*	1.54	*	0.0	*
FO	*	10.26	*	0.0	*	5.61	*	0.83	*	0.0	*
FA	*	2.47	*	0.0	*	3.19	*	0.70	*	0.0	*
LA	*	0.0	*	0.0	*	0.0	*	0.0	*	0.0	*
MT	*	3.19	*	2.16	*	3.26	*	5.39	*	1.96	*
ILM	*	2.29	*	2.09	*	2.94	*	6.56	*	1.20	*
AP	*	1.33	*	0.61	*	0.53	*	2.42	*	0.40	*
HM	*	0.0	*	0.0	*	0.0	*	0.0	*	0.0	*

RJ75-053 LATE DYKE LAMPROPHYRE GOOSE COVE WEST
 RJ75174A LATE DYKE DIABASE FISCHOT ISLAND
 RJ75-219 LATE DYKE DIABASE LOBSTER POINT
 RJ75-280 LATE DYKE DIABASE NORTHEAST ISLAND
 RJ75-158 MPF GREYWACKE IRELAND POINT

TABLE II.i(b). Amphibole analyses, structural formulae, and ferric iron estimates.

KAER = kaersutite
PG = pargasite
HS = hastingsite
COM HB = common hornblende
ED = edenite
TS = tschermakite
TR = tremolite
TI = titaniferous
FI = ferri-
FO = ferro-
MG = magnesian

		*	1 *	2 *	3 *	4 *	5 *	6 *	7
	SI02	*	39.21 *	38.99 *	39.93 *	39.10 *	39.38 *	38.89 *	39.11
	TI02	*	4.77 *	4.97 *	4.78 *	4.87 *	4.94 *	4.82 *	4.94
	AL203	*	12.01 *	12.34 *	11.95 *	12.04 *	11.97 *	12.01 *	11.89
	FE203	*	1.55 *	1.20 *	0.65 *	0.95 *	1.10 *	1.00 *	1.00
	FEO	*	15.06 *	15.31 *	15.76 *	15.28 *	15.63 *	15.96 *	16.35
	MNO	*	0.19 *	0.18 *	0.19 *	0.21 *	0.21 *	0.15 *	0.15
	MGO	*	10.41 *	10.57 *	10.40 *	10.24 *	10.27 *	10.02 *	9.70
	CAO	*	11.37 *	11.75 *	11.59 *	11.41 *	11.48 *	11.37 *	11.29
	NA2O	*	2.90 *	3.01 *	3.05 *	2.91 *	2.97 *	3.17 *	3.01
	K2O	*	0.64 *	0.64 *	0.64 *	0.65 *	0.66 *	0.64 *	0.64
	TOTAL	*	98.11 *	98.96 *	98.94 *	97.66 *	98.61 *	98.03 *	98.08
	FE203 MIN	*	0.0 *	0.0 *	0.0 *	0.0 *	0.0 *	0.0 *	0.0
	FE203 MAX	*	3.10 *	2.40 *	1.30 *	1.90 *	2.20 *	2.00 *	2.00
Z	SI	*	5.923 *	5.852 *	5.982 *	5.934 *	5.930 *	5.906 *	5.938
	AL(IV)	*	2.077 *	2.148 *	2.018 *	2.066 *	2.070 *	2.094 *	2.062
Y	AL(VI)	*	0.062 *	0.034 *	0.092 *	0.087 *	0.054 *	0.055 *	0.066
	FE3+	*	0.176 *	0.136 *	0.073 *	0.109 *	0.125 *	0.114 *	0.114
	TI	*	0.542 *	0.561 *	0.538 *	0.556 *	0.559 *	0.550 *	0.564
	FE2+	*	1.876 *	1.905 *	1.974 *	1.932 *	1.957 *	2.012 *	2.060
	MN	*	0.0 *	0.0 *	0.0 *	0.0 *	0.0 *	0.0 *	0.0
	MG	*	2.344 *	2.364 *	2.322 *	2.316 *	2.305 *	2.268 *	2.195
	CA	*	0.0 *	0.0 *	0.0 *	0.0 *	0.0 *	0.0 *	0.0
X	FE2+	*	0.026 *	0.017 *	0.0 *	0.006 *	0.011 *	0.014 *	0.016
	MN	*	0.024 *	0.023 *	0.024 *	0.027 *	0.027 *	0.019 *	0.019
	CA	*	1.840 *	1.889 *	1.860 *	1.855 *	1.852 *	1.850 *	1.837
	NA	*	0.109 *	0.071 *	0.116 *	0.111 *	0.110 *	0.116 *	0.128
A	NA	*	0.740 *	0.805 *	0.770 *	0.745 *	0.757 *	0.817 *	0.758
	K	*	0.123 *	0.123 *	0.122 *	0.126 *	0.127 *	0.124 *	0.124
1	KAER	*	75-283B	HE-1					
2	KAER	*	75-283B	HB-2					
3	KAER	*	75-283B	HB-3					
4	KAER	*	75-283B	HE-4					
5	KAER	*	75-283B	HB-5					
6	KAER	*	75-283B	HE-6					
7	KAER	*	75-283B	HB-7					

	*	1 *	2 *	3 *	4 *	5 *	6 *	7
SIO2	*	39.20 *	38.71 *	38.76 *	38.36 *	40.80 *	40.91 *	41.16
TIO2	*	4.60 *	4.74 *	4.64 *	4.56 *	4.00 *	4.05 *	3.96
AL2O3	*	11.95 *	12.01 *	11.58 *	12.31 *	10.78 *	10.55 *	10.58
FE2O3	*	1.35 *	1.40 *	1.25 *	2.10 *	1.25 *	1.35 *	1.40
FeO	*	16.34 *	15.78 *	16.63 *	15.85 *	14.77 *	14.84 *	14.77
MNO	*	0.27 *	0.22 *	0.21 *	0.21 *	0.20 *	0.15 *	0.18
MGO	*	9.73 *	10.22 *	9.59 *	9.89 *	11.21 *	11.20 *	11.48
CAO	*	11.42 *	11.27 *	11.33 *	11.25 *	11.17 *	11.14 *	11.10
NA2O	*	2.98 *	3.04 *	2.93 *	2.90 *	3.22 *	3.11 *	3.20
K2O	*	0.67 *	0.66 *	0.67 *	0.71 *	0.75 *	0.73 *	0.71
TOTAL	*	98.51 *	98.05 *	97.59 *	98.14 *	98.15 *	98.03 *	98.54
FE2O3 MIN	*	0.0 *	0.0 *	0.0 *	0.10 *	0.0 *	0.0 *	0.0
FE2O3 MAX	*	2.70 *	2.80 *	2.50 *	4.10 *	2.50 *	2.70 *	2.80
Z	SI	5.935 *	5.880 *	5.937 *	5.835 *	6.138 *	6.161 *	6.162
	AL(IV)	2.065 *	2.120 *	2.063 *	2.165 *	1.862 *	1.839 *	1.838
Y	AL(VI)	0.067 *	0.030 *	0.027 *	0.042 *	0.050 *	0.033 *	0.029
	FE3+	0.154 *	0.160 *	0.144 *	0.241 *	0.142 *	0.153 *	0.158
	TI	0.524 *	0.541 *	0.534 *	0.521 *	0.452 *	0.459 *	0.446
	FE2+	2.059 *	1.955 *	2.105 *	1.954 *	1.842 *	1.841 *	1.805
	MN	0.0 *	0.0 *	0.0 *	0.0 *	0.0 *	0.0 *	0.0
	MG	2.196 *	2.314 *	2.189 *	2.242 *	2.514 *	2.514 *	2.562
	CA	0.0 *	0.0 *	0.0 *	0.0 *	0.0 *	0.0 *	0.0
X	FE2+	0.009 *	0.050 *	0.025 *	0.063 *	0.015 *	0.027 *	0.044
	MN	0.035 *	0.028 *	0.027 *	0.027 *	0.025 *	0.019 *	0.023
	CA	1.853 *	1.834 *	1.859 *	1.833 *	1.801 *	1.797 *	1.781
	NA	0.104 *	0.088 *	0.089 *	0.077 *	0.159 *	0.156 *	0.153
A	NA	0.771 *	0.807 *	0.781 *	0.779 *	0.780 *	0.752 *	0.776
	K	0.129 *	0.128 *	0.131 *	0.138 *	0.144 *	0.140 *	0.136
1	KAER	*	75-283B	HB-8A				
2	KAER	*	75-283B	HB-8B				
3	KAER	*	75-283B	HB-9				
4	KAER	*	75-283B	HB-10				
5	TI-PG	*	75-286	HB-1				
6	TI-PG	*	75-286	HB-2				
7	TI-PG	*	75-286	HB-3				

		*	1	*	2	*	3	*
	SiO2	*	41.00	*	41.43	*	39.79	*
	TiO2	*	4.19	*	3.91	*	1.14	*
	Al2O3	*	10.95	*	10.49	*	10.59	*
	Fe2O3	*	1.45	*	1.30	*	4.30	*
	FeO	*	14.27	*	15.18	*	20.91	*
	MnO	*	0.18	*	0.19	*	0.31	*
	MgO	*	11.49	*	11.16	*	6.89	*
	CaO	*	11.29	*	11.08	*	10.59	*
	Na2O	*	3.04	*	3.29	*	3.25	*
	K2O	*	0.70	*	0.76	*	1.02	*
	TOTAL	*	98.56	*	98.79	*	98.79	*
	Fe2O3 MIN	*	0.0	*	0.0	*	1.00	*
	Fe2O3 MAX	*	2.90	*	2.60	*	7.60	*
Z	Si	*	6.124	*	6.196	*	6.183	*
	Al(IV)	*	1.876	*	1.804	*	1.817	*
Y	Al(VI)	*	0.051	*	0.045	*	0.119	*
	Fe3+	*	0.163	*	0.147	*	0.504	*
	Ti	*	0.470	*	0.440	*	0.133	*
	Fe2+	*	1.757	*	1.881	*	2.648	*
	Mn	*	0.0	*	0.0	*	0.0	*
	Mg	*	2.558	*	2.488	*	1.596	*
	Ca	*	0.0	*	0.0	*	0.0	*
X	Fe2+	*	0.024	*	0.018	*	0.069	*
	Mn	*	0.023	*	0.024	*	0.041	*
	Ca	*	1.807	*	1.775	*	1.763	*
	Na	*	0.146	*	0.183	*	0.127	*
A	Na	*	0.734	*	0.771	*	0.852	*
	K	*	0.133	*	0.145	*	0.202	*
1	TI-PG	*	75-286		HB-4			
2	TI-PG	*	75-286		HB-4B			
3	FI-MG HS	*	75-286		BL GR HB-1			

		*	1 *	2 *	3 *	4 *	5 *
	SiO ₂	*	48.18 *	47.94 *	48.49 *	46.56 *	43.49 *
	TiO ₂	*	0.28 *	0.17 *	0.40 *	0.16 *	0.18 *
	Al ₂ O ₃	*	6.17 *	6.27 *	5.67 *	6.79 *	9.37 *
	Fe ₂ O ₃	*	2.70 *	2.75 *	2.55 *	4.40 *	5.65 *
	FeO	*	13.54 *	13.01 *	14.11 *	13.72 *	14.12 *
	MnO	*	0.25 *	0.17 *	0.22 *	0.22 *	0.20 *
	MgO	*	12.31 *	12.63 *	12.29 *	11.35 *	9.89 *
	CaO	*	11.65 *	11.68 *	11.84 *	11.68 *	11.56 *
	Na ₂ O	*	1.04 *	1.11 *	1.01 *	1.06 *	1.52 *
	K ₂ O	*	0.12 *	0.16 *	0.13 *	0.17 *	0.22 *
	TOTAL	*	96.24 *	95.89 *	96.71 *	96.11 *	96.20 *
	Fe ₂ O ₃ MIN	*	0.70 *	0.90 *	1.00 *	2.80 *	4.10 *
	Fe ₂ O ₃ MAX	*	4.70 *	4.60 *	4.10 *	6.00 *	7.20 *
Z	SI	*	7.187 *	7.166 *	7.217 *	7.019 *	6.628 *
	AL(IV)	*	0.813 *	0.834 *	0.783 *	0.981 *	1.372 *
Y	AL(VI)	*	0.271 *	0.271 *	0.211 *	0.226 *	0.311 *
	FE3+	*	0.304 *	0.310 *	0.286 *	0.500 *	0.649 *
	TI	*	0.031 *	0.019 *	0.045 *	0.018 *	0.021 *
	FE2+	*	1.657 *	1.586 *	1.731 *	1.706 *	1.773 *
	MN	*	0.0 *	0.0 *	0.0 *	0.0 *	0.0 *
	MG	*	2.737 *	2.814 *	2.726 *	2.550 *	2.247 *
	CA	*	0.0 *	0.0 *	0.0 *	0.0 *	0.0 *
X	FE2+	*	0.032 *	0.039 *	0.024 *	0.024 *	0.026 *
	MN	*	0.032 *	0.022 *	0.028 *	0.028 *	0.026 *
	CA	*	1.862 *	1.871 *	1.888 *	1.887 *	1.888 *
	NA	*	0.074 *	0.068 *	0.060 *	0.062 *	0.060 *
A	NA	*	0.227 *	0.253 *	0.231 *	0.248 *	0.389 *
	K	*	0.023 *	0.031 *	0.025 *	0.033 *	0.043 *
1	COM HB	*	435-1	AM-1	LARGE		
2	COM HB	*	435-2	AM-2	LARGE		
3	COM HB	*	435-2	AM-3	LARGE		
4	FI-COM HB	*	435-3	AM-4	LARGE		
5	FI-FO-EO HB	*	435-3	AM-5	THIN		

		*	1 *	2 *	3 *	4 *	5 *	6 *
	SI02	*	50.21 *	52.61 *	46.97 *	48.47 *	48.79 *	49.03 *
	TI02	*	1.65 *	1.00 *	0.37 *	0.27 *	0.14 *	1.21 *
	AL203	*	5.06 *	3.59 *	10.91 *	9.91 *	6.60 *	5.69 *
	FE203	*	0.0 *	0.0 *	2.80 *	2.00 *	1.45 *	0.0 *
	FE0	*	7.58 *	7.50 *	10.60 *	11.33 *	11.00 *	11.36 *
	MNO	*	0.19 *	0.28 *	0.21 *	0.19 *	0.25 *	0.23 *
	MGO	*	16.53 *	17.17 *	13.06 *	13.32 *	14.05 *	14.23 *
	CA0	*	13.25 *	12.73 *	12.15 *	12.37 *	11.96 *	12.39 *
	NA20	*	0.61 *	0.49 *	1.29 *	1.11 *	0.97 *	0.92 *
	K20	*	0.06 *	0.04 *	0.10 *	0.09 *	0.23 *	0.13 *
	TOTAL	*	95.14 *	95.41 *	98.46 *	99.06 *	95.44 *	95.19 *
	FE203 MIN	*	0.0 *	0.0 *	0.90 *	0.40 *	0.0 *	0.0 *
	FE203 MAX	*	0.0 *	0.0 *	4.70 *	3.60 *	2.90 *	0.0 *
Z	SI	*	7.318 *	7.595 *	6.761 *	6.924 *	7.224 *	7.271 *
	AL(IV)	*	0.682 *	0.405 *	1.239 *	1.076 *	0.776 *	0.729 *
Y	AL(VI)	*	0.187 *	0.206 *	0.612 *	0.593 *	0.375 *	0.266 *
	FE3+	*	0.0 *	0.0 *	0.304 *	0.215 *	0.162 *	0.0 *
	TI	*	0.181 *	0.109 *	0.040 *	0.029 *	0.016 *	0.135 *
	FE2+	*	0.924 *	0.906 *	1.243 *	1.327 *	1.347 *	1.409 *
	MN	*	0.023 *	0.034 *	0.0 *	0.0 *	0.0 *	0.029 *
	MG	*	3.591 *	3.695 *	2.802 *	2.836 *	3.101 *	3.145 *
	CA	*	0.094 *	0.051 *	0.0 *	0.0 *	0.0 *	0.0 *
X	FE2+	*	0.0 *	0.0 *	0.033 *	0.027 *	0.015 *	0.0 *
	MN	*	0.0 *	0.0 *	0.026 *	0.023 *	0.031 *	0.0 *
	CA	*	1.975 *	1.918 *	1.874 *	1.893 *	1.897 *	1.952 *
	NA	*	0.025 *	0.082 *	0.067 *	0.057 *	0.057 *	0.048 *
A	NA	*	0.147 *	0.056 *	0.293 *	0.251 *	0.222 *	0.217 *
	K	*	0.011 *	0.007 *	0.018 *	0.016 *	0.043 *	0.025 *
1	ACT HB	*	033-1	AM-1				
2	ACT	*	033-1	AM-2				
3	COM HB	*	236-1	AMPH-1				
4	COM HB	*	236-2	AMPH-2				
5	ACT HB	*	530-1	AM-1				
6	ACT HB	*	530-1	AM-2				

	*	1 *	2 *	3 *	4 *	5 *	6 *	7
SiO2	*	52.95 *	53.05 *	43.98 *	44.61 *	49.91 *	46.22 *	52.47
TiO2	*	0.06 *	0.03 *	0.48 *	0.44 *	0.23 *	0.36 *	0.46
Al2O3	*	1.92 *	2.07 *	10.03 *	9.39 *	7.36 *	10.68 *	6.00
Fe2O3	*	0.10 *	0.45 *	3.90 *	3.95 *	2.40 *	2.80 *	0.70
FeO	*	10.87 *	9.19 *	12.50 *	11.24 *	9.80 *	12.08 *	9.18
MnO	*	0.25 *	0.25 *	0.25 *	0.23 *	0.17 *	0.19 *	0.18
MgO	*	15.94 *	16.95 *	11.38 *	12.21 *	14.69 *	12.31 *	15.36
CaO	*	12.80 *	12.68 *	12.07 *	12.14 *	11.67 *	12.11 *	11.46
Na2O	*	0.32 *	0.33 *	1.67 *	1.46 *	1.07 *	1.53 *	0.93
K2O	*	0.03 *	0.04 *	0.21 *	0.15 *	0.10 *	0.22 *	0.07
TOTAL	*	95.24 *	95.04 *	96.47 *	95.82 *	97.40 *	98.50 *	96.81
FE2O3 MIN	*	0.10 *	0.30 *	3.10 *	3.30 *	0.0 *	1.10 *	0.0
FE2O3 MAX	*	0.10 *	0.60 *	4.70 *	4.60 *	4.80 *	4.50 *	1.40

Z	SI	*	7.777 *	7.752 *	6.606 *	6.695 *	7.187 *	6.718 *	7.497
	AL(IV)	*	0.223 *	0.248 *	1.394 *	1.305 *	0.813 *	1.282 *	0.503
Y	AL(VI)	*	0.109 *	0.108 *	0.381 *	0.356 *	0.436 *	0.548 *	0.507
	FE3+	*	0.011 *	0.050 *	0.441 *	0.447 *	0.260 *	0.307 *	0.075
	TI	*	0.007 *	0.003 *	0.054 *	0.050 *	0.025 *	0.039 *	0.049
	FE2+	*	1.335 *	1.122 *	1.570 *	1.410 *	1.126 *	1.439 *	1.097
	MN	*	0.031 *	0.025 *	0.006 *	0.006 *	0.0 *	0.0 *	0.0
	MG	*	3.489 *	3.692 *	2.548 *	2.731 *	3.153 *	2.667 *	3.271
	CA	*	0.0 *	0.0 *	0.0 *	0.0 *	0.0 *	0.0 *	0.0
X	FE2+	*	0.0 *	0.0 *	0.0 *	0.0 *	0.054 *	0.029 *	0.0
	MN	*	0.0 *	0.006 *	0.026 *	0.023 *	0.021 *	0.023 *	0.022
	CA	*	1.997 *	1.985 *	1.942 *	1.952 *	1.800 *	1.886 *	1.754
	NA	*	0.003 *	0.009 *	0.031 *	0.025 *	0.125 *	0.062 *	0.224
A	NA	*	0.088 *	0.085 *	0.455 *	0.400 *	0.174 *	0.370 *	0.033
	K	*	0.006 *	0.007 *	0.040 *	0.029 *	0.018 *	0.041 *	0.013

1	ACT	*	112-1	AM-1	LARGE	IN EP BAND
2	ACT	*	112-1	AM-2	THIN IN LARGE	IM EP BAND
3	ED HB	*	112-2	AM-3	MARTIX	
4	ED HB	*	112-2	AM-4	MATRIX	
5	COM HB	*	114-1	AMPH-1	PORPHYROBLASTS	
6	COM HB	*	114-1	AMPH-2	MATRIX	
7	ACT HB	*	114-2	AMPH-3	CORE	

		*	1	*	2	*
	SI02	*	50.95	*	48.95	*
	TI02	*	0.21	*	0.22	*
	AL203	*	6.11	*	8.83	*
	FE203	*	1.70	*	3.30	*
	FEO	*	9.59	*	11.18	*
	MNO	*	0.18	*	0.22	*
	MGO	*	15.55	*	13.60	*
	CAO	*	12.12	*	11.89	*
	NA2O	*	0.95	*	1.20	*
	K2O	*	0.09	*	0.16	*
	TOTAL	*	97.45	*	99.55	*
	FE203 MIN	*	0.0	*	0.50	*
	FE203 MAX	*	3.40	*	6.10	*
Z	SI	*	7.312	*	6.976	*
	AL(IV)	*	0.688	*	1.024	*
Y	AL(VI)	*	0.346	*	0.459	*
	FE3+	*	0.184	*	0.354	*
	TI	*	0.023	*	0.024	*
	FE2+	*	1.121	*	1.274	*
	MN	*	0.0	*	0.0	*
	MG	*	3.327	*	2.889	*
	CA	*	0.0	*	0.0	*
X	FE2+	*	0.030	*	0.059	*
	MN	*	0.022	*	0.027	*
	CA	*	1.864	*	1.816	*
	NA	*	0.084	*	0.099	*
A	NA	*	0.180	*	0.233	*
	K	*	0.016	*	0.029	*
1	ACT HB	*	114-2	AMPH-3	RIM	
2	COM HB	*	114-2	AMPH-4	MATRIX	

[illegible]

		*	1 *	2 *	3 *	4 *	5 *	6 *	7
	SiO2	*	49.32 *	44.76 *	45.23 *	42.73 *	43.58 *	43.58 *	45.23
	TiO2	*	0.27 *	0.71 *	0.63 *	0.61 *	0.54 *	0.61 *	0.59
	Al2O3	*	6.66 *	10.71 *	10.70 *	11.72 *	11.08 *	11.20 *	10.22
	Fe2O3	*	0.50 *	5.25 *	2.90 *	8.45 *	5.85 *	6.65 *	4.50
	FeO	*	16.71 *	10.96 *	14.36 *	11.82 *	14.25 *	12.60 *	11.54
	MnO	*	0.35 *	0.39 *	0.41 *	0.27 *	0.37 *	0.37 *	0.33
	MgO	*	11.09 *	12.31 *	10.81 *	10.54 *	9.87 *	10.71 *	12.07
	CaO	*	12.20 *	12.53 *	12.81 *	12.48 *	12.36 *	12.38 *	12.24
	Na2O	*	1.03 *	1.61 *	1.54 *	1.52 *	1.54 *	1.58 *	1.42
	K2O	*	0.30 *	0.23 *	0.31 *	0.34 *	0.42 *	0.35 *	0.17
	TOTAL	*	98.43 *	99.46 *	99.70 *	100.48 *	99.86 *	100.03 *	98.31
	Fe2O3 MIN	*	0.0 *	4.50 *	2.90 *	7.80 *	5.20 *	5.80 *	3.80
	Fe2O3 MAX	*	1.00 *	6.00 *	2.90 *	9.10 *	6.50 *	7.50 *	5.20
Z	SI	*	7.251 *	6.498 *	6.606 *	6.239 *	6.421 *	6.375 *	6.616
	AL(IV)	*	0.749 *	1.502 *	1.394 *	1.761 *	1.579 *	1.625 *	1.384
Y	AL(VI)	*	0.405 *	0.331 *	0.447 *	0.255 *	0.344 *	0.306 *	0.378
	FE3+	*	0.055 *	0.574 *	0.319 *	0.930 *	0.649 *	0.733 *	0.496
	TI	*	0.030 *	0.077 *	0.069 *	0.067 *	0.060 *	0.067 *	0.065
	FE2+	*	2.054 *	1.330 *	1.754 *	1.443 *	1.755 *	1.541 *	1.412
	MN	*	0.025 *	0.024 *	0.051 *	0.011 *	0.024 *	0.017 *	0.018
	MG	*	2.430 *	2.664 *	2.353 *	2.294 *	2.167 *	2.335 *	2.632
	CA	*	0.0 *	0.0 *	0.0 *	0.0 *	0.0 *	0.0 *	0.0
X	FE2+	*	0.0 *	0.0 *	0.0 *	0.0 *	0.0 *	0.0 *	0.0
	MN	*	0.018 *	0.024 *	0.0 *	0.022 *	0.023 *	0.029 *	0.023
	CA	*	1.922 *	1.949 *	1.998 *	1.952 *	1.951 *	1.940 *	1.950
	NA	*	0.060 *	0.027 *	0.002 *	0.026 *	0.026 *	0.031 *	0.027
A	NA	*	0.233 *	0.426 *	0.434 *	0.405 *	0.413 *	0.417 *	0.376
	K	*	0.056 *	0.043 *	0.058 *	0.063 *	0.079 *	0.065 *	0.032
1	ACT HB	*			086-A7-A				
2	FI-FO-PG HB	*			087-A1-A				
3	ED HB	*			75-087 A2-AVE				
4	FI-MG HB	*			087-A2-3				
5	FI-MG-HS HB	*			087-A3-A				
6	FI-FO-PG HB	*			087-A4-A				
7	ED HB	*			087-A5-A				

		*	1 *	2 *	3 *	4 *	5 *	6 *	7
	SI02	*	44.05 *	44.73 *	44.76 *	44.29 *	42.76 *	44.14 *	42.99
	TI02	*	0.66 *	0.52 *	0.61 *	0.57 *	0.66 *	0.59 *	0.64
	AL203	*	11.10 *	10.65 *	10.71 *	10.78 *	11.48 *	10.96 *	11.58
	FE203	*	5.60 *	5.20 *	5.25 *	5.70 *	6.80 *	4.00 *	6.60
	FEO	*	12.67 *	12.97 *	11.90 *	11.35 *	12.29 *	14.22 *	12.45
	MNO	*	0.33 *	0.35 *	0.34 *	0.31 *	0.43 *	0.43 *	0.49
	MGD	*	10.95 *	11.04 *	11.60 *	11.77 *	10.55 *	10.28 *	10.64
	CAO	*	12.40 *	12.33 *	12.31 *	12.53 *	12.20 *	11.93 *	12.40
	NA2O	*	1.61 *	1.53 *	1.46 *	1.52 *	1.49 *	1.51 *	1.57
	K2O	*	0.23 *	0.25 *	0.28 *	0.25 *	0.66 *	0.60 *	0.64
	TOTAL	*	99.60 *	99.57 *	99.22 *	99.07 *	99.32 *	98.66 *	100.00
	FE203 MIN	*	4.80 *	4.20 *	4.20 *	5.20 *	5.80 *	2.50 *	5.90
	FE203 MAX	*	6.40 *	6.20 *	6.30 *	6.20 *	7.80 *	5.50 *	7.30
Z	SI	*	6.443 *	6.536 *	6.532 *	6.476 *	6.312 *	6.538 *	6.307
	AL(IV)	*	1.557 *	1.464 *	1.468 *	1.524 *	1.688 *	1.462 *	1.693
Y	AL(VI)	*	0.357 *	0.370 *	0.374 *	0.334 *	0.310 *	0.452 *	0.309
	FE3+	*	0.617 *	0.573 *	0.577 *	0.628 *	0.756 *	0.447 *	0.730
	TI	*	0.073 *	0.057 *	0.067 *	0.053 *	0.073 *	0.066 *	0.071
	FE2+	*	1.550 *	1.585 *	1.452 *	1.388 *	1.517 *	1.762 *	1.528
	MN	*	0.016 *	0.010 *	0.007 *	0.022 *	0.021 *	0.005 *	0.036
	MG	*	2.387 *	2.405 *	2.523 *	2.565 *	2.321 *	2.270 *	2.327
	CA	*	0.0 *	0.0 *	0.0 *	0.0 *	0.0 *	0.0 *	0.0
X	FE2+	*	0.0 *	0.0 *	0.0 *	0.0 *	0.0 *	0.0 *	0.0
	MN	*	0.025 *	0.033 *	0.035 *	0.016 *	0.032 *	0.049 *	0.024
	CA	*	1.943 *	1.930 *	1.925 *	1.963 *	1.930 *	1.893 *	1.949
	NA	*	0.031 *	0.037 *	0.041 *	0.021 *	0.038 *	0.057 *	0.027
A	NA	*	0.425 *	0.397 *	0.372 *	0.410 *	0.388 *	0.376 *	0.420
	K	*	0.043 *	0.047 *	0.052 *	0.047 *	0.124 *	0.113 *	0.120
1	FI-FO-PG	HB	*	087-A6-A					
2	FI-ED	HB	*	087-A7-A					
3	FI-ED	HB	*	087-A8-A					
4	FI-FO-PG	HB	*	087-A9-A					
5	FI-MG-HS	HB	*	089-A1-A					
6	ED	HB	*	089-A2-A					
7	FI-FO-PG	HB	*	089-A3-A					

	*	1 *	2 *	3 *	4 *	5 *	6 *	7
SiO2	*	43.36 *	42.82 *	42.70 *	43.16 *	44.24 *	43.14 *	43.24
TiO2	*	0.60 *	0.63 *	0.67 *	0.54 *	0.74 *	0.64 *	0.64
Al2O3	*	11.31 *	11.45 *	11.65 *	11.51 *	10.55 *	11.37 *	11.53
Fe2O3	*	6.25 *	6.75 *	7.35 *	6.35 *	6.10 *	5.85 *	6.50
FeO	*	12.62 *	12.48 *	12.30 *	12.50 *	11.93 *	12.45 *	12.64
MnO	*	0.43 *	0.43 *	0.42 *	0.36 *	0.39 *	0.42 *	0.38
MgO	*	10.56 *	10.52 *	10.38 *	10.89 *	11.53 *	10.93 *	10.74
CaO	*	12.04 *	12.12 *	12.09 *	12.24 *	12.12 *	12.24 *	12.12
Na2O	*	1.45 *	1.59 *	1.49 *	1.54 *	1.48 *	1.52 *	1.54
K2O	*	0.62 *	0.61 *	0.60 *	0.90 *	0.64 *	0.88 *	0.85
TOTAL	*	99.24 *	99.40 *	99.65 *	100.09 *	99.72 *	99.44 *	100.18
Fe2O3 MIN	*	4.80 *	5.60 *	6.00 *	5.20 *	4.60 *	4.90 *	5.10
Fe2O3 MAX	*	7.70 *	7.90 *	8.70 *	7.50 *	7.60 *	6.80 *	7.90
Z	SI	6.391 *	6.318 *	6.287 *	6.234 *	6.462 *	6.354 *	6.331
	AL(IV)	1.609 *	1.682 *	1.713 *	1.676 *	1.538 *	1.646 *	1.669
Y	AL(VI)	0.356 *	0.311 *	0.309 *	0.311 *	0.278 *	0.328 *	0.320
	Fe3+	0.694 *	0.751 *	0.816 *	0.701 *	0.671 *	0.649 *	0.717
	Ti	0.066 *	0.070 *	0.074 *	0.071 *	0.081 *	0.071 *	0.070
	Fe2+	1.555 *	1.540 *	1.514 *	1.531 *	1.457 *	1.533 *	1.548
	Mn	0.008 *	0.015 *	0.009 *	0.008 *	0.001 *	0.020 *	0.001
	Mg	2.320 *	2.314 *	2.278 *	2.378 *	2.510 *	2.399 *	2.344
	Ca	0.0 *	0.0 *	0.0 *	0.0 *	0.0 *	0.0 *	0.0
X	Fe2+	0.0 *	0.0 *	0.0 *	0.0 *	0.0 *	0.0 *	0.0
	Mn	0.046 *	0.039 *	0.043 *	0.037 *	0.047 *	0.033 *	0.046
	Ca	1.901 *	1.916 *	1.907 *	1.921 *	1.897 *	1.932 *	1.901
	Na	0.053 *	0.045 *	0.049 *	0.041 *	0.056 *	0.036 *	0.052
A	Na	0.362 *	0.410 *	0.376 *	0.396 *	0.363 *	0.398 *	0.385
	K	0.117 *	0.115 *	0.113 *	0.168 *	0.119 *	0.165 *	0.159
1	FI-FO-PG HB	*	089-A4-A					
2	FI-MG-HS HB	*	089-A5-A					
3	FI-MG-HS HB	*	089-A6-A					
4	FI-FO-PG HB	*	090-A1-RA					
5	FI-FO-PG HB	*	090-A1-CA					
6	FI-FO-PG HB	*	090-A2-A					
7	FI-FO-PG HB	*	090-A3-RA					

	*	1 *	2 *	3 *	4 *	5 *	6 *
SI02	*	44.72 *	43.31 *	42.44 *	38.53 *	45.33 *	44.81 *
TI02	*	0.67 *	0.55 *	0.66 *	0.67 *	0.45 *	0.44 *
AL203	*	10.32 *	11.68 *	11.39 *	12.01 *	10.52 *	9.83 *
FE203	*	5.90 *	5.90 *	5.90 *	10.70 *	3.65 *	4.75 *
FE0	*	12.23 *	12.69 *	12.73 *	9.24 *	10.13 *	9.89 *
MNO	*	0.42 *	0.43 *	0.45 *	0.40 *	0.28 *	0.32 *
MGO	*	11.56 *	10.56 *	10.57 *	10.58 *	13.18 *	12.90 *
CAO	*	12.07 *	12.06 *	12.27 *	12.25 *	11.86 *	11.73 *
NA2O	*	1.50 *	1.48 *	1.58 *	1.61 *	1.52 *	1.38 *
K2O	*	0.63 *	0.73 *	0.90 *	1.09 *	0.62 *	0.60 *
TOTAL	*	100.02 *	99.39 *	98.89 *	97.08 *	97.54 *	96.65 *
FE203 MIN	*	4.20 *	4.50 *	5.30 *	10.70 *	1.60 *	2.80 *
FE203 MAX	*	7.60 *	7.30 *	6.50 *	10.70 *	5.70 *	6.70 *

Z	SI	*	6.511 *	6.373 *	6.309 *	5.884 *	6.641 *	6.646 *
	AL(IV)	*	1.489 *	1.627 *	1.691 *	2.116 *	1.359 *	1.354 *
Y	AL(VI)	*	0.282 *	0.399 *	0.305 *	0.045 *	0.458 *	0.364 *
	FE3+	*	0.647 *	0.654 *	0.661 *	1.231 *	0.403 *	0.531 *
	TI	*	0.073 *	0.061 *	0.074 *	0.077 *	0.050 *	0.049 *
	FE2+	*	1.488 *	1.562 *	1.583 *	1.180 *	1.211 *	1.205 *
	MN	*	0.0 *	0.008 *	0.035 *	0.052 *	0.0 *	0.0 *
	MG	*	2.509 *	2.316 *	2.342 *	2.408 *	2.878 *	2.852 *
	CA	*	0.0 *	0.0 *	0.0 *	0.0 *	0.0 *	0.0 *
X	FE2+	*	0.001 *	0.0 *	0.0 *	0.0 *	0.029 *	0.022 *
	MN	*	0.052 *	0.045 *	0.021 *	0.0 *	0.035 *	0.040 *
	CA	*	1.883 *	1.901 *	1.954 *	1.998 *	1.862 *	1.864 *
	NA	*	0.064 *	0.053 *	0.024 *	0.002 *	0.074 *	0.074 *
A	NA	*	0.359 *	0.369 *	0.431 *	0.475 *	0.357 *	0.322 *
	K	*	0.117 *	0.137 *	0.171 *	0.212 *	0.116 *	0.114 *

1	FI-ED HB	*	090-A3-CA
2	FI-FQ-PG HB	*	090-A4-A
3	FI-FQ-PG HB	*	090-A5-1
4	FI-MG HS	*	090-A6-AVE
5	ED HB	*	133-1 AM-1
6	FI-ED HB	*	133-2 AM-2

	*	1 *	2 *	3 *	4 *	5 *	6 *	7
SI02	*	41.94 *	43.65 *	41.95 *	42.80 *	44.23 *	43.84 *	43.97
TI02	*	0.42 *	0.79 *	0.68 *	0.80 *	0.84 *	0.75 *	0.84
AL2O3	*	17.08 *	13.27 *	14.33 *	13.91 *	12.68 *	13.23 *	12.48
FE2O3	*	4.30 *	3.40 *	7.60 *	4.35 *	3.75 *	4.05 *	5.60
FeO	*	13.26 *	14.24 *	11.78 *	13.91 *	12.95 *	12.94 *	11.93
MNO	*	0.38 *	0.40 *	0.39 *	0.42 *	0.52 *	0.49 *	0.43
MGO	*	8.34 *	9.38 *	9.22 *	9.14 *	10.36 *	10.09 *	10.52
CAO	*	11.85 *	11.93 *	10.97 *	11.83 *	11.91 *	11.88 *	11.36
NA2O	*	1.15 *	1.12 *	1.02 *	1.18 *	1.11 *	1.15 *	1.13
K2O	*	0.39 *	0.56 *	0.54 *	0.59 *	0.62 *	0.56 *	0.50
TOTAL	*	99.11 *	98.74 *	98.48 *	98.93 *	98.97 *	98.98 *	98.76
FE2O3 MIN	*	2.20 *	1.70 *	4.00 *	2.40 *	1.80 *	2.00 *	2.40
FE2O3 MAX	*	6.40 *	5.10 *	11.20 *	6.30 *	5.70 *	6.10 *	8.80
Z	SI	6.126 *	6.425 *	6.191 *	6.312 *	6.466 *	6.412 *	6.433
	AL(IV)	1.874 *	1.575 *	1.809 *	1.688 *	1.534 *	1.588 *	1.567
Y	AL(VI)	1.066 *	0.728 *	0.683 *	0.724 *	0.651 *	0.693 *	0.585
	FE3+	0.473 *	0.377 *	0.845 *	0.482 *	0.413 *	0.446 *	0.617
	TI	0.046 *	0.087 *	0.075 *	0.089 *	0.092 *	0.082 *	0.092
	FE2+	1.599 *	1.750 *	1.369 *	1.700 *	1.583 *	1.578 *	1.411
	MN	0.0 *	0.0 *	0.0 *	0.0 *	0.003 *	0.0 *	0.0
	MG	1.816 *	2.058 *	2.028 *	2.005 *	2.258 *	2.200 *	2.294
	CA	0.0 *	0.0 *	0.0 *	0.0 *	0.0 *	0.0 *	0.0
X	FE2+	0.021 *	0.004 *	0.005 *	0.011 *	0.0 *	0.004 *	0.049
	MN	0.047 *	0.050 *	0.049 *	0.052 *	0.062 *	0.061 *	0.053
	CA	1.854 *	1.882 *	1.734 *	1.865 *	1.866 *	1.862 *	1.781
	NA	0.078 *	0.065 *	0.131 *	0.071 *	0.073 *	0.074 *	0.117
A	NA	0.248 *	0.255 *	0.160 *	0.265 *	0.242 *	0.253 *	0.203
	K	0.073 *	0.105 *	0.102 *	0.111 *	0.116 *	0.104 *	0.093
1	FO-TS	*	083-A1-1					
2	FO-TS HB	*	083-A1-A					
3	FI-FO TS	*	083-A2-A					
4	FO-TS HB	*	083-A3-A					
5	TS HB	*	083-A4-A					
6	TS HB	*	083-A5-A					
7	FI-TS HB	*	083-A6-1					

		*	1 *	2 *	3 *	4 *	5 *	6 *	7
	SiO2	*	42.45 *	42.61 *	41.18 *	43.49 *	41.82 *	41.31 *	40.70
	TiO2	*	1.20 *	1.24 *	0.92 *	1.30 *	0.90 *	1.24 *	1.32
	Al2O3	*	13.69 *	13.49 *	14.43 *	13.16 *	11.95 *	14.18 *	13.77
	Fe2O3	*	3.15 *	2.65 *	3.65 *	2.10 *	3.10 *	1.50 *	3.30
	FeO	*	19.19 *	19.08 *	18.23 *	18.79 *	17.85 *	19.58 *	19.53
	MnO	*	0.20 *	0.14 *	0.17 *	0.13 *	0.09 *	0.16 *	0.20
	MgO	*	6.40 *	6.50 *	6.27 *	7.19 *	7.20 *	6.08 *	5.50
	CaO	*	11.30 *	11.11 *	11.23 *	11.45 *	11.62 *	11.38 *	11.52
	Na2O	*	1.18 *	1.22 *	1.22 *	1.19 *	1.15 *	1.32 *	1.32
	K2O	*	0.74 *	0.74 *	0.79 *	0.81 *	0.64 *	1.05 *	0.64
	TOTAL	*	99.50 *	98.78 *	98.09 *	99.61 *	96.32 *	97.80 *	97.80
	Fe2O3 MIN	*	0.40 *	0.0 *	1.10 *	0.0 *	2.00 *	0.0 *	2.00
	Fe2O3 MAX	*	5.90 *	5.30 *	6.20 *	4.20 *	4.20 *	3.00 *	4.60
Z	SI	*	6.342 *	6.395 *	6.238 *	6.451 *	6.441 *	6.294 *	6.277
	AL(IV)	*	1.658 *	1.605 *	1.762 *	1.549 *	1.559 *	1.706 *	1.723
Y	AL(VI)	*	0.753 *	0.781 *	0.814 *	0.752 *	0.610 *	0.840 *	0.780
	FE3+	*	0.355 *	0.300 *	0.417 *	0.235 *	0.360 *	0.172 *	0.384
	TI	*	0.135 *	0.140 *	0.105 *	0.145 *	0.104 *	0.142 *	0.071
	FE2+	*	2.332 *	2.325 *	2.248 *	2.279 *	2.273 *	2.465 *	2.501
	MN	*	0.0 *	0.0 *	0.0 *	0.0 *	0.0 *	0.0 *	0.0
	MG	*	1.425 *	1.454 *	1.416 *	1.590 *	1.653 *	1.381 *	1.264
	CA	*	0.0 *	0.0 *	0.0 *	0.0 *	0.0 *	0.0 *	0.0
X	FE2+	*	0.065 *	0.069 *	0.061 *	0.052 *	0.026 *	0.030 *	0.018
	MN	*	0.025 *	0.018 *	0.022 *	0.016 *	0.012 *	0.021 *	0.026
	CA	*	1.809 *	1.787 *	1.823 *	1.820 *	1.918 *	1.858 *	1.904
	NA	*	0.101 *	0.126 *	0.095 *	0.112 *	0.044 *	0.092 *	0.052
A	NA	*	0.241 *	0.229 *	0.263 *	0.231 *	0.299 *	0.298 *	0.343
	K	*	0.141 *	0.142 *	0.153 *	0.153 *	0.126 *	0.204 *	0.126
1	FO-TS HB	*	131-1	HB-1	SEPT/77				
2	FO-TS HB	*	131-1	HB-1-CORE	SEPT/77				
3	MG HS	*	131-1	HB-2 RIM	SEPT/77				
4	FO-TS HB	*	131-1	HB-2 CORE	SEPT/77				
5	MG-HS HB	*	131-1	HB-2 CORE-2	SEPT/77				
6	MG-HS HB	*	131-2	HB-3	IN GNT SEPT/77				
7	MG-HS HB	*	131-2	HB-4	IN GNT SEPT/77				

	*	1 *	2 *	3 *	4 *	5 *	6 *	7
SI02	*	41.99 *	40.66 *	39.71 *	41.80 *	41.26 *	40.77 *	44.57
TI02	*	1.07 *	0.63 *	0.43 *	1.18 *	1.16 *	1.18 *	0.63
AL2O3	*	14.44 *	14.76 *	13.23 *	13.40 *	14.08 *	14.65 *	11.44
FE2O3	*	1.85 *	4.80 *	6.45 *	2.20 *	2.00 *	3.00 *	1.05
FeO	*	18.82 *	18.13 *	17.26 *	18.50 *	18.86 *	17.71 *	15.56
MNO	*	0.12 *	0.25 *	0.17 *	0.11 *	0.13 *	0.11 *	0.30
MGO	*	6.43 *	5.71 *	6.23 *	6.93 *	6.66 *	6.89 *	9.85
CAO	*	11.40 *	11.28 *	11.63 *	11.17 *	11.63 *	11.47 *	12.04
NA2O	*	1.28 *	1.20 *	1.31 *	1.33 *	1.33 *	1.33 *	1.08
K2O	*	0.76 *	0.64 *	0.78 *	1.03 *	1.04 *	1.03 *	0.93
TOTAL	*	98.15 *	98.06 *	97.20 *	97.65 *	98.15 *	98.14 *	97.45
FE2O3 MIN	*	0.0 *	2.50 *	5.40 *	0.0 *	0.50 *	1.00 *	0.0
FE2O3 MAX	*	3.70 *	7.10 *	7.50 *	4.40 *	3.50 *	5.00 *	2.10

Z	SI	*	6.330 *	6.180 *	6.136 *	6.352 *	6.258 *	6.169 *	6.657
	AL(IV)	*	1.670 *	1.820 *	1.864 *	1.648 *	1.742 *	1.831 *	1.343
Y	AL(VI)	*	0.896 *	0.824 *	0.546 *	0.752 *	0.775 *	0.781 *	0.671
	FE3+	*	0.210 *	0.550 *	0.751 *	0.252 *	0.229 *	0.342 *	0.118
	TI	*	0.121 *	0.072 *	0.050 *	0.135 *	0.132 *	0.134 *	0.071
	FE2+	*	2.328 *	2.261 *	2.218 *	2.292 *	2.358 *	2.189 *	1.943
	MN	*	0.0 *	0.0 *	0.0 *	0.0 *	0.0 *	0.0 *	0.004
	MG	*	1.445 *	1.294 *	1.435 *	1.570 *	1.506 *	1.554 *	2.193
	CA	*	0.0 *	0.0 *	0.0 *	0.0 *	0.0 *	0.0 *	0.0
X	FE2+	*	0.044 *	0.044 *	0.012 *	0.059 *	0.034 *	0.052 *	0.0
	MN	*	0.015 *	0.032 *	0.022 *	0.014 *	0.017 *	0.014 *	0.034
	CA	*	1.841 *	1.837 *	1.926 *	1.819 *	1.890 *	1.859 *	1.927
	NA	*	0.099 *	0.087 *	0.040 *	0.108 *	0.059 *	0.074 *	0.039
A	NA	*	0.275 *	0.266 *	0.353 *	0.284 *	0.332 *	0.316 *	0.274
	K	*	0.146 *	0.124 *	0.154 *	0.200 *	0.201 *	0.199 *	0.177

1	MG-HS	HB	*	131-2	HB -5 CORE	IN MATRIX	SEPT/77
2	FI-FO	TS	*	131-2	HB-5 RIM	IN MATRIX	SEPT/77
3	FI-MG	HS	*	131-1	HB-1-RIM	NOV/77	
4	MG-HS	HB	*	131-1	HB-1-CORE	NOV/77	
5	MG-HS	HB	*	131-2	HB-2 CORE	NOV/77	
6	MG HS		*	2-131-2	HB-1	LARGE MATRIX GRAINS	FEB/78
7	ED HB		*	477-1	HB-1	NOV/77	

	*	1 *	2 *	3 *	4 *
SI02	*	46.43 *	46.93 *	46.77 *	44.29 *
TI02	*	0.55 *	0.59 *	0.50 *	0.61 *
AL203	*	10.97 *	10.64 *	12.17 *	13.63 *
FE203	*	1.95 *	1.65 *	2.25 *	2.10 *
FEO	*	13.60 *	14.47 *	13.32 *	15.01 *
MNO	*	0.33 *	0.32 *	0.36 *	0.33 *
MGO	*	11.38 *	11.09 *	11.34 *	9.54 *
CAO	*	11.96 *	12.14 *	12.09 *	11.95 *
NA2O	*	1.01 *	0.86 *	0.96 *	1.09 *
K2O	*	0.82 *	0.80 *	0.76 *	0.98 *
TOTAL	*	99.00 *	99.49 *	100.52 *	99.53 *
FE203 MIN	*	0.0 *	0.0 *	0.0 *	0.20 *
FE203 MAX	*	3.90 *	3.30 *	4.50 *	4.00 *

Z	SI	*	6.750 *	6.803 *	6.679 *	6.468 *
	AL(IV)	*	1.250 *	1.197 *	1.321 *	1.532 *
Y	AL(VI)	*	0.629 *	0.620 *	0.727 *	0.813 *
	FE3+	*	0.214 *	0.180 *	0.242 *	0.231 *
	TI	*	0.060 *	0.064 *	0.054 *	0.067 *
	FE2+	*	1.631 *	1.739 *	1.563 *	1.812 *
	MN	*	0.0 *	0.0 *	0.0 *	0.0 *
	MG	*	2.466 *	2.396 *	2.414 *	2.076 *
	CA	*	0.0 *	0.0 *	0.0 *	0.0 *
X	FE2+	*	0.022 *	0.015 *	0.027 *	0.021 *
	MN	*	0.041 *	0.039 *	0.044 *	0.041 *
	CA	*	1.863 *	1.885 *	1.850 *	1.870 *
	NA	*	0.075 *	0.061 *	0.080 *	0.069 *
A	NA	*	0.210 *	0.181 *	0.186 *	0.240 *
	K	*	0.152 *	0.148 *	0.138 *	0.183 *

1	COM HB	*	477-2	HB-2	WITH BT	NOV/77
2	COM HB	*	2-477-1	HB-1	FEB/78	
3	COM HB	*	2-477-1	HB-2	MATRIX	FEB/78
4	MG-HS HB	*	2-477-1	HB-3	CHECK	FEB/78

	*	1 *	2 *	3 *	4 *	5 *	6 *	7
SI02	*	44.13 *	42.98 *	43.71 *	44.32 *	43.86 *	43.62 *	44.59
TI02	*	0.69 *	0.96 *	0.81 *	0.73 *	1.13 *	1.18 *	1.14
AL203	*	12.30 *	12.30 *	11.93 *	11.74 *	11.79 *	12.02 *	11.18
FE203	*	6.15 *	6.75 *	5.70 *	4.90 *	5.50 *	5.60 *	5.20
FEO	*	12.63 *	12.04 *	12.17 *	11.77 *	10.48 *	10.75 *	10.99
MNO	*	0.26 *	0.24 *	0.23 *	0.21 *	0.23 *	0.26 *	0.28
MGO	*	10.63 *	10.59 *	10.80 *	11.36 *	11.80 *	11.61 *	11.71
CAO	*	11.65 *	11.31 *	11.63 *	11.68 *	11.16 *	11.31 *	10.98
NA2O	*	1.60 *	1.73 *	1.58 *	1.56 *	1.62 *	1.70 *	1.50
K2O	*	0.29 *	0.30 *	0.20 *	0.20 *	0.10 *	0.10 *	0.07
TOTAL	*	100.33 *	99.20 *	98.76 *	98.47 *	97.67 *	98.15 *	97.64
FE2O3 MIN	*	3.30 *	3.50 *	3.20 *	2.40 *	1.90 *	2.30 *	1.20
FE2O3 MAX	*	9.00 *	10.00 *	8.20 *	7.40 *	9.10 *	8.90 *	9.20

Z	SI	*	6.390 *	6.304 *	6.413 *	6.487 *	6.441 *	6.393 *	6.546
	AL(IV)	*	1.610 *	1.696 *	1.587 *	1.513 *	1.559 *	1.607 *	1.454
Y	AL(VI)	*	0.489 *	0.430 *	0.476 *	0.512 *	0.482 *	0.469 *	0.480
	FE3+	*	0.671 *	0.746 *	0.630 *	0.540 *	0.609 *	0.618 *	0.575
	TI	*	0.075 *	0.106 *	0.089 *	0.080 *	0.125 *	0.130 *	0.126
	FE2+	*	1.470 *	1.403 *	1.443 *	1.389 *	1.202 *	1.247 *	1.257
	MN	*	0.0 *	0.0 *	0.0 *	0.0 *	0.0 *	0.0 *	0.0
	MG	*	2.294 *	2.315 *	2.362 *	2.478 *	2.583 *	2.536 *	2.562
	CA	*	0.0 *	0.0 *	0.0 *	0.0 *	0.0 *	0.0 *	0.0
X	FE2+	*	0.059 *	0.073 *	0.051 *	0.052 *	0.085 *	0.071 *	0.092
	MN	*	0.032 *	0.030 *	0.029 *	0.026 *	0.029 *	0.032 *	0.035
	CA	*	1.807 *	1.777 *	1.828 *	1.832 *	1.756 *	1.776 *	1.727
	NA	*	0.102 *	0.120 *	0.092 *	0.090 *	0.130 *	0.121 *	0.146
A	NA	*	0.347 *	0.372 *	0.357 *	0.353 *	0.331 *	0.362 *	0.281
	K	*	0.054 *	0.056 *	0.037 *	0.037 *	0.019 *	0.019 *	0.013

1	FI-FO-PG	HB	*	080-1	HB-1	RIM IN QZ BAND
2	FI-FO-PG	HB	*	080-1	HB-1	CORE IN QZ BAND
3	FI-TS	HB	*	080.2	HB-2	GRAINS ADJ QZ BAND
4	FI-TS	HB	*	080-3	HB-3	GRAINS IN MATRIX
5	FI-COM	HB	*	130-1	HB-1	
6	FI-COM	HB	*	130-1	HB-2	
7	FI-COM	HB	*	130-2	HB-3	WITH QZ

	*	1 *	2 *	3 *	4 *	5 *	6 *	7
SI02	*	44.13 *	43.37 *	43.41 *	44.63 *	44.05 *	44.11 *	43.95
TI02	*	0.97 *	0.95 *	0.90 *	1.03 *	1.99 *	1.63 *	1.74
AL2O3	*	12.12 *	12.86 *	13.60 *	12.55 *	12.51 *	12.52 *	13.30
FE2O3	*	4.50 *	4.75 *	3.40 *	5.80 *	5.05 *	1.63 *	5.60
FeO	*	11.63 *	9.95 *	10.43 *	10.19 *	11.64 *	10.61 *	10.96
MNO	*	0.23 *	0.21 *	0.23 *	0.23 *	0.20 *	0.23 *	0.23
MGO	*	11.33 *	11.85 *	11.36 *	12.18 *	11.82 *	12.04 *	11.77
CAO	*	11.39 *	11.03 *	10.91 *	11.67 *	10.70 *	10.50 *	10.46
NA2O	*	1.61 *	1.71 *	1.68 *	1.62 *	2.29 *	2.13 *	2.32
K2O	*	0.11 *	0.13 *	0.15 *	0.13 *	0.05 *	0.04 *	0.04
TOTAL	*	98.02 *	96.81 *	96.07 *	100.03 *	100.30 *	95.44 *	100.37
FE2O3 MIN	*	1.40 *	1.00 *	0.0 *	2.70 *	0.0 *	0.40 *	0.0
FE2O3 MAX	*	7.60 *	8.50 *	6.80 *	8.90 *	10.10 *	12.00 *	11.20
Z	SI	6.470 *	6.395 *	6.428 *	6.392 *	6.326 *	6.334 *	6.288
	AL(IV)	1.530 *	1.605 *	1.572 *	1.608 *	1.674 *	1.666 *	1.712
Y	AL(VI)	0.564 *	0.630 *	0.802 *	0.511 *	0.444 *	0.453 *	0.531
	FE3+	0.497 *	0.528 *	0.379 *	0.626 *	0.547 *	0.671 *	0.604
	TI	0.107 *	0.105 *	0.100 *	0.111 *	0.215 *	0.176 *	0.187
	FE2+	1.356 *	1.133 *	1.212 *	1.152 *	1.265 *	1.123 *	1.167
	MN	0.0 *	0.0 *	0.0 *	0.0 *	0.0 *	0.0 *	0.0
	MG	2.476 *	2.604 *	2.507 *	2.600 *	2.530 *	2.577 *	2.510
	CA	0.0 *	0.0 *	0.0 *	0.0 *	0.0 *	0.0 *	0.0
X	FE2+	0.070 *	0.093 *	0.080 *	0.069 *	0.133 *	0.151 *	0.144
	MN	0.029 *	0.026 *	0.029 *	0.028 *	0.024 *	0.028 *	0.028
	CA	1.789 *	1.742 *	1.731 *	1.791 *	1.646 *	1.615 *	1.604
	NA	0.112 *	0.138 *	0.160 *	0.112 *	0.196 *	0.205 *	0.224
A	NA	0.346 *	0.351 *	0.322 *	0.338 *	0.441 *	0.388 *	0.419
	K	0.021 *	0.024 *	0.028 *	0.024 *	0.009 *	0.007 *	0.007
1	TS HB	*	130-2	HB-4	WITH QZ			
2	FI-TS HB	*	136-1	HB-1				
3	TS HB	*	136-1	HB-2				
4	FI-TS HB	*	136-2	HB-3				
5	FI-PG HB	*	223-1	HB-1				
6	FI-TS HB	*	223-1	HB-2				
7	FI-PG HB	*	223-1	HB-3				

	*	1 *	2 *	3 *	4 *	5 *	6 *	7
SiO2	*	54.75 *	39.62 *	39.57 *	43.77 *	43.19 *	43.09 *	42.51
TiO2	*	0.06 *	1.43 *	1.42 *	1.05 *	1.02 *	0.95 *	1.09
Al2O3	*	1.52 *	13.39 *	13.55 *	12.86 *	13.13 *	13.00 *	13.32
Fe2O3	*	1.50 *	2.50 *	3.90 *	5.05 *	5.60 *	5.70 *	8.60
FeO	*	11.87 *	20.30 *	20.07 *	12.48 *	11.87 *	12.57 *	8.57
MnO	*	0.17 *	0.47 *	0.45 *	0.25 *	0.23 *	0.23 *	0.23
MgO	*	16.18 *	5.61 *	5.49 *	10.77 *	10.84 *	10.45 *	11.85
CaO	*	12.37 *	11.55 *	11.21 *	11.64 *	11.61 *	11.84 *	11.04
Na2O	*	0.32 *	1.32 *	1.37 *	1.63 *	1.70 *	1.65 *	1.73
K2O	*	0.01 *	1.71 *	1.67 *	0.35 *	0.35 *	0.38 *	0.18
TOTAL	*	98.75 *	97.90 *	98.70 *	99.85 *	99.54 *	99.86 *	99.12
Fe2O3 MIN	*	0.30 *	1.40 *	1.80 *	2.20 *	2.80 *	3.50 *	4.40
Fe2O3 MAX	*	2.70 *	3.60 *	6.00 *	7.90 *	8.40 *	7.90 *	12.80

Z	SI	*	7.786 *	6.142 *	6.092 *	6.350 *	6.285 *	6.279 *	6.166
	AL(IV)	*	0.214 *	1.858 *	1.908 *	1.650 *	1.715 *	1.721 *	1.834
Y	AL(VI)	*	0.041 *	0.588 *	0.551 *	0.549 *	0.537 *	0.511 *	0.443
	Fe3+	*	0.161 *	0.292 *	0.452 *	0.552 *	0.614 *	0.626 *	0.940
	TI	*	0.006 *	0.167 *	0.164 *	0.115 *	0.112 *	0.104 *	0.119
	Fe2+	*	1.362 *	2.632 *	2.573 *	1.455 *	1.386 *	1.489 *	0.937
	MN	*	0.0 *	0.025 *	0.0 *	0.0 *	0.0 *	0.0 *	0.0
	MG	*	3.430 *	1.296 *	1.260 *	2.329 *	2.351 *	2.270 *	2.562
	CA	*	0.0 *	0.0 *	0.0 *	0.0 *	0.0 *	0.0 *	0.0
X	Fe2+	*	0.049 *	0.0 *	0.012 *	0.058 *	0.059 *	0.043 *	0.103
	MN	*	0.020 *	0.037 *	0.059 *	0.031 *	0.028 *	0.028 *	0.028
	CA	*	1.885 *	1.918 *	1.849 *	1.809 *	1.810 *	1.848 *	1.716
	NA	*	0.045 *	0.045 *	0.081 *	0.102 *	0.102 *	0.080 *	0.153
A	NA	*	0.043 *	0.352 *	0.328 *	0.357 *	0.377 *	0.386 *	0.334
	K	*	0.002 *	0.338 *	0.328 *	0.065 *	0.065 *	0.071 *	0.033

1	ACT	*	223-2	AMPH-4	SECONDARY ACTINOLITE
2	MG HS	*	451-2	HB-1	
3	MG HS	*	451-2	HB-2	
4	FI-PG HB	*	458-1	HB-1	
5	FI-PG HB	*	458-1	HB-2	SURROUNDING OPAQUES
6	FI-PG HB	*	458-2	HB-3	MANY LARGE GRAINS
7	FI TS	*	459-1	HB-1	

	*	1 *	2 *	3 *	4 *	5 *	6 *	7
SI02	*	44.07 *	44.80 *	44.67 *	44.33 *	43.75 *	43.69 *	42.56
TIO2	*	0.98 *	0.91 *	0.96 *	1.61 *	1.55 *	1.63 *	1.81
AL2O3	*	12.95 *	12.05 *	12.58 *	11.24 *	11.32 *	11.64 *	11.59
FE2O3	*	7.00 *	6.00 *	6.65 *	6.90 *	5.90 *	6.10 *	3.95
FeO	*	9.79 *	9.71 *	9.96 *	8.88 *	9.87 *	9.55 *	11.34
MNO	*	0.23 *	0.25 *	0.23 *	0.27 *	0.28 *	0.26 *	0.19
MGO	*	12.02 *	12.35 *	12.11 *	13.08 *	12.60 *	12.72 *	11.80
CAO	*	10.99 *	10.88 *	10.86 *	10.87 *	11.33 *	11.45 *	10.75
NA2O	*	1.79 *	1.61 *	1.71 *	1.82 *	1.91 *	1.89 *	2.29
K2O	*	0.18 *	0.15 *	0.17 *	0.16 *	0.17 *	0.17 *	0.05
TOTAL	*	100.00 *	98.71 *	99.90 *	99.16 *	98.68 *	99.10 *	96.33
FE2O3 MIN	*	2.30 *	1.30 *	1.60 *	2.10 *	2.50 *	2.80 *	0.0
FE2O3 MAX	*	11.70 *	10.70 *	11.70 *	11.70 *	9.30 *	9.40 *	7.90
Z	SI	6.321 *	6.476 *	6.401 *	6.396 *	6.373 *	6.333 *	6.365
	AL(IV)	1.679 *	1.524 *	1.599 *	1.604 *	1.627 *	1.667 *	1.635
Y	AL(VI)	0.511 *	0.529 *	0.525 *	0.307 *	0.317 *	0.321 *	0.408
	FE3+	0.757 *	0.654 *	0.718 *	0.750 *	0.648 *	0.666 *	0.445
	TI	0.106 *	0.099 *	0.103 *	0.175 *	0.170 *	0.178 *	0.204
	FE2+	1.057 *	1.057 *	1.067 *	0.955 *	1.130 *	1.087 *	1.313
	MN	0.0 *	0.0 *	0.0 *	0.0 *	0.0 *	0.0 *	0.0
	MG	2.570 *	2.661 *	2.586 *	2.813 *	2.736 *	2.748 *	2.630
	CA	0.0 *	0.0 *	0.0 *	0.0 *	0.0 *	0.0 *	0.0
X	FE2+	0.118 *	0.117 *	0.126 *	0.116 *	0.073 *	0.071 *	0.104
	MN	0.028 *	0.031 *	0.028 *	0.033 *	0.035 *	0.032 *	0.024
	CA	1.689 *	1.685 *	1.667 *	1.680 *	1.768 *	1.778 *	1.722
	NA	0.165 *	0.168 *	0.179 *	0.170 *	0.124 *	0.119 *	0.149
A	NA	0.332 *	0.284 *	0.297 *	0.339 *	0.415 *	0.412 *	0.515
	K	0.033 *	0.028 *	0.031 *	0.029 *	0.032 *	0.031 *	0.010
1	FI-TS HB	*	459-1	HB-2				
2	FI-TS HB	*	459-2	HB-3				
3	FI-TS HB	*	459-2	HB-4				
4	FI-TS HB	*	551-1	HB-1				
5	FI-FO-PG HB	*	551-2	HB-2				
6	FI-FO-PG HB	*	551-2	HB-3				
7	FO-PG HB	*	552-1	HB-1				

		*	1 *	2 *	3 *	4 *	5 *	6 *	7
	SI02	*	43.91 *	43.75 *	43.38 *	42.77 *	43.48 *	43.34 *	43.32
	TI02	*	1.58 *	1.75 *	1.71 *	1.79 *	1.71 *	1.95 *	1.97
	AL203	*	11.01 *	11.28 *	11.48 *	11.44 *	11.15 *	11.49 *	12.27
	FE203	*	3.90 *	3.75 *	3.75 *	3.95 *	4.45 *	5.20 *	4.15
	FEO	*	11.38 *	11.52 *	11.40 *	11.95 *	11.34 *	11.23 *	13.29
	MNO	*	0.19 *	0.23 *	0.23 *	0.21 *	0.22 *	0.20 *	0.23
	MGO	*	12.09 *	12.15 *	11.91 *	11.60 *	12.04 *	12.08 *	11.10
	CAO	*	10.87 *	11.09 *	10.89 *	11.08 *	10.83 *	11.09 *	11.41
	NA2O	*	2.10 *	2.18 *	2.16 *	2.27 *	2.20 *	2.22 *	2.39
	K2O	*	0.05 *	0.05 *	0.05 *	0.05 *	0.05 *	0.05 *	0.0
	TOTAL	*	97.08 *	97.75 *	96.96 *	97.11 *	97.47 *	98.85 *	100.13
	FE203 MIN	*	0.0 *	0.10 *	0.0 *	0.60 *	0.30 *	1.30 *	0.80
	FE203 MAX	*	7.80 *	7.40 *	7.50 *	7.30 *	8.60 *	9.10 *	7.50
Z	SI	*	6.495 *	6.439 *	6.431 *	6.368 *	6.425 *	6.332 *	6.291
	AL(IV)	*	1.505 *	1.561 *	1.569 *	1.632 *	1.575 *	1.668 *	1.709
Y	AL(VI)	*	0.415 *	0.396 *	0.437 *	0.375 *	0.367 *	0.310 *	0.391
	FE3+	*	0.435 *	0.416 *	0.419 *	0.443 *	0.496 *	0.572 *	0.454
	TI	*	0.176 *	0.194 *	0.191 *	0.200 *	0.190 *	0.214 *	0.215
	FE2+	*	1.309 *	1.329 *	1.321 *	1.407 *	1.296 *	1.273 *	1.537
	MN	*	0.0 *	0.0 *	0.0 *	0.0 *	0.0 *	0.0 *	0.0
	MG	*	2.666 *	2.665 *	2.632 *	2.574 *	2.652 *	2.630 *	2.403
	CA	*	0.0 *	0.0 *	0.0 *	0.0 *	0.0 *	0.0 *	0.0
X	FE2+	*	0.099 *	0.088 *	0.092 *	0.080 *	0.105 *	0.099 *	0.077
	MN	*	0.024 *	0.029 *	0.029 *	0.026 *	0.028 *	0.025 *	0.028
	CA	*	1.723 *	1.749 *	1.730 *	1.767 *	1.715 *	1.736 *	1.775
	NA	*	0.154 *	0.135 *	0.150 *	0.126 *	0.153 *	0.140 *	0.120
A	NA	*	0.448 *	0.487 *	0.471 *	0.530 *	0.477 *	0.489 *	0.553
	K	*	0.009 *	0.009 *	0.009 *	0.009 *	0.009 *	0.009 *	0.0
1	FO-PG HB	*	552-1	HB-2					
2	FO-PG HB	*	552-2	HB-3					
3	FO-PG HB	*	552-2	HB-4					
4	FO-PG HB	*	552-3	HB-5					
5	FO-PG HB	*	552-3	HB-6					
6	FI-FO-PG HB	*	552-1	HB-7	CHECK				
7	FO-PG HB	*	553-1	HB-1					

	*	1 *	2 *	3 *	4 *	5 *
SI02	*	43.66 *	43.82 *	42.86 *	42.21 *	43.66 *
TI02	*	1.94 *	1.92 *	2.11 *	2.18 *	2.12 *
AL203	*	12.02 *	11.93 *	12.44 *	12.16 *	11.84 *
FE203	*	4.45 *	3.95 *	4.50 *	3.45 *	3.25 *
FEO	*	13.13 *	13.16 *	12.00 *	12.74 *	13.21 *
MNO	*	0.20 *	0.20 *	0.17 *	0.16 *	0.22 *
MGO	*	11.17 *	11.21 *	11.56 *	11.39 *	11.41 *
CAO	*	11.16 *	11.04 *	10.79 *	11.07 *	11.29 *
NA2O	*	2.30 *	2.29 *	2.46 *	2.66 *	2.40 *
K2O	*	0.0 *	0.05 *	0.05 *	0.05 *	0.05 *
TOTAL	*	100.03 *	99.57 *	98.94 *	98.07 *	99.45 *
FE203 MIN	*	0.50 *	0.0 *	0.0 *	0.0 *	0.0 *
FE203 MAX	*	8.40 *	7.90 *	9.00 *	6.90 *	6.50 *

Z	SI	*	6.336 *	6.377 *	6.264 *	6.250 *	6.363 *
	AL(IV)	*	1.664 *	1.623 *	1.736 *	1.750 *	1.637 *
Y	AL(VI)	*	0.391 *	0.423 *	0.407 *	0.372 *	0.397 *
	FE3+	*	0.487 *	0.433 *	0.496 *	0.385 *	0.357 *
	TI	*	0.212 *	0.210 *	0.232 *	0.243 *	0.232 *
	FE2+	*	1.494 *	1.502 *	1.347 *	1.486 *	1.535 *
	MN	*	0.0 *	0.0 *	0.0 *	0.0 *	0.0 *
	MG	*	2.416 *	2.432 *	2.518 *	2.514 *	2.479 *
	CA	*	0.0 *	0.0 *	0.0 *	0.0 *	0.0 *
X	FE2+	*	0.098 *	0.099 *	0.120 *	0.091 *	0.075 *
	MN	*	0.025 *	0.025 *	0.021 *	0.020 *	0.027 *
	CA	*	1.735 *	1.721 *	1.690 *	1.756 *	1.763 *
	NA	*	0.142 *	0.155 *	0.169 *	0.133 *	0.135 *
A	NA	*	0.505 *	0.492 *	0.528 *	0.631 *	0.543 *
	K	*	0.0 *	0.009 *	0.009 *	0.009 *	0.009 *

1	FO-PG	HB	*	553-1	HB-2
2	FO-PG	HB	*	553-2	HB-3
3	TI-FO-PG	HB	*	553-2	HB-4
4	TI-FO-PG	HB	*	553-2	HB-4-2
5	TI-FO-PG	HB	*	553-1	HB-5 CHECK

	*	1 *	2 *	3 *	4 *	5 *	6 *	7
SI02	*	47.06 *	46.41 *	46.46 *	47.38 *	47.86 *	47.51 *	47.91
TI02	*	1.05 *	0.89 *	0.88 *	0.56 *	0.41 *	0.46 *	0.65
AL203	*	9.66 *	9.71 *	9.75 *	10.25 *	10.29 *	10.11 *	10.22
FE203	*	2.70 *	2.85 *	2.60 *	5.45 *	3.60 *	4.20 *	5.50
FE0	*	9.15 *	8.85 *	8.86 *	6.53 *	7.53 *	6.98 *	6.57
MNO	*	0.14 *	0.18 *	0.17 *	0.18 *	0.16 *	0.14 *	0.16
MGO	*	14.39 *	14.21 *	14.21 *	15.27 *	15.14 *	15.23 *	15.38
CAO	*	11.97 *	12.23 *	12.07 *	12.30 *	12.28 *	12.18 *	12.09
NA2O	*	1.38 *	1.31 *	1.30 *	1.10 *	1.19 *	1.16 *	1.08
K2O	*	0.05 *	0.05 *	0.04 *	0.17 *	0.16 *	0.13 *	0.16
TOTAL	*	97.55 *	96.69 *	96.34 *	99.19 *	98.62 *	98.10 *	99.72
FE203 MIN	*	0.50 *	1.60 *	1.00 *	3.40 *	1.60 *	2.10 *	2.70
FE203 MAX	*	4.90 *	4.10 *	4.20 *	7.50 *	5.60 *	6.30 *	8.30

Z	SI	*	6.797 *	6.770 *	6.790 *	6.702 *	6.795 *	6.777 *	6.730
	AL(IV)	*	1.203 *	1.230 *	1.210 *	1.298 *	1.205 *	1.223 *	1.270
Y	AL(VI)	*	0.441 *	0.439 *	0.470 *	0.410 *	0.516 *	0.476 *	0.422
	FE3+	*	0.294 *	0.313 *	0.286 *	0.581 *	0.385 *	0.451 *	0.582
	TI	*	0.114 *	0.098 *	0.097 *	0.060 *	0.044 *	0.049 *	0.069
	FE2+	*	1.053 *	1.061 *	1.052 *	0.730 *	0.851 *	0.785 *	0.707
	MN	*	0.0 *	0.0 *	0.0 *	0.0 *	0.0 *	0.0 *	0.0
	MG	*	3.098 *	3.089 *	3.096 *	3.219 *	3.204 *	3.238 *	3.220
	CA	*	0.0 *	0.0 *	0.0 *	0.0 *	0.0 *	0.0 *	0.0
X	FE2+	*	0.053 *	0.018 *	0.031 *	0.042 *	0.043 *	0.048 *	0.065
	MN	*	0.017 *	0.022 *	0.021 *	0.022 *	0.019 *	0.017 *	0.019
	CA	*	1.852 *	1.911 *	1.890 *	1.864 *	1.868 *	1.861 *	1.820
	NA	*	0.078 *	0.048 *	0.058 *	0.072 *	0.070 *	0.074 *	0.097
A	NA	*	0.308 *	0.322 *	0.311 *	0.229 *	0.258 *	0.247 *	0.197
	K	*	0.009 *	0.009 *	0.007 *	0.031 *	0.029 *	0.024 *	0.029

1	COM HB	*	128-1	AM-1	
2	COM HB	*	128-2	AM-2	
3	COM HB	*	128-2	AM-3	
4	FI-COM HB	*	270-1	HB-1	SEVERAL GRAINS
5	COM HB	*	270-1	HB-2	LARGE PATCHY GRAIN
6	COM HB	*	270-2	HB-3	LARGE RAGGED GRAIN
7	FI-COM HB	*	270-2	HB-4	MATRIX

	*	1 *	2 *	3 *	4 *	5 *	6 *	7
SI02	*	46.25 *	46.94 *	46.46 *	46.93 *	46.86 *	45.82 *	51.13
TI02	*	0.84 *	0.89 *	0.68 *	0.88 *	0.64 *	0.90 *	0.34
AL2O3	*	9.93 *	9.04 *	9.99 *	9.67 *	9.38 *	12.46 *	5.25
FE2O3	*	3.45 *	3.30 *	4.70 *	3.85 *	2.90 *	3.35 *	2.45
FeO	*	9.49 *	9.64 *	9.40 *	10.68 *	10.69 *	7.31 *	7.98
MNO	*	0.25 *	0.19 *	0.26 *	0.26 *	0.23 *	0.11 *	0.10
MGO	*	13.71 *	14.04 *	13.59 *	13.32 *	13.31 *	14.93 *	16.65
CAO	*	12.61 *	12.38 *	11.66 *	12.00 *	12.15 *	11.95 *	12.25
NA2O	*	1.35 *	1.22 *	1.46 *	1.42 *	1.30 *	2.00 *	0.83
K2O	*	0.11 *	0.13 *	0.09 *	0.12 *	0.12 *	0.0 *	0.0
TOTAL	*	97.99 *	97.77 *	98.29 *	99.13 *	97.58 *	98.83 *	96.98
FE2O3 MIN	*	1.90 *	2.20 *	1.80 *	1.60 *	1.40 *	0.60 *	0.70
FE2O3 MAX	*	5.00 *	4.40 *	7.60 *	6.10 *	4.40 *	6.10 *	4.20

Z	SI	*	6.724 *	6.807 *	6.711 *	6.749 *	6.827 *	6.505 *	7.335
	AL(IV)	*	1.276 *	1.193 *	1.289 *	1.251 *	1.173 *	1.495 *	0.665
Y	AL(VI)	*	0.425 *	0.352 *	0.412 *	0.387 *	0.438 *	0.590 *	0.223
	FE3+	*	0.378 *	0.361 *	0.512 *	0.417 *	0.318 *	0.358 *	0.265
	TI	*	0.092 *	0.097 *	0.074 *	0.095 *	0.070 *	0.096 *	0.037
	FE2+	*	1.134 *	1.156 *	1.076 *	1.245 *	1.284 *	0.796 *	0.915
	MN	*	0.0 *	0.0 *	0.0 *	0.0 *	0.0 *	0.0 *	0.0
	MG	*	2.971 *	3.035 *	2.926 *	2.855 *	2.890 *	3.159 *	3.560
	CA	*	0.0 *	0.0 *	0.0 *	0.0 *	0.0 *	0.0 *	0.0
X	FE2+	*	0.019 *	0.013 *	0.059 *	0.039 *	0.019 *	0.071 *	0.041
	MN	*	0.031 *	0.023 *	0.032 *	0.032 *	0.028 *	0.013 *	0.012
	CA	*	1.894 *	1.923 *	1.805 *	1.849 *	1.897 *	1.818 *	1.883
	NA	*	0.056 *	0.040 *	0.104 *	0.081 *	0.056 *	0.098 *	0.063
A	NA	*	0.325 *	0.303 *	0.305 *	0.315 *	0.311 *	0.453 *	0.167
	K	*	0.020 *	0.024 *	0.017 *	0.022 *	0.022 *	0.0 *	0.0

1	COM HB	*	504-1	HB-1	
2	COM HB	*	504-1	HB-2	
3	FI-COM HB	*	504-2	HB-3	CORE LARGE GRAIN
4	COM HB	*	504-2	HB-3	RIM LARGE GRAIN
5	COM HB	*	504-2	HB-4	MATRIX COARSE GRAINED BAND
6	ED HB	*	554-2	AM-2	
7	ACT HB	*	554-1	AM-1	AFTER CPX

		*	1 *	2 *	3 *	4 *
	SI02	*	46.71 *	44.89 *	45.40 *	44.92 *
	TI02	*	0.57 *	0.72 *	0.59 *	0.55 *
	AL2O3	*	10.69 *	12.70 *	12.13 *	12.34 *
	FE2O3	*	7.55 *	7.50 *	6.30 *	7.85 *
	FE0	*	6.62 *	6.85 *	6.65 *	5.86 *
	MNO	*	0.15 *	0.11 *	0.10 *	0.10 *
	MGO	*	14.84 *	14.04 *	14.37 *	14.42 *
	CAO	*	11.48 *	11.60 *	11.77 *	11.68 *
	NA2O	*	1.57 *	1.83 *	1.61 *	1.65 *
	K2O	*	0.05 *	0.03 *	0.03 *	0.03 *
	TOTAL	*	100.23 *	100.27 *	98.95 *	99.40 *
	FE2O3 MIN	*	3.40 *	3.80 *	3.20 *	4.50 *
	FE2O3 MAX	*	11.70 *	11.20 *	9.40 *	11.20 *
Z	SI	*	6.577 *	6.343 *	6.465 *	6.379 *
	AL(IV)	*	1.423 *	1.657 *	1.535 *	1.621 *
Y	AL(VI)	*	0.351 *	0.458 *	0.501 *	0.444 *
	FE3+	*	0.801 *	0.799 *	0.676 *	0.840 *
	TI	*	0.060 *	0.076 *	0.063 *	0.059 *
	FE2+	*	0.673 *	0.709 *	0.709 *	0.605 *
	MN	*	0.0 *	0.0 *	0.0 *	0.0 *
	MG	*	3.115 *	2.957 *	3.050 *	3.052 *
	CA	*	0.0 *	0.0 *	0.0 *	0.0 *
X	FE2+	*	0.106 *	0.100 *	0.083 *	0.091 *
	MN	*	0.018 *	0.013 *	0.012 *	0.012 *
	CA	*	1.732 *	1.756 *	1.796 *	1.777 *
	NA	*	0.144 *	0.130 *	0.109 *	0.120 *
A	NA	*	0.285 *	0.371 *	0.335 *	0.334 *
	K	*	0.009 *	0.005 *	0.005 *	0.005 *
1	FI-COM HB	*	560-1	HB-1		
2	FI-TS HB	*	560-1	HB-2		
3	FI-TS HB	*	560-1	HB-3		
4	FI-TS HB	*	560-1	HB-4		

		*	1 *	2 *	3 *	4 *	5 *	6 *	7
	SiO2	*	49.91 *	50.48 *	51.47 *	48.55 *	49.90 *	51.60 *	53.44
	TiO2	*	0.03 *	0.07 *	0.61 *	0.87 *	0.70 *	0.43 *	0.29
	Al2O3	*	11.84 *	12.43 *	7.34 *	9.68 *	9.40 *	7.06 *	5.74
	Fe2O3	*	2.30 *	2.09 *	2.60 *	4.35 *	3.65 *	3.80 *	2.95
	FeO	*	1.89 *	1.88 *	6.61 *	6.25 *	6.66 *	5.45 *	5.97
	MnO	*	0.07 *	0.09 *	0.13 *	0.14 *	0.14 *	0.16 *	0.13
	MgO	*	19.36 *	19.30 *	17.29 *	16.12 *	16.41 *	17.77 *	18.50
	CaO	*	12.32 *	12.43 *	12.41 *	12.20 *	12.36 *	12.38 *	12.29
	Na2O	*	1.35 *	1.38 *	0.85 *	1.15 *	1.06 *	0.81 *	0.58
	K2O	*	0.02 *	0.02 *	0.04 *	0.05 *	0.04 *	0.02 *	0.03
	TOTAL	*	99.09 *	100.17 *	99.35 *	99.36 *	100.32 *	99.48 *	99.92
	Fe2O3 MIN	*	0.20 *	0.0 *	0.30 *	1.80 *	1.10 *	1.30 *	0.70
	Fe2O3 MAX	*	4.40 *	4.18 *	4.90 *	6.90 *	6.20 *	6.30 *	5.20
Z	SI	*	6.816 *	6.810 *	7.160 *	6.808 *	6.912 *	7.155 *	7.350
	AL(IV)	*	1.184 *	1.190 *	0.840 *	1.192 *	1.088 *	0.845 *	0.650
Y	AL(VI)	*	0.722 *	0.787 *	0.364 *	0.408 *	0.447 *	0.309 *	0.281
	FE3+	*	0.237 *	0.212 *	0.273 *	0.460 *	0.381 *	0.397 *	0.306
	TI	*	0.003 *	0.007 *	0.064 *	0.092 *	0.073 *	0.045 *	0.030
	FE2+	*	0.098 *	0.113 *	0.715 *	0.672 *	0.711 *	0.576 *	0.591
	MN	*	0.0 *	0.0 *	0.0 *	0.0 *	0.0 *	0.0 *	0.0
	MG	*	3.941 *	3.881 *	3.585 *	3.369 *	3.388 *	3.673 *	3.793
	CA	*	0.0 *	0.0 *	0.0 *	0.0 *	0.0 *	0.0 *	0.0
X	FE2+	*	0.118 *	0.099 *	0.055 *	0.060 *	0.060 *	0.056 *	0.095
	MN	*	0.008 *	0.010 *	0.015 *	0.017 *	0.016 *	0.019 *	0.015
	CA	*	1.803 *	1.797 *	1.850 *	1.833 *	1.834 *	1.839 *	1.811
	NA	*	0.071 *	0.094 *	0.080 *	0.090 *	0.089 *	0.086 *	0.078
A	NA	*	0.287 *	0.267 *	0.149 *	0.223 *	0.196 *	0.132 *	0.076
	K	*	0.003 *	0.003 *	0.007 *	0.009 *	0.007 *	0.004 *	0.005
1	COM HB	*	132-1	AM-1	CORONITE				
2	COM HB	*	132-1	AM-2	CORONITE				
3	COM HB	*	404-1	AM-1	LONG RIDGE				
4	COM HB	*	404-1	AM-2	MANY SMALL XLS AFTER CPX	LONG RIDGE			
5	COM HB	*	404-1	AM-3	MANY SMALL XLS AFTER CPX	LONG RIDGE			
6	COM HB	*	404-2	AM-4	ONE XL AFTER CPX				
7	ACT HB	*	404-2	AM-5	CLOT OF SMALL GRAINS				

		*	1 *	2 *	3 *	4 *	5 *	6 *	7
	SI02	*	52.45 *	48.23 *	48.50 *	48.24 *	49.01 *	48.50 *	50.08
	TI02	*	0.50 *	0.05 *	0.07 *	0.65 *	0.53 *	0.71 *	0.39
	AL203	*	5.10 *	13.54 *	13.67 *	9.64 *	8.89 *	8.84 *	9.71
	FE203	*	2.50 *	3.19 *	2.72 *	2.80 *	2.65 *	3.50 *	3.25
	FEO	*	5.41 *	1.79 *	2.27 *	6.64 *	6.19 *	5.96 *	5.82
	MNO	*	0.16 *	0.04 *	0.06 *	0.16 *	0.13 *	0.14 *	0.14
	MGO	*	18.51 *	18.68 *	18.48 *	16.06 *	16.51 *	16.39 *	16.79
	CAO	*	12.51 *	12.30 *	12.22 *	11.98 *	11.98 *	11.72 *	11.81
	NA2O	*	0.64 *	1.55 *	1.64 *	1.36 *	1.16 *	1.20 *	1.32
	K2O	*	0.03 *	0.05 *	0.06 *	0.03 *	0.02 *	0.02 *	0.04
	TOTAL	*	97.81 *	99.42 *	99.69 *	97.56 *	97.07 *	96.98 *	99.35
	FE203 MIN	*	0.70 *	1.20 *	0.20 *	0.20 *	0.10 *	0.40 *	0.0
	FE203 MAX	*	4.30 *	5.18 *	5.23 *	5.40 *	5.20 *	6.60 *	6.50
Z	SI	*	7.365 *	6.596 *	6.618 *	6.872 *	6.984 *	6.932 *	6.958
	AL(IV)	*	0.635 *	1.404 *	1.382 *	1.128 *	1.016 *	1.068 *	1.042
Y	AL(VI)	*	0.209 *	0.779 *	0.816 *	0.490 *	0.478 *	0.421 *	0.547
	FE3+	*	0.265 *	0.329 *	0.279 *	0.301 *	0.285 *	0.377 *	0.340
	TI	*	0.053 *	0.005 *	0.007 *	0.070 *	0.057 *	0.076 *	0.041
	FE2+	*	0.599 *	0.079 *	0.138 *	0.730 *	0.674 *	0.634 *	0.595
	MN	*	0.0 *	0.0 *	0.0 *	0.0 *	0.0 *	0.0 *	0.0
	MG	*	3.874 *	3.808 *	3.759 *	3.410 *	3.507 *	3.492 *	3.477
	CA	*	0.0 *	0.0 *	0.0 *	0.0 *	0.0 *	0.0 *	0.0
X	FE2+	*	0.036 *	0.126 *	0.120 *	0.061 *	0.063 *	0.079 *	0.081
	MN	*	0.019 *	0.005 *	0.007 *	0.019 *	0.016 *	0.017 *	0.016
	CA	*	1.882 *	1.802 *	1.787 *	1.828 *	1.829 *	1.795 *	1.758
	NA	*	0.062 *	0.067 *	0.086 *	0.091 *	0.092 *	0.110 *	0.145
A	NA	*	0.112 *	0.344 *	0.348 *	0.284 *	0.228 *	0.223 *	0.211
	K	*	0.005 *	0.009 *	0.010 *	0.005 *	0.004 *	0.004 *	0.007
1	ACT HB	*	404-1	AM-6	WITH CPX-2				
2	COM HB	*	408-1	HB-1					
3	COM HB	*	408-1	HB-2					
4	COM HB	*	LRC77-1	AM-1	MOST DEFORMED	NO CPX			
5	COM HB	*	LRC77-2	AM-2	WITH CPX				
6	COM HB	*	LRC77-3	AM-3	LEAST DEFORMED	WITH CPX			
7	COM HB	*	LRC77-2	ANPH-1					

		*	1 *	2 *	3 *	4 *	5 *	6 *	7
	SI02	*	37.00 *	37.06 *	37.28 *	37.42 *	36.64 *	36.70 *	37.23
	TI02	*	3.55 *	3.50 *	3.82 *	3.79 *	4.07 *	3.64 *	4.29
	AL203	*	14.95 *	14.98 *	14.39 *	14.57 *	15.15 *	14.34 *	14.38
	FE203	*	1.20 *	0.90 *	0.55 *	0.40 *	0.65 *	1.80 *	0.50
	FE0	*	18.21 *	18.33 *	18.28 *	17.94 *	18.92 *	18.04 *	19.43
	MNO	*	0.41 *	0.43 *	0.39 *	0.37 *	0.40 *	0.46 *	0.48
	MGO	*	6.66 *	6.54 *	6.96 *	6.94 *	6.23 *	6.94 *	6.40
	CAO	*	10.77 *	10.82 *	10.95 *	10.68 *	10.79 *	10.79 *	11.05
	NA2O	*	2.80 *	2.76 *	2.59 *	2.64 *	2.83 *	2.71 *	2.59
	K2O	*	1.12 *	1.12 *	1.46 *	1.53 *	1.21 *	1.25 *	1.44
	TOTAL	*	96.67 *	96.44 *	96.67 *	96.28 *	96.89 *	96.67 *	97.79
	FE203 MIN	*	0.0 *	0.0 *	0.0 *	0.0 *	0.0 *	0.0 *	0.0
	FE203 MAX	*	2.40 *	1.80 *	1.10 *	0.80 *	1.30 *	3.60 *	1.00
Z	SI	*	5.766 *	5.786 *	5.812 *	5.839 *	5.716 *	5.740 *	5.772
	AL (IV)	*	2.234 *	2.214 *	2.188 *	2.161 *	2.284 *	2.260 *	2.228
Y	AL (VI)	*	0.511 *	0.543 *	0.456 *	0.519 *	0.501 *	0.383 *	0.399
	FE3+	*	0.141 *	0.106 *	0.065 *	0.047 *	0.076 *	0.212 *	0.058
	TI	*	0.416 *	0.411 *	0.448 *	0.445 *	0.477 *	0.428 *	0.500
	FE2+	*	2.373 *	2.393 *	2.383 *	2.341 *	2.468 *	2.359 *	2.519
	MN	*	0.012 *	0.025 *	0.031 *	0.034 *	0.029 *	0.0 *	0.045
	MG	*	1.547 *	1.522 *	1.617 *	1.614 *	1.449 *	1.618 *	1.479
	CA	*	0.0 *	0.0 *	0.0 *	0.0 *	0.0 *	0.0 *	0.0
X	FE2+	*	0.0 *	0.0 *	0.0 *	0.0 *	0.0 *	0.0 *	0.0
	MN	*	0.043 *	0.032 *	0.020 *	0.015 *	0.024 *	0.061 *	0.018
	CA	*	1.798 *	1.810 *	1.829 *	1.786 *	1.803 *	1.808 *	1.835
	NA	*	0.159 *	0.158 *	0.151 *	0.199 *	0.172 *	0.131 *	0.146
A	NA	*	0.687 *	0.678 *	0.632 *	0.600 *	0.684 *	0.691 *	0.632
	K	*	0.223 *	0.223 *	0.290 *	0.305 *	0.241 *	0.249 *	0.285
1	TI-MG HS	*	486-1	HB-1	LARGE				
2	TI-MG HS	*	486-1	HB-2	LARGE				
3	TI-MG HS	*	486-1	HB-3	SMALL				
4	TI-MG HS	*	486-1	HB-4	SMALL				
5	TI-MG HS	*	486-2	HB-5	VERY LARGE				
6	TI-MG HS	*	486-3	HB-6					
7	KAEP	*	487-1	BR HB-1					

	*	1 *	2 *	3 *	4 *	5 *	6 *	7
SI02	*	37.07 *	37.16 *	36.94 *	37.52 *	36.55 *	36.81 *	36.42
TI02	*	3.98 *	3.91 *	0.64 *	0.61 *	4.88 *	4.24 *	4.63
AL2O3	*	14.51 *	14.73 *	13.85 *	13.50 *	16.52 *	15.94 *	16.77
FE2O3	*	0.35 *	1.30 *	6.65 *	6.70 *	1.40 *	1.35 *	1.15
FeO	*	19.49 *	18.35 *	18.53 *	18.72 *	18.25 *	18.58 *	18.04
MNO	*	0.44 *	0.46 *	0.47 *	0.49 *	0.25 *	0.26 *	0.27
MGO	*	6.07 *	6.34 *	5.54 *	5.59 *	6.59 *	6.77 *	6.69
CAO	*	11.03 *	10.53 *	10.96 *	11.21 *	11.06 *	11.29 *	10.96
NA2O	*	2.46 *	2.55 *	2.31 *	2.17 *	2.79 *	2.70 *	3.04
K2O	*	1.36 *	1.22 *	1.46 *	1.41 *	0.94 *	1.15 *	1.04
TOTAL	*	96.76 *	96.55 *	97.35 *	97.92 *	99.23 *	99.09 *	99.01
FE2O3 MIN	*	0.0 *	0.0 *	4.60 *	5.10 *	0.0 *	0.0 *	0.0
FE2O3 MAX	*	0.70 *	2.60 *	8.70 *	8.30 *	2.80 *	2.70 *	2.30

Z	SI	*	5.802 *	5.797 *	5.823 *	5.878 *	5.542 *	5.607 *	5.533
	AL(IV)	*	2.198 *	2.203 *	2.177 *	2.122 *	2.458 *	2.393 *	2.467
Y	AL(VI)	*	0.478 *	0.506 *	0.396 *	0.371 *	0.495 *	0.469 *	0.536
	FE3+	*	0.041 *	0.153 *	0.790 *	0.791 *	0.160 *	0.155 *	0.132
	TI	*	0.468 *	0.459 *	0.076 *	0.072 *	0.556 *	0.486 *	0.529
	FE2+	*	2.550 *	2.394 *	2.436 *	2.453 *	2.299 *	2.354 *	2.288
	MN	*	0.046 *	0.014 *	0.0 *	0.009 *	0.0 *	0.0 *	0.0
	MG	*	1.416 *	1.474 *	1.302 *	1.305 *	1.489 *	1.537 *	1.515
	CA	*	0.0 *	0.0 *	0.0 *	0.0 *	0.0 *	0.0 *	0.0
X	FE2+	*	0.0 *	0.0 *	0.006 *	0.0 *	0.015 *	0.013 *	0.003
	MN	*	0.012 *	0.046 *	0.063 *	0.056 *	0.032 *	0.034 *	0.035
	CA	*	1.850 *	1.760 *	1.851 *	1.882 *	1.797 *	1.843 *	1.784
	NA	*	0.138 *	0.194 *	0.080 *	0.062 *	0.156 *	0.111 *	0.178
A	NA	*	0.609 *	0.578 *	0.626 *	0.597 *	0.664 *	0.686 *	0.718
	K	*	0.272 *	0.243 *	0.294 *	0.282 *	0.182 *	0.223 *	0.202

1	TI-MG HS	*	487-1	BR HB-2
2	TI-MG HS	*	487-2	BR HB-3
3	MG HS	*	487-1	BL GR HB-1
4	HS	*	487-1	BL GR HB-2
5	KAER	*	488-1	HB-1
6	TI-MG HS	*	488-1	HB-2
7	KAER	*	488-2	HB-3

	*	1 *	2 *	3 *	4 *	5 *	6 *	7
SI02	*	37.05 *	36.38 *	36.80 *	37.45 *	37.67 *	37.88 *	38.03
TI02	*	2.32 *	4.59 *	4.58 *	5.23 *	5.23 *	4.07 *	3.88
AL203	*	18.09 *	16.65 *	15.72 *	15.08 *	13.80 *	15.76 *	16.36
FE203	*	1.05 *	1.40 *	0.0 *	0.80 *	1.30 *	1.20 *	1.20
FEO	*	18.66 *	17.61 *	17.98 *	17.24 *	17.67 *	15.52 *	14.88
MNO	*	0.20 *	0.23 *	0.27 *	0.23 *	0.25 *	0.31 *	0.27
MGO	*	6.19 *	6.97 *	7.12 *	7.79 *	7.89 *	8.85 *	8.86
CAO	*	12.29 *	10.95 *	11.25 *	11.25 *	10.98 *	11.63 *	11.39
NA2O	*	2.51 *	3.07 *	2.90 *	2.48 *	2.62 *	2.56 *	2.57
K2O	*	0.95 *	0.95 *	1.17 *	1.23 *	1.27 *	1.13 *	1.15
TOTAL	*	99.31 *	98.80 *	97.79 *	98.78 *	98.68 *	98.91 *	98.59
FE203 MIN	*	1.00 *	0.0 *	0.0 *	0.0 *	0.0 *	0.0 *	0.0
FE203 MAX	*	1.10 *	2.80 *	0.0 *	1.60 *	2.60 *	2.40 *	2.40

Z	SI	*	5.608 *	5.530 *	5.651 *	5.674 *	5.740 *	5.687 *	5.699
	AL(IV)	*	2.392 *	2.470 *	2.349 *	2.326 *	2.260 *	2.313 *	2.301
Y	AL(VI)	*	0.835 *	0.513 *	0.497 *	0.367 *	0.219 *	0.476 *	0.589
	FE3+	*	0.120 *	0.160 *	0.0 *	0.091 *	0.149 *	0.136 *	0.136
	TI	*	0.264 *	0.525 *	0.529 *	0.596 *	0.599 *	0.459 *	0.437
	FE2+	*	2.361 *	2.223 *	2.309 *	2.185 *	2.241 *	1.949 *	1.860
	MN	*	0.024 *	0.0 *	0.035 *	0.001 *	0.0 *	0.0 *	0.0
	MG	*	1.396 *	1.579 *	1.630 *	1.759 *	1.792 *	1.980 *	1.979
	CA	*	0.0 *	0.0 *	0.0 *	0.0 *	0.0 *	0.0 *	0.0
X	FE2+	*	0.0 *	0.016 *	0.0 *	0.0 *	0.011 *	0.0 *	0.005
	MN	*	0.002 *	0.030 *	0.0 *	0.028 *	0.032 *	0.039 *	0.034
	CA	*	1.993 *	1.783 *	1.851 *	1.826 *	1.793 *	1.871 *	1.829
	NA	*	0.005 *	0.184 *	0.149 *	0.146 *	0.164 *	0.090 *	0.132
A	NA	*	0.732 *	0.734 *	0.714 *	0.583 *	0.610 *	0.656 *	0.615
	K	*	0.183 *	0.184 *	0.229 *	0.238 *	0.247 *	0.216 *	0.220

1	TI-MG HS	*	488-2	HB-4
2	KAER	*	488-3	HB-5
3	KAER	*	488-3	HB-6
4	KAER	*	489-2	HB-1
5	KAER	*	489-2	HB-2
6	KAER	*	489-3	HB-3
7	TI-MG HS	*	489-3	HB-4

	*	1 *	2 *	3 *	4 *	5 *	6 *	7
SiO2	*	39.00 *	37.49 *	37.94 *	38.30 *	36.22 *	36.42 *	36.53
TiO2	*	3.73 *	4.14 *	4.04 *	3.54 *	4.51 *	4.51 *	4.87
Al2O3	*	15.57 *	14.64 *	14.77 *	14.89 *	15.51 *	15.76 *	15.48
Fe2O3	*	0.30 *	0.35 *	0.0 *	0.0 *	1.30 *	1.20 *	1.10
FeO	*	15.08 *	19.39 *	19.04 *	18.99 *	19.61 *	19.59 *	19.34
MnO	*	0.26 *	0.29 *	0.26 *	0.27 *	0.27 *	0.27 *	0.23
MgO	*	9.16 *	6.49 *	6.29 *	6.64 *	6.19 *	6.11 *	6.36
CaO	*	11.55 *	11.22 *	11.40 *	11.43 *	11.43 *	11.27 *	11.19
Na2O	*	2.68 *	2.41 *	2.32 *	2.35 *	2.35 *	2.38 *	2.39
K2O	*	0.98 *	1.50 *	1.64 *	1.54 *	1.42 *	1.55 *	1.56
TOTAL	*	98.31 *	97.92 *	97.70 *	97.95 *	98.81 *	99.06 *	99.05
Fe2O3 MIN	*	0.0 *	0.0 *	0.0 *	0.0 *	0.0 *	0.0 *	0.0
Fe2O3 MAX	*	0.60 *	0.70 *	0.0 *	0.0 *	2.60 *	2.40 *	2.20

Z	SI	*	5.841 *	5.790 *	5.853 *	5.882 *	5.576 *	5.587 *	5.596
	AL(IV)	*	2.159 *	2.210 *	2.147 *	2.118 *	2.424 *	2.413 *	2.404
Y	AL(VI)	*	0.590 *	0.455 *	0.538 *	0.577 *	0.390 *	0.436 *	0.391
	FE3+	*	0.034 *	0.041 *	0.0 *	0.0 *	0.151 *	0.139 *	0.127
	TI	*	0.420 *	0.481 *	0.469 *	0.409 *	0.522 *	0.520 *	0.561
	FE2+	*	1.889 *	2.504 *	2.456 *	2.439 *	2.516 *	2.508 *	2.469
	MN	*	0.022 *	0.026 *	0.034 *	0.035 *	0.0 *	0.0 *	0.0
	MG	*	2.045 *	1.494 *	1.446 *	1.520 *	1.420 *	1.397 *	1.452
	CA	*	0.0 *	0.0 *	0.057 *	0.020 *	0.0 *	0.0 *	0.0
X	FE2+	*	0.0 *	0.0 *	0.0 *	0.0 *	0.009 *	0.006 *	0.008
	MN	*	0.011 *	0.012 *	0.0 *	0.0 *	0.035 *	0.035 *	0.030
	CA	*	1.854 *	1.857 *	1.828 *	1.861 *	1.885 *	1.852 *	1.837
	NA	*	0.136 *	0.132 *	0.172 *	0.139 *	0.071 *	0.107 *	0.125
A	NA	*	0.643 *	0.590 *	0.522 *	0.561 *	0.631 *	0.601 *	0.585
	K	*	0.187 *	0.296 *	0.323 *	0.302 *	0.279 *	0.303 *	0.305

1	TI-FO PG	*	489-3	HB-5	REXLZED
2	TI-MG HS	*	490-1	HB-1	
3	TI-MG HS	*	490-1	HB-2	
4	TI-MG HS	*	490-1	HB-3	
5	KAER	*	490-2	HB-4	
6	KAER	*	490-2	HB-5	
7	KAER	*	490-3	HB-6	

	*	1 *	2 *	3 *	4 *	5 *	6 *	7
SI02	*	35.58 *	36.15 *	37.63 *	37.45 *	37.54 *	37.05 *	38.58
TI02	*	5.04 *	5.14 *	4.38 *	4.91 *	4.75 *	4.91 *	3.39
AL2O3	*	15.60 *	15.42 *	14.37 *	14.31 *	14.74 *	14.83 *	15.52
FE2O3	*	1.00 *	0.45 *	1.40 *	0.0 *	0.10 *	0.0 *	0.50
FEO	*	19.17 *	19.98 *	19.97 *	19.80 *	19.97 *	20.15 *	17.06
MNO	*	0.23 *	0.25 *	0.25 *	0.36 *	0.31 *	0.35 *	0.26
MGO	*	6.30 *	6.31 *	6.13 *	6.36 *	5.98 *	4.91 *	8.07
CAO	*	11.34 *	11.14 *	10.95 *	11.48 *	11.37 *	11.46 *	11.74
NA2O	*	2.35 *	2.33 *	2.27 *	1.66 *	1.67 *	1.60 *	2.94
K2O	*	1.49 *	1.52 *	1.49 *	2.26 *	1.97 *	2.07 *	0.44
TOTAL	*	98.10 *	97.69 *	98.84 *	98.59 *	98.40 *	97.33 *	98.50
FE2O3 MIN	*	0.0 *	0.0 *	0.0 *	0.0 *	0.0 *	0.0 *	0.0
FE2O3 MAX	*	2.00 *	0.90 *	2.80 *	0.0 *	0.20 *	0.0 *	1.00

Z	SI	*	5.513 *	5.601 *	5.779 *	5.770 *	5.782 *	5.736 *	5.819
	AL(IV)	*	2.487 *	2.399 *	2.221 *	2.230 *	2.218 *	2.264 *	2.181
Y	AL(VI)	*	0.362 *	0.417 *	0.380 *	0.369 *	0.458 *	0.442 *	0.578
	FE3+	*	0.117 *	0.053 *	0.162 *	0.0 *	0.012 *	0.0 *	0.057
	TI	*	0.587 *	0.599 *	0.506 *	0.569 *	0.550 *	0.572 *	0.384
	FE2+	*	2.480 *	2.459 *	2.549 *	2.551 *	2.572 *	2.609 *	2.152
	MN	*	0.0 *	0.016 *	0.0 *	0.047 *	0.035 *	0.046 *	0.014
	MG	*	1.455 *	1.457 *	1.403 *	1.461 *	1.373 *	1.325 *	1.814
	CA	*	0.0 *	0.0 *	0.0 *	0.003 *	0.0 *	0.006 *	0.0
X	FE2+	*	0.004 *	0.0 *	0.016 *	0.0 *	0.0 *	0.0 *	0.0
	MN	*	0.030 *	0.017 *	0.033 *	0.0 *	0.005 *	0.0 *	0.019
	CA	*	1.883 *	1.849 *	1.802 *	1.892 *	1.876 *	1.895 *	1.897
	NA	*	0.083 *	0.134 *	0.150 *	0.108 *	0.119 *	0.105 *	0.084
A	NA	*	0.623 *	0.566 *	0.526 *	0.388 *	0.380 *	0.375 *	0.776
	K	*	0.294 *	0.300 *	0.292 *	0.444 *	0.387 *	0.409 *	0.085

1	KAER	*	490-3	HB-7	
2	KAER	*	490-3	HB-8	REXLZED
3	TI-MG HS	*	490-3	HB-9	REXLZED
4	KAER	*	491-1	HB-1	
5	KAER	*	491-2	HB-2	
6	KAER	*	491-2	HB-3	
7	TI-MG HS	*	492-1	HB-1	

		*	1	*
	SI02	*	40.72	*
	TI02	*	3.13	*
	AL2O3	*	14.43	*
	FE2O3	*	0.65	*
	FeO	*	11.67	*
	MNO	*	0.07	*
	MGO	*	12.19	*
	CAO	*	11.53	*
	NA2O	*	2.94	*
	K2O	*	1.31	*
	TOTAL	*	98.64	*
	FE2O3 MIN	*	0.0	*
	FE2O3 MAX	*	1.30	*
Z	SI	*	5.988	*
	AL(IV)	*	2.012	*
Y	AL(VI)	*	0.488	*
	FE3+	*	0.072	*
	TI	*	0.346	*
	FE2+	*	1.422	*
	MN	*	0.0	*
	MG	*	2.672	*
	CA	*	0.0	*
X	FE2+	*	0.013	*
	MN	*	0.009	*
	CA	*	1.817	*
	NA	*	0.162	*
A	NA	*	0.676	*
	K	*	0.246	*

1 TI-F0 PG

*

T84-2

HB-2

BROWN

	*	1 *	2 *	3 *	4 *	5 *
SiO2	*	42.22 *	56.63 *	41.61 *	41.55 *	40.01 *
TiO2	*	2.11 *	0.03 *	2.95 *	3.04 *	3.85 *
Al2O3	*	14.79 *	0.30 *	14.46 *	14.41 *	15.31 *
Fe2O3	*	0.40 *	0.35 *	0.45 *	0.0 *	1.45 *
FeO	*	3.64 *	2.17 *	4.59 *	4.92 *	10.76 *
MnO	*	0.02 *	0.07 *	0.02 *	0.0 *	0.07 *
MgO	*	17.09 *	22.79 *	16.26 *	15.55 *	12.34 *
CaO	*	12.10 *	12.42 *	11.49 *	11.96 *	11.58 *
Na2O	*	3.25 *	0.30 *	2.97 *	2.82 *	2.75 *
K2O	*	0.51 *	0.01 *	1.22 *	1.16 *	1.16 *
TOTAL	*	96.13 *	95.07 *	96.02 *	95.41 *	99.28 *
Fe2O3 MIN	*	0.0 *	0.0 *	0.0 *	0.0 *	0.0 *
Fe2O3 MAX	*	0.80 *	0.70 *	0.90 *	0.0 *	2.90 *

Z	SI	*	6.100 *	7.958 *	6.065 *	6.098 *	5.833 *
	AL (IV)	*	1.900 *	0.042 *	1.935 *	1.902 *	2.167 *
Y	AL (VI)	*	0.619 *	0.008 *	0.550 *	0.590 *	0.463 *
	FE3+	*	0.044 *	0.037 *	0.049 *	0.0 *	0.159 *
	TI	*	0.229 *	0.003 *	0.323 *	0.335 *	0.422 *
	FE2+	*	0.428 *	0.179 *	0.545 *	0.604 *	1.274 *
	MN	*	0.0 *	0.0 *	0.0 *	0.0 *	0.0 *
	MG	*	3.680 *	4.773 *	3.533 *	3.401 *	2.681 *
	CA	*	0.0 *	0.0 *	0.0 *	0.069 *	0.0 *
X	FE2+	*	0.012 *	0.076 *	0.014 *	0.0 *	0.037 *
	MN	*	0.002 *	0.008 *	0.002 *	0.0 *	0.009 *
	CA	*	1.873 *	1.870 *	1.795 *	1.811 *	1.809 *
	NA	*	0.113 *	0.046 *	0.189 *	0.189 *	0.146 *
A	NA	*	0.798 *	0.036 *	0.651 *	0.613 *	0.631 *
	K	*	0.094 *	0.002 *	0.227 *	0.217 *	0.216 *

1	PG	*	493-2	HB-1	BROWN AMPHIBOLE
2	TR	*	493-1	AM-2	TREMOLITE AFTER TALC
3	TI PG	*	662-2	AM-1	
4	TI PG	*	662-3	HB-2	
5	TI-FO PG	*	G12-1	AM-1	IN BAND

Table II.ii. Pyroxene analyses, structural formulae, and end members.

	*	1 *	2 *	3 *	4 *	5 *	6 *	7
SI02	*	41.66 *	41.11 *	40.97 *	41.73 *	42.62 *	48.66 *	49.65
TI02	*	3.93 *	4.78 *	5.07 *	3.95 *	3.36 *	1.84 *	1.80
AL203	*	11.00 *	10.87 *	10.69 *	10.87 *	11.85 *	5.28 *	2.22
CR203	*	0.0 *	0.0 *	0.0 *	0.0 *	0.0 *	0.0 *	0.0
FE203	*	4.63 *	2.97 *	3.27 *	4.39 *	3.75 *	1.62 *	1.08
FEO	*	6.33 *	7.87 *	9.26 *	6.63 *	6.67 *	6.67 *	6.96
MNO	*	0.10 *	0.0 *	0.0 *	0.0 *	0.15 *	0.11 *	0.13
MGO	*	9.24 *	9.41 *	9.18 *	10.53 *	9.82 *	13.21 *	13.60
CAO	*	21.73 *	22.49 *	21.80 *	21.90 *	21.06 *	21.51 *	21.66
NA2O	*	0.57 *	0.0 *	0.0 *	0.0 *	0.58 *	0.42 *	0.41
NIO	*	0.0 *	0.0 *	0.0 *	0.0 *	0.0 *	0.0 *	0.0
TOTAL	*	99.19 *	99.50 *	100.24 *	100.00 *	99.86 *	99.32 *	97.51

SI	*	1.593 *	1.574 *	1.566 *	1.582 *	1.609 *	1.824 *	1.898
AL(IV)	*	0.407 *	0.426 *	0.434 *	0.418 *	0.391 *	0.176 *	0.100
AL(VI)	*	0.089 *	0.065 *	0.048 *	0.068 *	0.136 *	0.057 *	0.0
TI	*	0.113 *	0.138 *	0.146 *	0.113 *	0.095 *	0.052 *	0.052
CR	*	0.0 *	0.0 *	0.0 *	0.0 *	0.0 *	0.0 *	0.0
FE3+	*	0.133 *	0.085 *	0.094 *	0.125 *	0.107 *	0.046 *	0.029
FE2+	*	0.202 *	0.252 *	0.296 *	0.210 *	0.211 *	0.209 *	0.222
MG	*	0.527 *	0.537 *	0.523 *	0.595 *	0.552 *	0.738 *	0.775
MN	*	0.003 *	0.0 *	0.0 *	0.0 *	0.005 *	0.003 *	0.004
NI	*	0.0 *	0.0 *	0.0 *	0.0 *	0.0 *	0.0 *	0.0
CA	*	0.891 *	0.923 *	0.893 *	0.890 *	0.852 *	0.864 *	0.887
NA	*	0.042 *	0.0 *	0.0 *	0.0 *	0.042 *	0.031 *	0.030

WO	*	24.21 *	51.36 *	49.45 *	48.90 *	23.04 *	34.39 *	39.26
EN	*	26.33 *	29.88 *	28.96 *	32.69 *	27.62 *	36.90 *	38.74
FS	*	4.62 *	18.75 *	21.59 *	18.41 *	6.00 *	8.04 *	8.75
JD	*	4.23 *	0.0 *	0.0 *	0.0 *	4.25 *	3.05 *	0.0
AC	*	0.0 *	0.0 *	0.0 *	0.0 *	0.0 *	0.0 *	2.90
TI-TS	*	22.60 *	0.0 *	0.0 *	0.0 *	19.08 *	10.38 *	10.01
FE-TS	*	13.32 *	0.0 *	0.0 *	0.0 *	10.66 *	4.57 *	0.0
CA-TS	*	4.68 *	0.0 *	0.0 *	0.0 *	9.35 *	2.67 *	0.0

1 *	DFS73-112	*CPX-1	
2 *	DFS73-112	CPX-2	CAPE UNION VOLCANICS
3 *	DFS73-112	CPX-3	CAPE UNION VOLCANICS
4 *	DFS73-112	CPX-4	CAPE UNION VOLCANICS
5 *	76-545	CPX-U	
6 *	75-286	CPX-1	
7 *	75-286	DCPX-2	

	*	1 *	2 *	3 *	4 *	5 *	6 *	7
SiO2	*	48.49 *	48.50 *	48.19 *	47.24 *	47.59 *	50.71 *	50.59
TiO2	*	1.74 *	1.77 *	1.72 *	1.72 *	1.50 *	0.68 *	0.97
Al2O3	*	5.61 *	5.08 *	5.49 *	5.11 *	4.51 *	2.65 *	2.18
CR2O3	*	0.0 *	0.0 *	0.0 *	0.0 *	0.0 *	0.35 *	0.11
Fe2O3	*	3.08 *	4.12 *	4.41 *	7.37 *	7.79 *	2.96 *	3.42
FeO	*	4.86 *	4.49 *	3.71 *	2.39 *	1.52 *	4.56 *	7.12
MnO	*	0.13 *	0.14 *	0.13 *	0.15 *	0.13 *	0.20 *	0.25
MgO	*	13.70 *	13.65 *	13.93 *	13.24 *	14.20 *	16.92 *	15.64
CaO	*	22.08 *	22.47 *	22.34 *	23.12 *	23.06 *	19.55 *	19.28
Na2O	*	0.40 *	0.40 *	0.41 *	0.51 *	0.40 *	0.27 *	0.30
NiO	*	0.0 *	0.0 *	0.0 *	0.0 *	0.0 *	0.04 *	0.0
TOTAL	*	100.09 *	100.62 *	100.33 *	100.85 *	100.70 *	98.89 *	99.86
SI	*	1.800 *	1.796 *	1.785 *	1.754 *	1.764 *	1.886 *	1.886
Al(IV)	*	0.200 *	0.204 *	0.215 *	0.224 *	0.197 *	0.114 *	0.096
Al(VI)	*	0.045 *	0.018 *	0.025 *	0.0 *	0.0 *	0.002 *	0.0
TI	*	0.049 *	0.049 *	0.048 *	0.048 *	0.042 *	0.019 *	0.027
CR	*	0.0 *	0.0 *	0.0 *	0.0 *	0.0 *	0.010 *	0.003
Fe3+	*	0.086 *	0.115 *	0.123 *	0.206 *	0.218 *	0.083 *	0.096
Fe2+	*	0.151 *	0.139 *	0.115 *	0.074 *	0.047 *	0.142 *	0.222
MG	*	0.758 *	0.754 *	0.769 *	0.733 *	0.785 *	0.938 *	0.869
MN	*	0.004 *	0.004 *	0.004 *	0.005 *	0.004 *	0.006 *	0.008
NI	*	0.0 *	0.0 *	0.0 *	0.0 *	0.0 *	0.001 *	0.0
CA	*	0.878 *	0.892 *	0.887 *	0.920 *	0.916 *	0.779 *	0.770
NA	*	0.029 *	0.029 *	0.029 *	0.037 *	0.029 *	0.019 *	0.022
WO	*	33.92 *	34.44 *	33.62 *	33.82 *	34.11 *	34.21 *	34.19
EN	*	37.90 *	37.67 *	38.45 *	36.63 *	39.21 *	46.95 *	43.45
FS	*	5.32 *	4.71 *	3.56 *	1.55 *	0.47 *	7.40 *	11.50
JD	*	2.88 *	1.83 *	2.49 *	0.0 *	0.0 *	1.95 *	2.22
AC	*	0.0 *	1.05 *	0.45 *	3.67 *	2.88 *	0.0 *	0.0
TI-TS	*	9.72 *	9.86 *	9.58 *	9.61 *	8.36 *	1.90 *	2.72
FE-TS	*	8.60 *	10.44 *	11.84 *	12.56 *	11.11 *	4.66 *	4.96
CA-TS	*	1.67 *	0.0 *	0.0 *	0.0 *	0.0 *	2.93 *	0.96

1 * 75-286 CPX-3
 2 * 75-286 CPX-4
 3 * 75-286 CPX-5
 4 * 75-286 CPX-6
 5 * 75-286 CPX-7
 6 * 585-2 CPX-1
 7 * 588-1 CPX-1 MAIDEN POINT CROQUE

	*	1 *	2 *	3 *
SI02	*	50.75 *	50.84 *	51.39 *
TI02	*	0.77 *	0.91 *	0.71 *
AL203	*	2.64 *	2.96 *	2.59 *
CR203	*	0.16 *	0.33 *	0.37 *
FE203	*	3.07 *	2.71 *	3.21 *
FEO	*	6.38 *	5.99 *	4.51 *
MNO	*	0.22 *	0.22 *	0.20 *
MGO	*	16.15 *	16.23 *	17.00 *
CAO	*	19.24 *	19.55 *	20.10 *
NA2O	*	0.29 *	0.29 *	0.27 *
NIO	*	0.0 *	0.05 *	0.05 *
TOTAL	*	99.67 *	100.08 *	100.40 *

SI	*	1.886 *	1.878 *	1.884 *
AL(IV)	*	0.114 *	0.122 *	0.112 *
AL(VI)	*	0.001 *	0.007 *	0.0 *
TI	*	0.022 *	0.025 *	0.020 *
CR	*	0.005 *	0.010 *	0.011 *
FE3+	*	0.086 *	0.075 *	0.089 *
FE2+	*	0.198 *	0.185 *	0.138 *
MG	*	0.894 *	0.894 *	0.929 *
MN	*	0.007 *	0.007 *	0.006 *
NI	*	0.0 *	0.001 *	0.001 *
CA	*	0.776 *	0.774 *	0.790 *
NA	*	0.021 *	0.021 *	0.019 *

WO	*	33.67 *	33.88 *	34.70 *
EN	*	44.72 *	44.76 *	46.53 *
FS	*	10.26 *	9.60 *	7.23 *
JD	*	2.09 *	2.13 *	1.97 *
AC	*	0.0 *	0.0 *	0.0 *
TI-TS	*	2.15 *	2.53 *	1.96 *
FE-TS	*	4.52 *	4.25 *	4.96 *
CA-TS	*	2.59 *	2.86 *	2.66 *

1 *	588-2	CPX-2	MAIDEN POINT CROQUE
2 *	591-1	CPX-1	MATRIX MAIDEN POINT CROQUE
3 *	591-2	CPX-2	INCLUSION MAIDEN POINT CROQUE

	*	1 *	2 *	3 *	4 *	5 *	6 *	7
SI02	*	50.79 *	50.75 *	49.35 *	51.23 *	51.56 *	52.13 *	51.71
TI02	*	0.15 *	0.07 *	0.14 *	0.14 *	0.14 *	0.11 *	0.12
AL203	*	2.02 *	1.40 *	1.57 *	1.82 *	1.50 *	1.70 *	1.91
CR203	*	0.05 *	0.05 *	0.04 *	0.02 *	0.04 *	0.05 *	0.04
FE203	*	3.56 *	3.55 *	4.29 *	1.56 *	2.40 *	2.24 *	3.20
FEO	*	21.17 *	21.48 *	20.67 *	23.45 *	22.70 *	4.90 *	4.79
MNO	*	0.64 *	0.67 *	0.64 *	0.68 *	0.75 *	0.20 *	0.22
MGO	*	20.51 *	20.85 *	20.51 *	20.20 *	20.77 *	14.27 *	13.86
CAO	*	1.81 *	1.09 *	0.82 *	0.78 *	0.82 *	23.56 *	23.82
NA2O	*	0.04 *	0.01 *	0.04 *	0.04 *	0.04 *	0.37 *	0.37
NIO	*	0.0 *	0.0 *	0.05 *	0.06 *	0.07 *	0.0 *	0.0
TOTAL	*	100.74 *	99.92 *	98.12 *	99.98 *	100.79 *	99.53 *	100.04

SI	*	1.901 *	1.915 *	1.899 *	1.935 *	1.930 *	1.941 *	1.922
AL(IV)	*	0.089 *	0.062 *	0.071 *	0.065 *	0.066 *	0.059 *	0.078
AL(VI)	*	0.0 *	0.0 *	0.0 *	0.016 *	0.0 *	0.015 *	0.006
TI	*	0.004 *	0.002 *	0.004 *	0.004 *	0.004 *	0.003 *	0.003
CR	*	0.001 *	0.001 *	0.001 *	0.001 *	0.001 *	0.001 *	0.001
FE3+	*	0.103 *	0.104 *	0.124 *	0.044 *	0.068 *	0.064 *	0.091
FE2+	*	0.660 *	0.675 *	0.665 *	0.741 *	0.711 *	0.151 *	0.147
MG	*	1.144 *	1.173 *	1.176 *	1.137 *	1.159 *	0.792 *	0.768
MN	*	0.020 *	0.021 *	0.021 *	0.022 *	0.024 *	0.006 *	0.007
NI	*	0.0 *	0.0 *	0.002 *	0.002 *	0.002 *	0.0 *	0.0
CA	*	0.073 *	0.044 *	0.034 *	0.032 *	0.033 *	0.940 *	0.949
NA	*	0.003 *	0.001 *	0.003 *	0.003 *	0.003 *	0.027 *	0.027

WD	*	3.63 *	2.19 *	1.67 *	1.60 *	1.65 *	44.03 *	43.59
EN	*	57.20 *	58.14 *	58.25 *	57.80 *	58.16 *	39.60 *	38.40
FS	*	39.17 *	39.67 *	40.08 *	40.80 *	40.19 *	7.78 *	7.62
JD	*	0.0 *	0.0 *	0.0 *	0.0 *	0.0 *	1.54 *	0.63
AC	*	0.0 *	0.0 *	0.0 *	0.0 *	0.0 *	1.13 *	2.04
TI-TS	*	0.0 *	0.0 *	0.0 *	0.0 *	0.0 *	0.62 *	0.67
FE-TS	*	0.0 *	0.0 *	0.0 *	0.0 *	0.0 *	5.29 *	7.04
CA-TS	*	0.0 *	0.0 *	0.0 *	0.0 *	0.0 *	0.0 *	0.0

1 *	552-3	OPX-1
2 *	552-3	OPX-2
3 *	552-2-1	OPX-1
4 *	552-2-1	/OPX-2
5 *	552-2-1	OPX-3
6 *	128-1	CPX-1
7 *	128-2	CPX-2

	*	1 *	2 *	3 *	4 *	5 *	6 *	7
SI02	*	52.70 *	53.78 *	50.30 *	51.17 *	50.38 *	51.03 *	51.08
TI02	*	0.11 *	0.10 *	0.32 *	0.25 *	0.31 *	0.30 *	0.29
AL203	*	1.88 *	1.70 *	3.24 *	2.90 *	3.19 *	3.06 *	2.96
CR203	*	0.01 *	0.02 *	0.04 *	0.05 *	0.04 *	0.02 *	0.05
FE203	*	0.0 *	0.0 *	4.22 *	2.83 *	3.14 *	2.23 *	1.04
FEO	*	8.08 *	7.95 *	7.33 *	8.83 *	7.98 *	8.88 *	9.39
MNO	*	0.26 *	0.33 *	0.38 *	0.32 *	0.35 *	0.36 *	0.32
MGO	*	12.83 *	12.86 *	12.50 *	13.07 *	13.07 *	13.01 *	12.54
CAO	*	22.83 *	23.05 *	21.71 *	20.76 *	20.42 *	20.28 *	20.78
NA2O	*	0.45 *	0.50 *	0.57 *	0.51 *	0.59 *	0.62 *	0.57
NIO	*	0.04 *	0.03 *	0.0 *	0.0 *	0.0 *	0.0 *	0.0
TOTAL	*	99.19 *	100.32 *	100.61 *	100.69 *	99.47 *	99.79 *	99.02

SI	*	1.977 *	1.991 *	1.880 *	1.907 *	1.896 *	1.914 *	1.931
AL(IV)	*	0.023 *	0.009 *	0.120 *	0.093 *	0.104 *	0.086 *	0.069
AL(VI)	*	0.060 *	0.065 *	0.022 *	0.034 *	0.038 *	0.050 *	0.063
TI	*	0.003 *	0.003 *	0.009 *	0.007 *	0.009 *	0.008 *	0.008
CR	*	0.0 *	0.001 *	0.001 *	0.001 *	0.001 *	0.001 *	0.001
FE3+	*	0.0 *	0.0 *	0.121 *	0.081 *	0.091 *	0.064 *	0.031
FE2+	*	0.254 *	0.246 *	0.227 *	0.274 *	0.249 *	0.277 *	0.296
MG	*	0.717 *	0.710 *	0.696 *	0.726 *	0.733 *	0.727 *	0.707
MN	*	0.008 *	0.010 *	0.012 *	0.010 *	0.011 *	0.011 *	0.010
NI	*	0.001 *	0.001 *	0.0 *	0.0 *	0.0 *	0.0 *	0.0
CA	*	0.918 *	0.915 *	0.869 *	0.829 *	0.824 *	0.815 *	0.842
NA	*	0.033 *	0.036 *	0.041 *	0.037 *	0.043 *	0.045 *	0.042

WO	*	44.86 *	45.37 *	37.50 *	36.83 *	36.04 *	36.51 *	38.65
EN	*	36.12 *	36.02 *	34.83 *	36.30 *	36.68 *	36.38 *	35.33
FS	*	13.16 *	13.00 *	11.60 *	13.92 *	12.69 *	14.08 *	14.95
JD	*	3.34 *	3.64 *	2.28 *	3.46 *	3.83 *	4.51 *	4.18
AC	*	0.0 *	0.0 *	1.85 *	0.23 *	0.0 *	0.0 *	0.0
TI-TS	*	0.31 *	0.28 *	1.80 *	1.40 *	1.76 *	1.69 *	1.65
FE-TS	*	0.02 *	0.03 *	10.14 *	7.86 *	8.55 *	6.35 *	3.12
CA-TS	*	2.20 *	1.66 *	0.0 *	0.0 *	0.0 *	0.49 *	2.12

1 *	504-1	CPX-1
2 *	504-1	CPX-2
3 *	551-2	CPX-1
4 *	551-2	CPX-2
5 *	552-1	CPX-1
6 *	552-1	CPX-2
7 *	552-2	CPX-3

	*	1 *	2 *	3 *	4 *	5 *	6 *	7
SIO2	*	50.86 *	50.38 *	50.51 *	51.00 *	51.02 *	50.44 *	50.15
TIO2	*	0.30 *	0.34 *	0.26 *	0.30 *	0.27 *	0.27 *	0.33
AL2O3	*	2.91 *	2.79 *	1.98 *	2.45 *	2.38 *	3.09 *	3.36
CR2O3	*	0.04 *	0.04 *	0.03 *	0.04 *	0.05 *	0.04 *	0.05
FE2O3	*	1.12 *	2.47 *	3.50 *	2.40 *	2.42 *	2.15 *	3.27
FEO	*	8.71 *	7.89 *	7.28 *	7.59 *	7.23 *	9.67 *	8.64
MNO	*	0.33 *	0.30 *	0.32 *	0.30 *	0.30 *	0.37 *	0.34
MGO	*	12.86 *	12.46 *	13.27 *	12.88 *	12.96 *	12.55 *	12.10
CAO	*	20.66 *	21.32 *	20.98 *	21.71 *	21.80 *	20.01 *	20.99
NA2O	*	0.57 *	0.60 *	0.53 *	0.55 *	0.57 *	0.54 *	0.61
NIO	*	0.0 *	0.05 *	0.05 *	0.04 *	0.05 *	0.0 *	0.0
TOTAL	*	98.36 *	98.64 *	98.71 *	99.26 *	99.05 *	99.13 *	99.84

SI	*	1.930 *	1.914 *	1.917 *	1.922 *	1.925 *	1.911 *	1.891
AL(IV)	*	0.070 *	0.086 *	0.083 *	0.078 *	0.075 *	0.089 *	0.109
AL(VI)	*	0.061 *	0.039 *	0.006 *	0.031 *	0.031 *	0.050 *	0.040
TI	*	0.009 *	0.010 *	0.007 *	0.009 *	0.008 *	0.008 *	0.009
CR	*	0.001 *	0.001 *	0.001 *	0.001 *	0.001 *	0.001 *	0.001
FE3+	*	0.033 *	0.071 *	0.100 *	0.068 *	0.069 *	0.063 *	0.094
FE2+	*	0.275 *	0.251 *	0.231 *	0.239 *	0.228 *	0.305 *	0.271
MG	*	0.728 *	0.706 *	0.751 *	0.724 *	0.729 *	0.709 *	0.680
MN	*	0.011 *	0.010 *	0.010 *	0.010 *	0.010 *	0.012 *	0.011
NI	*	0.0 *	0.002 *	0.002 *	0.001 *	0.002 *	0.0 *	0.0
CA	*	0.840 *	0.868 *	0.853 *	0.877 *	0.882 *	0.813 *	0.848
NA	*	0.042 *	0.044 *	0.039 *	0.040 *	0.042 *	0.040 *	0.045

WO	*	38.56 *	39.10 *	38.54 *	39.98 *	40.34 *	36.58 *	37.40
EN	*	36.38 *	35.35 *	37.61 *	36.24 *	36.52 *	35.46 *	34.01
FS	*	13.93 *	12.53 *	11.70 *	12.02 *	11.50 *	15.85 *	14.09
JD	*	4.20 *	3.90 *	0.58 *	3.13 *	3.10 *	3.97 *	4.46
AC	*	0.0 *	0.0 *	3.32 *	0.89 *	1.07 *	0.0 *	0.0
TI-TS	*	1.71 *	1.94 *	1.48 *	1.70 *	1.53 *	0.77 *	0.94
FE-TS	*	3.32 *	6.65 *	6.76 *	6.04 *	5.94 *	3.21 *	4.80
CA-TS	*	1.89 *	0.0 *	0.0 *	0.0 *	0.0 *	4.15 *	4.30

1 *	552-3 CPX-4
2 *	552-2-1 CPX-1
3 *	552-2-1 CPX-2
4 *	552-2-2 CPX-3
5 *	552-2-3 CPX-4
6 *	553-1 CPX-1
7 *	553-1 CPX-2

	*	1 *	2 *	3 *	4 *	5 *	6 *	7
SI02	*	50.30 *	50.63 *	50.83 *	50.25 *	52.32 *	51.90 *	51.84
TI02	*	0.29 *	0.27 *	0.35 *	0.36 *	0.10 *	0.11 *	0.14
AL203	*	3.07 *	2.80 *	3.47 *	3.40 *	2.08 *	2.12 *	2.65
CR203	*	0.04 *	0.04 *	0.04 *	0.04 *	0.10 *	0.09 *	0.09
FE203	*	3.38 *	2.48 *	0.89 *	4.22 *	1.97 *	1.96 *	0.89
FE0	*	8.83 *	9.40 *	10.33 *	6.03 *	5.04 *	4.90 *	5.88
MNO	*	0.33 *	0.32 *	0.20 *	0.20 *	0.17 *	0.17 *	0.18
MGO	*	12.57 *	12.76 *	12.95 *	13.27 *	15.30 *	15.39 *	14.91
CAO	*	20.67 *	20.29 *	19.71 *	21.71 *	22.28 *	21.77 *	21.48
NA2O	*	0.51 *	0.50 *	0.48 *	0.59 *	0.35 *	0.38 *	0.42
NIO	*	0.0 *	0.0 *	0.0 *	0.0 *	0.0 *	0.0 *	0.0
TOTAL	*	99.99 *	99.49 *	99.25 *	100.07 *	99.71 *	98.79 *	98.48

SI	*	1.893 *	1.912 *	1.917 *	1.876 *	1.935 *	1.935 *	1.939
AL(IV)	*	0.107 *	0.088 *	0.083 *	0.124 *	0.065 *	0.065 *	0.061
AL(VI)	*	0.030 *	0.037 *	0.071 *	0.026 *	0.026 *	0.028 *	0.056
TI	*	0.008 *	0.008 *	0.010 *	0.010 *	0.003 *	0.003 *	0.004
CR	*	0.001 *	0.001 *	0.001 *	0.001 *	0.003 *	0.003 *	0.003
FE3+	*	0.098 *	0.072 *	0.027 *	0.121 *	0.057 *	0.057 *	0.026
FE2+	*	0.276 *	0.295 *	0.324 *	0.186 *	0.154 *	0.151 *	0.182
MG	*	0.705 *	0.718 *	0.728 *	0.738 *	0.843 *	0.855 *	0.831
MN	*	0.011 *	0.010 *	0.006 *	0.006 *	0.005 *	0.005 *	0.006
NI	*	0.0 *	0.0 *	0.0 *	0.0 *	0.0 *	0.0 *	0.0
CA	*	0.834 *	0.821 *	0.797 *	0.869 *	0.883 *	0.870 *	0.861
NA	*	0.037 *	0.037 *	0.035 *	0.043 *	0.025 *	0.027 *	0.030

WO	*	36.76 *	37.03 *	36.17 *	37.72 *	41.05 *	40.38 *	40.18
EN	*	35.28 *	35.93 *	36.42 *	36.94 *	42.20 *	42.78 *	41.58
FS	*	14.34 *	15.29 *	16.54 *	9.61 *	7.97 *	7.82 *	9.41
JD	*	3.72 *	3.66 *	3.51 *	4.27 *	2.51 *	2.75 *	3.05
AC	*	0.0 *	0.0 *	0.0 *	0.0 *	0.0 *	0.0 *	0.0
TI-TS	*	0.82 *	0.77 *	0.99 *	1.01 *	0.28 *	0.31 *	0.39
FE-TS	*	4.95 *	3.69 *	1.39 *	6.10 *	2.99 *	2.98 *	1.46
CA-TS	*	4.13 *	3.64 *	4.97 *	4.34 *	3.00 *	2.99 *	3.93

1 *	553-2 CPX-3
2 *	553-2 CPX-4
3 *	553-2 CPX-5
4 *	553-2 CPX-5-2
5 *	554-1 CPX-1
6 *	554-2 CPX-2
7 *	554.2 CPX-3

	*	1	*
SiO2	*	50.41	*
TiO2	*	0.14	*
Al2O3	*	8.73	*
CR2O3	*	0.06	*
FE2O3	*	7.22	*
FeO	*	0.0	*
MNO	*	0.17	*
MGO	*	12.25	*
CAO	*	21.33	*
NA2O	*	0.38	*
NIO	*	0.0	*
TOTAL	*	100.69	*

SI	*	1.849	*
AL(IV)	*	0.151	*
AL(VI)	*	0.226	*
TI	*	0.004	*
CR	*	0.002	*
FE3+	*	0.0	*
FE2+	*	0.199	*
MG	*	0.670	*
MN	*	0.005	*
NI	*	0.0	*
CA	*	0.838	*
NA	*	0.027	*

WO	*	34.09	*
EN	*	34.47	*
FS	*	10.54	*
JD	*	2.78	*
AC	*	0.0	*
TI-TS	*	0.40	*
FE-TS	*	0.09	*
CA-TS	*	17.64	*

1 * 554--2 CPX-3-AL RICH

	*	1 *	2 *	3 *	4 *	5 *	6 *	7
SI02	*	54.51 *	54.14 *	52.73 *	52.77 *	53.98 *	52.17 *	51.13
TI02	*	0.10 *	0.05 *	0.26 *	0.25 *	0.18 *	0.44 *	0.46
AL203	*	1.32 *	1.23 *	3.09 *	3.24 *	1.78 *	3.15 *	3.28
CR203	*	0.16 *	0.12 *	0.51 *	0.63 *	0.43 *	1.20 *	1.21
FE203	*	0.0 *	0.0 *	0.83 *	0.49 *	0.06 *	1.44 *	2.12
FEO	*	5.43 *	5.48 *	5.07 *	5.63 *	5.57 *	1.31 *	0.88
MNO	*	0.19 *	0.17 *	0.20 *	0.17 *	0.14 *	0.10 *	0.09
MGO	*	15.05 *	14.82 *	16.48 *	16.09 *	16.16 *	16.35 *	16.27
CAO	*	23.43 *	24.33 *	20.75 *	20.84 *	22.10 *	23.50 *	23.38
NA2O	*	0.32 *	0.30 *	0.43 *	0.45 *	0.39 *	0.45 *	0.35
NIO	*	0.04 *	0.04 *	0.04 *	0.03 *	0.08 *	0.0 *	0.0
TOTAL	*	100.55 *	100.68 *	100.39 *	100.59 *	100.87 *	100.11 *	99.17

SI	*	1.991 *	1.982 *	1.923 *	1.924 *	1.964 *	1.899 *	1.882
AL(IV)	*	0.009 *	0.018 *	0.077 *	0.076 *	0.036 *	0.101 *	0.118
AL(VI)	*	0.048 *	0.035 *	0.056 *	0.063 *	0.040 *	0.035 *	0.024
TI	*	0.003 *	0.001 *	0.007 *	0.007 *	0.005 *	0.012 *	0.013
CR	*	0.005 *	0.003 *	0.015 *	0.018 *	0.012 *	0.034 *	0.035
FE3+	*	0.0 *	0.0 *	0.023 *	0.014 *	0.0 *	0.039 *	0.059
FE2+	*	0.166 *	0.168 *	0.154 *	0.171 *	0.171 *	0.040 *	0.027
MG	*	0.819 *	0.809 *	0.896 *	0.874 *	0.876 *	0.887 *	0.892
MN	*	0.006 *	0.005 *	0.006 *	0.005 *	0.004 *	0.003 *	0.003
NI	*	0.001 *	0.001 *	0.001 *	0.001 *	0.002 *	0.0 *	0.0
CA	*	0.917 *	0.955 *	0.811 *	0.814 *	0.862 *	0.917 *	0.922
NA	*	0.023 *	0.021 *	0.030 *	0.032 *	0.028 *	0.032 *	0.025

WO	*	45.47 *	46.90 *	37.06 *	37.24 *	41.53 *	41.42 *	40.82
EN	*	41.56 *	40.54 *	44.85 *	43.76 *	43.91 *	44.37 *	44.62
FS	*	8.70 *	8.66 *	8.02 *	8.83 *	8.76 *	2.14 *	1.50
JD	*	2.30 *	2.13 *	3.09 *	3.23 *	2.75 *	3.22 *	2.50
AC	*	0.0 *	0.0 *	0.0 *	0.0 *	0.0 *	0.0 *	0.0
TI-TS	*	0.28 *	0.14 *	0.71 *	0.69 *	0.49 *	1.21 *	1.27
FE-TS	*	0.23 *	0.17 *	1.88 *	1.59 *	0.62 *	3.69 *	4.69
CA-TS	*	1.45 *	1.45 *	4.39 *	4.66 *	1.95 *	3.95 *	4.59

1 *	LRC77-3	CPX-1	
2 *	LRC77-2	CPX-2	
3 *	404-1	CPX-1	LONG RIDGE
4 *	404-1	CPX-2	L/NG RIDGE
5 *	404-2	CPX-3	LONG RIDGE
6 *	412-1	CPX-1	REACTION RIM
7 *	412-2	CPX-2	REACTION RIM

* 1 *

SI02	*	51.67	*
TI02	*	0.50	*
AL203	*	3.61	*
CR203	*	1.36	*
FE203	*	1.48	*
FEO	*	1.14	*
MNO	*	0.06	*
MGO	*	16.20	*
CAO	*	23.61	*
NA2O	*	0.41	*
NIO	*	0.01	*
TOTAL	*	100.05	*

SI	*	1.883	*
AL(IV)	*	0.117	*
AL(VI)	*	0.038	*
TI	*	0.014	*
CR	*	0.039	*
FE3+	*	0.041	*
FE2+	*	0.035	*
MG	*	0.880	*
MN	*	0.002	*
NI	*	0.0	*
CA	*	0.922	*
NA	*	0.029	*

WO	*	40.96	*
EN	*	44.02	*
FS	*	1.82	*
JD	*	2.90	*
AC	*	0.0	*
TI-TS	*	1.37	*
FE-TS	*	3.99	*
CA-TS	*	4.94	*

1 * 41.2-2 CPX-3 REACTION RIM ADJACENT SPINEL

	*	1 *	2 *	3 *	4 *	5 *	6 *	7
SIO2	*	46.78 *	46.70 *	47.85 *	46.78 *	46.58 *	45.23 *	45.00
TIO2	*	1.79 *	1.92 *	1.71 *	1.67 *	1.82 *	2.41 *	2.47
AL2O3	*	9.52 *	8.41 *	6.54 *	8.85 *	9.37 *	8.94 *	8.69
CR2O3	*	0.0 *	0.0 *	0.0 *	0.0 *	0.0 *	0.0 *	0.0
FE2O3	*	4.34 *	7.07 *	6.91 *	6.18 *	5.91 *	7.38 *	7.74
FEO	*	9.18 *	5.28 *	6.68 *	5.41 *	5.74 *	6.75 *	7.15
MNO	*	0.39 *	0.27 *	0.28 *	0.28 *	0.28 *	0.34 *	0.31
MGO	*	6.80 *	8.61 *	8.66 *	8.58 *	8.60 *	7.34 *	7.26
CAO	*	19.75 *	20.69 *	20.26 *	20.72 *	20.78 *	21.39 *	20.87
NA2O	*	2.28 *	2.21 *	2.26 *	2.15 *	2.03 *	1.89 *	1.94
NIO	*	0.0 *	0.0 *	0.0 *	0.0 *	0.0 *	0.0 *	0.0
TOTAL	*	100.83 *	101.16 *	101.15 *	100.62 *	101.11 *	101.67 *	101.43

SI	*	1.759 *	1.740 *	1.791 *	1.748 *	1.733 *	1.697 *	1.696
AL(IV)	*	0.241 *	0.260 *	0.209 *	0.252 *	0.267 *	0.303 *	0.304
AL(VI)	*	0.182 *	0.110 *	0.079 *	0.138 *	0.144 *	0.093 *	0.082
TI	*	0.051 *	0.054 *	0.048 *	0.047 *	0.051 *	0.068 *	0.070
CR	*	0.0 *	0.0 *	0.0 *	0.0 *	0.0 *	0.0 *	0.0
FE3+	*	0.124 *	0.202 *	0.198 *	0.177 *	0.169 *	0.212 *	0.224
FE2+	*	0.287 *	0.161 *	0.206 *	0.166 *	0.176 *	0.208 *	0.221
MG	*	0.381 *	0.478 *	0.483 *	0.478 *	0.477 *	0.410 *	0.408
MN	*	0.012 *	0.009 *	0.009 *	0.009 *	0.009 *	0.011 *	0.010
NI	*	0.0 *	0.0 *	0.0 *	0.0 *	0.0 *	0.0 *	0.0
CA	*	0.796 *	0.826 *	0.813 *	0.830 *	0.828 *	0.860 *	0.843
NA	*	0.166 *	0.160 *	0.164 *	0.156 *	0.146 *	0.138 *	0.142

WO	*	30.30 *	31.02 *	32.56 *	31.21 *	30.60 *	31.25 *	30.44
EN	*	19.07 *	23.92 *	24.16 *	23.90 *	23.85 *	20.53 *	20.40
FS	*	14.99 *	8.47 *	10.73 *	8.74 *	9.23 *	10.95 *	11.55
JD	*	16.63 *	15.98 *	16.41 *	15.58 *	14.65 *	13.75 *	14.18
AC	*	0.0 *	0.0 *	0.0 *	0.0 *	0.0 *	0.0 *	0.0
TI-TS	*	5.07 *	5.38 *	4.81 *	4.70 *	5.09 *	6.80 *	7.00
FE-TS	*	6.22 *	10.12 *	9.92 *	8.86 *	8.43 *	10.62 *	11.21
CA-TS	*	7.73 *	5.11 *	1.42 *	7.01 *	8.14 *	6.10 *	5.22

1 *	486-2	CPX-1
2 *	489-2	CPX-1
3 *	489-2	CPX-2
4 *	489-3	CPX-3
5 *	489-3	CPX-4
6 *	490-1	CPX-1
7 *	490-2	CPX-2

	*	1 *	2 *	3 *	4 *	5 *	6 *	7
SIO2	*	44.10 *	46.21 *	45.72 *	45.00 *	45.69 *	45.59 *	46.29
TIO2	*	2.79 *	1.73 *	1.78 *	1.94 *	2.07 *	1.90 *	1.96
AL2O3	*	9.77 *	7.02 *	7.36 *	7.85 *	8.43 *	7.91 *	8.36
CR2O3	*	0.0 *	0.0 *	0.0 *	0.0 *	0.0 *	0.0 *	0.0
FE2O3	*	7.83 *	6.97 *	7.17 *	7.72 *	5.84 *	7.20 *	5.11
FEO	*	6.47 *	7.29 *	7.01 *	6.68 *	8.00 *	7.15 *	8.51
MNO	*	0.35 *	0.42 *	0.42 *	0.43 *	0.42 *	0.39 *	0.39
MGO	*	7.04 *	7.97 *	7.84 *	7.80 *	7.63 *	7.67 *	7.42
CAO	*	21.13 *	21.94 *	22.14 *	22.01 *	21.84 *	22.18 *	22.16
NA2O	*	1.92 *	1.48 *	1.42 *	1.39 *	1.41 *	1.44 *	1.43
NIO	*	0.0 *	0.0 *	0.0 *	0.0 *	0.0 *	0.0 *	0.0
TOTAL	*	101.40 *	101.03 *	100.86 *	100.82 *	101.33 *	101.43 *	101.63

SI	*	1.661 *	1.748 *	1.733 *	1.708 *	1.722 *	1.719 *	1.738
AL(IV)	*	0.339 *	0.252 *	0.267 *	0.292 *	0.278 *	0.281 *	0.262
AL(VI)	*	0.095 *	0.061 *	0.062 *	0.059 *	0.096 *	0.071 *	0.109
TI	*	0.079 *	0.049 *	0.051 *	0.055 *	0.059 *	0.054 *	0.055
CR	*	0.0 *	0.0 *	0.0 *	0.0 *	0.0 *	0.0 *	0.0
FE3+	*	0.227 *	0.202 *	0.209 *	0.225 *	0.168 *	0.208 *	0.147
FE2+	*	0.200 *	0.227 *	0.218 *	0.208 *	0.250 *	0.222 *	0.265
MG	*	0.395 *	0.449 *	0.443 *	0.441 *	0.429 *	0.431 *	0.415
MN	*	0.011 *	0.013 *	0.013 *	0.014 *	0.013 *	0.012 *	0.012
NI	*	0.0 *	0.0 *	0.0 *	0.0 *	0.0 *	0.0 *	0.0
CA	*	0.853 *	0.889 *	0.899 *	0.895 *	0.882 *	0.896 *	0.892
NA	*	0.140 *	0.109 *	0.104 *	0.102 *	0.103 *	0.105 *	0.104

WO	*	29.65 *	34.31 *	34.15 *	32.92 *	33.10 *	33.45 *	34.28
EN	*	19.77 *	22.47 *	22.15 *	22.07 *	21.43 *	21.56 *	20.77
FS	*	10.55 *	12.03 *	11.60 *	11.08 *	13.15 *	11.71 *	13.88
JD	*	14.03 *	10.86 *	10.44 *	10.23 *	10.31 *	10.53 *	10.42
AC	*	0.0 *	0.0 *	0.0 *	0.0 *	0.0 *	0.0 *	0.0
TI-TS	*	7.91 *	4.92 *	5.08 *	5.54 *	5.87 *	5.39 *	5.54
FE-TS	*	11.33 *	10.11 *	10.43 *	11.26 *	8.42 *	10.42 *	7.35
CA-TS	*	6.78 *	5.31 *	6.16 *	6.91 *	7.71 *	6.93 *	7.77

1 *	490-2	CPX-3
2 *	491-1	CPX-1
3 *	491-1	CPX-2
4 *	491-1	CPX-3
5 *	491-1	CPX-4
6 *	491-2	CPX-5
7 *	491-2	CPX-6

	*	1	*	2	*	3	*	4	*	5	*	6	*	7
SI02	*	46.25	*	46.38	*	45.68	*	45.96	*	45.70	*	45.70	*	45.90
TI02	*	1.87	*	1.95	*	1.97	*	2.36	*	2.25	*	2.61	*	2.43
AL203	*	7.69	*	7.95	*	8.04	*	8.63	*	8.70	*	9.16	*	9.27
CR203	*	0.0	*	0.0	*	0.0	*	0.0	*	0.0	*	0.0	*	0.0
FE203	*	5.02	*	3.53	*	5.56	*	5.25	*	6.56	*	0.37	*	4.47
FEO	*	8.83	*	10.04	*	8.42	*	6.14	*	5.35	*	10.27	*	6.78
MNO	*	0.39	*	0.41	*	0.39	*	0.25	*	0.23	*	0.30	*	0.23
MGO	*	7.47	*	7.15	*	7.40	*	8.43	*	8.71	*	8.36	*	8.23
CAO	*	22.03	*	21.89	*	21.88	*	22.22	*	22.17	*	22.06	*	21.85
NA2O	*	1.35	*	1.29	*	1.38	*	1.56	*	1.56	*	1.55	*	1.60
NIO	*	0.0	*	0.0	*	0.0	*	0.0	*	0.0	*	0.0	*	0.0
TOTAL	*	100.90	*	100.59	*	100.72	*	100.80	*	101.23	*	100.38	*	100.76

SI	*	1.752	*	1.763	*	1.734	*	1.724	*	1.708	*	1.713	*	1.721
AL(IV)	*	0.248	*	0.237	*	0.266	*	0.276	*	0.292	*	0.287	*	0.279
AL(VI)	*	0.096	*	0.119	*	0.094	*	0.106	*	0.091	*	0.118	*	0.131
TI	*	0.053	*	0.056	*	0.056	*	0.067	*	0.063	*	0.074	*	0.069
CR	*	0.0	*	0.0	*	0.0	*	0.0	*	0.0	*	0.0	*	0.0
FE3+	*	0.145	*	0.102	*	0.161	*	0.151	*	0.188	*	0.135	*	0.128
FE2+	*	0.278	*	0.318	*	0.265	*	0.190	*	0.164	*	0.198	*	0.211
MG	*	0.422	*	0.405	*	0.419	*	0.471	*	0.485	*	0.467	*	0.460
MN	*	0.013	*	0.013	*	0.013	*	0.008	*	0.007	*	0.010	*	0.007
NI	*	0.0	*	0.0	*	0.0	*	0.0	*	0.0	*	0.0	*	0.0
CA	*	0.894	*	0.892	*	0.890	*	0.893	*	0.888	*	0.886	*	0.878
NA	*	0.099	*	0.095	*	0.102	*	0.113	*	0.113	*	0.113	*	0.116

WO	*	34.98	*	35.50	*	34.02	*	34.21	*	32.94	*	33.64	*	33.67
EN	*	21.10	*	20.26	*	20.94	*	23.58	*	24.27	*	23.36	*	23.00
FS	*	14.51	*	16.56	*	13.89	*	9.92	*	8.56	*	10.37	*	10.91
JD	*	9.92	*	9.51	*	10.16	*	11.35	*	11.31	*	11.27	*	11.64
AC	*	0.0	*	0.0	*	0.0	*	0.0	*	0.0	*	0.0	*	0.0
TI-TS	*	5.33	*	5.58	*	5.63	*	6.66	*	6.33	*	7.36	*	6.86
FE-TS	*	7.27	*	5.11	*	8.07	*	7.53	*	9.41	*	6.75	*	6.41
CA-TS	*	6.89	*	7.49	*	7.29	*	6.76	*	7.19	*	7.25	*	7.82

1	*	491-3	CPX-7
2	*	491-3	CPX-8
3	*	491-3	CPX-9
4	*	492-1	CPX-1
5	*	492-1	CPX-2
6	*	492-1	CPX-3
7	*	492-2	CPX-4

	*	1 *	2 *	3 *	4 *	5 *	6 *	7
SiO2	*	45.34 *	44.91 *	53.71 *	54.04 *	54.69 *	53.75 *	53.63
TiO2	*	2.57 *	2.46 *	0.09 *	0.08 *	0.07 *	0.08 *	0.05
Al2O3	*	9.20 *	8.78 *	5.92 *	4.70 *	4.82 *	5.28 *	5.62
Cr2O3	*	0.0 *	0.0 *	0.67 *	0.38 *	0.50 *	0.54 *	0.64
Fe2O3	*	6.33 *	7.09 *	0.57 *	3.49 *	0.37 *	1.35 *	1.24
FEO	*	4.94 *	4.29 *	6.25 *	4.25 *	6.54 *	5.99 *	5.91
MNO	*	0.25 *	0.28 *	0.10 *	0.10 *	0.13 *	0.12 *	0.11
MGO	*	9.05 *	9.11 *	31.24 *	33.28 *	32.61 *	32.21 *	31.99
CAO	*	22.39 *	22.58 *	1.55 *	0.59 *	0.39 *	0.43 *	0.85
NA2O	*	1.42 *	1.35 *	0.03 *	0.02 *	0.02 *	0.04 *	0.0
NiO	*	0.0 *	0.0 *	0.16 *	0.16 *	0.05 *	0.07 *	0.06
TOTAL	*	101.49 *	100.85 *	100.29 *	101.09 *	100.19 *	99.86 *	100.10
SI	*	1.688 *	1.684 *	1.861 *	1.854 *	1.889 *	1.866 *	1.859
AL(IV)	*	0.312 *	0.316 *	0.139 *	0.146 *	0.111 *	0.134 *	0.141
AL(VI)	*	0.091 *	0.072 *	0.103 *	0.044 *	0.086 *	0.082 *	0.088
TI	*	0.072 *	0.069 *	0.002 *	0.002 *	0.002 *	0.002 *	0.001
CR	*	0.0 *	0.0 *	0.018 *	0.010 *	0.014 *	0.015 *	0.018
FE3+	*	0.180 *	0.204 *	0.015 *	0.090 *	0.010 *	0.035 *	0.032
FE2+	*	0.151 *	0.131 *	0.181 *	0.122 *	0.189 *	0.174 *	0.171
MG	*	0.502 *	0.509 *	1.613 *	1.701 *	1.679 *	1.667 *	1.653
MN	*	0.008 *	0.009 *	0.003 *	0.003 *	0.004 *	0.004 *	0.003
NI	*	0.0 *	0.0 *	0.004 *	0.004 *	0.001 *	0.002 *	0.002
CA	*	0.893 *	0.907 *	0.058 *	0.022 *	0.014 *	0.016 *	0.032
NA	*	0.102 *	0.098 *	0.002 *	0.001 *	0.001 *	0.003 *	0.0
WO	*	32.62 *	33.02 *	3.07 *	1.12 *	0.76 *	0.84 *	1.67
EN	*	25.11 *	25.46 *	86.32 *	87.82 *	88.57 *	87.94 *	87.40
FS	*	7.93 *	6.99 *	10.61 *	11.07 *	10.67 *	11.21 *	10.93
JD	*	10.25 *	9.82 *	0.0 *	0.0 *	0.0 *	0.0 *	0.0
AC	*	0.0 *	0.0 *	0.0 *	0.0 *	0.0 *	0.0 *	0.0
TI-TS	*	7.20 *	6.94 *	0.0 *	0.0 *	0.0 *	0.0 *	0.0
FE-TS	*	9.02 *	10.21 *	0.0 *	0.0 *	0.0 *	0.0 *	0.0
CA-TS	*	7.87 *	7.57 *	0.0 *	0.0 *	0.0 *	0.0 *	0.0

- 1 * 492-3 CPX-5
- 2 * 492-3 CPX-6
- 3 * RJ75-124 OPX-1 CORE OF LARGE DEFORMED GRAIN
- 4 * RJ75-124-1 OPX-2 MATRIX
- 5 * 124-2 OPX-3 SMALL GRAIN ADJACENT SPINRL
- 6 * 124-2 OPX-4 LARGE DEFORMED GRAIN
- 7 * 124-3 OPX-5 CORE LARGE DEFORMED GRAIN

	*	1 *	2 *	3 *	4 *	5 *	6 *	7
SiO2	*	54.71 *	55.04 *	53.77 *	54.35 *	52.98 *	55.11 *	53.24
TiO2	*	0.05 *	0.05 *	0.10 *	0.10 *	0.13 *	0.11 *	0.15
Al2O3	*	3.70 *	4.16 *	4.44 *	4.36 *	5.95 *	4.20 *	6.31
CR2O3	*	0.30 *	0.38 *	0.40 *	0.42 *	0.68 *	0.46 *	0.70
FE2O3	*	1.15 *	0.49 *	1.89 *	0.84 *	2.70 *	1.12 *	2.57
FeO	*	6.26 *	6.58 *	5.56 *	5.92 *	4.83 *	6.15 *	4.59
MNO	*	0.11 *	0.11 *	0.13 *	0.13 *	0.13 *	0.13 *	0.13
MGO	*	32.82 *	32.88 *	32.27 *	32.48 *	32.32 *	33.04 *	32.57
CAO	*	0.41 *	0.42 *	0.62 *	0.60 *	0.50 *	0.48 *	0.64
NA2O	*	0.0 *	0.0 *	0.06 *	0.05 *	0.05 *	0.04 *	0.07
NiO	*	0.08 *	0.04 *	0.09 *	0.08 *	0.04 *	0.04 *	0.08
TOTAL	*	99.59 *	100.15 *	99.33 *	99.33 *	100.31 *	100.88 *	101.05
SI	*	1.904 *	1.902 *	1.878 *	1.893 *	1.832 *	1.893 *	1.826
AL(IV)	*	0.096 *	0.098 *	0.122 *	0.107 *	0.168 *	0.107 *	0.174
AL(VI)	*	0.055 *	0.072 *	0.061 *	0.072 *	0.075 *	0.063 *	0.081
TI	*	0.001 *	0.001 *	0.003 *	0.003 *	0.003 *	0.003 *	0.004
CR	*	0.008 *	0.010 *	0.011 *	0.012 *	0.019 *	0.012 *	0.019
FE3+	*	0.030 *	0.013 *	0.050 *	0.022 *	0.070 *	0.029 *	0.066
FE2+	*	0.182 *	0.190 *	0.162 *	0.172 *	0.140 *	0.177 *	0.132
MG	*	1.702 *	1.694 *	1.680 *	1.686 *	1.666 *	1.691 *	1.665
MN	*	0.003 *	0.003 *	0.004 *	0.004 *	0.004 *	0.004 *	0.004
NI	*	0.002 *	0.001 *	0.003 *	0.002 *	0.001 *	0.001 *	0.002
CA	*	0.015 *	0.016 *	0.023 *	0.022 *	0.019 *	0.018 *	0.024
NA	*	0.0 *	0.0 *	0.004 *	0.003 *	0.003 *	0.003 *	0.005
WO	*	0.79 *	0.81 *	1.21 *	1.17 *	0.98 *	0.92 *	1.24
EN	*	88.07 *	88.43 *	87.55 *	88.44 *	87.77 *	88.17 *	88.09
FS	*	11.14 *	10.76 *	11.24 *	10.39 *	11.26 *	10.91 *	10.66
JD	*	0.0 *	0.0 *	0.0 *	0.0 *	0.0 *	0.0 *	0.0
AC	*	0.0 *	0.0 *	0.0 *	0.0 *	0.0 *	0.0 *	0.0
TI-TS	*	0.0 *	0.0 *	0.0 *	0.0 *	0.0 *	0.0 *	0.0
FE-TS	*	0.0 *	0.0 *	0.0 *	0.0 *	0.0 *	0.0 *	0.0
CA-TS	*	0.0 *	0.0 *	0.0 *	0.0 *	0.0 *	0.0 *	0.0

1 *	124-3	OPX-6	MATRIX
2 *	124-1	OPX-7	REXLEZED ALONG KINK
3 *	493-3	OPX-1	GRAIN REPLACED BY TALC
4 *	493-3	OPX-2	DEFORMED GRAIN WITH OL
5 *	498-1	OPX-1	CORE WITH PLAG
6 *	498-1	OPX-1	RIM WITH PLAG
7 *	498-1	OPX-2	CORE WITH PLAG

	*	1 *	2 *	3 *	4 *	5 *	6 *	7
SiO2	*	54.19 *	54.32 *	52.94 *	54.35 *	55.11 *	53.26 *	54.91
TiO2	*	0.11 *	0.11 *	0.10 *	0.13 *	0.10 *	0.10 *	0.04
Al2O3	*	4.13 *	4.23 *	6.09 *	4.32 *	3.95 *	5.67 *	3.56
Cr2O3	*	0.48 *	0.38 *	0.68 *	0.40 *	0.35 *	0.61 *	0.08
Fe2O3	*	2.52 *	2.83 *	3.20 *	2.85 *	1.65 *	2.33 *	1.76
FeO	*	4.55 *	4.74 *	4.25 *	4.70 *	5.43 *	4.74 *	6.60
MnO	*	0.11 *	0.13 *	0.08 *	0.11 *	0.10 *	0.11 *	0.16
MgO	*	33.28 *	33.16 *	32.59 *	33.33 *	33.42 *	32.00 *	32.71
CaO	*	0.48 *	0.62 *	0.53 *	0.50 *	0.50 *	1.21 *	0.42
Na2O	*	0.05 *	0.04 *	0.05 *	0.04 *	0.04 *	0.06 *	0.01
NiO	*	0.08 *	0.11 *	0.08 *	0.08 *	0.08 *	0.07 *	0.03
TOTAL	*	99.98 *	100.67 *	100.59 *	100.81 *	100.73 *	100.16 *	100.28

SI	*	1.875 *	1.871 *	1.824 *	1.868 *	1.893 *	1.845 *	1.903
AL(IV)	*	0.125 *	0.129 *	0.176 *	0.132 *	0.107 *	0.155 *	0.097
AL(VI)	*	0.044 *	0.042 *	0.072 *	0.043 *	0.053 *	0.076 *	0.048
TI	*	0.003 *	0.003 *	0.003 *	0.003 *	0.003 *	0.003 *	0.001
CR	*	0.013 *	0.010 *	0.018 *	0.011 *	0.009 *	0.017 *	0.002
FE3+	*	0.066 *	0.073 *	0.083 *	0.074 *	0.043 *	0.061 *	0.046
FE2+	*	0.132 *	0.137 *	0.123 *	0.135 *	0.156 *	0.137 *	0.191
MG	*	1.716 *	1.702 *	1.674 *	1.707 *	1.711 *	1.652 *	1.689
MN	*	0.003 *	0.004 *	0.002 *	0.003 *	0.003 *	0.003 *	0.005
NI	*	0.002 *	0.003 *	0.002 *	0.002 *	0.002 *	0.002 *	0.001
CA	*	0.018 *	0.023 *	0.020 *	0.018 *	0.018 *	0.045 *	0.016
NA	*	0.003 *	0.003 *	0.003 *	0.003 *	0.003 *	0.004 *	0.001

WO	*	0.92 *	1.18 *	1.03 *	0.95 *	0.95 *	2.36 *	0.80
EN	*	88.73 *	87.82 *	88.05 *	88.12 *	88.62 *	87.04 *	86.78
FS	*	10.35 *	11.00 *	10.92 *	10.93 *	10.43 *	10.59 *	12.42
JD	*	0.0 *	0.0 *	0.0 *	0.0 *	0.0 *	0.0 *	0.0
AC	*	0.0 *	0.0 *	0.0 *	0.0 *	0.0 *	0.0 *	0.0
TI-TS	*	0.0 *	0.0 *	0.0 *	0.0 *	0.0 *	0.0 *	0.0
FE-TS	*	0.0 *	0.0 *	0.0 *	0.0 *	0.0 *	0.0 *	0.0
CA-TS	*	0.0 *	0.0 *	0.0 *	0.0 *	0.0 *	0.0 *	0.0

1 *	498-1	OPX-2 RIM WITH PLAG	
2 *	498-1	OPX-3 MATRIX	
3 *	498-2	OPX-4 CORE WITH CPX	
4 *	498-2	OPX-4 RIM WITH CPX	
5 *	498-2	OPX-5 MATRIX	
6 *	509-1	OPX-1 KINKED GRAIN AVERAGE	FERRIC IRON
7 *	509-2	OPX-2 SMALL MATRIX GRAINS IN PLAG BAND	

	*	1 *	2 *	3 *	4 *	5 *	6 *	7
SiO2	*	53.88 *	53.32 *	54.23 *	55.89 *	53.86 *	54.00 *	54.18
TiO2	*	0.07 *	0.20 *	0.10 *	0.11 *	0.11 *	0.09 *	0.11
Al2O3	*	4.93 *	5.19 *	4.21 *	3.57 *	5.20 *	3.93 *	3.73
Cr2O3	*	0.15 *	0.43 *	0.35 *	0.26 *	0.47 *	0.31 *	0.27
Fe2O3	*	2.22 *	2.46 *	1.42 *	0.0 *	1.02 *	2.74 *	1.73
FeO	*	6.39 *	5.43 *	6.54 *	8.11 *	6.83 *	5.32 *	6.32
MnO	*	0.13 *	0.11 *	0.13 *	0.18 *	0.11 *	0.13 *	0.11
MgO	*	31.95 *	31.99 *	32.04 *	31.68 *	31.39 *	32.79 *	32.37
CaO	*	0.69 *	0.78 *	0.70 *	0.46 *	0.99 *	0.43 *	0.48
Na2O	*	0.02 *	0.07 *	0.05 *	0.03 *	0.07 *	0.04 *	0.02
NiO	*	0.06 *	0.07 *	0.04 *	0.0 *	0.03 *	0.03 *	0.03
TOTAL	*	100.49 *	100.05 *	99.81 *	100.29 *	100.08 *	99.81 *	99.35

SI	*	1.867 *	1.853 *	1.889 *	1.936 *	1.873 *	1.878 *	1.895
AL(IV)	*	0.133 *	0.147 *	0.111 *	0.064 *	0.127 *	0.122 *	0.105
AL(VI)	*	0.068 *	0.065 *	0.062 *	0.081 *	0.086 *	0.039 *	0.048
TI	*	0.002 *	0.005 *	0.003 *	0.003 *	0.003 *	0.002 *	0.003
CR	*	0.004 *	0.012 *	0.010 *	0.007 *	0.013 *	0.009 *	0.007
FE3+	*	0.058 *	0.064 *	0.037 *	0.0 *	0.027 *	0.072 *	0.046
FE2+	*	0.185 *	0.158 *	0.191 *	0.235 *	0.199 *	0.155 *	0.185
MG	*	1.650 *	1.657 *	1.664 *	1.635 *	1.627 *	1.700 *	1.687
MN	*	0.004 *	0.003 *	0.004 *	0.005 *	0.003 *	0.004 *	0.003
NI	*	0.002 *	0.002 *	0.001 *	0.0 *	0.001 *	0.001 *	0.001
CA	*	0.026 *	0.029 *	0.026 *	0.017 *	0.037 *	0.016 *	0.018
NA	*	0.001 *	0.005 *	0.003 *	0.002 *	0.005 *	0.003 *	0.001

WD	*	1.33 *	1.57 *	1.36 *	0.90 *	1.95 *	0.82 *	0.93
EN	*	85.84 *	86.70 *	86.59 *	86.41 *	85.98 *	87.35 *	87.03
FS	*	12.83 *	11.78 *	12.05 *	12.69 *	12.07 *	11.83 *	12.05
JD	*	0.0 *	0.0 *	0.0 *	0.0 *	0.0 *	0.0 *	0.0
AC	*	0.0 *	0.0 *	0.0 *	0.0 *	0.0 *	0.0 *	0.0
TI-TS	*	0.0 *	0.0 *	0.0 *	0.0 *	0.0 *	0.0 *	0.0
FE-TS	*	0.0 *	0.0 *	0.0 *	0.0 *	0.0 *	0.0 *	0.0
CA-TS	*	0.0 *	0.0 *	0.0 *	0.0 *	0.0 *	0.0 *	0.0

- 1 * 509-2 OPX-3 CORES OF MEDIUM SIZED GRAINS IN PLAG BAND
- 2 * 662-1 OPX-1 CORE VERY LARGE GRAIN
- 3 * 662-1 OPX-1 RIM VERY LARGE GRAIN
- 4 * 662-1 OPX-2 CALCULATED FERRIC IRON
- 5 * 662-3 OPX-3 CORE VERY LARGE GRAIN
- 6 * 662-3 OPX-3 RIM VERY LARGE GRAIN
- 7 * 662-3 OPX-4 MATRIX

	*	1 *	2 *	3 *	4 *	5 *	6 *	7
SI02	*	53.98 *	54.71 *	51.24 *	51.63 *	50.88 *	51.85 *	50.41
TI02	*	0.16 *	0.08 *	0.29 *	0.30 *	0.24 *	0.26 *	0.80
AL203	*	4.93 *	3.84 *	6.09 *	4.83 *	6.10 *	4.40 *	7.93
CR203	*	0.43 *	0.29 *	0.95 *	0.70 *	0.97 *	0.70 *	1.16
FE203	*	1.81 *	1.36 *	1.22 *	1.77 *	1.50 *	1.00 *	1.77
FE0	*	6.50 *	7.27 *	1.72 *	1.01 *	1.06 *	1.53 *	0.97
MNO	*	0.14 *	0.14 *	0.09 *	0.07 *	0.06 *	0.07 *	0.03
MGO	*	31.64 *	32.19 *	15.37 *	16.03 *	15.57 *	16.03 *	14.04
CA0	*	0.97 *	0.45 *	23.53 *	23.91 *	23.52 *	23.92 *	21.82
NA2O	*	0.09 *	0.03 *	0.46 *	0.35 *	0.44 *	0.30 *	1.50
NIO	*	0.0 *	0.0 *	0.01 *	0.04 *	0.01 *	0.02 *	0.03
TOTAL	*	100.65 *	100.36 *	100.97 *	100.64 *	100.35 *	100.08 *	100.46

SI	*	1.869 *	1.899 *	1.849 *	1.867 *	1.844 *	1.885 *	1.822
AL(IV)	*	0.131 *	0.101 *	0.151 *	0.133 *	0.156 *	0.115 *	0.178
AL(VI)	*	0.070 *	0.056 *	0.108 *	0.073 *	0.105 *	0.074 *	0.159
TI	*	0.004 *	0.002 *	0.008 *	0.008 *	0.007 *	0.007 *	0.022
CR	*	0.012 *	0.008 *	0.027 *	0.020 *	0.028 *	0.020 *	0.033
FE3+	*	0.047 *	0.036 *	0.033 *	0.048 *	0.041 *	0.027 *	0.048
FE2+	*	0.188 *	0.211 *	0.052 *	0.030 *	0.032 *	0.047 *	0.029
MG	*	1.633 *	1.665 *	0.827 *	0.864 *	0.841 *	0.869 *	0.756
MN	*	0.004 *	0.004 *	0.003 *	0.002 *	0.002 *	0.002 *	0.001
NI	*	0.0 *	0.0 *	0.0 *	0.001 *	0.0 *	0.001 *	0.001
CA	*	0.036 *	0.017 *	0.910 *	0.927 *	0.914 *	0.932 *	0.845
NA	*	0.006 *	0.002 *	0.032 *	0.025 *	0.031 *	0.021 *	0.105

WO	*	1.89 *	0.87 *	38.32 *	40.12 *	38.21 *	41.23 *	34.41
EN	*	85.56 *	86.16 *	41.34 *	43.27 *	42.07 *	43.47 *	37.85
FS	*	12.55 *	12.97 *	2.73 *	1.63 *	1.69 *	2.43 *	1.51
JD	*	0.0 *	0.0 *	3.27 *	2.55 *	3.09 *	2.12 *	10.56
AC	*	0.0 *	0.0 *	0.0 *	0.0 *	0.0 *	0.0 *	0.0
TI-TS	*	0.0 *	0.0 *	0.79 *	0.82 *	0.65 *	0.71 *	2.17
FE-TS	*	0.0 *	0.0 *	3.01 *	3.41 *	3.44 *	2.38 *	4.06
CA-TS	*	0.0 *	0.0 *	10.54 *	8.21 *	10.83 *	7.66 *	9.44

1 *	662-5	OPX-5	CORE DEFORMED GRAIN
2 *	662-5	OPX-5	RIM DEFORMED GRAIN
3 *	124-1	CPX-1	LARGE GRAIN
4 *	124.1	CPX-2	MATRIX
5 *	124-3	CPX-3	CORE LARGE GRAIN
6 *	124-3	CPX-4	MATRIX
7 *	498-2	CPX-1	LAMELLAE IN OPX-4

	*	1	*	2	*	3	*	4	*	5	*	6	*	7
SI02	*	52.14	*	50.77	*	51.21	*	50.50	*	52.27	*	52.35	*	52.10
TI02	*	0.64	*	0.75	*	0.60	*	0.77	*	0.34	*	0.35	*	0.45
AL203	*	6.08	*	7.29	*	6.21	*	7.88	*	6.33	*	5.51	*	5.88
CR203	*	0.77	*	1.16	*	0.89	*	1.05	*	0.22	*	0.16	*	0.62
FE203	*	1.20	*	1.73	*	1.83	*	1.63	*	0.0	*	0.17	*	1.39
FEO	*	1.36	*	1.18	*	1.19	*	1.41	*	3.16	*	2.65	*	2.64
MNO	*	0.06	*	0.07	*	0.05	*	0.07	*	0.06	*	0.08	*	0.09
MGO	*	15.49	*	14.48	*	15.05	*	14.33	*	15.31	*	15.67	*	15.08
CAO	*	21.42	*	21.80	*	21.38	*	21.37	*	21.37	*	22.19	*	20.98
NA2O	*	1.27	*	1.36	*	1.35	*	1.43	*	0.92	*	0.82	*	1.34
NIO	*	0.04	*	0.02	*	0.02	*	0.01	*	0.04	*	0.02	*	0.0
TOTAL	*	100.47	*	100.61	*	99.78	*	100.45	*	100.02	*	99.97	*	100.57

SI	*	1.872	*	1.833	*	1.861	*	1.824	*	1.891	*	1.897	*	1.882
AL(IV)	*	0.128	*	0.167	*	0.139	*	0.176	*	0.109	*	0.103	*	0.118
AL(VI)	*	0.129	*	0.143	*	0.127	*	0.160	*	0.161	*	0.132	*	0.132
TI	*	0.017	*	0.020	*	0.016	*	0.021	*	0.009	*	0.010	*	0.012
CR	*	0.022	*	0.033	*	0.026	*	0.030	*	0.006	*	0.005	*	0.018
FE3+	*	0.033	*	0.047	*	0.050	*	0.044	*	0.0	*	0.005	*	0.038
FE2+	*	0.055	*	0.036	*	0.036	*	0.043	*	0.096	*	0.080	*	0.080
MG	*	0.829	*	0.779	*	0.815	*	0.772	*	0.826	*	0.846	*	0.812
MN	*	0.002	*	0.002	*	0.002	*	0.002	*	0.002	*	0.002	*	0.003
NI	*	0.001	*	0.001	*	0.001	*	0.0	*	0.001	*	0.001	*	0.0
CA	*	0.824	*	0.843	*	0.832	*	0.827	*	0.828	*	0.862	*	0.812
NA	*	0.088	*	0.095	*	0.095	*	0.100	*	0.065	*	0.058	*	0.094

WO	*	35.64	*	34.81	*	35.47	*	33.63	*	36.36	*	38.41	*	35.30
EN	*	41.50	*	38.98	*	40.78	*	38.60	*	41.58	*	42.35	*	40.59
FS	*	2.82	*	1.89	*	1.89	*	2.24	*	4.90	*	4.13	*	4.12
JD	*	8.93	*	9.61	*	9.56	*	10.06	*	6.54	*	5.76	*	9.39
AC	*	0.0	*	0.0	*	0.0	*	0.0	*	0.0	*	0.0	*	0.0
TI-TS	*	1.73	*	2.04	*	1.64	*	2.09	*	0.93	*	0.95	*	1.22
FE-TS	*	2.72	*	4.00	*	3.78	*	3.72	*	0.32	*	0.46	*	2.78
CA-TS	*	6.67	*	8.67	*	6.88	*	9.66	*	9.38	*	7.94	*	6.61

1	*	498-2	CPX-2	MATRIX
2	*	498-1	CPX-3	LAMELLAE IN OPX-2
3	*	498-1	CPX-4	MATRIX
4	*	498-1	CPX-5	LAMELLAE IN OPX-1
5	*	509-2	CPX-1	CORES OF MEDIUM SIZED GRAINS IN PLAG BAND
6	*	509-2	CPX-2	SNALL MATRIX GRAINS IN PLAG BAND
7	*	662-1	CPX-1	SMALL GRAINS ADJACENT LARGE OPX

	*	1 *	2 *	3 *	4 *
SiO2	*	52.22 *	50.05 *	49.09 *	50.05 *
TiO2	*	0.37 *	0.43 *	0.98 *	0.86 *
Al2O3	*	5.33 *	6.40 *	7.91 *	6.86 *
Cr2O3	*	0.76 *	0.79 *	0.02 *	0.02 *
Fe2O3	*	1.90 *	4.14 *	3.27 *	2.61 *
FEO	*	1.59 *	0.0 *	4.31 *	4.87 *
MNO	*	0.05 *	0.09 *	0.11 *	0.11 *
MGO	*	15.79 *	14.80 *	12.77 *	13.57 *
CAO	*	21.08 *	21.36 *	21.08 *	20.52 *
NA2O	*	1.29 *	1.37 *	1.15 *	1.10 *
NIO	*	0.0 *	0.08 *	0.04 *	0.04 *
TOTAL	*	100.38 *	99.51 *	100.73 *	100.61 *
SI	*	1.885 *	1.847 *	1.798 *	1.831 *
AL(IV)	*	0.115 *	0.153 *	0.202 *	0.169 *
AL(VI)	*	0.112 *	0.126 *	0.139 *	0.127 *
TI	*	0.010 *	0.012 *	0.027 *	0.024 *
CR	*	0.022 *	0.023 *	0.001 *	0.001 *
FE3+	*	0.052 *	0.0 *	0.090 *	0.072 *
FE2+	*	0.048 *	0.115 *	0.132 *	0.149 *
MG	*	0.850 *	0.814 *	0.697 *	0.740 *
MN	*	0.002 *	0.003 *	0.003 *	0.003 *
NI	*	0.0 *	0.002 *	0.001 *	0.001 *
CA	*	0.815 *	0.845 *	0.827 *	0.805 *
NA	*	0.090 *	0.098 *	0.082 *	0.078 *
WO	*	35.53 *	35.77 *	32.61 *	32.98 *
EN	*	42.48 *	39.30 *	34.91 *	37.06 *
FS	*	2.48 *	5.68 *	6.77 *	7.62 *
JD	*	9.03 *	9.48 *	8.21 *	7.85 *
AC	*	0.0 *	0.0 *	0.0 *	0.0 *
TI-TS	*	1.01 *	1.15 *	2.70 *	2.37 *
FE-TS	*	3.67 *	1.11 *	4.53 *	3.62 *
CA-TS	*	5.82 *	7.51 *	10.27 *	8.51 *

1 * 662-5 CPX-2 MATRIX
 2 * 662-3 CPX-3 ADJACENT SPINEL
 3 * G12-3 CPX-1
 4 * G12-3 CPX-2

Table II.iii. Feldspar analyses, structural formulae, and end members.

	*	1 *	2 *	3 *	4 *	5 *	6 *	7
SiO2	*	67.04 *	68.11 *	68.60 *	67.63 *	68.23 *	67.61 *	65.33
AL2O3	*	19.93 *	20.02 *	19.71 *	20.31 *	21.14 *	21.17 *	20.87
FE2O3	*	1.02 *	0.68 *	0.04 *	0.28 *	0.0 *	0.0 *	0.33
MGO	*	0.54 *	0.32 *	0.0 *	0.0 *	0.0 *	0.0 *	0.0
CAO	*	0.10 *	0.08 *	0.25 *	1.20 *	0.32 *	0.31 *	1.56
NA2O	*	12.35 *	12.67 *	12.73 *	12.51 *	12.44 *	12.79 *	12.11
K2O	*	0.17 *	0.21 *	0.07 *	0.09 *	0.04 *	0.03 *	0.04
SRO	*	0.0 *	0.0 *	0.0 *	0.12 *	0.12 *	0.46 *	0.18
BAO	*	0.0 *	0.0 *	0.04 *	0.18 *	0.05 *	0.01 *	0.02
TOTAL	*	101.15 *	102.09 *	101.44 *	102.32 *	102.34 *	102.38 *	100.44

SI	*	11.690 *	11.757 *	11.880 *	11.691 *	11.715 *	11.652 *	11.519
AL	*	4.098 *	4.075 *	4.025 *	4.140 *	4.280 *	4.302 *	4.339
FE3+	*	0.134 *	0.088 *	0.005 *	0.036 *	0.0 *	0.0 *	0.044
MG	*	0.140 *	0.082 *	0.0 *	0.0 *	0.0 *	0.0 *	0.0
CA	*	0.019 *	0.015 *	0.046 *	0.222 *	0.059 *	0.057 *	0.295
NA	*	4.176 *	4.241 *	4.275 *	4.194 *	4.142 *	4.274 *	4.141
K	*	0.038 *	0.046 *	0.015 *	0.020 *	0.009 *	0.007 *	0.009
SR	*	0.0 *	0.0 *	0.0 *	0.012 *	0.012 *	0.046 *	0.018
BA	*	0.0 *	0.0 *	0.003 *	0.012 *	0.003 *	0.001 *	0.001
OR	*	0.89 *	1.08 *	0.36 *	0.45 *	0.21 *	0.15 *	0.20
AB	*	98.66 *	98.58 *	98.57 *	94.54 *	98.39 *	98.53 *	93.17
AN	*	0.44 *	0.34 *	1.07 *	5.01 *	1.40 *	1.32 *	6.63

1 *	544-1	FD-1
2 *	544-2	FD-2
3 *	283B-1	FD-1
4 *	283B-2	FD-2
5 *	286-1	FD-1
6 *	286-2	FD-2
7 *	286-2	FD-3

	*	1	*	2	*	3	*	4	*	5	*	6	*	7
SiO2	*	63.06	*	61.88	*	62.98	*	64.30	*	64.62	*	65.25	*	65.41
Al2O3	*	22.82	*	23.30	*	23.31	*	22.38	*	21.71	*	21.93	*	22.32
Fe2O3	*	0.03	*	0.04	*	0.20	*	0.15	*	0.15	*	0.06	*	0.07
MgO	*	0.02	*	0.01	*	0.0	*	0.0	*	0.0	*	0.0	*	0.0
CaO	*	4.01	*	4.45	*	4.71	*	1.20	*	0.70	*	2.36	*	2.81
Na2O	*	10.02	*	9.45	*	9.19	*	10.47	*	10.97	*	10.51	*	10.38
K2O	*	0.06	*	0.06	*	0.14	*	0.99	*	0.77	*	0.11	*	0.12
SiO	*	0.02	*	0.0	*	0.0	*	0.0	*	0.0	*	0.0	*	0.0
BAO	*	0.0	*	0.0	*	0.0	*	0.0	*	0.0	*	0.0	*	0.0
TOTAL	*	100.04	*	99.19	*	100.53	*	99.49	*	98.92	*	100.22	*	101.11

SI	*	11.173	*	11.062	*	11.106	*	11.404	*	11.508	*	11.463	*	11.405
AL	*	4.767	*	4.911	*	4.847	*	4.680	*	4.559	*	4.543	*	4.589
FE3+	*	0.004	*	0.005	*	0.027	*	0.020	*	0.020	*	0.008	*	0.009
MG	*	0.005	*	0.003	*	0.0	*	0.0	*	0.0	*	0.0	*	0.0
CA	*	0.761	*	0.853	*	0.890	*	0.228	*	0.134	*	0.444	*	0.525
NA	*	3.443	*	3.276	*	3.143	*	3.601	*	3.789	*	3.581	*	3.510
K	*	0.014	*	0.014	*	0.032	*	0.224	*	0.175	*	0.025	*	0.027
SR	*	0.002	*	0.0	*	0.0	*	0.0	*	0.0	*	0.0	*	0.0
BA	*	0.0	*	0.0	*	0.0	*	0.0	*	0.0	*	0.0	*	0.0

OR	*	0.32	*	0.33	*	0.78	*	5.53	*	4.27	*	0.61	*	0.66
AB	*	81.63	*	79.09	*	77.32	*	88.85	*	92.47	*	88.42	*	86.41
AN	*	18.05	*	20.58	*	21.90	*	5.63	*	3.26	*	10.97	*	12.93

1	*	033-1	FD-1
2	*	033-2	FD-2
3	*	114-3	FD-1
4	*	236-1	FD-1
5	*	236-2	FD-2
6	*	236-3	FD-3
7	*	236-3	FD-4

	*	1 *	2 *	3 *	4 *	5 *	6 *	7
SI02	*	68.41 *	68.39 *	63.96 *	59.13 *	59.42 *	67.54 *	67.71
AL203	*	20.06 *	20.36 *	23.19 *	26.24 *	26.72 *	21.25 *	21.44
FE203	*	0.02 *	0.03 *	0.03 *	0.14 *	0.15 *	0.12 *	0.03
MGO	*	0.02 *	0.04 *	0.02 *	0.01 *	0.0 *	0.01 *	0.0
CAO	*	0.31 *	0.16 *	3.74 *	7.18 *	7.46 *	0.74 *	1.41
NA2O	*	11.84 *	12.61 *	8.57 *	6.88 *	6.22 *	10.68 *	10.20
K2O	*	0.08 *	0.04 *	0.17 *	0.11 *	0.04 *	0.05 *	0.10
SRO	*	0.0 *	0.0 *	0.32 *	0.11 *	0.0 *	0.13 *	0.27
BAO	*	0.0 *	0.0 *	0.0 *	0.01 *	0.0 *	0.01 *	0.02
TOTAL	*	100.74 *	101.63 *	100.00 *	99.81 *	100.01 *	100.53 *	101.23

SI	*	11.884 *	11.810 *	11.269 *	10.550 *	10.545 *	11.741 *	11.708
AL	*	4.109 *	4.146 *	4.818 *	5.520 *	5.591 *	4.356 *	4.371
FE3+	*	0.003 *	0.004 *	0.004 *	0.019 *	0.020 *	0.016 *	0.010
MG	*	0.005 *	0.010 *	0.005 *	0.003 *	0.0 *	0.003 *	0.0
CA	*	0.058 *	0.030 *	0.706 *	1.373 *	1.419 *	0.138 *	0.261
NA	*	3.988 *	4.223 *	2.928 *	2.381 *	2.141 *	3.600 *	3.420
K	*	0.018 *	0.009 *	0.038 *	0.025 *	0.009 *	0.011 *	0.022
SR	*	0.0 *	0.0 *	0.033 *	0.011 *	0.0 *	0.013 *	0.027
BA	*	0.0 *	0.0 *	0.0 *	0.001 *	0.0 *	0.001 *	0.001
OR	*	0.44 *	0.21 *	1.04 *	0.66 *	0.25 *	0.30 *	0.60
AB	*	98.14 *	99.10 *	79.73 *	63.00 *	59.99 *	96.03 *	92.35
AN	*	1.42 *	0.69 *	19.23 *	36.33 *	39.76 *	3.68 *	7.05

1 *	435-1	FD-1
2 *	435-2	FD-2
3 *	530-1	FD-1
4 *	085-1	FD-1
5 *	085-2	FD-2
6 *	086-1	FD-1
7 *	086-2	FD-2

	*	1 *	2 *	3 *	4 *	5 *	6 *	7
SI02	*	61.28 *	63.85 *	58.97 *	58.84 *	67.57 *	58.53 *	60.52
AL203	*	24.27 *	23.44 *	26.35 *	26.56 *	20.75 *	26.28 *	25.38
FE203	*	0.23 *	0.10 *	0.16 *	0.11 *	0.14 *	0.17 *	0.21
MGO	*	0.03 *	0.0 *	0.01 *	0.0 *	0.0 *	0.0 *	0.04
CAO	*	5.04 *	4.03 *	6.89 *	7.45 *	1.03 *	6.69 *	6.63
NA2O	*	8.44 *	8.71 *	7.60 *	7.37 *	10.27 *	7.31 *	6.29
K2O	*	0.12 *	0.06 *	0.09 *	0.05 *	0.04 *	0.04 *	0.18
SRO	*	0.20 *	0.20 *	0.04 *	0.16 *	0.13 *	0.12 *	0.14
BAO	*	0.02 *	0.0 *	0.02 *	0.0 *	0.0 *	0.03 *	0.03
TOTAL	*	99.63 *	100.39 *	100.13 *	100.54 *	99.93 *	99.17 *	99.42

SI	*	10.919 *	11.215 *	10.508 *	10.458 *	11.804 *	10.516 *	10.780
AL	*	5.099 *	4.854 *	5.536 *	5.566 *	4.274 *	5.567 *	5.330
FE3+	*	0.031 *	0.013 *	0.021 *	0.015 *	0.018 *	0.023 *	0.028
MG	*	0.008 *	0.0 *	0.003 *	0.0 *	0.0 *	0.0 *	0.011
CA	*	0.962 *	0.759 *	1.316 *	1.419 *	0.193 *	1.288 *	1.266
NA	*	2.916 *	2.967 *	2.626 *	2.540 *	3.479 *	2.547 *	2.173
K	*	0.027 *	0.013 *	0.020 *	0.011 *	0.009 *	0.009 *	0.041
SR	*	0.021 *	0.020 *	0.004 *	0.016 *	0.013 *	0.012 *	0.014
BA	*	0.001 *	0.0 *	0.001 *	0.0 *	0.0 *	0.0 *	0.002
OR	*	0.70 *	0.36 *	0.52 *	0.29 *	0.24 *	0.24 *	1.18
AB	*	74.66 *	79.35 *	66.28 *	63.98 *	94.52 *	66.25 *	62.45
AN	*	24.64 *	20.29 *	33.21 *	35.74 *	5.24 *	33.51 *	36.38

1 *	086-3	FD-3	
2 *	087-1	FD-1	GROUNDMASS
3 *	087-2	FD-2	LARGE GRAIN
4 *	087-2	FD-3	
5 *	089-1	FD-1	
6 *	089-1	FD-2	
7 *	090-1	FD-1	GROUNDMASS

	*	1	*	2	*	3	*	4	*
SI02	*	62.23	*	60.17	*	67.96	*	61.48	*
AL203	*	24.61	*	23.80	*	20.06	*	23.58	*
FE203	*	0.09	*	0.06	*	0.07	*	0.07	*
MGO	*	0.01	*	0.02	*	0.02	*	0.01	*
CAO	*	5.05	*	5.58	*	0.12	*	5.00	*
NA2O	*	7.88	*	8.81	*	11.95	*	9.35	*
K2O	*	0.27	*	0.05	*	0.07	*	0.05	*
SRO	*	0.21	*	0.0	*	0.04	*	0.03	*
BAO	*	0.02	*	0.0	*	0.0	*	0.0	*
TOTAL	*	100.37	*	98.49	*	100.29	*	99.57	*

SI	*	10.973	*	10.873	*	11.865	*	10.977	*
AL	*	5.117	*	5.071	*	4.129	*	4.964	*
FE3+	*	0.012	*	0.008	*	0.009	*	0.009	*
MG	*	0.003	*	0.005	*	0.005	*	0.003	*
CA	*	0.954	*	1.081	*	0.022	*	0.957	*
NA	*	2.695	*	3.087	*	4.046	*	3.237	*
K	*	0.061	*	0.012	*	0.016	*	0.011	*
SR	*	0.021	*	0.0	*	0.004	*	0.003	*
BA	*	0.001	*	0.0	*	0.0	*	0.0	*

OR	*	1.64	*	0.28	*	0.38	*	0.27	*
AB	*	72.64	*	73.87	*	99.07	*	76.98	*
AN	*	25.72	*	25.86	*	0.55	*	22.75	*

1	*	090-2	FD-2	LARGE	SAUSSERITIZED	GRAIN
2	*	133-1	FD-1			
3	*	133-1	FD-2			
4	*	133-2	FD-3			

	*	1 *	2 *	3 *	4 *	5 *	6 *	7
SI02	*	58.23 *	56.70 *	57.92 *	59.52 *	59.18 *	59.20 *	59.30
AL203	*	26.93 *	27.87 *	27.23 *	25.41 *	26.25 *	26.41 *	26.01
FE203	*	0.13 *	0.14 *	0.09 *	0.11 *	0.05 *	0.04 *	0.04
MGO	*	0.01 *	0.02 *	0.0 *	0.02 *	0.0 *	0.0 *	0.0
CAO	*	8.06 *	9.31 *	8.31 *	6.64 *	7.42 *	7.56 *	7.16
NA2O	*	6.20 *	5.86 *	6.54 *	7.21 *	7.13 *	7.10 *	7.08
K2O	*	0.09 *	0.08 *	0.05 *	0.09 *	0.13 *	0.17 *	0.16
SRO	*	0.23 *	0.06 *	0.21 *	0.23 *	0.24 *	0.27 *	0.20
BAO	*	0.04 *	0.03 *	0.03 *	0.0 *	0.01 *	0.0 *	0.03
TOTAL	*	99.92 *	100.07 *	100.38 *	99.23 *	100.41 *	100.75 *	99.98

SI	*	10.404 *	10.156 *	10.325 *	10.674 *	10.524 *	10.501 *	10.577
AL	*	5.673 *	5.886 *	5.723 *	5.373 *	5.504 *	5.524 *	5.470
FE3+	*	0.017 *	0.019 *	0.012 *	0.015 *	0.007 *	0.005 *	0.005
MG	*	0.003 *	0.005 *	0.0 *	0.005 *	0.0 *	0.0 *	0.0
CA	*	1.543 *	1.787 *	1.587 *	1.276 *	1.414 *	1.437 *	1.369
NA	*	2.148 *	2.035 *	2.261 *	2.507 *	2.459 *	2.442 *	2.449
K	*	0.021 *	0.018 *	0.011 *	0.021 *	0.029 *	0.038 *	0.036
SR	*	0.024 *	0.006 *	0.022 *	0.024 *	0.025 *	0.028 *	0.021
BA	*	0.003 *	0.002 *	0.002 *	0.0 *	0.001 *	0.0 *	0.002

OR	*	0.55 *	0.48 *	0.30 *	0.54 *	0.76 *	0.98 *	0.94
AB	*	57.87 *	53.00 *	58.57 *	65.91 *	63.01 *	62.34 *	63.54
AN	*	41.58 *	46.53 *	41.13 *	33.55 *	36.24 *	36.68 *	35.51

1 *	083-1	FD-1
2 *	083-1	FD-2
3 *	477-1	FD-1
4 *	477-1	FD-2
5 *	131-1	FD-1
6 *	131-1	FD-2
7 *	131-2	FD-3

	*	1 *	2 *	3 *	4 *	5 *	6 *	7
SI02	*	58.00 *	58.45 *	59.51 *	58.42 *	56.67 *	56.91 *	57.33
AL203	*	26.96 *	26.71 *	24.65 *	27.03 *	26.86 *	24.36 *	26.48
FE203	*	0.12 *	0.13 *	0.24 *	0.08 *	0.05 *	0.49 *	0.11
MGD	*	0.02 *	0.0 *	0.0 *	0.0 *	0.01 *	0.02 *	0.0
CAO	*	7.90 *	7.78 *	7.69 *	7.82 *	8.63 *	8.84 *	7.55
NA2O	*	6.92 *	7.59 *	7.56 *	7.46 *	7.34 *	8.17 *	7.41
K2O	*	0.09 *	0.04 *	0.05 *	0.04 *	0.02 *	0.02 *	0.05
SRO	*	0.23 *	0.0 *	0.0 *	0.0 *	0.0 *	0.0 *	0.0
BAO	*	0.01 *	0.0 *	0.0 *	0.0 *	0.0 *	0.0 *	0.0
TOTAL	*	100.25 *	100.70 *	99.70 *	100.85 *	99.58 *	98.81 *	98.93

SI	*	10.356 *	10.391 *	10.669 *	10.364 *	10.228 *	10.413 *	10.369
AL	*	5.676 *	5.599 *	5.211 *	5.654 *	5.716 *	5.255 *	5.647
FE3+	*	0.016 *	0.017 *	0.032 *	0.011 *	0.007 *	0.067 *	0.015
MG	*	0.005 *	0.0 *	0.0 *	0.0 *	0.003 *	0.005 *	0.0
CA	*	1.512 *	1.482 *	1.477 *	1.487 *	1.669 *	1.733 *	1.463
NA	*	2.396 *	2.617 *	2.628 *	2.566 *	2.569 *	2.899 *	2.599
K	*	0.021 *	0.009 *	0.011 *	0.009 *	0.005 *	0.005 *	0.012
SR	*	0.024 *	0.0 *	0.0 *	0.0 *	0.0 *	0.0 *	0.0
BA	*	0.001 *	0.0 *	0.0 *	0.0 *	0.0 *	0.0 *	0.0

OR	*	0.52 *	0.22 *	0.28 *	0.22 *	0.11 *	0.10 *	0.28
AB	*	61.00 *	63.70 *	63.84 *	63.18 *	60.55 *	62.52 *	63.80
AN	*	38.48 *	36.08 *	35.88 *	36.60 *	39.34 *	37.38 *	35.92

1 *	131-2	FD-4	
2 *	080-2	FD-1	MATRIX
3 *	080-2	FD-2	LARGE ALTERED AVERAGE OF CLEAR AND CLOUDTY PATCHES
4 *	080-3	FD-3	MATRIX
5 *	130-1	FD-1	FRESH
6 *	130-1	FD-2	ALTERED
7 *	136-2	FD-1	

	*	1 *	2 *	3 *	4 *	5 *	6 *	7
SiO2	*	64.29 *	65.43 *	65.58 *	63.38 *	58.53 *	58.89 *	59.05
AL2O3	*	18.75 *	18.66 *	18.89 *	19.12 *	26.57 *	26.09 *	26.21
FE2O3	*	0.08 *	0.07 *	0.07 *	0.19 *	0.15 *	0.15 *	0.14
MGO	*	0.0 *	0.0 *	0.0 *	0.0 *	0.0 *	0.0 *	0.0
CAO	*	0.0 *	0.0 *	0.0 *	0.02 *	7.43 *	6.81 *	7.03
NA2O	*	0.95 *	0.98 *	1.19 *	0.96 *	7.68 *	7.93 *	7.89
K2O	*	15.48 *	15.46 *	15.04 *	15.56 *	0.24 *	0.25 *	0.30
SRO	*	0.0 *	0.0 *	0.0 *	0.0 *	0.0 *	0.0 *	0.0
BAO	*	0.0 *	0.0 *	0.0 *	0.0 *	0.0 *	0.0 *	0.0
TOTAL	*	99.55 *	100.60 *	100.77 *	99.23 *	100.60 *	100.12 *	100.62

SI	*	11.917 *	11.981 *	11.965 *	11.814 *	10.418 *	10.514 *	10.498
AL	*	4.098 *	4.029 *	4.064 *	4.202 *	5.576 *	5.492 *	5.494
FE3+	*	0.011 *	0.010 *	0.010 *	0.027 *	0.020 *	0.020 *	0.019
MG	*	0.0 *	0.0 *	0.0 *	0.0 *	0.0 *	0.0 *	0.0
CA	*	0.0 *	0.0 *	0.0 *	0.004 *	1.417 *	1.303 *	1.339
NA	*	0.341 *	0.348 *	0.421 *	0.347 *	2.651 *	2.745 *	2.720
K	*	3.661 *	3.612 *	3.501 *	3.701 *	0.055 *	0.057 *	0.068
SR	*	0.0 *	0.0 *	0.0 *	0.0 *	0.0 *	0.0 *	0.0
BA	*	0.0 *	0.0 *	0.0 *	0.0 *	0.0 *	0.0 *	0.0
OR	*	91.47 *	91.21 *	89.27 *	91.34 *	1.32 *	1.39 *	1.65
AB	*	8.53 *	8.79 *	10.73 *	8.56 *	64.30 *	66.88 *	65.90
AN	*	0.0 *	0.0 *	0.0 *	0.10 *	34.38 *	31.74 *	32.45

1 *	451-4	KSP-1
2 *	451-3	KSP-2
3 *	451-2	KSP-3
4 *	451-1	KSP-4
5 *	451-1	PLAG-1
6 *	451-2	PLAG-2
7 *	451-3	PLAG-3

	*	1 *	2 *	3 *	4 *	5 *
SiO2	*	58.27 *	56.86 *	53.20 *	65.42 *	67.21 *
Al2O3	*	26.55 *	26.79 *	26.45 *	20.95 *	20.07 *
Fe2O3	*	0.12 *	0.53 *	0.55 *	0.13 *	0.10 *
MgO	*	0.0 *	0.0 *	0.02 *	0.0 *	0.0 *
CaO	*	7.41 *	7.24 *	12.86 *	0.69 *	0.74 *
Na2O	*	7.54 *	7.04 *	5.71 *	11.58 *	11.76 *
K2O	*	0.23 *	0.89 *	0.01 *	0.15 *	0.09 *
SR	*	0.0 *	0.0 *	0.0 *	0.0 *	0.0 *
BA	*	0.0 *	0.0 *	0.0 *	0.0 *	0.0 *
TOTAL	*	100.12 *	99.35 *	98.80 *	98.92 *	99.97 *

SI	*	10.415 *	10.288 *	9.829 *	11.624 *	11.799 *
AL	*	5.595 *	5.716 *	5.762 *	4.389 *	4.154 *
FE3+	*	0.016 *	0.072 *	0.076 *	0.017 *	0.013 *
MG	*	0.0 *	0.0 *	0.006 *	0.0 *	0.0 *
CA	*	1.419 *	1.404 *	2.546 *	0.131 *	0.139 *
NA	*	2.613 *	2.470 *	2.046 *	3.990 *	4.003 *
K	*	0.052 *	0.205 *	0.002 *	0.034 *	0.020 *
SR	*	0.0 *	0.0 *	0.0 *	0.0 *	0.0 *
BA	*	0.0 *	0.0 *	0.0 *	0.0 *	0.0 *
OR	*	1.28 *	5.04 *	0.05 *	0.82 *	0.48 *
AB	*	63.97 *	60.55 *	44.53 *	96.02 *	96.17 *
AN	*	34.74 *	34.41 *	55.42 *	3.16 *	3.34 *

1 *	451-4	PLAG-4
2 *	458-3	FD-1 ALTERED
3 *	128-1	FD-1 HIGHLY ALTERED
4 *	504-3	FD-1 ALTERED
5 *	504-3	FD-2 ALTERED

	*	1 *	2 *	3 *	4 *	5 *	6 *	7
SIO2	*	62.19 *	62.39 *	58.81 *	66.24 *	65.59 *	64.02 *	63.80
AL2O3	*	24.51 *	25.01 *	25.31 *	21.09 *	21.09 *	22.25 *	23.01
FE2O3	*	0.27 *	0.12 *	0.01 *	0.0 *	0.0 *	0.06 *	0.03
MGO	*	0.06 *	0.05 *	0.0 *	0.0 *	0.0 *	0.0 *	0.0
CAO	*	0.79 *	0.90 *	7.79 *	0.68 *	0.96 *	2.61 *	3.09
NA2O	*	8.98 *	8.87 *	7.61 *	11.42 *	11.04 *	10.25 *	9.95
K2O	*	1.58 *	2.20 *	0.10 *	0.04 *	0.09 *	0.04 *	0.05
SRO	*	0.27 *	0.17 *	0.38 *	0.25 *	0.61 *	0.48 *	0.0
BAO	*	0.0 *	0.0 *	0.0 *	0.0 *	0.0 *	0.0 *	0.0
TOTAL	*	98.65 *	99.71 *	100.01 *	99.72 *	99.38 *	99.71 *	99.93

SI	*	11.127 *	11.073 *	10.549 *	11.660 *	11.620 *	11.350 *	11.260
AL	*	5.171 *	5.234 *	5.353 *	***** *	4.406 *	4.651 *	4.788
FE3+	*	0.036 *	0.016 *	0.001 *	***** *	0.0 *	0.008 *	0.004
MG	*	0.016 *	0.013 *	0.0 *	0.0 *	0.0 *	0.0 *	0.0
CA	*	0.151 *	0.171 *	1.497 *	0.128 *	0.182 *	0.496 *	0.584
NA	*	3.116 *	3.053 *	2.647 *	3.899 *	3.793 *	3.524 *	3.405
K	*	0.361 *	0.498 *	0.023 *	0.009 *	0.020 *	0.009 *	0.011
SR	*	0.028 *	0.017 *	0.040 *	0.026 *	0.063 *	0.049 *	0.0
BA	*	0.0 *	0.0 *	0.0 *	0.0 *	0.0 *	0.0 *	0.0
DR	*	9.94 *	13.38 *	0.55 *	0.22 *	0.51 *	0.22 *	0.28
AB	*	85.88 *	82.02 *	63.52 *	96.60 *	94.93 *	87.47 *	85.11
AN	*	4.18 *	4.60 *	35.93 *	3.18 *	4.56 *	12.31 *	14.61

1 *	486-1	FD-1	ALTERED
2 *	486-1	FD-2	ALTERED
3 *	486-1	FD-3	
4 *	487-3	FD-1	
5 *	487-3	FD-2	
6 *	489-1	FD-1	
7 *	489-2	FD-2	

	*	1 *	2 *	3 *	4 *	5 *	6 *	7
SiO2	*	56.26 *	55.99 *	55.98 *	55.52 *	56.59 *	56.52 *	53.00
Al2O3	*	28.07 *	28.24 *	28.38 *	27.91 *	28.65 *	29.59 *	30.01
Fe2O3	*	0.22 *	0.15 *	0.09 *	0.14 *	0.23 *	0.13 *	0.09
MgO	*	0.0 *	0.0 *	0.0 *	0.0 *	0.0 *	0.0 *	0.0
CaO	*	9.20 *	9.41 *	10.15 *	9.50 *	9.09 *	9.68 *	9.73
Na2O	*	6.76 *	6.58 *	6.33 *	6.52 *	6.50 *	6.10 *	7.00
K2O	*	0.0 *	0.0 *	0.01 *	0.0 *	0.01 *	0.01 *	0.14
SR	*	0.0 *	0.0 *	0.0 *	0.0 *	0.0 *	0.0 *	0.0
BA	*	0.0 *	0.0 *	0.0 *	0.0 *	0.0 *	0.0 *	0.0
TOTAL	*	100.51 *	100.37 *	100.94 *	99.59 *	101.07 *	102.03 *	99.97

SI	*	10.067 *	10.034 *	9.992 *	10.034 *	10.048 *	9.944 *	9.610
AL	*	5.923 *	5.967 *	5.973 *	5.947 *	5.998 *	6.138 *	6.416
FE3+	*	0.030 *	0.020 *	0.012 *	0.019 *	0.031 *	0.017 *	0.012
MG	*	0.0 *	0.0 *	0.0 *	0.0 *	0.0 *	0.0 *	0.0
CA	*	1.764 *	1.807 *	1.942 *	1.840 *	1.730 *	1.825 *	1.891
NA	*	2.346 *	2.287 *	2.191 *	2.285 *	2.238 *	2.081 *	2.461
K	*	0.0 *	0.0 *	0.002 *	0.0 *	0.002 *	0.002 *	0.032
SR	*	0.0 *	0.0 *	0.0 *	0.0 *	0.0 *	0.0 *	0.0
BA	*	0.0 *	0.0 *	0.0 *	0.0 *	0.0 *	0.0 *	0.0

OR	*	0.0 *	0.0 *	0.06 *	0.0 *	0.06 *	0.06 *	0.74
AB	*	57.07 *	55.86 *	52.99 *	55.40 *	56.38 *	53.25 *	56.14
AN	*	42.93 *	44.14 *	46.96 *	44.60 *	43.57 *	46.70 *	43.12

1 *	498-1	FD-1	LAMELLAE IN CPX-1
2 *	498-1	FD-2	LAMELLAE IN CPX-2
3 *	498-1	FD-3	CORE MATRIX
4 *	498-1	FD-3	RIM MATRIX
5 *	498-1	PL-1	ESTIMATE LAMELLAE IN OPX
6 *	498-1	PL-2	ESTIMATE MATRIX
7 *	509-4	FD-1	ALTERED

	*	1	*	2	*
SI02	*	53.37	*	54.36	*
AL2O3	*	29.43	*	31.02	*
FE2O3	*	0.20	*	0.19	*
MGO	*	0.0	*	0.0	*
CAO	*	11.12	*	10.95	*
NA2O	*	5.46	*	5.44	*
K2O	*	0.01	*	0.0	*
SRO	*	0.0	*	0.0	*
BAO	*	0.0	*	0.0	*
TOTAL	*	99.59	*	101.96	*

SI	*	9.691	*	9.618	*
AL	*	6.301	*	6.472	*
FE3+	*	0.027	*	0.025	*
MG	*	0.0	*	0.0	*
CA	*	2.164	*	2.076	*
NA	*	1.923	*	1.867	*
K	*	0.002	*	0.0	*
SR	*	0.0	*	0.0	*
BA	*	0.0	*	0.0	*

OR	*	0.06	*	0.0	*
AB	*	47.02	*	47.34	*
AN	*	52.92	*	52.66	*

1 *	G12-4	FD-1	IN SPINEL
2 *	G12-4	PL-1	ESTIMATE

Table II.iv. Olivine analyses, structural formulae, and end members.

SiO2	*	39.78	*	39.45	*	41.21	*
FeO	*	12.24	*	12.27	*	10.81	*
MnO	*	0.13	*	0.14	*	0.08	*
MgO	*	48.09	*	48.17	*	50.20	*
CaO	*	0.02	*	0.02	*	0.0	*
NiO	*	0.26	*	0.21	*	0.34	*
Cr2O3	*	0.02	*	0.02	*	0.0	*
TOTAL	*	100.54	*	100.28	*	102.64	*

SI	*	0.983	*	0.978	*	0.989	*
FE	*	0.253	*	0.254	*	0.217	*
MN	*	0.003	*	0.003	*	0.002	*
MG	*	1.771	*	1.780	*	1.796	*
CA	*	0.001	*	0.001	*	0.0	*
NI	*	0.005	*	0.004	*	0.007	*
CR	*	0.0	*	0.0	*	0.0	*

FO	*	87.42	*	87.39	*	89.18	*
FA	*	12.58	*	12.61	*	10.82	*

1	*	412-1	OL-1
2	*	412-2	OL-2
3	*	401-2	OL-1 ESTIMATE

SiO2	*	33.09	*	41.92	*	41.52	*	39.75	*	40.35	*	41.10	*	40.21
FeO	*	51.49	*	11.27	*	10.14	*	10.70	*	10.26	*	10.77	*	10.62
MnO	*	0.45	*	0.14	*	0.14	*	0.10	*	0.12	*	0.11	*	0.10
MgO	*	15.25	*	48.76	*	49.11	*	47.99	*	48.50	*	50.28	*	48.69
CaO	*	0.0	*	0.0	*	0.01	*	0.02	*	0.03	*	0.04	*	0.02
NiO	*	0.07	*	0.37	*	0.37	*	0.29	*	0.39	*	0.44	*	0.33
Cr2O3	*	0.04	*	0.0	*	0.01	*	0.02	*	0.03	*	0.03	*	0.01
TOTAL	*	100.39	*	102.46	*	101.30	*	98.87	*	99.68	*	102.77	*	99.98

SI	*	0.0	*	1.008	*	1.005	*	0.992	*	0.995	*	0.986	*	0.991
FE	*	0.0	*	0.227	*	0.205	*	0.223	*	0.212	*	0.216	*	0.219
MN	*	0.0	*	0.003	*	0.003	*	0.002	*	0.003	*	0.002	*	0.002
MG	*	0.0	*	1.747	*	1.773	*	1.784	*	1.782	*	1.798	*	1.789
CA	*	0.0	*	0.0	*	0.0	*	0.001	*	0.001	*	0.001	*	0.001
NI	*	0.0	*	0.007	*	0.007	*	0.006	*	0.008	*	0.008	*	0.007
CR	*	0.0	*	0.0	*	0.0	*	0.0	*	0.001	*	0.001	*	0.0

FO	*	0.0	*	88.43	*	89.53	*	88.82	*	89.32	*	89.22	*	89.04
FA	*	0.0	*	11.57	*	10.47	*	11.18	*	10.68	*	10.78	*	10.96

1	*	651-2	OL-1	
2	*	124-1	OL-1	ESTIMATE
3	*	124-2	OL-2	ESTIMATE
4	*	124-3	OL-3	
5	*	493-3	OL-1	ESTIMATE IN CPX
6	*	498-2	OL-1	ESTIMATE IN OPX
7	*	498-1	OL-2	ESTIMATE

SiO2	*	40.31	*	39.94	*	41.11	*
FeO	*	10.18	*	10.50	*	11.91	*
MnO	*	0.09	*	0.13	*	0.11	*
MgO	*	49.51	*	49.21	*	49.82	*
CaO	*	0.01	*	0.02	*	0.0	*
NiO	*	0.37	*	0.42	*	0.43	*
Cr2O3	*	0.01	*	0.02	*	0.01	*
TOTAL	*	100.48	*	100.24	*	103.39	*

SI	*	0.987	*	0.983	*	0.985	*
FE	*	0.208	*	0.216	*	0.239	*
MN	*	0.002	*	0.003	*	0.002	*
MG	*	1.807	*	1.805	*	1.780	*
CA	*	0.0	*	0.001	*	0.0	*
NI	*	0.007	*	0.008	*	0.008	*
CR	*	0.0	*	0.0	*	0.0	*

FO	*	89.61	*	89.23	*	88.12	*
FA	*	10.39	*	10.77	*	11.88	*

1 *	498-1	OL-3	ESTIMATE
2 *	509-1	OL-1	IN DEFORMED CPX
3 *	2662-5	OL-1	ESTIMATE

Table II.v. Epidote analyses and structural formulae.

SiO2	*	37.72	*	38.49	*	36.55	*	37.45	*	37.54	*	38.11	*	38.00
AL2O3	*	23.34	*	25.70	*	23.78	*	23.78	*	25.21	*	23.11	*	23.82
FE2O3	*	12.66	*	8.56	*	13.09	*	13.03	*	10.64	*	14.19	*	13.20
FeO	*	0.58	*	0.94	*	0.0	*	0.0	*	0.0	*	0.0	*	0.0
MNO	*	0.27	*	0.11	*	0.15	*	0.13	*	0.14	*	0.11	*	0.12
MGO	*	0.06	*	0.02	*	0.04	*	0.02	*	0.01	*	0.04	*	0.05
CAO	*	22.77	*	23.23	*	23.19	*	23.21	*	23.60	*	23.14	*	23.21
NA2O	*	0.03	*	0.02	*	0.03	*	0.03	*	0.04	*	0.0	*	0.0
TOTAL	*	97.43	*	97.07	*	96.83	*	97.65	*	97.18	*	98.70	*	98.40

SI	*	3.010	*	3.046	*	2.936	*	2.984	*	2.980	*	3.016	*	3.004
AL	*	2.196	*	2.398	*	2.252	*	2.233	*	2.359	*	2.156	*	2.220
FE3+	*	0.760	*	0.510	*	0.792	*	0.782	*	0.637	*	0.846	*	0.786
FE2+	*	0.038	*	0.062	*	0.0	*	0.0	*	0.0	*	0.0	*	0.0
MN	*	0.018	*	0.007	*	0.010	*	0.0	*	0.009	*	0.007	*	0.008
MG	*	0.007	*	0.002	*	0.005	*	*****	*	0.001	*	0.005	*	0.006
CA	*	1.947	*	1.970	*	1.996	*	*****	*	2.007	*	1.962	*	1.966
NA	*	0.005	*	0.003	*	0.005	*	*****	*	0.006	*	0.0	*	0.0

1	*	033-1	EP-1
2	*	033-2	EP-2
3	*	033-2	EP-3
4	*	033-3	EP-4
5	*	033-3	EP-5
6	*	086-1	EP-1
7	*	086-2	EP-2

SiO2	*	37.26	*	38.02	*	37.86	*	37.71	*	37.52	*	37.84	*	38.13
AL2O3	*	23.48	*	24.13	*	23.88	*	23.09	*	23.26	*	23.32	*	23.89
FE2O3	*	14.24	*	10.95	*	13.62	*	13.44	*	13.75	*	13.95	*	13.59
FE0	*	0.0	*	1.34	*	0.33	*	0.55	*	0.0	*	0.45	*	0.13
MNO	*	0.08	*	0.14	*	0.14	*	0.14	*	0.11	*	0.18	*	0.14
MGO	*	0.04	*	0.10	*	0.04	*	0.04	*	0.04	*	0.06	*	0.05
CAO	*	23.03	*	22.54	*	23.15	*	22.96	*	23.41	*	22.98	*	23.50
NA2O	*	0.0	*	0.0	*	0.0	*	0.0	*	0.0	*	0.0	*	0.0
TOTAL	*	98.13	*	97.22	*	99.02	*	97.93	*	98.09	*	98.78	*	99.43

SI	*	2.963	*	3.030	*	2.981	*	3.006	*	2.983	*	2.992	*	2.987
AL	*	2.201	*	2.267	*	2.216	*	2.170	*	2.180	*	2.174	*	2.206
FE3+	*	0.853	*	0.657	*	0.807	*	0.806	*	0.824	*	0.830	*	0.801
FE2+	*	0.0	*	0.089	*	0.021	*	0.037	*	0.0	*	0.029	*	0.009
MN	*	0.005	*	0.009	*	0.009	*	0.009	*	0.007	*	0.012	*	0.009
MG	*	0.005	*	0.012	*	0.005	*	0.005	*	0.005	*	0.007	*	0.006
CA	*	1.962	*	1.925	*	1.953	*	1.961	*	1.995	*	1.947	*	1.973
NA	*	0.0	*	0.0	*	0.0	*	0.0	*	0.0	*	0.0	*	0.0

1 * 086-3 EP-3
 2 * 087-1 EP-1
 3 * 087-2 EP-2
 4 * 089-1 EP-1
 5 * 089-2 EP-2
 6 * 090-1 EP-1
 7 * 090-2 EP-2

SI02	*	38.35	*	37.79	*	37.23	*	37.68	*	37.06	*	37.70	*	38.40
AL203	*	23.20	*	24.59	*	23.45	*	25.55	*	22.53	*	22.97	*	25.99
FE203	*	12.95	*	11.67	*	12.49	*	12.13	*	13.71	*	13.43	*	10.22
FEO	*	1.00	*	0.22	*	0.0	*	0.0	*	0.0	*	0.20	*	0.13
MNO	*	0.20	*	0.10	*	0.08	*	0.0	*	0.45	*	0.18	*	0.0
MGO	*	0.04	*	0.04	*	0.06	*	0.0	*	0.04	*	0.05	*	0.0
CAO	*	23.05	*	23.13	*	23.02	*	23.79	*	22.61	*	23.10	*	23.59
NA2O	*	0.0	*	0.03	*	0.04	*	0.03	*	0.04	*	0.03	*	0.06
TOTAL	*	98.79	*	97.57	*	96.37	*	99.18	*	96.44	*	97.66	*	98.39

SI	*	3.029	*	3.000	*	2.997	*	2.941	*	3.002	*	3.011	*	3.005
AL	*	2.160	*	2.301	*	2.226	*	2.351	*	2.151	*	2.163	*	2.398
FE3+	*	0.769	*	0.697	*	0.757	*	0.736	*	0.837	*	0.807	*	0.602
FE2+	*	0.066	*	0.015	*	0.0	*	0.0	*	0.0	*	0.013	*	0.009
MN	*	0.013	*	0.007	*	0.005	*	0.0	*	0.031	*	0.012	*	0.0
MG	*	0.005	*	0.005	*	0.007	*	0.0	*	0.005	*	0.006	*	0.0
CA	*	1.951	*	1.967	*	1.986	*	1.990	*	1.962	*	1.977	*	1.978
NA	*	0.0	*	0.005	*	0.006	*	0.005	*	0.006	*	0.005	*	0.009

1	*	090-3	EP-3
2	*	112-1	EP-1
3	*	112-2	EP-2
4	*	114-3	EP-1
5	*	133-1	EP-1
6	*	133-2	EP-2
7	*	236-1	EP-1

Table II.vi. Chlorite analyses and structural formulae.

SI22	*	26.87	*	27.48	*	27.22	*	26.90	*	27.64	*	25.75	*	26.02
TI22	*	0.02	*	0.05	*	0.07	*	0.01	*	0.05	*	0.02	*	0.04
AL273	*	20.59	*	21.75	*	22.13	*	21.70	*	22.91	*	19.91	*	21.15
CF203	*	1.61	*	0.07	*	0.07	*	0.01	*	0.07	*	0.0	*	0.13
FE0	*	11.78	*	18.46	*	17.64	*	20.04	*	16.77	*	24.73	*	18.09
MNO	*	0.11	*	0.19	*	0.16	*	0.22	*	0.16	*	0.15	*	0.17
AGE	*	23.39	*	21.18	*	21.15	*	18.93	*	21.22	*	15.96	*	19.82
CAF	*	0.02	*	0.07	*	0.06	*	0.01	*	0.02	*	0.0	*	0.09
NA27	*	0.01	*	0.03	*	0.03	*	0.0	*	0.0	*	0.05	*	0.03
K27	*	0.0	*	0.0	*	0.0	*	0.0	*	0.0	*	0.0	*	0.11
NI7	*	0.07	*	0.03	*	0.02	*	0.03	*	0.0	*	0.03	*	0.01
TOTAL	*	84.47	*	89.31	*	88.55	*	87.85	*	88.90	*	86.60	*	85.71

SI	*	5.492	*	5.462	*	5.433	*	5.482	*	5.457	*	5.467	*	5.408
AL(IV)	*	2.503	*	2.538	*	2.567	*	2.512	*	2.543	*	2.513	*	2.592
AL(VI)	*	2.454	*	2.559	*	2.640	*	2.719	*	2.789	*	2.489	*	2.590
CF	*	0.260	*	0.011	*	0.011	*	0.002	*	0.011	*	0.0	*	0.030
FE	*	2.014	*	3.060	*	2.945	*	3.431	*	2.769	*	4.407	*	3.144
MN	*	0.019	*	0.032	*	0.027	*	0.038	*	0.027	*	0.027	*	0.030
MG	*	7.125	*	6.274	*	6.291	*	5.749	*	6.244	*	5.068	*	6.139
CA	*	0.004	*	0.015	*	0.013	*	0.002	*	0.017	*	0.0	*	0.020
NA	*	0.004	*	0.012	*	0.012	*	0.0	*	0.0	*	0.021	*	0.012
K	*	0.0	*	0.0	*	0.0	*	0.0	*	0.0	*	0.0	*	0.029
NI	*	0.012	*	0.005	*	0.003	*	0.005	*	0.0	*	0.005	*	0.002

1 * 033-1 CHL-1
 2 * 114-2 CHL-1
 3 * 114-1 CHL-2
 4 * 236-2 CHL-1
 5 * 236-1 CHL-2
 6 * 435-1 CHL-1
 7 * 530-1 CHL-1

Table II.vii. Mica analyses and structural formulae.

	*	1 *	2 *	3 *	4 *	5 *	6 *	7
SiO2	*	36.50 *	37.45 *	37.41 *	37.66 *	36.80 *	35.80 *	36.49
TiO2	*	1.57 *	1.19 *	1.31 *	1.46 *	1.31 *	2.43 *	2.34
Al2O3	*	19.53 *	18.07 *	19.01 *	19.17 *	19.24 *	18.72 *	19.29
CR2O3	*	0.12 *	0.02 *	0.05 *	0.04 *	0.07 *	0.0 *	0.0
FeO	*	18.58 *	19.63 *	19.68 *	19.10 *	19.79 *	23.89 *	24.43
MnO	*	0.11 *	0.21 *	0.16 *	0.19 *	0.19 *	0.10 *	0.09
MgO	*	11.80 *	11.05 *	11.14 *	11.34 *	11.56 *	7.37 *	7.65
CaO	*	0.06 *	0.11 *	0.17 *	0.06 *	0.05 *	0.0 *	0.02
Na2O	*	0.14 *	0.05 *	0.07 *	0.08 *	0.07 *	0.14 *	0.15
K2O	*	8.20 *	7.99 *	8.43 *	8.54 *	8.14 *	6.04 *	6.10
NiO	*	0.0 *	0.0 *	0.0 *	0.0 *	0.0 *	0.0 *	0.0
TOTAL	*	96.61 *	95.77 *	97.43 *	97.64 *	97.22 *	94.49 *	96.56

Si	*	5.401 *	5.605 *	5.512 *	5.520 *	5.436 *	5.492 *	5.476
Al(IV)	*	2.599 *	2.395 *	2.488 *	2.480 *	2.564 *	2.508 *	2.524
Al(VI)	*	0.808 *	0.793 *	0.814 *	0.833 *	0.786 *	0.877 *	0.889
Ti	*	0.175 *	0.134 *	0.145 *	0.161 *	0.146 *	0.280 *	0.264
Cr	*	0.014 *	0.002 *	0.006 *	0.005 *	0.008 *	0.0 *	0.0
Fe	*	2.299 *	2.457 *	2.425 *	2.341 *	2.521 *	3.065 *	3.066
Mn	*	0.014 *	0.027 *	0.020 *	0.024 *	0.025 *	0.013 *	0.011
Mg	*	2.602 *	2.465 *	2.446 *	2.477 *	2.624 *	1.689 *	1.715
Ni	*	0.0 *	0.0 *	0.0 *	0.0 *	0.0 *	0.0 *	0.0
Ca	*	0.010 *	0.018 *	0.027 *	0.009 *	0.008 *	0.0 *	0.003
Na	*	0.040 *	0.015 *	0.020 *	0.023 *	0.021 *	0.042 *	0.044
K	*	1.548 *	1.526 *	1.585 *	1.597 *	1.582 *	1.182 *	1.168

1 *	083-1-2	BT-1	WITH GARNET
2 *	477-2	BT-2	GROUNDMASS
3 *	477-1-2	BT-1	WITH HORNBLENDE
4 *	477-1-2	BT-2	ADJACENT TO GARNET
5 *	477-1-2	BT-3	GROUNDMASS
6 *	131-1	BT-1	GROUNDMASS
7 *	131-1	BT-2	GROUNDMASS

	*	1 *	2 *	3 *	4 *	5 *	6 *	7
SiO2	*	36.27 *	36.54 *	36.54 *	36.21 *	36.19 *	36.43 *	36.21
TiO2	*	4.41 *	2.61 *	3.21 *	2.93 *	2.67 *	2.46 *	2.50
Al2O3	*	14.50 *	17.85 *	17.62 *	18.35 *	19.10 *	18.43 *	19.41
CR2O3	*	***** *	0.0 *	0.0 *	0.0 *	0.0 *	0.0 *	0.0
FeO	*	23.60 *	23.52 *	23.46 *	23.10 *	24.90 *	24.00 *	24.25
MnO	*	0.0 *	0.08 *	0.07 *	0.09 *	0.10 *	0.10 *	0.07
MgO	*	***** *	8.20 *	7.76 *	7.62 *	6.80 *	7.18 *	6.77
CaO	*	***** *	0.02 *	0.01 *	0.02 *	0.04 *	0.0 *	0.09
Na2O	*	***** *	0.12 *	0.17 *	0.06 *	0.09 *	0.08 *	0.13
K2O	*	***** *	6.13 *	5.70 *	7.36 *	6.37 *	7.55 *	7.25
NiO	*	0.0 *	0.0 *	0.0 *	0.0 *	0.0 *	0.0 *	0.0
TOTAL	*	***** *	95.07 *	94.54 *	95.74 *	96.26 *	96.23 *	96.68

SI	*	5.682 *	5.559 *	5.830 *	5.500 *	5.475 *	5.530 *	5.464
AL(IV)	*	2.318 *	2.441 *	2.170 *	2.500 *	2.525 *	2.470 *	2.536
AL(VI)	*	0.364 *	0.761 *	1.144 *	0.786 *	0.881 *	0.828 *	0.917
TI	*	0.520 *	0.299 *	0.385 *	0.335 *	0.304 *	0.281 *	0.284
CR	*	0.0 *	0.0 *	0.0 *	0.0 *	0.0 *	0.0 *	0.0
FE	*	3.092 *	2.993 *	3.131 *	2.935 *	3.150 *	3.047 *	3.060
MN	*	0.012 *	0.010 *	0.009 *	0.012 *	0.013 *	0.013 *	0.009
MG	*	1.706 *	1.863 *	1.849 *	1.729 *	1.536 *	1.628 *	1.526
NI	*	0.0 *	0.0 *	0.0 *	0.0 *	0.0 *	0.0 *	0.0
CA	*	0.007 *	0.003 *	0.002 *	0.003 *	0.006 *	0.0 *	0.015
NA	*	0.036 *	0.035 *	0.053 *	0.018 *	0.026 *	0.024 *	0.038
K	*	1.479 *	1.190 *	1.160 *	1.426 *	1.229 *	1.462 *	1.396

1 *	131-1	BT-3	IN PLAG
2 *	131-2	BT-4	IN GARNET
3 *	131-2	BT-5	GROUNDMASS
4 *	131-2	BT-6	GROUNDMASS
5 *	131-3	BT-8	RIM IN GARNET
6 *	131-3	BT-9	CORE IN GARNET
7 *	131-3	BT-10	GROUNDMASS

	*	1	*	2	*	3	*	4	*
SI02	*	35.71	*	35.57	*	35.63	*	34.93	*
TI02	*	2.29	*	2.47	*	3.34	*	2.80	*
AL203	*	17.70	*	18.41	*	17.23	*	17.10	*
CR203	*	0.0	*	0.05	*	0.04	*	0.04	*
FE0	*	22.64	*	24.22	*	25.98	*	26.56	*
MNO	*	0.06	*	0.04	*	0.24	*	0.21	*
MGO	*	8.29	*	8.39	*	6.68	*	6.61	*
CA0	*	0.0	*	0.06	*	0.05	*	0.05	*
NA20	*	0.09	*	0.10	*	0.06	*	0.04	*
K20	*	8.47	*	8.76	*	8.65	*	8.52	*
NIO	*	0.0	*	0.0	*	0.06	*	0.08	*
TOTAL	*	95.25	*	98.07	*	97.96	*	96.94	*

SI	*	5.494	*	5.359	*	5.429	*	5.404	*
AL(IV)	*	2.506	*	2.641	*	2.571	*	2.596	*
AL(VI)	*	0.704	*	0.629	*	0.525	*	0.523	*
TI	*	0.265	*	0.280	*	0.383	*	0.326	*
CR	*	0.0	*	0.006	*	0.005	*	0.005	*
FE	*	2.913	*	3.052	*	3.311	*	3.437	*
MN	*	0.008	*	0.005	*	0.031	*	0.028	*
MG	*	1.901	*	1.884	*	1.517	*	1.524	*
NI	*	0.0	*	0.0	*	0.007	*	0.010	*
CA	*	0.0	*	0.010	*	0.008	*	0.008	*
NA	*	0.027	*	0.029	*	0.018	*	0.012	*
K	*	1.663	*	1.684	*	1.682	*	1.682	*

1	*	2-131-1	BT-1	
2	*	3-131-2	BT-1	
3	*	451-1	BT-1	SEVERAL SMALL GRAINS
4	*	451-1	BT-2	SEVERAL SMALL GRAINS

	*	1 *	2 *	3 *	4 *	5 *	6 *	7
SiO2	*	33.41 *	33.37 *	33.17 *	33.39 *	33.41 *	35.23 *	38.46
TiO2	*	8.37 *	8.92 *	7.70 *	8.18 *	8.85 *	6.70 *	4.63
Al2O3	*	16.00 *	16.04 *	15.97 *	16.07 *	16.27 *	13.10 *	17.74
CR2O3	*	0.0 *	0.0 *	0.0 *	0.0 *	0.0 *	0.02 *	0.53
FeO	*	17.51 *	17.95 *	17.08 *	20.06 *	19.10 *	26.14 *	5.49
MnO	*	0.20 *	0.16 *	0.21 *	0.22 *	0.20 *	0.03 *	0.01
MgO	*	6.51 *	6.70 *	6.52 *	6.38 *	5.72 *	7.20 *	21.43
CaO	*	0.0 *	0.0 *	0.03 *	0.0 *	0.0 *	0.0 *	0.05
Na2O	*	0.35 *	0.35 *	0.30 *	0.36 *	0.39 *	0.32 *	0.84
K2O	*	7.98 *	7.89 *	7.88 *	7.12 *	7.98 *	8.14 *	8.34
NiO	*	0.0 *	0.0 *	0.0 *	0.0 *	0.0 *	0.0 *	0.15
TOTAL	*	90.33 *	91.38 *	88.86 *	91.78 *	91.92 *	96.88 *	97.67

Si	*	5.097 *	5.083 *	5.072 *	5.129 *	5.146 *	0.0 *	5.330
Al(IV)	*	2.878 *	2.881 *	2.879 *	2.871 *	2.854 *	0.0 *	2.670
Al(VI)	*	0.0 *	0.0 *	0.0 *	0.039 *	0.102 *	0.0 *	0.229
Ti	*	0.961 *	1.022 *	0.886 *	0.945 *	1.025 *	0.0 *	0.483
Cr	*	0.0 *	0.0 *	0.0 *	0.0 *	0.0 *	0.0 *	0.058
Fe	*	2.900 *	2.834 *	3.018 *	3.023 *	2.848 *	0.0 *	0.636
Mn	*	0.026 *	0.021 *	0.027 *	0.029 *	0.026 *	0.0 *	0.001
Mg	*	1.480 *	1.521 *	1.486 *	1.461 *	1.313 *	0.0 *	4.427
Ni	*	0.0 *	0.0 *	0.0 *	0.0 *	0.0 *	0.0 *	0.017
Ca	*	0.0 *	0.0 *	0.005 *	0.0 *	0.0 *	0.0 *	0.007
Na	*	0.104 *	0.103 *	0.089 *	0.107 *	0.116 *	0.0 *	0.226
K	*	1.554 *	1.534 *	1.537 *	1.395 *	1.568 *	0.0 *	1.475

1 * 491-1 BT-1
 2 * 491-1 BT-2
 3 * 491-1 BT-3
 4 * 491-2 BT-4
 5 * 491-3 BT-5
 6 * 651-1 BT-1 IN ZIRCON
 7 * 662-2 MICA-1 FLAKES IN AMPHIBOLE

Table II.viii. Oxide analyses, structural formulae, and end members.

	*	1 *	2 *	3 *	4 *	5 *	6 *	7
SI02	*	0.36 *	0.24 *	0.38 *	0.32 *	0.33 *	0.20 *	0.18
TI02	*	0.01 *	0.51 *	0.45 *	0.07 *	0.08 *	0.12 *	0.04
AL203	*	68.47 *	19.41 *	25.80 *	54.27 *	54.64 *	56.57 *	63.96
CR203	*	0.02 *	44.27 *	41.89 *	12.92 *	12.81 *	11.80 *	2.63
FE203	*	0.0 *	3.15 *	0.0 *	0.83 *	0.17 *	0.0 *	0.11
FEO	*	12.48 *	21.94 *	20.79 *	13.48 *	13.47 *	12.59 *	12.71
MNO	*	0.09 *	0.26 *	0.25 *	0.09 *	0.09 *	0.09 *	0.09
MGO	*	17.47 *	8.55 *	9.15 *	17.98 *	17.95 *	17.78 *	19.10
CAO	*	0.04 *	0.03 *	0.03 *	0.0 *	0.01 *	0.01 *	0.03
TOTAL	*	98.94 *	98.37 *	98.74 *	99.96 *	99.55 *	99.16 *	98.85

SI	*	0.073 *	0.062 *	0.095 *	0.140 *	0.160 *	0.042 *	0.037
TI	*	0.006 *	0.100 *	0.085 *	13.610 *	13.520 *	0.019 *	0.006
AL	*	16.304 *	5.958 *	7.609 *	0.0 *	0.0 *	14.068 *	15.471
CR	*	0.003 *	9.097 *	8.270 *	71.550 *	71.570 *	1.964 *	0.426
FE3+	*	0.0 *	0.620 *	0.0 *	13.870 *	14.600 *	0.0 *	0.018
FE2+	*	2.108 *	4.779 *	4.350 *	0.0 *	0.0 *	2.221 *	2.180
MN	*	0.015 *	0.057 *	0.053 *	0.830 *	0.150 *	0.016 *	0.016
MG	*	5.259 *	3.318 *	3.411 *	0.0 *	0.0 *	5.590 *	5.840
CA	*	0.009 *	0.008 *	0.008 *	0.0 *	0.0 *	0.002 *	0.007

UVSP	*	0.02 *	1.26 *	1.10 *	0.07 *	0.07 *	0.24 *	0.08
CHR	*	0.02 *	57.37 *	53.61 *	0.01 *	0.01 *	12.59 *	2.68
SP	*	71.42 *	37.57 *	44.23 *	2.16 *	2.14 *	71.63 *	73.40
HERC	*	28.54 *	0.0 *	1.06 *	0.13 *	0.03 *	15.54 *	23.82
MGFER	*	0.0 *	3.80 *	0.0 *	2.39 *	2.39 *	0.0 *	0.0
MT	*	0.0 *	0.0 *	0.0 *	0.02 *	0.02 *	0.0 *	0.03

1 *	132-1	SP-1F
2 *	401-3	CHR-1
3 *	412-2	CHR-1
4 *	124-2	SP-1
5 *	493-4	SP-1 RIMMED BY MT & CHL
6 *	0498-3	SP-1
7 *	509-2	GREEN SPINEL-1

	*	1 *	2 *	3 *	4 *	5 *	6 *	7
SI02	*	0.36 *	0.45 *	0.58 *	0.41 *	0.0 *	0.0 *	0.0
TI02	*	55.55 *	53.69 *	51.62 *	49.94 *	50.00 *	49.35 *	47.89
AL203	*	0.17 *	0.21 *	0.21 *	0.18 *	0.0 *	0.0 *	0.0
FE203	*	0.0 *	0.0 *	0.0 *	0.0 *	6.23 *	9.89 *	13.51
FEO	*	43.67 *	42.71 *	44.65 *	48.14 *	43.76 *	43.15 *	41.86
MNO	*	0.86 *	1.92 *	2.80 *	1.04 *	1.19 *	1.21 *	1.19
TOTAL	*	100.61 *	98.98 *	99.86 *	99.71 *	101.18 *	103.60 *	104.45
SI	*	0.018 *	0.022 *	0.030 *	0.020 *	0.0 *	0.0 *	0.0
AL	*	0.010 *	0.012 *	0.012 *	0.010 *	0.0 *	0.0 *	0.0
TI	*	2.056 *	2.026 *	1.948 *	1.890 *	1.883 *	1.818 *	1.753
FE3+	*	0.0 *	0.0 *	0.032 *	0.166 *	0.235 *	0.365 *	0.495
FE2+	*	1.798 *	1.792 *	1.840 *	1.860 *	1.832 *	1.767 *	1.704
MN	*	0.036 *	0.082 *	0.118 *	0.044 *	0.050 *	0.050 *	0.049
UVSP	*	0.0 *	0.0 *	0.0 *	0.0 *	0.0 *	0.0 *	0.0
MT	*	0.0 *	0.0 *	0.0 *	0.0 *	0.0 *	0.0 *	0.0
ILM	*	100.00 *	100.00 *	98.32 *	95.18 *	93.98 *	90.65 *	87.32
HM	*	0.0 *	0.0 *	1.68 *	4.82 *	6.02 *	9.35 *	12.86

1 *	130-3	ILM-1F
2 *	451-2	ILM-1F
3 *	458-1	ILM-2F
4 *	459-1	ILM-1F
5 *	552-6	ILM-1
6 *	552-6	ILM-2A
7 *	552-6	ILM-3A

	*	1	*	2	*	3	*	4	*	5	*	6	*	7
SI02	*	0.0	*	0.0	*	0.0	*	0.0	*	0.0	*	0.33	*	0.0
TI02	*	47.31	*	48.94	*	48.60	*	48.05	*	50.57	*	54.32	*	1.84
AL203	*	0.0	*	0.0	*	0.0	*	0.0	*	0.0	*	0.33	*	0.0
FE203	*	12.64	*	11.61	*	11.58	*	13.20	*	8.42	*	0.0	*	66.33
FE0	*	41.04	*	42.73	*	42.13	*	42.15	*	44.30	*	43.99	*	33.01
MNO	*	1.48	*	1.26	*	1.55	*	1.05	*	1.16	*	0.99	*	0.14
TOTAL	*	102.47	*	104.54	*	103.86	*	104.45	*	104.45	*	99.96	*	101.32
SI	*	0.0	*	0.0	*	0.0	*	0.0	*	0.0	*	0.020	*	0.0
AL	*	0.0	*	0.0	*	0.0	*	0.0	*	0.0	*	0.012	*	0.0
TI	*	1.764	*	1.788	*	1.787	*	1.758	*	1.846	*	1.962	*	0.420
FE3+	*	0.472	*	0.424	*	0.426	*	0.483	*	0.308	*	0.024	*	15.160
FE2+	*	1.702	*	1.736	*	1.723	*	1.715	*	1.798	*	1.920	*	8.384
MN	*	0.062	*	0.052	*	0.064	*	0.043	*	0.048	*	0.056	*	0.036
UVSP	*	0.0	*	0.0	*	0.0	*	0.0	*	0.0	*	0.0	*	5.12
MT	*	0.0	*	0.0	*	0.0	*	0.0	*	0.0	*	0.0	*	94.88
ILM	*	87.83	*	0.0	*	89.00	*	87.64	*	92.12	*	98.85	*	0.0
HM	*	12.17	*	89.11	*	11.00	*	12.36	*	7.88	*	1.15	*	0.0

1	*	552-6	ILM-4
2	*	552-6	ILM-5B
3	*	552-6	ILM-6
4	*	552-6	ILM-7C
5	*	552-6	UILM-8
6	*	552-1	ILM-1F
7	*	552-6	MT 1-A

	*	1	*	2	*	3	*	4	*	5	*	6	*	7
SI02	*	0.0	*	0.0	*	0.0	*	0.0	*	0.0	*	0.0	*	0.0
TI02	*	1.06	*	3.14	*	2.00	*	1.05	*	2.07	*	1.48	*	1.97
AL203	*	0.0	*	0.0	*	0.0	*	0.0	*	0.0	*	0.0	*	0.0
FE203	*	68.86	*	62.16	*	66.45	*	67.11	*	65.23	*	66.03	*	64.28
FEO	*	32.80	*	33.42	*	33.36	*	31.96	*	32.95	*	32.25	*	32.32
MNO	*	0.09	*	0.19	*	0.13	*	0.12	*	0.12	*	0.12	*	0.14
TOTAL	*	102.81	*	98.91	*	101.94	*	100.24	*	100.37	*	99.88	*	98.71
SI	*	0.0	*	0.0	*	0.0	*	0.0	*	0.0	*	0.0	*	0.0
AL	*	0.0	*	0.0	*	0.0	*	0.0	*	0.0	*	0.0	*	0.0
TI	*	0.239	*	0.734	*	0.454	*	0.243	*	0.477	*	0.343	*	0.462
FE3+	*	15.522	*	14.533	*	15.093	*	15.515	*	15.046	*	15.314	*	15.077
FE2+	*	8.216	*	8.683	*	8.420	*	8.211	*	8.446	*	8.312	*	8.424
MN	*	0.023	*	0.050	*	0.033	*	0.031	*	0.031	*	0.031	*	0.037
UVSP	*	2.89	*	8.99	*	5.55	*	2.91	*	5.85	*	4.17	*	5.63
MT	*	97.11	*	91.01	*	94.45	*	97.09	*	94.15	*	95.83	*	94.37
ILM	*	0.0	*	0.0	*	0.0	*	0.0	*	0.0	*	0.0	*	0.0
HM	*	0.0	*	0.0	*	0.0	*	0.0	*	0.0	*	0.0	*	0.0

1	*	552-6	MT-2A
2	*	552-6	MT-3
3	*	552-6	MT-4
4	*	552-6	MT-5B
5	*	552-6	MT-6
6	*	552-6	MT-7C
7	*	552-6	MT-8

	*	1 *	2 *	3 *	4 *	5 *
SIO2	*	0.91 *	0.85 *	0.01 *	0.64 *	0.63 *
TIO2	*	47.88 *	0.80 *	0.59 *	50.59 *	52.70 *
AL2O3	*	0.30 *	0.96 *	0.77 *	0.54 *	0.26 *
FE2O3	*	0.0 *	64.43 *	65.83 *	0.0 *	0.0 *
FEO	*	40.49 *	33.07 *	31.07 *	43.56 *	39.15 *
MNO	*	2.41 *	0.07 *	0.05 *	1.21 *	2.24 *
TOTAL	*	91.99 *	100.18 *	98.32 *	96.54 *	94.98 *

SI	*	0.049 *	0.258 *	0.003 *	0.033 *	0.033 *
AL	*	0.019 *	0.344 *	0.283 *	0.033 *	0.016 *
TI	*	1.956 *	0.183 *	0.138 *	1.965 *	2.054 *
FE3+	*	0.0 *	14.727 *	15.435 *	0.0 *	0.0 *
FE2+	*	1.840 *	8.400 *	8.095 *	1.882 *	1.697 *
MN	*	0.111 *	0.018 *	0.013 *	0.053 *	0.098 *

UVSP	*	0.0 *	2.42 *	1.77 *	0.0 *	0.0 *
MT	*	0.0 *	97.58 *	98.23 *	0.0 *	0.0 *
ILM	*	100.00 *	0.0 *	0.0 *	100.00 *	100.00 *
HM	*	0.0 *	0.0 *	0.0 *	0.0 *	0.0 *

1 *	491-3	ILM HOST-2
2 *	491-2	MT LAM-1
3 *	491-3	MT LAM-2
4 *	492-2	ILM-1
5 *	492-3	ILM-2

Table II.ix. Garnet analyses, structural formulae, and end members

	*	1 *	2 *	3 *	4 *	5 *	6 *	7
SI02	*	37.63 *	37.42 *	36.94 *	37.90 *	38.04 *	38.69 *	37.27
TI02	*	0.09 *	0.14 *	0.02 *	0.28 *	0.12 *	0.11 *	0.31
AL203	*	21.98 *	21.81 *	21.23 *	20.83 *	21.52 *	21.69 *	21.23
CR203	*	0.02 *	0.02 *	0.04 *	0.02 *	0.03 *	0.04 *	0.02
FE0	*	29.84 *	24.53 *	29.47 *	19.66 *	27.62 *	28.52 *	26.05
MNO	*	0.97 *	4.08 *	3.42 *	11.04 *	2.52 *	1.87 *	3.55
MGO	*	2.03 *	1.84 *	1.29 *	2.16 *	1.82 *	2.11 *	1.77
CA0	*	8.09 *	10.54 *	7.88 *	7.50 *	8.67 *	8.34 *	8.94
NA2O	*	0.01 *	0.0 *	0.0 *	0.01 *	0.01 *	0.0 *	0.04
TOTAL	*	100.66 *	100.38 *	100.29 *	99.40 *	100.35 *	101.37 *	99.18

SI	*	5.950 *	5.922 *	5.933 *	6.058 *	6.022 *	6.050 *	5.978
AL (IV)	*	0.050 *	0.078 *	0.067 *	0.0 *	0.0 *	0.0 *	0.022
AL (VI)	*	4.048 *	3.991 *	3.954 *	4.032 *	4.061 *	4.099 *	3.993
TI	*	0.011 *	0.017 *	0.002 *	0.034 *	0.014 *	0.013 *	0.037
CR	*	0.002 *	0.002 *	0.005 *	0.003 *	0.004 *	0.005 *	0.003
FE	*	3.947 *	3.247 *	3.959 *	2.628 *	3.657 *	3.730 *	3.495
MN	*	0.013 *	0.547 *	0.465 *	1.495 *	0.338 *	0.248 *	0.482
MG	*	0.478 *	0.434 *	0.309 *	0.515 *	0.429 *	0.492 *	0.423
CA	*	1.371 *	1.787 *	1.356 *	1.285 *	1.471 *	1.398 *	1.537
NA	*	0.003 *	0.0 *	0.0 *	0.003 *	0.003 *	0.0 *	0.012

PY	*	7.765 *	7.086 *	5.112 *	8.684 *	7.104 *	8.171 *	6.979
SPESS	*	2.109 *	8.931 *	7.703 *	25.226 *	5.591 *	4.116 *	7.955
UV	*	0.061 *	0.061 *	0.126 *	0.064 *	0.093 *	0.123 *	0.063
SCHLOR	*	0.174 *	0.272 *	0.040 *	0.568 *	0.236 *	0.215 *	0.617
GROSS	*	22.015 *	29.851 *	22.287 *	21.047 *	24.001 *	22.881 *	24.663
ALM	*	67.877 *	54.799 *	64.732 *	44.411 *	62.975 *	64.494 *	59.724

1 *	083-1	GNT-1	
2 *	477-1	GNT-1	PORPHYROBLAST
3 *	477-2	GNT-2	SEVERAL SMALL XLS
4 *	131-1	GNT-1	CORE
5 *	131-1	GNT-1	RIM
6 *	131-2	GNT-2	RIMS OF LARGE GARNETS
7 *	131-3	GNT-3	SMALL EUHEDRAL

	*	1	*	2	*
SI02	*	39.02	*	39.30	*
TI02	*	0.04	*	0.04	*
AL203	*	22.85	*	22.83	*
CR203	*	0.03	*	0.01	*
FEO	*	27.68	*	27.25	*
MNO	*	1.34	*	1.42	*
MGO	*	6.58	*	6.54	*
CAO	*	3.95	*	4.23	*
NA2O	*	0.01	*	0.0	*
TOTAL	*	101.50	*	101.62	*

SI	*	5.969	*	5.995	*
AL(IV)	*	0.031	*	0.005	*
AL(VI)	*	4.090	*	4.102	*
TI	*	0.005	*	0.005	*
CR	*	0.004	*	0.001	*
FE	*	3.542	*	3.477	*
MN	*	0.174	*	0.184	*
MG	*	1.500	*	1.487	*
CA	*	0.648	*	0.692	*
NA	*	0.003	*	0.0	*

PY	*	24.249	*	24.117	*
SPESS	*	2.804	*	2.976	*
UV	*	0.088	*	0.029	*
SCHLOR	*	0.074	*	0.074	*
GROSS	*	10.295	*	11.111	*
ALM	*	62.489	*	61.692	*

1	*	223-1	GNT-1
2	*	223-1	GNT-2

